Search for Squarks and Gluinos in τ-lepton Final States with the ATLAS Experiment

Dissertation
zur
Erlangung des Doktorgrades (Dr. rer. nat.)
der
Mathematisch-Naturwissenschaftlichen Fakultät
der
Rheinischen Friedrich-Wilhelms-Universität Bonn

von
Oliver Patrick Ricken
aus
Bergisch Gladbach

Bonn, Oktober 2018

Dieser Forschungsbericht wurde als Dissertation von der Mathematisch-Naturwissenschaftlichen Fakultät der Universität Bonn angenommen und ist auf dem Hochschulschriftenserver der ULB Bonn http://nbn-resolving.de/urn:nbn:de:hbz:5n-55288 elektronisch publiziert.

1. Gutachter:	Prof. Dr. Klaus Desch
2. Gutachter:	Prof. Dr. Jochen Dingfelder
Tag der Promotion:	03.12.2018
Erscheinungsjahr:	2019

One equal temper of heroic hearts,
made weak by time and fate, but strong in will
to strive, to seek, to find, and not to yield.

Ulysses - by Alfred, Lord Tennyson

Abstract

The successful and well-established Standard Model of Particle Physics is able to describe the majority of observed phenomena at the microscopic scale of elementary particles. Despite its high predictive power, it is also subject to certain manifest shortcomings. It is, for example, unable to explain the experimentally confirmed existence of dark matter or provide a description of gravity at the quantum scale. Supersymmetry is a versatile and long sought model that provides solutions to these shortcomings and into which the Standard Model can be fully embedded as a low-energy approximation. The ATLAS experiment at the Large Hadron Collider poses a unique experimental environment to search for first signs of Supersymmetry. The presence of new strongly interacting particles—squarks and gluinos—would be a strong indicator for the existence of Supersymmetry. Promising and experimentally accessible signatures of the decays of short-lived squarks and gluinos can comprise the presence of τ-leptons. This thesis presents the analysis carried out in the search for squarks and gluinos decaying to τ-leptons as signs for Supersymmetry. The analysis strategy comprises a sophisticated procedure to estimate the influence of Standard Model processes to the search. Different approaches in the actual search for signals of Supersymmetry are implemented and their performance is compared. The findings are made subject to a detailed statistical evaluation and subsequent interpretation. As no discovery of the sought new particles can be claimed, upper limits on the model parameters of Supersymmetry as well as on the general presence of any model of new physics are set.

Zusammenfassung

Das erfolgreiche und wohletablierte Standardmodell der Teilchenphysik ist in der Lage, die Mehrheit der beobachteten Phänomene auf der mikroskopischen Skala der Elementarteilchen zu beschreiben. Trotz seiner hohen Vorhersagekraft zeigt es offensichtliche Unzulänglichkeiten. Es ist zum Beispiel nicht in der Lage, die experimentell bestätigte Beobachtung von dunkler Materie zu erklären oder Gravitation auf der Quantenskala zu beschreiben. Supersymmetrie ist eine vielseitige und lange verfolgte Theorie, die Lösungen zu diesen Unzulänglichkeiten bietet und in die das Standardmodell als niederenergetische Näherung vollständig eingebettet werden kann. Das ATLAS Experiment am Large Hadron Collider stellt eine einzigartige Forschungsumgebung dar, um nach ersten Anzeichen von Supersymmetrie zu suchen. Die Präsenz neuer, stark wechselwirkender Teilchen—Squarks und Gluinos—wäre ein starker Indikator für die Existenz von Supersymmetrie. Vielversprechende und experimentell zugängliche Signaturen der Zerfälle kurzlebiger Squarks und Gluinos können die Präsenz von τ-Leptonen beinhalten. Diese Arbeit präsentiert die durchgeführte Analyse in der Suche nach in τ-Leptonen zerfallenden Squarks und Gluinos als Hinweise auf Supersymmetrie. Die Analysestrategie beinhaltet ein fortgeschrittenes Verfahren zur Abschätzung des Einflusses von Prozessen des Standardmodells auf die Suche. Verschiedene Ansätze in der eigentlichen Suche nach Signalen von Supersymmetrie werden implementiert und ihre Verhalten verglichen. Die Ergebnisse der Suche werden einer detaillierten statistischen Analyse und anschließender Interpretation unterzogen. Da diese Arbeit die Entdeckung der gesuchten neuen Teilchen nicht für sich beanspruchen kann, werden obere Ausschlussgrenzen auf die Modellparameter von Supersymmetrie sowie die generelle Anwesenheit beliebiger Modelle neuer Physik gesetzt.

Contents

CHAPTER 1

Introduction

The innate curiosity for insight into the very nature of the universe and everything in it has always been a driving force of humankind. Physics in particular represents a discipline that addresses everything, which is at any time perceived as a fundamental question about Nature. It reaches from the description of the universe itself, to an understanding of the structure and formation of touchable matter to knowledge about elementary particles and their interactions. The physics topic covering the smallest building blocks of matter has significantly developed over time. More than two thousand years passed from first considerations of the indivisibility of atoms, to the dawn of modern experimental particle physics, initiated by the discovery of the electron more than a hundred years ago. The subsequent rapid progress culminated in the postulation of the Standard Model [1–3] of particle physics more than fifty years ago and its final experimental confirmation in 2012 by the discovery of the Higgs-boson [4]. The way to ever smaller length scales and the search for new fundamental particles still drives the technological progress in the fields – particle accelerators and detectors. A technological apex of experimental high-energy particle physics are the world's largest particle accelerator, the Large Hadron Collider [5], and its experiments. It was in this experimental environment, where in 2012 the existence of the last missing piece of the Standard Model, the Higgs-boson has been confirmed by the joint efforts of the ATLAS [6] and CMS [7] experiments. The Higgs-boson is the last discovered elementary particle predicted by the Standard Model. The enormous success of the Standard Model is not just rooted with the prediction of particles before their discovery in experiments over a period of about fifty years, but also in the description of the vast majority of observed phenomena in a multitude of experiments. Despite its success, the Standard Model has never been the final theory to describe every aspect of the microscopic quantum world of elementary particles. Ever since its postulation, extensions and more complex models have been proposed to remedy its various shortcomings. One of the oldest and still sought for models to embed the Standard Model into is Supersymmetry (SUSY). This thesis presents the search for experimental evidence of SUSY in data taken with the ATLAS experiment at the Large Hadron Collider.

In SUSY, an additional fundamental symmetry between bosonic and fermionic elementary particles is introduced. The multitude of new particles and their ways of interacting with the Standard Model particles enables SUSY to address various shortcomings of the Standard Model simultaneously. The fact that SUSY is not just an extension to the Standard Model but a model in which the latter is fully embedded, renders SUSY complex. This complexity is reflected in a high degree of polymorphism. Over the time, SUSY has been searched for without discovering it, the large set of experimental results has led to various constraints. These, in turn, limit the possible realisations of SUSY in nature. In addition to constraints from the side of the model itself, the experimental environment also limits the possible phase-space of interest. The result of many years of searches for SUSY at different particle

physics experiments and the environment of the Large Hadron Collider motivate the representation of SUSY searched for in the present thesis. The collisions of high-energy protons as provided by the Large Hadron Collider allow access to virtually all kinds of particle physics scenarios. The highest abundance is expected for the production of particles being able to interact via the strong force of the Standard Model. Consequently, the production of the lightest strongly interacting particles predicted by SUSY is a promising hint towards the model and hence searched for in this thesis – the search for squarks and gluinos.

The polymorphism of SUSY is not only represented by its rich spectrum of new particles with respect to the Standard Model but also in the individual new particle signatures left in the experiment for detection and identification. It is hence possible to search for squarks and gluinos in various ways, utilising different experimental signatures. While the the presented analysis [8, 9] makes use of the increased probability of squarks and gluinos to be detectable through the presence of τ-leptons, other analyses search for the presence of these new particles in more generic deviations from the Standard Model prediction [10, 11]. These rare Standard Model particles are challenging to detect in an experiment but they pose a unique source of evidence for theories beyond the Standard Model. Since its start of operation in 2010, the centre-of-mass energy of the Large Hadron Collider increased from $\sqrt{s} = 7\,\text{TeV}$ over $\sqrt{s} = 8\,\text{TeV}$ to $\sqrt{s} = 13\,\text{TeV}$, enlarging the accessible phase-space for a search of SUSY continuously. While this thesis is based on data recorded at $\sqrt{s} = 13\,\text{TeV}$, similar searches for the strong production of SUSY involving the presence of τ-leptons have already been performed at lower energies of $\sqrt{s} = 7\,\text{TeV}$ [12] and $\sqrt{s} = 8\,\text{TeV}$ [13].

The presented thesis first introduces the Standard Model of particle physics as the starting point for the development of SUSY and its representations searched for. The scene is further set by a description of the experimental environment of the ATLAS detector at the Large Hadron Collider and the techniques used to produce the predictions of the Standard Model and SUSY by means of simulations of the underlying particle physics.

The search for the rare signals of SUSY in the vast amount of data dominated by the Standard Model requires a sophisticated and tailor-made strategy. The large amount of collected data available to this analysis allows for the pursuit of two different signal extraction approaches and their qualitative and quantitative comparison. The approach already established in [9, 12, 13], tries to isolate the expected signal as effectively as possible from the predicted background by strongly limiting the available phase-space. This approach relies on the reduction of both signal and background until as little as possible background remains. It is applicable already to smaller sets of data and has been successfully pursued in the past. The novel technique utilised in this thesis relies not exclusively on the total suppression of background but on the separation of signal from background based on the different distribution of kinematic observables they predict. This new level of available information allows for access to new regions of phase-space and provides more confidence in the final statements regarding the realisation of the models searched for. Regardless of the pursued signal extraction strategy, the quality of statements about SUSY requires the best possible knowledge about the Standard Model background. This analysis comprises dedicated studies of the predicted Standard Model backgrounds and the quality of their modelling. The known and newly found imperfections in the background predictions, the description of the expected signal, the experimental environment, and the utilised techniques are considered as systematic uncertainties to the analysis. The various sources of systematic uncertainty, their implementation in this analysis, and their effects are introduced and discussed in detail.

Considering all sources of uncertainty, the results of both approaches are evaluated by means of hypothesis tests, utilising the profile log-likelihood technique. They are interpreted with respect to a possible realisation of the SUSY models searched for and the prospects of general theories beyond the Standard Model.

CHAPTER 2

Basic Theoretical Principles – from Particle Physics to the Standard Model and Beyond

In the ever-ongoing quest for understanding of the Universe and everything in it, the typical approach applied by science is the testing of a hypothesised model in an experiment. The outcome of an experiment can be used to falsify the hypothesised model – in the end, no model can be confirmed but every experiment confirming its predictions creates confidence into the model. Across all sciences, an enormous multitude of models has been developed, experimentally tested and falsified over time, leaving a still vast number of models deemed true that describe the observed Universe. In the field of physics, the most fundamental principles are studied, reaching from theories about the expansion of the Universe and space itself to the smallest particles that make up all matter. The discipline of particle physics, the habitat of the presented analysis, addresses the latter end of this scale, the realm of elementary particles, their interactions and schemes of composing all matter in the Universe.

The model of elementary particle physics that is able to describe the majority of observations made in between everyday life experiences and the smallest of quantum scales is the so-called *Standard Model of Particle Physics* (SM). The forthcoming section is dedicated to a detailed description of the SM, including its shortcomings. It is loosely based on [14] and [15]. Said shortcomings can be remedied by a variety of different models of *physics beyond the Standard Model* (BSM). The model of BSM physics searched for in the context of this thesis is *Supersymmetry* (SUSY), which is introduced and discussed afterwards, again, loosely based on [16] and [15].

2.1 The Standard Model of Particle Physics

The Standard Model is a relativistic quantum field theory of fermionic matter particles whose interactions among each other are conveyed by the exchange of bosonic messenger particles. An overview of the particle content of the SM is provided in fig. 2.1. The set of fermions, depicted in the left half of the diagram, forms all known matter. It can be sub-structured into three generations, summarised in each row of the illustration. The fermions of the same row differ only by their mass, increasing from the first to the third generation. While ordinary, stable matter, i.e. protons, neutrons, and electrons, is solely composed of the particles of the first generation, the second and third generation fermions and their bound states have to be produced in laboratory experiments and are short-lived. The different interactions between the fermions, conveyed by the messenger bosons in the right half, are visualised by the different boxes. The particular role of the scalar Higgs-boson is emphasised by its separated location in the illustration. As a hypothetical messenger particle of the gravitational force, the graviton is depicted outside of the SM.

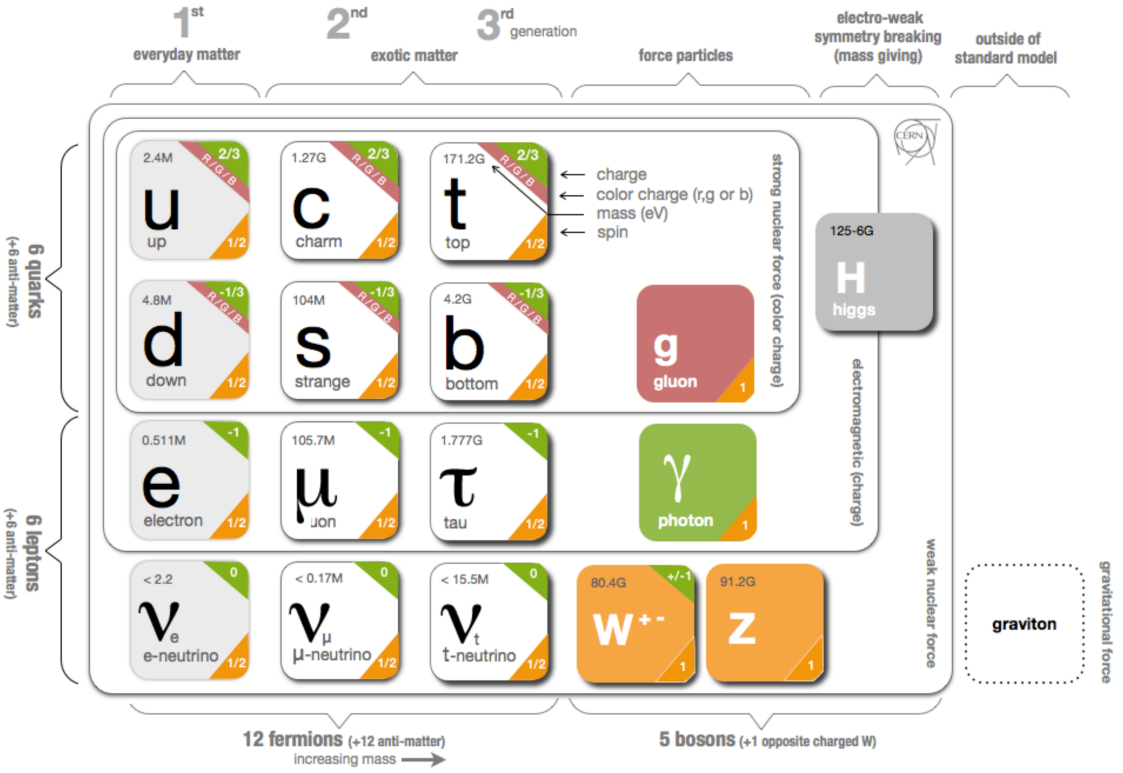

Figure 2.1: Schematic overview of the particle content of the Standard Model of Particle Physics [17], giving the mass, electric charge, and spin of the elementary particles as well as visualising the interactions they take part in.

In the quantum field theoretical approach of the Standard Model, the fundamental fermions are described by components of a field Ψ. Their behaviour and properties are parametrised by a Lagrange energy density $\mathcal{L}$, referred to as the *Lagrangian*, and the Euler-Lagrange equations. A procedure that is used to build the mathematical foundation of the SM in the forthcoming paragraphs can be summarised in the following way: the requirement of the Lagrangian to be invariant under local gauge transformations leads to the introduction of additional gauge fields that couple to the fermion fields. These gauge fields can be interpreted as the aforementioned messengers that convey the interactions between the fermions. The following sections introduce the theoretical basic principles of the Standard Model, focussing on the formalisms of the interactions it considers. Details on the background of the matter particles and their discoveries can be found in, for example, [18].

2.1.1 The electroweak interaction

The electroweak interaction represents the unification of the two separate interactions, electrodynamics and the weak force, into one gauge theory. A quantum gauge theory of electrodynamics (Quantum-electrodynamics, QED) already existed in the first half of the twentieth century [19]. It was able to describe observed phenomena on microscopic scales and could be transformed into the well-known Maxwell Equations. The weak interaction, on the other hand, was first considered as a contact interaction between four fermions in order to describe the decays of radioactive nuclei. This first formulation did not

embed a gauge symmetry and hence, among other flaws, comprised the divergence of cross-sections for increasing energies. These shortcomings can be overcome by formulating a unified quantum field theory of the electromagnetic and weak interactions, based on a common set of gauge groups and exchange particles. The forthcoming sections briefly introduce QED as an example of gauge theories as well as the weak force and the unification of the two.

Quantum-electrodynamics In classical electrodynamics, the relativistic interaction of an electron with four-momentum p^μ and a electromagnetic field A^μ is described by adding the field-based energy term to the momentum expression $p^\mu \rightarrow p^\mu + eA^\mu$, e denoting the elementary charge of the electron [20]. This approach is also referred to as *minimal coupling*.

The general transition to the quantum theory of the electron is performed by replacing the classical equation of motion with the Dirac-Equation:

$$(i\gamma^\mu \partial_\mu - m)\Psi = 0 \, .$$

In this notation, the partial derivative acting on the electron wave function Ψ replaces the classical momentum expression. The electromagnetic interaction is introduced similarly as in the classical case by replacing the momentum operator, giving

$$(i\gamma^\mu(\partial_\mu - ieA_\mu) - m)\Psi = 0 \, .$$

Although the given formulation seems ad-hoc, it can also be obtained ab initio. A general property of physical observables in quantum mechanics is their independence of phases of the wave function. This results in a phase α transforming $\Psi(x) \rightarrow e^{i\alpha}\Psi(x)$ not changing the free Lagrangian

$$\mathcal{L} = i\overline{\Psi}\gamma^\mu \partial_\mu \Psi - m\overline{\Psi}\Psi \, .$$

Here, $\overline{\Psi} = \Psi^\dagger \gamma^0$ is the Dirac adjoint wave function defined via the Hermitian adjoint wave function $\Psi^\dagger$ and the time-like Dirac matrix γ^0. The promotion of a global gauge transformation to a local one results in the invariance of the equation of motion under application of a phase that is dependent on phase-time itself $\Psi(x) \rightarrow e^{i\alpha(x)}\Psi(x)$. Due to its momentum term including ∂_μ, the current form of the Dirac-Equation needs to be modified to be become invariant under local gauge transformation. A replacement of the derivative by the so-called *covariant derivative*

$$D_\mu = \partial_\mu - ieA_\mu$$

enables invariance under local gauge transformation. The transformation applied here is a general element of the U(1) gauge group. Consequently, the electromagnetic field A_μ transforms via its adjoint representation $A_\mu \rightarrow A_\mu + \frac{1}{e}\partial_\mu \alpha$, giving the following Lagrangian:

$$\mathcal{L} = i\overline{\Psi}\gamma^\mu D_\mu \Psi - m\overline{\Psi}\Psi = \overline{\Psi}(i\gamma^\mu(\partial_\mu - ieA_\mu))\Psi \, .$$

In order for the electromagnetic field to propagate without being related to a matter particle, another gauge-invariant term can be added. The introduction of the field strength tensor $F_{\mu\nu} = \partial_\mu A_\nu - \partial_\nu A_\mu$ yields the final Lagrangian of QED in eq. (2.1). The last term added represents the free propagation of the photon field. It is the field quantum of QED and conveys interactions between charged fields by coupling to them.

$$\mathcal{L}_{\text{QED}} = \underbrace{\overline{\Psi}(i\gamma^\mu\partial_\mu - m)\Psi}_{\substack{\text{Free fermion}\\ \text{propagation}}} + \underbrace{e\overline{\Psi}\gamma^\mu A_\mu \Psi}_{\substack{\text{Fermion–photon}\\ \text{interaction}}} \underbrace{-\frac{1}{4}F_{\mu\nu}F^{\mu\nu}}_{\substack{\text{Free photon}\\ \text{propagation}}} . \tag{2.1}$$

The described procedure can be summarised to a recipe that is applicable to mathematically model the other interactions of the fermion fields of the SM: First, the invariance of a field under a given group transformation is imposed. The invariance of the full Lagrangian is then ensured by the introduction of additional fields. The resulting gauge theory is completed by adding a propagating term for the gauge field to the Lagrangian that is also invariant under the transformation.

From a historical point of view, QED was the first gauge quantum field theory. It allowed for precise calculations and the explanation of differences between measurements and classical quantum dynamics such as, for example, the Lamb shift in the energy spectrum of the hydrogen atom [21].

Among the advantages of quantum field theories such as QED is the possibility to compute predictions of observables in perturbation theory in orders of the coupling constant between the matter field and the gauge boson. The lowest possible order, referred to as *leading-order* (LO), considers only the minimum of possible interactions between incoming and outgoing particles. The established way of visualisation of such processes are tree-like Feynman diagrams. They picture particles by lines and interactions between particles by vertices connecting those lines. An example LO QED diagram for a simple scattering process is depicted in fig. 2.2(a). The solid lines represent the incoming and outgoing fermions, the dashed line illustrates the photon being exchanged. At next-to-leading-order (NLO), one additional interaction is considered in the diagram. Two of the various possibilities for NLO diagrams in QED are shown in figs. 2.2(b) and 2.2(c). Allowing for corrections beyond next-to-leading-order leads to diagrams with correspondingly more loops.

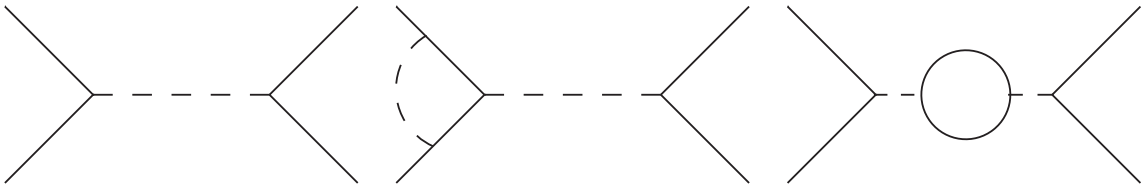

(a) Leading-order (b) Next-to-leading order vertex (c) Next-to-leading order propagator

Figure 2.2: Example Feynman diagrams in QED, (a) showing a scattering process at leading-order, (b) and (c) depicting diagrams with a next-to-leading-order vertex and propagator, respectively [15].

Electroweak unification Experiments in the 1950s [22, 23] already showed that the weak interaction does not conserve parity and acts only on left-handed particles and right-handed antiparticles. This observation can be incorporated into the description of the SM by splitting matter fermions into their left- and right-chiral components and associating different gauge quantum numbers to them. Whilst chirality denotes the transformation behaviour of a fermion field under Lorentz transformations, it is strongly linked to the handedness of a fermion, i.e. the relation of the spin axis and the direction of motion. A unified theory of the chirality-sensitive weak and the chirality-blind electromagnetic interaction hence needs to consider two symmetry transformations. The $\mathrm{U}_{\mathrm{em}}(1)$ transformation acts on the electric charge and is independent of chirality, while the weak force is introduced by an $\mathrm{SU}_L(2)$ transformation which acts on the *isospin* of left-handed fermions (and right-handed antifermions) only [1–3]. Above a certain energy scale, the two forces can be unified into one fundamental force, based on the $\mathrm{SU}_L(2)\times\mathrm{U}_Y(1)$ gauge

group. It is to be noted that $\mathrm{U}_Y(1)$ is now dependent on the so-called *weak hypercharge* Y and is no longer chirality-blind[1]. Below this electroweak energy scale, the electroweak symmetry is broken and QED as the interaction associated to $\mathrm{U}_{\mathrm{em}}(1)$ exists as introduced. In analogy to the photon field of QED, both transformations come with their own respective gauge fields. Due to its more complex group structure, the $\mathrm{SU}_L(2)$ transformation has three gauge fields instead of one as for the $\mathrm{U}_{\mathrm{em}}(1)$ transformation.

Another aspect arising from the chirality dependence and which has to be included in the structure of the SM stems from the fact that, for example, a right-handed electron couples to the photon while a right-handed neutrino would not participate in any interaction at all[2]. Moreover, phenomenology shows that the weak interaction treats left-handed charged and neutral leptons equally. This outcome of the aforementioned considerations is reflected in the electroweak theory by grouping the leptons into chirality multiplets. The left-handed leptons form a doublet (ν_L, ℓ_L) that couples to both the isospin- and the hypercharge-based interactions, while the right-handed charged leptons ℓ_R carry only a hypercharge and remain a singlet. Right-handed neutral leptons are not considered as they would be complete gauge-singlets and hence not have any observable gauge interactions with the remaining SM particles. All of these considerations culminate in the electroweak Langrangian

$$\begin{aligned}\mathcal{L}_{\mathrm{ew}} = &\overbrace{(\overline{\nu_L}, \overline{\ell_L})\gamma^\mu \left(i\partial_\mu - g\frac{\vec{\tau}}{2}\cdot\vec{W}_\mu - g'\frac{Y_L}{2}B_\mu\right)\begin{pmatrix}\nu_L\\ \ell_L\end{pmatrix}}^{\substack{\text{left-chiral lepton interactions}\\ \text{free propagation, isospin coupling, hypercharge coupling}}} + \\ &\underbrace{\overline{\ell_R}\gamma^\mu\left(i\partial_\mu - g'\frac{Y_R}{2}B_\mu\right)\ell_R}_{\substack{\text{right-chiral lepton interactions}\\ \text{free propagation, hypercharge coupling}}} - \underbrace{\frac{1}{4}\vec{W}_{\mu\nu}\vec{W}^{\mu\nu}}_{\substack{\text{isospin messenger}\\ \text{free propagation}}} - \underbrace{\frac{1}{4}B_{\mu\nu}B^{\mu\nu}}_{\substack{\text{hypercharge messenger}\\ \text{free propagation}}},\end{aligned} \tag{2.2}$$

with $B^{\mu\nu} = \partial^\mu B^\nu - \partial^\nu B^\mu$ and $W_i^{\mu\nu} = \partial^\mu W_i^\nu - \partial^\nu W_i^\mu - \varepsilon^{ijk} W_j^\mu W_k^\nu$.

For the doublet of charged and neutral left-chiral leptons, the expression comprises the free propagation term as well as the interaction with the isospin messengers $\vec{W}$ as well as with the hypercharge messenger B. The singlet of right-chiral charged leptons is able to propagate freely and couples to the hypercharge messenger B. Moreover, the free propagation of the messenger field quanta is considered. In this notation, $\vec{\tau}$, ε^{ijk}, and g are the generators, the structure constant, and the coupling of the SU(2) symmetry, respectively[3]. $Y_{R/L}$ and g' denote the charge and the coupling of the U(1) symmetry, respectively. Comparing the electroweak Langrangian in eq. (2.2) to the one of QED in eq. (2.1), the similar structure as well as the separation of left- and right-chiral particles becomes visible. The two gauge-field terms of eq. (2.2) now introduce four new vector fields W_1^μ, W_2^μ, W_3^μ, and B^μ. In order to form fields that explain the results of experiments, i.e. mediators that induce chirality-dependent flips of the charge and a chirality-blind neutral mediator, the physically realised fields can arise from a mixing mechanism:

$$W_\mu^\pm = \frac{1}{\sqrt{2}}(W_\mu^1 \mp iW_\mu^2)$$

$$\begin{pmatrix} A_\mu \\ Z_\mu \end{pmatrix} = \begin{pmatrix} \cos\theta_W & \sin\theta_W \\ -\sin\theta_W & \cos\theta_W \end{pmatrix}\begin{pmatrix} B_\mu \\ W_\mu^3 \end{pmatrix}.$$

[1] The weak hypercharge Y is defined as $Q_{\mathrm{em}} = T_3 + Y$ via the electric charge Q_{em} and the third component of the weak isospin T_3.

[2] Note that within the SM, neutrinos are massless and that a right-handed neutrino would hence not even couple to gravity [15].

[3] The generators of the electroweak gauge group $\mathrm{SU}_L(2) \times \mathrm{U}_Y(1)$ are related to the Pauli matrices via $\vec{\tau} = \frac{1}{2}\vec{\sigma}$.

The weak mixing angle θ_W, often referred to as the *Weinberg angle*, relates the couplings to the electric charge via

$$g \sin\theta_W = g' \cos\theta_W = e \ .$$

It is to be noted that the physical representation of the gauge fields does not yet feature masses. In order to introduce masses to the electroweak gauge bosons, the theory needs to be extended further as described in section 2.1.3. The description of the electroweak force up to this point only holds for leptons. For quarks, however, it is very similar. Left-handed up- and down-type quarks, i.e. positively and negatively charged quarks, respectively, are grouped into an $\mathrm{SU}_L(2)$ doublet, similar to the left-handed leptons. As for the right-handed leptons, all right-handed quarks remain singlets, only coupling to the hypercharge. Another difference with respect to the lepton-sector is the fact that all quarks are massive. In general, the experimentally accessible mass eigenstates are not necessarily identical to the eigenstates under the electroweak interaction. In the lepton-sector, there are no mass eigenstates for the up-type fermions, the neutrinos. Hence only their weak eigenstate is well defined. Without loss of generality, up-type quarks are chosen to have congruent eigenstates in the both bases. The full set of $\mathrm{SU}_L(2)$ doublets hence comes as pairs

$$\begin{pmatrix} u \\ d' \end{pmatrix}_L, \begin{pmatrix} c \\ s' \end{pmatrix}_L, \begin{pmatrix} t \\ b' \end{pmatrix}_L \ ,$$

in which the down-type weak eigenstates arise from mixing of the mass eigenstates by means of the Cabibbo-Kobayashi-Maskawa matrix [24, 25] (CKM matrix).

$$\begin{pmatrix} d' \\ s' \\ b' \end{pmatrix} = \begin{pmatrix} V_{ud} & V_{us} & V_{ub} \\ V_{cd} & V_{cs} & V_{cb} \\ V_{td} & V_{ts} & V_{tb} \end{pmatrix} \begin{pmatrix} d \\ s \\ b \end{pmatrix} \ .$$

2.1.2 The strong interaction

The concept of the strong force as it is comprised in the SM was developed in the 1960s. After a large set of new particles with similar properties had been discovered in accelerator experiments, it became evident that they could not be fundamental and had to share some common underlying structure. It was proposed that this new *particle zoo* was actually composed of a few new fundamental particles named *quarks* [26, 27]. A proposed ordering scheme was able to relate the collection of new composite particles to only three underlying quarks, which formed either states of three quarks, so-called *baryons*, or pairs of a quark and an antiquark, so-called *mesons* [28]. The structure of this ordering scheme strongly resembles the arrangement of chemical elements in the periodic table of elements [29] based on the configuration of their electron shells. The quark model became widely accepted when the Ω^- state it had predicted, was discovered, showing the exact predicted properties [30].

The force binding quarks to form composite states, so-called *hadrons*, can neither be the electromagnetic force—same charged quarks would repel each other instead of being bound—nor the weak force, which is too weak to compensate the electromagnetic repulsion. The newly introduced force is hence referred to as the *strong* force. Observations within the quark model conclude that the charge of quarks under the strong force needs to have three values[4], referred to as *red*, *blue*, and *green*, the *colour charge*.

[4] An example for this conclusion is the observation of the Δ^{++} resonance of the proton [31]. For it to exist, the strong interaction contribution to the total wave function needs to be antisymmetric. Since it is composed of three quarks, this is only possible if three values of the strong charge exist and not just two.

As for the electroweak force, the strong interaction is described by a gauge symmetry. The requirement of the Lagrangian of *Quantum chromodynamics* (QCD) [32] to be invariant under the underlying $SU_C(3)$ transformation gives the following expression:

$$\mathcal{L}_{\text{QCD}} = \overline{q}(i\gamma^\mu \partial_\mu - m)q - g_s(\overline{q}\gamma^\mu T_a q)G_\mu^a - \frac{1}{4}G_{\mu\nu}^a G_a^{\mu\nu} \ .$$

In this notation, q is a quark field – there is a total of six quark fields, one for each *flavour*, i.e. up, down, charm, strange, top, and bottom. G_μ^a ($a = 1 \ldots 8$) represent the eight massless gluon fields, g_s the coupling constant, and T_a the generators of the $SU_C(3)$ transformation. It is to be noted that the quark fields are also subject to the electroweak force, i.e. they decompose into left- and right-handed chiral components that couple to the gauge bosons of the electroweak interaction. The structure of the gluon field tensor $G_{\mu\nu}$ is of particular importance:

$$G_{\mu\nu}^a = \partial_\mu G_\nu^a - \partial_\nu G_\mu^a - g_s f_{abc} G_\mu^b G_\nu^c \ ,$$

with f_{abc} being the structure constant of $SU_C(3)$. Comparing the gluon field tensor to its electromagnetic counterpart, the additional term containing the structure and coupling constants marks a difference. Due to this term, the gluon field quanta of the strong force are, in contrast to the field quanta of the electromagnetic force, able to couple to each other. This gives rise to phenomena unique to QCD and two additional diagrams of the strong interaction, the full set being depicted in fig. 2.3.

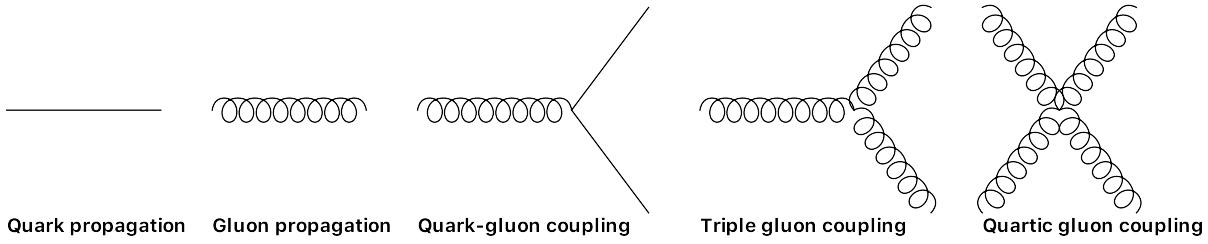

Figure 2.3: Schematic example diagrams of the different contributions to the Langrangian of QCD. From left to right: propagation of quark, propagation of gluons, coupling of a gluon to a quark, and triple and quartic gluon self-coupling.

The first two diagrams represent the propagation of quarks and gluons, while the third graph illustrates the coupling of a gluon to a quark. The fourth and fifth graphs represent a unique feature of QCD, the self-coupling of gluons. The self-coupling of the strong force gauge bosons has some implicit consequences for the nature of QCD. Despite gluons being massless just as photons, the strong interaction is not infinite-ranged but limited to short distances between the interacting particles.

When separating two quarks, the self-coupling of gluons leads to an increase of the force between the quarks, growing further with distance. The increase in binding energy will eventually surpass the production threshold of additional quark-antiquark pairs, rendering it energetically preferable to produce two new particles. The newly produced coloured particles bind with the separated quarks and prevent the observation of bare colour charge – a property of the strong force known as *confinement*. This feature is also reflected in the strong dependence of the coupling constant α_s on the energy scale Q the process happens at. The current status of experimental measurements of this dependence is depicted in fig. 2.4: At low energies—corresponding to large separation—the coupling becomes strong, driving the process of confinement. At high energies—corresponding to small length scales—the coupling is small, rendering the quarks quasi-free inside bound states. This property of QCD is referred to as *asymptotic freedom* [33, 34]. As a consequence, the perturbative description of QCD is only possible at high energies.

In the regime of low energies, the coupling becomes too strong, forcing quarks into the aforementioned bound states. A possible approach to describe masses and decays of bound quark states are phenomenological models such as the *Bonn Model* [35–37].

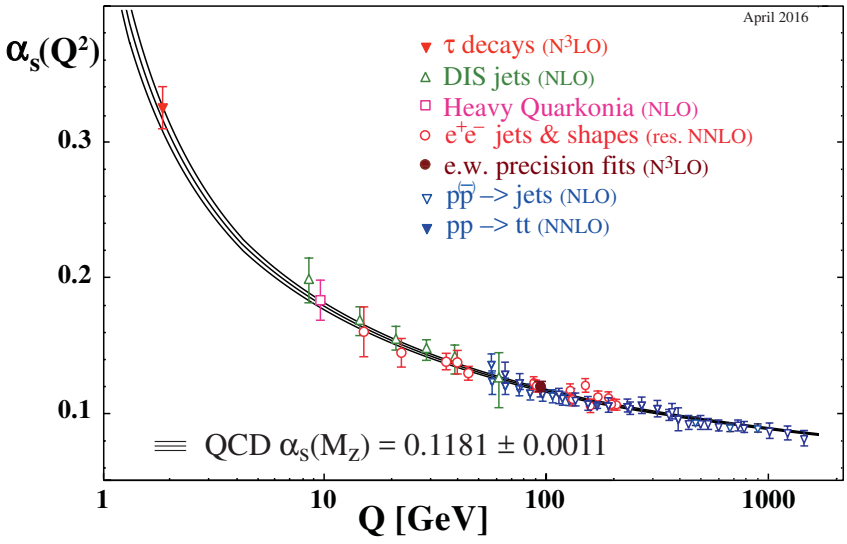

Figure 2.4: Dependence of the strong coupling constant α_s on the energy scale Q as measured by various experiments [38]

For comprehension of the physics at the LHC, knowledge about the structure of the proton is necessary. In an over-simplified quark model, the proton consists only of two up quarks and one down quark, bound together by gluons. The results of a broad range of scattering experiments at different energy scales and momentum transfers, however, require a more complex picture in order to be explained. Similar to the creation and annihilation of electron-positron pairs due to fluctuations of the QED vacuum, the strong force acting on the constituents of the proton allows for creation and annihilation of quark-antiquark pairs as well as for radiation and re-absorption of gluons. In that picture, the proton consists of a multitude of different quarks of all flavours and gluons, the entire set of them being referred to as *partons*. The quarks inside the proton are separated into *valence quarks* (uud), which give the proton quantum numbers, and *sea quarks* arising from QCD vacuum fluctuations.

If now two protons collide, e.g. at an accelerator like LHC, only two of the partons are assumed to collide while the rest of them remains relatively unaffected, giving rise to the name of *spectators*. This behaviour is reflected in the cross-section for producing any particle X in a proton-proton collision $\sigma_{pp\to X}$, which factorises as

$$\sigma_{pp\to X} = \sum_{a,b} \int_0^1 \int_0^1 \mathrm{d}x_1 \mathrm{d}x_2 f_a(x_1, Q^2) f_b(x_2, Q^2) \hat{\sigma}_{ab\to X}(\hat{s}) \,.$$

Here, a and b denote the interacting partons, while x_1 and x_2 represent the fraction of the proton momentum that is carried by the respective partons. The center-of-mass energy of the parton collision

originating from a proton-proton collision at a center-of-mass energy of $\sqrt{s}$ is given as $\sqrt{\hat{s}} = \sqrt{x_1 x_2}\sqrt{s}$. The *parton distribution function* (PDF) $f_a(x_1, Q^2)$ parametrises the probability to find a parton a with a fraction of momentum x_1 in a scattering process with momentum transfer Q^2. The PDFs are obtained from fitting analytical relations to several measurements from scattering experiments at various energy scales. An example of proton PDFs at different values of Q^2 ($\equiv \mu^2$) is depicted in fig. 2.5. In order to predict the outcome of proton-proton collisions at the LHC, a precise knowledge of the underlying proton PDFs is crucial.

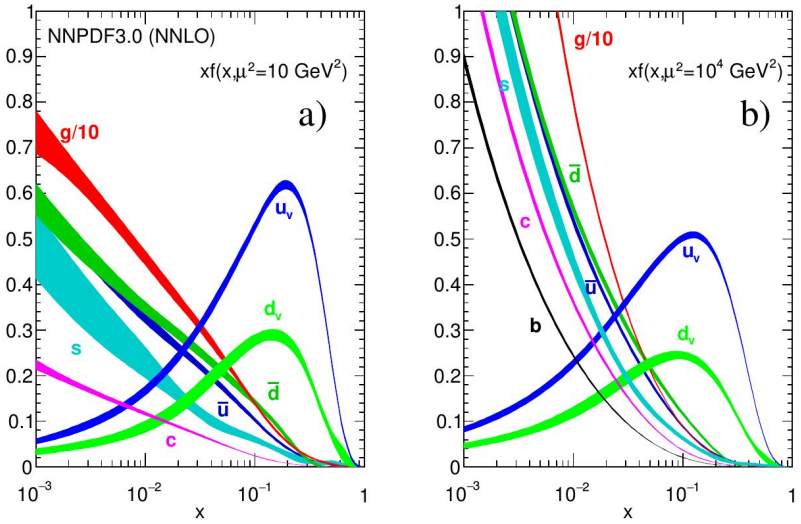

Figure 2.5: Parton distribution functions from a global fit to experimental data using NNPDF 3.0 [39]. The bands give the product of the momentum fraction and the actual distribution function $x \times f(x)$ for two different values of the momentum transfer μ^2 for $\alpha_s = \alpha_s(M_Z^2) = 0.118$ [38].

2.1.3 The Higgs mechanism

Except for the Lagrangian of QED, no formulation introduced in the preceeding sections contains any mass-terms for neither the fermion nor the gauge fields. Experiments, however, do measure non-vanishing masses for the charged leptons, the quarks, and for the weak gauge bosons. The reason for this non-intuitive formulation is the fact that any explicit mass-terms, be it for fermions or gauge bosons, would break the gauge invariance of the formulation. For fermions, an explicit mass-term would result in a coupling of right- and left-handed fields, which, in turn, would break the gauge invariance of the electroweak interaction[5]. This major flaw of the SM is overcome by the Higgs mechanism [40–43]. First, the Higgs-field ϕ is introduced as a doublet of the weak isospin, containing two complex fields with hypercharge $Y = 1$ in eq. (2.3).

$$\phi = \begin{pmatrix} \phi^+ \\ \phi^0 \end{pmatrix} \tag{2.3}$$

The doublet components $\phi^+ = \frac{1}{\sqrt{2}}(\phi_1 + i\phi_2)$ and $\phi^0 = \frac{1}{\sqrt{2}}(\phi_3 + i\phi_4)$ hence give a total of four new scalar field components.

[5] Note that in QED as a gauge theory of its own, a mass-term for the electron is not a problem due to the chirality of particles not playing a role.

In addition to the regular electroweak operators of the SM acting on the Higgs-field, a potential $V(\phi)$ is subjoined, giving the Higgs Lagrangian:

$$\mathcal{L}_{\text{Higgs}} = \left| \left(i\partial_\mu - g\frac{\vec{\tau}}{2} \cdot \vec{W}_\mu - g' \frac{Y_L}{2} B_\mu \right) \phi \right|^2 + V(\phi) \, .$$

The Higgs-potential comes with an expression similar to a mass-term and a term reflecting the Higgs-field self-interaction:

$$V(\phi) = \underbrace{\mu^2 \phi^\dagger \phi}_{\text{mass-term}} + \underbrace{\lambda (\phi^\dagger \phi)^2}_{\text{self-interaction}} \, .$$

The form of the potential is described by the two parameters λ and μ^2. For the potential to have a lower bound, λ needs to be positive, whereas μ^2 can be chosen to be negative. In that case, the potential takes a shape referred to as *Mexican Hat*. Its minimum is given by a rim that is shifted with respect to the origin, expressed by its expectation value not vanishing and hence introducing the vacuum expectation value v as

$$\langle \phi \rangle = \sqrt{\frac{-\mu^2}{2\lambda}} =: \frac{1}{\sqrt{2}} v \, .$$

A graphical representation of the Higgs potential for $\mu^2 < 0$ is shown in fig. 2.6.

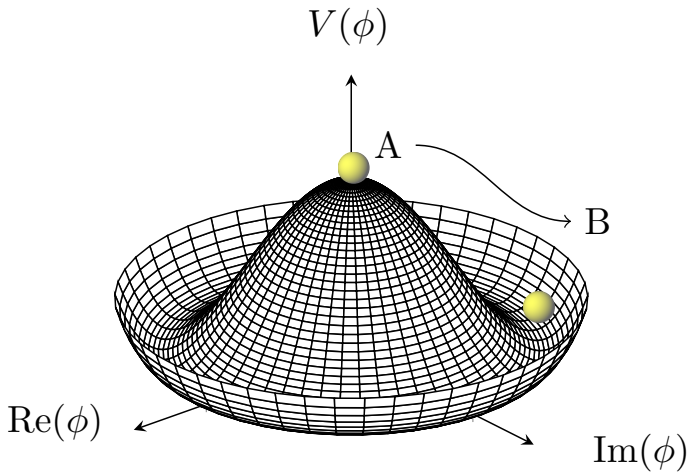

Figure 2.6: Illustration of the potential of a complex scalar field of type $V(\phi) = \mu^2 \phi^\dagger \phi + \lambda (\phi^\dagger \phi)^2$ with $\lambda > 0$ and $\mu^2 < 0$. The potential is symmetric around the origin A, the ground state is a degenerate circle where one arbitrary ground state B is chosen, breaking the electroweak symmetry [44].

While in general, the potential conserves electroweak symmetry, its ground state does not – this property is referred to as *spontaneous breaking* of the electroweak symmetry. Due to its rotational symmetry, the ground state of the potential can be chosen anywhere around the rim.

A typical choice is to fix it in the electrically neutral part of the doublet to also conserve the symmetry of QED and the afore made choice of arrangements in the Higgs-field and fermion doublets:

$$\phi_0 = \frac{1}{\sqrt{2}} \begin{pmatrix} 0 \\ v \end{pmatrix} .$$

Since the electrically charged component of the Higgs-field does not acquire a vacuum expectation value, the photon remains massless. A parametrisation of fluctuations around the ground state is found by means of adding another scalar field h that to the ground state and redefining the Higgs-field, giving it a space-dependence as

$$\phi(x) = \frac{1}{\sqrt{2}} \begin{pmatrix} 0 \\ v + h(x) \end{pmatrix} .$$

Fluctuations in the remaining three components of the Higgs-field can be absorbed by a phase of the $SU_L(2)$ gauge group, leaving physical observables unchanged. The chosen ground state of ϕ is now inserted into the original Higgs Lagrangian, giving mass-terms for the weak gauge bosons as well as for the field h. Moreover, couplings of the weak gauge bosons and the field h arise: hW^+W^-, hhW^+W^-, hZZ, $hhZZ$, hhh, $hhhh$. In terms of these physical fields, the mass-terms follow eq. (2.4).

$$m_W = \frac{1}{2} v g, \qquad m_Z = \frac{1}{2} v \sqrt{g^2 + g'^2} = \frac{m_W}{\cos\theta_W}, \qquad m_\gamma = 0, \qquad \text{and} \quad m_h = \sqrt{2\lambda} v \, . \tag{2.4}$$

This construction gives masses to the electroweak gauge bosons and the scalar field h, which manifests in this basis as the physically observable Higgs-boson. Note that the Higgs-boson mass-expression is only valid at LO. Higher orders introduce loops of all other SM fermions correcting the term, giving rise to the hierarchy problem as discussed in section 2.1.5.

The same field that gives masses to the electroweak gauge bosons can also be utilised to provide masses to the charged fermions. The field's quantum numbers allow it to couple to one isospin doublet and one singlet at a time. The general Lagrangian for this so-called *Yukawa*-coupling in the example case of the electron then reads

$$\mathcal{L}_{\text{Yukawa}} = -G_e \left[(\overline{\nu_{Le}}, \overline{e_L}) \begin{pmatrix} \phi^+ \\ \phi^0 \end{pmatrix} e_R + \overline{e_R} (\phi^-, \phi^0) \begin{pmatrix} \nu_e \\ e \end{pmatrix}_L \right]$$

At the ground state of the Higgs-potential, this equation simplifies to

$$\mathcal{L}_{\text{Yukawa}} = -\frac{G_e}{\sqrt{2}} v (\overline{e_L} e_R + \overline{e_R} e_L) - \frac{G_e}{\sqrt{2}} (\overline{e_L} e_R + \overline{e_R} e_L) h = -m_e \bar{e} e - \frac{m_e}{v} \bar{e} e h \, ,$$

where the first term can be related tot electron mass by choosing $G_e = \sqrt{2} \frac{m_e}{v}$. This Yukawa-coupling of the fermions to the Higgs-field provides mass-terms for the fermions and parametrises their coupling to the Higgs-boson.

The two different coupling mechanisms that give rise to the masses of all elementary particles, i.e. the gauge coupling of the electroweak bosons and the Yukawa-coupling of the fermions[6], render it necessary to search for the physical Higgs-boson in bosonic and fermionic decay channels.

[6] Note that, in a strict sense, the description of the Yukawa-coupling of the fermions to the Higgs-field and boson is equivalent to the description of an additional fundamental interaction itself.

The discovery of the Higgs-boson is hence reported across the bosonic channels $H \to ZZ$, $H \to \gamma\gamma$[7], $H \to WW$ as well as the fermionic channels $H \to bb$ and $H \to \tau\tau$ [4]. While at the time of the discovery the combination of multiple channels across the ATLAS and CMS experiments was necessary to gain enough statistical significance, different individual decay channels have developed sufficient sensitivity to claim a discovery on their own, e.g. the ATLAS discovery of the $H \to \tau\tau$ decay mode [45].

2.1.4 Physics of the τ-lepton decay

One of the core characteristics of the analysis presented in this thesis is the involvement of τ-leptons. As a charged lepton, the τ-lepton shares many features with the electron and the muon. The striking difference with respect to the muon is its high mass. While the muon can only decay into the electron and two neutrinos, the 1.78 GeV heavy τ-lepton features a large set of decay modes that include hadrons.

The τ-lepton exclusively decays weakly via a virtual W boson and emission of a tau-neutrino. The W, in turn, can decay either to a pair of the lighter leptons and corresponding neutrinos or into two quarks, cf. fig. 2.7(b). Due to the undetermined initial state of the partons participating in the collision at a hadron collider like LHC, light leptons from the decay of a τ-lepton are barely distinguishable from prompt leptons. As a consequence, only hadronically decaying τ-leptons are considered as τ-leptons in this thesis. Figure 2.7(a) gives a breakdown of the branching fractions of the different τ-lepton decay-modes, including the predominant hadronic modes.

Charge conservation dictates the allowed multiplicities of charged hadrons in the hadronic τ-lepton decay modes, only odd numbers are allowed. Conservation of helicity makes adding a neutral pion to the the decay into one charged pion the by far most abundant one. The category *Other* includes signatures involving Kaons which, however, only amount to a small fraction of all hadronic decays. In addition to the low multiplicity of charged hadrons, the small vicinity in which the particles are produced and propagate around the axis of the τ-lepton is another distinct characteristic of the τ-lepton decay. Both features become important when comparing the signature of a hadronic τ-lepton decay to the one of a quark- or gluon-initiated jet[8] trying to separate them in experimental data. As mentioned in section 2.1.2, quarks and gluons carry colour themselves which makes them subject to confinement. The resulting need to *dress* their colour to ultimately form colour-neutral objects makes them interact vividly with their colour-sensitive environment. Particles in this environment may be other quarks or gluons that exist in the same time-frame, or remnants from the proton-proton collision. This extensive *colour-flow* is a higher-order effect of QCD at low energies and is hence only accessible phenomenologically (cf. e.g. [47]). The effect, however, is evident: jets arising from single coloured particles feature a wider cone around the propagation axis of the initiating particle and exhibit a generally higher activity than a low-multiplicity, narrow-cone τ-lepton decay. These typical behaviours are schematically illustrated in fig. 2.7(c).

Despite these hypothetically strong separation criteria, the overlap between jet and τ-lepton signatures is considerable. The sophisticated methods developed to separate the two from each other in experimental environments are described in detail later. The theoretical understanding of the interplay of such high-order QCD effects mimicking τ-lepton decays and its realisation in physics simulations is an utmost complicated endeavour. The resulting experimental challenges and how to overcome them is a major part of the analysis presented in this thesis.

[7] Although there is no direct coupling of the Higgs-boson to the photon, a measurement of this process becomes possible due to loops including top-quarks and the electromagnetic charge of the top-quark.

[8] Collimated sprays of charged and neutral particles that originate from the production of a strongly interacting particle or hadron are referred to as *jets*. A precise description under particular considerations of their signatures in the ATLAS detector is provided in section 3.3.1.

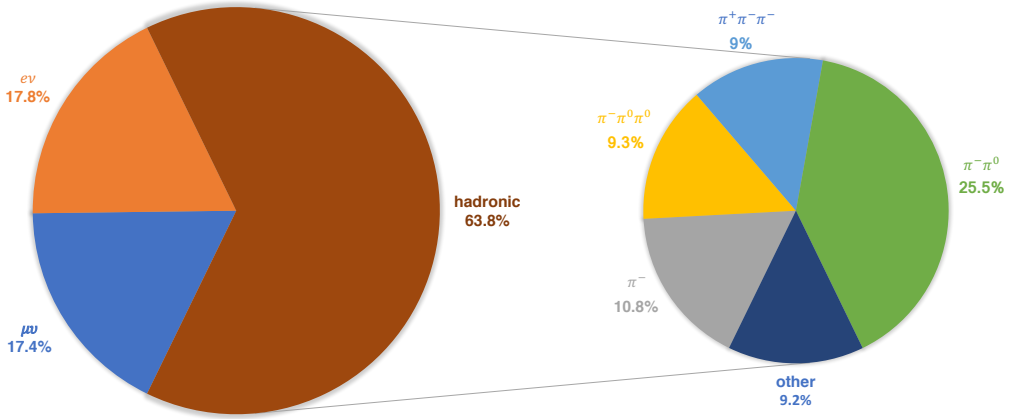

(a) Branching fractions

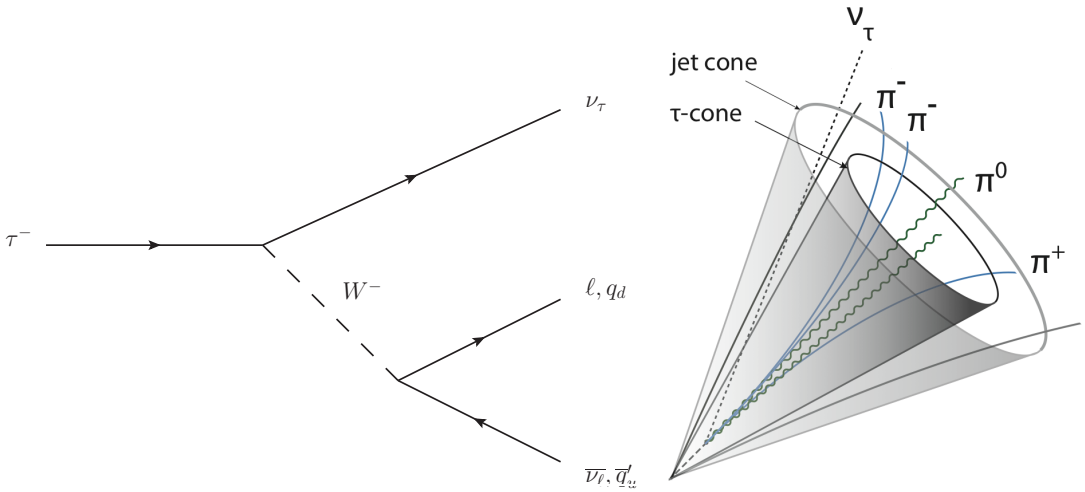

(b) Decay diagram

(c) τ-lepton/jet cones

Figure 2.7: Physics of the τ-lepton decay. Figure (a) gives a breakdown of the branching fractions of its most important decay channels (data from [38]), (b) shows the diagram of the hadronic decay of a τ-lepton, and (c) schematically depicts the difference between quark/gluon jets and hadronic decays of the τ-lepton [46].

2.1.5 Shortcomings of the SM

With respect to several criteria, the Standard Model of Particle Physics can be regarded as good and successful.

- Over the time since its postulation, it has been able to explain a multitude of observations and discoveries.
- It predicted the existence of several particles before their actual discovery in laboratory experiments, including the top quark [48, 49], the tau neutrino [50], and the Higgs-boson [4].
- Its descriptive power covers a large range of different phenomena, from the quantum scale of elementary particles to the macroscopic representations of electromagnetism.
- It is confirmed by an enormous set of independent laboratory experiments up to relative precisions of $O(10^{-9})$ for the electromagnetic coupling constant α_{EM}, cf. fig. 2.8.
- With 19 free parameters, it represents the most compact of models that are able to achieve the aforementioned successes and is hence the preferred model to describe the most microscopic part of the known universe.

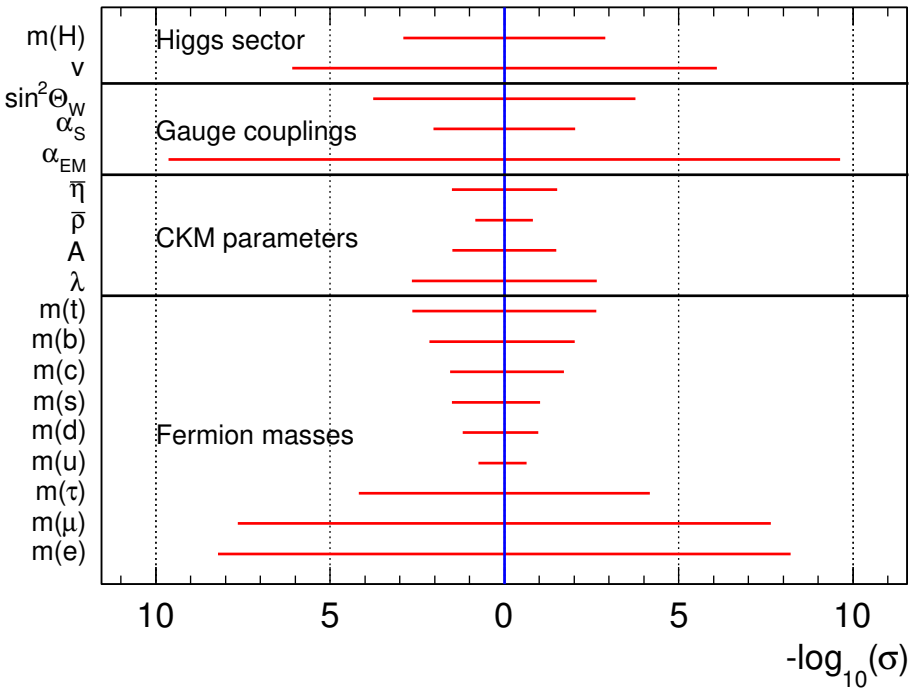

Figure 2.8: Experimental precision of the free parameters of the Standard Model. Centred around the value of a perfect measurement at 0, the x-axis gives $-\log_{10}(\sigma)$ of the relative up- and downward uncertainties σ for each parameter, i.e. larger bars correspond to smaller uncertainties and a higher precision. The vacuum angle of QCD θ_{QCD} is not considered. Data taken from [38].

Despite its predictive power, versatility and success, the SM is subject to shortcomings of different kinds.

The hierarchy problem Although the prediction of the Higgs-boson is regarded a major success of the SM, the mass of the observed particle can only be predicted by including large corrective terms into the underlying calculations, giving rise to the so-called *hierarchy problem* [51–54]. The coupling structure of the Higgs-boson to the Standard Model fermions leads to corrections of the Higgs-boson mass at one-loop level as illustrated in fig. 2.9(a). Due to its high mass and correspondingly high Yukawa-coupling, the top quark contributes the strongest to these corrections. Under the assumption of a Yukawa-coupling of $-\lambda_f H\bar{f}f$, a fermion loop yields a correction to the Higgs-boson mass of

$$\Delta m_H^2 = -\frac{|\lambda_f^2|}{8\pi^2}\Lambda_{\mathrm{UV}} + \dots \ .$$

Here, Λ_{UV} represents a mass scale at which the SM becomes invalid. A natural upper bound for this scale parameter is the Planck scale $M_P = 2.4 \times 10^{18}$ GeV at which quantum gravity effects start to play a non-negligible role. At the Planck scale, the corrections would amount to more than 30 orders of magnitude more than the measured value. This, in turn, would have to be countered by a correspondingly high bare mass of the Higgs-boson and result in a huge *fine-tuning problem*. This mathematically aesthetic flaw can be corrected by considering the Yukawa-coupling of scalar particles to the Higgs-boson as $-\lambda_S |H|^2 |S|^2$, resulting in one-loop corrections of the form

$$\Delta m_H^2 = \frac{\lambda_s}{16\pi^2}\Lambda_{\mathrm{UV}} + \dots \ ,$$

depicted in fig. 2.9(b). Postulating the existence of two scalars for every SM fermion, fulfilling $\lambda_S = |\lambda_f|^2$, would then exactly cancel all contributions to the Higgs-boson mass naturally. This elegant solution to the fine-tuning or hierarchy problem is one of the key motivational features of Supersymmetry, introduced in section 2.2 [55–60].

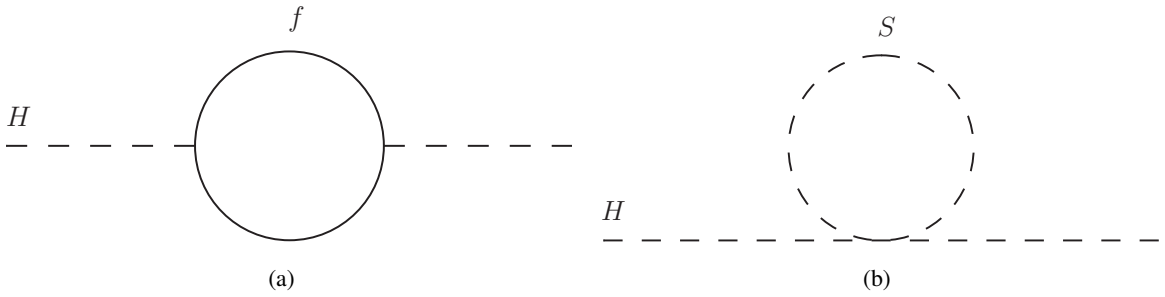

Figure 2.9: One-loop level contributions of fermions (a) and scalars (b) to the mass of the Higgs-boson. The Higgs-boson itself being a scalar particle, acquires positive contributions to its mass-term by both types of graphs, giving rise to the hierarchy problem.

Dark matter Indirect observations from cosmology reveal another shortcoming of the SM. Based on measurements of e.g. the rotational velocity of stars in galaxies, anisotropies in the cosmic microwave background or the expansion behaviour of the Universe, the distribution of energy and matter in the Universe is accessible. As depicted in fig. 2.10, the share of matter that is described by the Standard Model, i.e. baryonic matter, is less than 5% [38]. More than 25% are attributed to so-called *dark matter*, which is hypothesised to only interact weakly and gravitationally. The major share of the total energy balance is taken by a yet unaccessible form referred to as *dark energy*.

While dark energy remains mysterious and an exciting topic for the farther future, Supersymmetry is able to provide a candidate for dark matter on the level of elementary particles [61, 62].

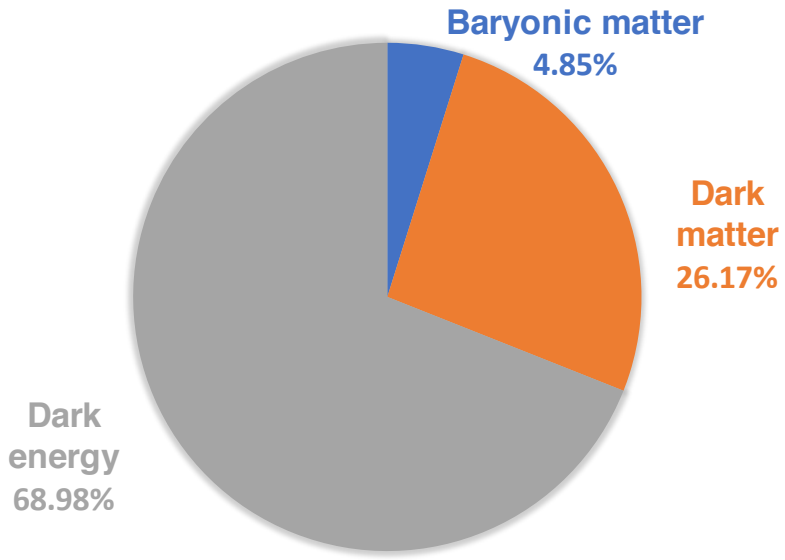

Figure 2.10: Distribution of energy and matter in the Universe. Data taken from [38].

Unification of forces One of the mathematically elegant features of the Standard Model is the unification of the electromagnetic and the weak force, the underlying symmetry and its breaking in the Higgs mechanism. A natural continuation of this pattern would be a unification of the electroweak and the strong force at a certain energy scale. As depicted in fig. 2.11, the dependence of the three coupling constants on the energy scale does not allow for a common intersection and hence a unification. More explicitly, electroweak precision measurements, particularly of the electroweak mixing angle θ_W, exclude unification of all three forces in the SM by more than seven standard deviations. When imposing Supersymmetry, on the other hand, the energy-dependencies of the coupling constants are modified such that a unification is possible [59, 63–70] as depicted in fig. 2.11. Here, the predicted couplings meet in one point, regardless of the underlying SUSY particle mass scale (cf. section 2.2.1). The predicted value of the electroweak mixing angle under that assumption of Supersymmetry would well match the values measured at existing experiments [71].

Gravitation In the light of the unification of forces, one of the major shortcomings of the Standard Model becomes visible. Although the electroweak and the strong force cover already many of the known phenomena of physics, the driving force of astrophysics and the most intuitively accessible force of every-day life is not addressed by the SM: gravitation. Due to its small coupling constant on the microscopic scale of elementary particles with respect to the other three fundamental forces[9], it is entirely neglected in the formalism of the SM.

[9] A simple comparison of the gravitational force F_G between two electrons and the Coulomb force F_C gives a ratio of $F_F/F_C = (m_e^2 \cdot 4\pi\epsilon_0)/(e^2 \cdot G) \approx O(10^{-61})$, resulting in the gravitational coupling constant being $O(10^{-31})$ of the electromagnetic coupling constant.

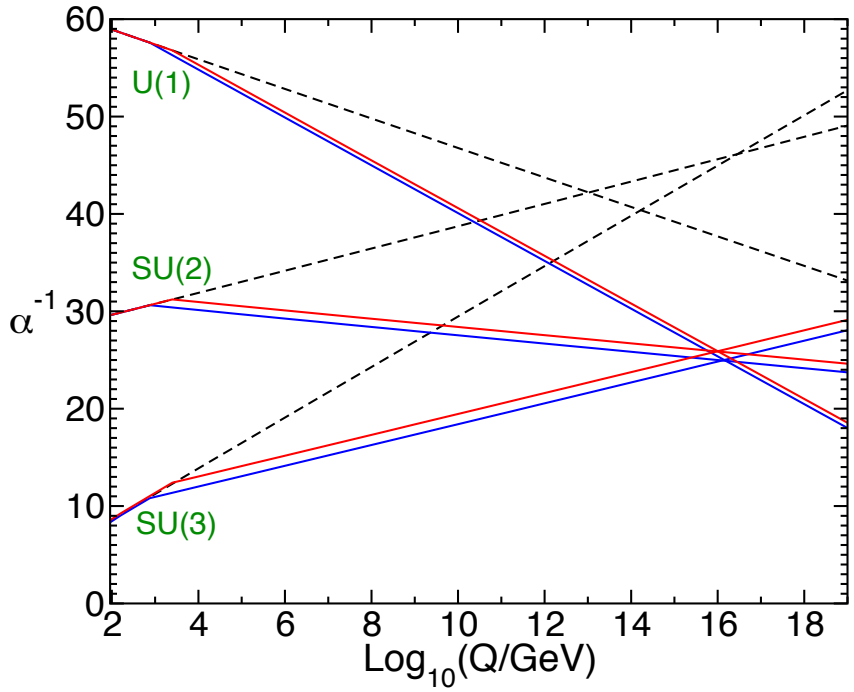

Figure 2.11: Dependence of the three SM gauge coupling constants on the energy scale Q with (solid lines) and without Supersymmetry (dashed lines) [16]. Supersymmetry is realised by the MSSM, treating the sparticle masses as a common threshold, varied between 750 GeV (blue) and 2.5 TeV.

Although many different theories (e.g. [72, 73]) try to describe gravity on the quantum scale, no experimental studies probing its effects have been carried out successfully yet.

Current status In addition to these design flaws and the incompatibility with astrophysical observations, a most recent precision measurements of observables that are predicted by the Standard Model show signifiant deviations from the predictions. As example measurements, the magnetic moment of the muon [74], the ratio of the branching fractions of the weak gauge boson decays $W \to \mu + \nu_\mu$ and $W \to \tau + \nu_\tau$ [75] as well as the ratio of the branching fractions of the heavy-flavour mesons $B \to D^{(*)}\tau\nu$ and $B \to D^{(*)}\ell\nu$ [76] are particularly noteworthy.

All of the above points give rise to the design of extensions to the Standard Model or higher-order models in which the SM is fully comprised. The Two-Higgs-Doublet model [77] can serve as an example for an extension to the Standard Model. It extends the Higgs sector of the SM by introducing an additional neutral, heavier CP-even Higgs-boson, a CP-odd neutral Higgs-boson, and a pair of charged Higgs-bosons, allowing for explanations of the observed excesses in the aforementioned heavy-flavour decays by means of the Yukawa-coupling to a charged Higgs-boson in addition to the W-boson.

Supersymmetry, in turn, represents the most scrutinised higher-order model that is still searched for. It is able to address multiple shortcomings of the Standard Model at once and would fully comprise the SM as a low-energy approximation, similar to classical mechanics representing the low-velocity limit of special relativity. A detailed introduction to Supersymmetry, its benefits and the representations searched for in the context of this thesis are provided in the forthcoming section.

2.2 Supersymmetry

The subtle mathematical beauty of SUSY [16, 78–83] lies within its simple, yet intriguing concept: It postulates a fundamental symmetry between bosons and fermions. A new operator Q transfers bosons into fermions and vice versa:

$$Q|\text{boson}\rangle = |\text{fermion}\rangle, \qquad Q|\text{fermion}\rangle = |\text{boson}\rangle \, .$$

These transformation properties render Q a fermionic operator and make SUSY a fermionic extension of the Poincaré spacetime. Following the Haag-Łopuszańnski-Sohnius extension [84] of the Coleman-Mandula theorem [85], the Poincaré group only contains all possible symmetry generators in four-dimensional space-time when including an additional fermionic symmetry, which follows the algebra

$$\begin{aligned} \{Q, Q^\dagger\} &= P^\mu \\ \{Q, Q\} &= \{Q^\dagger, Q^\dagger\} = 0 \\ [P^\mu, Q] &= [P^\mu, Q^\dagger] = 0 \, . \end{aligned}$$

In fact, SUSY can be deduced ab-initio from considerations of the Poincaré group itself.

Moreover, the SUSY generator commutes with the gauge generators. This fact leads to SM and SUSY particles of the same type behaving equally under gauge interactions and makes them have identical masses.

2.2.1 The Minimal Supersymmetric Standard Model

The SM as introduced in section 2.1 does not provide the particle content necessary to realise SUSY as introduced above. The SM particle content essentially needs to be doubled, giving the so-called *Minimal Supersymmetric Standard Model* (MSSM) [86–88]. In the MSSM, for each fermionic SM degree of freedom, one additional scalar superpartner of equal mass is introduced. SM fermions are treated as Weyl-spinors, i.e. $e = (e_L, e_R)$, being two eigenstates of the weak interaction rather than the spin. This fact leads to the introduction of individual superpartners for each degree of freedom of those Weyl-spinor components in the form of a complex scalar superpartner for the Weyl-spinor component, i.e. $(\tilde{e}_L, \tilde{e}_L^*)$ and $(\tilde{e}_R, \tilde{e}_R^*)$. The asterisk denotes the corresponding anti sparticle. Here, the subscripts only denote the charges under the weak interaction, i.e. chirality. Since the fermion superpartners are (complex) scalars, the subscript labelling does not reflect any information on helicity.

For each SM gauge boson, a fermionic superpartner is introduced. In contrast to the fermion sector of the SM, the massless gauge bosons before electroweak symmetry breaking can take only two spin states already. The degrees of freedom in the gauge sector hence even out after application of the Q operator.

Finally, the Higgs sector of the SM is extended as well, exhibiting certain difficulties. The complex SU(2) Higgs-doublet of the SM receives a Weyl-fermion superpartner. This, however, would lead to so-called *triangle gauge anomalies*. These would break the gauge invariance of the coupling of three gauge bosons by loops containing the fermionic Higgs-partners. In addition, the neat feature of giving Yukawa-couplings to both up- and down-type quarks by means of an additional, conjugate Higgs-field does not work in SUSY anymore. As a consequence, a second Higgs-doublet is introduced. One doublet H_u with hypercharge $Y = \frac{1}{2}$ couples to up-type fermions, the other doublet H_d with hypercharge $Y = -\frac{1}{2}$ couples to down-type fermions. Both fields consist of an electrically charged and a neutral component.

For all particles being introduced in the MSSM, a naming scheme is applied. The bosonic superpartners

of SM fermions receive an *s*-prefix, e.g. giving the *stau* as the superpartner of the τ-lepton. The *s*-prefix is also appended when referring to classes of fermion superpartners such as *squarks* and *sleptons*, as well as SUSY particles in general – so-called *sparticles*. The fermionic superpartners of the SM gauge and Higgs-bosons are referenced by adding an *ino*-suffix, e.g. giving the *gluino* and the set of *gauginos* or *Higgsinos*.

The SM fields and their SUSY counterparts can be grouped into supermultiplets which share the same charge under SM gauge interactions. Table 2.1 summarises the chiral supermultiplets with a spin-0 and a spin-$\frac{1}{2}$ part, table 2.2 lists the gauge supermultiplets.

Names and notation		Spin 0	Spin $\frac{1}{2}$	$SU(3)_C$, $SU(2)_L$, $U(1)_Y$
Squarks, quarks (3 families)	Q	$(\tilde{u}_L, \tilde{d}_L)$	(u_L, d_L)	$(3, 2, \frac{1}{6})$
	$\overline{u}$	$\tilde{u}_R^*$	$u_R^\dagger$	$(\overline{3}, 1, -\frac{2}{3})$
	$\overline{d}$	$\tilde{d}_R^*$	$d_R^\dagger$	$(\overline{3}, 1, \frac{1}{3})$
Sleptons, leptons (3 families)	L	$(\tilde{\nu}, \tilde{e}_L)$	(ν, e_L)	$(1, 2, -\frac{1}{2})$
	$\overline{e}$	$\tilde{e}_R^*$	$e_R^\dagger$	$(1, 1, 1)$
Higgs, Higgsinos	H_u	(H_u^+, H_u^0)	$(\tilde{H}_u^+, \tilde{H}_u^0)$	$(1, 2, \frac{1}{2})$
	H_d	(H_d^0, H_d^-)	$(\tilde{H}_d^0, \tilde{H}_d^-)$	$(1, 2, -\frac{1}{2})$

Table 2.1: Chiral supermultiplets of the MSSM and their respective transformation properties under the SM gauge groups as well as the U(1) hypercharge. Spin-0 fields are complex scalars, spin-$\frac{1}{2}$ fields are represented as left-chiral Weyl-spinors [16].

Names	Spin $\frac{1}{2}$	Spin 1	$SU(3)_C$, $SU(2)_L$, $U(1)_Y$
gluino, gluon	$\tilde{g}$	g	$(8, 1, 0)$
Wino, W boson	$\tilde{W}^{(1,2,3)}$	$W^{(1,2,3)}$	$(1, 3, 0)$
Bino, B boson	$\tilde{B}^0$	B^0	$(1, 1, 0)$

Table 2.2: Gauge supermultiplets of the MSSM and their respective quantum numbers und the SM gauge interactions [16].

Based on those supermultiplets, a superpotential can be constructed in analogy to the Higgs-potential and the Yukawa-couplings of the SM:

$$W_{\text{MSSM}} = \overline{u}\boldsymbol{y_u} Q H_u - \overline{d}\boldsymbol{y_d} Q H_d - \overline{e}\boldsymbol{y_e} L H_d + \mu H_u H_d \,. \tag{2.5}$$

Here, $\boldsymbol{y_u}$, $\boldsymbol{y_d}$, and $\boldsymbol{y_e}$ are 3×3 matrices in family-space. They give the Yukawa-couplings of the up-type and down-type quarks as well as the charged leptons after electroweak symmetry breaking. It is possible to simplify the matrices by neglecting the first two SM fermion families due to their low masses, giving

$$\boldsymbol{y_u} = \begin{pmatrix} 0 & 0 & 0 \\ 0 & 0 & 0 \\ 0 & 0 & y_t \end{pmatrix}, \qquad \boldsymbol{y_d} = \begin{pmatrix} 0 & 0 & 0 \\ 0 & 0 & 0 \\ 0 & 0 & y_b \end{pmatrix}, \qquad \boldsymbol{y_e} = \begin{pmatrix} 0 & 0 & 0 \\ 0 & 0 & 0 \\ 0 & 0 & y_\tau \end{pmatrix}.$$

The breaking of electroweak symmetry in the MSSM works similarly as in the SM, despite the new Higgs-fields. It is again possible to exploit gauge symmetries to rotate the ground states of the

superpotential into the neutral components fo the Higgs doublets, giving individual vacuum expectation values for the neutral fields as

$$v_u = \left\langle H_u^0 \right\rangle, \qquad v_d = \left\langle H_d^0 \right\rangle \ .$$

Constraints on the vacuum expectation values are imposed by fixing their quadratic sum relative to the mass of the Z-boson and the gauge couplings. Furthermore, their ratio is parametrised by an angle β:

$$v_u^2 + v_d^2 = v^2 = 2\frac{m_Z^2}{g^2 + g'^2} \approx (174\,\mathrm{GeV})^2 \,, \qquad \frac{v_u}{v_d} =: \tan\beta \,.$$

Three degrees of freedom of the MSSM Higgs-field are used to generate the masses of the physical gauge bosons. The remaining five degrees of freedom give five physical Higgs-bosons, two CP-even scalars h^0 and H^0, one CP-odd scalar A^0 and two charged states $H^\pm$. In the common notation, h^0 labels the lightest of the neutral Higgs-bosons. At tree-level, its mass has an upper bound given by the mass of the Z-boson. Similar to the loop-induced corrections introduced in the section 2.1.3, contributions of heavy fermions and scalars, predominantly top and stop quarks, correct this upper bound to

$$m_{h^0} \lessapprox 135\,\mathrm{GeV} \ .$$

This number [16] agrees well with the mass of the Higgs-boson observed at the LHC [4].

External constraints The mathematically aesthetic and elegant concept of the MSSM neither withstands all fundamental observations nor general theoretical considerations. In the following, information on some of these constraints and how to refine the MSSM to overcome them is presented.

The superpotential as introduced in eq. (2.5) is, in a strict sense, not complete. It does not contain all terms that are invariant under SM gauge and SUSY transformations; terms that violate conservation of the lepton-number L or the baryon-number B have been omitted. Their presence in the superpotential would have dramatic effects on resulting predictions, rendering SUSY incompatible with established observations and measurements. One of the most striking contradictions to including all L- and B-violating terms into the eq. (2.5) would be the prediction of a rapid decay of the proton, whose lifetime is measured to be $\geq 2.1 \times 10^{29}$ yr [38]. In the SM, on the other hand, no allowed terms violate L or B, providing a natural conservation of both quantum numbers.

Instead of forcing the conservation of lepton- and baryon-number onto the MSSM, the introduction of a new fundamental symmetry called *R-parity* provides a solution to the problem. For a particle with spin s it is defined as

$$P_R = (-1)^{3(B-L)+2S} \ .$$

In fact, this new symmetry can be considered a multiplicative SUSY quantum number: while all SM particles have $R_P = 1$, all sparticles are characterised by $R_P = -1$. Conservation of R-parity gives rise to several important consequences:

- The lightest sparticle (LSP) is stable. If it is electrically neutral and interacts only weakly with the SM, it poses a candidate for cosmological dark matter at the elementary particle scale, cf. section 2.1.5.
- Every heavier sparticle has a finite lifetime and decays to an odd number of LSPs and an arbitrary number of SM particles.

- Arising from collisions of SM-particles ($R_P = 1$), e.g. at the LHC, sparticles can only be produced in pairs.

The fact that SUSY has not been discovered to date marks another important constraint. If SUSY as proposed by eq. (2.5) and conservation of R-parity were realised in nature, the selectron, i.e. a scalar electrically charged particle with a mass of approximately 511 keV would have been discovered already. Since this is not the case, the selectron and consequently all other sparticles need to be heavier than their SM counterparts. SUSY hence needs to be a broken symmetry. In the framework of the MSSM, SUSY is broken but—in contrast to the electroweak symmetry of the SM—the exact breaking mechanism is not specified. Extending the MSSM by additional fields at a higher mass scale, however, can introduce different mechanisms for the breaking of SUSY as discussed in more detail in the respective paragraph.

Mass mixing As already mentioned and visualised in tables 2.1 and 2.2, the superpartners of the SM Higgs-bosons and the electroweak gauge bosons carry the same quantum numbers. They can hence mix to form mass eigenstates, referred to as neutralinos $\tilde{\chi}^0_{1,2,3,4}$ for the neutral fields $\tilde{B}$, $\tilde{W}^0$ and $\tilde{H}^0_{u,d}$ and charginos $\tilde{\chi}^\pm_{1,2}$ for the charged fields $\tilde{W}^\pm$ and $\tilde{H}^\pm_{u,d}$, respectively. In the neutral sector, the corresponding mass matrix is given by

$$\boldsymbol{M}_{\tilde{\chi}^0} = \begin{pmatrix} M_1 & 0 & -c_\beta s_W m_Z & s_\beta s_W m_Z \\ 0 & M_2 & c_\beta c_W m_Z & -s_\beta c_W m_Z \\ -c_\beta s_W m_Z & c_\beta C_W m_Z & 0 & -\mu \\ s_\beta s_W mZ & -s_\beta c_W m_Z & -\mu & 0 \end{pmatrix}.$$

Here, the short-hand notation $s_\beta \equiv \sin\beta$, $c_\beta \equiv \cos\beta$, $s_W \equiv \sin\theta_W$, and $c_W \equiv \cos\theta_W$ is used, with β being the already introduced angle describing the ratio of the two Higgs vacuum expectation values and θ_W the Weinberg angle of the SM. μ represents the Higgs mass parameter of the superpotential (cf. eq. (2.5)), while M_1 and M_2 are mass parameters of the MSSM. The mixing matrix can be diagonalised to obtain the masses of the four neutralinos. For scenarios where $m_Z \ll |\mu \pm M_{1,2}|$, the lightest neutralino is mainly bino-like, $\tilde{\chi}^0_2$ is mainly wino-like and $\tilde{\chi}^0_{3,4}$ are Higgsino-like. $\tilde{\chi}^0_1$ is often the LSP and stable in scenarios that conserve R-parity. Due to its weak coupling, it is deemed a suitable candidate for dark matter on the elementary particle scale [61, 62].

For the charginos, the charge-conjugate states have equal mass, resulting in a 2×2 matrix that can explicitly give the masses as

$$m^2_{\tilde{\chi}^\pm_{1,2}} = \frac{1}{2}\left[|M_2|^2 + |\mu|^2 + 2m_W^2 \mp \sqrt{(|M_2|^2 + |\mu|^2 + 2m_W^2)^2 - 4|\mu M_2 - m_w^2 \sin 2\beta|^2}\right].$$

For the same scenario of $m_Z \ll |\mu \pm M_{1,2}|$, $\tilde{\chi}^\pm_1$ becomes wino-like while $\tilde{\chi}^\pm_2$ is Higgsino-like.

As in the SM, mixing also occurs in the sfermionic sector of SUSY. The Yukawa-coupling terms in the superpotential and trilinear couplings in the SUSY Langrangian as introduced later couple the scalar $\tilde{f}_L$ and $\tilde{f}_R$ partners and give hence rise to a mixture of the respective sparticles. However, due to the large differences in mass between the third and the first two families and strong experimental constraints on flavour-changing processes, the mixing of sfermions is expected to only play a role for the third generation. The mixing of the superpartners of the τ-lepton is described by the matrix $\boldsymbol{M}^2_{\tilde{\tau}}$ in eq. (2.6).

$$\boldsymbol{M}^2_{\tilde{\tau}} = \begin{pmatrix} m^2_{\tilde{\tau}_L} + m^2_\tau + \Delta_L & m_\tau(A_0 + \mu \tan\beta) \\ m_\tau(A_0 + \mu \tan\beta) & m^2_{\tilde{\tau}_R} + m_\tau + \Delta_R \end{pmatrix} \tag{2.6}$$

$$\Delta_L = \left(-\frac{1}{2} + \sin^2\theta_W\right) m_Z^2 \cos 2\beta \tag{2.7}$$

$$\Delta_R = \frac{1}{3}\sin^2\theta_W m_Z^2 \cos 2\beta\,. \tag{2.8}$$

The off-diagonal elements mix L and R states[10], forming two mass eigenstates $\tilde{\tau}_{1,2}$. Certain configurations of the other parameters in the mixing matrix can result in the $\tilde{\tau}_1$ being substantially lighter than the chirality eigenstates of the first two slepton generations, rendering it the lightest slepton. Since for the other two slepton generations corresponding mixing matrices exist and the magnitude of the off-diagonal elements depends on the mass of the SM partner, mixing can be neglected for selectrons and smuons. For them, the mass eigenstates are equal to the gauge eigenstates.

For squarks, the mixing procedure follows a similar pattern, being also strongest in the third generation, i.e. for stop and sbottom quarks. Of particular importance in this context is the mixing of the stop quarks. For SUSY to provide the proposed solution to the hierarchy problem of section 2.1.5, the masses of the sfermions need not to be too large. Due to the large Yukawa-coupling of the top quark, the $\tilde{t}$ mass-terms are most important in this respect. The Yukawa-coupling of the top quark also induces large mixing of the states $\tilde{t}_{L,R}$, making the $\tilde{t}_1$ the lightest of squarks.

Symmetry breaking in the MSSM As already mentioned, SUSY needs to be a broken symmetry. A pragmatic approach to address this issue is to comprise all possible *soft* SUSY breaking terms in a Lagrangian. In this context, the attribute *soft* refers to the fact that the breaking terms give masses to the sparticles in the TeV range and still enable SUSY to be a possible remedy for the shortcomings of the SM. In eq. (2.9), $M_{1,2,3}$ denote gaugino mass parameters and $\boldsymbol{a_{u,d,e}}$ are 3×3 matrices in family-space which parametrise trilinear couplings. The family-space matrices $\boldsymbol{m^2_{Q,L,\bar{u},\bar{d},\bar{e}}}$ yield the sparticle masses, while $m^2_{H_u,H_d}$ and b represent additional Higgs-mass contributions. In this approach, the breaking of SUSY takes place in a *hidden* high-energy sector beyond the mass scales of the sparticles.

$$\begin{aligned} \mathcal{L}^{\text{MSSM}}_{\text{soft}} = &-\frac{1}{2}\left(M_3\tilde{g}\tilde{g} + M_2\tilde{W}\tilde{W} + M_1\tilde{B}\tilde{B} + \text{h. c.}\right) \\ &-\left(\tilde{\bar{u}}\boldsymbol{a_u}\tilde{Q}H_u - \tilde{\bar{d}}\boldsymbol{a_d}\tilde{Q}H_d - \tilde{\bar{e}}\boldsymbol{a_e}\tilde{Q}H_e + \text{h. c.}\right) \\ &-\tilde{Q}^\dagger \boldsymbol{m^2_Q}\tilde{Q} - \tilde{L}^\dagger \boldsymbol{m^2_L}\tilde{L} - \tilde{\bar{u}}\boldsymbol{m^2_{\bar{u}}}\tilde{\bar{u}}^\dagger - \tilde{\bar{d}}\boldsymbol{m^2_{\bar{d}}}\tilde{\bar{d}}^\dagger - \tilde{\bar{e}}\boldsymbol{m^2_{\bar{e}}}\tilde{\bar{e}}^\dagger \\ &-m^2_{H_u}H^*_u H_u - m^2_{H_d}H^*_d H_d - (bH_u H_d + \text{h. c.}) \end{aligned} \tag{2.9}$$

The soft breaking of SUSY introduces more than 100 additional parameters [89] to the theory, rendering it far from simple. The number of free parameters can be reduced though when considering experimental constraints such as SUSY-induced flavour-changing in the SM fermion sector. In addition to experimental results limiting the set of parameters, theoretically well motivated models of more concrete forms of the

[10] It is again to be noted that the subscripts L and R of SUSY sfermions, i.e. scalar particles, only denote the relationship to the SM partners and do not represent chirality or helicity.

breaking mechanism exist, simplifying the theory further. The forthcoming sections introduce the models of SUSY studied in and searched for in the context of this thesis. Further information on the breaking of SUSY and designated breaking mechanisms can be found in [16].

The gravitino It is in general possible to extend SUSY to also incorporate gravity. By promoting the global symmetry to a local symmetry, *Supergravity* [72, 73] is introduced. From a theoretical point of view, supergravity is interesting to study, at collider experiments, however, it is of minor importance. Only its gauge field of the local SUSY transformation, the graviton g (spin $s = 2$) and its superpartner, the gravitino $\tilde{G}$ (spin $s = 3/2$), are relevant.

In unbroken SUSY, both the graviton and the gravitino are massless. After spontaneous breaking of the symmetry, however, the gravitino absorbs the arising degrees of freedom associated with the breaking in a similar fashion as the W and Z bosons absorb degrees of freedom in the breaking of the electroweak symmetry[11]. The mass acquired by the gravitino this way depends on the breaking scale:

$$m_{3/2} \sim \frac{\langle F \rangle}{M_P} \, .$$

Here, $\langle F \rangle$ denotes the energy scale associated to the breaking process and M_P represents the Planck mass. In contrast to the graviton coupling only via the gravitational interaction, the gravitino can also couple to any particle-sparticle pair via its goldstino component. The exact coupling strength depends on the particles involved, the gravitino itself as well as the energy scale of the breaking. Although it is generally smaller than the other couplings in the MSSM, it can still be large enough to give rise to prompt decays.

2.2.2 Gauge-mediated SUSY breaking

Out of the many different mechanisms of symmetry breaking that are hypothesised, gauge-mediated SUSY breaking (GMSB) [90–92] is of particular interest for the presented analysis.

GMSB is one of the breaking mechanisms where the symmetry is broken in a hidden sector. In this sector, additional multiplets of so-called *messenger* fields exist. They acquire their high mass by coupling to a gauge singlet S. This mass generation process makes S acquire a two-fold vacuum expectation value $\langle S \rangle$ and $\langle F_S \rangle$ that breaks the mass degeneracy for the messenger multiplets. They then fulfil the relation

$$m^2_{\text{fermions}} = \left| y_S \langle S \rangle \right|^2 , \qquad m^2_{\text{scalars}} = \left| y_S \langle S \rangle \right| \pm \left| y_S \langle F_S \rangle \right| \, .$$

The symmetry is hence broken for the case $\langle F_S \rangle \neq 0$. The symmetry is propagated to the MSSM via loop diagrams. The MSSM particles couple to messenger loops by means of regular gauge couplings, giving rise to the name of the breaking mechanism. Figure 2.12 depicts an example diagram for such a coupling. While the gaugino masses are generated via one-loop diagrams, the scalar masses require two loops.

An attractive feature of GMSB lies within the fact that its symmetry breaking is based on SM quantum numbers, it is hence intrinsically blind to flavour. As a consequence, the suppression of flavour-changing terms in the superpotential and the soft breaking Langrangian as well as other simplifying features introduced in section 2.2.1 come naturally.

[11] In analogy to the Goldstone-bosons of electroweak symmetry breaking, so-called *goldstinos* absorb the degrees of freedom in this breaking process.

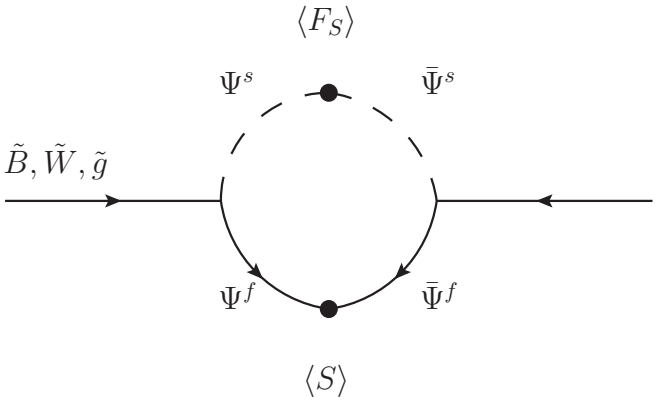

Figure 2.12: Contributions to the gaugino masses by one-loop diagrams in GMSB. Ψ^f and Ψ^s denote the fermionic and scalar content of messenger multiples, respectively [15].

Phenomenology The characteristic feature of GMSB is the gravitino always being the LSP. Due to the breaking happening around the GUT scale and well below the Planck scale, the gravitino mass is in the keV range. The low coupling of the gravitino makes it predominantly relevant in the last step of a SUSY decay cascade, i.e. NLSP $\rightarrow \tilde{G}$: the next-to-lightest sparticle (NLSP) decays into the gravitino and a matching SM particle.

In contrast to the unconstrained breaking of SUSY, GMSB can be described by only six parameters:

- $\langle S \rangle$ denotes the mass of the messenger fields.
- Λ gives the ratio of the two vacuum expectation values associated to the generation process of mass for the supermultiplet S: $\Lambda = \frac{\langle F_S \rangle}{\langle S \rangle}$.
- The number of messenger fields is N_5, the index arising from the assumption to unify all SM couplings in an SU(5) GUT.
- The mass of the gravitino is related to a scale parameter $C_{\tilde{G}}$.
- The ratio of the vacuum expectation values of the two Higgs fields $\tan\beta$ has already been introduced.
- sgn(μ) denotes the sign of the Higgs mass parameter μ.

The sparticle masses in GMSB depend on these six parameters. Λ and N_5 have the largest influence on the mass spectrum, resulting in a simplified proportionality of

$$M_{\text{gauginos}} \propto \Lambda N_5, \qquad M_{\text{scalars}} \propto \Lambda \sqrt{N_5}\,.$$

While Λ provides an overall mass scale for sparticles in GMSB, N_5 determines the hierarchy between gauginos and scalars. The different dependence on N_5 originates from the different loop order in which the messenger fields give mass to the sparticles. This dependence on N_5 hence also influences the nature of the NLSP. For $N_5 = 1$, the NLSP is the lightest neutralino, for higher values of N_5, the gauginos gain more mass than the scalars. In such scenarios, the NLSP is typically the lightest slepton. The phenomenology of GMSB thus strongly depends on the value of N_5:

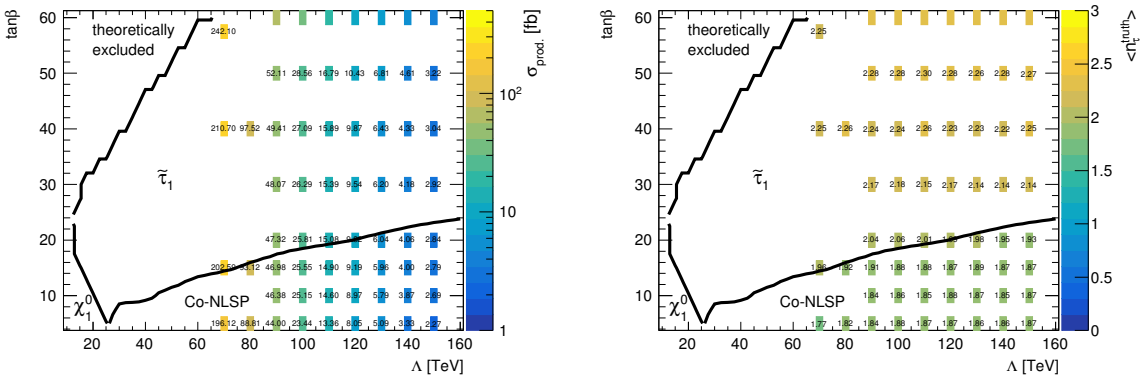

(a) (b)

Figure 2.13: Production cross-sections $\sigma_{\text{prod.}}$ at NLO integrated over all sub-processes (a) and the average number of truth-level τ-leptons with $p_{\text{T}} > 20\,\text{GeV}$ $\langle n_\tau^{\text{truth}} \rangle$ per event (b) across the GMSB parameter-grid. The lines sketch regimes of different NLSPs. The data displayed is generated using the SPheno [93] program and preprocessed by the PySLHA program [94].

$$N_5 = 1: \quad \tilde{\chi}_1^0 \to \gamma\tilde{G}$$
$$N_5 = 3: \quad \tilde{\ell} \to \ell\tilde{G}\,.$$

The influence of $\tan\beta$ is also significant. It determines the mixing both in the gaugino and the scalar sector. For low values, the mixing is small and the masses of the sτ-leptons are more or less degenerate. At higher values, the mixing increases, making the $\tilde{\tau}_1$ the NLSP.

The mass parameter of the messenger fields $\langle S \rangle$ needs to be large enough for the messengers to only play an indirect role. The influence of $\text{sgn}(\mu)$ is generally small at the electroweak scale and hence at the LHC. $C_{\tilde{G}}$ determines the lifetime of the NLSP. For large values, the NLSP becomes metastable, yielding long-lived and eventually charged particles. For the analysis presented in this thesis, a GMSB model with four fixed parameters is chosen:

$$N_5 = 3, \qquad \langle S \rangle = 250\,\text{TeV}, \qquad C_{\tilde{G}} = 1, \qquad \mu > 1\,.$$

The remaining free parameters are varied between $70\,\text{TeV} \leq \Lambda \leq 160\,\text{TeV}$ and $2 \leq \tan\beta \leq 60$, respectively. Due to limitations in available computing resources, the range of parameters is sampled with a limited rate, giving rise to a grid of in the two-dimensional parameter-space, each pair of parameters referred to as a *signal point* or *scenario*. An overview of the parameter-space is provided in fig. 2.13.

Across the parameter-grid, different regions of dominating NLSPs are sketched. For low values of Λ, the lightest neutralino is still the favoured NLSP. Since this regime is not expected to produce sufficient numbers of τ-leptons, it is neither considered in this analysis, nor in its predecessors [9, 12, 13]. For the remaining grid, $\tan\beta$ determines the nature of the NLSP.

For low values of $\tan\beta$, a so-called *Co-NLSP* region exists. There, all sleptons are of similar mass and hence decay to the gravitino LSP with similar probabilities. At larger values, the mixing increases and makes the $\tilde{\tau}_1$ the lightest slepton and NLSP. Once the difference of masses between the slepton generations exceeds twice the mass of the τ-lepton, the three-body-decay $\tilde{\ell} \to \tilde{\tau}^{\pm}\tau^{\mp}\tau$ becomes accessible.

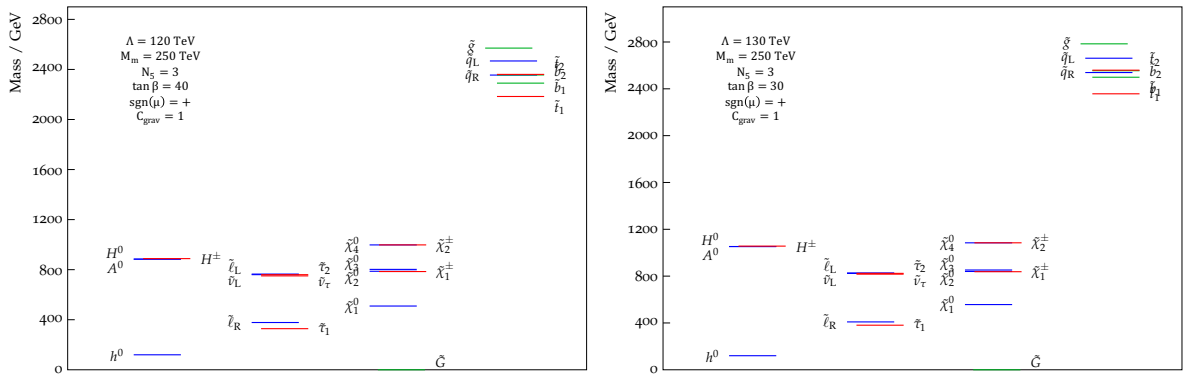

(a) $\Lambda = 120\,\text{TeV}$, $\tan\beta = 40$ (b) $\Lambda = 130\,\text{TeV}$, $\tan\beta = 30$

Figure 2.14: Example mass spectra for the scenarios of $\Lambda = 120\,\text{TeV}$, $\tan\beta = 40$ (a) and $\Lambda = 130\,\text{TeV}$, $\tan\beta = 30$ (b). The data displayed is generated using the SPheno [93] program and visualised by the PySLHA program [94].

The number of expected τ-leptons consequently increases over the parameter-grid. For high values of $\tan\beta$ and low values of Λ, a region of unphysical mass spectra due to tachyonic matter states is theoretically excluded.

In contrast to the τ-lepton multiplicity, the production cross-section is largely independent of $\tan\beta$. It is predominantly driven by the masses of the produced sparticles and hence strongly correlated with Λ. Example mass spectra of the studied GMSB model are depicted in fig. 2.14.

Apart from its attractive features and phenomenology, GMSB is subject to one severe drawback: it is barely able to provide a lightest Higgs-boson with a mass equal to the one found at the LHC. There are, however, different possibilities to remedy this shortcoming, e.g. the introduction of additional vector-like quarks [95]. The general signatures provided by a model of GMSB are hence nevertheless worth studying, which is why this flaw is ignored in the model studied in this thesis.

These considerations converge in a multitude of different signatures, which a model of GMSB can produce at a hadron collider such as LHC. An example decay cascade for the prominent case of squark–squark production is depicted in fig. 2.15(a).The current state of GMSB at the LHC, searched for using the ATLAS experiment, is depicted in fig. 2.15(b), including parts of the earlier results obtained at $\sqrt{s} = 8\,\text{TeV}$ in Run-1 of the LHC [13]. The former results have been obtained in a similar fashion in an earlier version of the analysis presented here [9]. Values of the free parameters Λ and $\tan\beta$ below the contour-lines are excluded. The parameter-space of interest to this analysis is hence $\Lambda > 100\,\text{TeV}$ for all available values of $\tan\beta$.

2.2.3 SUSY at the LHC

The majority of new particles predicted by SUSY are heavier than all SM particles. The LHC providing the highest of available center-of-mass energies in collider experiments hence poses the ideal environment to search for SUSY – or any other BSM theory involving new heavy particles. The ATLAS and CMS multipurpose experiments are sufficiently versatile to search for virtually any SUSY signature. The following paragraphs briefly summarise the predominant production and decay processes of SUSY at the LHC.

Production The characteristics of SUSY introduced in section 2.2.1 render possible production signatures at the LHC evident.

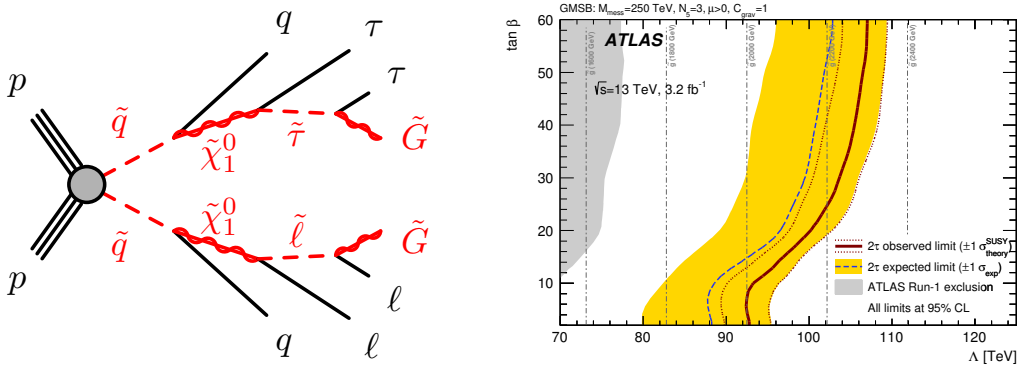

(a) (b)

Figure 2.15: Example decay cascade of a typical GMSB process in a proton–proton collision (a) and the first exclusions in the parameter-space at $\sqrt{s} = 13\,\text{TeV}$ (b) [9].

The assumption of R-parity being conserved results in sparticles being produced via gauge interactions and in pairs. Since the initial particles in a hadron collider carry colour charge, interactions via the strong force dominate over electroweak processes.

This first consideration is the key motivation to search for squarks and gluinos as envoys of SUSY in the context of this thesis.

Production diagrams of squarks and gluinos at LO via the strong force are depicted in figs. 2.16 and 2.17. The u- and t-channel diagrams feature virtual sparticles, i.e. they can be suppressed for cases where the respective sparticle is too heavy.

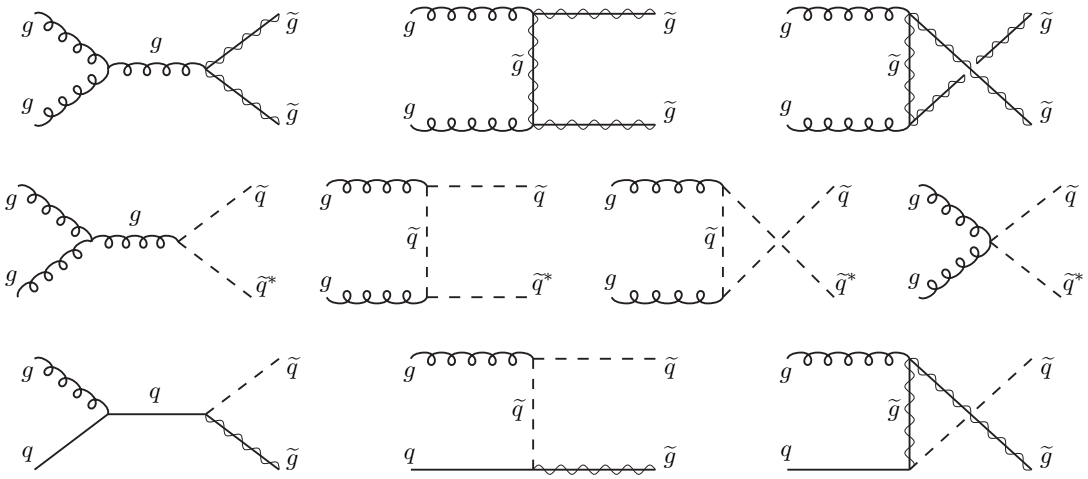

Figure 2.16: Production diagrams for SUSY particles via the strong force from initial states of gluons, or quarks and gluons [16].

Due to their smaller relative coupling strength with respect to the strong interaction, electroweak production processes only play a subdominant role at the LHC. They are only relevant when the coloured sparticles are too heavy to be accessible at the available energy scale. This is, for example, the case for the higher values of Λ in the GMSB model. A detailed breakdown of the different processes contributing to the production of the model of GMSB is depicted in fig. A.1 of appendix A.1. Possible LO electroweak production diagrams of charginos and neutralinos are depicted in fig. 2.18. It is to be noted that the

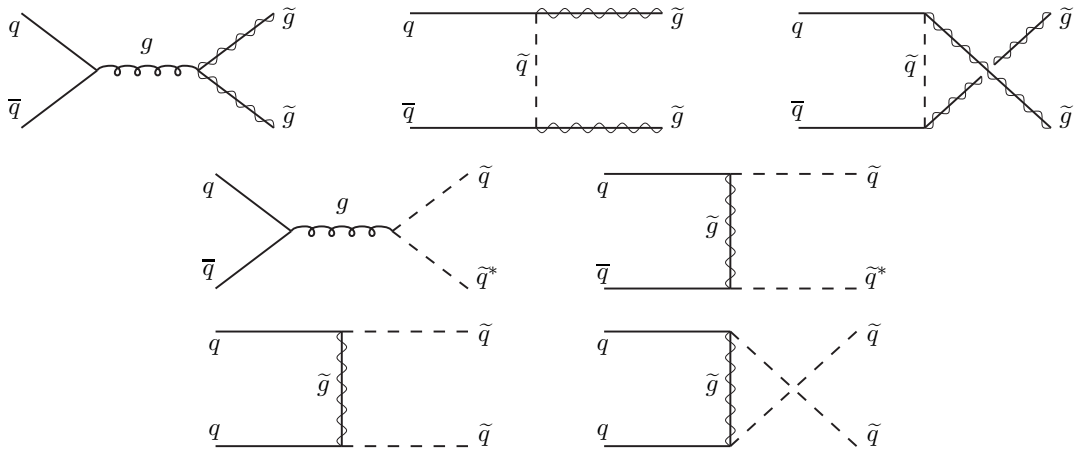

Figure 2.17: Production diagrams for SUSY particles via the strong force from initial states of quarks and/or antiquarks [16].

couplings of charginos and neutralinos can be either of gauge or Yukawa kind, depending on the process and mixing configuration. In general, the associated production of a neutralino or chargino with a squark or gluino is possible, its lower cross-section rendering it even more subdominant, though.

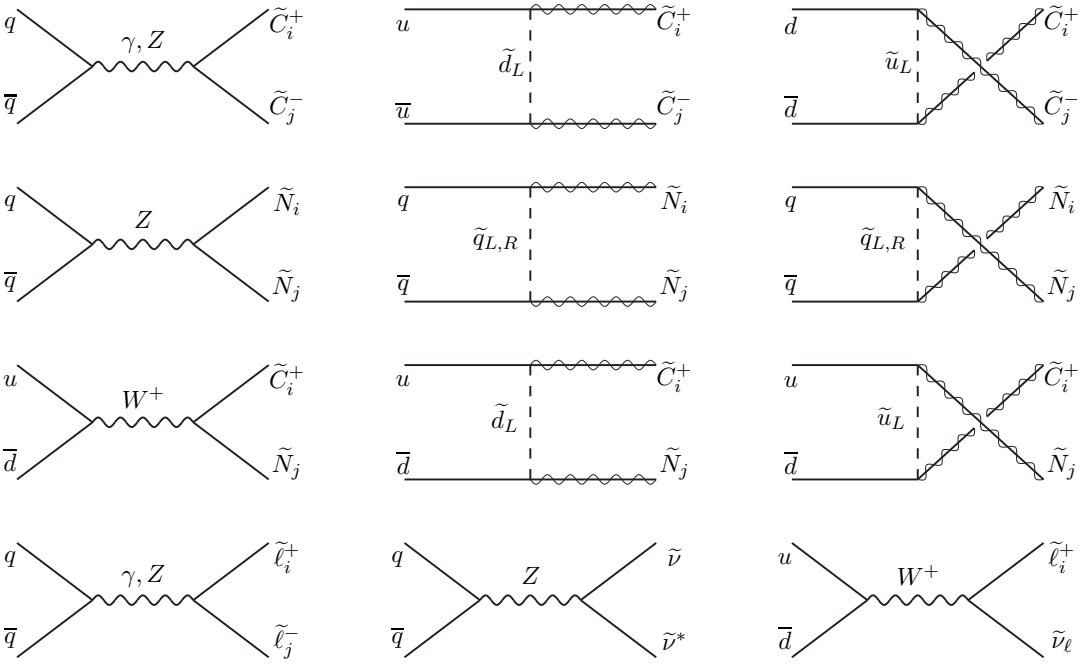

Figure 2.18: Production diagrams for SUSY particles via the electroweak force from initial states of quarks and/or antiquarks. In contrast to the usual notation, here, *C* denotes charginos and *N* neutralinos [16].

Decay While the production process determines the cross-section and hence the probability of a particle to be produced, its decay gives the signature that is observable in the detector. Assuming a typical mass hierarchy as e.g. depicted in fig. 2.14, decay chains begin with coloured particles.

For starters, the gluino almost always decays to squark-quark pair

$$\tilde{g} \to \tilde{q}q \,.$$

Subsequent decays of the squark then require gauginos

$$\tilde{q} \to \tilde{\chi}^0 q, \qquad \tilde{q} \to \tilde{\chi}^\pm q' \,.$$

The nature of the neutralino/chargino the squark decays into depends on the quantum numbers of the squark and the mixing configuration of the gaugino sector. A right-handed squark will prefer a decay into a bino-like gaugino, while a left-handed squark will prefer a wino-like state due to the stronger isospin coupling – even if its heavier. Higgsino-like states only play a role for squarks of the third generation due to their Yukawa-coupling.

Inverting the mass hierarchy in the coloured sector basically inverts the decay scheme of squarks and gluinos:

$$\begin{aligned} &\tilde{q} \to \tilde{g}q \\ &\tilde{g} \to \tilde{\chi}^0 qq', \qquad \tilde{g} \to \tilde{\chi}^\pm qq' \,. \end{aligned}$$

Independent of the mass hierarchy are the decays of the gauginos. They decay via their gauge or Higgs content, depending on the mixing. The most likely two-body-decays are

$$\begin{aligned} &\tilde{\chi}_i^0 \to Z\tilde{\chi}^0, \quad W\tilde{\chi}_j^\pm, \quad h^0\tilde{\chi}_j^0, \quad \ell\tilde{\ell}, \quad \nu\tilde{\nu}, \\ &\tilde{\chi}_i^\pm \to W\tilde{\chi}_j^0, \quad Z\tilde{\chi}_j^\pm, \quad h^0\tilde{\chi}_j^\pm, \quad \ell\tilde{\nu}, \quad \nu\tilde{\ell} \,. \end{aligned}$$

In principle, decays into heavier Higgs-bosons or a quark–squark pair are also allowed. In a typical mass scheme, however, these modes are highly suppressed or not allowed. Three-body-decays may occur e.g. for small differences in mass between the two lightest neutralinos. The heavier particle can then decay into the lighter one and an off-shell gauge or Higgs-boson.

Similar as for the squarks, the sleptons decay to gauginos and corresponding leptons, depending on their quantum numbers and the mixing configuration. Slepton decays involving Yukawa-couplings are rare due to the small coupling constants and the typically heavier Higgsino-like gauginos. Typical two-body-decays of sleptons are

$$\tilde{\ell} \to \ell\tilde{\chi}_i^0, \quad \tilde{\ell} \to \nu\tilde{\chi}_i^\pm, \quad \tilde{\nu} \to \nu\tilde{\chi}_i^0, \quad \tilde{\nu} \to \ell\tilde{\chi}_i^\pm \,.$$

For the model of GMSB, the light gravitino is the LSP every other sparticle ultimately decays into. Due to its small coupling, this decay usually marks the last step of a decay cascade. Here, the involved NLSP is only able to decay into the gravitino.

The majority of these considerations holds for any SUSY model, most notably for the model of GMSB introduced in section 2.2.2 as depicted in fig. 2.15(a). However, they do not only describe models such as GMSB and their manifold signatures, but they also motivate the more phenomenological approach in the search for SUSY introduced in the forthcoming section.

2.2.4 Simplified model of gluino pair-production

The requirement of SUSY being broken and the desire to describe it by only few parameters lead to the development of a multitude of different *full-scale* models such as GMSB[12]. They often propose a specific mechanism of SUSY breaking and impose requirements to simplify the model under consideration of experimental results or theoretical constraints. Since apart from said constraints and measurements, no further information on BSM physics let alone SUSY is yet available, there is no reason for Nature to prefer one breaking mechanism, i.e. full-scale model, over another. As long as a model is not excluded, it is thus as legitimate to be searched for as any other model. The choice to search for a model of GMSB in the context of this thesis, for example, was predominantly due to its abundance of τ-lepton signatures.

The experimental accessibility of signatures of full-scale models is another debatable point. GMSB is able to produce a wealth of SM final state signatures. Even upon only considering τ-leptons final states, the potential presence of additional lighter leptons, or more or fewer strongly interacting particles poses a challenge to the design of any analysis.

Although a full-scale model such as GMSB covers, in principle, all available phase-space including a multitude of signatures, its realisation in an actual analysis context is subject to limitations. In order to keep the number of free parameters small, the remaining parameters are fixed, cf. section 2.2.2 for the assumptions on the GMSB parameters beyond Λ and $\tan\beta$. Any result obtained in an analysis of such a full-scale model reduced to few parameters is only valid under said constraints and does hence not convey information on the theory behind the model in general.

Ultimately, no experimental hint for the highly desirable theory of SUSY has been found yet. In addition to the aforementioned ignorance of which a full-scale model is realised in nature, this striking point gave rise to a shift in the paradigm of SUSY searches. The focus of most SUSY searches shifts to the search for a new kind of models, so-called *simplified models* [96–98].

A simplified model comprises only few if not just one diagram – the number of possible decays is small as is the number of involved particles. It uses effective vertices instead of more complex couplings if need be. It is typically parametrised by pseudo-observables such as the masses of the involved particles or the branching fractions of their decays instead of experimentally inaccessible parameters like Λ or $\tan\beta$. This practically inverted approach with respect to the search for full-scale models comes with several desirable features.

Among the phenomenological advantages is the fact that the model can be designed such that its production cross-section is high by choosing abundant initial state particles. Moreover, the decay cascade of the model can be designed to have distinct features to allow for high separation from SM processes or high acceptance and efficient detection in the experiment.

The limitation to a small set of processes and hence final states allows for precisely tailored analyses. The level of information extracted from the experimental results is thus higher as for full-scale models where only a fraction of the total final states can be analysed at a time.

Ambivalent features lie with the results and their interpretation as well as their re-usability. Since simplified models are often parametrised by the masses of the involved particles, the results in the case of no discovery comprise upper limits on said particle masses. While the limits obtained on the parameters of full-scale models are valid for any process allowed within the model, limits on particle masses obtained with simplified models only hold for the exact model. Although the simplified model results are not particularly useful when considered stand-alone, they can be of great help when recasting obtained results to new models of theory for which no designated analysis yet exists. A newly proposed model may produce physics signatures which are covered by simplified models for which analysis results exist.

[12] The term *full-scale model* is only used to distinguish models of SUSY that target a particular breaking mechanism and which are inclusive in their particle content from the *simplified models* introduced in this section and studied in this thesis.

These results may now be re-used to assess the probability of the new model being realised in nature without the need to perform a full data analysis tailored towards the model. In addition to providing comprehensive results, i.e. upper limits on particle masses instead of upper limits on model parameters from which masses first need to be calculated, the striking advantage of simplified model searches hence is the usage in studies of other, new models. More specifically, the independence of a simplified model of any higher-level theoretical considerations such as symmetry breaking mechanisms, make it so versatile.

The ultimate goal in searches for new physics using simplified models can be considered twofold: while the analysis of many simplified models allows for reliable statements about models not yet searched for, each analysis on its own still possesses discovery potential in the specific piece of phase-space it covers. Simplified models can thus also be used to cover much phase-space of interest rather efficiently. The latter argument in particular motivates the efforts of the ATLAS and CMS collaboration in searches for simplified models at the beginning of Run-2 of the LHC.

Since the number of potential simplified models is as large as the number of available processes in any new model of BSM physics, the choice which model to search for in an analysis is crucial. The key design aspects of abundance, detectability, and distinction have already been mentioned earlier. They can be extended by the question of usability for re-interpretation. The more generic a simplified model is, the more versatile it is for the recasting of results. The balance between all of these characteristics is challenging to find and an art on its own.

The simplified model searched for in the presented analysis is inspired by signatures of the GMSB model and conserves R-parity. At a hadron collider like the LHC, the choice to search for gluinos is evident. Studies in [99] have found that abundant and well-detectable decay cascades involve two intermediate steps via a gaugino and a slepton of the third generation to the LSP. Pair-produced gluinos, e.g. via the diagrams depicted in fig. 2.16, decay into two quarks and a gaugino. The three-body-decay of the gluino occurs at an effective vertex. The decay into either the light chargino or the second-to-lightest neutralino are equally probable. The gauginos then decay into pairs of a third generation slepton—the NLSP—and the corresponding lepton. The NLSP finally decays into the lightest neutralino LSP and a corresponding lepton.

The choice to allow two decays modes of both the gluino and the gauginos as well as the decision for a neutralino LSP add more generality and flexibility to the model. It is more versatile and can be part of a substantially larger number of more complex models, allowing for a broader range of re-interpretation. The diagram showing the possible decay cascades and summarising these considerations is depicted in fig. 2.19.

With the branching fractions of all involved sparticles fixed, only their masses remain as potential free parameters. The masses in each decay step are fixed to be equal, i.e. $m(\tilde{\tau}) = m(\tilde{\nu}_\tau)$, $m\left(\tilde{\chi}_1^\pm\right) = m\left(\tilde{\chi}_2^0\right)$, leaving four possible free parameters. The dimensionality of the model's parameter-space is reduced further. The gluino mass drives the cross-section and is hence chosen as one of two final parameters. Since the LSP mass is crucial as well on the theory side, e.g. in models of particle dark matter, as for experiments, cf. chapter 5, it is chosen to be the second free parameter. The masses of the intermediate gauginos and sleptons are coupled to the difference of the gluino and LSP masses, cf. eq. (2.10).

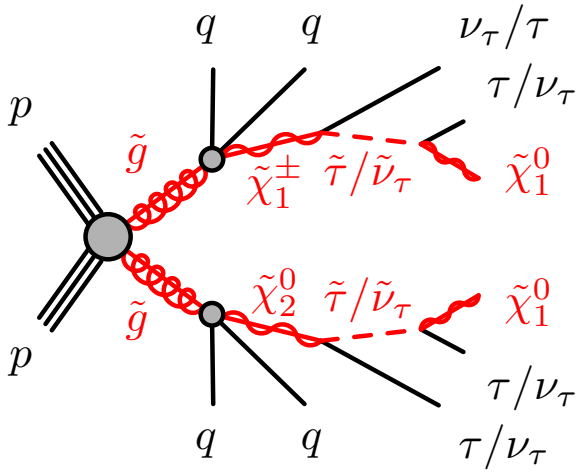

Figure 2.19: Decay cascade of the simplified model of gluino pair-production in proton–proton collisions [9].

$$\begin{aligned} \Delta_m &= m(\tilde{g}) - m\left(\tilde{\chi}_1^0\right) , \\ m(\tilde{\tau}, \tilde{\nu}_\tau) &= m\left(\tilde{\chi}_1^0\right) + \frac{\Delta_m}{4} , \\ m\left(\tilde{\chi}_1^\pm, \tilde{\chi}_2^0\right) &= m\left(\tilde{\chi}_1^0\right) + \frac{\Delta_m}{2} \\ &= m(\tilde{\tau}, \tilde{\nu}_\tau) + \frac{\Delta_m}{4} \end{aligned} \tag{2.10}$$

Early results of a search for this simplified model are displayed as an exclusion contour in the two-dimensional parameter-plane of the gluino and the LSP mass, depicted in fig. 2.20. These results have been obtained in a similar fashion in an earlier version of the analysis presented here [9] and represent its starting point.

The following point regarding the choice of parametrisation of the simplified model is to be noted: although the choice for the gluino and LSP mass to be the two free parameters can be motivated, any choice is just as legitimate. In fact, the choice of parameters is almost never optimal. The complexity of this *simplified model* would, in principle, require eight free parameters (all sparticle masses and the two branching fraction) and could even comprise more (e.g. gaugino or slepton mixing). With eight free parameters, it is already less *simplified* than the full-scale model of GMSB. In addition to the debatable attribute of being *simplified*, practical aspects such as sampling the parameter-space with limited computing resources or aspects of comprehension such as visualisation of the parameter-space, are to be considered.

The parametrisation of an ever so aesthetic and attractive phenomenological model to make it a simplified model is hence challenging. The compromise between the adequate description of the model's complexity and a feasible realisation for it to be analysed is difficult to make.

A possible tonic though not a remedy to this issue has been found in [99]. Explorations have shown that a coarse-grained evaluation of the influence of so-called *hidden parameters*, i.e. the model parameters that are not free but could still be important, can help to ensure the validity of results obtained using the model – despite a possible over-simplification.

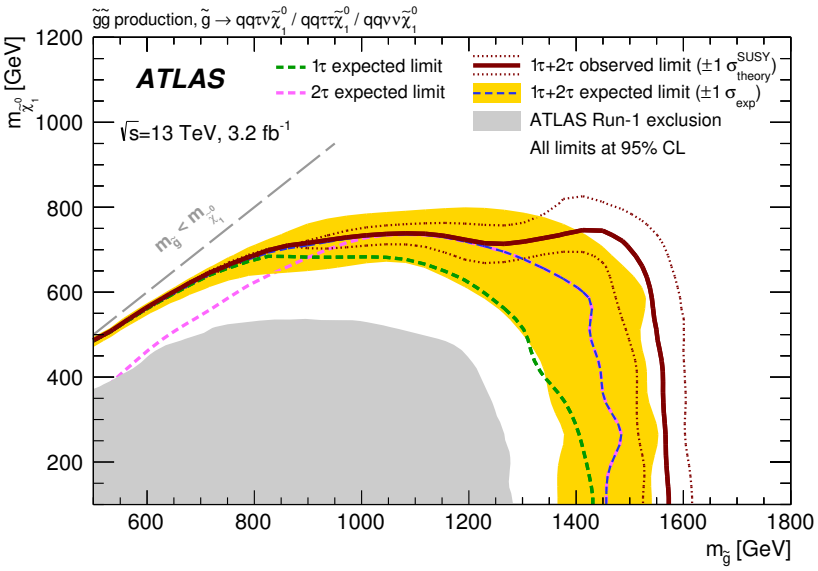

Figure 2.20: Simplified model, first exclusions in the parameter-space at $\sqrt{s} = 13\,\text{TeV}$ [9].

2.2.5 Current status of SUSY

Despite its aesthetics and versatility, no experimental sign of SUSY has been observed yet. The ongoing endeavours of searches for full-scale models such as GMSB or simplified models try to infer properties of SUSY if it should exist and narrow down the remaining available parameter-space further. Elaborate searches for specific models in data are extended by low energy measurements, results from flavour physics, astronomical observations and, in particular, precision measurements of properties of the SM Higgs-boson, limiting the possibilities for SUSY to exist further.

The impact of all these constraints is evaluated simultaneously by fits of global likelihoods, comprising a vast set of seemingly uncorrelated measurements. The utilisation of these likelihoods allows to sample large parameter-spaces of different SUSY models. This way, areas of parameter-space are found where SUSY predictions are at least as compatible with measurements as the SM or predict the observation with even less tension. A quantification is achieved by means of a p-value for each sampled point in parameter-space, obtained using Monte Carlo pseudo-experiments.

Indeed, these sampling approaches find that many full-scale models are under severe tension by current measurements. A strongly simplified version of the MSSM, the *constrained MSSM* (cMSSM) [100–102], is, in fact, even excluded [103]. Two-dimensional projections of scans across the five-dimensional parameter-space of the cMSSM performed by the Fittino collaboration are depicted in figs. 2.21(a) and 2.21(b). The χ^2 distribution at the best fit point on which the p-value calculation is based in shown in fig. 2.21(c), giving a p-value smaller than 5%, resulting in an exclusion of the model at a confidence level of 95%.

Models like the cMSSM only cover a small fraction of possible solutions to the entire MSSM. Condoning a reduced predictive power and only considering the most stringent theoretical constraints, it is possible to construct slightly more complex models which are still able to predict the current set of observations, such as the *phenomenological MSSM* (pMSSM)[104, 105]. With $O(20)$ free parameters, such models are still not arbitrary and allow for more possible mass spectra and coupling structures within the MSSM than e.g. the cMSSM. Similar studies as for the cMSSM, indeed, suggest enough free parameter-space for the pMSSM to exist [106, 107]. Similar to the two-dimensionally projected scans in

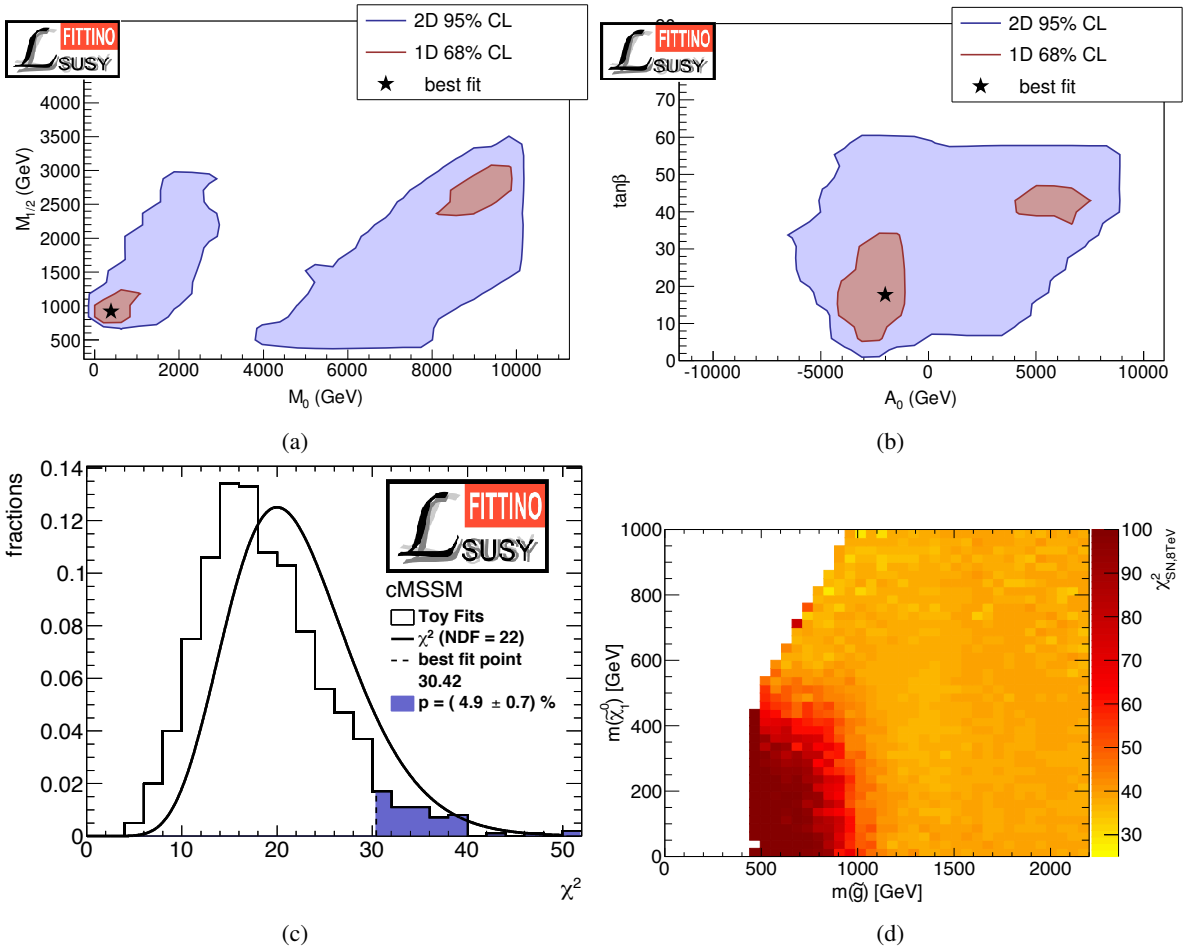

Figure 2.21: Results of a parameter scan for the cMSSM in the m_0–$m_{1/2}$ plane (a) and the A_0–$\tan\beta$ plane (b), as well as the χ^2 distribution used to obtained the $p-$value at the best fit point (c) by the Fittino collaboration [103]. A two-dimensional χ^2 distribution in the gluino–neutralino mass-plane obtained by the SCYNet collaboration [107] is depicted in (d).

the cMSSM, fig. 2.21(d) shows a χ^2 distribution for the pMSSM-11 in the gluino–neutralino mass-plane. Phenomenologically motivated models such as the pMSSM are key motivational aspects as well as use cases for searches for simplified models as the one presented in the context of this thesis.

CHAPTER 3

The Large Hadron Collider and the ATLAS Experiment – The Biggest Tools to Study the Smallest Objects

The most probable manifestations of SUSY in experimental observations are expected to be the decay patterns of new heavy particles. The discovery of SUSY in this fashion depends upon the capability to produce said new particles, to measure the signatures of their decay products, and to reconstruct their properties from these measurements. These fundamental requirements are well met by the ATLAS experiment at Large Hadron Collider. The following sections introduce the experimental environments as well as the techniques employed to reconstruct and identify individual objects from the measured signatures in the ATLAS detector. They are loosely based on [15].

3.1 The LHC accelerator

The Large Hadron Collider (LHC) [5] is a particle accelerator and collider, housed in an underground tunnel of approximately 27 km underground the Swiss–French border near Geneva, Switzerland. It features two rings, each storing protons of energies up to 7 TeV. The highly relativistic protons circulate in the rings grouped into up to 2800 so-called *bunches* of 25 ns time distance from each other.

The protons are accelerated in multiple stages of an injector complex before entering the LHC at energies of 450 GeV. Starting from the Proton Synchrotron Booster (PSB) [108] via the Proton Synchrotron (PS) [109] and the Super Proton Synchrotron (SPS) [110], the LHC pre-accelerator chain is schematically depicted in fig. 3.1. The bunch structure of the LHC is built up by staggering subsequent fills of protons from one pre-accelerator to the next, larger one. In the LHC, the beam is then stored and accelerated to the desired energy while circulating in opposite directions in the respective rings.

The acceleration process of an electrically charged particle with charge q can be described by its energy gain ΔE_{kin} on traversing an electrical field $\vec{E}$ along a path $\vec{s}$:

$$\Delta E_{\text{kin}} = \int_{\vec{s}} \left(\vec{F} \cdot \mathrm{d}\vec{s}\right) = q \int_{\vec{s}} \left(\vec{E} \cdot \mathrm{d}\vec{s}\right) \tag{3.1}$$

The technical realisation of this process is similar for all involved accelerators. By feeding high-frequency (HF) radio waves into a cylindrical conducting cavity, a standing wave can be formed. Upon traversing the cavity, the particle is accelerated by the longitudinal component of that wave, gaining energy. In the optimal case, the particle is in phase with the HF field in the cavity.

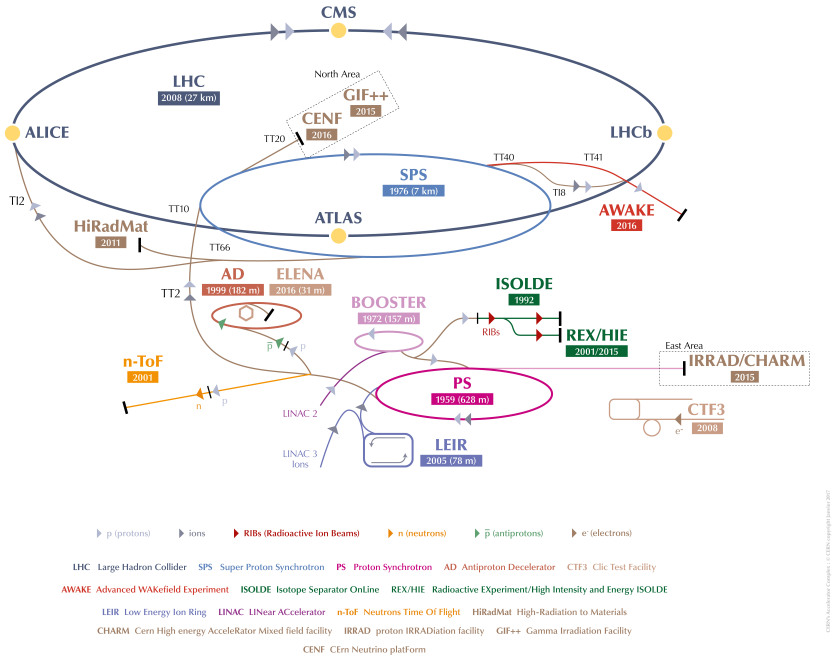

Figure 3.1: The CERN accelerator complex, including the LHC and its pre-accelerators [111].

In the LHC, eight such superconducting cavities are present in every ring, operated at a frequency of 400.8 MHz, producing field gradients of 5.5 MV m^{-1}. The ring-structure[1] of the LHC allows the particles to pass each acceleration complex multiple times, gaining energy every time until the desired beam energy is reached.

The motion of the particles inside the ring is controlled by exploitation of the Lorentz force. An electrically charged particle moving at velocity $\vec{v}$ inside a magnetic field $\vec{B}$ experiences a force perpendicular to its direction of motion and the magnetic field:

$$F_{\text{Lorentz}} = q\left(\vec{v} \times \vec{B}\right) .$$

A total of 1232 dipole magnets along the LHC ring keep the particle beams on their circular track. The coils of each of these 15 m long magnets is made of superconducting Nb-Ti cables, cooled down to 1.9 K. The dipole magnets reach up to 8.36 T in field strength. Their *two-in-one* design allows for both beams of same charged particles circulating in opposite directions to be deflected by the same magnetic field. In addition to the dipole magnets used for confining the beams to their circular track, a total of 858 quadrupole magnets are employed to focus the beam from all directions. Multipole magnets of up to dodecapoles are used to correct for aberration effects during the focusing and further losses of beam quality due to other disturbances.

The advantage of the ring-structure of using the same acceleration complex in every revolution of the beam comes at the price of synchrotron radiation. Deflection of an electrically charged particle results in

[1] An alternative to circular accelerators using one acceleration complex multiple times, is a linear accelerator. Here, one long straight line of many cavities is traversed by the particles. This setup, however, is less cost-effective for protons as for lighter leptons. Proposed future linear lepton colliders are the ILC [112] and CLIC [113].

an energy loss of the particle in the form of radiation. The amount of energy lost for a highly relativistic particle in synchrotron radiation follows the proportionality

$$\Delta E_{\text{sync}} \propto \frac{q^2 E^4}{R m^4} .$$

Synchrotron radiation losses increase with the energy of the particle E in fourth power while they decrease with its mass m in fourth power and the radius R of the trajectory. The consequence of this proportionality is the fact that circular accelerators at high energies are preferred for heavy particles such as protons or even ions, while linear accelerators are preferred for light particles such as electrons[2].

After their acceleration phase, the protons are stored for up to 24 h and brought to collision at four interaction points along the ring, each housing one of the large LHC experiments, cf. fig. 3.1. The ATLAS (A Toroidal LHC ApparatuS) detector is used in the presented analysis and introduced in detail in the forthcoming section 3.2. The CMS (Compact Muon Solenoid) experiment [7] is located at the beam intersection opposite of ATLAS. It is similarly designed multi-purpose detector as ATLAS and features a similarly broad physics program. The LHCb detector [115] is specifically designed to detect b-quarks, focussing on a heavy-flavour physics program. The ALICE (A Large Ion Collider Experiment) experiment [116] is designed to detect and study collisions of heavy ions, which is another physics program of the LHC in addition to collisions of protons.

3.2 The ATLAS detector

The data of proton–proton collisions provided by the LHC and analysed in this thesis is recorded by the ATLAS detector. It is one of the two multipurpose experiments in the LHC project and primarily designed to detect the decay products of heavy particles produced in collisions. A computer generated schematic of the ATLAS detector and all its sub-systems is depicted in fig. 3.2.

It is designed in a typical onion-like multilayer fashion of different sub-detectors surrounding the collision point in its centre. Its cylindrical shape is sub-structured into a barrel part for the detection of particles emerging transversely to the beam direction, and two end-cap parts detecting measuring particles close to the beam. The coordinate system of ATLAS is right-handed, its origin placed in the nominal interaction point (IP) in the centre of the detector. The z-axis is oriented along the beam pipe, the x-axis points from the IP to the centre of the LHC ring, and the y-axis points upwards. In the transverse plane, cylindrical coordinates (r, ϕ) are used, ϕ being the azimuthal angle around the beam pipe. As the third component, the pseudorapidity η is defined as $\eta = -\ln\tan(\theta/2)$, θ being the polar angle. Usage of the pseudorapidity instead of the polar angle is well motivated at hadron colliders: in contrast to the polar angle, the pseudorapidity is invariant under longitudinal Lorentz boosts[3], i.e. the difference in pseudorapidity between two particles $\Delta\eta$ is invariant under a boost parallel to the beam axis. The latter is neither known nor accessible at a hadron collider due to energy of the interacting partons being unknown, in contrast to the energy of the accelerated proton.

[2] Before the LHC, the same tunnel housed the Large Electron Positron collider (LEP) [114]. With the same radius as the LHC, the synchrotron radiation losses per revolution for an electron at an energy of 100 GeV in the LEP accelerator amounted to 3 GeV. At the nominal beam energy of the LHC, the losses per turn for a proton only amount to 6 keV. The necessary compensation of these losses by the HF power supplied for the cavities effectively limits the maximum energy for electrons in circular colliders.

[3] This statement is only exactly true for massless particles. For these, the pseudorapidity is exactly equal to the relativistic rapidity $y = \frac{1}{2}\ln\frac{E+p_L}{E-p_L}$ with p_L being the longitudinal momentum, parallel to the beam direction. Due to the high energies of particles produced at the LHC with respect to their masses, it is, however, safe to assume that $\eta = y$ holds

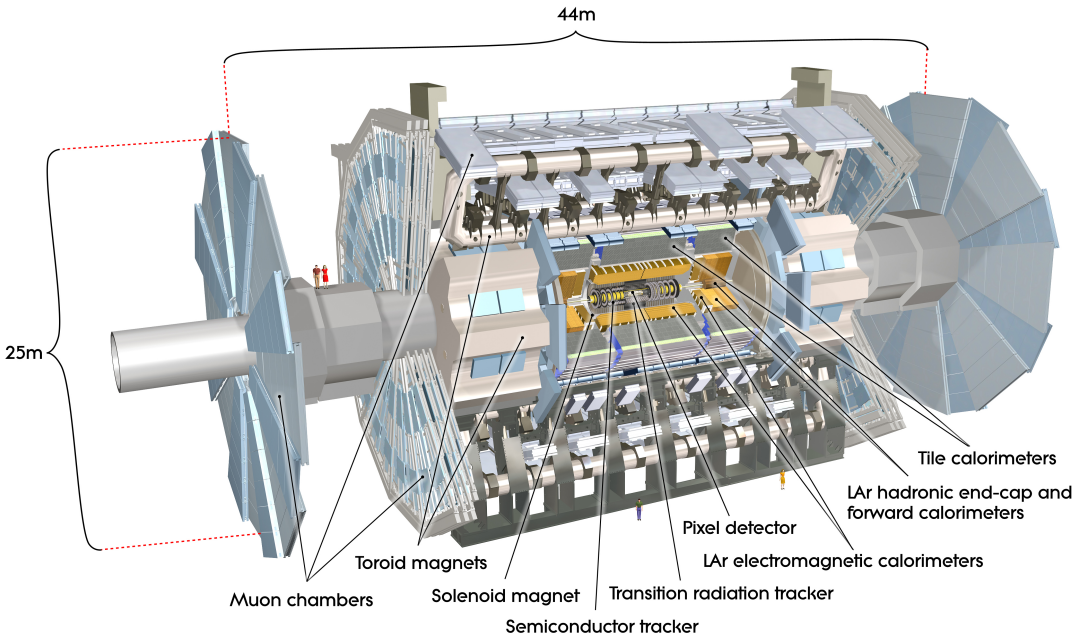

Figure 3.2: Schematic overview of the ATLAS detector and its sub-systems [117].

Using these coordinates, it is convenient to introduce a measure of distance that is also invariant under longitudinal Lorentz boosts:

$$\Delta R = \sqrt{(\Delta\eta)^2 + (\Delta\phi)^2} \, .$$

ΔR can be universally employed to quantify distances between objects in detectors at hadron colliers.

The forthcoming sections provide a brief overview of the different sub-detectors of ATLAS and their working principles. A detailed overview can be found in [6].

3.2.1 The inner detector and solenoid magnet

The very centre of the ATLAS experiment is taken up by the inner detector (ID). It is designed to record the tracks of electrically charged particles traversing it and to measure their momentum. The latter is possible due to the immersion of the ID in a 2 T magnetic field, generated by a superconducting solenoid coil enclosing the entire ID volume. Similar to protons on their tracks in the LHC, the trajectories of charged particles in this magnetic field are bent by the Lorentz force. The sign of a particles's charge can be inferred from the direction of deflection, while their momenta can be determined from the radius of curvature given the value of the charge. Measurements of particle properties in the ID are supposed to affect the particle as little as possible in order to make energy measurements in the calorimeter system as precise as possible. The material budget of the ID is hence kept to a minimum. A schematic overview of the ATLAS ID and its sub-systems is depicted in fig. 3.3. The individual sub-detectors are briefly described in the forthcoming paragraphs.

The pixel detector The pixel detector is the innermost sub-system of the ATLAS ID. In the barrel region, it consists of four layers of silicon pixel sensors, the end-cap regions are covered each by three

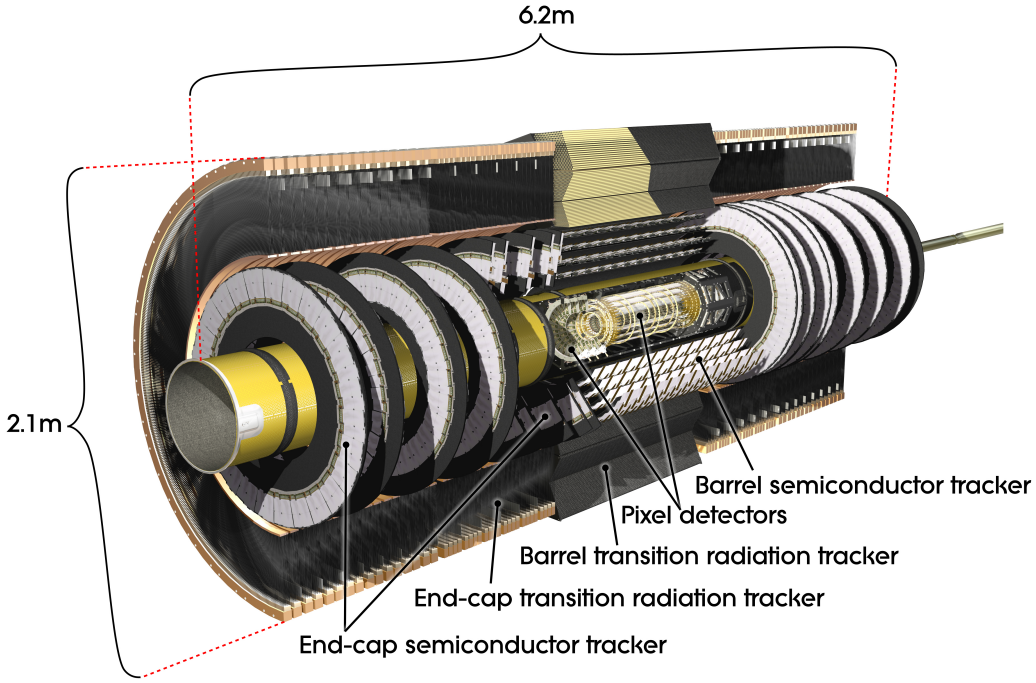

Figure 3.3: Schematic overview of the ATLAS inner detector and its sub-systems [118].

discs of the same pixels. This setup allows for detection in the range of $|\eta| < 2.5$. The innermost barrel layer has a radius of 25.7 mm [119], the outermost layer resides at a radial distance of 122.5 mm. The total of over 86 million pixels with a size of 400 µm × 50 µm are grouped into multiple chips and modules. A decrease in the density of employed sensors with increasing vicinity to the IP accounts for the high occupancy of the system with traversing particles closest to the IP. The main purpose of the pixel detector is the provision of high-precision measurements of the innermost hits. This way it helps to extrapolate tracks to the primary or secondary vertices and allows for the reconstruction of the latter.

The silicon tracker The next layer in the onion-like structure of the ATLAS detector, enclosing the pixel detector, is the silicon tracker (SCT). In the barrel, four layers extend from radii of 299 to 514 mm. The end-caps are covered by nine discs each, allowing for a total coverage of again $|\eta| < 2.5$. The SCT is also grouped into modules of two layers, each comprising 768 active silicon stripes with a pitch of 80 µm in a back-to-configuration. The two layers of each module are tilted with respect to each other by 20 mrad. This setup enables spatial resolution also along the longitudinal axis of the strip. Depending on the position of the strip inside the SCT, the strip length varies between 5 cm and 12 cm. The design of the SCT provides at least four hits to the measurement of a charged particle's track with a resolution in the r–ϕ-plane of 17 µm and 580 µm in the z-direction.

The transition radiation tracker The transition radiation tracker (TRT) is the outermost of the three ID sub-systems. It extends the ID volume to radii of up to 1 082 mm from the IP. While the pixel detector and the SCT aim at a high spatial resolution, particularly in the harsh environment close to the IP, the design goal of the TRT is different: it aims at providing many hits for the reconstruction of tracks and the capability of particle identification.

The TRT follows the basic principle of a gaseous drift-tube detector. Small straws of 4 mm in diameter are filled with a gas mixture of Xe:CO_2:O_2 (70:27:3)[4]. Charged particles traversing a gas-filled straw cause ionisation in the gas. Between the inner wall of a straw and a 30 µm thin gold-plated tungsten wire [120] in its centre, a voltage is applied, causing an avalanche-like amplification of ionisation primary electrons. The electrons generated in the avalanche drift towards the wire and are collected as an analog signal. In the barrel region of $|\eta| \leq 1.0$, 52 544 straws of 144 cm length are aligned parallel to the beam axis, arranged in 73 layers [121]. The end-cap region $1 < |\eta| < 2.1$ is covered by 122 880 straws of 37 cm in length, arranged in 160 layers [122]. In contrast to the barrel region, here, the straws are aligned radially in 20 wheel-like modules of 8 layers each. On average, a charged track traverses 35 TRT straws, allowing the TRT to significantly enhance the track reconstruction capability of the ATLAS detector.

In addition to its contribution to the track reconstruction, the TRT allows for the identification of particles exploiting the phenomenon of transition radiation [123]. When a charged particle passes the boundary between two materials of different relative permittivities, there is a probability for it to emit an X-ray photon, referred to as *transition radiation* (TR). The energy of the photon depends on the difference in permittivity, while the emission probability is proportional to the Lorentz boost γ of the particle. By interleaving thin foils of radiator material, i.e. alternating layers of materials of different permittivity, between the straws, the probability for the emission of TR is enhanced. The detection of TR photons is realised by means of the photo-electric effect in the noble gas of the straw-tubes and the subsequent detection of the freed electron in a similar fashion as for the ionisation electrons. Due to their low mass compared to, e.g. muons or pions, electrons come with a substantially higher γ-value, and are hence more likely to emit TR. By discriminating ionisation from TR signals in the readout process of the straws, it is possible to distinguish electrons from other charged particles, particularly pions. Information from the TRT particle identification (PID) then contributes to the overall identification of electrons.

Another distinct feature of the ATLAS TRT is its capability to measure the specific energy deposition of a traversing particle in the gas $\mathrm{d}E/\mathrm{d}x$, also feeding into the TRT PID and allowing for the identification of multi-charged particles [124].

3.2.2 The calorimeter system

The calorimeter system is intended to fully stop arriving particles and measure their energies. Due to the manifold spectrum of particles that pass the ID and the solenoid magnet, and their different preferred interactions, the calorimeter system consists of different sub-detectors. A schematic overview of the ATLAS calorimeter sub-systems enclosing the ID and solenoid magnet is depicted in fig. 3.4.

The first layer of the central calorimeter system is referred to as the *electromagnetic calorimeter* (ECAL). Its purpose lies with the detection of electrons and photons. Both of these particle types undergo cascade reactions, producing electrons, positrons, and photons upon reacting electromagnetically with the detector matter. The resulting detector signature is referred to as an *electromagnetic shower*[5]. In contrast to electrons and photons, most stable or longer-lived hadrons (i.e. protons, neutrons, charged pions and kaons) do not leave fully contained signatures in the ECAL and cannot be measured completely there. They undergo similar cascade reactions as electrons and photons, referred to as *hadronic showers*. They exhibit a larger extension—both lateral and longitudinal—and are subject to larger fluctuations[6].

[4] Due to irreparable gas leakage of the TRT during operation in Run-1 of the LHC, parts of the system are operated using a more cost-effective Ar:CO_2:O_2 (70:27:3) mixture instead of the expensive Xe-mixture.

[5] Electromagnetic showers are characterised by the radiation length X_0 as the distance after which the average energy of an incoming electron has decreased to $1/e$ of its initial energy due to bremsstrahlung [15].

[6] Similar to electromagnetic showers, hadronic showers are characterised by the interaction length λ via the the free path length of a pion or neutron, depending on the definition, cf. [38].

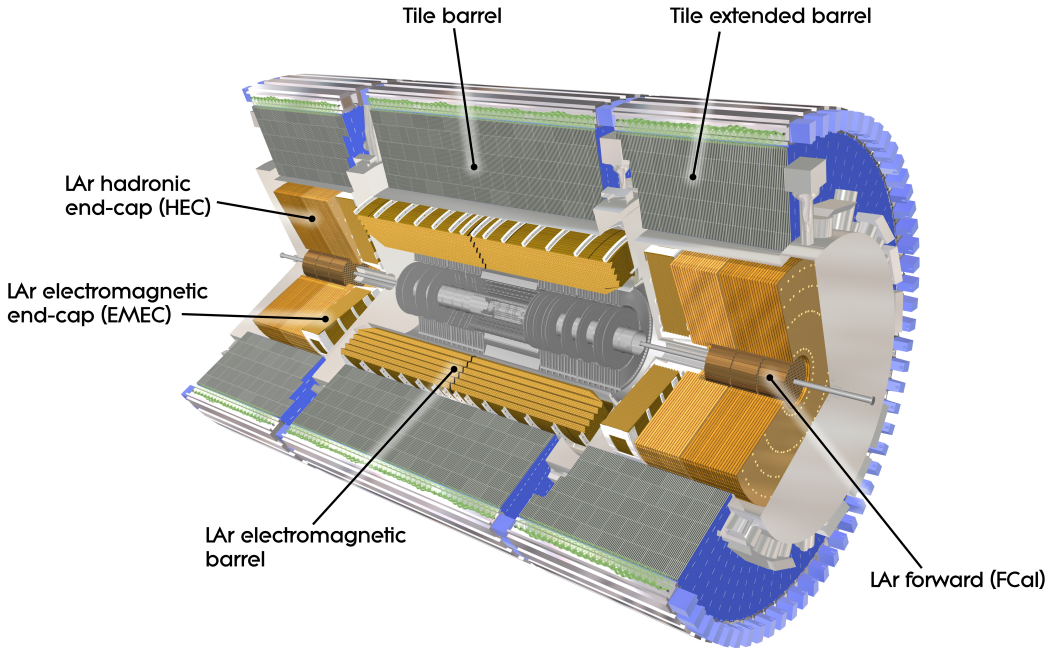

Figure 3.4: Schematic overview of the ATLAS calorimeter system and its sub-systems [125].

The layer enclosing the ECAL is thus dedicated to those particles, their containment and measurement of their properties – the hadronic[7] calorimeter (HCAL).

Dedicated calorimeter systems are used in the forward regions of the ATLAS experiment. Due to the boost of the colliding protons, the flux of incoming particles is particularly high here. The calorimeter design for these regions is hence accounts for the more demanding conditions to prevent e.g. radiation damage. The forthcoming paragraphs briefly introduce the aforementioned calorimeter sub-systems.

The electromagnetic calorimeter The general structure of the ECAL is similar to the ID: a barrel part covers the region of $|\eta| < 1.475$, while the end-cap region extends to $|\eta| < 3.2$. The ECAL central part up to $|\eta| < 2.5$ comes in three layers. The innermost layer is of fine granularity, allowing for precise photon detection with a resolution of $\Delta\eta \approx 0.003$. The second layer is the largest and provides a granularity of $\Delta\eta \times \Delta\phi = 0.025 \times 0.025$. Depending on η, the depth of the ECAL varies between 22 and 38 X_0 .

The ECAL is composed of steel-clad lead plates which are folded in an accordion-like fashion. They serve as absorber plates and are interleaves with electrodes. In a 2.1 mm gap between the absorber and the electrode, a honeycomb spacer structure is filled with liquid Ar, which acts as an ionisation and detection medium simultaneously. Due to the boiling point of Ar being 87 K, the ECAL system is operated at cryogenic temperatures within three cryostats, one for each end-cap and the barrel module.

The hadronic calorimeter Enclosing the ECAL system, the different components of the HCAL measure properties of hadronic particles. The barrel part up to $|\eta| < 1.7$ is formed by a sandwich structure

[7] Although in a strict sense, the term *hadronic* would refer to the calorimeter being composed of hadrons, it has been established as reference to a calorimeter system designed to detect hadrons. A more proper wording would be *hadron calorimeter*.

of steel and plastic scintillator tiles referred to as *Tile Calorimeter* or *Tilecal*. The Tilecal consists of 64 wedge-like modules, forming a hermetic barrel of a length of 7.4 λ. The signal of the scintillator tiles is passed to photomultipliers and is propagated further by wavelength-shifting fibres. Fibres from multiple tiles are grouped together, forming three layers of cells of depths of 1.5, 4.1, and 1.8 λ, respectively. While the lateral size of the first two layers is $\Delta\eta \times \Delta\phi = 0.1 \times 0.1$, the third layer is grained twice as coarse with $\Delta\eta \times \Delta\phi = 0.2 \times 0.1$.

The hadronic end-cap calorimeter (HEC) covers $1.5 < |\eta| < 3.2$. Similar to the ECAL, the HEC utilises liquid Ar as an active medium and is housed in the same cryostat as the end-cap ECAL. The absorber material is exchanged for copper plates stacked parallel to the beam direction. The HEC is structured into two sub-modules of 24 copper plates of 25 mm and 16 plates of 50 mm thickness, respectively. The 8.5 mm gap between two absorption layers is filled with liquid Ar. A segmented readout electrode in the centre of each gap provides a spatial granularity of $\Delta\eta \times \Delta\phi = 0.1 \times 0.1$ for $|\eta| < 2.5$ and $\Delta\eta \times \Delta\phi = 0.2 \times 0.2$ for regions closer to the beam direction.

The forward calorimeter The calorimeter system is completed by the forward calorimeter (FCAL), covering the region of up to $|\eta| < 4.9$. Due to the high occupancy and radiation doses the detector material has to withstand in this region, the FCAL also utilises the liquid Ar technique. The high particle flux is coped with by a substantially reduced gap size between the absorption layers, allowing for a faster timing. The absorber material is a metal matrix in which ten-thousands of holes are drilled, parallel to the beam axis. Into these holes, small rods serving as electrodes are inserted. The remaining sub-millimetre gap between a rod and the matrix is then filled with liquid Ar. The FCAL is sub-structured into three modules on each side. The innermost modules are machined from copper, the outer ones from tungsten. The copper modules are optimised for the measurement of electromagnetic showers and have a depth of 28 X_0 (2.7 λ). The tungsten modules, in turn, are designed to measure hadronic showers and come at a depth of 3.6 λ (90 X_0) each.

3.2.3 The muon system and toroid magnet

The outermost detector is the muon system. Since muons neither undergo hadronic interactions nor do they emit substantial amounts of bremsstrahlung, they are the only detectable particles that traverse all of the aforementioned systems. For the detection and identification of muons, an additional independent tracking system is installed. A schematic overview of the muons system is depicted in fig. 3.5. The muon tracking detectors are marked in light blue, while the magnet system necessary for particle tracking is drawn in yellow.

The muon system covers the range of $|\eta| < 2.7$ and is designed to achieve a momentum resolution of 10% for a muon track of $p_{\mathrm{T}} = 1\,\mathrm{TeV}$. The magnet system necessary for the track measurement in the barrel region consists of eight air-core coils aligned to provide a magnetic field parallel to the beam axis. They generate a toroidal magnetic field of approximately 0.5 T around the detector. In the end-cap region, eight similar coils generate a toroidal field of approximately 1.0 T. While each barrel coil is housed in a separate cryostat, the coils of each end-cap region share one common cryostat.

The muon detection system consists of different components, tailored towards different tasks. Precision measurements of the muon tracks are performed by the Monitored Drift Tube (MDT) chambers. In the barrel region, they are installed as three cylinders of 5 m, 7.5 m, and 10 m, respectively, enclosing the barrel toroid coils. In the forward region, they come as four wheel-modules at distances of 7.4 m, 10.8 m, 14 m, and 21.5 m from the IP, respectively. Only in the very forward region of the innermost wheels, $2 < |\eta| < 2.7$, Cathode Strip Chambers (CSCs) are used to provide better time resolution under consideration of the high particle flux.

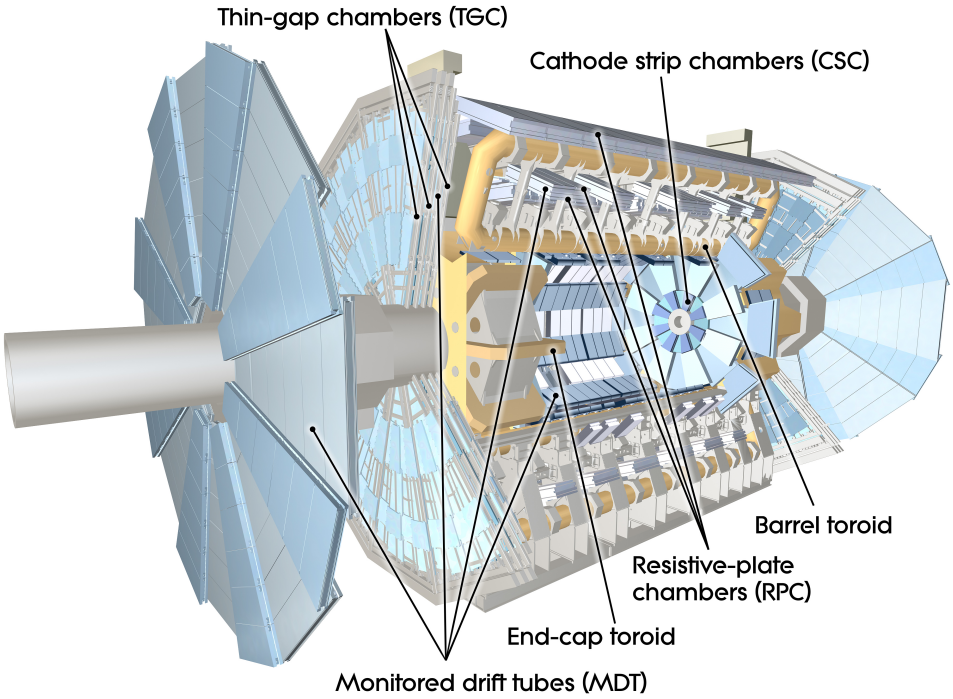

Figure 3.5: Schematic overview of the ATLAS muon system and its sub-systems [126].

The underlying technology of the MDTs is similar to that of the TRT: 432 drift tubes of approximately 3 cm diameter are filled with $ArCO_2$ at a pressure of 3 bar. The achieved position resolution of a single tube of 80 µm gives a resolution of approximately 35 µm for each chamber. The necessary precision of the alignment of the MDT chambers is ensured by a dedicated optical monitoring system in combination with information from the ID tracking, allowing positioning in the 100 µm range.

Also the CSCs are also gaseous detectors. The resemble multi-wire proportional chambers but with a segmented cathode plane. In contrast to the MDTs, the CSCs exhibit a planar geometry and readout. They are segmented perpendicular to the their cathodes to allow for a two-dimensional readout by considering signals from both cathodes, not reading out the wire signal. Said segmentation in the plane of curvature of a track is of $O(5\,\text{mm})$, giving a resolution of 60 µm per plane. In the other direction, a coarser segmentation gives a resolution of 5 mm. The desired high-rate capability of the CSCs is reflected in their read-out rate of up to $1\,000\,\text{Hz}\,\text{cm}^{-2}$ compared to the lower rate of $150\,\text{Hz}\,\text{cm}^{-2}$ for the MDTs.

The muon system is enhanced by two designated sub-components designed for the fast detection of muons, so-called muon *triggers*. Special trigger chambers are interleaved with the tracking chambers, providing low detection times at high time resolutions. A coarse spatial resolution allows for an additional rough estimate of the track momentum. This segmentation also completes the MDT measurement setup. It provides a second spatial coordinate in regions where the MDT design only allows to measure one component perpendicular to the straw direction.

The barrel and end-cap regions are instrumented differently due to their individual requirements. Resistive Plate Chambers (RPCs) are installed in the barrel regions. They are designed as gaseous detectors with two parallel plate electrodes and segmentation into 25 to 35 mm strips perpendicular to each other. Their time jitter of < 10 ns suffices to assign individual muon tracks to single LHC bunches, cf. section 3.1.

The muon trigger system in the end-cap region is formed by the Thin Gap Chambers (TGCs). Similar to the CSCs, the TGC design is based on multi-wire proportional chambers. The distance between the wire and the cathode is smaller than between adjacent wires. In combination with a highly quenching gas mixture, this setup provides stability at high rates as well as fast timing. As for the RPCs, a cathode segmentation perpendicular to the wire direction allows for a two-dimensional read-out and reconstruction. The wire signal is used to determine the track curvature while the cathode signal measures the azimuthal direction. The number of read-out channels is kept to a minimum by grouping wires depending on their position in the module under consideration of the desired resolution in η. The achieved time resolution is high enough to allow for 99% of the muon tracks being correctly assigned to LHC bunch crossings.

3.2.4 The trigger system

The design goal of the LHC to run at a bunch spacing of 25 ns, resulting in a collision-rate of 40 MHz in the centre of the ATLAS detector renders recording all available collision data technically impossible. The challenge of deciding which data to store for analysis is taken up by the two-stage trigger system [127, 128].

In the context of data acquisition (DAQ), the term of a particle physics *event* as it is used in this analysis can be introduced. A pure quantum mechanical approach would define an *event* as the interaction of two particles and everything originating from it. Since at a hadron collider, not only two partons interact but rather a multitude of different hadron substructure particles, multiple interactions already within the collision of two protons need to be considered. The interactions of proton remnants are referred to as the *underlying event*. While the main parton interaction and the underlying event can still be covered by a quantum mechanical description, the definition of an event in the context of an LHC experiment is enhanced further. The bunch structure of the colliding beams leads to multiple interactions per bunch-crossing on hadron-level, referred to as *pile-up*. Motivated by these considerations, the technical aspects of the beam and the trigger system give rise to a more practical definition of an event. In the context of the ATLAS experiment, a particle physics *event* refers to the collision data recorded in a 25 ns timeframe between two bunch-crossings, triggered by the initial bunch-crossing.

The first of two trigger levels (L1) is run on custom hardware close to the detector. The second trigger stage is operated on commercial-grade computer systems comprised in the regular CERN IT infrastructure. It is referred to as the *high-level trigger* (HLT).

The L1-trigger utilises detector information of reduced granularity. Based on signal input only from the calorimeter system, muon trigger chambers and topological considerations, it pre-selects data of interest to be passed on to the HLT. Moreover, the L1-trigger is able to identify regions of interest for the HLT to work on and increase its efficiency. A latency of 2.5 µs, i.e. maximum decision time, results from the limitations in the buffers of the detector electronics. The latter are only able to store information on single bunch-crossings for that amount of time. The L1-trigger is reduces the data rate from potential 40 MHz down to a maximum of 100 kHz.

The software-based HLT uses fine-granularity calorimeter information, precision measurements from the muon system, as well as tracking information from the ID. A first trigger sub-stage performs a fast but coarse reconstruction, further filtering the input to a full reconstruction of an event similar to the later reconstruction used for analysis, cf. section 3.3. The rate of event data written to the storage facilities is reduced to a maximum of 1 kHz after the HLT. Although the HLT has access to the full event information needed for a complete reconstruction, measurable quantities still may differ from their counterparts used for analysis. The main reason for this difference lies with a lack of calibration and correction information that is applied a-posteriori based on the data taken. Furthermore, limitations in computing resources render the utilisation of e.g. complex multivariate reconstruction techniques impossible at this stage.

The term *trigger* is not only used for the hard- and software of the trigger-system itself, but also for a set of requirements which need to be fulfilled for an event to be written to disc, or *to be triggered*. The ATLAS experiment has a rich menu of different triggers, each targeting different purposes and hence reconstructed quantities. Example triggers include requirements on the presence of jets, leptons, or combinations of the latter, as well as more complex quantities such as the overall measured energy in an event. If an event passes the threshold(s) set for a trigger, the trigger induces the storage of the event on disc for later access. Setting the thresholds of the triggers is obviously correlated to the rate of the trigger accepting events – an event is more likely to contain a low-energy muon than a high-energy muon. In order to keep the acceptance rate of triggers with low requirements within the given bounds of the trigger system, a so-called *pre-scale* mechanism is used. By randomly selecting events that a low-threshold trigger accepted to be written to disc, the data-rate can be kept constant. In a subsequent analysis, events accepted by such a pre-scaled trigger can be scaled back to their originally accepted number by application of a weight-factor corresponding to the inverse of the randomisation.

3.2.5 Operation of the detector

Despite its sophisticated design, operation of and data-taking with the ATLAS experiment still requires human attention. The large number of different sub-systems and their individual complexity make monitoring of the experiment's operation challenging. While the status of the whole detector and its components is continuously monitored live by shifters in the ATLAS control room, a post-data-taking assessment completes the set of quality assurance measures taken to ensure stable quality of the data taken. A typical data-taking period, referred to as a *run*, ends when the beam has reached a lower bound of proton density due to collisions and starts when a new particle fill of the LHC is stable enough. The taken dataset is sub-structured in so-called *luminosity blocks* (LBs) of approximately 60 s of data-taking. In the first 36 h of the aftermath of a run, the data quality (DQ) is assessed by a team of detector experts. The dataset is sub-structured in so-called *luminosity blocks* (LBs) of approximately 60 s of data-taking. Immediately after a run, approximately 10% of the taken data—the so-called *express stream*—is examined by the DQ experts to spot possible problems that have not been noticed during the data-taking process. The express stream data is also used to verify or, if need be, update the calibration of the different sub-detectors. After all DQ experts have signed a run off as being of optimal quality, the full dataset undergoes reconstruction and is calibrated using the updated conditions. Based on the experts' findings, the so-called *Good Runs List* (GRL) is created, containing all data-taking periods with optimal detector performance.

Data-taking performance The analysis presented in the context of this thesis is based on $\sqrt{s} = 13\,\text{TeV}$ p–p collision data recorded by the ATLAS experiment between February 2015 and December 2016. As displayed in fig. 3.6(a), in this period of time, a total of $42.7\,\text{fb}^{-1}$ of integrated luminosity[8] has been provided by the LHC in 567 individual runs[9]. The luminosity and its uncertainty of 2.1% are determined as described in [129]. A total of $39.5\,\text{fb}^{-1}$ has been recorded by the ATLAS detector, resulting in a recording efficiency of 92.5%. The inefficiencies in the data-taking are mainly due to the time lost

[8] A general quantity to describe the reaction rate $\dot{N}$ of a certain particle physics process at a collider experiment is given by its quantum mechanical probability, expressed by the cross-section σ and the luminosity of the experiment $\mathcal{L}$ as $\dot{N} = \sigma\mathcal{L}$. The luminosity depends on characteristic parameters of the accelerator, i.e. the number of particles in the two colliding bunches $n_{1,2}$, the number of bunches per beam n_b, the revolution frequency of the beams f, and the longitudinal beam widths $\sigma_{x,y}$ as $\mathcal{L} = f n_b n_1 n_2 (4\pi\sigma_x\sigma_y)^{-1}$. The integrated luminosity over time $\mathcal{L}_{\text{int.}}$ is hence proportional to the number of recorded events in a given period of time.

[9] While a typical run takes approximately 12 h, the longest p–p in this data-taking period has been recorded in June 2016, lasting for > 40 h and delivering $\mathcal{L}_{\text{int.}} = 716\,\text{pb}^{-1}$ of data, corresponding to approximately 150 000 000 events.

while ramping up the detector systems after the LHC has been flagged for stable beam conditions. The aforementioned DQ measures leave the 36.1 fb^{-1} of integrated luminosity for analysis in this thesis, giving a DQ-efficiency of 91.4%. This further reduction of available data ensures that the detector was working in a stable way and under optimal conditions.

The large increase in integrated luminosity between the years 2015 and 2016 over a similar time of data-taking is achieved by an increase in the luminosity of the beams. This aspect is reflected in the peak luminosity distribution of each run, depicted in figs. 3.6(c) and 3.6(d). The higher luminosity is correlated with an increase in the number of interactions per bunch-crossing, the pile-up, as depicted in fig. 3.6(e). In order for the data-recording-rate to still be constant around 1 kHz, the pre-scales of the majority of triggers was increased between 2015 and 2016, resulting in a non-linear increase in the number of recorded events: 2 219 697 577 were recorded in 2015, 8 369 013 278 in 2016, amounting to total of more than 10 Billion events available for analysis.

Event data and computing model The vast number of events saved to disc is stored using a sophisticated event data and computing model [131, 132], developed to efficiently handle such amounts of data. The ATLAS computing model is sub-structured into different data formats targeting the different steps of the DAQ chain. In the first step, the byte-stream data from the detector itself is grouped into *Raw Data Objects* (RDOs), representing a computational model of the ATLAS detector. The reconstruction of low-level objects such as tracks from hits in the ID or calorimeter clusters from calorimeter cell signals is carried out on RDOs, giving Event Summary Data (ESD) files. ESDs represent intermediate collections of basic detector data such as hit and cell information but also the first reconstructed objects such as tracks or clusters. The next step performs reconstruction and identification of so-called *physics objects*, i.e. the reconstructed representations of what is deemed to have been actual particles or e.g. jets. The resulting data format is referred to as Analysis Object Data (AOD). Its data size is drastically reduced by mainly storing information on high-level physics objects and dropping most information on basic objects.

The last step of general data preparation is the transition of the barely human-readable AOD to a data format that is both well machine- and human-readable, the xAOD [132]. The aspect of human-readability is ensured by re-organising the information stored in AODs in *arrays of structures* (containers) corresponding to different physics objects, e.g. τ-leptons. For every event, the τ-lepton container provides structures representing τ-lepton objects. Every τ-lepton object, in turn, provides access to the quantities associated to it, e.g. its transverse momentum, as well as links to objects associated to it, e.g. its decay products. This way, human users can easily and intuitively navigate the objects and properties of a reconstructed particle physics event. The machine-friendly aspect is realised by storing the information, e.g. the τ-lepton transverse momentum of all τ-leptons in an event, in an array, providing only links between the human-friendly frontend and the array. The xAOD data format is, in contrast to the AOD, directly readable by the commonly used ROOT [133] software package for high-energy physics data analysis. While xAODs are typically stored centrally in large data facilities, smaller, Derived xAODs (DxAODs) can also be stored locally on small-scale computer clusters. The DxAOD formats used in the presented analysis are tailored towards the needs of the ATLAS SUSY community. The SUSY3 format is the one used the most in this analysis. It requires events to have been accepted by any single-τ-lepton trigger, missing momentum trigger, light lepton trigger or combined missing momentum and single-jet trigger. Moreover, the presence of a τ-lepton with either one, two, or three reconstructed tracks, $|\eta| < 2.6$, and $p_{\text{T}} \geq 15\,\text{GeV}$ after calibration is required. For the special case of studies requiring the explicit absence of any τ-lepton, the format SUSY5 is used. It requires light lepton triggers or missing momentum triggers to have accepted the stored events. While always the presence of a light lepton ($|\eta_e| < 2.6$, $|\eta_\mu| < 2.7$) is required, the specific lepton requirements depend on the trigger decision.

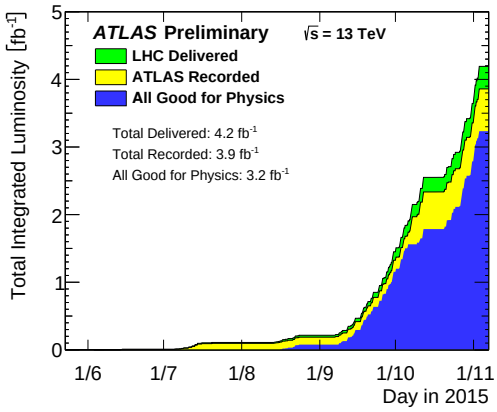

(a) Integrated luminosity in 2015

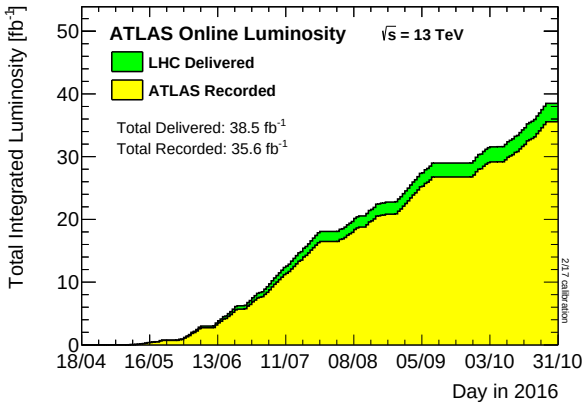

(b) Integrated luminosity in 2016

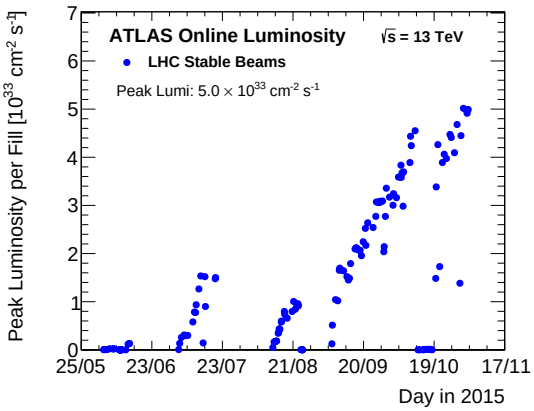

(c) Peak luminosity in 2015

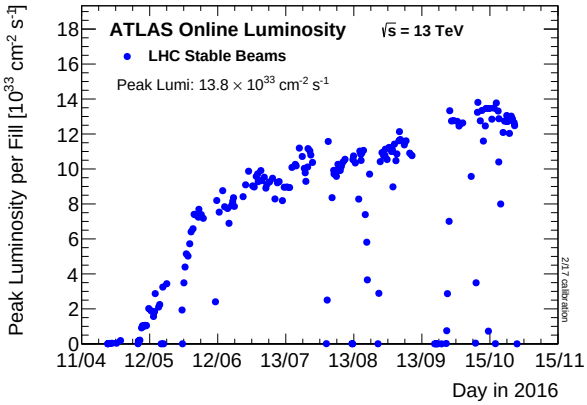

(d) Peak luminosity in 2016

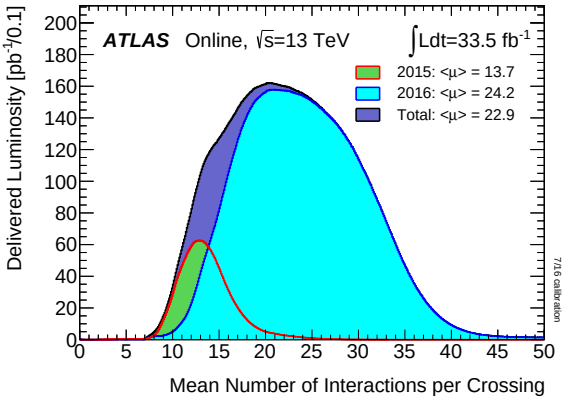

(e) Pile-up in 2015/2016

Figure 3.6: Machine parameters of the LHC and the ATLAS detector associated to data-taking and its performance in the years 2015 and 2016 [130]. Depicted are the integrated luminosity as a function of time for 2015 (a) and 2016 (b), the peak luminosity in each run as a function of time for 2015 (c) and 2016 (d), and the mean number of interactions per bunch-crossing (e) as a measure for pile-up.

If a light lepton trigger accepted the event, electrons and muons need to have $p_{\mathrm{T}} \geq 25\,\mathrm{GeV}$, while electrons (muons) need to fulfil $4.5\,\mathrm{GeV} \leq p_{\mathrm{T}} \leq 25\,\mathrm{GeV}$ ($3.5\,\mathrm{GeV} \leq p_{\mathrm{T}} \leq 25\,\mathrm{GeV}$) if only a missing momentum trigger accepted the event. The assessment of multi-jet processes is performed on SUSY11 data which only requires a stored event to have been accepted by a single-jet trigger.

In principle, the xAOD and the DxAOD formats already allow for ROOT-based analyses. In the context of this thesis, however, an additional data-preparation step is performed to further optimise the computational performance of the analysis. Due to its structure similar to the mathematical equivalent, the final data format is referred to as *n-tuples*. The convenient structure of physics objects and their properties is broken up into a list of vectors of float and integer variables per event, collected in a ROOT *TTree* [133] structure.

Since a coherent treatment of all involved samples of data and simulation along all steps of the data-preparation chain is crucial, the individual software is versioned. For data, the xAOD-tag `p2950` is used, for all simulated samples the tag `p2949`. An overview of all samples used is provided in appendix F.

3.3 Object and event reconstruction

The many specialised sub-detectors of the ATLAS experiment described in section 3.2 allow to reconstruct and identify the majority of (meta-)stable particles being present in the recorded collision events. The procedure of reconstruction and identification starts from the signatures the particles leave in the various sub-systems. A schematic illustration of different particle signatures in the transverse projection of the ATLAS detector is depicted in fig. 3.7.

In general, signatures are reconstructed under all available particle hypotheses. Each object is then assigned an identification tag for each tested hypothesis. Identification tags correspond to certain working points in the signal-to-background efficiency diagrams of the identification algorithms. They hence reflect the likelihood of the hypothesis being true given the imposed requirements. The distinct trace of a muon, for example, is characterised by hits in the ID, forming a bent track, hit-like signals in the calorimeter system and hits forming a track again in the muon system. This signature leaves little room for ambiguity and is hence used to identify a reconstructed object as a muon. By deciding for identification working points and procedures to remove leftover ambiguities as introduced later, every analysis can chose which type is assigned to the reconstructed objects. The forthcoming sections present the reconstruction and identification of the physics objects used in this analysis.

3.3.1 Jets

Strongly interacting particles, i.e. quarks and gluons, are subject to confinement (cf. section 2.1.2). When attempting to exist freely, e.g. by being ripped from a colliding proton, they hadronise immediately to form colour-neutral states. The result of this hadronisation process of a once pseudo-free coloured particle is a more or less collimated spray of particles, spreading through the detector. Another consequence of confinement is the fact that the initial particle of the jet cannot be identified anymore. It is hence necessary to unambiguously classify a bundle of final state particles as one physics object, a so-called *jet*. Theoretical considerations need to be taken into account, too: the coupling structure of the strong force allows for the additional emission of low-energy partons as well as the collinear splitting. Both of these likely processes are not fundamentally distinguishable from higher-order calculations of a single parton. The definition of a jet hence needs to be both *collinear safe* and *infrared safe*, i.e. the observable must neither change when a high-energy object is split into two lower-energy, collinear objects, nor when an extra low-energy object is added, respectively.

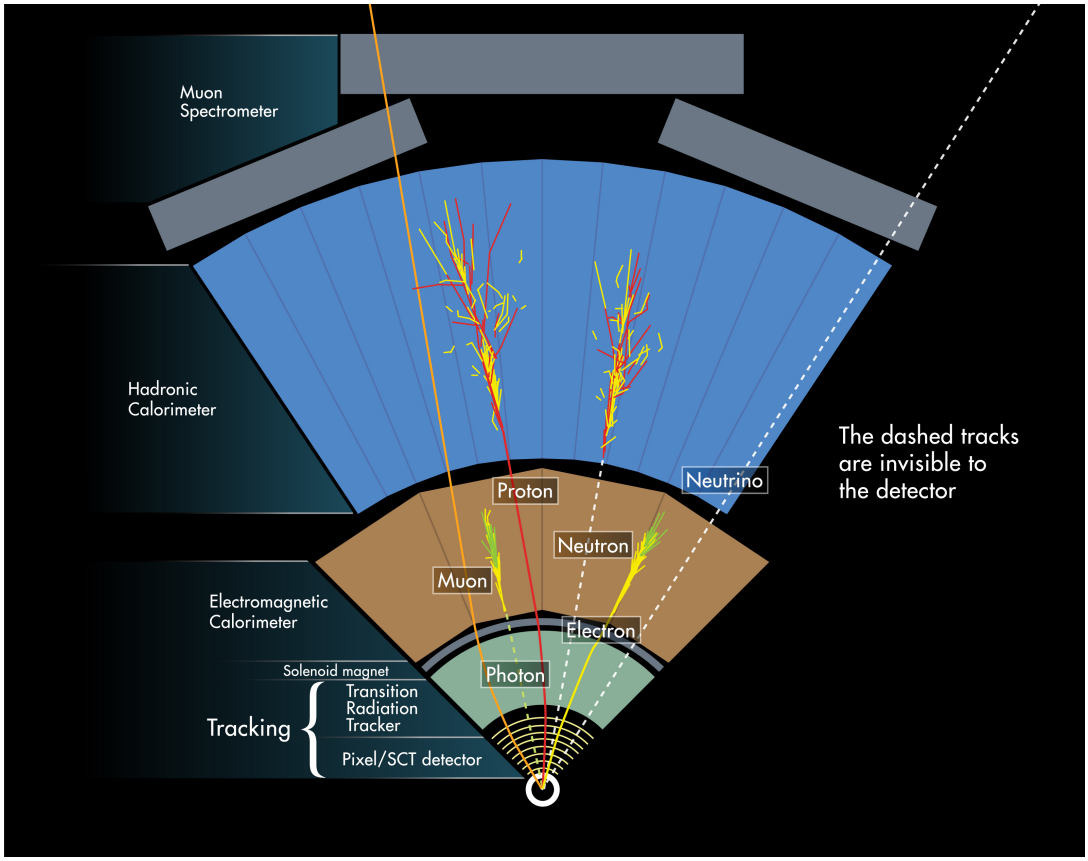

Figure 3.7: Schematic signatures of different particles as they are reconstructed by the different ATLAS sub-detectors in the transverse plane [134].

A final aspect is the jet-finding algorithm itself: it needs to perform in the same way on detector-level, i.e. calorimeter cells and tracks, as on simulation-level, i.e. simulated final state particles. A common class of jet-finding algorithms that fulfils the aforementioned criteria forms jets by clustering objects. Typically, an iterative approach is used, that clusters possible constituents pairwise until a defined stop condition is met. For the jet-clustering algorithms used by the ATLAS collaboration, two measures of distance are defined:

$$d_{ij} = \min\left(\left(k_t^{2p}\right)_i, \left(k_t^{2p}\right)_j\right) \frac{(\Delta R_{ij})^2}{R} ,$$
$$d_{iB} = \left(k_t^{2p}\right)_i .$$

In this notation, k_t^{2p} denotes the magnitude of the transverse momentum of an object and ΔR_{ij} the distance in the η–ϕ-plane between objects i and j. R and p are free parameters. In each iteration, d_{ij} is computed for each pair of objects ij, while d_{ib} is calculated for each object individually. Once they are calculated for all (combinations of) objects in an event, they are collected in a mutual list, sorted by magnitude. If d_{ij} is the smallest entry, the objects i and j are grouped together, the original constituents are removed, and the procedure is repeated. If d_{iB} is the smallest entry of the list, object i is considered a fully clustered jet and removed from the list.

The free parameters control the clustering procedure. R addresses the size of a jet, with larger values allowing for larger jets to be clustered. On the other hand, p controls the priorities of the clustering. Typical values are $p = 1$ (k_t-algorithm [135]), $p = 0$ (Cambridge/Aachen-algorithm [136, 137]), and $p = -1$ (anti-k_t-algorithm [138]).

The k_t-algorithm starts the clustering process from soft objects, preserving the substructure of the jet. A disadvantage of this approach is the large number of jets that remain not merged and are lost. On the theory-level, this algorithm somewhat mimics the soft radiation processes of QCD. The Cambrdige/Aachen-version objects are only based on their geometrical vicinity, neglecting their momenta. Although this approach preserves the structure of the jet, it leads to highly irregular structures. The anti-k_t-algorithm starts from the hardest object and consecutively merges softer objects around them into the jet. This approach leads to a highly regular structure of the jet-space, allowing for easier application of calibration or corrections of e.g. pile-up effects. On the down-side, any information on the jet substructure is lost.

Among others, these jet-finding algorithms have been tested by the ATLAS collaboration. The anti-k_t-algorithm with a distance parameter of $R = 0.4$ is the best-suited algorithm for the majority of physics analyses, including the presented one. For analyses requiring jet substructure information, different approaches are also used, e.g. separating quark- from gluon-initialised jets [139], identifying jets from heavy vector boson decays [140], or the reconstruction of highly boosted top-quark jets [141].

The basis of jet reconstruction in the detector are so-called *topo-clusters* of calorimeter cells [142]. Topo-clusters originate from grouping of calorimeter cells with energy entries above a defined noise threshold. The clustering starts from a cell with signal-to-noise ratio of $S/N > 4$, adding all neighbours and neighbours-of-neighbours with $S/N > 2$ to a cluster. In the last step, all neighbouring cells of that cluster are added regardless of their signal. For the special case of a cluster having two maxima, it is split in two and cells in between the two sub-clusters are shared. Next, the built clusters undergo a calibration procedure, the so-called *local hadronic calibration*. A prerequisite to this procedure is the knowledge about how "hadronic" a cluster is, based on its determined properties. The calibration is then applied based on the estimated fraction of hadronic energy in the cluster. This process includes corrections undetected as well as escaped energy, and dead material or detector effects. Furthermore, the calibration partially cancels the non-compensating[10] properties of the ATLAS calorimeter system.

The jets found by clustering calibrated topo-clusters of calorimeter cells are then further calibrated to the so-called *Jet Energy Scale* [143–145]. The JES corrects for pile-up effects [146, 147] as well as for the direction of the jet relative to the reconstructed vertex. The JES is derived from a comparison of reconstructed and true jet energy in simulations and measurements in data.

For the presented analysis, jets are required to have $p_{\mathrm{T}} > 20\,\mathrm{GeV}$ and $|\eta| < 2.8$. The jet collection is cleared off spurious calorimeter measurements associated to beam particles, cosmic particles, or noise is procedure referred to as *jet cleaning* [148]. The jet cleaning is performed at the *loose* working point, ibid.. Jets failing the cleaning procedure but fulfilling the other minimal requirements are labelled as *bad* jets.

Due to the challenging pile-up conditions of the LHC, ATLAS utilises a technique to further relate jet and vertex information, the so-called *jet vertex tagging* (JVT) [149]. It is a multi-variate procedure that allows for a separation of pile-up jets and those arising from the initial hard interaction.

[10] A calorimeter is called *compensating* if its response only depends on the energy deposition of a stopped particle and not the particle type. A benchmark is hence an identical response to electrons and charged pions.

3.3.2 *b*-Jets

Jets originating from *b*-quarks exhibit a different detector signature than jets from lighter quarks. In the first step of the hadronisation process, the *b*-quark binds with a lighter quark to form a hadron. The typically longer lifetime of *b*-hadrons compared to light-flavour hadrons results in a measurable flight distance they traverse before their decay. In the detector, a slightly displaced vertex of *b*-jets relative to other jets from the same interaction vertex is visible. The distinct decay modes of *b*-hadrons, e.g. involving a light lepton that can be detected even inside the residual jet, also help distinguishing *b*-jets from light-flavour jets.

The ATLAS collaboration has developed various algorithms exploiting the aforementioned features of *b*-hadrons to identify and *tag* jets as *b*-jets [150]. The lifetime of *b*-hadrons and hence the displaced vertex is exploited by the IP3D tagger, the SV1 tagger, and the JetFitter. The IP3D algorithm uses the so-called *impact parameter* of the reconstructed jet, i.e. the displacement of its axis relative to the reconstructed primary vertex[11]. The SV1 tagger tries to actually reconstruct the secondary vertex from the constituent tracks of the jet in a similar fashion as the hard collision vertices are reconstructed. The JetFitter algorithm not only reconstructs the secondary vertex but also the tertiary vertex of the light-flavour quark decay inside the jet along with the entire jet substructure. It exploits the jet topology by means of a Kalman filter [152, 153].

In contrast to the regular jet reconstruction, all available algorithms are used simultaneously. Their individual results are combined into an artificial neural network, the MV1 tagger. The output of the MV1 algorithm, in turn, is a flavour weight defined between zero and one for each jet. The higher the value of the flavour weight, the more likely the jet originiates from a *b*-quark. A resulting property of this multivariate approach are defined efficiencies for successful *b*-detection and rejection of light-flavour jets. The efficiencies for different requirements on the flavour weight are calibrated in dedicated analyses [150], stuying *b*-quark production in decays of top-quark pairs. The mis-tagging rate of falsely identifying a light-flavour jet as a *b*-jet is also calibrated in $t\bar{t}$-samples but in different analyses [154]. The underlying algorithm used to obtain the flavour-weight in ibid. and in the presented analysis is the MV2c20 [152] algorithm, a successor of the aforementioned MV1. The used working point corresponds to a *b*-tag efficiency of 77% and rejection factors of τ-lepton jets (cf. section 3.3.4), *c*-jets, as well as light-flavour and gluon jets of approximately 22, 6, and 130, respectively [152]. In the presented analysis, the discrimination of *b*-jets from other quark- or gluon-initiated jets is only needed to separate the Standard Model processes of W + jets from top-quark production. The actual choice of the working point is thus only of minor importance as it still provides good separation of the two processes, cf. e.g. section 6.1.

3.3.3 Light leptons and photons

Light leptons only play a minor role in the context of the presented analysis. While the analysis is fully inclusive with respect to electrons, not addressing them in any way, muons are only used in the estimation process of minor SM processes. Photons only play in a role in the calculation of the missing transverse momentum and are not considered as individual objects in this analysis at all. Details on the reconstruction of electrons and muons as they are present in the simulated and recorded samples used in this analysis can be found in [155] for electrons and in [156] for muons. The ATLAS photon reconstruction and calibration is described in [157].

[11] The primary vertex of an event is defined as the vertex with the highest $\sum p_{\mathrm{T}}^2$ of all tracks associated to it and fulfils further quality criteria [151].

3.3.4 τ-leptons

The crucial role of τ-leptons in the search for SUSY is evident from sections 2.2.2 and 2.2.4. They are the key signature particles of the models searched for, and many design and evaluation aspects of this analysis are driven by their properties. In the general jargon of hadron collider experiments, *τ-lepton* only refers to the hadronic decay products of an original τ-lepton. The unknown initial state of the collision in combination with different sources of unmeasured energy contributions due to e.g. additional neutrinos render the reconstruction and identification of leptonic decay modes difficult. The separation of light leptons emerging from leptonic τ-lepton decays requires dedicated studies of the whole event topology and a sophisticated treatment of the multiple undetectable neutrinos. Already in the reconstruction of a hadronic τ-lepton decay, the single present neutrino spoils the complete reconstruction of the τ-lepton. In the environment of hadron colliders, however, the remaining *visible*, i.e. hadronic, part is the only way of clearly separating τ-leptons from prompt light leptons. Based on [158, 159], the following paragraphs introduce the reconstruction and calibration of the τ-leptons as used in the presented analysis. A more detailed overview is provided ibid..

Reconstruction Due to the similarities of hadronically decaying τ-leptons and QCD jets (cf. section 2.1.4), the τ-lepton reconstruction chain is seeded by already reconstructed but yet uncalibrated jets with $p_{\mathrm{T}} > 10\,\mathrm{GeV}$ and $|\eta| < 2.5$, neglecting seed-jets from the barrel-end-cap transition region $1.37 < |\eta| < 1.52$. The first step is to find the decay vertex of the τ-lepton. In a cone of $\Delta R = 0.2$ around the jet axis, tracks of good quality are used to find potential τ-lepton decay vertices of the event. The vertex with the highest fraction of associated track p_{T} relative to the total p_{T} of the jet is chosen as reference for the further reconstruction steps. Depending on the total energy converted in the event, the tau-vertex is likely to coincide with the primary vertex of the event, varying from approximately 90% for low-energy events such as $Z \to \tau\tau$ to more than 99% for higher-energy topologies. Once the tau-vertex is found, the visible component of the τ-lepton transverse momentum $p_{\mathrm{T}}^{\mathrm{vis}}$ is calculated from the topo-clusters of the seed-jet. The barycentre of the set of jet clusters is calculated under the hypothesis of all cells being activated by massless particles. The four-vectors of all cells in a $\Delta R = 0.2$ cone around the barycentre-tau-vertex axis are recalculated using the tau-vertex. The sum of all these constituents then gives the visible four-momentum of the τ-lepton candidate, again under the assumption of the τ-lepton being massless. Tracks are considered depending on their presence in either the *core region* ($\Delta R < 0.2$) of the τ-lepton candidate or its *isolation region* ($0.2 < \Delta R < 0.4$) relative to its visible direction. Tracks in the core are associated to the τ-lepton candidate if they have $p_{\mathrm{T}} > 10\,\mathrm{GeV}$ and at least seven hits in the silicon trackers (Pixel and SCT, cf. section 3.2.1) of which at least two need to be in the Pixel detector. Moreover, their transversalal and longitudinal impact parameters needs to fulfil $|d_0| < 1\,\mathrm{mm}$ and $|z_0 \sin\theta| < 1.5\,\mathrm{mm}$, respectively. Tracks in the isolation region are not associated to the final τ-lepton object but are used in its identification process. Particular care is taken of possible neutral pions in the τ-lepton decay. They are assigned a likelihood based on cluster shape and track information in the core region. The obtained information is further used in the identification process described in the subsequent paragraph.

Identification (ID) The τ-lepton candidates reconstructed in the described fashion are not easily distinguished from QCD jets. The subtle differences outlined in section 2.1.4 can be exploited to provide discrimination power and identify τ-lepton candidates as actual τ-leptons. A first coarse separation can be obtained by a requirement on the track multiplicity. Since > 99.9% of all hadronic τ-lepton decays feature either one (1-prong) or three (3-prong) charged particles [38], jets with different track multiplicities can be safely ruled out. The separation power against remaining jets, particularly against

quark-initiated high-p_{T} jets, is increased by a multivariate discriminant, a *boosted decision tree* (BDT) implemented using the TMVA software package [160]. Simulated example distributions of two selected input variables for 1-prong and 3-prong τ-lepton candidates from both signal and multi-jet background sources are depicted in fig. 3.8. The fraction of EM energy from charged pions $f_{\mathrm{EM}}^{\mathrm{track-HAD}}$ is defined as the fraction of the energy, deposited in the electromagnetic calorimeter, of tracks associated with the τ-lepton candidate in the core region. The ratio of track-plus-EM-system to p_{T} $p_{\mathrm{T}}^{\mathrm{EM+track}}/p_{\mathrm{T}}$ is defined as the ratio of the τ-lepton p_{T}, estimated using the vector sum of track momenta and up to two most energetic electromagnetic calorimeter clusters in the core region, to the calorimeter-only measurement of the τ-lepton p_{T}. In addition, the following variables feed into the jet-discrimination BDT [159]: the centrality fraction f_{cent}, the ratio of EM energy to track momentum $f_{\mathrm{EM}}^{\mathrm{track}}$, the leading track momentum fraction $f_{\mathrm{leadtrack}}^{-1}$, the track radius R_{track}, the leading track IP significance $S_{\mathrm{leadtrack}}$, the track-plus-EM-system mass $R_{\pi^0+\mathrm{track}}$, the fraction of tracks-p_{T} in the isolation region $f_{\mathrm{iso}}^{\mathrm{track}}$, the maximum ΔR_{max}, the track mass m_{track}, and the transverse flight path significance $S_{\mathrm{T}}^{\mathrm{flight}}$. Potential biases due to pile-up effects on variables such as e.g. f_{cent} or $f_{\mathrm{leadtrack}}^{-1}$ are removed by application of a correction based on the number of primary vertices in the event n_{PV}.

Separate BDTs are trained for 1-prong and 3-prong candidates based on simulated $Z/\gamma^* \to \tau\tau$ signal samples and di-jet background events selected from data. A signal efficiency is defined as the fraction of true τ-leptons with n tracks being reconstructed as τ-leptons with n tracks and passing the identification criteria. Similarly, a background efficiency is defined as the fraction of jets from a background-dominated sample being reconstructed as τ-leptons with n tracks and passing the identification. An illustration of the inverse background efficiency as a function of the signal efficiency for τ-leptons with $p_{\mathrm{T}} \geq 20\,\mathrm{GeV}$ is depicted in fig. 3.9. Along the determined efficiency curve, three working points referred to as *loose*, *medium*, and *tight* are defined, providing fixed values of the signal and background efficiencies, independently of the τ-lepton p_{T}. Due to the selection of BDT input variables, the τ-lepton ID working points also independent of pile-up.

For the presented analysis, the *medium* ID working point is selected for all reconstructed τ-leptons. While the *loose* working point would cause too much background to enter the analysis phase-space, the *tight* working point would suppress too much signal, particularly upon requiring multiple τ-leptons.

Although quark- and gluon-initiated jets are by far the major source of falsely identified τ-leptons, electrons still pose a source of potential mis-identification, particularly at low p_{T} where their cluster shapes are difficult to distinguish. A dedicated BDT to discriminate electrons from single charged pions is trained in the context of electron identification. This BDT is utilised in the τ-lepton identification by tuning the required score for an electron candidate to pass its *very loose* working point such that it is 95% efficient for hadronically decaying τ-leptons. This optimisation is performed in different ranges of p_{T} and $|\eta|$ of the τ-lepton. τ-lepton candidates with only one associated track in the $\Delta R < 0.4$ vicinity of such a *very loose* electron are rejected.

Energy calibration The energy of τ-leptons reconstructed to this stage is calibrated in a similar fashion as for regular jets, but due to their different nature at a different energy scale. The final calibration of the τ-lepton energy is obtained by feeding the output of two different calibration approaches into a multivariate *boosted regression tree* (BRT), based on the TMVA software package [160]. The first calibration procedure entering the BRT is referred to as the *baseline* calibration, similar to the calibration already used in Run-1 of the LHC [158]. The energy of the topo-clusters obtained at the local hadron calibration (cf. section 3.3.1) E_{LC} is corrected by the energy contribution from pile-up $E_{\mathrm{pile-up}}$ and the detector response function $\mathcal{R}$ as shown in eq. (3.2).

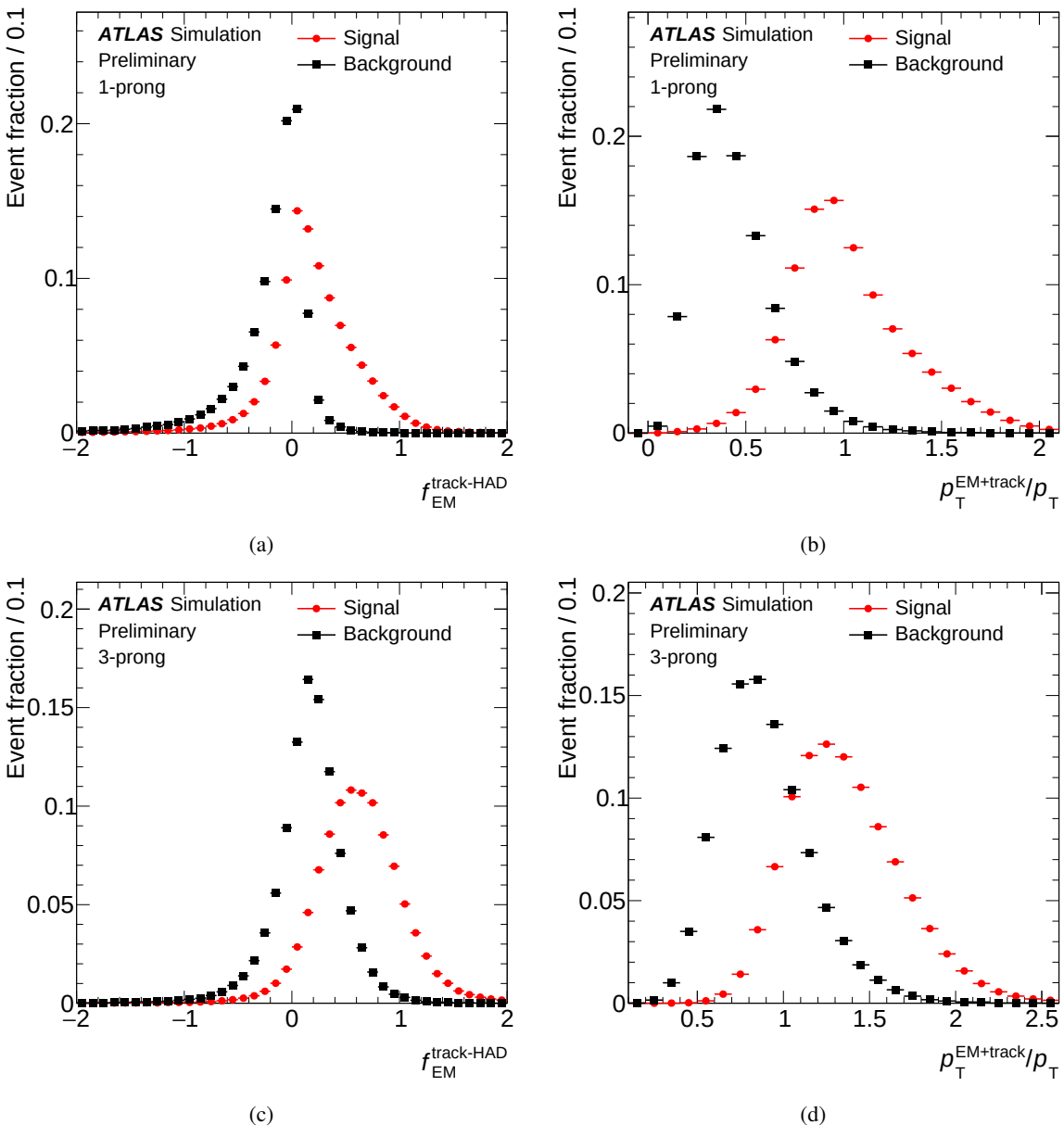

Figure 3.8: Example distributions of input variables to the jet-discrimination BDT of the τ-lepton identification procedure. The fraction of EM energy from charged pions $f_{\mathrm{EM}}^{\mathrm{track-HAD}}$ for 1-prong and 3-prong τ-lepton candidates is shown in (a) and (c), respecitvely. The ratio of track-plus-EM-system to p_{T} $p_{\mathrm{T}}^{\mathrm{EM+track}}/p_{\mathrm{T}}$ for 1-prong and 3-prong τ-lepton candidates is shown in (b) and (d), respectively. The depicted distributions are purely simulation-based [161].

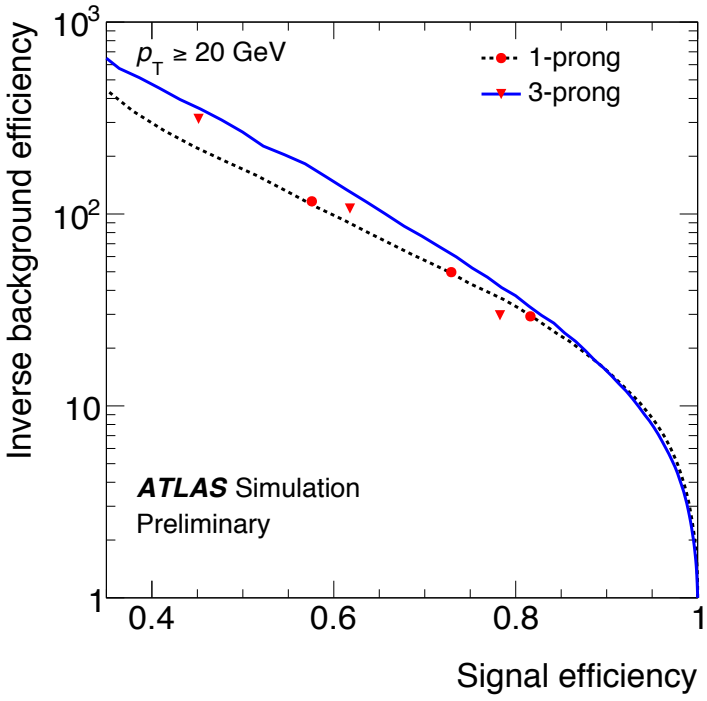

Figure 3.9: Expected inverse background efficiency as a function of the signal efficiency for 1-prong and 3-prong τ-lepton candidates fulfilling $p_T \geq 20\,\text{GeV}$. The dotted and solid lines represent the results of scans of the underlying BDT distributions. The red markers correspond to the three working points of *loose*, *medium*, and *tight* ID requirements. The working points do not stay exactly on the line because they implement variable cuts to achieve a reduced p_T-dependency of the efficiency [161].

$$E_{\text{calib}} = \frac{E_{\text{LC}} - E_{\text{pile-up}}}{\mathcal{R}\left(E_{\text{LC}} - E_{\text{pile-up}}, |\eta|, n_{\text{PV}}\right)} \,. \tag{3.2}$$

Here, the pile-up contribution to the measured energy is found to be a linear function of the number of primary vertices n_{PV} and is applied in bins of the pseudorapidity η. The response function $\mathcal{R}$ is given by the Gaussian mean of the $E_{\text{LC}} - E_{\text{pile-up}}/E^{\text{vis}}_{\text{true}}$ distribution, with $E^{\text{vis}}_{\text{true}}$ denoting the simulated energy of the τ-lepton decay products without the neutrino contribution. The response functions for τ-leptons with one reconstructed track and multiple tracks (multi-prong) are depicted in figs. 3.10(a) and 3.10(b), respectively. The drop towards low energies stems from the increasing influence of pile-up effects and needs to be approximated by linear function due to the energy threshold for τ-lepton reconstruction. The achieved resolution of the baseline calibration is depicted separately for 1-prong and multi-prong τ-leptons in figs. 3.10(c) and 3.10(d), respecitvely. It follows the typical parametrisation of calorimeter energy resolutions as

$$\frac{\sigma_E}{E} = \frac{a}{\sqrt{E}} \oplus \frac{b}{E} \oplus c \,,$$

with a, b, and c denoting the sampling term, the noise term, and the constant term, respectively.

The second calibration approach targets the weak spot of the baseline calibration at lower energies. It exploits the better energy measurement capabilities of the tracking system for of low-energy charged pions and is referred to as *Tau Particle Flow* (TPF) [162].

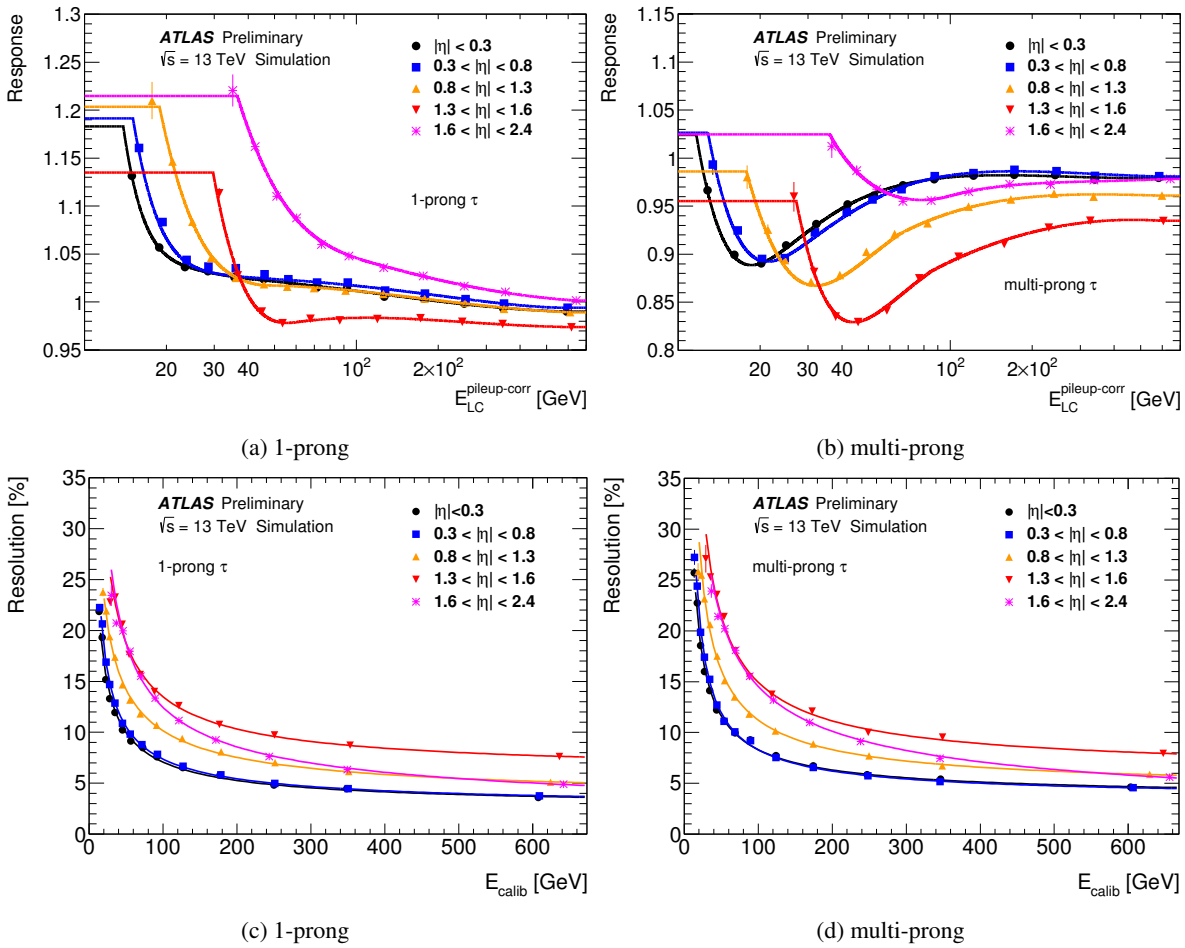

(a) 1-prong

(b) multi-prong

(c) 1-prong

(d) multi-prong

Figure 3.10: Detector response as a function of the topo-cluster energy at the local hadron calibration corrected for pile-up (a) and (b), and the τ-lepton energy resolution as a function of the calibrated energy (c) and (d) for 1-prong and multi-prong τ-leptons in the baseline calibration procedure [161]

The BRT used to obtain the final energy calibration is trained using a large set of discriminating variables as described in detail in [159]. The performance of the BRT-based energy calibration with respect to the baseline calibration is depicted in fig. 3.11. While for high transverse momenta, the baseline calibration performs equally well, the contribution of the TPF calibration to the BRT is clearly visible at low p_{T}.

The energy of τ-leptons used in the presented analysis is calibrated using the BRT-based approach.

Performance of the algorithms The performance of the sophisticated algorithms to reconstruct hadronically decaying τ-leptons and to separate them from QCD jets can be studied in various ways. A cross-check between data and simulation is performed in a so-called *tag-and-probe* analysis [159] of $Z \to \tau\tau$ events. Here, one τ-lepton is required to decay hadronically while the second needs to decay to via a muon. The muon is considered the *tag*, the hadronically decaying τ-lepton the *probe*. In that analysis, the V + jets and top-quark contributions are estimated from simulation, while the multi-jet contribution is estimated in a data-driven procedure. The agreement between the simulated prediction and data is studied in the distribution of reconstructed tracks in a wider cone of $\Delta R < 0.6$ around the

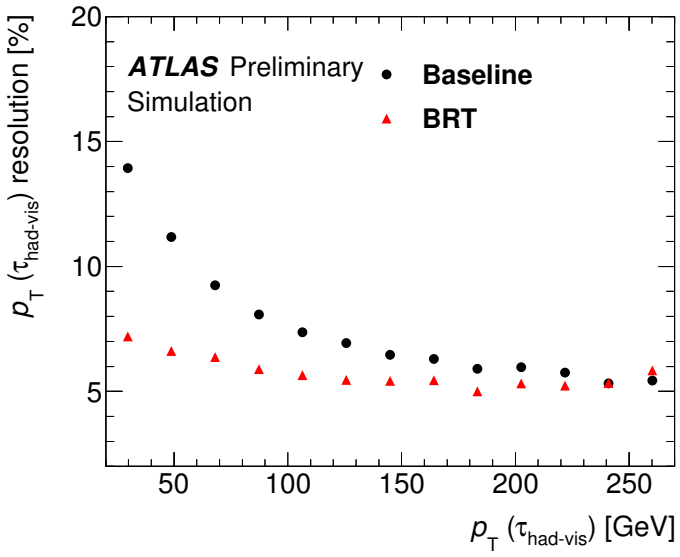

Figure 3.11: Resolution of baseline and BRT-based energy calibration. The p_T-resolution of the reconstructed τ-lepton is shown as a function of the generated τ-lepton p_T [159].

τ-lepton axis after a suitable event selection. The influence of the *medium* ID requirement on genuine τ-leptons and different sources of faked τ-leptons is depicted in figs. 3.12(a) and 3.12(b), respectively.

By fitting the contributions from true and misidentified τ-leptons from jets before and after application of the ID requirement, the effective efficiency and rejection can be determined from these distributions. The deviation of the simulation from data is overcome by the application of correction factors obtained in a comparison of the prediction to data. Since no significant deviation between different regions of the τ-lepton p_T or $|\eta|$ are found, inclusive correction factors for 1-prong and 3-prong τ-leptons are provided for all three working points. The results including statistical and systematical uncertainties are summarised in fig. 3.12(c). The total uncertainties amount to $< 5\%$. They are dominated by a systematic uncertainty due to the modelling of the τ-lepton template used in the fit. The correction factors for the *medium* ID working point are applied per object to the events containing reconstructed τ-leptons in this analysis. The uncertainties on the correction factors are accounted for by designated systematic uncertainties (cf. section 7.2).

In addition to the track multiplicity, the reconstruction of the τ-lepton energy is studied in the same tag-and-probe analysis of $Z \to \tau_\mu \tau_{\text{had}}$ events. In this notation, the regular hadronic τ-lepton is referred to as τ_{had}, while τ_μ labels a the leptonic decay of a τ-lepton into a muon. Based on the same event selection, the invariant mass m_{vis} of the system formed by the muon and the τ-lepton is used as an in-situ measurement of the tau energy scale used for calibration[12]. The different predicted contributions to the event spectrum are fitted to data, allowing the tau energy calibration to float around its nominal value. Any deviations found are accounted for by correction factors in a similar fashion as for the n_{track} distributions. The resulting distributions of m_{vis} for 1-prong and 3-prong τ-leptons are depicted in fig. 3.13.

The variations of the tau energy scale using the BRT-approach are found to be approximately 1% for 1-prong τ-leptons and approximately 3% for 3-prong τ-leptons, each with a total uncertainty of approximately 2% [159]. As for the studies of the track multiplicity, the correction factors for the tau

[12] Since the neutrinos are neglected, the invariant mass of the τ-lepton-muon system is referred to as the *visible* mass m_{vis}, defined as $m_{\text{vis}} = \sqrt{\boldsymbol{p}_\tau + \boldsymbol{p}_\mu}$.

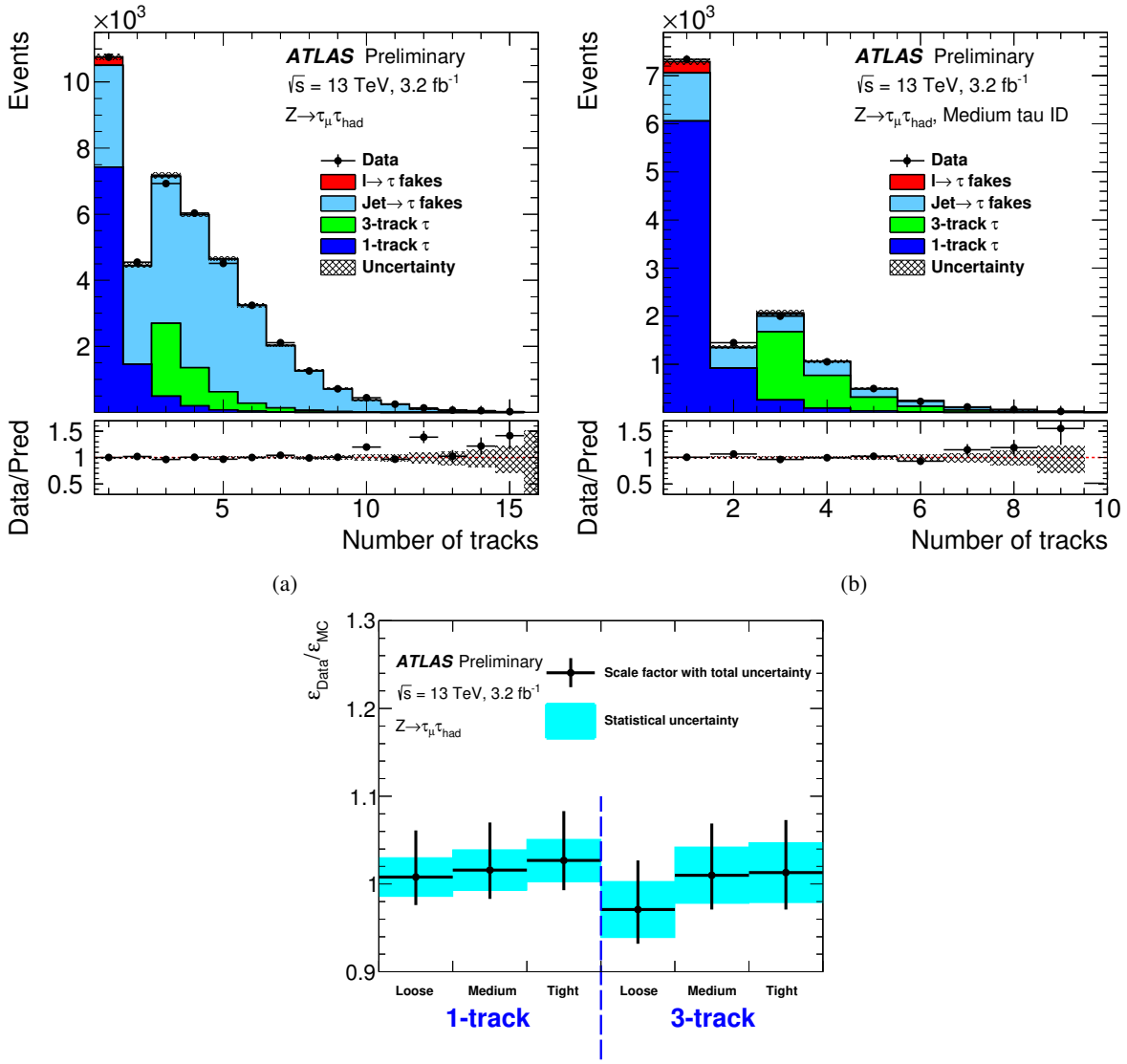

Figure 3.12: Distributions of the track multiplicity n_{track} of τ-leptons before (a) and after application of the *medium* ID requirement (b). The track multiplicity is determined in cone of $\Delta R < 0.6$ around τ-lepton axis. The true-tau and jet contributions are fitted to the observed data while the fake-tau contribution from light leptons is fixed to its nominal prediction from simulation. The uncertainties shown are statistical only. The correction factors needed to match the predicted τ-lepton identification efficiency to the observation in data for different ID working points are depicted in (c), including the total systematic and statistical uncertainties. All results are taken from [159].

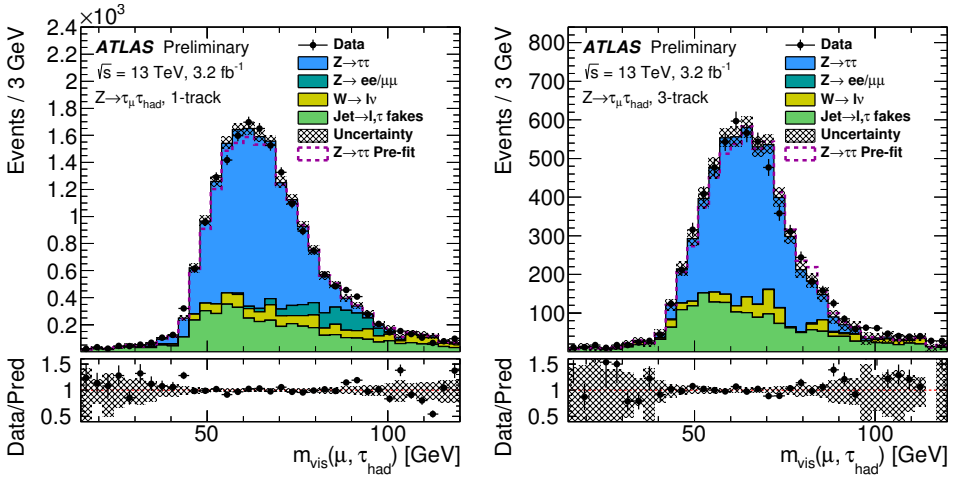

(a) (b)

Figure 3.13: Distributions of the visible mass m_{vis} of τ-leptons for 1-prong (a) and 3-prong (a) τ-leptons after application of the *medium* ID requirement. The visible mass is the invariant mass of the system formed by the muon and the τ-lepton. The distributions of $Z \to \tau\tau$ signal events and $Z \to \ell\ell$, $W \to \ell\nu$ as well as Jet $\to \ell\tau$ faking τ-leptons are fitted to data. The uncertainties shown are statistical only [159].

energy scale are applied to the simulation of τ-leptons in this analysis. The uncertainties are again considered as designated systematic uncertainties.

3.3.5 Missing transverse momentum

For the presented analysis and many searches for Supersymmetry in general, the missing transverse momentum $\boldsymbol{p}_{\text{T}}^{\text{miss}}$ and its magnitude, the missing transverse energy $E_{\text{T}}^{\text{miss}}$, are the most crucial physics objects besides jets and τ-leptons. Conservation of momentum ensures the overall balance of all transverse momenta in one collision. If, however, particles escape detection and hence carry away a fraction of the total energy, this balance is disturbed. In the Standard Model, only neutrinos should contribute to the $E_{\text{T}}^{\text{miss}}$ of an event. On the other, a multitude of electrically neutral and only weakly interacting particles are postulated, resulting in $E_{\text{T}}^{\text{miss}}$-based experimental signatures. Obviously, a measurement of the $E_{\text{T}}^{\text{miss}}$ is only possible through already measured other physics objects and eventually present unassociated energy depositions in the calorimeter system [163]:

$$E_{x(y)}^{\text{miss}} = E_{x(y)}^{\text{miss},e} + E_{x(y)}^{\text{miss},\gamma} + E_{x(y)}^{\text{miss,jets}} + E_{x(y)}^{\text{miss,SoftTerm}} + E_{x(y)}^{\text{miss},\mu} \,.$$

Every term in this representation is the x and y projection, respectively, of the negative sum of the four-momenta of the underlying objects. The reconstruction and calibration of all contributing objects is performed in the regular ways as introduced in the former paragraphs. Since signatures in the detector can be reconstructed as multiple objects of different types, e.g. jets and τ-leptons, terms in the $E_{\text{T}}^{\text{miss}}$-calculation are ranked. If a signature entered as an electron, for example, it cannot enter again as a τ-lepton. The order of the summation of terms is hence important. The $E_{x(y)}^{\text{miss,SoftTerm}}$ contribution contains all jets below the reconstruction threshold of $p_{\text{T}} > 20\,\text{GeV}$ as well as all tracks and clusters which have not been assigned to any physics object. The $E_{x(y)}^{\text{miss},\mu}$ term covers all combined muons which have matched

measurements in both the inner detector and muon system and segment-tagged muons[13]. For combined muons, the estimated energy loss in the calorimeter system is subtracted from the other calorimeter contributions.

The obvious question of whether to calibrate the $E_{\mathrm{T}}^{\mathrm{miss}}$ contributions of decay products of hadronically decaying τ-leptons as jets or as τ-leptons is not further pursued in this thesis. Its $\sqrt{s} = 8\,\mathrm{TeV}$ predecessor, however, found that no significant impact is to be expected [15]. Hence, contributions from τ-leptons enter the calculation of $E_{\mathrm{T}}^{\mathrm{miss}}$ calibrated at the tau energy scale.

3.3.6 Overlap removal

As already briefly mentioned in the calculation of the missing transverse momentum, it is generally possible for one particle to be reconstructed as different objects. Hadronically decaying τ-leptons, for example, are obviously overlapping with the definition if regular jets as the reconstruction process of the former is seeded by the latter. In such cases, the multiple-assigned objects point in the same direction in the detector.

The necessary absence of any ambiguity is addressed by a procedure referred to as *overlap removal*, applied to all events after the reconstruction and calibration of the physics objects. In general, light leptons can be reconstructed with the highest precision and identified with the highest confidence, followed by τ-leptons. Jets, on the other hand, are the most inclusive of objects. Genuine jets, along with τ-leptons and electrons are reconstructed as jets regardless of their true nature, a removal of ambiguity is hence indispensable. The following scheme of subsequently applied steps ensures that each signature in the detector is assigned to its mostly likely source[14]:

1. A *loose* τ-lepton is discarded if it overlaps with an electron within $\Delta R_y = 0.2$.
2. A *loose* τ-lepton is discarded if it overlaps with a muon within $\Delta R_y = 0.2$.
3. An electron is removed if it shares an inner-detector track with a muon.
4. A jet is removed if it overlaps with an electron within $\Delta R_y = 0.2$ and if it is not b-tagged.
5. An electron is removed if it overlaps with a jet within $\Delta R_y = 0.4$.
6. A jet with $N_{\mathrm{track}}(\mathrm{jet}) \leq 2$ is removed if it overlaps with a muon within $\Delta R_y = 0.2$ and if it is not b-tagged.
7. A muon is removed if it overlaps with a jet within $\Delta R_y = 0.4$.
8. A jet is removed if it overlaps with a *loose* τ-lepton within $\Delta R_y = 0.2$, regardless of the jet flavour-tag.

The first four steps account for the higher confidence in the reconstruction of light leptons with respect to τ-leptons and jets, as well as among each other. Steps 5–7 address the cases of light leptons emerging from the decays of heavy flavour quarks inside of jets, while the last step represents the confidence in the identification of τ-leptons once the event is cleared of other ambiguities.

Based on now ambiguity-free events, selection criteria towards an analysis of simulated physics and data can begin.

[13] A muon candidate is referred to as *segment-tagged* if an inner detector track is matched to a signal in the muon system but the energy of the object is not sufficient to allow for an independent measurement in the outer tracking system.

[14] For the overlap removal, the angular distance measure ΔR_y is used. Its definition substitutes the pseudorapidity η for the rapidity of a particle y.

CHAPTER 4

Simulation Procedures – Casting Models to Reality

For many science experiments in general and the majority of particle physics experiments in particular, reliable simulations are indispensable. The general idea is always to predict the outcome of the performed experiment in either or a combination of the two following ways. Predictions of well-established and precisely known theories, e.g. the Standard Model, allow for studies of the experiment's performance and estimation of systematic uncertainties. Simulations of new proposed models are necessary to gain knowledge of how to search for the desired model. Analyses searching for models of new physics typically require sufficient simulation-based predictive power from both sides. Knowledge of the Standard Model and the desired BSM theory is necessary to separate the two from each other in order to make any reliable statement about the new model's compatibility with data. Precision of both simulated models is needed to keep uncertainties low and the statistical predictive power high for interpretation. The forthcoming sections present general considerations about simulations in particle physics and provide a more detailed overview of the ones utilised in the context of the presented analysis.

4.1 Simulation of particle physics

It is natural to expect the first appearance of models of new physics in the tails of kinematic distributions of predicted Standard Model processes – it is obvious to assume they would have been discovered already if they were expected in the cores of distributions. Said tails, however, are typically difficult to model. Theory-based predictions of extreme kinematic configurations often suffer from a lack of precision and the challenge of calculation in general. A notorious example is the description of the transverse momentum of the vector boson in V + jets processes. The simulation of SM processes for a BSM search is complicated further by the fact that the kinematic regimes of interest typically come at a low production cross-section. It is thus necessary to simulate a vast number of events to achieve sufficiently precise modelling in the desired regions of phase-space.

For the simulation of particle physics at hadron colliders, the concept of *factorisation* is important. It describes the separation of the hard scattering process and the long distance process of a collision event. The hard scattering happens at short distances and can be predicted using perturbation theory. The long distance process, on the other hand, can only be described phenomenologically. It covers the sub-processes of hadronisation and the modelling of the underlying event. A schematic representation of an example proton–proton collision illustrating the factorisation is depicted in fig. 4.1.

The hard scattering component of the event is depicted in red. It can be computed to higher orders of

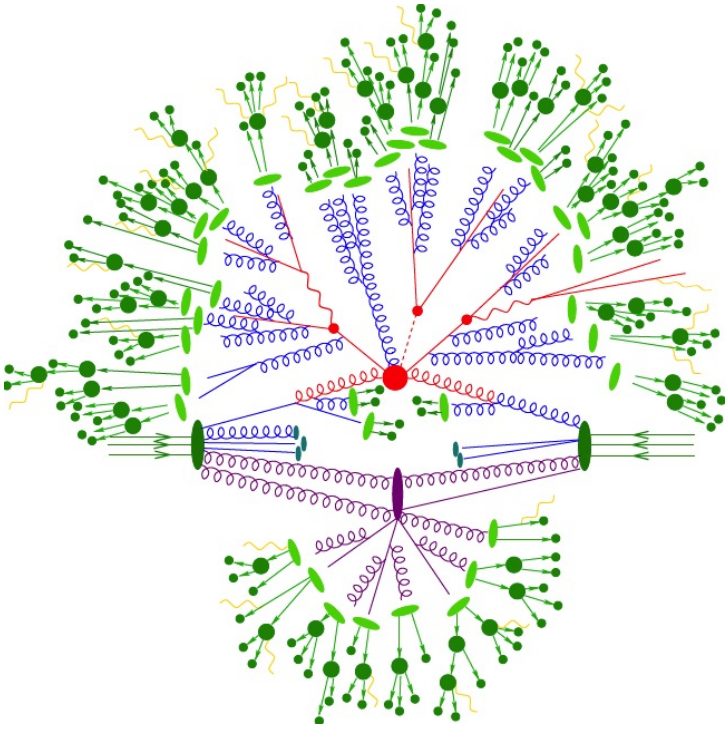

Figure 4.1: Schematic representation of an example proton–proton collision at the LHC [164]. The hard scattering process is shown in red. Blue lines illustrate radiation process, the underlying event of interacting proton remnants is depicted in purple. The hadronisation and showering of partons is coloured green.

perturbation theory. Initial and final state radiation produced by the high-energy incoming and outgoing particles are coloured blue. The underlying event is highlighted in purple. It represents interactions of the proton parts that do not participate in the hard scattering process. Due to their typically low momentum transfer, processes of the underlying event are not accessible via perturbation theory. The hadronisation of partons and their subsequent showering to the formation of jets is depicted in green. These processes can only be modelled phenomenologically. An additional challenge at hadron colliders is given by the substructure of the proton. The probability to find a certain parton at a certain fraction of the proton momentum is described by the parton distribution function and needs to be taken into account (cf. section 2.1.2).

The feature of factorisation can be exploited to divide the challenge of event simulation into smaller subtasks. Before starting the actual chain of simulation steps, the input parameters to the simulation need to be defined. While for Standard Model processes the inputs are known to high precision (cf. fig. 2.8), the spectrum of particle masses and their couplings or branching fractions of BSM theories need to be calculated for every signal scenario first.

For the different simulation steps, a multitude of software packages referred to as *generators* is available. Integrated frameworks of generators such as Pythia [165, 166], Herwig [167–169], or Sherpa [170–173] cover the entire chain of simulation. The starting point of the simulation process is the tree-level matrix element of the hard interaction, followed by an integration over phase-space. In this way, parton-level events are generated. Their final state particles undergo subsequent decay, hadronisation, and showering, allowing for multi-particle final states. The integrated frameworks also take care of initial and final state radiation, gluon emission, and further higher-order processes as well as simulation of the underlying event.

More specialised generators besides the integrated frameworks offer improvement in different steps. The matrix element calculation with respect to multi-parton final states is addressed by ALPGEN [174]. It also computes the matrix element at tree-level but in slices of final state partons. In this way, it is easily possible to simulate the production of e.g. a W-boson with up to six additional final state partons at matrix element level. Typically, this approach yields a better description than calculation of the boson production at tree-level and acquisition of the additional partons from showering. Since ALPGEN only covers the matrix element calculation, it needs to be be complemented by other generators for hadronisation, parton showering and the underlying event simulation. A different approach is pursued by the generators aMC@NLO [175–179] and POWHEG [180, 181] as well as the successor of the latter POWHEG-BOX [182]. These generators offer computation of the matrix element at NLO. In such computations, however, an overlap between the matrix element and the showering can occur which needs to be resolved. The aMC@NLO generator introduces counter-events to subtract the showering effects while keeping the NLO precision for inclusive observables. This approach requires prior knowledge of the showering process, e.g. the showering algorithm the generator is interfaced to. The generators from the POWHEG-family chose a different approach. Here, the showering process is required to be ordered in p_{T}. The matrix element calculations are then performed up to the first emission at NLO, vetoing the subsequent showering (e.g. from PYTHIA or HERWIG) above the obtained momentum threshold of the computed first emission in the matrix element.

Once the physics process from the proton–proton collision up to the showering and hadronisation is simulated, the events are forwarded to a simulation of the ATLAS detector. Depending on the required precision of the simulation and the available computing resources, either the complete GEANT4-based [183] model of the detector or the fast simulation framework AFII [184] are used. In the latter case, computing efforts are reduced substantially by substituting the individual shower interaction of a particle with the detector with a parametrised description and keeping the rest of the detector model in GEANT4. The fast simulation approach is only used for the signal samples of the models searched for in this thesis, the Standard Model samples are all produced using the full detector simulation. The subsequent sections provide an overview of the Standard Model and signal samples used in the context of this thesis as well as the tools used to generate them.

4.2 Simulation of Standard Model physics

From the full set of Standard Model processes, the most relevant ones to this analysis are the production of weak vector bosons V + jets and top quarks. These processes are assessed with utmost care in a set of dedicated control regions (cf. section 6.1), where their agreement with the observed data is studied and their prediction is corrected accordingly. Moreover, the influence of the chosen simulation setup on the predicted physics is studied and parametrised by a large set of systematic uncertainties (cf. section 7.3). In principle, the production of multiple weak vector bosons, referred to as VV processes, can also produce signal-like detector signatures. Due to the low production cross-section of such events and the difficult challenge of their isolation, VV contributions are considered by its nominal prediction without corrections of its normalisation. Due to its large cross-section and challenging non-perturbative underlying calculations, the irreducible contribution arising from QCD-induced multi-jet production is not simulated but estimated from data directly (cf. section 6.2). At the starting point of this analysis as presented in the forthcoming chapters, the SM processes are considered at the highest available order of cross-section calculations.

V + jets The samples for V + jets processes are generated by Sherpa. The matrix element (ME) calculations include up to two partons at next-to-leading order (NLO) and up to four additional partons at leading order (LO) in perturbative QCD using the OpenLoops [185] and Comix [172] ME generators, respectively [8]. The phase-space merging between the Sherpa parton shower [173] (PS) and the MEs follows the ME+PS@NLO prescription [171]. The inclusive cross-sections are normalised to a next-to-next-to-leading order (NNLO) calculation in QCD [186] based on the FEWZ program [8, 187]. The simulation process is performed separately for events containing only light quarks (u, d, s, assumed to be massless), events containing c- but no b-quarks, and events with b-quarks. Furthermore, the simulation is binned in the p_{T} of the vector boson and the truth-level H_{T} (cf. section 5.4). This segmented simulation process ensures better populated tails of various kinematic distributions that are crucial to a multitude of analyses. For studies of systematic uncertainties introduced due to the choice of the used generators, an additional comparison sample for $W(\tau\nu)$ + jets processes is used. It is generated using MG5_aMC@NLO interfaced to Pythia. The ME calculation is performed at tree-level and includes the emission of up to four additional partons [8].

Top-quarks The samples for the production of pairs of top-quarks as well as single top-quarks are simulated using the Powheg-Box generator for calculations of the MEs. The subsequent modelling of the PS, the hadronisation, and the underlying event are simulated using Pythia. The cross-section calculations are carried out at NNLO in perturbative QCD with the resummation of next-to-next-to-leading-logarithm (NNLL) soft gluon terms using the Top++ 2.0 program [8, 188]. Potential overlap between $t\bar{t}$ and single-t events beyond LO is avoided by the removal of the corresponding diagrams from the ME calculation step. The $t\bar{t}$ samples are segmented in a similar fashion as the V + jets samples, binned in truth-level $E_{\mathrm{T}}^{\mathrm{miss}}$ and H_{T}. In order to have the highest possible amount of statistics available, a dedicated merging scheme of the individual is developed [189]. The single-t samples are produced separately for s-channel and t-channel diagrams, Wt-production as well as the individual cases of weak vector or Higgs-bosons associated to the production.

For the evaluation of systematic uncertainties due to the chosen generator for $t\bar{t}$ production, additional comparison samples are used. Uncertainties due to variations in the used PDF set and the hadronisation scale are derived on PowhegBox+Pythia8 samples and applied to the nominal PowhegBox+Pythia6 prediction. The influence of the model of the hard scattering process is evaluated by a comparison of MG5_aMC@NLO and Powheg-Box samples both interfaced to Herwig++. Uncertainties due to the hadronisation model and underlying event are assessed by a comparison of Powheg-Box samples interfaced to Pythia and Herwig++. Finally, an uncertainty due to the modelling of ISR is studied by varying the Powheg-Box parameter, which controls the p_{T} of the first additional parton emission beyond the Born configuration [8]. Due to the minor influence of single-t processes (cf. section 7.3), no additional systematic uncertainty samples are considered. Instead, overall cross-section uncertainties are considered obtained by the Hathor 2.1 program [190, 191] using the PDF4LHC [192] prescription with the MSTW2006 68% CL NLO [193, 194], CT10 NLO [195], and NNPDF2.3 [196] PDF sets.

The usage of Sherpa as the nominal generator also for the simulation top-quark events has been studied to a greater extend [189] but found to be unfeasible due to an incorrect modelling of the τ-lepton spins and their correlation. Although a recovery of these crucial pieces of information is in principle possible using the TauSpinner tool [197] as performed in the early version of the presented analysis [9], the results found are not convincing [189]. Moreover, the chosen Powheg-Box samples are available with a substantially larger number of simulated events.

VV Processes involving the production of multiple weak vector bosons are generated using Sherpa. The amount of available statistics is enhanced by merging samples from two generation periods with different software versions. Processes with fully leptonic final states are calculated with up to one parton for the 4ℓ and $2\ell + 2\nu$ samples or no parton for the $3\ell + 1\nu$ samples at NLO, and up to three additional partons at LO. Processes with one of the bosons decaying hadronically and the other leptonically are simualted with up to one parton for the ZZ or no parton for the WW and WZ samples at NLO, and up to three additional partons at LO [8]. An overview of the generator configurations of all samples used in the context of this thesis is provided in table 4.1. A detailed list of all used samples is compiled in appendix F.

	Sample	Generator	PDF set	Showering prescription	Underlying event tune
Nominal samples	Pile-up	Pythia 8.186 [198]	MSTW2008LO [193]	—	A2 [199]
	W + jets	Sherpa 2.2.1 [170]	NNPDF3.0nnlo [200]	—	Sherpa default
	Z + jets	Sherpa 2.2.1	NNPDF3.0nnlo	—	Sherpa default
	$t\bar{t}$	Powheg-Box v2 [182]	CT10 [195]	Pythia 6.428 [165]	CTEQ6L1 [201] + Perugia2012 [202]
	Single-t	Powheg-Box [182] v1	CT10	Pythia 6.428	CTEQ6L1 + Perugia2012
	VV	Sherpa 2.2.2 [170]	NNPDF3.0nnlo	—	Sherpa default
		Sherpa 2.2.1	NNPDF3.0nnlo	—	Sherpa default
Systematic samples	$W(\tau\nu)$ + jets	MG5_aMC@NLO v2.2.3 [205]	NNPDF2.3lo [203]	Pythia 8.186	A14 [204]
	$t\bar{t}$	Powheg-Box v2	NNPDF3.0nlo	Pythia 8.210 [198]	NNPDF2.3lo + A14
		MG5_aMC@NLO v2.2.3	CT10	Herwig++ 2.7.1 [168]	UE-EE-5-CTEQ6L1 [206]
		Powheg-Box v2	CT10	Herwig++ 2.7.1	UE-EE-5-CTEQ6L1
Signal samples	$\tilde{g}\tilde{g}$ model	MG5_aMC@NLO v2.2.3	NNPDF2.3lo	Pythia 8.186	A14
	GMSB	Herwig++ 2.7.1	CTEQ6L1	—	UE-EE-5-CTEQ6L1

Table 4.1: Overview of the simulated SM and signal samples used in the context of this thesis, the used generators, parton distribution functions, showering models, and the underlying event models. For setups where the matrix element calculation tool is different from the tool for the modelling of the underlying event, the used PDF sets can differ.

4.3 Signal simulation

The signal models introduced in sections 2.2.2 and 2.2.4 are each described by two free parameters. The two-dimensional parameter-space of each model is covered by a finite selection of parameter pairs for which a similar simulation process as for the Standard Model processes is performed, giving rise to the nomenclature of a parameter *grid*. For the simplified model grid, 169 points are simulated, covering the ranges of 665 to 2 425 GeV in $m(\tilde{g})$ and 105 to 1 305 GeV in $m(\tilde{\chi}_1^0)$. The spacing of the grid is chosen such that in addition to the overall range, different mass splitting scenarios between $m(\tilde{g})$ and $m(\tilde{\chi}_1^0)$ are accessible. The simplified model is simulated using MG5_aMC@NLO interfaced to Pythia. The ME–PS matching is performed using the CKKW-L prescription, with a matching scale set to one quarter of the gluino mass [8]. For grid points with a small difference between the masses of the gluino and the LSP, a generator-level requirement on the p_{T} of the highest-energy jet is imposed to enforce a higher boost of the SUSY particles recoiling against the jet. In this way, a better detector acceptance of the decay products is ensured.

The GMSB model is simulated using Herwig++. The input SUSY spectra are provided in the SLHA format, generated using SPheno v3.1.12 [93]. The PS evolution is performed using algorithms described in [168, 207–209]. For the GMSB model, 71 grid points are simulated, covering a range of 70 to 150 TeV in equidistant steps of 10 TeV in Λ and 2 to 60 in $\tan\beta$. For $\tan\beta < 20$, the step-size is smaller, allowing for a more precise assessment of the Co-NLSP regime.

Signal cross-sections for both models are calculated to next-to-leading order in the strong coupling constant, adding the resummation of soft gluon emission at next-to-leading-logarithm accuracy (NLO+NLL) [210–214] using the Prospino program [210]. The nominal cross-section and its uncertainty are taken from an envelope of cross-section predictions using different PDF sets and factorisation and renormalisation scales, as described in [8, 215]. An overview of all studied signal samples is again compiled in appendix F, including the filter efficiencies of the simplified model jet filter.

4.4 Corrections of the simulation

Different sources limitations render any particle physics simulation an imperfect description of reality. Limited mathematical precision (e.g. the order of perturbation theory calculations) or computational efforts (e.g. the number of simulated events) cannot be remedied once the simulation has been performed. Deviations due to assumptions of the experimental model made prior to the simulation process can be corrected a-posteriori. An example of such a correction is the application of scale factors to an event for every reconstructed τ-lepton to match the reconstruction performance in simulation to the one in data. Other corrections may depend on properties of the overall event. The forthcoming paragraphs briefly explain the implementation of corrections of the latter type applied in the presented analysis.

4.4.1 Pile-up reweighting

The simulation of particle collisions a priori to the recording of data faces the challenge of unknown operation conditions of the accelerator and the detector. A particular obstacle is simulation of pile-up. Ideally, the simulation is performed based on data taken under the actual experimental conditions. The development and testing of analysis strategies prior to the data taking, however, requires the availability of simulated events.

The contradiction is overcome by assuming a hypothetical pile-up model as input to the simulation. The characteristic distribution of the average number of interactions per bunch-crossing $\langle\mu\rangle$ is taken as a measure of agreement between simulation and data[1]. The distribution of $\langle\mu\rangle$ after application of the 1τ pre-selection (cf. section 5.6) is shown in fig. 4.2. The shape of the originally simulated distribution (green) in the MC15c simulation campaign clearly deviates from the one measured in the combined data (black) taken in 2015 and 2016. It is more narrow and pronounced.

The discrepancy between the input $\langle\mu\rangle$ profile and data is corrected by the application of re-weighting factors, ultimately matching the distributions of data and simulation (red) in fig. 4.2. The remaining deviations between data and the re-weighted simulation are addressed by a designated systematic uncertainty as described in section 7.2.

[1] Since the actual number of interactions per bunch-crossing cannot be measured directly, its average is the chosen as a measure of pile-up.

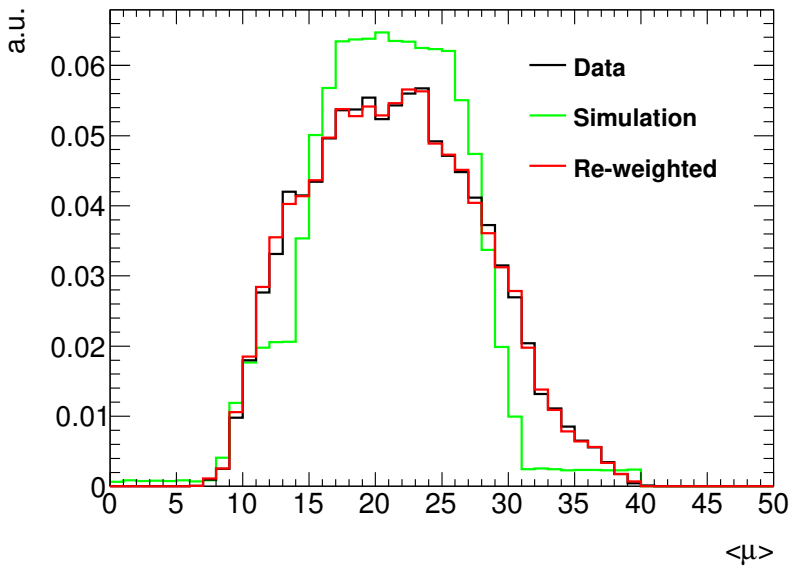

Figure 4.2: Distribution of the average number of interactions per bunch-crossing $\langle\mu\rangle$ in data and simulation. The pre-selection of the 1τ channel (cf. section 5.6 is applied. The simulation distributions comprise all simulated SM samples used in this analysis. The distributions are normalised to unity to allow for a comparison of the shape.

4.4.2 *b*-tag reweighting

Processes involving top-quarks pose one of the major and irreducible Standard Model contributions to this analysis (cf. section 5.2). The modelling of simulated top-quark events is assessed in dedicated regions of phase-space, which ensure a high top-quark contribution by requiring *b*-tagged jets (cf. section 6.1). The correct simulation of the *b*-tagging as introduced in section 3.3.2) is hence a crucial aspect. As explained ibid., dedicated analyses are used to calibrate the efficiency of the selection algorithms. Despite the dedicated calibration procedures, no a priori agreement between the simulated *b*-tag selection and the one obtained from data is observed. Similar as for the pile-up or τ-lepton corrections, scale factors are introduced to measured performance in simulation. The correction applied depends on the overall kinematics of the events, the number of real *b*- and *c*-jets, and the response of the tagging algorithm. It is thus calculated on an event-by-event basis rather than for individual objects. Any bias in selection not requiring *b*-tagged jets is avoided by only applying the re-weighting to events that fulfil all kinematic requirements on the control sample.

4.4.3 Further corrections

Similar considerations as for τ-leptons and *b*-tagged jets can be made for electrons and muons, too. In a similar fashion, corresponding correction factors are obtained and applied to the respective events in the presented analysis. Corrections that are unique to the presented analysis and not prescribed for other ATLAS studies are introduced in section 7.4 and supported by appendix D.

CHAPTER 5

Analysis Design and Strategy – The Map to SUSY

The search for squarks and gluinos as first hints towards the existence of Supersymmetry is an ambitious endeavour. The ATLAS detector at the $\sqrt{s} = 13\,\text{TeV}$ Large Hadron Collider provides both the unique opportunity to search for SUSY at the highest available energies as well as a challenging experimental environment. The multitude of experimental and theoretical results obtained in the last decades motivate the choice of the models introduced in section 2.2. The ever increasing limits on the masses of sparticles and SUSY parameters narrow down the available phase-space and require new, tailor-made analysis procedures for further assessment. The analysis presented in the context of this thesis represents the advancement of searches for SUSY at $\sqrt{s} = 8\,\text{TeV}$, involving the presence of jets, missing transverse momentum and τ-leptons [13, 15]. It makes use of more advanced procedures of signal extraction and estimation of the Standard Model contributions based on the increased amount of available statistics. This chapter describes the general strategy of the analysis in the search for signals of SUSY and discusses the different approaches that are pursued. The introduction of the tools used for signal isolation, assessment of the Standard Model processes and extraction of the results is motivated by the expected physics signatures.

5.1 Expected physics signatures

The long ongoing search for hints towards the existence of SUSY has lead to models of ever smaller production cross-sections. Their expected occurrence is hence rare with respect to processes arising from the Standard Model. An illustration of the expected abundance of Standard Model physics with respect to an example SUSY model is given in fig. 5.1. It displays measured and predicted production cross-sections of various SM processes and an example simplified model signal scenario. For the majority of SM processes relevant in the context of this analysis, i.e. the production of top-quarks and electroweak gauge bosons (W + jets, Z + jets, VV), the production cross-sections are expected to exceed those of SUSY models by several orders of magnitude. In order to find any SUSY signal, it is hence necessary to develop a selection mechanism.

The extraction of signal events from the vast amount of recorded data can be carried out by imposing selection criteria that only signal events are expected to pass. The design process of such a suite of criteria—each being referred to as a *cut*—starts with the characteristics of the signal models of interest. In a nutshell, the simplified model is characterised by the following list of features that can be inferred from fig. 5.2(a) and their correlations amongst each other.

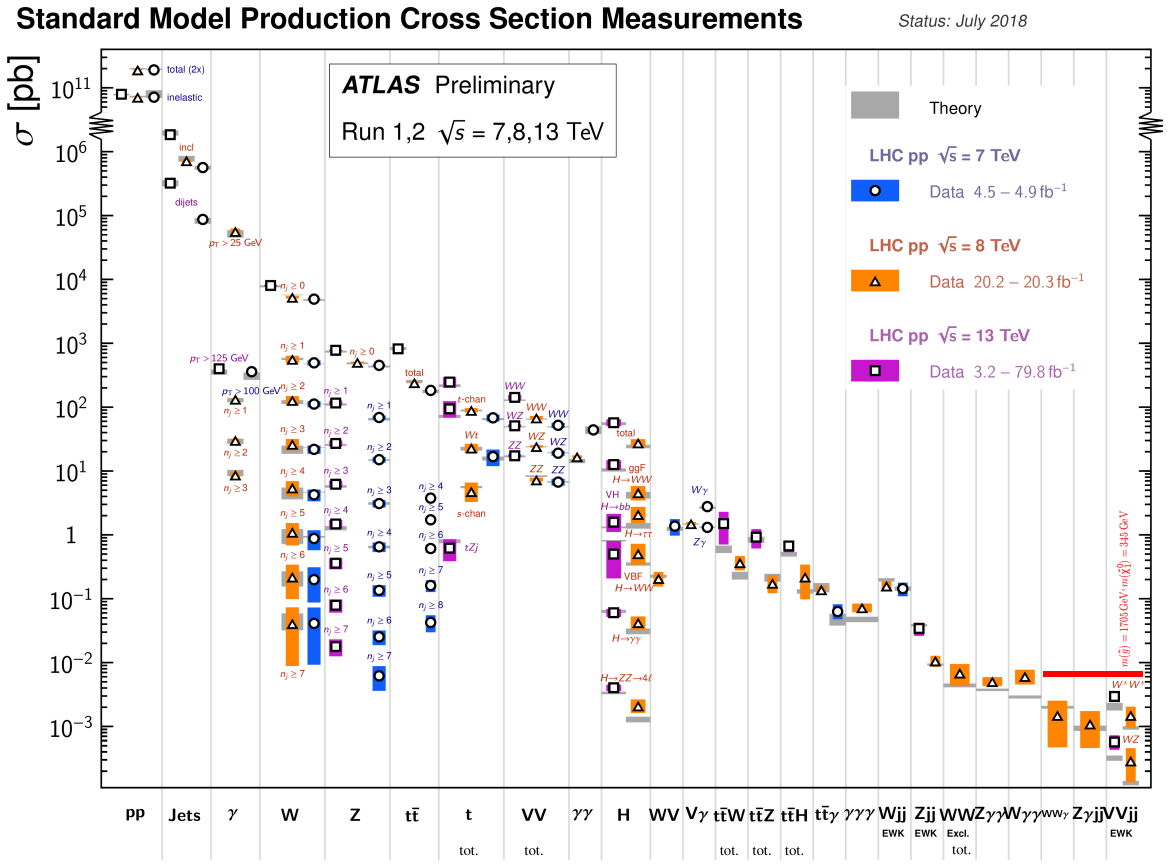

Figure 5.1: Summary of several Standard Model total and fiducial production cross-section measurements, corrected for leptonic branching fractions, compared to the corresponding theoretical expectations. All theoretical expectations were calculated at NLO or higher. The luminosity used for each measurement is indicated in the legend. Uncertainties for the theoretical predictions are quoted from the original ATLAS papers. They were not always evaluated using the same prescriptions for PDFs and scales. The $W\gamma$ and $Z\gamma$ theoretical cross-sections have non-perturbative corrections applied to the NNLO fixed order calculations (PRD 87, 112003 (2013)). Not all measurements are statistically significant yet [216]. To the right, a red line marks the total production cross-section of an example simplified model point ($m(\tilde{g}) = 1\,705\,\text{GeV}$, $m(\tilde{\chi}_1^0) = 345\,\text{GeV}$, $\sigma_{\text{tot.}} = 4.57\,\text{fb}$). An example for the GMSB model with $\Lambda = 120\,\text{TeV}$ and $\tan\beta = 40$ would have a production cross-section of $\sigma_{\text{tot.}} = 11.10\,\text{fb}$.

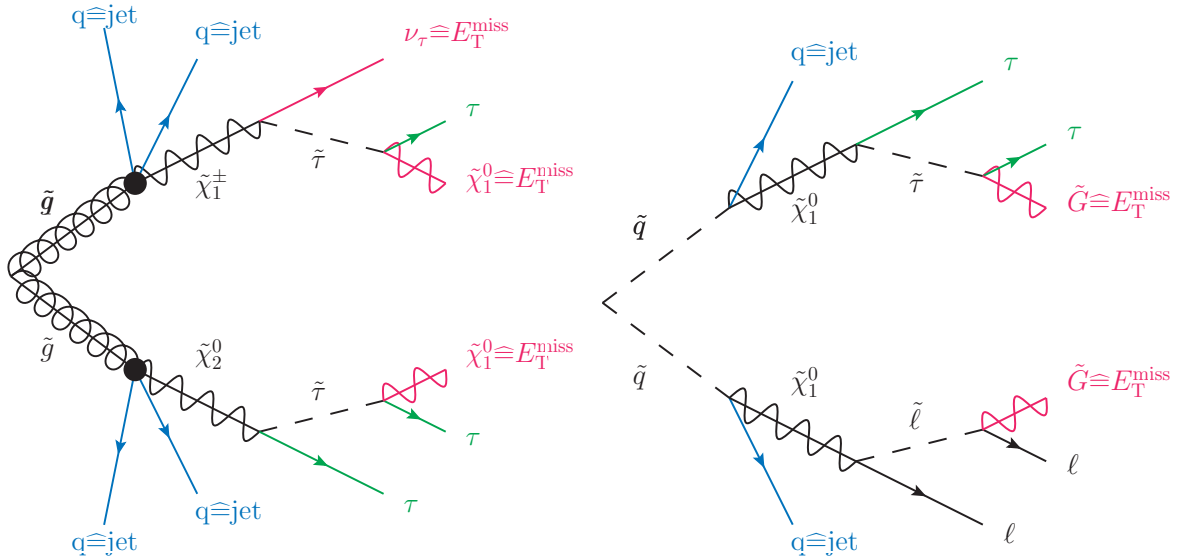

(a) Simplified model (b) Example GMSB diagram

Figure 5.2: Reconstructable physics objects in the simplified model of gluino pair-production (a) and for an example diagram of the GMSB model (b). Particles reconstructed as jets are marked in blue, τ-leptons in green and contributions to the event's overall missing transverse momentum in red. Light leptons are displayed in black.

- the presence of numerous jets with properties depending on the energy available in the decay of the gluino,
- the presence of (multiple) τ-leptons, their properties also depending on the available energy in the decay of the mother sparticle
- and the presence of missing momentum due to escaping particles such as neutrinos (also introduced from decays of the τ-leptons themselves) and the LSPs. As for the jets and τ-leptons, the available energy in the production process of the neutrinos and the LSP is expected to drive the amount of missing momentum.
- Besides, the absence of any prompt light lepton is noteworthy. Electrons or muons are only expected in the case of leptonic decays of τ-leptons – a case which is not considered here but which has been subject to exploration [217, 218].
- The list of reconstructible physics objects is completed by jets arising from bottom-quark decays. Since the decay of the gluino is inclusive with respect to quark flavours, no requirements regarding the presence of *b*-tagged jets are imposed in the search for signal.

The experimentally accessible signatures of the GMSB model can be inferred from the production and decay diagram in fig. 5.2(b): the characteristic τ-leptons are accompanied by multiple jets arising from decays of squarks (or gluinos), as well as missing momentum from the undetectable gravitino LSPs and neutrinos in the τ-lepton decays. The most striking difference can also directly be inferred from said figure: the GMSB model does allow for the presence of light leptons, e.g. emerging from decaying sleptons.

A special characteristic of both models is the number of produced τ-leptons. Due to the different possible decays of gluinos and gauginos in the simplified model and due to the rich sparticle spectrum of

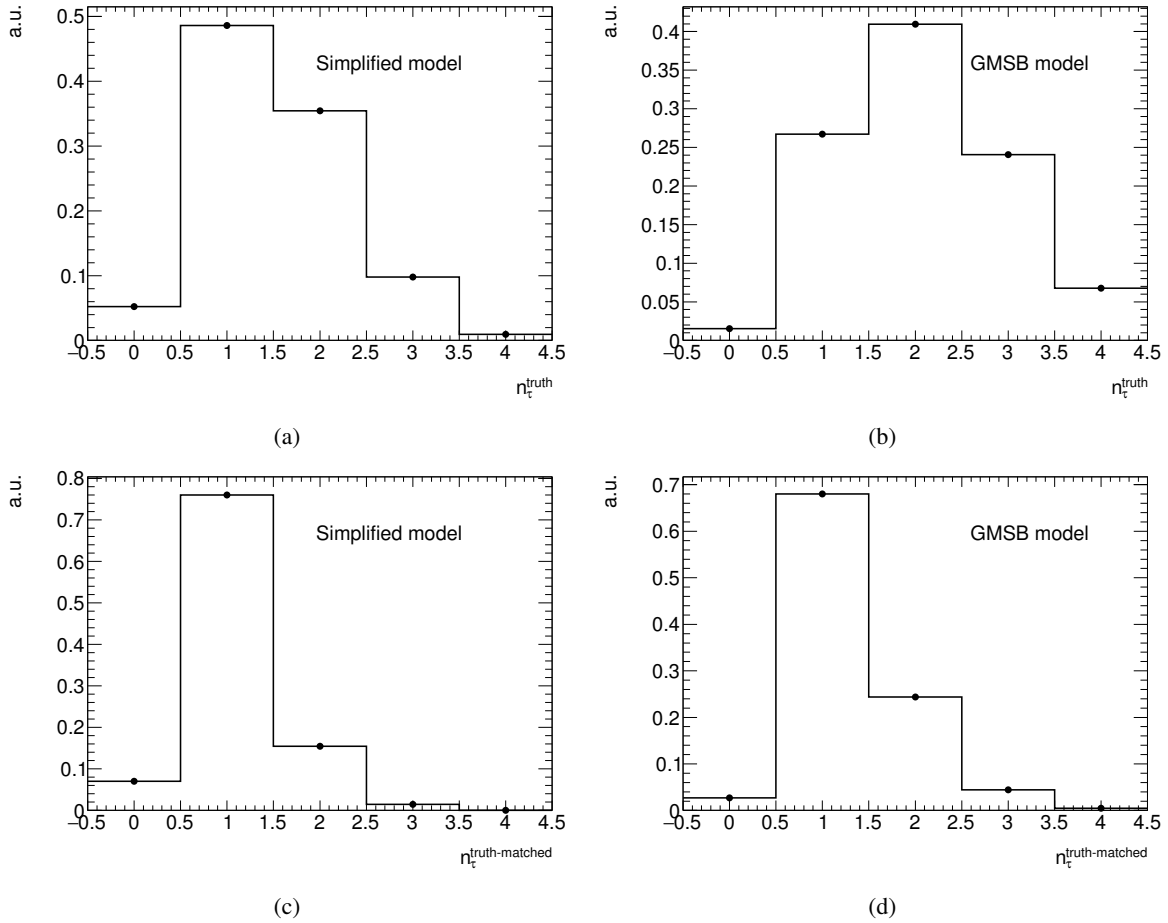

Figure 5.3: Number of truth-level τ-leptons n_τ^{truth} (truth-matched τ-leptons $n_\tau^{\text{truth-matched}}$) summed up for all signal points of the simplified model of gluino production (a) ((c)) and the GMSB Model (b) ((d)). The distributions are normalised to unity to ensure comparability.

the GMSB model in general, the τ-lepton multiplicity can vary. Folding this effect with the reconstruction efficiencies for one or multiple τ-leptons in the ATLAS detector, the number of expected τ-leptons that can actually be used for signal extraction from data becomes a crucial variable. For both models, the number of generated or *truth-level*[1] τ-leptons and of reconstructed τ-leptons that are matched to a truth-level τ-lepton [2] is depicted in fig. 5.3. While both models are initially rich in signatures involving multiple τ-leptons, the number of actually reconstructed τ-leptons is likely to be smaller. This effect is later exploited for the design of the search.

[1] Quantities as predicted by the simulation before interaction with and reconstruction by the detector are referred to as *truth-level* quantities. They are to be distinguished from *reconstruction-level* quantities that are obtained after an event has undergone the detector simulation and reconstruction.

[2] A *truth-matched* reconstructed τ-lepton has a truth-level τ-lepton within a cone of $\Delta R = 0.2$ around its reconstructed four-vector axis.

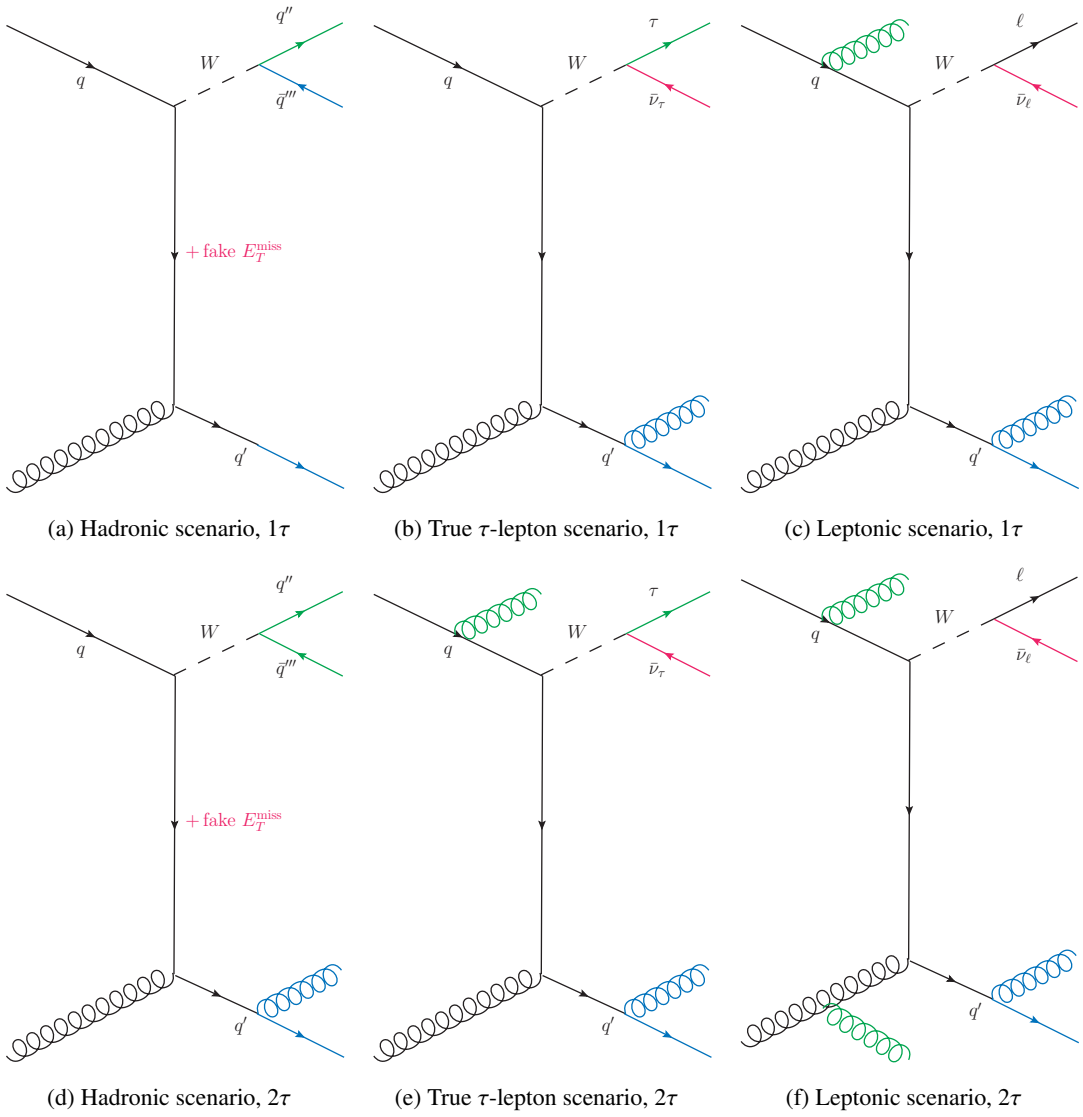

(a) Hadronic scenario, 1τ (b) True τ-lepton scenario, 1τ (c) Leptonic scenario, 1τ

(d) Hadronic scenario, 2τ (e) True τ-lepton scenario, 2τ (f) Leptonic scenario, 2τ

Figure 5.4: Example production diagrams for W + jets processes with one ((a), (b), (c)) or two ((d), (e), (f), [15]) detectable τ-leptons in the final state. Objects marked in blue are detected as jets, green ones as τ-leptons, while red ones contribute to the measured missing transverse momentum.

5.2 Standard Model background processes

From the example SM processes depicted in fig. 5.1, some can exhibit detector signatures that resemble the ones that are expected for the signal models. The set of those processes is referred to as *background*. The largest contribution to the background spectrum by far originates from multi-jet production – fig. 5.1 shows $O(5 \times 10^5$ pb) for di-jet production and $O(10^6$ pb) for fully inclusive jet production. Since multi-jet production due to the strong force does not allow for the production of any escaping particle nor any τ-lepton, such events are intrinsically suppressed in this analysis. However, small contributions due to mis-measurements of jets, jets falsely being identified as τ-leptons, or from semi-leptonic decays of b-jets are still possible and have to be considered in the overall background estimation.

Of major importance are processes where the charged weak gauge boson W is produced, typically in association with additional jets from initial or final state radiation. Example diagrams illustrating different kinds of W + jets production that contribute to the background spectrum are shown in fig. 5.4. The fully hadronic case where the W-boson decays into two quarks contributes with the largest cross-section. Although without any selection applied, this background is indistinguishable from multi-jet production, it is still two orders of magnitude less abundant than the latter. The decay of the W-boson into a τ-lepton and the corresponding neutrino poses the only source of genuine τ-leptons from W + jets production. Here, missing momentum can originate from the neutrinos in the decay of the W-boson and the further decay of the τ-lepton. Any τ-lepton required beyond the first one has to be a mis-identified jet. Finally, the decay of the W-boson into any light lepton and the corresponding neutrino contributes the smallest. Although genuine missing transverse momentum can be measured in this scenario, any reconstructed τ-lepton has to a mis-identified jet from a QCD process. Considering the cross-section visualisation in fig. 5.1, the different numbers of necessary additional jets and the probabilities of jets being mistaken for τ-leptons, it becomes clear that W + jets poses a stronger background contribution when requiring only one τ-lepton than multiple.

Already with a smaller inclusive cross-section, production of the neutral weak gauge boson Z contributes to the background spectrum. Example diagrams of signatures that can mimic physics of signal models are depicted in fig. 5.5. As for the W + jets scenarios, in the fully hadronic case τ-leptons have to be mis-identified jets and missing transverse momentum has to arise from jet mis-measurements or semi-leptonic decays of b-jets. Again, without any selection applied, this scenario is indistinguishable from multi-jet production but comes at much lower cross-sections. In contrast to any W + jets scenario, two genuine τ-leptons can be produced by the decay of the Z-boson, along with missing momentum from the involved neutrinos. The decay of the Z-boson to a neutrino pair leaves genuine missing transverse momentum in the detector but requires additional jets to be mis-identified as τ-leptons. Not displayed is the decay of the Z-boson to a pair of light leptons. It resembles the latter scenario but would require jet mis-measurements or the presence of semi-leptonically decaying b-jets to incorporate the missing transverse momentum. Depending on the number of required final state τ-leptons, different decay patterns of the Z-bosons contribute. The decay to two τ-leptons is relevant when two τ-leptons are required, the decay to two neutrinos poses a background in scenarios with only one τ-lepton.

Finally, production of top-quarks poses an important background to this analysis. Due to their high mass, top-quarks can decay via real W-bosons into a rich spectrum of lighter particles, including all lepton flavours and all lighter quarks. This unique feature enables decays of top-quark pairs to virtually mimic any signal signature. This includes multiple genuine and fake τ-leptons, genuine missing transverse momentum, as well as multiple jets. This fact renders the $t\bar{t}$ background irreducible to this analysis. For final states where two τ-leptons are required, example diagrams of the production and decay of top-quark pairts are shown in fig. 5.6. Due to their smaller production cross-section and the reduced possibility to produce detected τ-leptons, the production of single top-quarks is only a minor background to this analysis. The low cross-section of $t\bar{t}$ production in association with additional gauge bosons renders it also negligible. The remaining parts of the background spectrum are production processes of two weak gauge bosons (referred to as VV or *di-boson*). In principle, they can exhibit signatures as rich as those of $t\bar{t}$ processes. Their lower production cross-section, however, makes such events a minor background. The rare processes including the presence of more than two gauge bosons or a Higgs boson are not considered due to their low cross-section as studied in [13, 15].

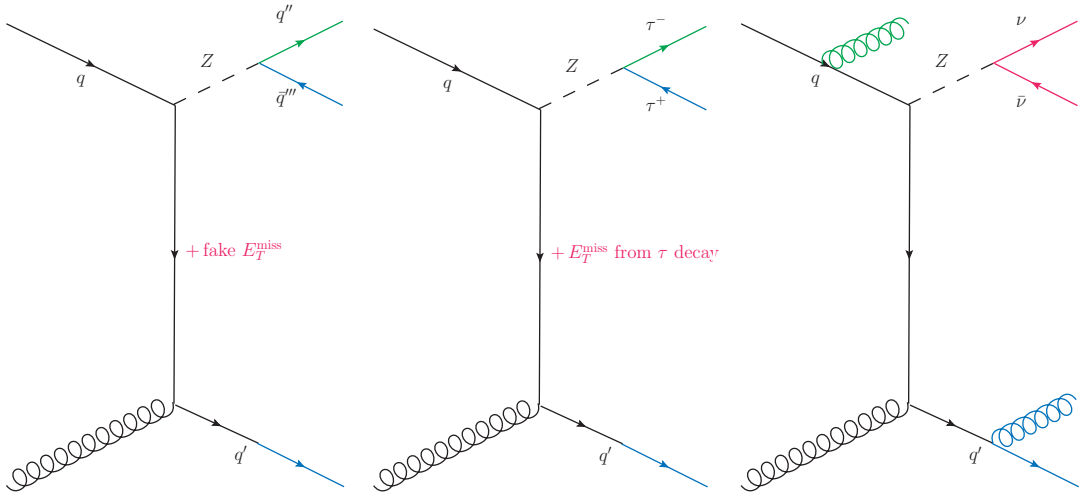

(a) Hadronic scenario, 1τ (b) True τ-lepton scenario, 1τ (c) Invisible scenario, 1τ

(d) Hadronic scenario, 2τ (e) True τ-lepton scenario, 2τ (f) Invisible scenario, 2τ

Figure 5.5: Example production diagrams for Z + jets processes with one ((a), (b), (c)) or two ((d), (e), (f), [15]) detectable τ-leptons in the final state. Objects marked in blue are detected as jets, green ones as τ-leptons while red ones contribute to the measured missing transverse momentum.

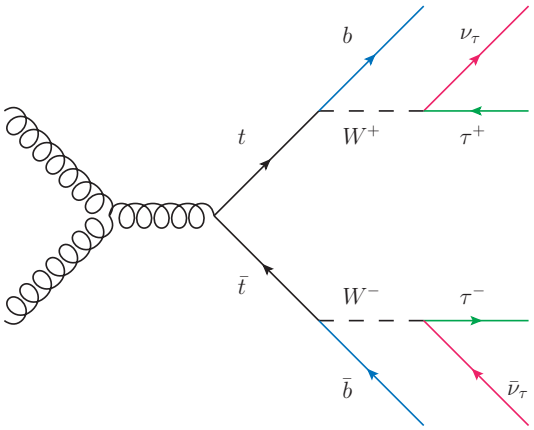

(a) Two true τ-leptons scenario, 2τ

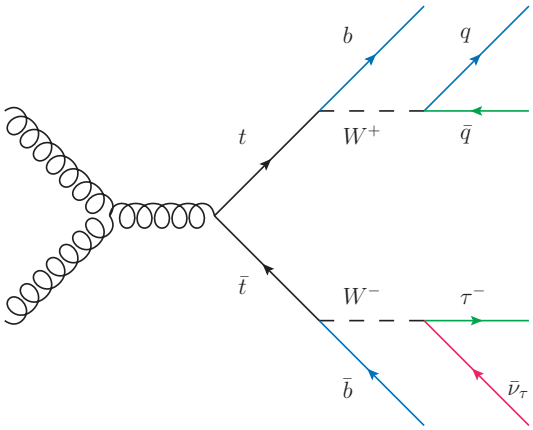

(b) True τ-lepton scenario, 2τ

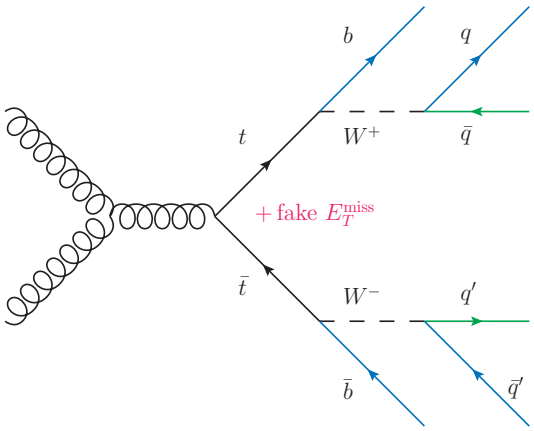

(c) Hadronic scenario, 2τ

Figure 5.6: Example production diagrams for $t\bar{t}$ processes with two detectable τ-leptons in the final state [15]. Objects marked in blue are detected as jets, green ones as τ-leptons while red ones contribute to the measured missing transverse momentum.

5.3 Analysis strategy

With knowledge about the signal models and the background processes to be expected in this search, the general analysis strategy can be introduced. The first step is to develop selection criteria that suppress background but affect the signal models as little as possible. By imposing cuts on data and simulation alike, signal-like events are filtered. Since this procedure is equivalent to narrowing down the available phase-space into smaller regions, such a suite of cuts is also referred to as a *signal region* (SR). The extraction of results in a SR is performed by means of hypothesis tests. The agreement between the combined signal-plus-background hypothesis and the background-only hypothesis with the observed data is quantified by fitting the the respective simulations to data. The results of these hypothesis tests or fits are the foundation for any further statements about the validity of the tested models. A detailed explanation of the utilised fitting procedures and the interpretation of their results is provided in appendix G.

Signal region concepts Depending on the desired approach of result extraction, the available amount of data, and the statistical tools, the design of SRs can follow different paradigms. An approach that has been used frequently in the past [9, 12, 13, 219] is to suppress the background of the Standard Model as strongly as possible, condoning a simultaneous loss in signal events due to strong selection criteria being imposed. Following this paradigm, the extraction of results is based on the overall number of events (so-called *yields*) in the recorded data, the expected background and predicted signal, and their uncertainties – all being measured in the respective signal regions. This procedure is particularly effective for analyses that suffer from little data to base the evaluation on since only the overall yields and uncertainties are of interest. Due to the low available amount of recorded data in the first $\sqrt{s} = 13\,\text{TeV}$ period of LHC in 2015, this has been the sole approach also in the exploration phase of this thesis [9]. Although more integrated luminosity has been collected in the $\sqrt{s} = 8\,\text{TeV}$ periods of the LHC, limitations in statistical tools constrained [12, 13, 219] to use only this approach. Since under this paradigm, the normalisation of the signal and background predictions is fitted to data, such an SR is referred to as *normalisation-fit* SR.

Once the basic number of events available for an evaluation is higher, a more refined procedure can be applied more reliably. Instead of only counting data and simulated events, the comparison of of characteristic distributions can be exploited to discriminate signal from background. The higher statistics allow for studies of binned distributions which look different for signal and background. In the this approach, the normalisation of signal and background is fitted using bins of a given distribution, resembling a fit of the shape of that distribution. This technique is hence referred to as *shape-fit* or *multi-bin fit*, introducing a corresponding nomenclature for SRs designed under this paradigm. Since the shape of the distribution in which the multi-bin fit is performed is not a free parameter of the underlying signal models, the term *multi-bin fit* is used for further reference. In accordance to that choice, the normalisation-fit approach is further referred to as *single-bin fit*.

The general idea of this approach is illustrated in a simplified example in fig. 5.7. Two different signals that have identical yields in a SR but look different in a binned histogram of a variable that has discriminating power. They can be separated by using said distribution instead of only the total yields. More important than discriminating two signals from each other is the enhancement of the confidence into hypothesis tests that quantify the agreement between observed data and different proposed hypotheses. While a single-bin fit is equivalent to merging all bins of a distribution, only considering the significance[3] of the overall yields, a multi-bin fit gives more weight to significant bins than to insignificant ones. This way, the outcome of a multi-bin fit arises from a more constrained foundation and can give more trustworthy result. These aspects are covered in extensive detail in appendix G, motivating and illustrating the benefits of this technique further. The multi-bin fit approach does not only come with statistical benefits, but also enables a SR to probe a wider phase-space. The higher number of events that are used to build the distribution that is fitted later, arise from less strict cuts. This softer selection does not only allow for more background and signal alike that can be separated by the shape differences. It also allows signals to enter the evaluation process in the SR, which would not enter stricter single-bin SRs. Thus the multi-bin fit approach can probe areas of the model phase-space that a single-bin fit would not address because it is simply not tailored towards it. While in the SR design process for the single-bin fit a compromise between signal significance and signal diversity has to be found, the multi-bin fit intrinsically fosters both. Both of these approaches, the single-bin fit and the multi-bin fit, are used in this analysis. The necessary developments are presented, and a comparison and discussion of their performance is carried out.

Regardless of the chosen fitting approach, the exact design of the different SRs is dependent on the number of τ-leptons available. Sections 5.1 and 5.2 have outlined that the number of τ-leptons, which are to be expected, strongly varies depending on the type of background or signal.

[3] There are different ways of defining *significance*. For additional details see appendix B.

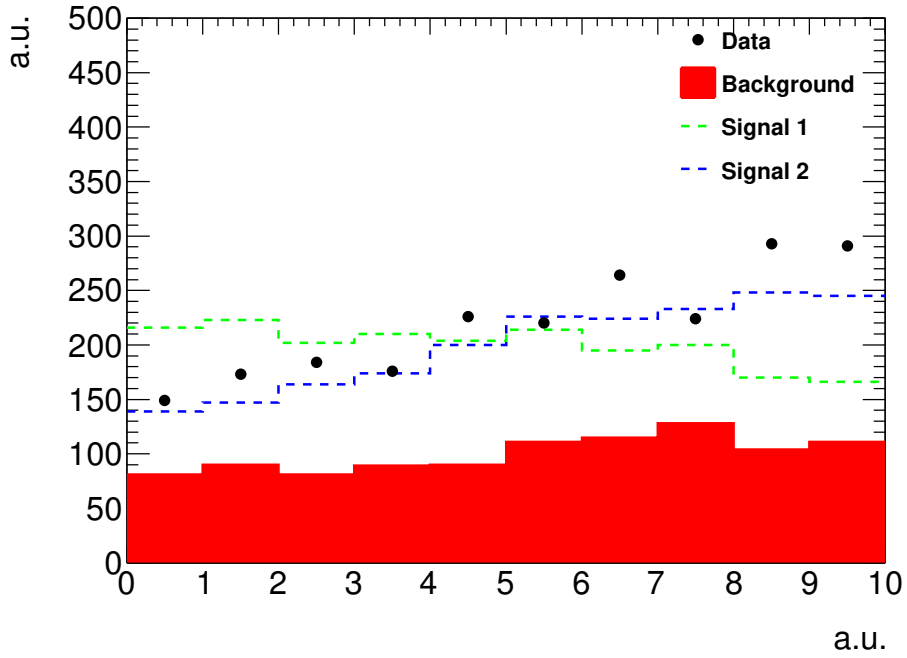

Figure 5.7: Example distribution for a multi-bin fit. In multiple bins of an arbitrary observable, two signals with the same event yield but different shapes are displayed above the same background. The difference in the signal shapes can be exploited to determine the signal model that agrees better with the observed data.

As a consequence of these expectations, the analysis is split into two so-called *signal channels*, separating signatures depending on the number of reconstructed τ-leptons. The 1τ channel exclusively considers signatures with exactly one reconstructed τ-lepton. The 2τ channel addresses all signatures containing multiple τ-leptons, requiring at least two reconstructed τ-leptons. In the 1τ channel, two single-bin fit SRs are designed that are tailored towards the simplified model. They are complemented by two single-bin fit SRs in the 2τ channel. The set of these four SRs is mutually exclusive, each SR probing a different part of the simplified model phase-space. A multi-bin fit SR is developed in the 2τ channel to explore the potential gain of this approach. It is a substitute for the 2τ high-mass single-bin SR and hence mutually exclusive with respect to the other three single-bin fit SRs of both channels.

Based on earlier sensitivity studies [9], a designated single-bin fit SR tailored towards the GMSB model is only developed in the 2τ channel. It is based on stricter requirements on the same observables as the high-mass SR of the 2τ channel and hence also mutually exclusive with respect to the other three single-bin fit SRs of both channels. As mentioned in section 3.3.4, τ-leptons that are reconstructed and properly identified are reconstructed only from hadronic decays – leptonic tau decays are not reconstructed as τ-leptons but as the corresponding leptons. This fact has been exploited in the $\sqrt{s} = 8\,\text{TeV}$ studies [12, 13, 219, 220] by means of additional signal channels that target $\tau + e$ and $\tau + \mu$ signatures, effectively looking for signatures of two τ-leptons with one of the τ-leptons decaying leptonically. Due to the small branching fraction of these τ-lepton decays, the expected benefit of incorporating these additional signal channels is small. These analysis strategies are hence neither pursued any further in the studies with $\sqrt{s} = 13\,\text{TeV}$ data [8, 9] nor in this analysis.

Background estimation Regardless of the technique used for the extraction of results, it is necessary to have a reliable prediction of the expected Standard Model background in the SRs. In this analysis, the background model is studied, constrained, and validated to ensure its reliability.

In a first step of the background prediction procedure, so-called *control regions* (CRs) are designed. In contrast to SRs, CRs are signal-free regions of phase-space tailored to study specific kinds of background. A CR is built for every major contribution to the background spectrum of this analysis, e.g. W + jets processes with decays into genuine τ-leptons. Each CR is designed such that its composition is dominated by the respective type of background process.

As computational power and precision as well as analytical knowledge are limited, the simulated background prediction does not describe the observed data perfectly. The quality of the description is improved by performing an adjustment of the different backgrounds to data in all CRs. All background normalisations are varied simultaneously until the best possible agreement across all CRs is found. Each CR hence contributes the strongest to the normalisation of its respective background component and acts as a simultaneous constraint on all other background normalisations. In order for this approach to work, the individual CRs need to be mutually exclusive to avoid any double-counting of events when carrying out the fit of the normalisations[4] and hence avoiding unnecessary bias. While the absence of any signal is crucial to not spoil the adjustment of the background to data, it is helpful to ensure an as high as possible purity of the backgrounds of interest in their respective CRs. However, leaving a sufficient amount of events to perform the adjustment with is also of major importance to not be subject to unnecessarily high statistical fluctuations and hence uncertainties on the obtained normalisation. The output of this procedure are *normalisation-factors* (NFs) that are used as additional scaling factors for the backgrounds to match the prediction in the best possible way to the observed data in all regions of phase-space. While an NF close to 1.0 with a small uncertainty indicates good modelling of the corresponding background process in a CR with good statistics, NFs deviating from unity point towards potential modelling issues of the process of interest. High uncertainties on the NFs indicate insufficient statistics to carry out a proper fit or the influence of systematic uncertainties. More details on the concept of adjusting the Standard Model background and the NFs are provided in chapter 6.

The modelling of the backgrounds is not only assessed by evaluation of the resulting NFs but also by means of so-called *validation regions* (VRs). While the mutually exclusive CRs do not share any phase-space with the signal-rich SRs, the VRs are, in every respect, just in between CRs and SRs: validation regions are designed such that they probe the phase-space gap between CRs and SRs and hence the extrapolation from the the background-fit regime to the application in the SRs. Since no fit of any kind is performed in the VRs, they do not necessarily need to be mutually exclusive with respect to each other – which they are nevertheless in this analysis. The assessment of the extrapolation is carried out by application of the NFs to the backgrounds in the VRs and a following check of the modelling of backgrounds in the variables that are used for the definition of the SRs. Agreement between the background prediction and data in the VRs is an indicator for a reliable background estimation in the SRs later on where the same NFs are applied in the same way. In order for this assessment to work, the absence of signal in the VRs needs to be ensured, just as for the CRs.

As a novelty with respect to earlier studies [9, 13, 219], this analysis uses one mutual set of CRs for both channels, estimating the background to each SR, regardless of the channel, in the very same way and free of any overlap in phase-space (cf. fig. 6.11 in section 6.4). Since VRs are supposed to probe the transfer from the CRs to the SRs, their design depends on the SRs and hence on the signal channel.

[4] The adjustment of the Standard Model background prediction to the observed data in the CRs is performed by treating individual normalisations as free parameters in a simultaneous fit. This fit is referred to as *background-only* fit and to be distinguished from the fit performed to extract signal information as introduced before. Further details on the background-only fit can be found in section 6.1 and in appendix G.

As a consequence, VRs are designed for each signal channel individually. The set of mutual CRs in combination with the aforementioned set of signal regions allows for several major advancements of this analysis with respect to [9, 13, 219].

A) It marks the first attempt to utilise the multi-bin fit approach for result extraction and allows for a direct comparison with the single-bin fit approach that is carried out in parallel.

B) The mutual exclusiveness of the four single-bin fit SRs and their mutual background estimation allow for a simultaneous fit of the four SRs. This point marks a substantial improvement of this analysis over earlier studies [9, 13, 219] in terms of sensitivity to the signal models searched for: the ability to use four different SRs, each addressing a different part of phase-space, allows for inclusion of all possible signatures into the search for signal – particularly considering 1τ and 2τ signatures at the same time. This approach is superior to the combination of SRs that are not mutually exclusive based on the best expected performance. In the case of [9, 13, 219], for example, only results of one of the two channels—either the 1τ or the 2τ channel—were used, neglecting any potential information the other channel could have held. By considering all possible final state signal signatures at the same time, the less sensitive SRs can still enhance the sensitivity of the strongest stand-alone SRs, hence, increasing the overall sensitivity. This effect is illustrated by a comparison of the expected limits of both of these approaches in fig. 5.8. The increase in sensitivity and thus exclusion power when using all available signatures in the simultaneous fit over only choosing the best-performing single SR at each point is clearly visible. At high values of $m(\tilde{g})$ and $m(\tilde{\chi}_1^0)$, the limit is mainly driven by the 2τ channel, the increase due to information from the 1τ channel is small. The benefit from already using more than just the strongest of the 2τ SRs can be inferred from the 2τ limit being stronger than the Best-$\mathrm{CL}_\mathrm{S}^{\mathrm{exp.}}$ limit of both channels. At highest gluino and lowest neutralino masses, both channels perform similarly when considered individually. When utilising information from both channels simultaneously, however, the limit is improved substantially.

C) The arguments given under **B)** are also applicable to the search for the GMSB model. While only the 2τ channel has a designated GMSB SR, there are still three SRs to which this SR is mutually exclusive. Since also for the 2τ GMSB SR the same background estimation from the same set of CRs is used, it is possible to combine the remaining simplified model SRs in one simultaneous fit with the 2τ GMSB SR to exploit any potential sensitivity they hold.

5.4 Important observables and variables

The characteristic signatures of the models, represented by numerous observables and variables, are used to distinguish the different regions of phase-space from each other. The following paragraph introduces the list of used variables and observables in accordance with [8].

- The multiplicity of the characteristic particles helps to distinguish signal channels or control regions from each other. Here, the number of τ-leptons n_τ, the number of jets and b-tagged jets n_{jet}, $n_{b-\mathrm{jet}}$, respectively, and the number of muons n_μ are used.

- Apart from the pure presence of particles, some regions of phase-space impose additional requirements on the individual properties of particles such as their transverse momentum, e.g. p_T^j or p_T^τ, or topological properties with respect to the rest of the event, e.g. the azimuthal angle separation with the missing transverse momentum $\Delta\phi(\tau, \boldsymbol{p}_\mathrm{T}^{\mathrm{miss}})$ and $\Delta\phi(\mathrm{jet}, \boldsymbol{p}_\mathrm{T}^{\mathrm{miss}})$, respectively. While the

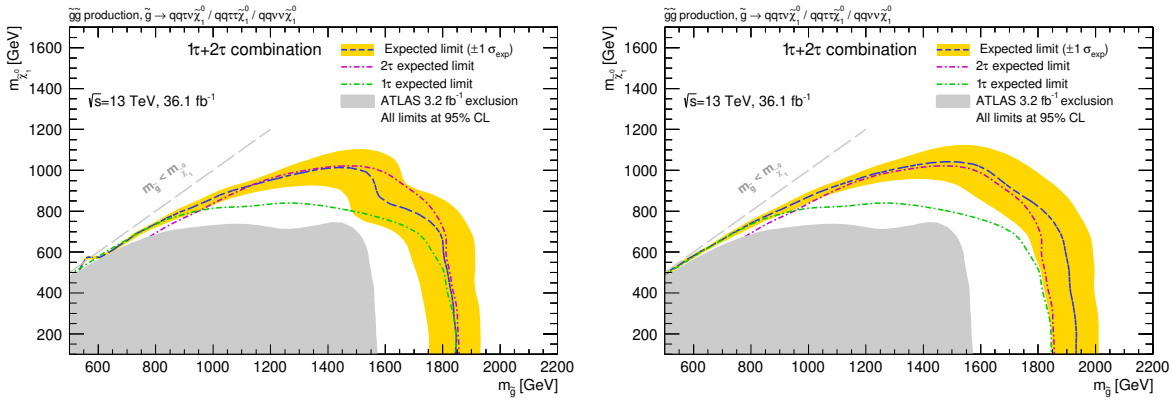

(a) Best-$CL_S^{exp.}$ combination

(b) Simultaneous fit

Figure 5.8: Expected exclusion contours at 95% confidence level for the simplified model of gluino pair-production for the Best-$CL_S^{exp.}$ combination (a) and the simultaneous fit (b) of all single-bin fit SRs. The yellow band shows the one-standard-deviation spread of the expected limit around the median. The previous observed ATLAS result [9] obtained with $\mathcal{L} = 3.2\,\text{fb}^{-1}$ of $\sqrt{s} = 13\,\text{TeV}$ data is shown as the grey filled area. The magenta and green dashed lines show the expected limits of the individual signal channels.

transverse momentum also helps to separate different signals from each other, topological cuts are only used to separate different Standard Model backgrounds from each other or the signals.

- The scalar sum of the transverse momenta of all τ-leptons and jets in the event is a measure for the amount of *hadronic activity*.

$$H_\text{T} = \sum_i p_\text{T}^{\tau_i} + \sum_j p_\text{T}^{\text{Jet}_j} \tag{5.1}$$

- The magnitude of the missing transverse momentum E_T^miss is of importance, e.g. for the trigger used in this analysis or to foster particular signal signatures. Its relative contribution to the overall energy measured in an event is calculated with respect to the so-called *effective mass*

$$m_\text{eff} = H_\text{T} + E_\text{T}^\text{miss}. \tag{5.2}$$

- The transverse mass [38] of the system formed by $\boldsymbol{p}_\text{T}^\text{miss}$ and the momentum $\boldsymbol{p}$ of a reconstructed object that is assumed to be massless – this definition also covers τ-leptons.

$$m_\text{T}^\ell \equiv m_\text{T}(\boldsymbol{p}, \boldsymbol{p}_\text{T}^\text{miss}) = \sqrt{2 p_\text{T}^l E_\text{T}^\text{miss}(1 - \cos\Delta\phi(\boldsymbol{p}, \boldsymbol{p}_\text{T}^\text{miss}))} \tag{5.3}$$

The transverse mass is an analogue to the invariant mass of a two-particle system where the longitudinal component is neglected (cf. chapter 3) and one of the particles escapes detection, leaving only a contribution to the missing momentum. These features render it particularly useful in identifying leptonic decays of the W-boson as during its confirmation and mass measurement at the Tevatron in 1995 [221]. For events where a lepton ℓ and the missing transverse momentum both originate from a $W \to \ell\nu$ decay, the m_T^ℓ distribution exhibits a Jacobian peak at the W-boson mass. In events with two reconstructed τ-leptons, the sum of their transverse masses $m_\text{T}^{\tau_1} + m_\text{T}^{\tau_2}$ can be used to isolate and suppress contributions Z + jets processes.

- The so-called *stransverse mass* variable $m_{\mathrm{T2}}^{\tau\tau}$ [222, 223]

$$m_{\mathrm{T2}}^{\tau\tau} = \sqrt{\min_{\boldsymbol{p}_{\mathrm{T}}^{a}+\boldsymbol{p}_{\mathrm{T}}^{b}=\boldsymbol{p}_{\mathrm{T}}^{\mathrm{miss}}} \left(\max\left[m_{\mathrm{T}}^{2}(\boldsymbol{\tau}_1, \boldsymbol{p}_{\mathrm{T}}^{a}), m_{\mathrm{T}}^{2}(\boldsymbol{\tau}_2, \boldsymbol{p}_{\mathrm{T}}^{b})\right]\right)} \tag{5.4}$$

  is of particular use in the search for signals with small mass differences between the sparticles. It originates from searches for pairs of heavy particles that each decay to a visible component (e.g. a τ-lepton) and an invisible one (e.g. the LSP, denoted a or b) that is assumed to be massless. While the visible components are directly measurable, the invisible ones can only be assessed altogether as the total missing transverse momentum. The mass of the heavy new particle is an upper bound for each computable transverse mass $m_{\mathrm{T}}^{2}(\boldsymbol{\tau}_{1,2}, \boldsymbol{p}_{\mathrm{T}}^{a,b})$, where $\boldsymbol{p}_{\mathrm{T}}^{a,b}$ can be any two-momentum that does not contradict $\boldsymbol{p}_{\mathrm{T}}^{\mathrm{miss}}$. The upper bound is reflected by choosing the maximum of all possible transverse masses. A minimisation of the possible two-momenta such that their sum gives the total observed missing transverse momentum ensures that the two transverse masses, from which the maximum is chosen, deviate as little as possible from each other. The distribution of $m_{\mathrm{T2}}^{\tau\tau}$ hence has a kinematic endpoint if the afore introduced requirements are met. This is the case for simplified model scenarios where the mass differences between the sparticles are small and the LSP can be assumed to be massless. In the case of multiple τ-leptons being present in an event, there is no a priori way to select the two τ-leptons on which the calculation of $m_{\mathrm{T2}}^{\tau\tau}$ is based. In such cases, all possible permutations are considered and the highest value of $m_{\mathrm{T2}}^{\tau\tau}$ is chosen to represent the event.

- The sum of the transverse masses of all jets and the two leading τ-leptons,

$$m_{\mathrm{T}}^{\mathrm{sum}} = m_{\mathrm{T}}^{\tau_1} + m_{\mathrm{T}}^{\tau} - + \sum_{i} m_{\mathrm{T}}^{\mathrm{Jet}_i}, \tag{5.5}$$

  where $m_{\mathrm{T}}^{\mathrm{Jet}}$ is defined analogously to m_{T}^{ℓ}, makes use of high τ-lepton and jet multiplicities as well as large missing momentum to separate signal from background.

- The invariant mass of a the $\tau - \mu$ system $m_{\mathrm{inv}}(\tau\mu)$ helps to probe the physics of decaying W bosons that mimic decays to τ-leptons.

5.5 Trigger strategy

In order to carry out any search, recorded data needs to be available for analysis. The necessity of having a trigger to filter the desired data already at recording level has been explained in detail in section 3.2.4. The physics objects that are characteristic to the signals searched for narrow down the natural choices of triggers for this analysis. Since no exceptionally high jet multiplicities are expected for the signal models (cf. fig. 5.9), triggers based exclusively on jets are not a sensible choice. The remaining items of interest are hence τ-leptons and the missing momentum. Studies carried out in [9, 224] have shown that using the presence of one or two τ-leptons and possibly additional missing momentum is not as effective as using the missing momentum as a stand-alone requirement for recorded data to be accepted by the trigger system. These observations, and the fact that the use of pre-scaled triggers could result in undesired loss of events of interest, lead to the choice of the $E_{\mathrm{T}}^{\mathrm{miss}}$-based trigger with the lowest threshold that is still not pre-scaled as the trigger for this analysis. Due to the fact that during the data taking periods of 2015 and 2016 the lowest-threshold $E_{\mathrm{T}}^{\mathrm{miss}}$-Trigger without pre-scaling changed over time, the actually queried trigger information depends on the time the data has been taken. In the case of Monte Carlo simulations, this effect is emulated by randomly assigning data taking time-stamps to the MC events and imposing

the corresponding trigger requirements. The chosen trigger reaches its plateau of a stable efficiency $\geq 99\%$ when requiring $E_{\mathrm{T}}^{\mathrm{miss}} > 180\,\mathrm{GeV}$ and the presence of a jet with $p_{\mathrm{T}} > 120\,\mathrm{GeV}$. The additional requirement on a high p_{T} jet allows to operate at lower missing transverse momentum thresholds opposed to a pure $E_{\mathrm{T}}^{\mathrm{miss}}$ based selection while it does not limit the acceptance for possible signal significantly [8]. Details on the development of the trigger strategy and the evaluation of its performance are documented in appendix C.

5.6 Event quality and pre-selection

The different phase-space regions designed and investigated in this analysis share a set of mutual requirements to ensure that only well-reconstructed events that have been recorded with a fully functional detector enter the subsequent analysis steps. These selection criteria are referred to as *event quality cuts*, listed below.

- The event is recorded in a luminosity block (cf. section 3.2.5) that is part of the Good Runs List (ibid.).
- The event does not contain hadronic objects, i.e. τ-leptons and jets, in uncommonly noisy calorimeter parts (both, the LAr and Tile calorimeter—cf. section 3.2.2—are affected) or any other malfunctioning detector section. These conditions are separately listed from the Good Runs List (GRL) requirement because at the time of recording, they were not part of the criteria being checked for the GRL but discovered later.
- The primary vertex has at least two tracks associated to it.
- After overlap removal (cf. section 3.3.6) no cosmic muon candidate (i.e. a muon that cannot be associated to the primary vertex or its vicinity, showing $|z_0^{\mathrm{PV}}| > 1\,\mathrm{mm}$ or $d_0^{\mathrm{PV}} > 2\,\mathrm{mm}$) is present.
- The event is not allowed to contain a badly-reconstructed muon (defined as a muon found before overlap removal with a large curvature uncertainty, $\sigma(q/p)/|q/p| > 0.2$).
- The absence of any jet being classified as *loose bad* (cf. section 3.3.1) after overlap removal is required.
- The leading jet has to pass the "tight bad jet" cleaning criteria (ibid.), helping to suppress beam-halo background (ibid.) and ensuring its proper reconstruction outside of malfunctioning tile-calorimeter module. For details see [189] and [224].

After the event quality is ensured, additional selection criteria that are common to both signal channels are applied:

- The presence of a second jet with $p_{\mathrm{T}} > 25\,\mathrm{GeV}$ is required to suppresses background in general since the signal models are not expected to produce many events with only one jet, rendering it safe to use this cut. For illustration purposes, the jet multiplicity of the signal models is depicted in fig. 5.9.
- At this stage, the τ-leptons that characterise the individual channels are required, exactly one *medium*-ID τ-lepton in the 1τ channel and at least two *medium*-ID τ-leptons in the 2τ channel (cf. section 5.7). The *medium* ID working point is chosen to already suppress background contributions from fake τ-leptons, especially in the 1τ channel. In the $\sqrt{s} = 8\,\mathrm{TeV}$ analysis [13], the 2τ channel

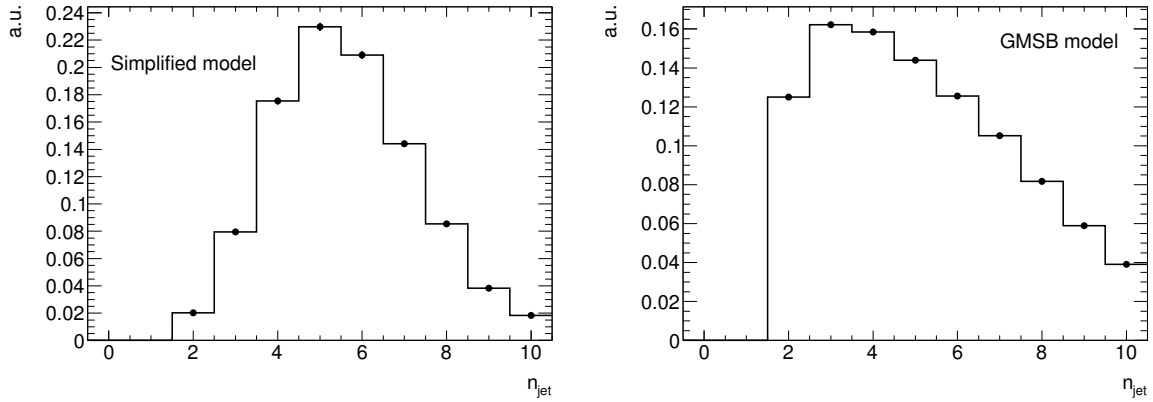

(a) (b)

Figure 5.9: The number of reconstructed jets n_{jet} summed up for all signal points of the simplified model of gluino pair-production, (a), and the GMSB model, (b). The distributions are normalised to unity to ensure comparability.

	Signal channel	
	1τ channel	2τ channel
Trigger requirements	$E_{\text{T}}^{\text{miss}} > 180\,\text{GeV}$ $p_{\text{T}}^{\text{j}_1} > 120\,\text{GeV}$	
Additional requirements	$n_{\text{jet}} \geq 2$ $p_{\text{T}}^{\text{j}_2} > 25\,\text{GeV}$	
τ-leptons	$n_\tau = 1$	$n_\tau \geq 2$

Table 5.1: Summary of the pre-selection and τ-lepton multiplicity requirements for both signal channels.

needed to be based on the *loose* ID working point to have avoid critical signal losses. Improvements in the ATLAS τ-lepton reconstruction routines upon the LHC upgrade to $\sqrt{s} = 13\,\text{TeV}$, however, lead to comparable signal efficiencies already at the *medium* ID working point. This way, both channels can use the same τ-lepton requirements and can be based on the same background estimation.

- To allow for the aforementioned combination of the simplified model and GMSB SRs, neither of the two channels imposes any requirement on electrons or muons at this stage. The design of particular control regions will later on require the presence of muons (cf. section 6.1).

The entire collection of trigger requirements, event quality criteria and additional mutual cuts is referred to as *pre-selection* in the following sections and chapters. The analysis-specific criteria are summarised in table 5.1.

In order to access any signal processes or to study electroweak backgrounds (i.e. W + jets, Z + jets, VV and processes involving top quarks), the generally large abundance of multi-jet events (cf. section 5.1) is suppressed already at this stage, extending the pre-selection by two additional cuts. Due to the requirements on the missing transverse momentum already at trigger-level, multi-jet events entering at this stage of the analysis are most likely subject to mis-measurements of the jet energy, introducing artificial missing transverse momentum to the event. Such events are likely to have $\boldsymbol{p}_{\text{T}}^{\text{miss}}$ pointing in a

similar direction as the high-energy jets. This feature is exploited to suppress the multi-jet background by requiring $\Delta\phi(\text{jet}, \boldsymbol{p}_{\text{T}}^{\text{miss}}) > 0.4$ for the two highest-energy jets. This cut is always applied with the exception of phase-space regions designed to probe the multi-jet background directly, cf. table 6.2.

5.7 Design of signal regions

With recorded data of ensured quality available, the actual analysis design process starts with defining the set of signal regions that have been introduced in section 5.3. The definition of the individual SRs depends on the signal channel and the approach used for extraction of the results. Common to all design processes is the goal of keeping the SRs free of any overlap in phase-space, i.e. ensuring that not a single event can end up in two SRs at the same time and be double-counted in the evaluation. Such signal regions are referred to as being *orthogonal* to each other. As introduced in section 5.3, this feature is of particular importance when aiming for the strongest possible conclusions to be drawn from the final results by combining individual SRs in a simultaneous fit.

In general, the final variables and their values cut on are chosen based on several considerations [189]:

- The final number of cut variables is desired to be small. The fewer variables are used to select the signal region, the less susceptible the entire analysis becomes to systematic mis-modelling and extrapolation effects that have to be investigated, parametrised and quantified. In the end, the analysis is more robust.

- The optimal values of the selection variables to separate the desired SUSY signal from its Standard Model background are obtained by scanning a corresponding distribution of the modified Asimov significance for discovery z_{A}. This approach is already used in [9, 13], details of the exact procedure are provided in appendix B. In addition to maximising the discovery significance based on signal benchmark scenarios, close attention is paid to not select too strictly to avoid a loss of sensitivity towards other scenarios than the benchmarks.

- Variables that ensure the orthogonality of the signal regions amongst each other are chosen such that the desired signal types (e.g. represented by the different benchmark scenarios) remain in the corresponding parts of phase-space.

The design process for all SRs is carried out by solely looking at the simulated background and signal, not by taking distributions of data into account. This so-called *blind* optimisation process ensures that no human bias due to the distribution of observed data is introduced to artificially enhance the contribution of the desired signal. In general, the single-bin fit SRs of this analysis are based on the ones used in the exploration phase of this study [9]. The presented setup, however, aims for a simplification of these SRs, i.e. a reduced number of variables used to define them.

The following paragraphs introduce the individual SRs and guide through the underlying design process. The optimisation is based on four benchmark signal scenarios, three for the simplified model and one for the GMSB model. The scenarios are chosen such that they lie just beyond the parameter-space excluded in the exploration study [9] and, in the case of the simplified model, target different splittings of the gluino and LSP mass. Table 5.2 provides an overview of the four selected benchmark signal scenarios.

Benchmark scenario	$m(\tilde{g})$	$m(\tilde{\chi}_1^0)$
Low-mass, LM	1 065 GeV	825 GeV
Medium-mass, MM	1 265 GeV	905 GeV
High-mass, HM	1 705 GeV	345 GeV
	Λ	$\tan\beta$
GMSB	120 TeV	40

Table 5.2: Overview of the four benchmark signal scenarios.

5.7.1 Signal regions of the 1τ channel

The signal region design process in the 1τ channel is driven by the expected background composition that is to be controlled. Figure 5.10 shows distributions of the kinematic variables used in the design process after the pre-selection step, the application of the multi-jet suppression and the requirement of exactly one *medium*-ID τ-lepton. The different background contributions are normalised using the normalisation-factors obtained in the background fit (cf. sections 5.3, 6.1 and 6.2). In addition, the four signal benchmark scenarios are displayed. They are not subject to any fit at this stage. From these distributions, the background composition to the 1τ channel can be inferred: predominantly, $W(\tau\nu)$ + jets and $t\bar{t}$ production are present, with sub-dominant contributions from $Z(\nu\nu)$ + jets and $Z(\tau\tau)$ + jets. This result is expected due to several reasons: $W(\tau\nu)$ + jets produces exactly one τ-lepton, has genuine missing transverse momentum due to the escaping neutrino and contributes additional jets. This is the exact signature the 1τ channel is looking for. Top quark pairs pose a background that is in general hard to suppress and hence almost omnipresent. Events from the production of two heavy gauge bosons, decays of the Z-boson to electrons or muons or multi-jet production form the smallest contributions to the 1τ channel background spectrum.

While these observations allow for designated background suppression if need be, isolating the signals of interest is the main goal of the SR design process. Considering the structure of the simplified model of gluino pair-production and the sets of parameters—namely sparticle masses—for which signal events are simulated, the variety of different scenarios, particularly after reconstruction in the detector, becomes visible: scenarios in which the mass splitting between the gluino and the LSP is low ($\Delta m(\tilde{g},\chi_1^0) \leq 300\,\text{GeV}$), i.e. close to and along the dashed diagonale in the model parameter-plane, cf. figs. 2.20 and 5.11, exhibit substantially different characteristics than scenarios with medium ($300\,\text{GeV} < \Delta m(\tilde{g},\chi_1^0) \leq 1\,000\,\text{GeV}$) or high mass splittings ($\Delta m(\tilde{g},\chi_1^0) > 1\,000\,\text{GeV}$). Those three cases are represented by the three corresponding simplified model benchmark signal scenarios. In order to cover the parameter-space as broadly as possible, different signal regions are designed to address the signatures of the different parts of phase-space.

For this analysis, two signal regions are designed in the 1τ channel—the *compressed* SR and the *medium-mass* SR—in each of which the final results are extracted by means of a single-bin fit. While in [9] the 1τ channel also comprises a third *high-mass* SR, no such region is designed here due to the higher sensitivity of the corresponding SR in the 2τ channel (cf. [189, 224] and section 5.7.2.

The compressed SR of the 1τ channel targets the most compressed part of the sparticle mass spectrum of the simplified model (cf. section 2.2.4). In events where a high-momentum jet recoils against the pair of gluinos and gives the visible decay products of the SUSY decay chain a strong boost in the transverse plane. Only this boost enables their detection, without it, they would not be

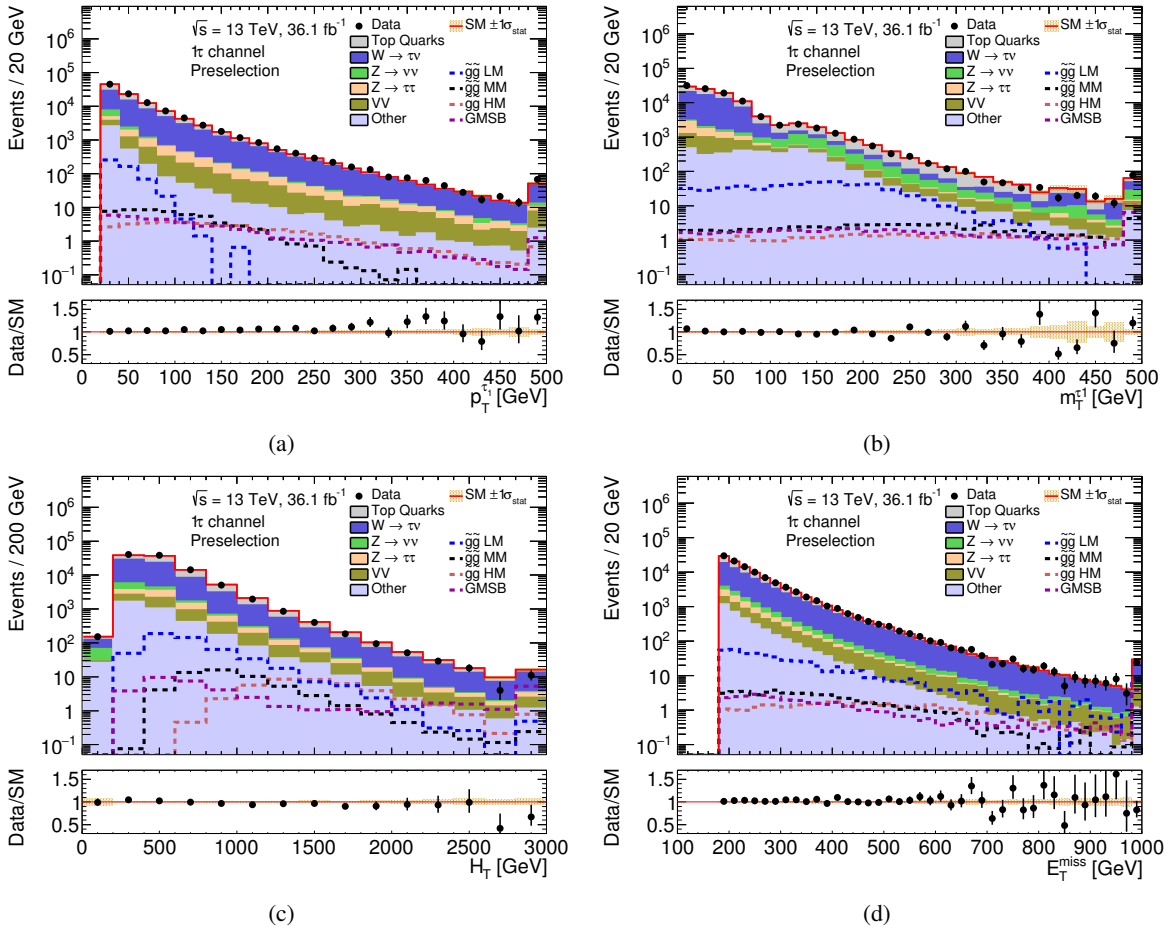

Figure 5.10: Kinematic distributions after the pre-selection in the 1τ channel. The results shown are obtained after fitting the normalisation of the background in the control regions. The last bin of each distribution contains the overflow events. The uncertainties displayed consider only statistical limitations in the background modelling, illustrated by the shaded bands. The contribution labelled as *other* includes multi-jet events and V + jets processes not explicitly listed in the legend. The dashed lines represent the four signal model benchmark scenarios used in the design process of the analysis.

resolvable by the detector or reconstructable afterwards [189]. The final selection criteria summarised in table 5.3 can be motivated from the distributions in fig. 5.10: despite the jet-induced boost of the SUSY decay products, the τ-leptons are still low in energy – for the low-mass benchmark scenario, addressing highly compressed scenarios, the p_{T}^{τ} distribution peaks at low values while for the other benchmarks it flattens out slowly. In addition to selecting the desired signals, requiring $p_{\mathrm{T}}^{\tau} < 45\,\mathrm{GeV}$ also separates the compressed SR from the medium-mass SR of the 1τ channel. In order to suppress background from fake τ-leptons and genuine $W(\tau\nu)$ + jets, $m_{\mathrm{T}}^{\tau} > 80\,\mathrm{GeV}$ is required. As can be seen in fig. 5.10(b), the distribution of m_{T}^{τ} is falling slowly for the low-mass benchmark while it peaks at low values for said backgrounds. This cut hence preserves much signal and suppresses most background. The final cut of $E_{\mathrm{T}}^{\mathrm{miss}} > 400\,\mathrm{GeV}$ can be motivated by the distribution in fig. 5.10(d), where the background is peaking at low values and the shape of the low-mass benchmark flattens out again slowly. Table 5.4 provides an overview of the background composition of the compressed signal region and the expected signal yields of the four benchmark scenarios. The design goal is successfully met since the low-mass benchmark signal is by far the strongest of all tested signals, the compressed SR hence is expected to perform at its best. Furthermore, table A.15 summarises the signal losses at each step of the event selection chain.

The medium-mass SR of the 1τ channel, on the other hand, addresses larger values of $\Delta m(\tilde{g},\chi_1^0)$. Such scenarios do not require a recoil jet to become kinematically accessible – reconstructed physics objects of produced particles are expected to be detectable without an additional boost. This statement can be fostered by the distribution of the τ-lepton transverse momentum in fig. 5.10(a). For the medium-mass benchmark scenario, the distribution stretches further than for the low-mass scenario, allowing for separation of the signal scenarios and suppression of further background by requiring a lower boundary of $p_{\mathrm{T}}^{\tau} > 45\,\mathrm{GeV}$. Also the transverse mass of the τ-lepton is used for stronger background suppression by tightening the cut to $m_{\mathrm{T}}^{\tau} > 250\,\mathrm{GeV}$ without loosing much signal due to the flatness of the distribution. For the same reasons as for the compressed SR, the $E_{\mathrm{T}}^{\mathrm{miss}} > 400\,\mathrm{GeV}$ requirement is imposed also in the medium-mass SR. The final cut on the hadronic activity $H_{\mathrm{T}} > 1\,000\,\mathrm{GeV}$ is introduced to foster the presence of the medium-mass benchmark scenario, simultaneously suppressing background.

Table 5.3 also summarises the selection criteria for the medium-mass SR of the 1τ channel and allows for a direct comparison with the cuts used to design the compressed SR of the 1τ channel. A breakdown of the background composition and the yields of the different benchmark signals for the medium-mass signal region is displayed in table 5.4 and table A.8 of appendix A.3. Here, the desired medium-mass benchmark is not the most dominant signal scenario. However, all three signal benchmarks are abundant and can be accessed by this SR, rendering it a well-designed region in the set of all signal regions, completing the parameter-space coverage. Table A.15 summarises the signal losses at each step of the event selection chain.

Studying the expected results of the two signal regions of the 1τ channel in fig. 5.11, their feature of being complementary to each others becomes clear. The expected exclusion contours overlap only slightly but rather probe different areas of the model parameter-space, they cover a broad parameter-space.

Sensitivity studies in [224] show that the design of a designated signal region targeting the GMSB model in the 1τ channel is not particularly helpful due to the larger number of recorded τ-leptons. In fact, the two simplified model SRs of the 1τ channel are designed to be orthogonal to the GMSB SR of the 2τ channel, allowing for a statistical combination with said designated GMSB SR to exploit any potential sensitivity in the 1τ channel without further ado.

	1τ SRs	
	Compressed	Medium-mass
Pre-selection	$E_{\mathrm{T}}^{\mathrm{miss}} > 180\,\mathrm{GeV},\ p_{\mathrm{T}}^{\mathrm{j}_1} > 120\,\mathrm{GeV}$	
	$n_{\mathrm{jet}} \geq 2,\ p_{\mathrm{T}}^{\mathrm{j}_2} > 25\,\mathrm{GeV}$	
Multi-jets	$\Delta\phi(\boldsymbol{p}_{\mathrm{T}}^{\mathrm{j}_{1,2}}, \boldsymbol{p}_{\mathrm{T}}^{\mathrm{miss}}) > 0.4$	
τ-leptons	$n_\tau = 1$	
	$p_{\mathrm{T}}^{\tau} < 45\,\mathrm{GeV}$	$p_{\mathrm{T}}^{\tau} > 45\,\mathrm{GeV}$
Event properties	$E_{\mathrm{T}}^{\mathrm{miss}} > 400\,\mathrm{GeV}$	
	$m_{\mathrm{T}}^{\tau} > 80\,\mathrm{GeV}$	$m_{\mathrm{T}}^{\tau} > 250\,\mathrm{GeV}$
	—	$H_{\mathrm{T}} > 1\,000\,\mathrm{GeV}$

Table 5.3: Summary of the Simplified Model signal region definitions in the 1τ channel.

1τ SR	Medium-mass	Compressed
Fitted Standard Model events	15.92 ± 2.99	319.61 ± 27.49
Fitted $Z(\nu\nu)$ + jets events	2.20 ± 0.50	110.16 ± 23.64
Fitted VV events	2.95 ± 0.57	28.18 ± 4.54
Fitted $W(\tau\nu)$ + jets events	2.15 ± 1.69	50.54 ± 17.79
Fitted other V + jets events	1.67 ± 0.38	44.85 ± 9.56
Fitted top quarks events	5.78 ± 1.56	76.78 ± 21.23
Fitted Multi-jet events	1.14 ± 0.14	9.22 ± 1.17
Nominal LM signal events	8.54 ± 2.41	59.26 ± 4.94
Nominal MM signal events	6.44 ± 0.38	2.78 ± 0.23
Nominal HM signal events	16.83 ± 0.46	1.93 ± 0.16
Nominal GMSB signal events	6.32 ± 0.41	2.48 ± 0.23

Table 5.4: Yields of the expected backgrounds from the SM in the SRs of the 1τ channel. The expectation is given with the scalings computed in the combined fit applied. Uncertainties are statistical plus systematical for the SM backgrounds. Only the subsamples contributing in the respective region are considered. In addition, the nominal expected yields of the four signal benchmarks are displayed – here, only the statistical uncertainty is given.

5.7.2 Signal regions of the 2τ channel

As for the 1τ channel, the expected background composition of the 2τ channel drive parts of the signal region design process. The background spectrum can be inferred from the distributions of the signal region defining variables shown in fig. 5.12. At the pre-selection stage, the 2τ channel background is dominated by $t\bar{t}$ events, followed by $W(\tau\nu)$ + jets and $Z(\tau\tau)$ + jets events. Other heavy gauge boson processes or multi-jet production do not contribute significantly. For the same reasons as in the 1τ channel, top quark production is highly present also in the 2τ channel. In the case of $W(\tau\nu)$ + jets events, the second τ-lepton is a mis-identified jet faking a tau while the missing transverse energy can arise naturally from the present neutrino. Decays of a Z-boson into two τ-leptons are a natural source of two real τ-leptons with missing transverse energy also coming from the neutrinos being involved. The minor backgrounds are stronger suppressed in the 2τ channel since they are not giving any genuine τ-leptons and the probability of having two fake τ-leptons is low at the *medium*-ID working point (cf. section 3.3.4).

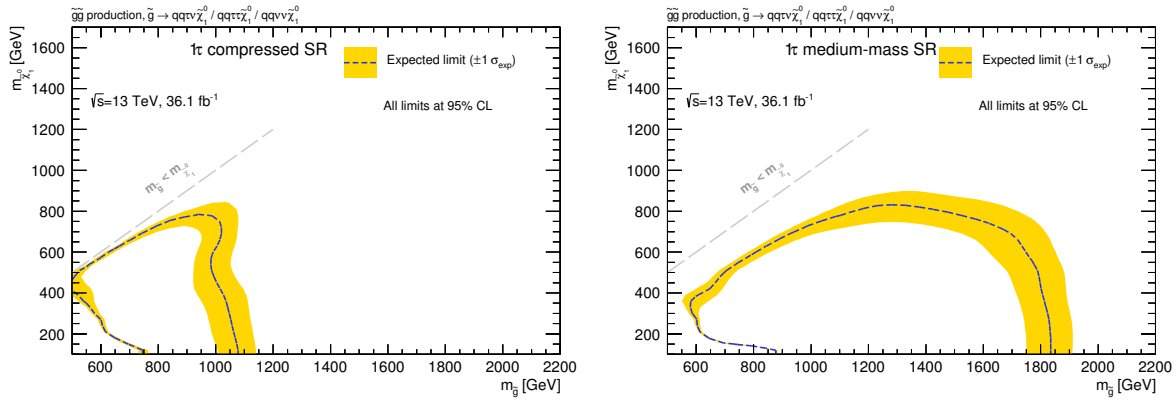

(a) (b)

Figure 5.11: Expected exclusion contours at 95% confidence level for the simplified model of gluino pair-production for the compressed (a) and the medium-mass SR (b) in the 1τ channel. The yellow band shows the one-standard-deviation spread of the expected limit around the median. The previous observed ATLAS result [9] obtained with $\mathcal{L} = 3.2\,\text{fb}^{-1}$ of $\sqrt{s} = 13\,\text{TeV}$ data is shown as the grey filled area.

The compressed SR marks the first of the two single-bin fit SRs that are developed to search for the simplified model in the 2τ channel. In analogy to its namesake in the 1τ channel, it addresses scenarios in which the mass differences between the sparticles are small. This point is reflected in a focus on the LM and MM benchmarks in the kinematic plots. The presence of multiple jets and τ-leptons is exploited by the $m_{\text{T}}^{\text{sum}}$ variable, depicted in fig. 5.12(d). The stringent cut of $m_{\text{T}}^{\text{sum}} > 1\,600\,\text{GeV}$ is a major background suppressor, while preserving the majority of all signal benchmark scenarios. The unique attribute of this SR is the cut on $m_{\text{T2}}^{\tau\tau} > 70\,\text{GeV}$. Due to the strict requirements and assumptions that are made in its calculation, the topologies addressed by the this SR are the only target for this variable. The requirement of two identical decays of heavy particles is only given when two τ-leptons are required. Moreover, the assumption of the invisible decay products being massless is best justified for small LSP masses. The distribution of $m_{\text{T2}}^{\tau\tau}$ in fig. 5.12(c) emphasis the value of this variable: while for the background $m_{\text{T2}}^{\tau\tau}$ drops, it increases for all benchmarks with the LM scenario being the most abundant one. Finally, the cut on $H_{\text{T}} < 1\,100\,\text{GeV}$ is not used to suppress background or enrich signal in first place but to make the compressed SR orthogonal to the high-mass SR. This, however, is achieved without condoning a substantial loss in signal: fig. 5.12(a) illustrates that the target signal benchmarks are located at low values of H_{T}, keeping the losses due to the cut low.

The cuts defining the compressed SR of the 2τ channel are summarised in table 5.5. Its predicted background composition after the fit in the CRs along with the expected yields of the signal benchmarks are compiled in table 5.6 and table A.9 of appendix A.3. Here, the goal of the design is successfully met: the LM benchmark is the strongest present signal while the MM signal is still well present. Furthermore, table A.16 summarises the signal losses at each step of the event selection chain.

The high-mass SR is the sole single-bin fit SR that addresses the scenarios of highest gluino masses with large mass differences to the lighter sparticles in the decay chain. The variables used in the design process reflect the higher amount of available energy in the decays along the cascade by exploiting detectable decay products of higher energies. Since only the high-mass SR targets the corresponding benchmark scenario and coverage of the other two scenarios is already established, its design process focusses on enriching this one signal and applies strong background suppression criteria.

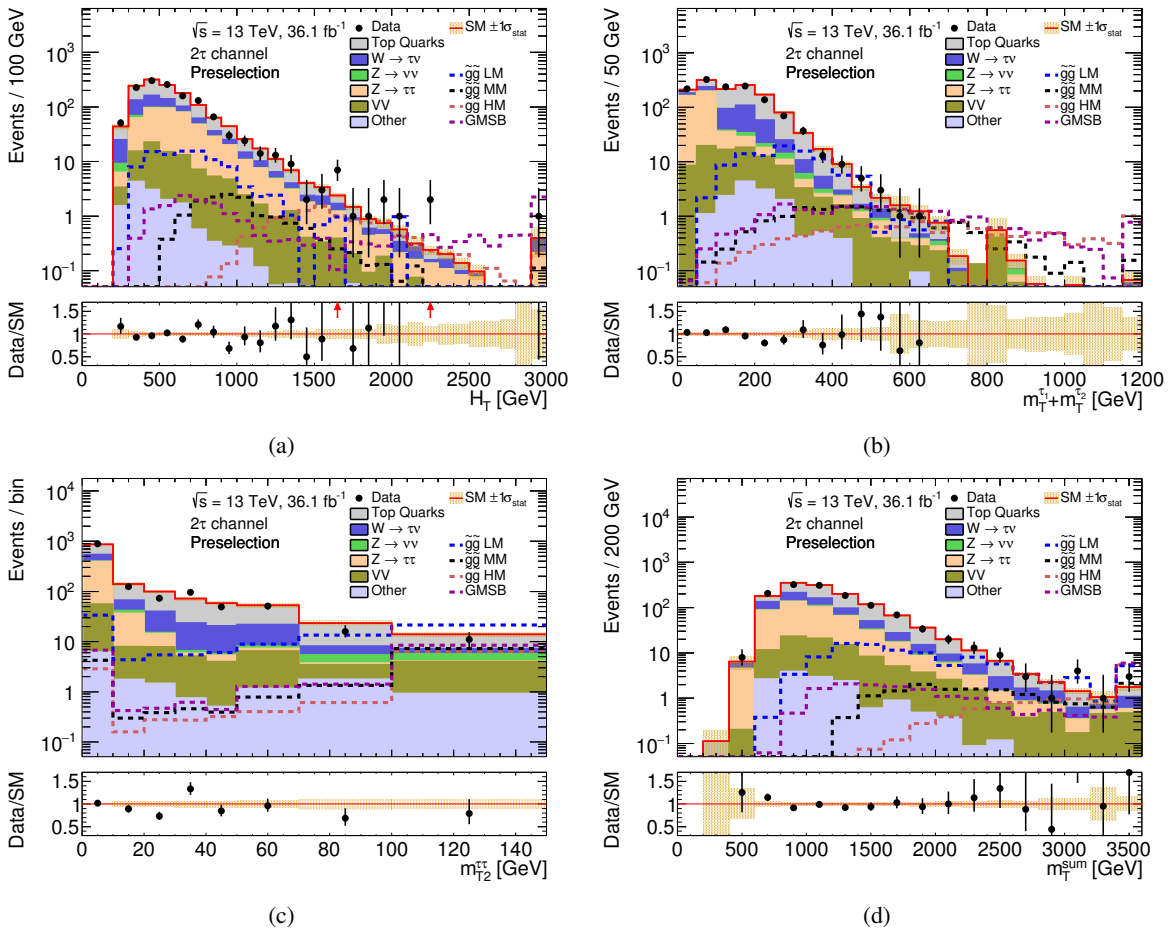

Figure 5.12: Kinematic distributions after the pre-selection in the 2τ channel. The results shown are obtained after fitting the normalisation of the background in the control regions. The last bin of each distribution contains the overflow events. The uncertainties displayed consider only statistical limitations in the background modelling, illustrated by the shaded bands. Red arrows in the Data/SM ratio indicate bins where the corresponding entry falls outside the plotted range. The contribution labelled as *other* includes multi-jet events and V + jets processes not explicitly listed in the legend. The dashed lines represent the four signal model benchmark scenarios used in the design process of the analysis.

	2τ SRs			
	Compressed	High-mass	Multibin	GMSB
Pre-selection	$E_{\mathrm{T}}^{\mathrm{miss}} > 180\,\mathrm{GeV}$, $p_{\mathrm{T}}^{\mathrm{j}_1} > 120\,\mathrm{GeV}$ $n_{\mathrm{jet}} \geq 2$, $p_{\mathrm{T}}^{\mathrm{j}_2} > 25\,\mathrm{GeV}$			
Multi-jets	$\Delta\phi(\boldsymbol{p}_{\mathrm{T}}^{\mathrm{j}_{1,2}}, \boldsymbol{p}_{\mathrm{T}}^{\mathrm{miss}}) > 0.4$			
τ-leptons	$n_\tau \geq 2$			
Event properties	$m_{\mathrm{T2}}^{\tau\tau} > 70\,\mathrm{GeV}$ $H_{\mathrm{T}} < 1\,100\,\mathrm{GeV}$ $m_{\mathrm{T}}^{\mathrm{sum}} > 1\,600\,\mathrm{GeV}$	$m_{\mathrm{T}}^{\tau_1} + m_{\mathrm{T}}^{\tau_2} > 350\,\mathrm{GeV}$ $H_{\mathrm{T}} > 1\,100\,\mathrm{GeV}$ —	$m_{\mathrm{T}}^{\tau_1} + m_{\mathrm{T}}^{\tau_2} > 150\,\mathrm{GeV}$ $H_{\mathrm{T}} > 800\,\mathrm{GeV}$ binned in $m_{\mathrm{T}}^{\tau_1} + m_{\mathrm{T}}^{\tau_2}$	$m_{\mathrm{T}}^{\tau_1} + m_{\mathrm{T}}^{\tau_2} > 150\,\mathrm{GeV}$ $H_{\mathrm{T}} > 1\,900\,\mathrm{GeV}$ —

Table 5.5: Summary of the simplified model and GMSB signal region definitions in the 2τ channel.

2τ SR	GMSB	High-mass	Compressed
Fitted Standard Model events	1.42 ± 0.61	2.37 ± 0.74	5.37 ± 2.05
Fitted $Z(\tau\tau)$ + jets events	0.28 ± 0.10	0.32 ± 0.11	0.03 ± 0.01
Fitted $Z(\nu\nu)$ + jets events	0.01 ± 0.01	0.09 ± 0.03	0.67 ± 0.35
Fitted VV events	0.29 ± 0.08	0.56 ± 0.15	1.06 ± 0.25
Fitted $W(\tau\nu)$ + jets events	$0.37^{+0.38}_{-0.37}$	$0.36^{+0.43}_{-0.36}$	$0.40^{+0.47}_{-0.40}$
Fitted other V + jets events	$0.00^{+0.00}_{-0.00}$	0.02 ± 0.01	0.29 ± 0.08
Fitted top quarks events	0.39 ± 0.23	0.99 ± 0.47	2.89 ± 1.68
Fitted Multi-jet events	0.06 ± 0.01	0.01 ± 0.00	0.02 ± 0.00
Nominal LM signal events	0.98 ± 0.98	4.35 ± 1.39	20.17 ± 2.8
Nominal MM signal events	0.58 ± 0.10	3.56 ± 0.24	5.32 ± 0.31
Nominal HM signal events	2.75 ± 0.17	9.12 ± 0.35	0.42 ± 0.07
Nominal GMSB signal events	5.71 ± 0.42	6.18 ± 0.41	3.52 ± 0.29

Table 5.6: Yields of the expected backgrounds from the SM in the single-bin SRs of the 2τ channel. The expectation is given with the scalings computed in the combined fit applied. Uncertainties are statistical plus systematics for the SM backgrounds. Only the subsamples contributing in the respective region are considered. In addition, the nominal expected yields of the four signal benchmarks are displayed – here, only the statistical uncertainty is given.

The distribution of $m_{\mathrm{T}}^{\tau_1}+m_{\mathrm{T}}^{\tau_2}$ in fig. 5.12(b) shows the expected behaviour for the $Z(\tau\tau)$+jets background: two genuine τ-leptons and only small amounts of missing transverse momentum aligned with them make it predominantly occupy low values of the $m_{\mathrm{T}}^{\tau_1}+m_{\mathrm{T}}^{\tau_2}$ distribution. Already a moderate cut is able to suppress most $Z(\tau\tau)$ + jets contributions. The targeted HM benchmark signal, however, peaks towards higher values of $m_{\mathrm{T}}^{\tau_1}+m_{\mathrm{T}}^{\tau_2}$, enabling a stricter cut of $m_{\mathrm{T}}^{\tau_1}+m_{\mathrm{T}}^{\tau_2} > 350\,\mathrm{GeV}$ to suppress more background, also from other sources than $Z(\tau\tau)$ + jets. The higher τ-lepton and jet energies from the decays of the sparticles make the hadronic activity H_{T} a helpful variable for separating the HM benchmark signal from background. As expected, the H_{T} distribution at pre-selection level in fig. 5.12(a) peaks at higher values for the HM benchmark and thus allows for a hard cut of $H_{\mathrm{T}} > 1\,100\,\mathrm{GeV}$, keeping most signal and suppressing the majority of all backgrounds. Table 5.5 summarises the cuts defining the high-mass SR while table 5.6 and table A.9 in appendix A.3 give an overview of the remaining backgrounds after the fit and the expected signal yields. Table A.16 summarises the signal losses at each step of the event selection chain.

A statement about the complementarity of the two single-bin fit signal regions of the 2τ channel that are tailored towards the simplified model is possible when looking at figs. 5.13(a) and 5.13(b). Although they are not as complementary as the 1τ SRs, their expected limits in the gluino-neutralino mass plane

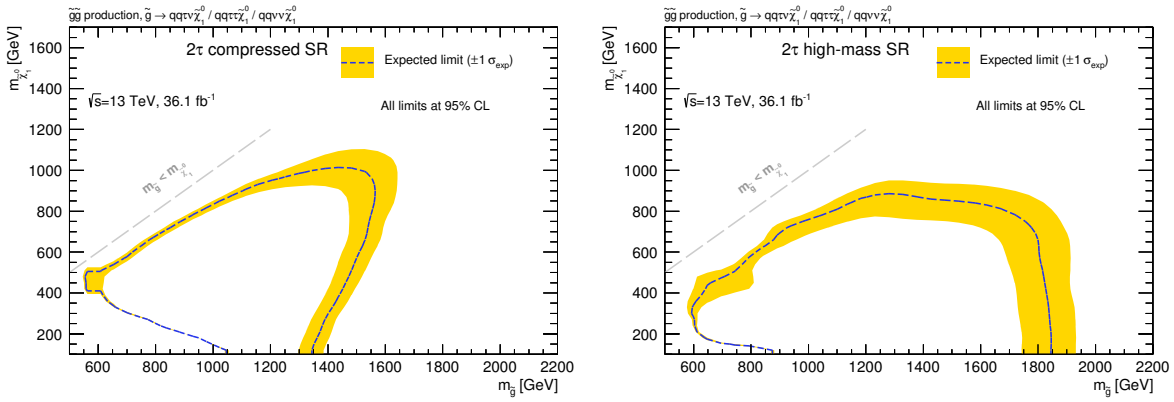

(a) (b)

Figure 5.13: Expected exclusion contours at 95% confidence level for the simplified model of gluino pair-production for the compressed (a) and the high-mass SR (b) of the 2τ channel. The yellow band shows the one-standard-deviation spread of the expected limit around the median. The previous observed ATLAS result [9] obtained with $\mathcal{L} = 3.2\,\text{fb}^{-1}$ of $\sqrt{s} = 13\,\text{TeV}$ data is shown as the grey filled area.

illustrate that they probe the desired different parts of phase-space. While the high-mass SR gives a strong increase towards high gluino masses, the compressed SR provides a limit at intermediate gluino masses and towards higher neutralino masses, accounting for the compressed part of the mass spectrum. The visible overlap of the two expected limits is originating from remaining sensitivity towards other signal scenarios than the pre-defined benchmarks. Furthermore, it gives rise to the question whether it is possible to form a signal region that combines features of both SRs knowingly, providing a similarly strong limit as the combination of the two. Such an SR would, consequentially, be a hybrid of the two.

The multibin SR of the 2τ channel is a direct consequence of this consideration. Instead of optimising single signal regions for the search for one small set of signatures—e.g. the HM SR for signatures such as the HM benchmark scenario—by cutting hard to suppress as much background as possible, this region pursues a different approach. Starting from the setup of the HM SR, the multibin SR releases cuts to allow the presence of both, more signal and background. Not only does it comprise more HM-like signal but it also contains signals that are not accessible to the HM SR, signals with much lower hadronic activity and different configurations of the missing transverse momentum. To compensate for the more and substantially different signals that enter this SR as well as for the increased background, the multibin SR uses a multi-bin fit for extraction of the final results.

As outlined in section 5.3, a multi-bin fit uses the shape of the distribution of a discriminating variable to separate signal from background based. The challenges in the design of such a multi-bin fit SR are manifold and different from the ones faced in the development of single-bin fit SRs. While releasing cuts to let in more background and allow for fitting a smooth background shape with enough statistics, a basic background suppression is still needed. If the background were to exceed the signal globally beyond statistical fluctuations, a fit of the shape would not give a usable result. This basic background suppression is achieved by imposing softer but still effective cuts on $m_{\text{T}}^{\tau_1} + m_{\text{T}}^{\tau_2}$ and H_{T}. A cut of $m_{\text{T}}^{\tau_1} + m_{\text{T}}^{\tau_2} > 150\,\text{GeV}$ excludes most of the $Z(\tau\tau)$ + jets background and already smaller contributions from other Standard Model processes. The cut on H_{T} is loosened to only $H_{\text{T}} > 800\,\text{GeV}$, suppressing the majority of the

remaining background from $W(\tau\nu)$ + jets, top quark and VV production [5]. The effects of these cuts can be inferred from figs. 5.12(a) and 5.12(b).

With this foundation of background reduction, the most crucial step in the development of the multibin SR can be addressed: the choice and binning of the discriminating variable in which the actual fit of the shape is performed later on. As potential variables whose shapes look different for signals and background, the discriminating variables that define the HM SR—from which the design process of the multibin SR started—are manifest. Explorations of the multi-bin fit are hence performed on distributions of H_{T} and $m_{\mathrm{T}}^{\tau_1}+m_{\mathrm{T}}^{\tau_2}$.

The binning of these variables is the next challenge. The number and width of the bins must fulfil certain requirements, each bin has to contain enough background and signal events to perform a sensible fit with. By the time of the design process, no simulation samples for consideration of systematic detector or theory-related effects were available. As a consequence, the optimisation of the binning is based on statistical uncertainties only. Starting from an equidistant binning of both variables as depicted in figs. 5.14(a) and 5.14(b), adjacent bins are sequentially merged. In this process, the number of background and signal events before and after application of all necessary correction-factors (cf. section 4.4) are considered as well as the resulting shape of both distributions. Each bin that is dominated by background should contain enough background events to not be subject to unnecessarily high statistical fluctuations. As a rule-of-thumb, the relative statistical uncertainty should not exceed 30%. For bins which contain more signal of any benchmark scenario than background, the number of un-corrected signal events has to be > 3 to exclude downward fluctuations that would be in agreement with the actual absence of signal[6]. The resulting distributions of H_{T} and $m_{\mathrm{T}}^{\tau_1}+m_{\mathrm{T}}^{\tau_2}$ are shown in fig. 5.14(c) and fig. 5.14(d), respectively.

For both cases, the distributions fulfil the requirements of sufficient statistics and shape differences. The choice which of the two distributions to finally use is now based on the expected performance in the limit setting procedure. Without studying observed data or systematic uncertainties, the multi-bin fit based on $m_{\mathrm{T}}^{\tau_1}+m_{\mathrm{T}}^{\tau_2}$ performs slightly better as can be inferred from fig. 5.15. The stronger expected limit is visible for high values of the neutralino mass at high values of the gluino mass, i.e. for models with intermediate mass splitting. Based on this assessment, the binning of the multibin SR in $m_{\mathrm{T}}^{\tau_1}+m_{\mathrm{T}}^{\tau_2}$ as shown in fig. 5.14(d) is chosen to be used for the final multi-bin fit. A breakdown of the exact background composition and the expected yields of the signal benchmark scenarios is given in tables 5.8 and 5.9 and tables A.10 and A.11 of appendix A.3. For sake of a clearer visualisation, a short-hand notation is introduced for the seven bins of the $m_{\mathrm{T}}^{\tau_1}+m_{\mathrm{T}}^{\tau_2}$-based multibin SR, summarised in table 5.7. Table A.17 summarises the signal losses at each step of the event selection chain. As the amount of required $m_{\mathrm{T}}^{\tau_1}+m_{\mathrm{T}}^{\tau_2}$ increases in the selection, the number of events of benchmark scenarios with higher $\Delta m(\tilde{g},\chi_1^0)$ increases, too. This expected behaviour emphasis the achieved design goal of the multibin SR addressing different signal scenarios in its different bins, all at the same time and hence providing an increased sensitivity with respect to a conventional single-bin fit SR.

[5] The same cuts are used in [9] to define the early version of the 2τ HM SR used for studies of only $\mathcal{L} = 3.2\,\mathrm{fb}^{-1}$ of $\sqrt{s} = 13\,\mathrm{TeV}$ data in the exploration study preceding this analysis.

[6] The Poisson distribution for a mean value of 3 events or less allows for an observation of 0 events with more than 5% probability.

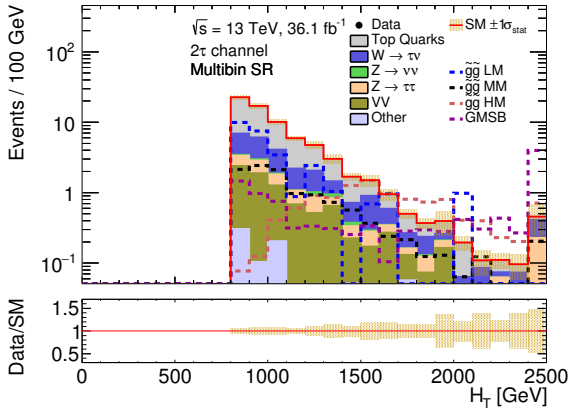

(a) H_{T}, unmodified binning

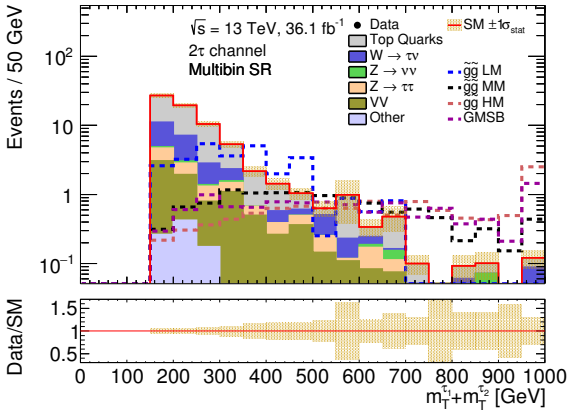

(b) $m_{\mathrm{T}}^{\tau_1}+m_{\mathrm{T}}^{\tau_2}$, unmodified binning

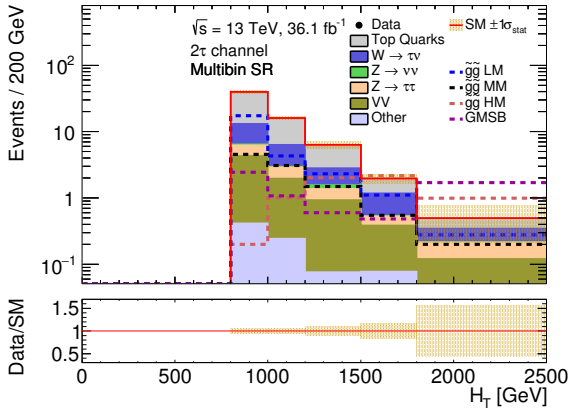

(c) H_{T}, modified binning

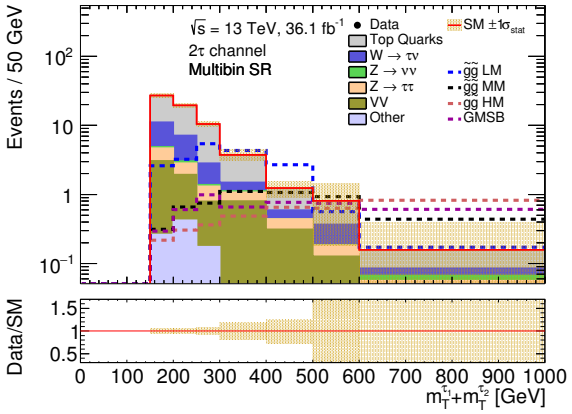

(d) $m_{\mathrm{T}}^{\tau_1}+m_{\mathrm{T}}^{\tau_2}$, modified binning

Figure 5.14: Kinematic distributions of the potential discriminating variables H_{T} and $m_{\mathrm{T}}^{\tau_1}+m_{\mathrm{T}}^{\tau_2}$ before ((a), (b)) and after the optimisation of the binning ((c), (d)) in the multibin SR of the 2τ channel. The results shown are obtained after fitting the normalisation of the background in the control regions. The last bin of each distribution contains the overflow events. The uncertainties displayed consider only statistical limitations in the background modelling, illustrated by the shaded bands. The contribution labelled as *other* includes multi-jet events and V + jets processes not explicitly listed in the legend. The dashed lines represent the four signal model benchmark scenarios used in the design process of the analysis.

Bin label	$m_{\mathrm{T}}^{\tau_1}+m_{\mathrm{T}}^{\tau_2}$-interval
Bin $\mathcal{A}$	$150\,\mathrm{GeV} \leq m_{\mathrm{T}}^{\tau_1}+m_{\mathrm{T}}^{\tau_2} < 200\,\mathrm{GeV}$
Bin $\mathcal{B}$	$200\,\mathrm{GeV} \leq m_{\mathrm{T}}^{\tau_1}+m_{\mathrm{T}}^{\tau_2} < 250\,\mathrm{GeV}$
Bin $\mathcal{C}$	$250\,\mathrm{GeV} \leq m_{\mathrm{T}}^{\tau_1}+m_{\mathrm{T}}^{\tau_2} < 300\,\mathrm{GeV}$
Bin $\mathcal{D}$	$300\,\mathrm{GeV} \leq m_{\mathrm{T}}^{\tau_1}+m_{\mathrm{T}}^{\tau_2} < 400\,\mathrm{GeV}$
Bin $\mathcal{E}$	$400\,\mathrm{GeV} \leq m_{\mathrm{T}}^{\tau_1}+m_{\mathrm{T}}^{\tau_2} < 500\,\mathrm{GeV}$
Bin $\mathcal{F}$	$500\,\mathrm{GeV} \leq m_{\mathrm{T}}^{\tau_1}+m_{\mathrm{T}}^{\tau_2} < 600\,\mathrm{GeV}$
Bin $\mathcal{G}$	$600\,\mathrm{GeV} \leq m_{\mathrm{T}}^{\tau_1}+m_{\mathrm{T}}^{\tau_2}$

Table 5.7: Look-up of the short-hand notation of the $m_{\mathrm{T}}^{\tau_1}+m_{\mathrm{T}}^{\tau_2}$-based 2τ multibin SR bins.

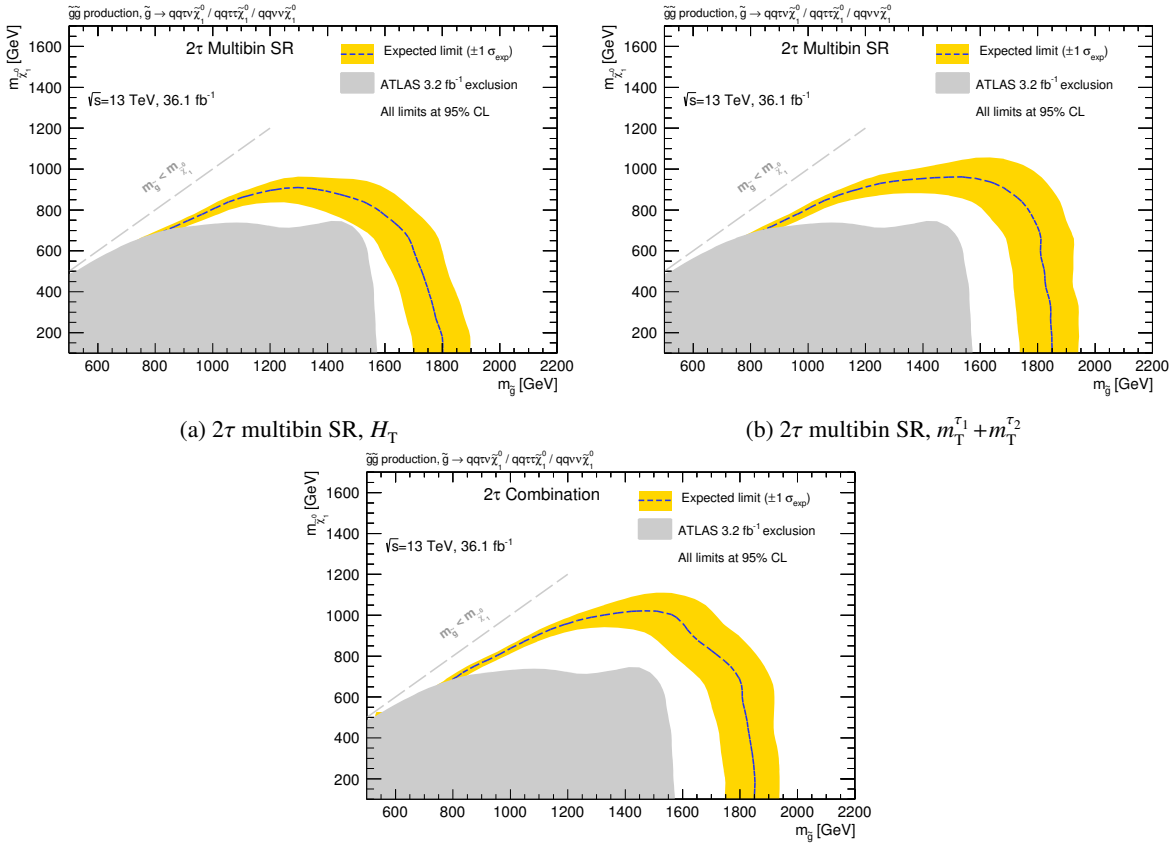

(a) 2τ multibin SR, H_{T}

(b) 2τ multibin SR, $m_{\mathrm{T}}^{\tau_1}+m_{\mathrm{T}}^{\tau_2}$

(c) 2τ (compressed + high-mass) SRs

Figure 5.15: Expected exclusion contour at 95% confidence level for the simplified model of gluino pair-production in the final setup of the 2τ channel multibin SR binned in H_{T} (a) and $m_{\mathrm{T}}^{\tau_1}+m_{\mathrm{T}}^{\tau_2}$ (b) compared to the simultaneous fit combination of the two single-bin fit SRs of the 2τ channel (c). The yellow band shows the one-standard-deviation spread of the expected limit around the median. The previous observed ATLAS result [9] obtained with $\mathcal{L} = 3.2\,\mathrm{fb}^{-1}$ of $\sqrt{s} = 13\,\mathrm{TeV}$ data is shown as the grey filled area.

2τ Multibin SR	Bin $\mathcal{A}$	Bin $\mathcal{B}$	Bin C	Bin $\mathcal{D}$
Fitted bkg events	27.13 ± 6.44	19.51 ± 3.97	10.44 ± 2.88	7.51 ± 1.61
Fitted $Z(\tau\tau)$ + jets events	1.62 ± 0.40	0.92 ± 0.28	0.51 ± 0.14	0.55 ± 0.21
Fitted $Z(\nu\nu)$ + jets events	0.20 ± 0.07	0.19 ± 0.06	0.07 ± 0.04	0.09 ± 0.04
Fitted V events	2.80 ± 0.62	1.51 ± 0.39	0.62 ± 0.22	1.53 ± 0.37
Fitted $W(\tau\nu)$ + jets events	6.22 ± 3.91	4.09 ± 1.79	1.46 ± 0.79	0.76 ± 0.70
Fitted other V + jets events	0.15 ± 0.09	0.30 ± 0.12	0.11 ± 0.05	0.07 ± 0.05
Fitted top quarks events	16.03 ± 5.04	12.38 ± 3.55	7.60 ± 2.72	4.50 ± 1.22
Fitted Multi-jet events	0.11 ± 0.01	0.12 ± 0.02	0.07 ± 0.01	0.01 ± 0.00
Nominal LM signal events	2.59 ± 0.97	3.23 ± 1.05	5.44 ± 1.28	8.66 ± 1.84
Nominal MM signal events	0.31 ± 0.07	0.66 ± 0.11	0.75 ± 0.12	2.21 ± 0.21
Nominal HM signal events	0.22 ± 0.05	0.31 ± 0.06	0.36 ± 0.06	0.97 ± 0.10
Nominal GMSB signal events	0.31 ± 0.11	0.62 ± 0.11	1.00 ± 0.18	1.33 ± 0.18

Table 5.8: Yields of the expected backgrounds from the SM in the first four bins of the Multibin SR of the 2τ channel. Uncertainties are statistical plus systematics for the SM backgrounds. Only the subsamples contributing in the respective region are considered. In addition, the nominal expected yields of the four signal benchmarks are displayed – here, only the statistical uncertainty is given.

2τ Multibin SR	Bin $\mathcal{E}$	Bin $\mathcal{F}$	Bin $\mathcal{G}$
Fitted bkg events	2.47 ± 0.80	1.63 ± 1.60	1.26 ± 0.52
Fitted $Z(\tau\tau)$ + jets events	$0.26^{+0.30}_{-0.26}$	0.12 ± 0.09	$0.07^{+0.10}_{-0.07}$
Fitted $Z(\nu\nu)$ + jets events	$0.00^{+0.00}_{-0.00}$	$0.00^{+0.01}_{-0.00}$	0.08 ± 0.03
Fitted VV events	0.60 ± 0.22	0.24 ± 0.11	0.37 ± 0.11
Fitted $W(\tau\nu)$ + jets events	$0.30^{+0.36}_{-0.30}$	$0.36^{+0.46}_{-0.36}$	$0.15^{+0.21}_{-0.15}$
Fitted other V + jets events	$0.00^{+0.00}_{-0.00}$	0.01 ± 0.01	$0.01^{+0.10}_{-0.01}$
Fitted top quarks events	1.29 ± 0.56	$0.89^{+1.48}_{-0.89}$	0.58 ± 0.45
Fitted Multi-jet events	0.02 ± 0.00	0.00 ± 0.00	0.01 ± 0.00
Nominal LM signal events	5.40 ± 1.54	1.12 ± 0.57	1.37 ± 0.62
Nominal MM signal events	2.13 ± 0.20	1.86 ± 0.18	3.53 ± 0.24
Nominal HM signal events	1.31 ± 0.13	1.26 ± 0.12	6.57 ± 0.31
Nominal GMSB signal events	1.62 ± 0.21	1.58 ± 0.20	5.23 ± 0.38

Table 5.9: Yields of the expected backgrounds from the SM in the last three bins of the Multibin SR of the 2τ channel. Uncertainties are statistical plus systematics for the SM backgrounds. Only the subsamples contributing in the respective region are considered. In addition, the nominal expected yields of the four signal benchmarks are displayed – here, only the statistical uncertainty is given.

The expected performance can already be evaluated at this stage. The expected limit of the multi-bin fit in the multibin SR in the gluino-neutralino mass plane in fig. 5.14(d) can be compared to the expected limit of the HM single-bin fit SR from which the design process started in fig. 5.13(b).

The multibin SR performs better at high values of the neutralino mass, i.e. for scenarios with more compressed mass spectra, over the full range of gluino masses the 2τ channel is sensitive to. Its performance beyond the limit of the HM SR is compatible with the limit obtained in the compressed SR (cf. fig. 5.13(a)) which is specifically designed to address this region of phase-space. The performance increase of the multi-bin fit with respect to a single single-bin fit SR is hence evident.

With the multibin SR probing not only the phase-space of its single-bin fit counterpart—the HM SR—a comparison of its exclusion power to the combination of both single-bin fit SRs is the next benchmark test. Figures 5.15(b) and 5.15(c) oppose both approaches directly. The expected limits are well compatible within the one-standard-deviation uncertainty band with the combined approach being slightly stronger for the scenarios with the heaviest neutralinos. In terms of extending the parameter-space excluded at 95% CL, both approaches give similar results. However, apart from this comparison, a look the expected CL_S values allows for a more refined statement about the performance of the multi-bin fit with respect to the single-bin fit approach. Due to the consideration of several bins with different signal significance and a much richer signal spectrum that can be probed, the multi-bin fit is expected to exhibit lower CL_S values across the model parameter-space and hence giving the more confident result. As a measure, the ratios of the expected CL_S values of the HM SR on its own and of the combination of both single-bin fit SRs over the multibin SR are presented in fig. 5.16. Since a smaller CL_S value marks a stronger exclusion and hence a better result, a ratio > 1 indicates regions of the parameter-space where the multibin SR performs better (coloured in red). Cyan coloured areas indicate values of the ratio < 1, illustrating regimes where the single-bin fit combination performs better, while white areas indicate parameter regions where both approaches perform comparably. The exact values of the ratio are given as numbers written onto the parameter plane. Areas with no such labels mark scenarios for which either or both of the exclusion fits did not perform properly.

Results that can actually be used for further studies and model-building are the 95% CL upper limits on the excluded production cross-section over the model parameter-space as outlined in more detail in chapter 8. In the same colour-coding and for the same setup, the ratios of these are also visualised in

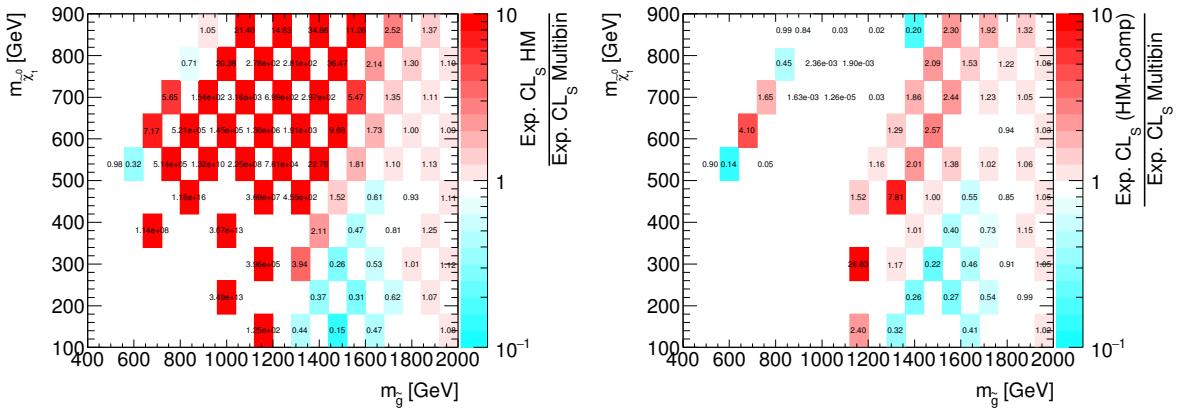

(a) 2τ HM vs. multibin SR

(b) 2τ (Comp. + HM) SR

Figure 5.16: Ratio of the $CL_S^{exp.}$ values of the high-mass SR and the multibin SR (a) and of the combination of the compressed and high-mass SRs and the multibin SR (b)in the 2τ channel evaluated over the parameter-plane of the simplified model. The numbers written onto the parameter grid give the exact ratio. Parameter points without such a printed value show insufficient quality of the underlying fit and cannot be evaluated. Overlaid values that fall beyond the range of the z-axis are printed without on a white background, too.

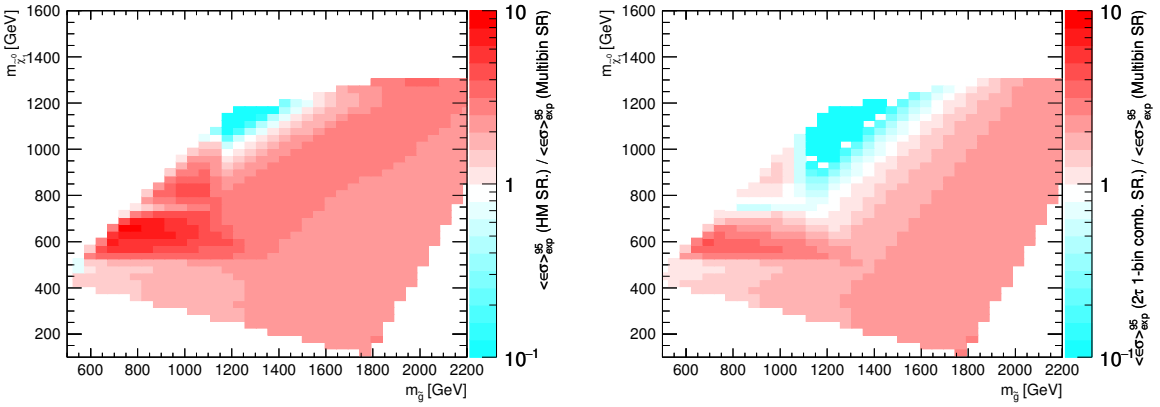

(a) 2τ HM vs. multibin SR

(b) 2τ (Comp + HM) vs. multibin SR

Figure 5.17: Ratio of the 95% CL upper limits on the expected excluded production cross-section of the high-mass SR and the multibin SR (a) and of the combination of the compressed and high-mass SRs and the multibin SR (b) in the 2τ channel evaluated over the parameter-plane of the simplified model.White areas at the bottom left and right are not evaluated due to insufficient quality of the underlying fit.

fig. 5.17. These results speak a similar language and emphasise the strength of the Shape Fit approach even more. Here, the results are stronger in even more parts of the parameter-space.

Due to its increased sensitivity towards signal scenarios which are not accessible to the HM SR—i.e. scenarios with lighter gluinos and neutralinos alike—the multibin SR gives the much stronger exclusion than the HM SR particularly in said regime: the bottom left and intermediate top part of figs. 5.16(a) and 5.17(a) are dominated by red colouring. The HM SR, however, does perform better for higher gluino masses and large mass difference to the neutralino while along the actual 95% exclusion contour their performance is comparable. Since the 2τ compressed SR is not sensitive to the highest gluino masses, this

statement still holds for the comparison to the combination of the two single-bin fit regions in figs. 5.16(b) and 5.17(b). The multibin SR being sensitive towards signals scenarios with intermediate gluino masses but high neutralino masses is visible in the white area at the top of said figure. As for the comparison of the exclusion contours, also the ratio of the expected CL_S values fosters the compatibility of the single multi-bin fit SR with the combination of the single-bin fit SRs.

Concluding, the presented analysis design and strategy offer various improvements with respect to the early $\sqrt{s} = 13\,\text{TeV}$ exploration study [9] and its $\sqrt{s} = 8\,\text{TeV}$ predecessor [13], and gives rise to the expectation of strongly improved results. Due to the more compact design of mutually exclusive signal regions and the set of fully orthogonal control regions, the combination of all single-bin fit SR into one simultaneous fit is possible – not only for the simplified model but also for the GMSB model. The hence possible consideration of many more physics topologies in the result extraction are expected to increase the sensitivity towards not yet excluded regions of the model parameter-spaces. A novel multi-bin fit based SR is designed in the 2τ channel and its performance is scrutinised. This new approach is expected to provide comparably strong exclusion limits and give even more confidence in already excluded areas of the model parameter-space.

The GMSB SR of the 2τ channel is the only SR tailored specifically towards the expected signatures of the GMSB model. The early $\sqrt{s} = 13\,\text{TeV}$ exploration studies to this analysis [9] have shown that dedicated sensitivity towards GMSB signals is gained the best for selections including multiple τ-leptons and jets, all at high energies. These findings are supported by the distributions shown in figs. 5.12(a) and 5.12(d), studying the behaviour of the GMSB signal benchmark scenario, as well as fig. 2.13(b). The optimal cuts on H_T and $m_\text{T}^{\tau_1} + m_\text{T}^{\tau_2}$ are found to be $H_\text{T} > 1\,900\,\text{GeV}$ and $m_\text{T}^{\tau_1} + m_\text{T}^{\tau_2} > 150\,\text{GeV}$. While the $m_\text{T}^{\tau_1} + m_\text{T}^{\tau_2}$ requirement predominantly suppresses background arising from $Z(\tau\tau)$ + jets processes as in the 2τ multibin SR, the stringent H_T cut accounts for the numerous high-energy jets and τ-leptons. The resulting yields in the GMSB SR are compiled in table 5.6, the signal loss at each selection step is documented in table A.17. The quality of the signal region design is considered good, given the high abundance of expected signal and the low predicted background. Due to its strong resemblance to the 2τ HM SR, the corresponding benchmark exhibits an also high abundance. The GMSB is mutually exclusive with respect to all the 2τ compressed SR and the 1τ channel. This fact later allows for exploitation of any remaining sensitivity in these SRs in a simultaneous result extraction, collecting even the smallest of GMSB signal yields.

CHAPTER 6

Background Estimation – Establishing Control over the Known

The last chapter outlined how the search for the sought signal models is carried out. The regions of phase-space in which the signal dominates the Standard Model background are designed. However, the background prediction in those signal regions is not yet robust. Due to computational and intellectual limitations, the simulated backgrounds as they are provided by the MC generators do not necessarily describe the observed data flawlessly. In addition, computation is also a major limiting factor of the precision of the data-driven estimation of the multi-jets background. As a consequence, the necessity of adjusting the nominal background prediction to the observed data arises. This endeavour is carried out in a simultaneous fit of all backgrounds in a set of control regions and afterwards evaluated in validation regions. Due to the differences in the estimation procedure of MC-based simulations used for electroweak backgrounds and the data-driven approach used for the multi-jets contribution, those two topics are addressed individually, as is the validation of the background fit.

Mutual to all CRs is the used approach of *normalisation-factors* as already mentioned in section 5.3. Considering a CR enriched in a background A, where $N_{\mathrm{CR}}^{\mathrm{data}}$ events are observed in data, and $N_{\mathrm{CR}}^{\mathrm{A,MC}}$ are expected for background A from simulation (or the data-driven estimation) [189]. The prediction for this background in the signal region is then obtained as

$$N_{\mathrm{SR}}^{\mathrm{A,scaled}} = \omega_A N_{\mathrm{SR}}^{\mathrm{A,MC}} = \frac{N_{\mathrm{CR}}^{\mathrm{data}} - N_{\mathrm{CR}}^{\mathrm{other,MC}}}{N_{\mathrm{CR}}^{\mathrm{A,MC}}} N_{\mathrm{SR}}^{\mathrm{A,MC}} \tag{6.1}$$

where the nominal MC prediction is corrected by a normalisation-factor

$$\omega_A = \frac{N_{CR}^{\mathrm{data}} - N_{CR}^{\mathrm{other,MC}}}{N_{CR}^{\mathrm{A,MC}}} \quad . \tag{6.2}$$

All normalisation-factors that are defined are obtained in one simultaneous fit across all CRs using the HistFitter software package [225] and the profile log-likelihood approach that is described in appendix G. All NFs are varied simultaneously until the best possible agreement between the total background spectrum across all CRs is found. Due to the optimised isolation of the backgrounds in dedicated CRs, the influence of every CR on the NF in the combined fit is strongest for the respective background. This procedure enables the correct handling of correlations between different samples as well as between CRs. Moreover, this fit considers all available uncertainties, statistical and systematical ones alike, and their correlations. The results of this fit and its validation are covered in section 6.4.

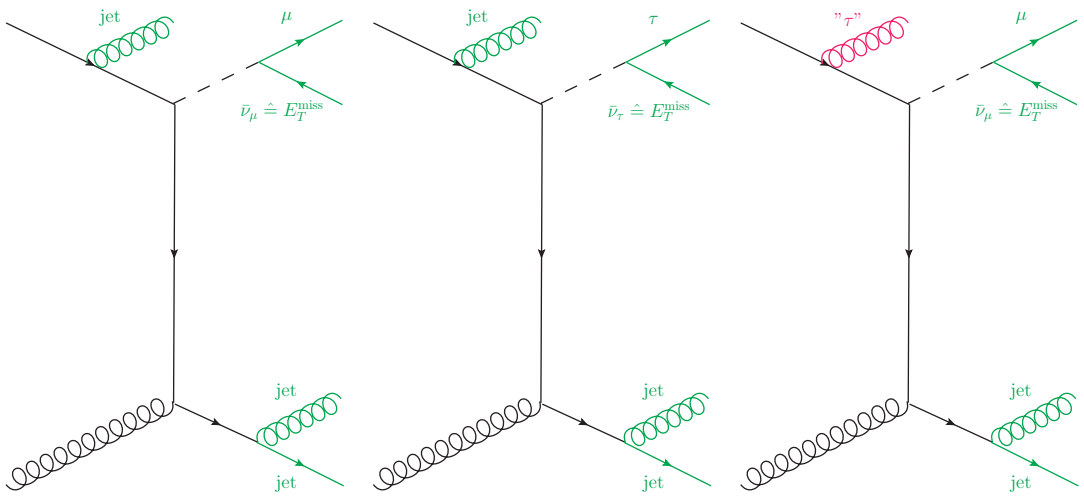

(a) τ-lepton-independent kinematics (b) True τ-lepton assessment (c) Fake τ-lepton assessment

Figure 6.1: Example production diagrams for W + jets processes that are used to probe different aspects of τ-lepton-related topologies [15]. Objects marked in green are identified correctly, while red coloured objects are misidentified.

6.1 Electroweak backgrounds: top quarks and V + jets

Events arising from top quark production and V + jets processes pose the major background contributions to both signal channels and all of their SRs (cf. sections 5.2 and 5.7). While the contributions from top quarks and W-bosons are addressed in similar CRs, individual regions are designed for Z + jets processes.

Top and W CRs As illustrated in figs. 5.4 and 5.6, the underlying structure of events from top quark production and W + jets processes that resemble signal events can be substantially different. There can be different variations of fake or true τ-leptons, fake or true missing transverse momentum etc.. To account for these differences properly, the background estimation for top quark and W + jets processes is carried out separately for fake and true τ-lepton contributions as proposed in [15]. The original proposal only covers the 2τ channel and has been successfully implemented in [9]. This analysis extends the field of application also to the 1τ channel to provide the important mutual background estimation for both signal channels. The different ways of assessing true and fake τ-lepton physics to address them individually are illustrated by diagrams of possible underlying processes, depicted in fig. 6.1.

The approach becomes clearest when starting from the fake τ-lepton assessment[1]. A fake τ-lepton in decays of W-bosons most likely arises from an additional jet that is misidentified – the misidentification probabilities for light leptons are much smaller, as is the combined probability to misidentify both the a real τ-lepton and a jet. In order to not be subject to unnecessarily large amounts of missing transverse momentum introduced by mis-measurements, the W-boson for the assessment of fake τ-lepton physics is required to decay leptonically. The requirement of a light lepton hence ensures the presence of a W-boson, while the detected τ-lepton is most likely a misidentified jet. Thus topologies such as fig. 6.1(c) probe the physics of fake τ-leptons. This analysis only makes use of muons as probes for the W-boson due to their cleaner signature and their smaller probability to be misidentified as τ-leptons (cf. [9]). No criteria are imposed on the presence of electrons. True τ-leptons, on the other hand, are assessed by requiring the

[1] This procedures relies on the assumption that processes containing single and multiple fake τ-leptons are uncorrelated.

CR	Top/W Kinematic	Top/W true-τ	Top/W fake-τ
Pre-selection	$E_{\mathrm{T}}^{\mathrm{miss}} > 180\,\mathrm{GeV},\ p_{\mathrm{T}}^{\mathrm{j}_1} > 120\,\mathrm{GeV}$ $n_{\mathrm{jet}} \geq 2,\ p_{\mathrm{T}}^{\mathrm{j}_2} > 25\,\mathrm{GeV}$		
Multi-jet	$\Delta\phi(\boldsymbol{p}_{\mathrm{T}}^{\mathrm{j}_{1,2}}, \boldsymbol{p}_{\mathrm{T}}^{\mathrm{miss}}) > 0.4$		
τ-leptons	$n_\tau = 0$	$n_\tau = 1$	
Jets	$n_{\mathrm{jet}} \geq 3$		—
Muons	$N_\mu = 1$	$N_\mu = 0$	$N_\mu = 1$
Top separation	$n_{b-\mathrm{jet}} = 0/\geq 1$		
Event properties	$H_{\mathrm{T}} < 800\,\mathrm{GeV}$ $E_{\mathrm{T}}^{\mathrm{miss}} < 300\,\mathrm{GeV}$		
	$m_{\mathrm{T}}^{\mu} < 100\,\mathrm{GeV}$	$m_{\mathrm{T}}^{\tau} < 80\,\mathrm{GeV}$	$m_{\mathrm{T}}^{\mu} < 100\,\mathrm{GeV}$
	—	—	$m_{\mathrm{inv}}(\tau\mu) > 60\,\mathrm{GeV}^{\dagger}$

Table 6.1: Summary of the Top/W CRs used across both channels. The Top and W regions of each type are separated by requiring the presence/absence of a b-tagged jet. The requirement marked with a † is only applied in the W fake-τ CR.

presence of exactly one τ-lepton and not allowing for the presence of muons – again, no requirements are imposed on electrons. The presence of the τ-lepton ensures the underlying process to be the decay of a W-boson, while an additional jet is required to keep the minimal number of reconstructed objects constant with respect to the fake τ-lepton case. The targeted topology for the studies of true τ-leptons is depicted in fig. 6.1(b). With fake and true τ-leptons being covered, the remaining event topology of additional jets needs to be addresses. To decouple the ISR/FSR contributions from the also hadronically interacting τ-lepton, the absence of any τ-lepton is explicitly required as illustrated in fig. 6.1(a). This criterion furthermore ensures orthogonality with respect to the other two W CRs. To still probe the physics of W-boson decays and to suppress the influence of multi-jet processes, a muon is required. As in the true τ-lepton case, an extra jet accounts for the minimum number of detected objects to be constant.

For contributions from single or pairs of top quarks, similar considerations can be made and, in principle, the same selection criteria can be applied – in a top quark decay, the same statements hold due to the W boson being involved. The major difference with respect to the decays of directly produced W-bosons lies within the presence of jets arising from b-quarks. While in the decays of top quarks, b-tagged jets are almost obligatory, the probability of an ISR/FSR jet to be b-tagged is low. This distinct feature helps in separating the otherwise similar topologies of W + jets and top quark processes that are assessed in this endeavour.

For each of the presented cases, a designated CR is designed in which the corresponding NFs are obtained. The cuts defining said control regions are summarised in table 6.1.

In addition to the selection criteria motivated by the underlying diagrams of fig. 6.1 and the considerations regarding b-tagged jets, several cuts listed as *event properties* are applied. Imposing upper bounds of $H_{\mathrm{T}} < 800\,\mathrm{GeV}$ and $E_{\mathrm{T}}^{\mathrm{miss}} < 300\,\mathrm{GeV}$ ensures the presence of the desired Standard Model processes along with the absence of any signal. Moreover, any overlap of the CRs with the SRs of both channels is avoided (cf. tables 5.3 and 5.5). The upper bounds on the transverse masses of the involved muons ($m_{\mathrm{T}}^{\mu} < 100\,\mathrm{GeV}$) and τ-leptons ($m_{\mathrm{T}}^{\tau} < 80\,\mathrm{GeV}$) foster the desired nature of the CR: due to the high

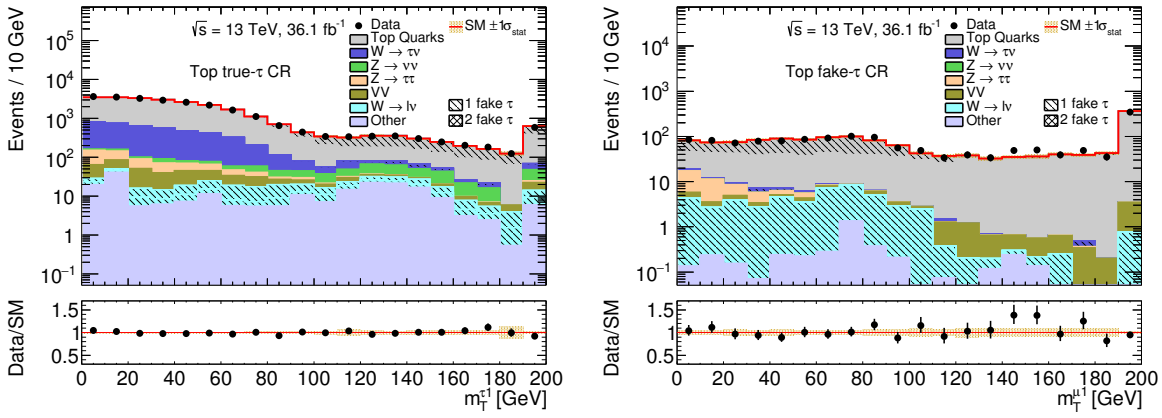

(a) (b)

Figure 6.2: Distributions of m_{T}^{τ} in the Top true-τ (a) and m_{T}^{μ} in the fake-τ CR (b). The cuts on $m_{\mathrm{T}}^{\tau} < 80\,\mathrm{GeV}$ and $m_{\mathrm{T}}^{\mu} < 100\,\mathrm{GeV}$ as given in table 6.1 are not applied. The results shown are obtained after fitting the normalisation of the background in the control regions. The last bin of each distribution contains the overflow events. The uncertainties displayed consider only statistical limitations in the background modelling, illustrated by the shaded bands. The contribution labelled as *other* includes multi-jet events and V + jets processes not explicitly listed in the legend. The black hatch-pattern illustrates contributions with fake τ-leptons.

mass of the W-boson with respect to any lepton and the resulting boost of the decay products, genuine decays of a W-boson to a muon or τ-lepton are expected to have the corresponding neutrinos aligned with the charged leptons. As a result, the transverse mass of the muon and τ-lepton is expected to be rather low, i.e. around and below the W-boson mass. Processes with fake $E_{\mathrm{T}}^{\mathrm{miss}}$, e.g. from multi-jet, or hadronic top quark or W-boson decays, on the other hand, do not have a preferred direction of the missing transverse momentum vector. They can hence be effectively suppressed by this measure. This goal is successfully met as shown in fig. 6.2: in the Top true-τ CR, the contributions without fake τ-leptons accumulate towards low values, as do the fake τ-lepton contributions in the distribution of the muon transverse mass in the Top fake-τ CR. A cut on the invariant mass of the system formed by the muon and the τ-lepton $m_{\mathrm{inv}}(\tau\mu) > 60\,\mathrm{GeV}$ helps to suppress contributions from $Z(\tau\tau)$ + jets events where one τ-lepton is accidentally identified as a muon, the corresponding distribution of $m_{\mathrm{inv}}(\tau\mu)$ being depicted in fig. 6.3. The $Z(\tau\tau)$ + jets background component shows a clear tendency to values below the mass of the Z-boson and can hence be cut away easily. All six CRs are mutually exclusive due to the requirements they impose on the multiplicities of muons, τ-leptons, and b-tagged jets.

Figures 6.4(a) to 6.4(c) depict example distributions of important variables in three example CRs for the estimation of top quark and W + jets backgrounds. In addition, figs. A.2 to A.7 in appendix A.2 show distributions of numerous variables in all six Top and W CRs. These sets of plots allow for several statements regarding the quality of this part of the background estimation.

In general, all CRs are based on high statistics to allow for further statements and a reliable fit. The indicated bands of the statistical uncertainties are small with respect to the amount of events in each bin, as can be inferred from the provided ratio plots in the bottom panes. Each CR is predominantly occupied by events of the background contribution it is entitled to probe: top quark contributions in all Top CRs, $W(\tau\nu)$ + jets in the W True-Tau CR and $W(\ell\nu)$ + jets in the W fake-τ and kinematic CRs, where the absence of τ-leptons is required. Thus the results obtained from fits in these CRs can be considered to be based on the correct input and to address the desired processes.

Furthermore, the modelling of most of the important variables that are used for SR and VR design is

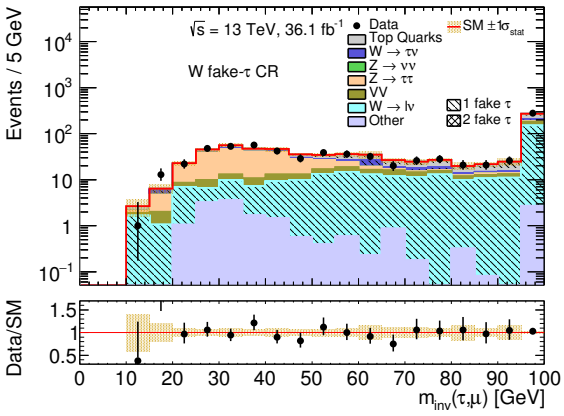

(a)

Figure 6.3: Distribution of $m_{\text{inv}}(\tau\mu)$ in the W fake-τ CR without before application of the cut on $m_{\text{inv}}(\tau\mu) > 60\,\text{GeV}$. The results shown are obtained after fitting the normalisation of the background in the control regions. The last bin of each distribution contains the overflow events. The uncertainties displayed consider only statistical limitations in the background modelling, illustrated by the shaded bands. The contribution labelled as *other* includes multi-jet events and V + jets processes not explicitly listed in the legend.

in good agreement with the observed data, well within the statistical uncertainties. An exception to this statement pose distributions of the jet multiplicity n_{jet} at high values. This, however, is a long-known effect that is due to the difficult description of high jet multiplicities already on the level of MC generators and their calculation of matrix elements [189]. Also fig. A.7(a) (and to a lower extend fig. A.3(a)), show a harder H_{T} distribution for the background spectrum than for the observed data. Since this trend is not observed in the Top kinematic CR, this feature is attributed to a mis-modelling of the W + jets contribution. A potential explanation is the absence of high-order electroweak corrections in the used samples generated with Sherpa 2.2 – Sherpa 2.3 is expected to comprise these but has not yet been available to this analysis [189]. This effect is addressed by a designated systematic uncertainty (cf. section 7.4) with additional information presented in appendix D. The background from $W(e\nu)$ + jets processes is assigned the same NF as the $W(\mu\nu)$ + jets contribution that is assessed in the kinematic and fake-τ W CRs.

Z + jets CRs The background contributions from Z + jets processes are assessed individually and inclusively with respect to the origin of τ-leptons. While the branching fraction for $Z(\tau\tau)$ + jets is small ($\mathcal{B}(Z \to \tau\tau) \approx 3.4\%$ [38]) and a breakdown into more specific components would result in too few events for a sensible further analysis, $Z(\nu\nu)$ + jets is difficult to isolate. The selection criteria that are used to define the respective CRs for $Z(\tau\tau)$ + jets and $Z(\nu\nu)$ + jets are summarised in table 6.2.

The two major Z + jets background components contribute to the two signal channels differently: in the 1τ channel, $Z(\nu\nu)$ + jets poses a background—genuine missing transverse momentum and a misidentified ISR/FSR jet characterise this process—while two τ-leptons and missing transverse momentum from $Z(\tau\tau)$ + jets processes are a distinct feature of the 2τ channel. As a consequence, the CR design for those two cases is inspired by the considerations of the respective SR designs in sections 5.2 and 5.7.

As can be inferred from fig. 5.12(b), $Z(\tau\tau)$ + jets events tend to low values of $m_{\text{T}}^{\tau_1} + m_{\text{T}}^{\tau_2}$ – the missing transverse momentum originates from the neutrinos of the τ-lepton decays and is hence likely to point in the same direction as the visible τ-lepton decay products. The strict upper cut of $m_{\text{T}}^{\tau_1} + m_{\text{T}}^{\tau_2} < 100\,\text{GeV}$ suppresses most other background and keeps almost all $Z(\tau\tau)$ + jets events in the selection.

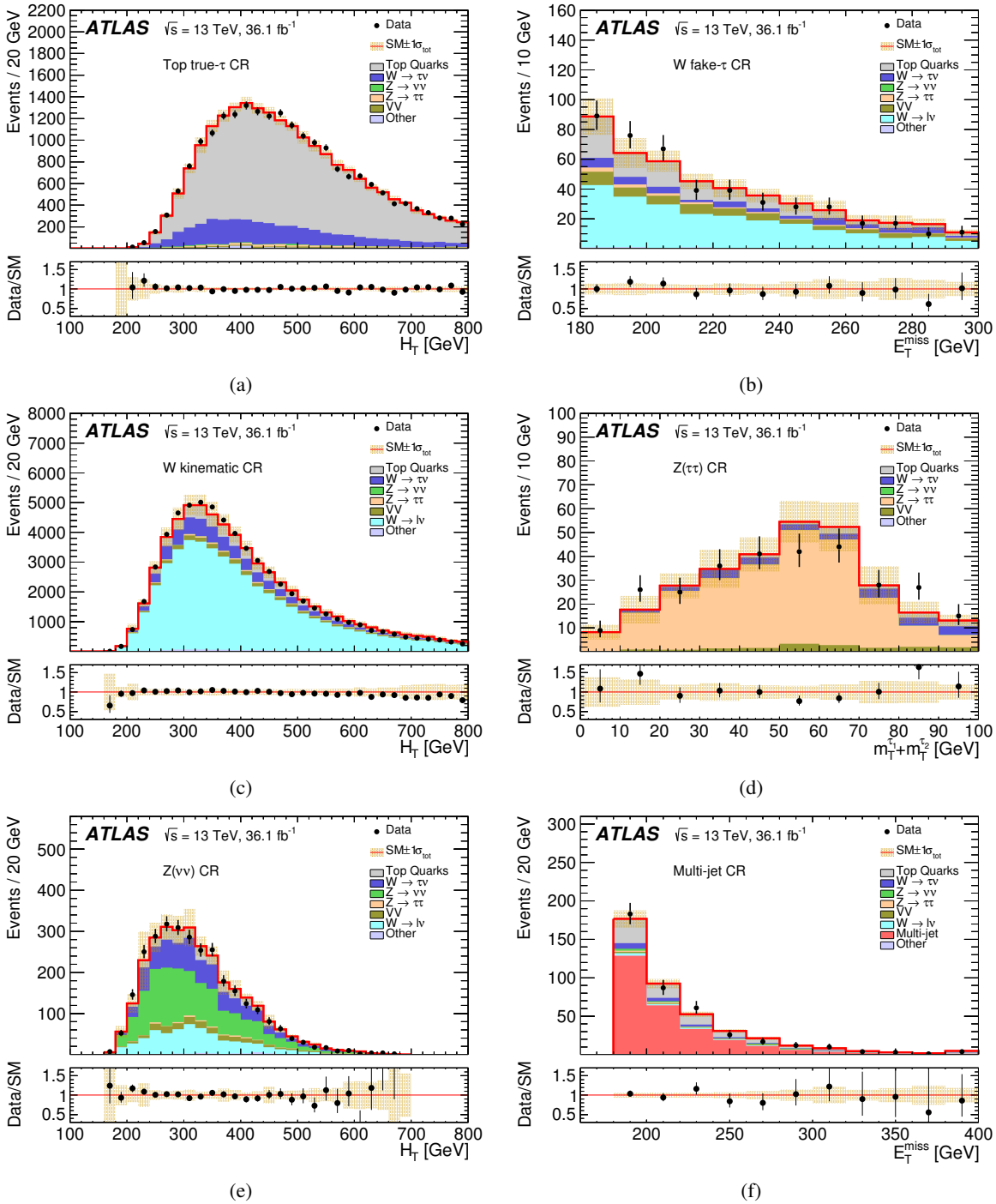

Figure 6.4: Example kinematic distributions of characteristic variables in the CRs [8]. The results shown are obtained after fitting the normalisation of the background in the control regions. The last bin of each distribution contains the overflow events. The uncertainties displayed consider statistical limitations in the background modelling as well as all experimental and theoretical systematic uncertainties, illustrated by the shaded bands. Red arrows in the Data/SM ratio indicate bins where the corresponding entry falls outside the plotted range. The contribution labelled as *other* includes multi-jet contributions (except for (f)) and V + jets processes not explicitly listed in the legend.

CR	$Z(\nu\nu)$	$Z(\tau\tau)$	Multi-jet
Pre-selection	$E_{\mathrm{T}}^{\mathrm{miss}} > 180\,\mathrm{GeV},\ p_{\mathrm{T}}^{\mathrm{j}_1} > 120\,\mathrm{GeV}$ $n_{\mathrm{jet}} \geq 2,\ p_{\mathrm{T}}^{\mathrm{j}_2} > 25\,\mathrm{GeV}$		
Multi-jet	$\Delta\phi(\boldsymbol{p}_{\mathrm{T}}^{\mathrm{j}_{1,2}}, \boldsymbol{p}_{\mathrm{T}}^{\mathrm{miss}}) > 0.4$		$\Delta\phi(\boldsymbol{p}_{\mathrm{T}}^{\mathrm{j}_{1,2}}, \boldsymbol{p}_{\mathrm{T}}^{\mathrm{miss}}) < 0.3$
τ-leptons	$n_\tau = 1$	$n_\tau \geq 2,\ q_{\tau_1} = -q_{\tau_2}$	$n_\tau = 1$
Muons	$n_\mu = 0$	—	—
Top separation	$n_{b-\mathrm{jet}} = 0$		—
Event properties	$H_{\mathrm{T}} < 800\,\mathrm{GeV}$		—
	$E_{\mathrm{T}}^{\mathrm{miss}} < 300\,\mathrm{GeV}$	—	—
	$100\,\mathrm{GeV} \leq m_{\mathrm{T}}^{\tau} < 200\,\mathrm{GeV}$	$m_{\mathrm{T}}^{\tau_1} + m_{\mathrm{T}}^{\tau_2} < 100\,\mathrm{GeV}$	$100\,\mathrm{GeV} < m_{\mathrm{T}}^{\tau} < 200\,\mathrm{GeV}$
	$E_{\mathrm{T}}^{\mathrm{miss}}/m_{\mathrm{eff}} > 0.3$	$m_{\mathrm{T2}}^{\tau\tau} < 70\,\mathrm{GeV}$	$E_{\mathrm{T}}^{\mathrm{miss}}/m_{\mathrm{eff}} < 0.2$
	$\Delta\phi(\mathrm{j}_1, \boldsymbol{p}_{\mathrm{T}}^{\mathrm{miss}}) > 2.0$	—	—
	$\Delta\phi(\tau, \boldsymbol{p}_{\mathrm{T}}^{\mathrm{miss}}) > 1.0$	—	—

Table 6.2: Summary of the Z + jets and Multi-jet CRs used across both channels.

A consequent next step is to require at least two τ-leptons of which the two highest in energy should have opposite signs in their electric charge. This kind of signature is expected for genuine $Z(\tau\tau)$ + jets events while any other background or signal should not prefer any τ-lepton charge configuration. Requiring the absence of any b-tagged jet reduces the amount of remaining top quark contributions while the upper cut of $m_{\mathrm{T2}}^{\tau\tau} < 70\,\mathrm{GeV}$ ensures orthogonality to the 2τ compressed SR. The upper cut on H_{T} removes any overlap with the 2τ High-Mass SR. Due to the fact that the $Z(\tau\tau)$ CR is the only CR requiring the presence of more than one τ-lepton, it is orthogonal to any other CR without any additional cuts.

Studying fig. 5.10, the challenge of isolating the $Z(\nu\nu)$+jets contribution in the 1τ background spectrum becomes clear: the usually helpful discriminating variables do not indicate significant separation power. However, combining them allows for a first increase in isolation. Upper cuts of $H_{\mathrm{T}} < 800\,\mathrm{GeV}$ and $E_{\mathrm{T}}^{\mathrm{miss}} < 300\,\mathrm{GeV}$ select not only the small $Z(\nu\nu)$ + jets contribution but ensure orthogonality with respect to the compressed 1τ SR. The mutual exclusiveness to the 1τ medium-mass SR requires a window cut of $100\,\mathrm{GeV} \leq m_{\mathrm{T}}^{\tau} < 200\,\mathrm{GeV}$, selecting again the majority of $Z(\nu\nu)$ + jets. Since$Z(\nu\nu)$ + jets events only pose a substantial background to the 1τ channel, this CR requires the presence of exactly one τ-lepton. The absence of muons is needed to remove any overlap with the W fake-τ CR. At this point, further refinement is needed to increase the purity of the $Z(\nu\nu)$ + jets contribution. Considerations regarding topological characteristics of $Z(\nu\nu)$ + jets events with a faked τ-lepton provide helpful tools here: for the invisible decay of the Z-boson to produce enough missing transverse momentum, the Z-boson needs to be rather strongly boosted by recoiling against a high-energy jet. This recoil would result in the leading jet to be antiparallel or at least well separated from the vector of missing transverse momentum, motivating the cut of $\Delta\phi(\mathrm{j}_1, \boldsymbol{p}_{\mathrm{T}}^{\mathrm{miss}}) > 2.0$. The same considerations can be made for the required τ-lepton: since it has to arise from an ISR or FSR jet and hence needs to be uncorrelated to the neutrino-induced missing transverse momentum, it is also expected to be well separated from the vector of missing transverse momentum. However, for the τ-lepton, the separation is not expected to be as strong as for the leading jet against the Z-boson recoils, introducing an angular separation requirement of $\Delta\phi(\tau, \boldsymbol{p}_{\mathrm{T}}^{\mathrm{miss}}) > 1.0$. Since the Z-boson is the only non-hadronic particle in a $Z(\nu\nu)$ + jets event, the neutrinos are expected to be

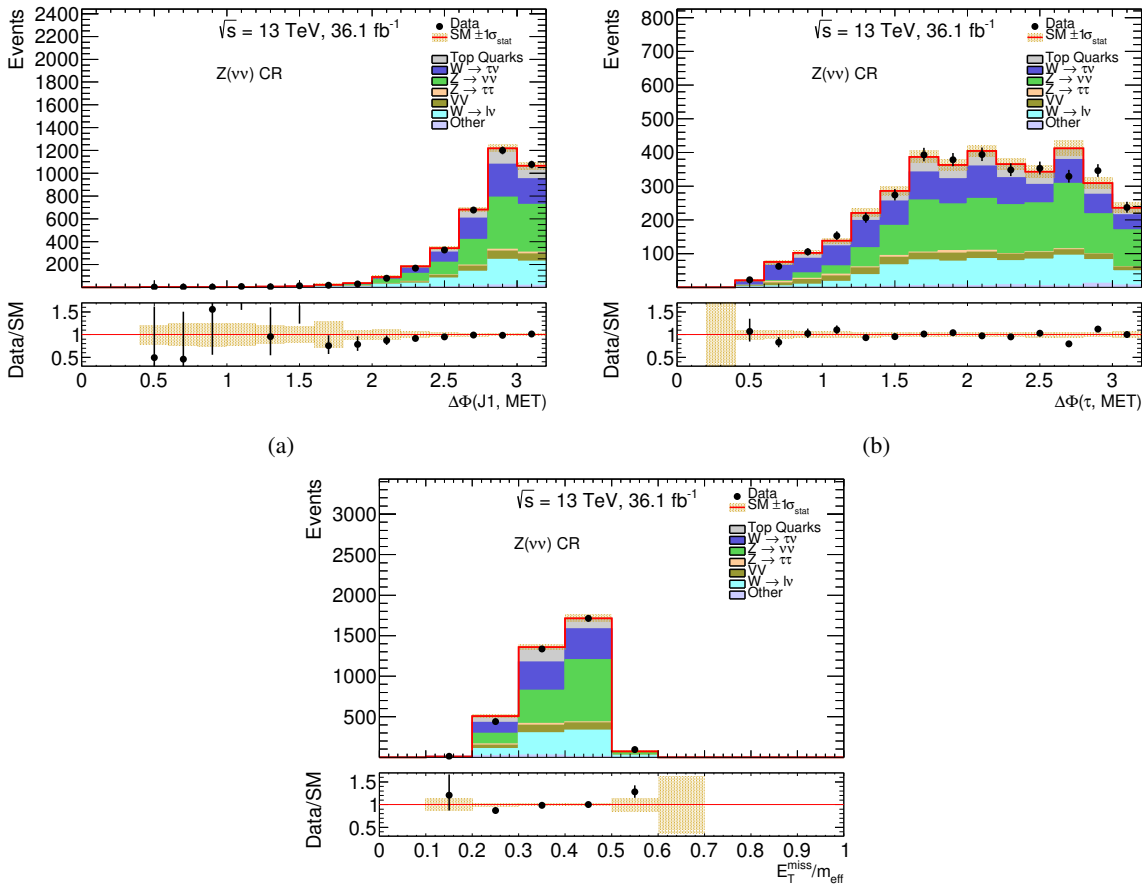

Figure 6.5: Kinematic distributions of characteristic variables in the $Z(\nu\nu)$ CR without the cuts of $\Delta\phi(\mathrm{j}_1, \boldsymbol{p}_{\mathrm{T}}^{\mathrm{miss}}) > 2.0$, $\Delta\phi(\tau, \boldsymbol{p}_{\mathrm{T}}^{\mathrm{miss}}) > 1.0$, and $E_{\mathrm{T}}^{\mathrm{miss}}/m_{\mathrm{eff}} > 0.3$ applied. The results shown are obtained after fitting the normalisation of the background in the control regions. The last bin of each distribution contains the overflow events. The uncertainties displayed consider only statistical limitations in the background modelling, illustrated by the shaded bands. The contribution labelled as*other* includes multi-jet events and V + jets processes not explicitly listed in the legend.

the only source of missing transverse momentum. Moreover, the Z-boson should carry a substantial amount of energy, similar to the hadronic rest of the event. Requiring the missing transverse energy to be in of a the magnitude than the effective mass should hence separate $Z(\nu\nu)$ + jets topologies from top quark and W + jets processes where the fraction of missing transverse momentum is smaller due to more visible particles. The considerations are reflected in a cut on the ratio $E_{\mathrm{T}}^{\mathrm{miss}}/m_{\mathrm{eff}} > 0.3$. Distributions of these three discriminating variables are depicted in fig. 6.5. The gain in $Z(\nu\nu)$ + jets purity is not big but nevertheless visible.

Statements about the final CRs for the major Z-boson based background contributions can be made based on figs. 6.4(d) and 6.4(e) and figs. A.8 and A.9 in appendix A.2. While the $Z(\tau\tau)$ CR is dominated by the desired events, the $Z(\nu\nu)$ CRs is still well populated by the corresponding background type. Studying the individual distributions of important variables, the good modelling of the two processes in the simulation becomes visible: all distributions of the predicted background are in agreement with the observed data, already within the statistical uncertainties. Both regions are hence expected to probe and

provide reliable information on the backgrounds they are designed for. In each of these two regions, an NF for the corresponding contribution is obtained by means of the simultaneous background fit, rendering this analysis [8] the first in its line [9, 13] to address the $Z(\nu\nu)$ + jets component of the background spectrum individually. Fort the negligible background contributions from $Z(ee)$ + jets and $Z(\mu\mu)$ + jets (cf. appendix A.3), the same considerations regarding fake τ-leptons can be made as for the $Z(\nu\nu)$ + jets contribution. They are hence treated in the same way and get assigned the same NF.

Due to their low production cross-sections (cf. fig. 5.1), the contribution of VV processes is low (cf. ibid.). In combination with its rich spectrum of potential final state signatures, this background is also difficult to isolate. Its small abundance, though, justifies the choice of taking it into account without fitting it individually but keeping its contribution as predicted by the MC generators.

6.2 Multi-jet background

As already mentioned in sections 5.1 and 5.2 and visualised in fig. 5.1, the production of multiple jets in an event via the strong force—referred to as multi-jet events—poses the most abundant of all Standard Model processes that contribute to the background spectrum. As a consequence of the high production cross-section and the additional fact that processes involving the strong force are difficult to model at low energies (cf. chapter 4), it is challenging to simulate this background using MC techniques. Besides, multi-jet events contain neither prompt τ-leptons nor genuine $E_{\mathrm{T}}^{\mathrm{miss}}$– except for the rare cases of semi-leptonic decays of heavy-flavour jets [189]. Hence, any τ-lepton and missing transverse momentum contribution have to originate from jet mis-identification or mis-measurements for a multi-jet event to be found in a signal region of this analysis. The low probability for this to happen and the challenge to model the detector-induced misidentification correctly are two additional reasons to not estimate this background contribution using MC simulations.

While the challenge of fake τ-leptons is a feature specific to this analysis, fake $E_{\mathrm{T}}^{\mathrm{miss}}$ in multi-jet events is a common issue in various SUSY searches. As a result, the so-called *jet smearing technique* [226] has been developed and first used in a search for SUSY with multiple jets, $E_{\mathrm{T}}^{\mathrm{miss}}$ and no light leptons. This method is based on the idea that the dominant source of $E_{\mathrm{T}}^{\mathrm{miss}}$ in multi-jet events arises from a mis-measurement of the energy of one or multiple jets. It is hence possible to generate a pseudo-dataset of multi-jet events with artificially generated fake $E_{\mathrm{T}}^{\mathrm{miss}}$ by varying properties of well-measured jets in the observed data (so-called *seed events*) within their calorimeter resolution distributions. These distributions are computed as ratios between reconstructed $p_{\mathrm{T}}^{\mathrm{j}}$ and truth-level $p_{\mathrm{T}}^{\mathrm{j}}$. Here, truth jets include neutrinos while both, truth and reconstructed jets, include muons. The latter aspect is of particular importance for jets from b-quarks that can decay semileptonically. The jet resolution distributions are initially derived using MC simulations of dijet events. Data-driven corrections are then applied to better describe the resolution measured in data, especially in the distribution tails [189].

The procedure itself is schematically illustrated in fig. 6.6. A well-measured multi-jet seed event without significant $E_{\mathrm{T}}^{\mathrm{miss}}$ is the starting point. In a next step, the measured energies of the reconstructed jets are recalculated by multiplication with a smearing factor that is randomly drawn from the normalised jet energy resolution distribution –an example is provided in fig. 6.7. In the subsequent step, the vector sum of the reconstructed jet energies is recalculated, giving rise to a vector of missing transverse momentum. This procedure is carried out multiple times for each seed event (here, 200 times), creating an, in principle, arbitrarily large pseudo-dataset of multi-jet events with artificially generated $E_{\mathrm{T}}^{\mathrm{miss}}$. More details on the technique, the underlying measurements and the parametrisation used in Run-1 of the LHC can be found in [226]. Additional information on explorations and contributions to the underlying development of the multi-jet estimation for this analysis are documented in [227].

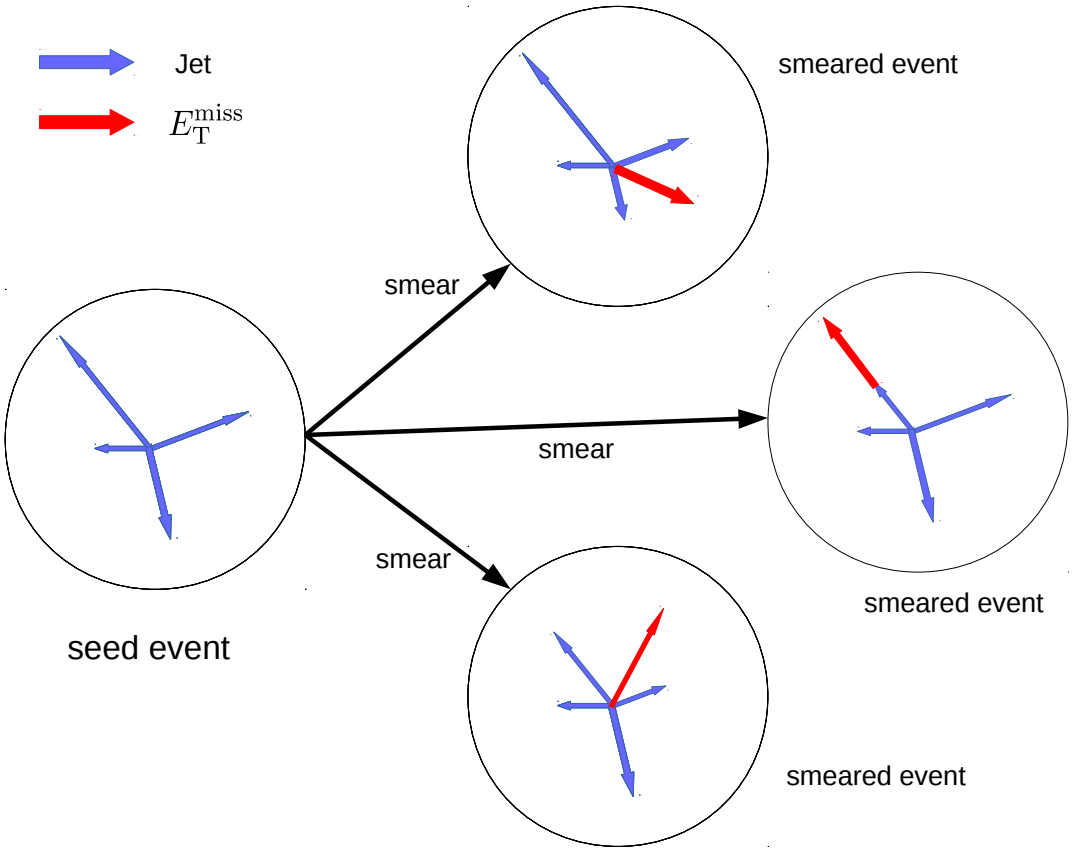

Figure 6.6: Schematic illustration of the jet smearing procedure [227].

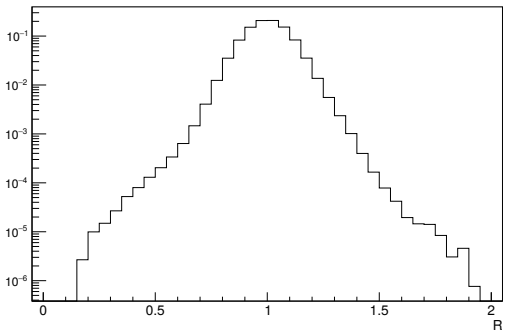

Figure 6.7: An example jet resolution function as obtained in [227]. The response value $R = p_{\mathrm{T}}^{\mathrm{true}}/p_{\mathrm{T}}^{\mathrm{reco}}$ is a measure for the resolution of the measured jet energy. The shapes of the Gaussian core due to statistical fluctuations and the non-Gaussian sidebands due to, for example, neutrinos or malfunctioning detector parts, are visible. The displayed distribution is for illustration purposes only and not used in the presented analysis.

While creating artificial $E_{\mathrm{T}}^{\mathrm{miss}}$ is sufficient in the absence of τ-leptons, e.g. for the aforementioned analysis, the studies presented here face an additional challenge. In multi-jet events, τ-leptons have to originate from misidentified jets. The advantage of using the data-driven jet smearing method to obtain an estimation for that background contribution is that this required fake τ-lepton content is intrinsically present. There is consequently no need for corrections of the jet–τ-lepton fake probabilities – in contrast to MC-based estimates.

Since the only reconstructed τ-leptons decay hadronically and their reconstruction is seeded from jets (cf. section 3.3.4), it would be consequent to make them subject to a similar smearing procedure as jets. Different approaches for *τ-lepton smearing* have been studied and evaluated in [227]. However, no measurable increase in the agreement between observed data and the generated pseudo-data has been found and the endeavour of τ-lepton smearing is not pursued for this analysis.

While the jet smearing approach has already been studied in [15] and successfully used in the $\sqrt{s} = 8\,\mathrm{TeV}$ analysis [13], statistical limitations of the small early $\sqrt{s} = 13\,\mathrm{TeV}$ dataset of ATLAS limit its application in the exploration study [9] to the 1τ channel. Since the multi-jet background component in the 2τ channel is, in general, small, a less sophisticated approach compensating its short-comings by means of a larger systematic uncertainty, is deemed a sensible solution ibid.. The increased $\sqrt{s} = 13\,\mathrm{TeV}$ dataset that is available to this analysis and more refined selection techniques allow for usage of the jet smearing technique in both signal channels and to hence provide a mutual multi-jet estimate to this analysis..

Multi-jet CR As for the electroweak contributions to the background spectrum, the design of a dedicated multi-jet CR is necessary and of even more importance. While the MC-based simulation of backgrounds is a well-established, frequently applied and evaluated approach, data-driven methods require a special level of attention. With rather well-known cross-sections, the normalisation of MC-simulations to a given amount of integrated luminosity can be easily performed. The proper normalisation of data-driven background estimates, on the other hand, requires careful design of control regions to obtain the normalisation by means of only the observed data, without knowledge about an underlying cross-section. The correct normalisation is a particular challenge for the jet smearing method: since even from a small number of seed events, in principle, an arbitrarily large pseudo-dataset can be produced by smearing each seed event as often as desired, the only handle to properly normalise the multi-jet sample is by means of a fit to data.

Exploration studies in [9] show that two features predominantly characterise the multi-jet background and explain its abundance:

- The region of low $E_{\mathrm{T}}^{\mathrm{miss}}$ values exhibits the expected higher abundance of multi-jet events. The less $E_{\mathrm{T}}^{\mathrm{miss}}$ has to be faked, the easier a multi-jet event can end up in an $E_{\mathrm{T}}^{\mathrm{miss}}$-based selection. In [9], such a region is used as the multi-jet CR of the 1τ channel. Due to the inefficiency of $E_{\mathrm{T}}^{\mathrm{miss}}$-based triggers in regimes of low $E_{\mathrm{T}}^{\mathrm{miss}}$, that study uses a single-jet trigger to select events for its multi-jet CR. This approach, however, is problematic. Since all other regions of phase-space, particularly SRs, comprise high-$E_{\mathrm{T}}^{\mathrm{miss}}$ selection criteria, it does not provide representative modelling for any other region of interest. Most of its events exhibit only small mis-measurements of the jet energy and are hence located in the Gaussian core of the resolution function, while high-$E_{\mathrm{T}}^{\mathrm{miss}}$ events are subject to larger mis-measurements and are found in the non-Gaussian tails of the resolution distributions as depicted in fig. 6.7. As a consequence, the low-$E_{\mathrm{T}}^{\mathrm{miss}}$ approach of estimating the multi-jet background as in [9] is not chosen for the presented analysis.

- The other characteristic of the multi-jet component of the background is the missing transverse momentum being aligned with high-energy jets. The absence of genuine $E_{\mathrm{T}}^{\mathrm{miss}}$—that could, in

principle, point anywhere—and the fact that mis-measurements of higher-energy jets contribute more to the fake missing transverse momentum, are reflected in the multi-jet background peaking at low values of $\Delta\phi(\text{jet}, \boldsymbol{p}_{\text{T}}^{\text{miss}})$, particularly for the two jets highest in energy. Since this requirement is independent of the magnitude of $E_{\text{T}}^{\text{miss}}$, it can also be used on events that are triggered by the common $E_{\text{T}}^{\text{miss}}$-trigger of this analysis.

Based on these observations, the multi-jet CR of this analysis is designed to fit into the ensemble of the other regions of phase-space. It uses the same $E_{\text{T}}^{\text{miss}}$-based trigger and applies the corresponding efficiency and event quality criteria. The contribution of the desired multi-jet events is enhanced by requiring the missing transverse momentum vector to be aligned with at least one of the two leading jets in the polar plane.

As already mentioned, the probability of two τ-leptons originating from misidentified jets is so low that the multi-jet background mainly contributes to 1τ signatures, motivating the requirement of only reconstructed tau. As in the Top and W fake-τ CRs (cf. section 6.1), a cut on the transverse mass of the τ-lepton suppresses the small contributions from genuine τ-lepton sources. In analogy to the $Z(\nu\nu)$ CR, a cut on the ratio $E_{\text{T}}^{\text{miss}}/m_{\text{eff}}$ is applied. Here, however, its purpose is to ensure that the event is dominated by hadronic activity and to suppress events with genuine $E_{\text{T}}^{\text{miss}}$ such as leptonic W-boson or top quark decays. In order to allow for an as broadly applicable as possible prediction, no criteria regarding light leptons are imposed. The full set of selection requirements describing the Multi-jet CR is summarised in table 6.2.

Seed selection The first step in the generation of the pseudo-dataset of multi-jet events is to select proper seed events from data. As already outlined, a useful seed event is characterised by the presence of jets and only an insignificant amount of missing transverse energy. Triggers based on a $E_{\text{T}}^{\text{miss}}$ requirement are hence not a sensible choice. Instead, single-jet triggers are used to select events to undergo the jet smearing process. In order to maximise the size of the seed dataset, various single-jet triggers with different $p_{\text{T}}^{\text{j}_1}$ requirements, ranging from `HLT_j15` to `HLT_j460` are used. Since all triggers below a threshold of 380 GeV in $p_{\text{T}}^{\text{j}_1}$ were pre-scaled during the data taking periods of 2015 and 2016, a pre-scale weight based on the highest-threshold trigger that accepted the event is applied to correct the number of selected events to the right level. All triggers are used in a $p_{\text{T}}^{\text{j}_1}$ region where they are fully efficient.

Since a seed event is expected to be a genuine multi-jet event, its quality can be determined by assessing how well the jet energies are measured. This aspect is quantified by the aforementioned prerequisite of an insignificant $E_{\text{T}}^{\text{miss}}$ contribution to the total energy of the event. Earlier studies [228] have shown that a cut on $E_{\text{T}}^{\text{miss}}$ alone leads to strong kinematic biases in the generated pseudo-dataset, particularly in p_{T}^{j} [189]. Instead, a cut on the so-called E_T^{miss}*-significance* is used. Different definitions are possible for determination of the $E_{\text{T}}^{\text{miss}}$-significance:

$$S_{1/2} = \frac{E_{\text{T}}^{\text{miss}}}{\sqrt{\sum E_{\text{T}}}}\,, \quad \text{or} \quad S_{1/3} = \frac{E_{\text{T}}^{\text{miss}}}{(\sum E_{\text{T}})^{1/3}}\,, \quad \text{or} \quad S_{1/2^{\text{sub}}} = \frac{E_{\text{T}}^{\text{miss}} - 8\,\text{GeV}}{\sqrt{\sum E_{\text{T}}}} \quad . \tag{6.3}$$

While in Run-1 of the LHC, the resolution of $E_{\text{T}}^{\text{miss}}$ at ATLAS essentially followed a $\sqrt{\sum E_{\text{T}}}$-behaviour, motivating the use of $S_{1/2}$, it changed with the utilisation of more sophisticated $E_{\text{T}}^{\text{miss}}$-reconstrcution approaches . For $E_{\text{T}}^{\text{miss}}$ in Run-2 of ATLAS, [228] found that a cut on $S_{1/2}$ introduces the aforementioned biases in, e.g. p_{T}^{j}. The alternative definition $S_{1/3}$ has been found to not do so. It is used in the exploration study [9] for the jet smearing approach in the 1τ channel. In 2016, however, $S_{1/2^{\text{sub}}}$ has been proposed, accounting for the slight biases in the calculation of $E_{\text{T}}^{\text{miss}}$ due to the calorimetric evolution of the $E_{\text{T}}^{\text{miss}}$-

significance with respect to $\sqrt{\sum E_{\mathrm{T}}}$. All three version have been tested for this analysis, keeping $S_{1/3}$ as it provides the best modelling of kinematic distributions [189].

The optimal cut value for the $E_{\mathrm{T}}^{\mathrm{miss}}$-significance to select useful seed events is determined to be $s_{1/3} < 1.2\,\mathrm{GeV}^{2/3}$. However, this simple seed selection causes mis-modelling of observables in the multi-jet CR that are related to b-tagged jets such as $n_{b-\mathrm{jet}}$, $p_{\mathrm{T}}^{b-\mathrm{jet}}$ or $\Delta\phi(b\text{-jet}, \boldsymbol{p}_{\mathrm{T}}^{\mathrm{miss}})$. These biased distributions are shown in figs. 6.8(a), 6.8(c) and 6.8(e). The topology which is present in data but not in the pseudo-data are events with high-p_{T} b-tagged jets undergoing a semileptonic decay to hadrons, non-isolated leptons and neutrinos. Such seed events have substantial genuine $E_{\mathrm{T}}^{\mathrm{miss}}$ (high-p_{T} neutrinos from the b-jet decay) and do not pass the $E_{\mathrm{T}}^{\mathrm{miss}}$-significance cut. These events also tend to exhibit a low $\Delta\phi(b\text{-jet}, \boldsymbol{p}_{\mathrm{T}}^{\mathrm{miss}})$, which is precisely the kind of configurations selected in the multi-jet CR, rendering this bias visible.

To restore the proper amount of pseudo-data events with this topology, seed events where the leading b-jet is collimated with $E_{\mathrm{T}}^{\mathrm{miss}}$ in the transverse plane are kept, regardless of the $E_{\mathrm{T}}^{\mathrm{miss}}$-significance. Quantitatively, this is expressed by requiring $\Delta\phi(b\text{-jet}, \boldsymbol{p}_{\mathrm{T}}^{\mathrm{miss}}) < 0.13$, a cut found to give the best modelling in b-tag related kinematic distributions in the multi-jet CR. The large improvement due to this refined selection can be inferred by comparing the left (no b-sensitive selection) to the right (b-sensitive selection applied) column in fig. 6.8. Particularly the modelling in $\Delta\phi(b\text{-jet}_1, \boldsymbol{p}_{\mathrm{T}}^{\mathrm{miss}})$ is improved.

A side-effect of this selection criteria are additionally selected events from $t\bar{t}$ processes that fulfil this exact requirement. A subtraction is performed to account for their small contribution to the seed events in data in the following way: the seed selection is applied to the $t\bar{t}$ MC sample, jets are then smeared (50 smearing iterations for MC, instead of 200 for data). The subtraction of the resulting $t\bar{t}$ pseudo-dataset is carried out by means of a designated nuisance parameter in the set of systematic uncertainties (cf. section 7.4) when performing the background normalisation fit. The impact of the $t\bar{t}$ subtraction on multi-jet yields is small, as can be seen in fig. 6.9 and by comparing it to the right column in fig. 6.8, as it mostly affects the relative fraction of events with and without b-jets.

The results of using the jet smearing approach to estimate the multi-jet contribution to the background spectrum of this analysis is depicted in fig. 6.4(f) and fig. A.10 in appendix A.2. After smearing each seed event 200 times, the multi-jet contribution is fitted to the observed data in the multi-jet CR in the same simultaneous fit as the electroweak backgrounds. Since the latter are constrained across all CRs, the multi-jet CR can safely be assumed to normalise the multi-jet component properly. This statement is supported by the good overall agreement of both the normalisation and the shape of the variables displayed. Particular emphasis is put onto variables that are sensitive to the characteristics and weaknesses of the underlying jet smearing technique, i.e. variables which are related to the artificially enhanced missing transverse momentum. As can be inferred from fig. A.10(e), the τ-lepton transverse momentum is well described although it is not subject to a smearing routine.

Despite the strict selection criteria that already suppress much multi-jet influence, the multi-jet CR is well populated with multi-jet events and exhibits a high level of purity to allow for a reliable statements in other CRs, the VRs, and later in the SRs.

6.3 Application and results of the background fit

While for the multi-jet, $Z(\tau\tau)$+jets, and $Z(\nu\nu)$+jets samples it is possible to directly infer the corresponding NFs ω(Multi-jet), $\omega(Z \to \tau\tau)$, and $\omega(Z \to \nu\nu)$,respectively, from the fit, the definitions of the Top and W control regions still do not allow for a determination of the correction factors for the different mis-modelled effects. Except for the kinematic CR, where only the kinematic normalisation-factor contributes, all regions feature combinations of different effects.

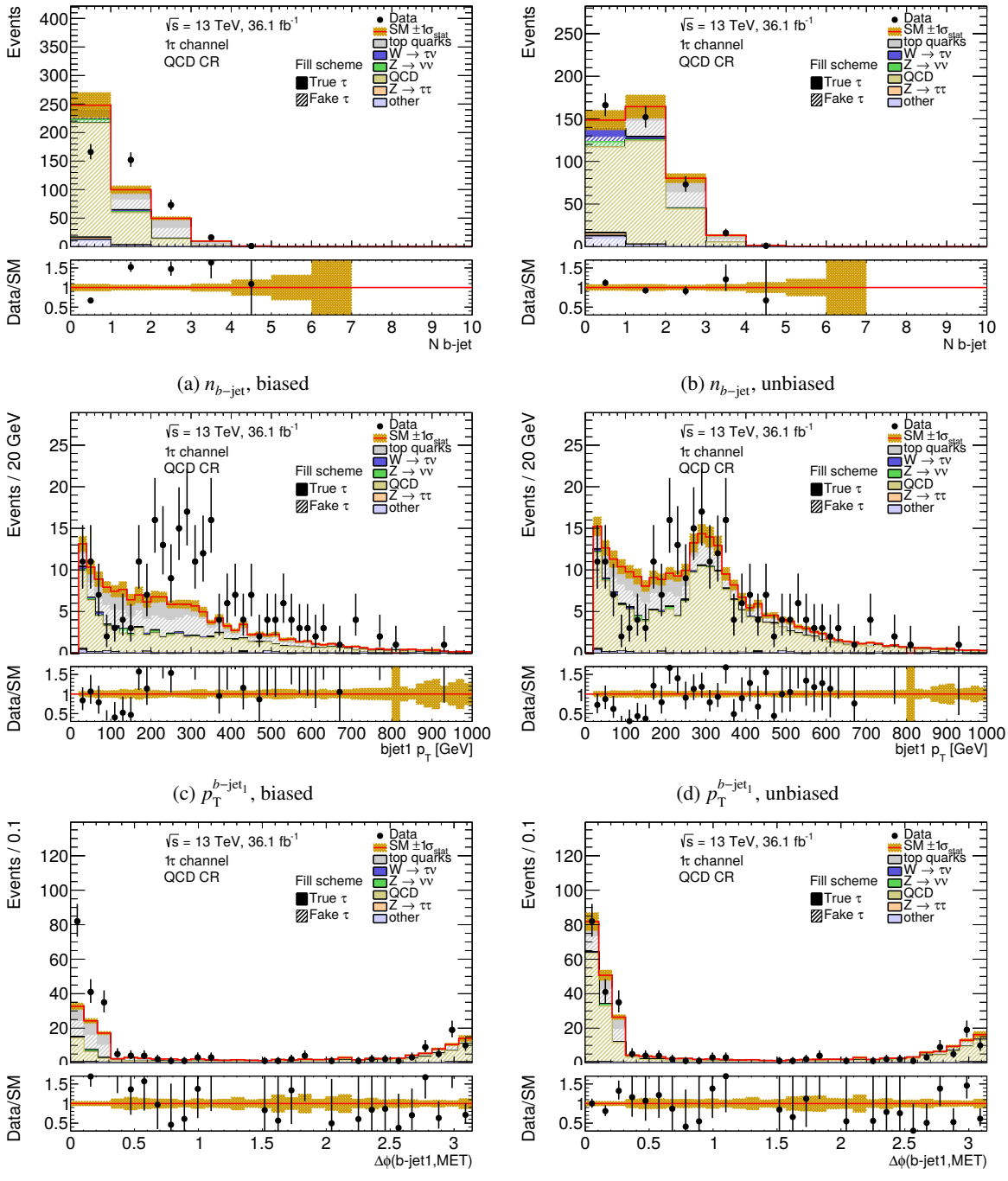

(a) $n_{b-\text{jet}}$, biased

(b) $n_{b-\text{jet}}$, unbiased

(c) $p_{\text{T}}^{b-\text{jet}_1}$, biased

(d) $p_{\text{T}}^{b-\text{jet}_1}$, unbiased

(e) $\Delta\phi(b\text{-jet}_1, \boldsymbol{p}_{\text{T}}^{\text{miss}})$, biased

(f) $\Delta\phi(b\text{-jet}_1, \boldsymbol{p}_{\text{T}}^{\text{miss}})$, unbiased

Figure 6.8: Kinematic distributions of variables affected by the b-jet bias in the multi-jet CR without (left column) and with (right column) the b-sensitive seed selection applied [189]. The results shown are obtained before fitting the normalisation of the background in the control regions. The last bin of each distribution contains the overflow events. The uncertainties displayed consider only statistical limitations in the background modelling, illustrated by the shaded bands. The contribution labelled as *other* includes multi-jet events and V + jets processes not explicitly listed in the legend. The hatch-pattern illustrates contributions from true and fake τ-leptons.

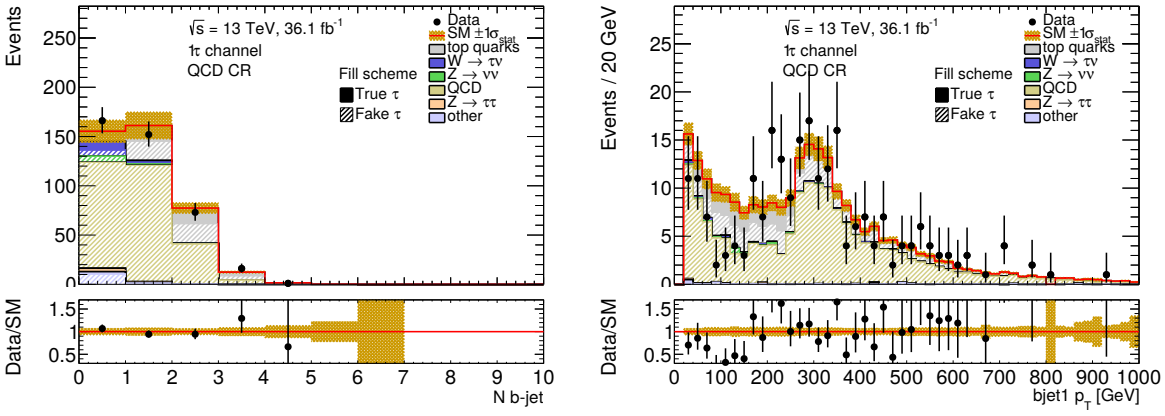

(a) $n_{b\text{-jet}}$, unbiased, $t\bar{t}$ corrected

(b) $p_{\mathrm{T}}^{b\text{-jet}_1}$, unbiased, $t\bar{t}$ corrected

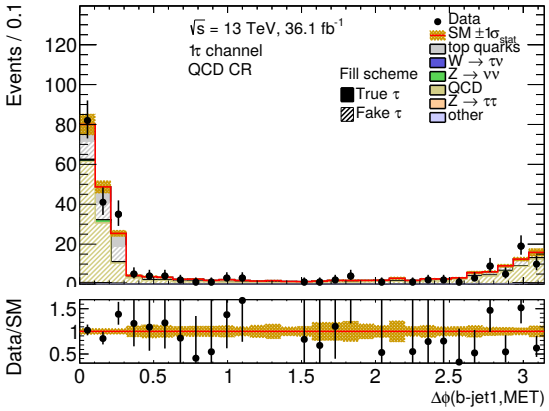

(c) $\Delta\phi(b\text{-jet}_1, \boldsymbol{p}_{\mathrm{T}}^{\mathrm{miss}})$, unbiased, $t\bar{t}$ corrected

Figure 6.9: Kinematic distributions of variables affected by the b-jet bias in the multi-jet CR with the b-sensitive seed selection applied and corrected for overestimation of the $t\bar{t}$ contribution [189]. The results shown are obtained before fitting the normalisation of the background in the control regions. The last bin of each distribution contains the overflow events. The uncertainties displayed consider only statistical limitations in the background modelling, illustrated by the shaded bands. The contribution labelled as *other* includes multi-jet events and V + jets processes not explicitly listed in the legend. The hatch-pattern illustrates contributions from true and fake τ-leptons.

	$n_\tau^{\text{reco}} = 0$	$n_\tau^{\text{reco}} = 1$	$n_\tau^{\text{reco}} \geq 2$
$n_\tau^{\text{truth}} = 0$ ($W \to \ell\nu$, top quarks)	$\omega_{\text{kin.}}$	$\omega_{\text{kin.}} \times \omega_{\text{fake}}$	$\omega_{\text{kin.}} \times \omega_{\text{fake}} \times \omega_{\text{fake}}$
$n_\tau^{\text{truth}} = 1$ ($W \to \tau\nu$, top quarks)	–	$\omega_{\text{kin.}} \times \omega_{\text{true}}$	$\omega_{\text{kin.}} \times \omega_{\text{true}} \times \omega_{\text{fake}}$
$n_\tau^{\text{truth}} = 2$ (top quarks)	–	–	$\omega_{\text{kin.}} \times \omega_{\text{true}} \times \omega_{\text{true}}$

Table 6.3: Sub-division of simulated top quark and W + jets samples according to their content of true and reconstructed τ-leptons and the respective combination of normalisation factors for each sub-sample.

Moreover, to use this method as a background estimate, the corresponding NFs have to be applied to events with one or two τ-leptons depending on the true τ-lepton content of the individual event. To achieve the separation and correct application, the simulation samples for top quarks and W + jets (with all lepton final states) are subdivided according to their multiplicity of true and reconstructed τ-leptons. The resulting sub-samples are normalised using an according product of normalisation-factors. Table 6.3 provides an overview of the sub-division and the applied NFs.

The fit of the nine normalisation-factors in the nine mutually exclusive control regions using HistFitter provides an overall, combined estimate of the different sources of mis-description. While some plots shown so far in this chapter only contain uncertainties due to statistical limitations, the background fit considers all experimental and theoretical systematic uncertainties that affect the background prediction as described in more detail later in chapter 7. In order to estimate the influence of all uncertainties, the following results are given also for a background fit that only considers statistical uncertainties.

The NFs obtained in the fit are summarised in table 6.4 and graphically illustrated in fig. 6.10. While all obtained normalisation-factors except for $\omega(Z \to \nu\nu)$ are in agreement with unity well within one standard deviation (approximately 1.5σ for $\omega(Z \to \nu\nu)$) when considering systematic uncertainties, for W-boson and top quark processes involving true τ-leptons almost no change to the nominal prediction is necessary. The generally difficult description of fake τ-leptons is reflected in the corresponding NFs, including $\omega(Z \to \nu\nu)$, that deviate stronger from unity and come with larger uncertainties. An observation that has already been made in the exploration phase [9] is the fact that W + jets contributions are, on average, overestimated while top quark process are rather underestimated, leading to correspondingly compensating NFs. The normalisation-factor of the multi-jet background ω(Multi-jet) is an exception to the way of interpretation of the formerly discussed results. Due to the unique normalisation issue of the multi-jet background (cf. section 6.2), the multi-jet pseudo-dataset is pre-normalised in the multi-jet CR under consideration of the nominal MC prediction of the electroweak backgrounds and the observed data. With the pre-normalisation factor of $O(100)$ being applied before the combined background fit, the actual NF presented here hence represents the influence of the fit on the electroweak components in the multi-jet CR. Since this graphical representation does not consider any correlations, the visualisation of the results in the form of Gaussian functions is for illustration purposes only.

Having obtained the fitted normalisation-factors, it is possible to calculate the total background composition of all regions. For the set of control regions, an overview of the expected (pre-fit) and fitted (post-fit) yields of the different background components and the number of observed data events is provided in tables A.1 to A.4 in appendix A.3. Here, all uncertainties, statistical and systematic alike, are considered. The presented overview allows for a detailed deduction of the composition of the kinematic distributions shown in sections 6.1 and 6.2.

NF	Value
$\omega_{\text{kin}}(\text{top})$	1.08 ± 0.01
$\omega_{\text{true}}(\text{top})$	0.97 ± 0.01
$\omega_{\text{fake}}(\text{top})$	1.16 ± 0.10
$\omega_{\text{kin}}(\text{W})$	0.91 ± 0.00
$\omega_{\text{true}}(\text{W})$	1.00 ± 0.01
$\omega_{\text{fake}}(\text{W})$	0.95 ± 0.09
$\omega(Z \to \tau\tau)$	0.86 ± 0.07
$\omega(Z \to \nu\nu)$	1.44 ± 0.15
$\omega(\text{Multi-jet})$	0.93 ± 0.07

(a) Statistical only

NF	Value
$\omega_{\text{kin}}(\text{top})$	1.08 ± 0.21
$\omega_{\text{true}}(\text{top})$	0.97 ± 0.09
$\omega_{\text{fake}}(\text{top})$	1.16 ± 0.24
$\omega_{\text{kin}}(\text{W})$	0.91 ± 0.19
$\omega_{\text{true}}(\text{W})$	1.00 ± 0.18
$\omega_{\text{fake}}(\text{W})$	0.95 ± 0.17
$\omega(Z \to \tau\tau)$	0.86 ± 0.22
$\omega(Z \to \nu\nu)$	1.44 ± 0.29
$\omega(\text{Multi-jet})$	0.93 ± 0.38

(b) Statistical ⊕ systematic

Table 6.4: Resulting normalisation factors and their uncertainties for both signal channels, without (a) and with (b) all systematic uncertainties considered.

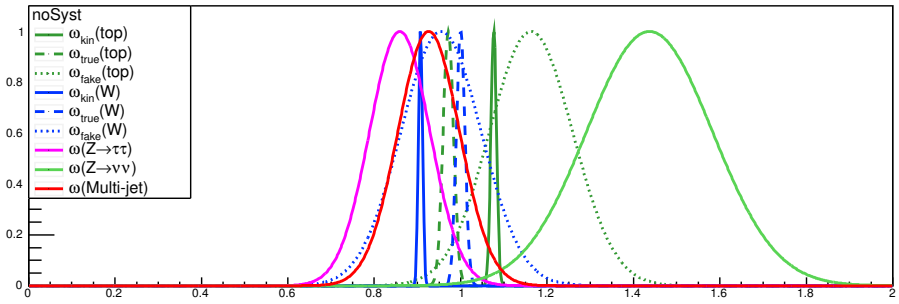

(a) Statistical only

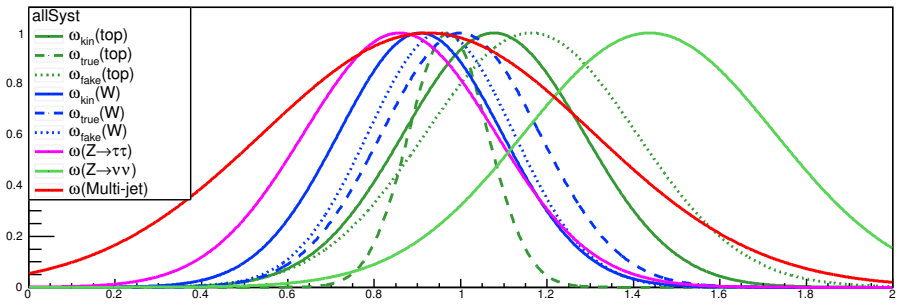

(b) Statistical ⊕ systematic

Figure 6.10: Graphical representation of the normalisation-factors obtained without (a) and with (b) systematic uncertainties considered. The representation as individual Gaussian functions is somewhat misleading since it does not show any correlations between the different NFs.

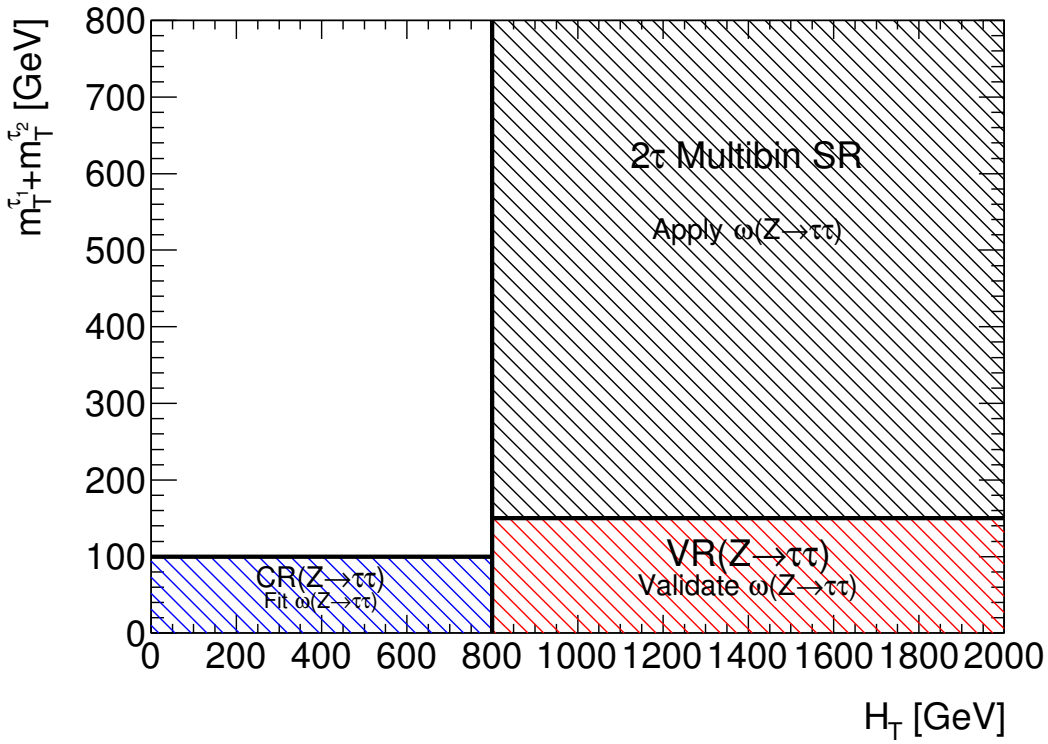

Figure 6.11: Schematic illustration of the separation of phase-space into a set of mutually exclusive regions using the example of the $Z(\tau\tau)$ + jets background and the 2τ multibin SR.

6.4 Validation of the extrapolation of the fit results

With the results of the background fit being available, the modelling in the control regions has already been assessed. Since the signal regions in which the fit results are going to be used to predict the background composition are quite different in the phase-space they probe—e.g. more stringent cuts on $E_{\mathrm{T}}^{\mathrm{miss}}$, H_{T} or m_{T}^{τ} ($m_{\mathrm{T}}^{\tau_1}+m_{\mathrm{T}}^{\tau_2}$, respectively)— it is necessary to study how well the fit results can be extrapolated from the CRs to the SRs. This evaluation is carried out in designated regions of phase-space which are neither used in the background fit nor for the final result extraction, the validation regions (VRs). In phase-space, VRs are located in between CRs and SRs. Figure 6.11 illustrates such a configuration using the example of the $Z(\tau\tau)$ + jets background and the 2τ multibin SR. Typically, single cuts that would define SRs are dropped to define VRs. They are thus able to probe the extrapolation across the phase-space gap in that variable. In the provided example, the $Z(\tau\tau)$ VR probes the extrapolation in H_{T} from the $Z(\tau\tau)$ CR to the 2τ multibin SR. Due to their phase-space vicinity to the SRs, the necessary absence of signal in the VRs is subject to dedicated studies documented in [189]. In order to be able to probe the extrapolation to the signal regions, the validation regions of this analysis are also designed for each signal channel individually.

Validation regions of the 1τ channel The validation regions of the 1τ channel are designed in accordance with the respective SR-defining variables. For each variable listed under *event kinematics* in table 5.3, a dedicated VR is constructed by imposing the SR-cut on the variable to be probed and inverting the remaining cuts to ensure both orthogonality with respect to the corresponding SR and the

extrapolation variable	H_{T}	$E_{\mathrm{T}}^{\mathrm{miss}}$	m_{T}^{τ}
τ-leptons	$p_{\mathrm{T}}^{\tau} > 45\,\mathrm{GeV}$		
Event kinematics	$m_{\mathrm{T}}^{\tau} < 250\,\mathrm{GeV}$		$m_{\mathrm{T}}^{\tau} > 250\,\mathrm{GeV}$
	$E_{\mathrm{T}}^{\mathrm{miss}} < 400\,\mathrm{GeV}$	$E_{\mathrm{T}}^{\mathrm{miss}} > 400\,\mathrm{GeV}$	$E_{\mathrm{T}}^{\mathrm{miss}} < 400\,\mathrm{GeV}$
	$H_{\mathrm{T}} > 1\,000\,\mathrm{GeV}$	$H_{\mathrm{T}} < 1\,000\,\mathrm{GeV}$	

(a) 1τ medium-mass VRs

extrapolation variable	$E_{\mathrm{T}}^{\mathrm{miss}}$	m_{T}^{τ}
τ-leptons	$p_{\mathrm{T}}^{\tau} < 45\,\mathrm{GeV}$	
Event kinematics	$m_{\mathrm{T}}^{\tau} < 80\,\mathrm{GeV}$	$m_{\mathrm{T}}^{\tau} > 80\,\mathrm{GeV}$
	$E_{\mathrm{T}}^{\mathrm{miss}} > 400\,\mathrm{GeV}$	$E_{\mathrm{T}}^{\mathrm{miss}} < 400\,\mathrm{GeV}$

(b) 1τ compressed VRs

Table 6.5: Validation regions of the 1τ channel. These requirements are applied in addition to the pre-selection.

absence of signal events. As a result, five VRs are developed in the 1τ channel. Their exact descriptions are summarised in table 6.5.

The qualitative agreement between the observed data and the background prediction, and hence the quality of the fit in terms of modelling of the extrapolation, can be inferred from fig. 6.12. For all five VRs the background and data shapes agree well within the total uncertainty bands. Discrepancies in the total yields are visible but small. An overview of the exact composition of all VRs after the fit is compiled in the upper pane of fig. 6.13. Its lower pane illustrates the relative deviation between total pre- and post-fit yields in every VR, normalised to the total uncertainty. Here, the mismatch becomes visible and can be considered small, well covered by a standard deviation of uncertainty. In addition, the expected and fitted yields of the different background components and the number of observed data events are provided in tables 6.5(a) and 6.5(b) of appendix A.3.

Validation regions of the 2τ channel The three SR-defining variables of the 2τ channel are H_{T}, $m_{\mathrm{T}}^{\tau_1}+m_{\mathrm{T}}^{\tau_2}$ and $m_{\mathrm{T2}}^{\tau\tau}$. Inverting these cuts, even individually, however, leads to scarcely occupied regions of phase-space that suffer from strong presence of signal. A different approach for the validation regions of the 2τ channel is hence necessary. The solution is an assessment of the different major background contributions in individual VRs rather than addressing the overall modelling of the extrapolation in particular variables. Studying the extrapolation of H_{T}, for example, by inverting the multibin SR requirement on $m_{\mathrm{T}}^{\tau_1}+m_{\mathrm{T}}^{\tau_2}$ leads to a $Z(\tau\tau)$ + jets-dominated phase-space. This outcome is expected since such a selection strongly resembles the setup of the $Z(\tau\tau)$ CR. As a consequence, the $Z(\tau\tau)$ VR is the only 2τ VR in which the extrapolation of H_{T} is possible. In order to keep it mutually exclusive with respect to the 2τ compressed SR, an additional upper cut of $m_{\mathrm{T2}}^{\tau\tau} < 60\,\mathrm{GeV}$ is imposed. Trying to assess the extrapolation of $m_{\mathrm{T}}^{\tau_1}+m_{\mathrm{T}}^{\tau_2}$, on the other side, allows for validation of the modelling of the $W(\tau\nu)$ + jets and top quark background components only. Requiring an SR-like minimum of $m_{\mathrm{T}}^{\tau_1}+m_{\mathrm{T}}^{\tau_2} > 150\,\mathrm{GeV}$ suppresses most $Z(\tau\tau)$ + jets events while the upper cuts of $H_{\mathrm{T}} < 800\,\mathrm{GeV}$ and $m_{\mathrm{T2}}^{\tau\tau} < 60\,\mathrm{GeV}$ ensure orthogonality with respect to any 2τ SR and suppress the presence of signal.

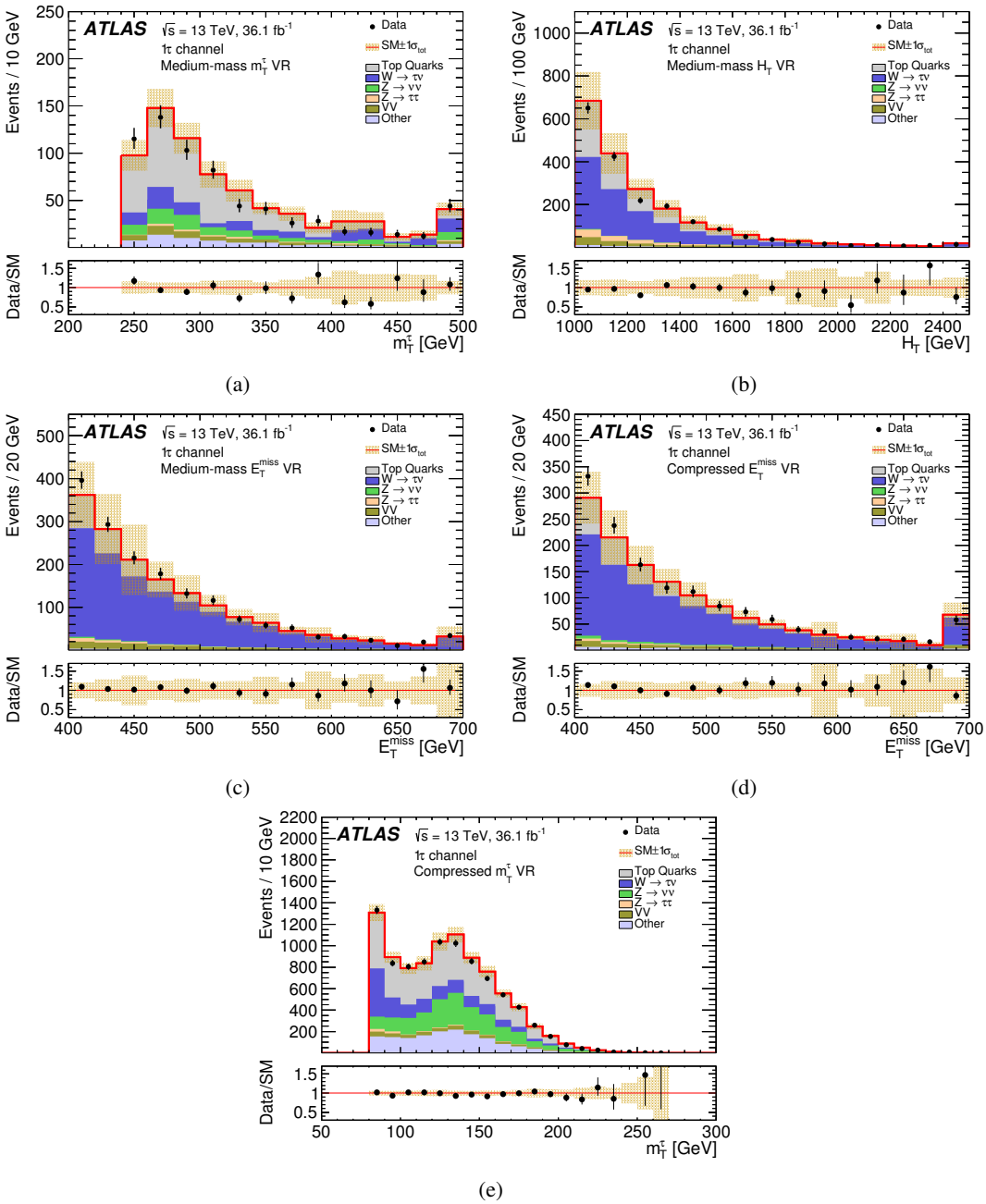

Figure 6.12: Kinematic distributions of characteristic variables in the VRs of the 1τ channel [8], (a) to (c) probing the extrapolation to the medium-mass SR, (d) and (e) probing the extrapolation to the compressed SR. The results shown are obtained after fitting the normalisation of the background in the control regions. The last bin of each distribution contains the overflow events. The uncertainties displayed consider statistical limitations in the background modelling as well as all experimental and theoretical systematic uncertainties, illustrated by the shaded bands. Red arrows in the Data/SM ratio indicate bins where the corresponding entry falls outside the plotted range. The contribution labelled as *other* includes the multi-jet contribution and V + jets processes not explicitly listed in the legend.

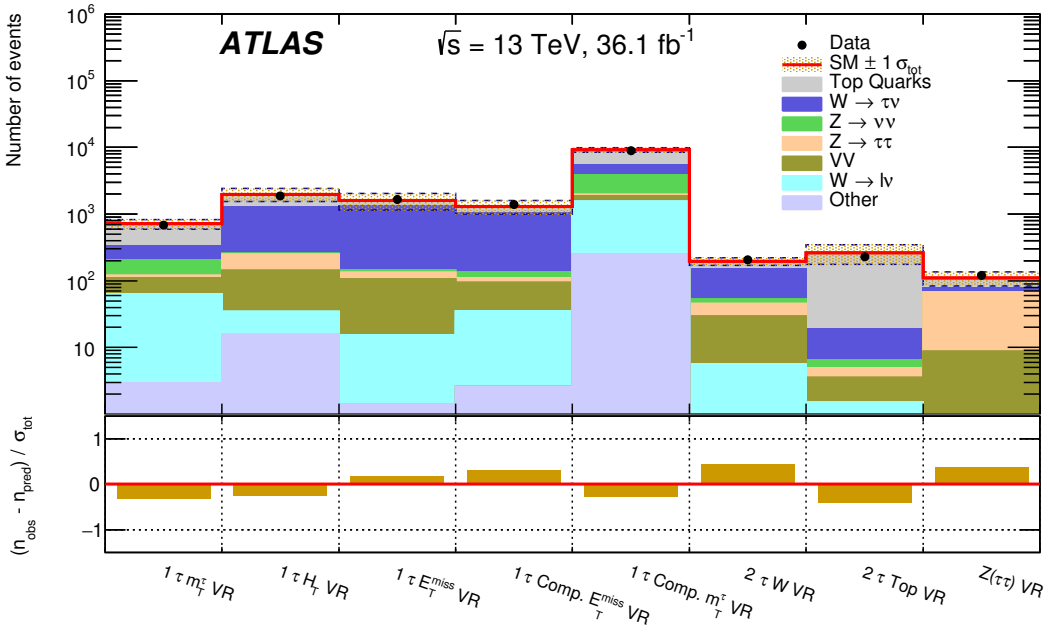

Figure 6.13: Number of observed events, n_{obs}, and predicted background yields after the fit, n_{pred}, in the validation regions of the 1τ and 2τ channels. The background predictions are scaled using the normalisation-factors derived in the control regions. The total uncertainty in the background predictions, σ_{tot}, is shown as a shaded band [8]. The error bars of the data points only represent the Poissonian statistical uncertainty of the measurement.

	2τ W/Top VR	2τ $Z(\tau\tau)$ VR
W/Top separation	$n_{b-\text{jet}} = 0 / \geq 1$	—
Event kinematics	$H_{\text{T}} < 800\,\text{GeV}$ $m_{\text{T}}^{\tau_1} + m_{\text{T}}^{\tau_2} > 150\,\text{GeV}$ $m_{\text{T2}}^{\tau\tau} < 60\,\text{GeV}$	$H_{\text{T}} > 800\,\text{GeV}$ $m_{\text{T}}^{\tau_1} + m_{\text{T}}^{\tau_2} < 150\,\text{GeV}$

Table 6.6: Validation regions for the 2τ channel. These requirements are applied in addition to the pre-selection.

A separation of the $W(\tau\nu)$ + jets and top quark contributions based on the number of b-tagged jets leads to the definition of the Top and W VRs of the 2τ channel. The exact definitions of the 2τ VRs are summarised in table 6.6. Example distributions of important variables are provided in fig. 6.14 and figs. A.11 to A.13 of appendix A.2. The exact composition of the background spectrum in the 2τ VRs can be inferred from the illustration in fig. 6.13 as can be the post-fit agreement of the total yields. A breakdown of the expected and fitted yields of the different background components and the number of observed data events is provided in table 6.6 of appendix A.3. Here, all uncertainties, statistical and systematic alike, are considered.

As for the VRs of the 1τ channel, the agreement in both, the total yields as well as the modelling in all important variables, is good in all 2τ VRs. The extrapolation of the fit results of the combined background fit can be applied safely to estimate the background in the SRs and to use it for extraction of results and their statistical interpretation.

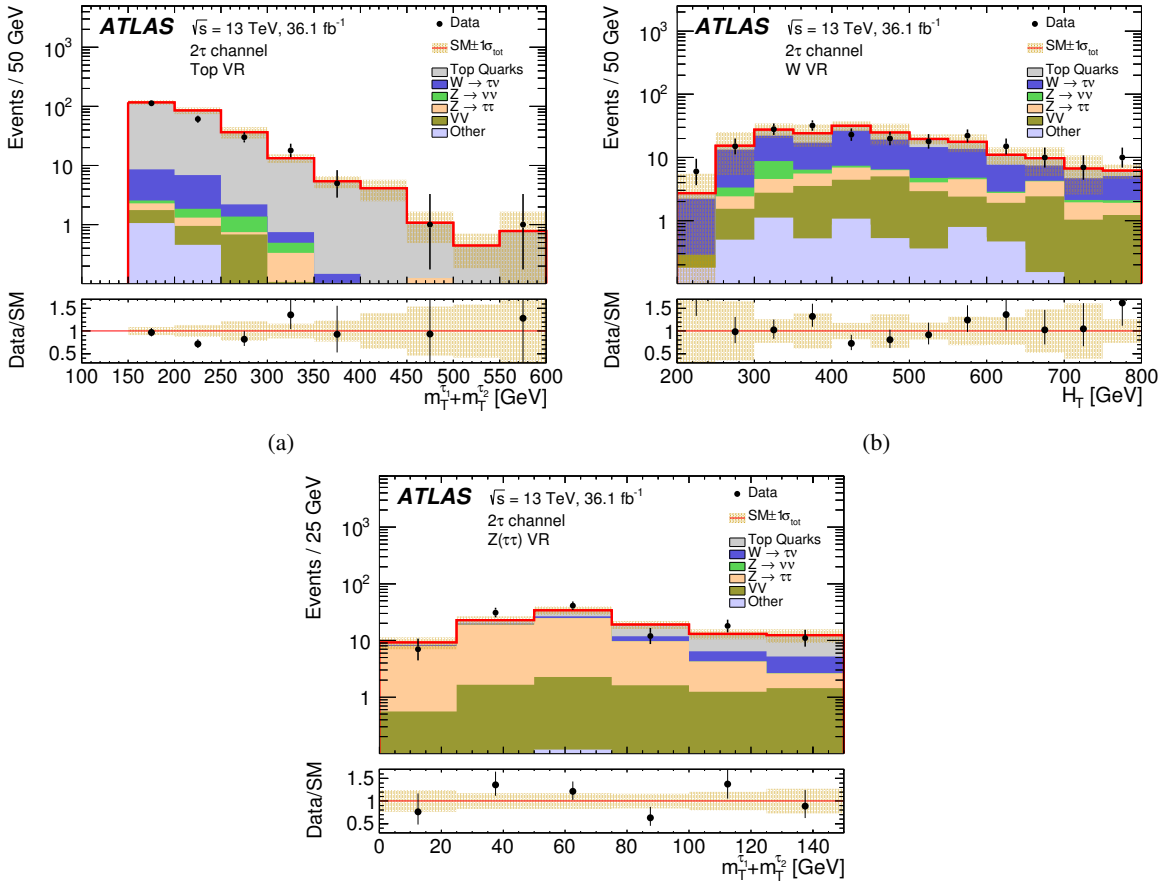

(a) (b) (c)

Figure 6.14: Kinematic distributions of characteristic variables in the VRs of the 2τ channel [8], (a) ((b), (c)) probing the extrapolation of top quark ($W \to \tau\nu$, $Z \to \tau\tau$) contributions to all 2τ SRs. The results shown are obtained after fitting the normalisation of the background in the control regions. The last bin of each distribution contains the overflow events. The uncertainties displayed consider statistical limitations in the background modelling as well as all experimental and theoretical systematic uncertainties, illustrated by the shaded bands. Red arrows in the Data/SM ratio indicate bins where the corresponding entry falls outside the plotted range. The contribution labelled as *other* includes the multi-jet contribution and V + jets processes not explicitly listed in the legend.

CHAPTER 7

Systematic Uncertainties – Parametrising the Ignorance

Every experimental measurement is subject to uncertainties. The finite amount of individual measurements available for an analysis introduces statistical uncertainties. Limited knowledge of the experimental setup and the theoretical predictions, on the other hand, gives rise to systematical uncertainties – they parametrise the ignorance about the measurement. While the former can be reduced by repeating the experiment, the latter typically do not scale with the amount of available statistics and require detailed studies in order to be understood. Before this chapter elaborates on the different concepts of systematical uncertainties and the ones considered in this analysis, a brief discussion of statistical limitations is presented.

At the ATLAS experiment, measured data is considered a priori true. Error bars on data points in histograms only illustrate the uncertainty the mean value of a Poissonian counting experiment would have in the corresponding bin. No systematic uncertainties are attributed to data. However, statements made based on taken data are still limited by the amount of available data and hence subject to statistical uncertainties. They are considered in the evaluation of results by treating the underlying statistics as the outcome of a correspondingly performed counting experiment.

Any prediction of MC-based signal or background, on the other hand, is attributed all potential uncertainties. The data-driven estimation of the multi-jets background is treated individually (cf. section 7.4). Here, statistical uncertainties are also due to the finite binning of visualisation in histograms. In addition, the combined systematic uncertainty can be considered to form a total uncertainty. Limitations due to a finite number of simulated events are treated as systematic uncertainties and discussed in the following paragraphs.

The major contributions to the total systematic uncertainty in the presented analysis stem from the estimation of the number of background events in the signal regions. They are pre-dominantly due to limitations in the modelling of the detector response or identification efficiencies for certain physics objects.

7.1 General concepts

The influence of systematic uncertainties on the presented analysis is studied by modifying every event according to the studied systematic uncertainty (e.g. rescaling jet energies to study the influence of a possible bias in the their measurement). The analysis is then re-run on all signal and background samples under the same systematic variation [15]. The results of the background estimation using

systematically varied inputs may differ from the nominal case. These deviations of all systematic variations are considered as individual nuisance parameters (NPs) in the simultaneous fits that are carried out to obtain the background (and signal) predictions as described in appendix G. While the different systematic uncertainties are considered to be a priori uncorrelated, this fitting technique is able to consider all correlations between the systematic uncertainty NPs and the resulting normalisation-factors. Since the fit is configured such that the overall normalisation in the CRs is conserved due to the fit being performed to observed data, strong correlations between the nuisance parameters of the systematic uncertainties and the normalisation-factors are to be expected[1]. As a result of this approach, the total correlated systematic uncertainty can deviate from the uncorrelated quadratic sum of the individual contributions.

Since the systematic variation of detector or generator parameters is often only sensible in a certain range—negative values of a measured jet energy are unphysical, for example—and since the used fitting approach does not distinguish between such unphysical effects and physically sensible variations, all NPs of systematic uncertainties that go into the fit are constrained. For experimental uncertainties, such constraints can be obtained from auxiliary measurements as the in-situ determination of the uncertainty on the jet energy calibration scale. Also uncertainties arising from theory sources can be constrained by imposing sensible boundaries on the varied parameters of interest, for example by taking the uncertainties of a fit to extrapolate the value of the strong coupling constant α_s to the center-of-mass energy of the LHC. For both these kinds of systematic uncertainties, no additional constraining function in the total likelihood is required due to their intrinsic constraining properties (cf. appendix G).

The procedure described up to this point is valid for systematic uncertainties that arise from effects which are well accessible and common to many analyses carried out in the ATLAS collaboration since they require extensive computing efforts to be studied and made available for analysis. Apart from those most common effects, this analysis considers different additional systematic uncertainties which are unique to it and which require designated treatment. The implementation of these special cases is described in more detail in the corresponding paragraphs of section 7.3.1 and section 7.4, respectively. For these autonomously estimated uncertainties, no intrinsic constraints are available from auxiliary studies or measurements. The hence necessary constraining functions in the likelihood of the combined fit are imposed in from of (asymmetric) Gaussian functions with a mean of one and half the width corresponding to the estimated variation.

The systematic uncertainties introduced in the next sections come in different implementations in the combined fit setup. Those which affect individual physics objects in an event come as full comparison samples. For them, an event-by-event comparison of the systematically varied sample and the nominal one is performed. This approach allows for changes in individual distributions and bin-by-bin migrations of single events. Uncertainties which only affect the total event itself come as modifications of the different corrections factors, resulting in changes of the event weight in distributions it is contributing to. In most cases, the underlying variations of the uncertainty are performed both up- and downwards, e.g. an up- and downward change in the calibration scale of jet energies. They give rise to up- and downward varied samples and weights that constrain the range of the nuisance parameter to be fitted in. For one-sided uncertainties such as a resolution, e.g. the jet energy resolution, the constraint is given by only one comparison sample which provides both kinds of variations within the allowed boundaries. The implementations of systematic uncertainties unique to this analysis come as up- and downward varied weight-based systematic uncertainties, or as single modified weights which are used as symmetrical variations.

[1] A simplified example could be the following: the fit of a single background with 10% pre-fit uncertainty in a single CR is fitted under consideration of a single systematic uncertainty of equal influence 10%. Due to the conservation of the overall normalisation in the CR, the result will be a strong correlation of the normalisation-factor and the NP of the systematic uncertainty for them to cancel out when considered simultaneously.

7.2 Experimental uncertainties

Experimental uncertainties cover all aspects, which originate from imperfections, limited precision, or knowledge of the experimental setup, i.e. the ATLAS detector in general. The different sources of experimental uncertainties are grouped to affect particular physics objects on reconstruction-level. Common to all experimental uncertainties is their validity across all regions of phase-space without the need for extrapolation. As they are provided for every sample, signal and background alike, correlations between the different regions of phase-space are intrinsically present and preserved. The following paragraphs describe the most dominant experimental uncertainties and the way they are determined and applied. In contrast to systematic uncertainties originating from theory-level effects, experimental uncertainties are applied likewise to both signal and background simulation.

Jet energy scale Transferring a measured electronics signal from the calorimeter system into a value of jet energy is done using a calibration at the so-called *jet energy scale* (JES), cf. section 3.3.1. Since this relation is known only with limited precision, studies of variations of the JES lead to a systematic uncertainty. By comparisons of nominal and MC samples with varied hadronic shower and physics models, and alternative detector configurations as well as by a comparison of the jet response as function of η in MC and data, systematic variations of the JES are obtained. As additional contributions to the JES uncertainties, changes due to variations in residual pile-up being removed from the jet cone and uncertainties in the jet flavour composition are taken into account. Further considered aspects for high-energy jets include uncertainties such as a so-called *punch-through* uncertainty if a jet is not fully contained in the calorimeter system, or an uncertainty on the response to single hadrons.

Wherever possible and appropriate, measurements to determine and constrain these uncertainties and their contributions are carried out in situ, on measured data. Due to more feasible conditions including lower pile-up and lower trigger thresholds for jets, these studies have been performed only on the $\sqrt{s} = 7\,\text{TeV}$ ATLAS set. The results and details on the applied techniques are documented in [143]. For the presented analysis using $\sqrt{s} = 13\,\text{TeV}$ data as well as for its exploration study [9], the uncertain prescriptions are adapted to properly describe $\sqrt{s} = 13\,\text{TeV}$ data and simulation as described in [144, 145]. Since the missing transverse energy is calculated from the jet measurements, changes in the jet energy are propagated according to eq. (7.1) [15].

$$E_{x,y}^{\text{miss,new}} = E_{x,y}^{\text{miss,old}} + \sum_{\text{jets}} p_{x,y}^{\text{old}} - \sum_{\text{jets}} p_{x,y}^{\text{new}} \tag{7.1}$$

In order to account for the influence of modified jet energies in the context of τ-leptons, these changes are applied before the jet–τ-lepton overlap removal step (cf. section 3.3.6) This way, ambiguities between low-energy jets that pass baseline selection criteria after being subject to JES variations and τ-leptons are removed.

The presented analysis considers four individual nuisance parameters in its combined fit model to account for the JES uncertainty. Three of these parameters represent combined parameters, being comprised of many more different parameters that account for individual contributions to the total JES uncertainty such as the aforementioned pile-up effect. The fourth NP is assigned to account for the η interpolation between well-measured jets and jets that are more difficult to access due to their η-position in the detector. The jet energy scale uncertainty is implemented as a comparison of individual up- and downward variations with respect to the nominal sample, being available as event-by-event input considering the smallest correlations.

Jet energy resolution In addition to JES-based uncertainties on the transfer from detected signal to measured energy value, the finite energy resolution of the ATLAS detector poses a source of systematic uncertainty. Since the resolution of a measurement can only be obtained if the real value is known, MC simulations of such measurements are necessary. Due to the limited precision of the GEANT4 model of the ATLAS detector in these simulations and other aspects such as the hadronic shower shape, the jet energy resolution (JER) is also only known to finite precision. This limited knowledge of the JER hence introduces an uncertainty on the uncertainty of a jet energy measurement. The arising systematic uncertainty accounting for this effect is determined by smearing every jet energy by a factor drawn from a Gaussian distribution with mean one and standard deviation according to the JER measurement depending on p_{T}- and η-values of the jet. Just like the JES uncertainties, these modified jet energies due to variations of the JER are applied before the jet–τ-lepton overlap removal and also considered in a re-calculation of the missing transverse energy (cf. eq. (7.1)).

As for the JES uncertainties, the underlying in situ studies for quantification of the JER uncertainty have been performed using the $\sqrt{s} = 7\,\mathrm{TeV}$ ATLAS dataset, being presented in more detail in [143]. Extensive studies of the changed conditions of the $\sqrt{s} = 13\,\mathrm{TeV}$ period of data taking with respect to the in situ studies are documented in [144], allowing again for a transfer to be applied in [9] and the presented analysis. The JER is considered with one designated nuisance parameter and implemented as a one-sided event-by-event comparison.

Flavour tagging The identification of jets as being produced by heavy-flavour quarks, is used to separate the top quark from the W + jets components in the background spectrum of the control regions of this analysis. As a consequence, the influence of systematic uncertainties due to flavour tagging effects needs to be studied. Considered aspects are the efficiencies and mis-tag rates for b- and c-quarks as well as a general uncertainty for the tagging of light quark jets. A total of five nuisance parameters, implemented as up- and downward variations influencing every event individually is added to the combined fit. Details on the estimation technique of the systematic variations can be found in [150].

Jet vertex tagging The JVT likelihood for the suppression of pile-up influence on the jet reconstruction (cf. section 3.3.1) introduces a source of systematic uncertainty that is addressed individually in this analysis. Based on variations of the fragmentation model in different studied generators and additional smaller effects of other origin, [149] provides weight-based up- and downward variations that are covered by an additional nuisance parameter in the fit, accounting for uncertainties in the efficiency of the JVT procedure.

Tau energy scale As for jets, the energy of reconstructed τ-leptons is subject to uncertainties due to the energy scale they are calibrated at. Systematic variations of the tau energy scale (TES) are obtained by varying different parameters in the simulation, for example the description of the detector and its material or the underlying event and hadronic shower model of the τ-lepton decay. An additional in situ variation is obtained by comparing measurements of the visible mass of reconstructed τ-leptons in data to TES-varied simulation results. Just as for the changes in the jet energy measurements due to JES variations, changes of τ-lepton contributions to the calculation of the missing transverse energy are propagated according to eq. (7.1). Extensive details on studies of the TES systematic uncertainty in $\sqrt{s} = 13\,\mathrm{TeV}$ ATLAS data and simulation can be found in [159, 161]. The effects considered for obtaining the TES variation are addressed by three nuisance parameters in the combined fit that are considered in this analysis for the TES systematic uncertainty. Each of them is implemented as an event-by-event up- and downward variation.

τ-lepton identification and reconstruction The complex reconstruction approach of hadronically decaying τ-leptons also poses a source of systematic uncertainty, which are summarised as τ-lepton identification uncertainties. They depend on a multitude of different parameters such as the event and τ-lepton kinematics, the number of tracks and pixel hits that are associated to the hadronic τ-lepton decay, or the used identification algorithm. The contributions studied in the context of this analysis are due to three sources, each accounted for by dedicated nuisance parameters in the combined fit, implemented as event-based up- and downward re-weighting: an uncertainty on the identification scaling factor (cf. section 3.3.4) is propagated from the fit of said factor and the uncertainty of that fit. The reconstruction algorithm introduces uncertainties due to various effects, including pile-up, the detector material, and threshold effects, all of which are assessed by varying input parameters in the simulation. For high-energy τ-leptons, the systematic uncertainties due to identification and reconstruction uncertainties are studied separately, doubling the number of fitted nuisance parameters to four. A third component is introduced by the overlap removal procedure applied between τ-leptons and electrons (cf. section 3.3.6). Variations of the aforementioned parameters also influence the kinematic properties of τ-leptons that are used to remove overlap with electrons. Variations of electron parameters in the simulation also affect the procedure. Both of these effects are addressed by an individual nuisance parameter each. A detailed overview including a breakdown of the individual sub-components of the different uncertainty contributions is provided in [159, 161].

While all of these effects are only studied for true τ-leptons, the assessment of jets being mis-identified as τ-leptons is addressed by the dedicated separation of the control region space for fake and true τ-leptons. Most deviations of the simulation from data are covered by application of the obtained normalisation-factors. The uncertainties on the latter are also obtained in the combined fit and hence include systematic uncertainties on the fake τ-lepton modelling. In the data-driven estimate of the multi-jet background, no evaluation of systematic uncertainties on any τ-lepton property is necessary since τ-leptons in this background contribution are directly obtained from data.

Missing transverse energy The calculation of the missing transverse momentum and its magnitude is a complex endeavour as it depends on the reconstruction of every other reconstructed physics objects. The effects of the τ-lepton and jet reconstruction have already been discussed, being the main sources of variations of $E_{\mathrm{T}}^{\mathrm{miss}}$. Contributions from light leptons energy uncertainties are considered in the same fashion but found to be negligible for this analysis. In addition to the contributions from reconstructed physics objects, the influence of so-called *soft terms* and its uncertainty is studied and evaluated. The soft-term contribution to $E_{\mathrm{T}}^{\mathrm{miss}}$ is composed of objects below the reconstruction thresholds and calorimeter depositions which are not assigned to any reconstructed object. Two nuisance parameters are assigned to energy scale variations of this soft term. An additional third NP accounts for an uncertainty on the resolution of the soft-term measurement like the JER contribution does for the energy resolution of jet measurements. Detailed studies on the measurement of $E_{\mathrm{T}}^{\mathrm{miss}}$ and its systematic uncertainties are provided in [163].

Light lepton reconstruction and identification As for jets and τ-leptons, effects on the reconstruction and identification of electrons and muons are investigated for ATLAS analyses and documented in [156, 229], respectivbely. They include the energy and momentum calibration as well as corrections for the efficiency of reconstruction, identification and isolation. They are considered in the fit of the signal and backgrounds in this analysis by means of three dedicated nuisance parameters for electrons and twelve for muons but found to be of negligible influence.

Pile-Up The weight-based re-weighting procedure correcting for differences in the pile-up descriptions between data and simulation (cf. section 4.4.1) is subject to a designated systematic uncertainty. The distribution of the average number of interactions per bunch-crossing $\langle\mu\rangle$ in the simulation is varied and the resulting changes in the pile-up weight are applied on an event-by-event basis, giving the systematic variation. The range of the variation is determined by studying the correlation in data and simulation between $\langle\mu\rangle$ and the number of primary vertices n_{PV} [189].

Luminosity The measurement of the integrated luminosity recorded by ATLAS is also subject to uncertainties. A detailed description of the measurement procedure and the determination of its uncertainty are documented in [129], quoting a total uncertainty of 2.1% for the combined $\sqrt{s} = 13\,\mathrm{TeV}$ dataset of 2015 and 2016. This uncertainty, however, affects only the prediction of the diboson background and the signal yields since their normalisation is estimated solely from the simulation and not via a fit to data.

Trigger For the $E_{\mathrm{T}}^{\mathrm{miss}}$-based trigger used in this analysis, no dedicated treatment of systematic uncertainties is necessary. Requirements on the leading jet transverse momentum and $E_{\mathrm{T}}^{\mathrm{miss}}$ make it 100% efficient without being pre-scaled (cf. section 3.2.4 and appendix C). In MC simulations, its performance is emulated as outlined ibid. with the same plateau requirements being applied.

7.3 Theory uncertainties

In addition to limited knowledge or performance of the experimental environment, effects that are introduced by the simulation before the detector interaction pose sources of systematic uncertainties. They are referred to as theory uncertainties, introduced separately for background and signal samples in the following paragraphs.

7.3.1 Background uncertainties

Since the background to the search performed in this analysis arises from well-understood Standard Model processes, it can be estimated to a higher degree of precision than the signal models. Moreover, the different contributions to the background spectrum are not simulated using the same generator and configuration, giving rise to a dedicated and detailed description of the theory uncertainties on the background samples.

PDF and α_{s} In proton–proton collisions the parton distribution function (PDF) of the proton plays an important role in predicting the expected physics. In addition to the uncertainties on the measurement of the proton PDF, systematic variations are introduced due to various competing fits of different models to the observed data in said measurement. Furthermore, the extrapolation from the phase-space of the PDF measurements to the kinematic regimes in which this analysis is performed is covered. Additional influence on the proton PDF due to variations in the strong coupling constant α_{s} is also evaluated.

For MC samples generated using Sherpa 2.2.1 or 2.2.2, the NNPDF3.nnlo PDF set is used. It contains a nominal PDF set and 100 PDF variations as well as two variations of α_{s} corresponding to $\alpha_{\mathrm{s}}(m_Z) = 0.117$ and $\alpha_{\mathrm{s}} = 0.119$. The PDF uncertainty arising from the available variations is computed as the RMS of these variations according to eq. (7.2).

$$\Delta N_{\mathrm{PDF}} = \sqrt{\frac{1}{99}\sum_{i=1}^{100}(N_i - N_0)^2} \tag{7.2}$$

In this notation, N_i and N_0 correspond to the number of events for PDF variation i and for the nominal PDF set, respectively. The additional uncertainty due to the variation of α_s is computed as $(N_{\alpha_s=0.119} - N_{\alpha_s=0.117}/2)$. The uncorrelated sum of the two contributions is considered as the total PDF uncertainty that is added to the combined fit as weight-based up- and downward variations, evaluated for every sample in every region of phase-space individually. Since the same PDF set is used for all samples, the PDF uncertainty is fully correlated and one common NP is assigned for all background contributions in all regions. In the case of V + jets samples where the necessary input is only available in Sherpa 2.2.1 but not in Sherpa 2.2.0, the variation is computed using Sherpa 2.2.1 samples and applied to (2.2.1 + 2.2.0)/2. For VV samples, the input is available in Sherpa 2.2.1 and 2.2.2, but not in Sherpa 2.1. Since the contribution of the 2.1 samples is only at the percent-level in most regions of phase-space, reaching 16% for the 2τ high-mass SR where MC statistics are scarce, the uncertainty is evaluated using Sherpa 2.2.1 and 2.2.2, and is applied also to 2.1. This approach is conservative but still better motivated than an overall estimation as performed in the exploration study [9]. Since for the PowhegBox+Pythia6-generated $t\bar{t}$ samples, the required input is not available, the necessary calculations are performed using PowhegBox+Pythia8 samples with the same NNPDF3.0nnlo PDF set. Due to its negligible influence across all regions of phase-space, no PDF uncertainty is considered for single-top samples.

Renormalisation- and factorisation-scales In addition to uncertainties arising from the used PDF and value of α_s, changes in the renormalisation- and factorisation-scales influence the background prediction. In the same fashion as for the approach outlined for the PDF uncertainty, variations of the scale parameters μ_R and μ_F are provided already by the generators used. The available setups vary both scales up and down by a factor of two, giving a total of eight possible combinations of which six are used – the sets $(2\mu_R, \frac{1}{2}\mu_F)$ and $(\frac{1}{2}\mu_R, 2\mu_F)$ are not evaluated due to too large $\log(\mu_R/\mu_F)$ contributions to the cross-section. A total scale uncertainty is computed as the average between the two combinations that give the largest and smallest deviations from the nominal prediction, implemented as weight-based up- and downward variations. Due to its process-dependence, the scale uncertainty is evaluated individually for every sample in every region of phase-space and considered with a designated NP for every sample in the combined fit. The same considerations regarding the exchange or mixing of different generators and the negligible influence of single-top samples as for the PDF uncertainty also apply here. Uncertainties due to CKKW matching scales and re-summation for V + jets samples are found to be negligible [8].

Additional $t\bar{t}$ generator uncertainties For the $t\bar{t}$ contribution of the background spectrum, additional effects of varying the input to the used MC generator are studied, evaluated, and accounted for by means of systematic uncertainties. The influence of the hard scattering model is assessed by comparing $t\bar{t}$ samples of different matrix element calculators but the same showering and hadronisation tool, here, MG5_aMC@NLO+Herwig++ is compared to PowhegBox+Herwig++. As neither of the two comparison generators is the nominal one used for this analysis and both are subject strong statistical limitations, a different approach of estimating the influence of the systematic variation is pursued. In a first step, the correct normalisation of both comparison samples is obtained by performing the full background-only fit with the exchanged $t\bar{t}$ samples. Due to the conservation of the overall normalisation of in CRs, this fit already covers the influence of the exchange samples in the CRs. Based on the normalised comparison samples, the relative difference between them is studied in the regular VRs and SRs of a looser selection due to statistical limitations, cf. appendix E. The obtained results are implemented as symmetrised up- and downward variations and one NP in the fit, applied in the VRs and SRs. Since these variations are obtained without any closure, this uncertainty is subject to an a priori constraint by means of a symmetrical Gaussian distribution.

Also the influence of exchanging the underlying parton shower and hadronisation models is evaluated by means of a generator comparison. By comparing the nominal PowhegBox+Pythia6 setup to a $t\bar{t}$ sample generated with PowhegBox+Herwig++, differences can be studied directly and can be used as variations to derive systematic uncertainties from. As for the matrix element uncertainty, the systematic uncertainty due to changes in the parton shower and hadronisation model is implemented by means of symmetrised up- and downward variations and one NP in the combined fit. Finally, the modelling of initial state radiation (ISR) is studied by a comparison of the nominal sample to $t\bar{t}$ samples with varied Powheg-Box parameters that control the transverse momentum of the first additional parton emission beyond the Born configuration [189]. For this ISR uncertainty, designated up- and downward varied samples provide the variations, addressed by one NP in the fit.

Single-top and $t\bar{t}+V$ uncertainties In principle, the same considerations as for the aforementioned $t\bar{t}$ uncertainties also hold for the single-top and $t\bar{t}+V$ samples that are used in this analysis. However, supported by tables A.1 to A.11 in appendix A.3 , their influence can be classified as minor. Instead of separating the uncertainties on the theoretical components of the single-top and $t\bar{t}$ contributions into sub-contributions from the PDF model, variations in α_s, the renormalisation and factorisation scale, the matrix element calculation, the parton showering and hadronisation model, and the ISR modelling, one inclusive uncertainty on the production cross-section of the combined contributions from single-top and $t\bar{t}$ processes is assigned to the corresponding samples as a symmetrised weight-based variation with one NP in the combined fit. In accordance with the latest results, the total cross-section uncertainty is assigned to be 10%, obtained from calculations as described in section 4.2.

$W(\tau\nu)$ + jets alternative generator comparison Together with $t\bar{t}$ events, the background arising from $W(\tau\nu)$ + jets production poses the most important and abundant component of the Standard Model background in this analysis. In order to cover dependencies of the prediction on the generator used (Sherpa), a comparison to an alternative generator (MG5_aMC@NLO+Pythia8) is performed. The $W(\tau\nu)$ + jets MG5_aMC@NLO+Pythia8 sample is used as a direct comparison sample to the nominal Sherpa sample and their deviation is treated as a symmetric variation, considered by means of one designated NP in the fit.

7.3.2 Signal uncertainties

The afore introduced experimental uncertainties also apply to the signal samples. The respective theory uncertainties, however, are addressed in a more exclusive way. While for the Standard Model processes, cross-section measurements allow for constraints and the estimation of uncertainties, the SUSY signal production cross-section is predicted entirely from theory, rendering its total uncertainty an important quantity. The calculation of SUSY cross-sections is performed depending on the production process, at NLO level for electroweak and mixed processes, and with NLO+NLL accuracy for production via the strong force (cf. section 4.3). Sources of systematic uncertainty contributing to these calculations comprise the choice of parameters in the generation process, the chosen PDF set and the knowledge about the strong coupling constant α_s. Variations of these parameters are evaluated by re-computation of the cross-section with different values, similarly to the individual evaluations considered for the Standard Model processes. The resulting cross-section values form an envelope whose median is taken as the nominal value and whose minimum and maximum are symmetrised to yield the total uncertainty as described in [215] [15]. This total uncertainty on the signal cross-section hence absorbs all effects which are studied separately for the backgrounds. Typically, its influence is depicted as contour lines indicating the $\pm 1\sigma$ cross-section variation in plots across the model parameter-space. This way of illustration allows

for a disentanglement of the effect of unavoidable systematic uncertainties from external sources and the ones from the definition of the signal models.

In contrast to the background samples, the signal samples used in this analysis are simulated using the AFII fast calorimeter simulation [230] for the modelling of shower shapes in the calorimeters and the corresponding determination of energy depositions (cf. chapter 4). The deviations of this approximation from the full GEANT4 simulation is studied ibid.. For the major sources of experimental systematic uncertainties as described in section 7.2, additional nuisance parameters accounting for AFII-induced deviations are introduced to the fit. They address jet-based uncertainties inclusively and put a special focus on τ-lepton, treating TES variations, the τ-lepton–electron overlap removal procedure as well as reconstruction and identification effects individually. In total, five additional nuisance parameters are introduced to the fit to account for potential deviations due to this simplified simulation setup. Each of these uncertainties is implemented as a weight-based up- and downward variation with a designated NP.

7.4 Uncertainties on external corrections

While most of the aforementioned systematic uncertainties, their underlying variations and constraints are provided by either theory groups having predicted parameters or ATLAS in-situ measurements and estimations, this analysis also considers sources of systematic uncertainty which are unique to it and which require dedicated estimation techniques.

W + jets H_{T}-corrections The discrepancies in the distribution of H_{T} in the W kinematic and true-τ CRs discussed in section 6.1 are attributed to inaccurate modelling of electroweak processes in the generator used. This limitation of the predictive power is accounted for by the introduction of an additional systematic uncertainty. The weights computed as bin-specific correction-factors (cf. appendix D) are used as input variations to a symmetrised uncertainty applied to the $W(\tau\nu)$ + jets sample, considered with one designated NP in the combined fit.

Uncertainties on the data-driven multi-jet estimate The contribution from multi-jet events play a special role in the determination of the Standard Model background spectrum to this analysis. Due to its estimation in a data-driven way and not based on MC simulations, none of the aforementioned uncertainties, neither those of experimental nor theory origin, apply to it. Although the input to the multi-jet estimation is recorded data and hence a priori not subject to systematic uncertainties of any kind, the applied jet smearing technique introduces different sources of systematic uncertainty. While the influence of limited seed statistics and multiple smearing of single events is considered in the statistical uncertainty of the background (cf. section 6.2), variations in the shape of the used response functions and bin-by-bin migration and correlation effects are not evaluated in dedicated ways – detailed studies, particularly on the latter, can be found in [227]. Instead, one inclusive overall uncertainty is estimated and used as a symmetric up- and downward weight-based variation, considered with one dedicated NP in the combined fit. Since the modelling of the missing transverse momentum is crucial for the presented analysis and it is particularly affected by the jet smearing technique, the $E_{\mathrm{T}}^{\mathrm{miss}}$ distribution in the multijet CR is used to estimate the overall systematic uncertainty on the multi-jet prediction. The largest deviation of the predicted background from data in fig. 6.4(f) is observed in second-to-last bin, motivating a 40% uncertainty on the multi-jet estimation before the combined fit.

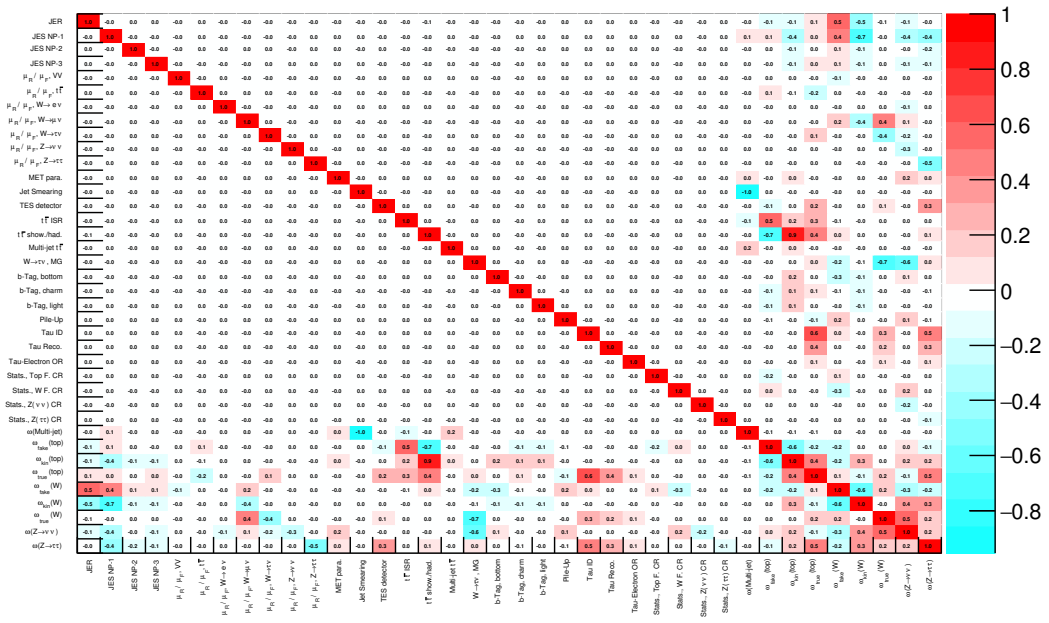

Figure 7.1: Correlation (covariance) matrix of the most dominant nuisance parameters in the combined background-only fit, considering all systematic uncertainties. The x- and y-axes give the nuisance parameters. In the colour-code of the z-axis, white corresponds to two NPs being uncorrelated while red (cyan) indicates (anti-)correlation. The overlaid numbers give the exact value of the correlation. In addition to the NPs introduced for systematic uncertainties in chapter 7, the normalisation-factors of the Standard Model backgrounds (cf. section 6.3) are considered as are further nuisance parameters accounting for insufficient MC statistics.

In section 6.2, a slight overestimation of the multi-jet background due to $t\bar{t}$ events entering the seed selection is observed and discussed. The effect is studied by exposing the nominal MC $t\bar{t}$ sample to the same jet smearing procedure and evaluated by fitting the smeared sample as a subtraction sample in the Multijet CR with a designated nuisance parameter.

7.5 Systematic uncertainties after the fits

Adding all the introduced systematic variations to the combined fit provides not only the results already presented in section 6.3 and extended by those in appendix A, but also insight into the structure of the set of systematic uncertainties. This section summarises the picture of systematic uncertainties of both the full background-only fit in the CRs as well as the fits including signal contributions.

Systematic uncertainties in the background-only fit The fit of the Standard Model backgrounds in the nine control regions as described in section 6.3, taking into account all the experimental and theory-based systematic uncertainties introduced in sections 7.2 and 7.3.1, paints a detailed picture of the behaviour of the systematic uncertainties. The total post-fit background composition of the different CRs, VRs and SRs is summarised in tables A.1 to A.11 of appendix A.3. An overview of the influence of the underlying sources of systematic uncertainty for selected regions of phase-space is provided in table 7.1. For the other regions, tables A.12 to A.14 of appendix A.4 provide the respective results.

Uncertainty of CR	W True-τ	W Fake-τ	Top True-τ	Top Fake-τ
Total background expectation	31374.01	451.97	20963.73	829.06
Total statistical $\left(\sqrt{N_{\text{exp.}}}\right)$	±177.13	±21.26	±144.79	±28.79
Total background systematic	±232.35 [0.74%]	±21.09 [4.67%]	±148.02 [0.71%]	±28.26 [3.41%]
Background estimation	±7136.85 [22.7%]	±50.80 [11.2%]	±4322.88 [20.6%]	±134.26 [16.2%]
Jet reconstruction	±5504.58 [17.5%]	±32.26 [7.1%]	±1861.41 [8.9%]	±58.59 [7.1%]
Electroweak theory	±4254.28 [13.6%]	±18.57 [4.1%]	±405.23 [1.9%]	±4.42 [0.53%]
Tau identification	±2009.28 [6.4%]	±5.55 [1.2%]	±1344.69 [6.4%]	±23.85 [2.9%]
Flavour tagging	±820.63 [2.6%]	±16.90 [3.7%]	±734.59 [3.5%]	±23.15 [2.8%]
Tau energy measurement	±579.14 [1.8%]	±0.41 [0.09%]	±416.26 [2.0%]	±2.20 [0.27%]
Top quark theory	±406.81 [1.3%]	±14.62 [3.2%]	±3531.68 [16.8%]	±110.33 [13.3%]
PDF variations	±305.14 [0.97%]	±5.83 [1.3%]	±167.51 [0.80%]	±5.61 [0.68%]
Diboson theory	±182.23 [0.58%]	±5.82 [1.3%]	±38.12 [0.18%]	±0.88 [0.11%]
$E_{\text{T}}^{\text{miss}}$ reconstruction	±135.66 [0.43%]	±3.70 [0.82%]	±161.21 [0.77%]	±8.35 [1.0%]
Pile-up	±63.38 [0.20%]	±7.74 [1.7%]	±232.89 [1.1%]	±11.34 [1.4%]
Electron reconstruction	±17.55 [0.06%]	±0.43 [0.09%]	±12.07 [0.06%]	±0.78 [0.09%]
Multi-jet estimation	±9.81 [0.03%]	±0.07 [0.02%]	±118.30 [0.56%]	±5.91 [0.71%]
Muon reconstruction	±0.84 [0.00%]	±4.09 [0.91%]	±1.14 [0.01%]	±6.85 [0.83%]
MC statistics	±0.00 [0.00%]	±12.16 [2.7%]	±0.00 [0.00%]	±14.07 [1.7%]

Uncertainty of 1τ medium-mass VR	m_{T}^{τ}	H_{T}	$E_{\text{T}}^{\text{miss}}$
Total background expectation	716.03	1981.56	1588.74
Total statistical ($\sqrt{N_{\text{exp.}}}$)	±26.76	±44.51	±39.86
Total background systematic	±113.29 [15.82%]	±438.63 [22.14%]	±441.33 [27.78%]
Top quark theory	±126.31 [17.6%]	±231.23 [11.7%]	±98.08 [6.2%]
Background estimation	±94.89 [13.3%]	±362.05 [18.3%]	±340.94 [21.5%]
Tau energy measurement	±41.74 [5.8%]	±16.18 [0.82%]	±64.61 [4.1%]
Jet reconstruction	±41.53 [5.8%]	±183.94 [9.3%]	±103.06 [6.5%]
Electroweak theory	±38.84 [5.4%]	±493.37 [24.9%]	±578.72 [36.4%]
Tau identification	±23.30 [3.3%]	±123.86 [6.3%]	±100.02 [6.3%]
MC statistics	±19.45 [2.7%]	±12.99 [0.66%]	±13.70 [0.86%]
PDF variations	±8.71 [1.2%]	±28.48 [1.4%]	±24.90 [1.6%]
Diboson theory	±6.76 [0.94%]	±17.40 [0.88%]	±10.97 [0.69%]
$E_{\text{T}}^{\text{miss}}$ reconstruction	±5.03 [0.70%]	±8.29 [0.42%]	±6.94 [0.44%]
Multi-jet estimation	±3.81 [0.53%]	±17.33 [0.87%]	±3.09 [0.19%]
Flavour tagging	±2.49 [0.35%]	±7.07 [0.36%]	±5.71 [0.36%]
Electron reconstruction	±1.71 [0.24%]	±1.11 [0.06%]	±0.50 [0.03%]
Pile-up	±0.86 [0.12%]	±20.57 [1.0%]	±16.47 [1.0%]
Muon reconstruction	±0.84 [0.12%]	±0.64 [0.03%]	±0.25 [0.02%]

Uncertainty of SR	2τ GMSB	2τ high-mass	2τ compressed	1τ medium-mass	1τ compressed
Total background expectation	1.41	2.34	5.36	15.90	319.74
Total statistical $\left(\sqrt{N_{\text{exp.}}}\right)$	±1.19	±1.53	±2.32	±3.99	±17.88
Total background systematic	±0.53 [37.63%]	±0.70 [29.75%]	±1.90 [35.39%]	±2.95 [18.56%]	±31.90 [9.98%]
Electroweak theory	±0.29 [20.7%]	±0.36 [15.4%]	±0.40 [7.4%]	±0.80 [5.0%]	±21.71 [6.8%]
MC statistics	±0.29 [20.6%]	±0.19 [8.2%]	±0.51 [9.5%]	±0.90 [5.7%]	±5.64 [1.8%]
Top quark theory	±0.20 [14.3%]	±0.42 [17.7%]	±1.67 [31.2%]	±1.67 [10.5%]	±17.77 [5.6%]
Background estimation	±0.18 [12.7%]	±0.31 [13.3%]	±0.70 [13.1%]	±1.66 [10.5%]	±36.72 [11.5%]
PDF variations	±0.14 [9.8%]	±0.10 [4.1%]	±0.11 [2.0%]	±2.11 [13.3%]	±6.06 [1.9%]
Tau identification	±0.12 [8.7%]	±0.23 [9.9%]	±0.29 [5.4%]	±0.52 [3.3%]	±4.85 [1.5%]
Jet reconstruction	±0.07 [5.1%]	±0.21 [8.9%]	±0.82 [15.2%]	±1.09 [6.9%]	±23.28 [7.3%]
Pile-up	±0.04 [2.5%]	±0.05 [2.0%]	±0.07 [1.3%]	±0.13 [0.83%]	±3.23 [1.0%]
Multi-jet estimation	±0.03 [2.0%]	±0.02 [1.00%]	±0.04 [0.72%]	±0.47 [2.9%]	±3.96 [1.2%]
Tau energy measurement	±0.02 [1.7%]	±0.15 [6.2%]	±0.20 [3.7%]	±0.46 [2.9%]	±0.24 [0.07%]
$E_{\text{T}}^{\text{miss}}$ reconstruction	±0.01 [0.84%]	±0.03 [1.5%]	±0.19 [3.5%]	±0.03 [0.22%]	±2.99 [0.94%]
Flavour tagging	±0.01 [0.67%]	±0.02 [0.70%]	±0.07 [1.3%]	±0.07 [0.43%]	±1.26 [0.39%]
Electron reconstruction	±0.00 [0.04%]	±0.00 [0.11%]	±0.01 [0.22%]	±0.04 [0.23%]	±0.45 [0.14%]
Muon reconstruction	±0.00 [0.04%]	±0.00 [0.12%]	±0.01 [0.18%]	±0.03 [0.19%]	±0.36 [0.11%]
Diboson theory	±0.00 [0.00%]	±0.00 [0.00%]	±0.00 [0.00%]	±0.00 [0.00%]	±0.00 [0.00%]

Table 7.1: Breakdown of the dominant systematic uncertainties on background estimates in selected CRs, VRs, and SRs in the background-only fit. It is to be noted that the individual nuisance parameters can be correlated, and do not necessarily add up quadratically to the total background uncertainty. The percentages show the size of the uncertainty relative to the total expected background. Uncertainties on the present signals are not given here.

The uncertainty spectrum of the control regions is dominated by the uncertainties on the fitted background normalisation-factors with sub-dominant contributions from jet reconstruction uncertainties. In the Top CRs, the additional uncertainties on the theory modelling are of compatible order, while the multi-jet estimation uncertainty introduced by the jet smearing technique is prominent in the respective CR. Noteworthy is the minor influence of τ-lepton-related uncertainties, an evolution that is visible through [9, 12, 13] and which can be attributed to the advanced way of estimating contributions from real and fake τ-leptons as well as non-τ-lepton related event aspects separately.

Due to the requirement of the fit to conserve the overall normalisation of all CRs, the expected effect of strong correlations leading to compensations is visible for all CRs is visible. From the complete correlation matrix depicted in fig. 7.1, it is possible to infer the exact contexts. While the fit finds the nuisance parameters of the systematic uncertainties to be as uncorrelated as they were a priori, strong correlations of the systematic uncertainty NPs and the background normalisation-factors are found. The fit hence compensates changes of the background yields due to systematic uncertainties by the normalisation-factors, conserving the total normalisation of the CRs as designed. Quantitatively, this feature is reflected in the total systematic uncertainties in the CRs being substantially smaller than the quadratic sum of all individual uncertainties. In fact, the total systematic uncertainty deviates only little from the statistical uncertainty here, painting a coherent picture of the fit setup.

The less exclusively designed validation regions, on the other hand, present a different picture. Since they are not used in the fit to constrain the background spectrum, the results are extrapolations from the CRs and not subject to a conservation of the overall normalisation. The correlations between the nuisance parameters found in the CRs are hence propagated to the VRs. Due to the different background compositions, this extrapolation can give rise to substantial deviations of the systematic uncertainty from the statistical. While in the 2τ channel, the dominant sources of uncertainty are still the normalisation-factors and the $t\bar{t}$ theory uncertainties with sub-dominant contributions from the jet reconstruction, the 1τ channel VRs are now dominated by uncertainties arising from predictions of the electroweak theory components.

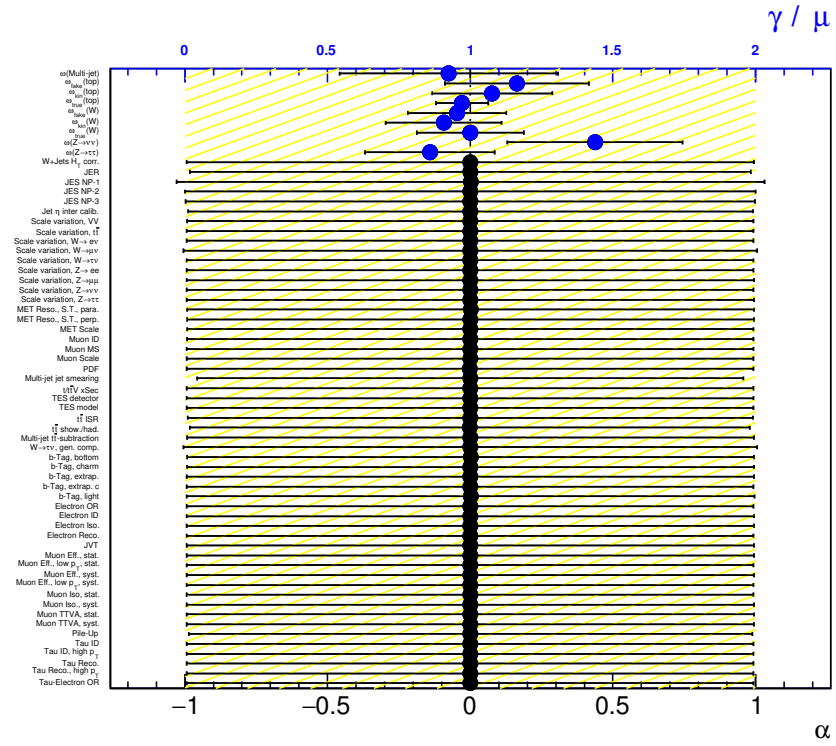

Figure 7.2: Pull-plot of the nuisance parameters (NPs) of the combined background-only fit, considering all systematic uncertainties. The y-axis gives the list of nuisance parameters. Here, ω represents the normalisation-factors of the Standard Model backgrounds as introduced in section 6.3. For NPs related to systematic uncertainties, the lower black x-axis provides information on the constraint of the NP in the fit. A central value of 0 indicates agreement between the fitted value of the NP and the predicted central value of constraint from external sources. The length of the error bar with respect to unity—indicated by the yellow hatched area—indicates the agreement between the spread of the fitted NP and the width of the external constraint. Smaller error bars point towards the fit constraining the systematic uncertainty stronger than the prediction from theory or the experimental measurement. For the normalisation-factors ω, the upper blue x-axis indicates their deviation from unity and their post-fit uncertainty, rendering it a representation equivalent to table 6.4(b) and fig. 6.10(b).

Looking at a detailed breakdown of the individual components [189], this statement can be further refined to attribute the influence to the generator comparison between the nominal Sherpa and MG5_aMC@NLO+Herwig++ for the 1τ channels major background component $W(\tau\nu)$ + jets.

The extrapolation of the background-only results to the SRs follows the same considerations as the ones for the VRs and allows for further statements: the signal regions for which only little background is predicted, are subject to uncertainties due to low MC statistics and uncertainties related to their major background contributions, e.g. $t\bar{t}$ theory uncertainties in the 2τ compressed SR. Here, another expected feature of the fit becomes visible. While in 1τ SRs, the influence of uncertainties due to the reconstruction of τ-leptons is small, it is larger in the 2τ channel. This effect can be explained by the similarity of the 1τ regions to the majority of CRs due to the requirement of the presence of one τ-lepton. The 2τ channel, on the other hand, is based on different signatures and is thus more susceptible to extrapolation effects.

In addition to the influence of the different uncertainties on the predictions in phase-space, the fit results can be used to study the quality of the fit itself. Figure 7.2 provides an overview of the different nuisance parameters after the fit. In addition to visualising the normalisation-factors and their uncertainties as in

fig. 6.10(b) and table 6.4(b), the influence of the dominant systematic uncertainties and a comparison of the nuisance parameter estimation is presented: for all considered NPs, the fit finds no deviation from the constraints provided by external measurements or theory predictions, neither for the central values nor for the NPs variation width. This observation supports the quality of the chosen fit setup: it is based on sufficiently inclusive control regions that can access all necessary physics processes and has enough freedom to cover any potential disagreements between observation and prediction easily.

Results of the exclusion fit The results in the signal regions presented in the last paragraph are based on extrapolation of the background-only fit results from the CRs to the SRs – in the SRs, no fit is performed, nor is any signal model considered in the fit. Performing an exclusion fit instead of a background-only fit (cf. appendix G) enables statements under consideration of the signal samples and the signal regions, taking uncertainties on the tested signal models into account.

For the five single-bin signal regions of both channels, table 7.2 provides an overview of the systematic uncertainties on both, signal expectation and background prediction under consideration of the target signal scenarios. In all presented cases, the largest contribution to the overall uncertainty is the prediction of the signal cross-section. The signal-induced uncertainty due to the fast calorimeter simulation AFII also becomes one of the most relevant contributions in all evaluated setups. As for the background-only case, the quality of the fit is assessed by a visualisation of the fit results of the considered nuisance parameters. As an example, fig. 7.3 shows such an evaluation for the GMSB benchmark scenario in the 2τ GMSB SR. As for the background-only fit, all nuisance parameters are fitted to the values predicted by the external sources and only few are differently constrained. Since in an exclusion fit, the signal regions serve as additional constraints of the background and signal model, a different result is expected: a different measurement prefers a different fit result and gives different constraints. The picture of a correctly working and trustworthy fitting procedure is thus still considered valid.

7.6 Conclusions

The last sections have presented the different sources of systematic uncertainty as well as their ways of determination and implementation into this analysis. In addition to uncertainties due to experimental or theory-related limitations, uncertainties that are specific to this analysis and which are estimated in designated ways have been introduced. The behaviour of the used fitting procedures, the background-only and the exclusion fit, under consideration of these systematic uncertainties has been studied and found to be stable, allowing for reliable further evaluation of obtained results and their statistical interpretation. For the background-only fit, the dominant sources of systematic uncertainty have been found to be the prediction of the background normalisation and the additional top quark theory uncertainties. In general, regions of phase-space which are easier to model and assess (e.g. Top/W true-τ or kinematic CRs) are more well described than more challenging (e.g. Top/W fake-τ CRs) or less inclusive regions (VRs, SRs). Considering the influence of the signal regions as additional constraints and the uncertainties on the signal prediction, the exclusion fits show that the driving uncertainty arises from the signal cross-section calculation and the simplified modelling used in the calorimeter simulation upon reconstruction of signal events.

Potential improvements of this analysis by external sources lie once more [9, 13] with an improved modelling of jets being mis-reconstructed as τ-leptons in the simulation and more precise predictions of the signal cross-sections. Additional computing resources to allow for utilisation of the full calorimeter simulation for the signal scenarios or an improvement of fast simulation also hold possible advancement.

Single-bin SR	1τ compressed SR	1τ medium-mass SR	
Evaluated	$m(\tilde{g})$ = 1 065 GeV	$m(\tilde{g})$ = 1 265 GeV	$m(\tilde{g})$ = 1 705 GeV
signal scenario	$m(\tilde{\chi}_1^0)$ = 825 GeV	$m(\tilde{\chi}_1^0)$ = 905 GeV	$m(\tilde{\chi}_1^0)$ = 345 GeV
Total background expectation	59.26	6.44	16.86
Total statistical $\left(\sqrt{N_{\text{exp.}}}\right)$	±7.70	±2.54	±4.11
Total background systematic	±12.02 [20.28%]	±1.83 [28.45%]	±4.78 [28.38%]
Signal cross-section	±10.26 [17.3%]	±1.60 [24.9%]	±4.44 [26.4%]
Tau identification	±3.95 [6.7%]	±0.41 [6.4%]	±1.12 [6.6%]
AFII simulation	±3.48 [5.9%]	±0.48 [7.5%]	±1.13 [6.7%]
Jet reconstruction	±2.64 [4.5%]	±0.47 [7.3%]	±0.19 [1.1%]
Flavour tagging	±1.28 [2.2%]	±0.08 [1.2%]	±0.23 [1.4%]
MC statistics	±1.24 [2.1%]	±0.29 [4.6%]	±0.53 [3.1%]
$E_{\text{T}}^{\text{miss}}$ reconstruction	±0.69 [1.2%]	±0.04 [0.63%]	±0.03 [0.18%]
Tau energy measurement	±0.53 [0.90%]	±0.21 [3.3%]	±0.39 [2.3%]
Pile-up	±0.47 [0.80%]	±0.18 [2.7%]	±0.27 [1.6%]
Electron reconstruction	±0.02 [0.03%]	±0.01 [0.09%]	±0.03 [0.15%]
Muon reconstruction	±0.02 [0.03%]	±0.01 [0.14%]	±0.02 [0.14%]
Multi-jet estimation	±0.00 [0.00%]	±0.00 [0.00%]	±0.00 [0.00%]
Background estimation	±0.00 [0.00%]	±0.00 [0.00%]	±0.00 [0.00%]
Diboson theory	±0.00 [0.00%]	±0.00 [0.00%]	±0.00 [0.00%]
Top quark theory	±0.00 [0.00%]	±0.00 [0.00%]	±0.00 [0.00%]
PDF variations	±0.00 [0.00%]	±0.00 [0.00%]	±0.00 [0.00%]
Electroweak theory	±0.00 [0.00%]	±0.00 [0.00%]	±0.00 [0.00%]

Single-bin SR	2τ GMSB	2τ compressed	2τ high-mass
Evaluated	Λ = 120 TeV	$m(\tilde{g})$ = 1 065 GeV	$m(\tilde{g})$ = 1 705 GeV
signal scenario	$\tan\beta$ = 40	$m(\tilde{\chi}_1^0)$ = 825 GeV	$m(\tilde{\chi}_1^0)$ = 345 GeV
Total background expectation	5.75	20.17	9.12
Total statistical $\left(\sqrt{N_{\text{exp.}}}\right)$	±2.40	±4.49	±3.02
Total background systematic	±1.82 [31.74%]	±5.91 [29.27%]	±3.01 [32.98%]
Signal cross-section	±1.34 [23.4%]	±3.49 [17.3%]	±2.40 [26.4%]
Tau identification	±0.82 [14.3%]	±2.61 [13.0%]	±1.27 [13.9%]
AFII simulation	±0.77 [13.4%]	±2.38 [11.8%]	±1.19 [13.1%]
MC statustucs	±0.42 [7.3%]	±2.31 [11.4%]	±0.32 [3.5%]
Flavour tagging	±0.17 [3.0%]	±0.18 [0.91%]	±0.22 [2.5%]
Pile-up	±0.15 [2.6%]	±0.01 [0.03%]	±0.25 [2.8%]
Jet reconstruction	±0.13 [2.3%]	±1.98 [9.8%]	±0.12 [1.3%]
Electron reconstruction	±0.05 [0.84%]	±0.01 [0.03%]	±0.01 [0.11%]
Muon reconstruction	±0.05 [0.82%]	±0.00 [0.02%]	±0.01 [0.07%]
Tau energy measurement	±0.04 [0.77%]	±0.40 [2.0%]	±0.06 [0.67%]
$E_{\text{T}}^{\text{miss}}$ reconstruction	±0.00 [0.00%]	±0.81 [4.0%]	±0.07 [0.79%]
Multi-jet estimation	±0.00 [0.00%]	±0.00 [0.00%]	±0.00 [0.00%]
Background estimation	±0.00 [0.00%]	±0.00 [0.00%]	±0.00 [0.00%]
Diboson theory	±0.00 [0.00%]	±0.00 [0.00%]	±0.00 [0.00%]
Top quark theory	±0.00 [0.00%]	±0.00 [0.00%]	±0.00 [0.00%]
PDF variations	±0.00 [0.00%]	±0.00 [0.00%]	±0.00 [0.00%]
Electroweak theory	±0.00 [0.00%]	±0.00 [0.00%]	±0.00 [0.00%]

Table 7.2: Breakdown of the dominant systematic uncertainties on background and signal estimates in the single-bin SRs. It is to be noted that the individual nuisance parameters can be correlated, and do not necessarily add up quadratically to the total background uncertainty. The percentages show the size of the uncertainty relative to the total expected background.

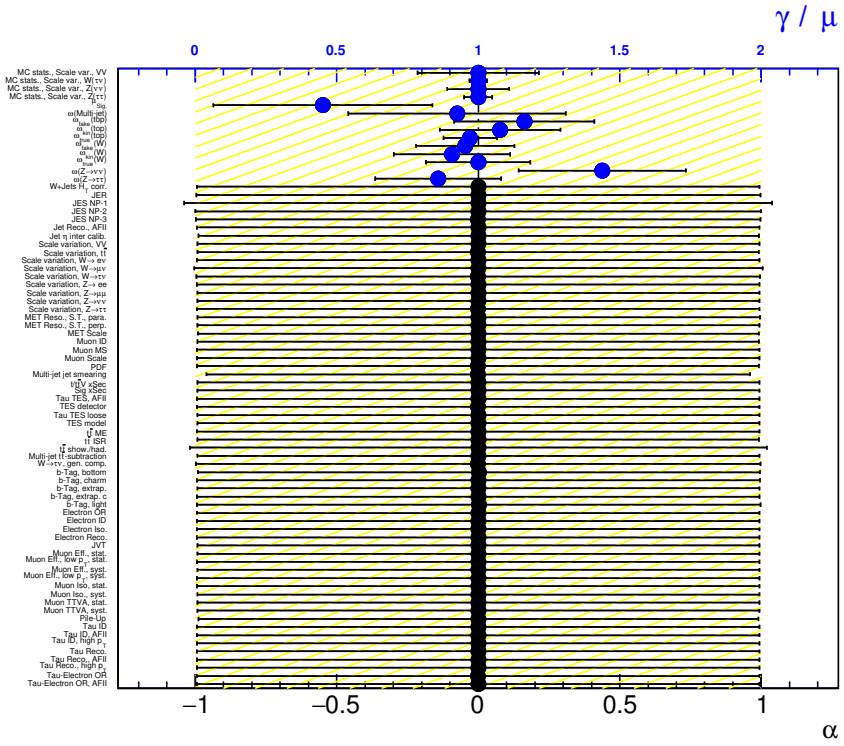

Figure 7.3: Pull-plot of the nuisance parameters (NPs) of the combined fit of the GMSB signal and background model, considering all systematic uncertainties. For illustration purposes, the GMSB benchmark scenario (Λ = 120 TeV, $\tan\beta$ = 40) is used the tested signal model in the 2τ GMSB signal region. The y-axis gives the list of nuisance parameters. Here, ω represents the normalisation-factors of the Standard Model backgrounds as introduced in section 6.3. For NPs related to systematic uncertainties, the lower black x-axis provides information on the constrain of the NP in the fit. A central value of 0 indicates agreement between the fitted value of the NP and the predicted central value of constraint from external sources. The length of the error bar with respect to unity—indicated by the yellow hatched area—indicates the agreement between the spread of the fitted NP and the width of the external constraint. Smaller error bars point towards the fit constraining the systematic uncertainty stronger than the prediction from theory or the experimental measurement. For the normalisation factors ω, the upper blue x-axis indicates their deviation from unity and their post-fit uncertainty, rendering it a representation equivalent to table 6.4(b) and fig. 6.10(b).

CHAPTER 8

Results and Interpretation – Evaluating the Loot

Having introduced the estimation and validation of Standard Model background processes in chapter 6 and the spectrum of systematic uncertainties as well as their effects on the analysis in chapter 7, the scene is set to study and evaluate the results from the strategy introduced in chapter 5. This chapter first presents the general results of the combined background-only fit in the signal regions by unblinding the observed data in the SRs and studying their kinematic distributions. Subsequently, the findings are made subject to a detailed quantitative evaluation. The statistical measures of interest are introduced and utilised for statements about the general potential of this analysis to find physics beyond the Standard Model. Furthermore, the compatibility of the SUSY models searched for in the light of the predicted Standard Model processes and given the observed data is studied. The results of different exclusion fit configurations are presented and discussed, concluding with an outlook towards future scenarios of interest and analysis prospects.

8.1 Event kinematics in the unblinded signal regions

The full control established over the background spectrum in the control and validation regions allows for a detailed look into the signal regions. The overall composition of the signal and background spectrum in the SRs as presented in tables 5.4, 5.8, 5.9 and A.9 can be scrutinised by a look at the distributions of the final discriminating variables. Now that the background estimation can be considered reliable, a comparison of the predicted background and expected signal distributions to the observed data is also possible. For the 1τ channel, fig. 8.1 provides examples of the distributions of discriminating variables. In each shown distribution, the cut on the displayed variable is not applied but indicated by an arrow, allowing for statements about the overall modelling and extrapolation.

In the 1τ compressed signal region in fig. 8.1(a), the predicted background and data both below and above the final cut agree well. The upward fluctuation of the background for $100\,\text{GeV} \leq m_{\text{T}}^{\tau} \leq 200\,\text{GeV}$ has been studied in detail [8, 189] and found to be attributed to single multi-jet events that arise from the same seed event and come with high weights. The deviation is hence artificial but can be safely neglected due to the overall compatibility of data and the background prediction within the total uncertainty. Due to the excellent agreement even towards higher values of m_{T}^{τ}, no excess of data over the predicted Standard Model spectrum can be claimed.

The 1τ medium-mass SR is subject to stronger fluctuations, both below and above the final cut. For high values of H_{T}, a small excess of data is visible in fig. 8.1(b) that is, however, still in agreement with the background due to its large uncertainties and the chosen binning.

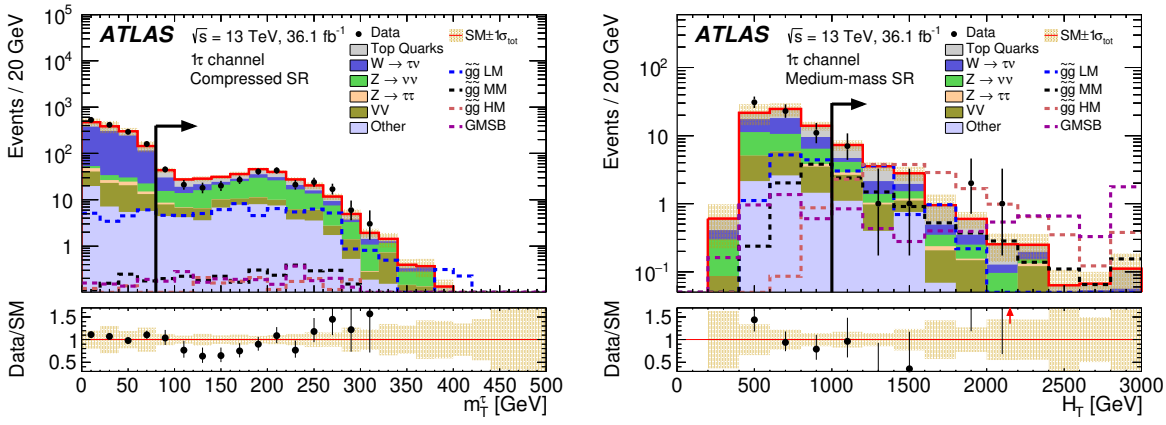

(a) (b)

Figure 8.1: Kinematic distributions for extended SR selections of the 1τ channel after the fit [8]: (a) m_{T}^{τ} in the compressed SR without the $m_{\mathrm{T}}^{\tau} > 80\,\mathrm{GeV}$ requirement and (b) H_{T} in the medium-mass SR without the $H_{\mathrm{T}} > 1\,000\,\mathrm{GeV}$ requirement. The contribution labeled as *other* includes multi-jet events and the V + jets processes not explicitly listed in the legend. The last bin of each distribution includes overflow events. The total uncertainty in the background prediction is shown as a shaded band. Red arrows in the Data/SM ratio indicate bins where the entry is outside the plotted range. A red arrow in the Data/SM ratio indicates a bin where the entry is outside the plotted range. The signal region is indicated by the black arrow. Signal predictions are overlaid for several benchmark models. For the simplified model, LM, MM and HM refer to low, medium and high mass splitting scenarios, with $m_{\tilde{g}}$ ($m_{\tilde{\chi}_1^0}$) set to 1 065 GeV (825 GeV), 1 625 GeV (905 GeV) and 1 705 GeV (345 GeV), respectively. The GMSB benchmark scenario corresponds to $\Lambda = 120\,\mathrm{TeV}$ and $\tan\beta = 40$.

Already from these distributions of kinematic variables, qualitative statements about the discovery potential of these two SRs are possible. Since the final fit setup is treating both 1τ signal regions as single-bin SRs, the overall yields are fitted and not the bin-wise accessible shape of a distribution. As a consequence, the small excess towards higher H_{T}-values in the medium-mass SR will be countered by the lower-H_{T} bins where no data is observed to give a good overall agreement between data and the predicted Standard Model background. Here, the design of a Multibin SR could have provided additional statistical power. In the compressed SR, the background prediction already agrees well in the majority of bins. No discovery potential in any 1τ SR is hence expected.

Results in the four SRs of the 2τ channel are provided in fig. 8.2. In the compressed SR, qualitatively good compatibility of the Standard Model prediction and data can be observed. The strongly correlated high-mass and GMSB SRs exhibit a comparable behaviour in their H_{T}-distributions as depicted in figs. 8.2(b) and 8.2(d). Good agreement between data and the background spectrum is observed before application of the final cut on H_{T} while at higher values, a small excess of data is visible. In contrast to the 1τ medium-mass SR, this preference of data towards higher values of H_{T} is not easily absorbed by the uncertainties but rather poses a genuine small excess that needs to be evaluated further. The 2τ multibin SR, originally designed to provide sensitivity towards signal scenarios that the compressed and high-mass SRs would address individually, is depicted in its final representation in fig. 8.2(c). Here, small deviations of the background prediction from data are observed in all bins, each of them still being in agreement within the found uncertainties. Considering the aforementioned small excess in the H_{T}-distributions of the high-mass and GMSB SRs, the H_{T}-based variation of the multibin SR may have exhibited an increased sensitivity. Such a result-driven design choice, however, is considered biased and shows the exact motivation why the development process is performed blindly, solely based on the expected results. The intrinsic strength of the multibin SR, on the other hand, is not accessible from these figures but lies

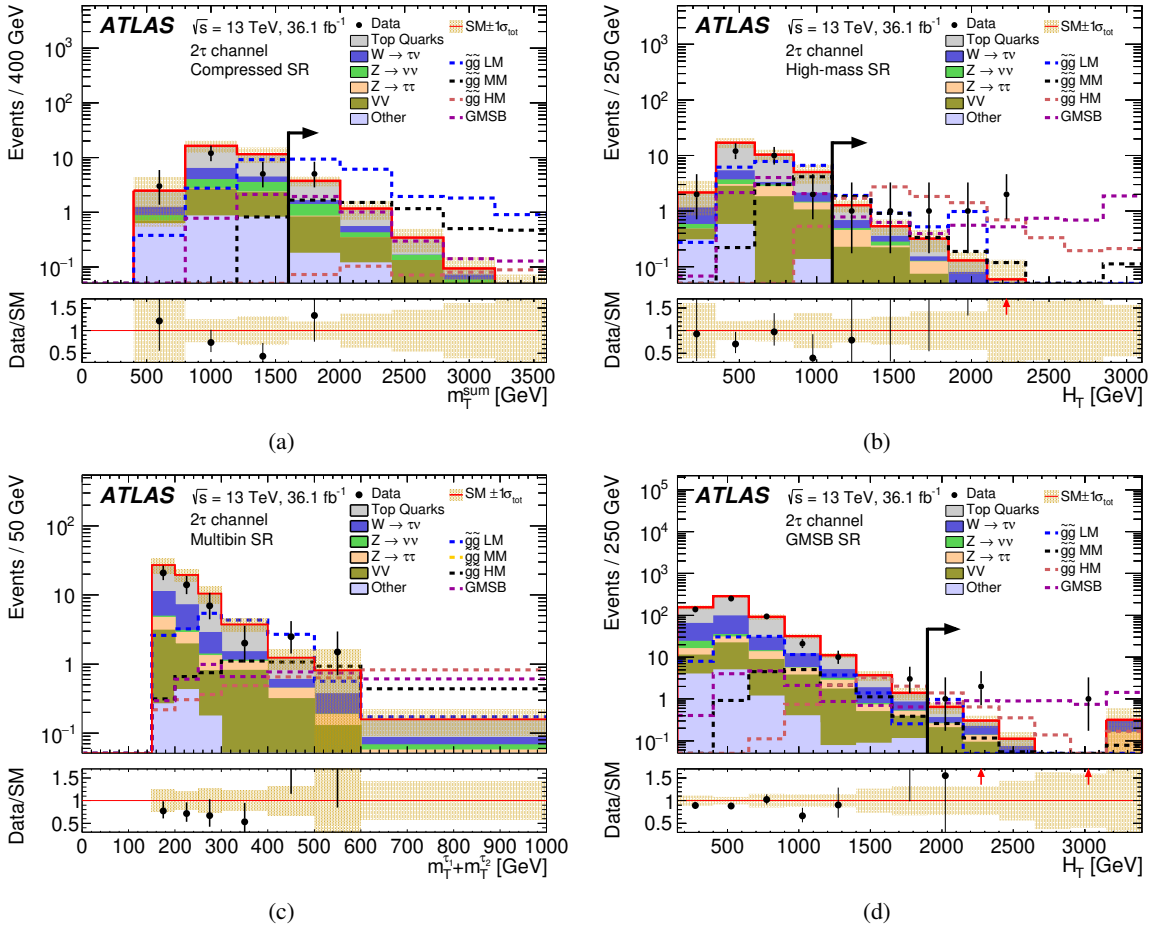

Figure 8.2: Kinematic distributions for extended SR selections of the 2τ channel after the fit [8]: (a) $m_{\mathrm{T}}^{\mathrm{sum}}$ in the compressed SR without the $m_{\mathrm{T}}^{\mathrm{sum}} > 1\,600\,\mathrm{GeV}$ requirement, (b) H_{T} in the high-mass SR without the $H_{\mathrm{T}} > 1\,100\,\mathrm{GeV}$ requirement, (c) $m_{\mathrm{T}}^{\tau_1} + m_{\mathrm{T}}^{\tau_2}$ in the multibin SR, and (d) H_{T} in the GMSB SR without the $H_{\mathrm{T}} > 1\,900\,\mathrm{GeV}$ requirement. The contribution labeled as *other* includes multi-jet events and the $V+\mathrm{jets}$ processes not explicitly listed in the legend. The last bin of each distribution includes overflow events. The total uncertainty in the background prediction is shown as a shaded band. Red arrows in the Data/SM ratio indicate bins where the entry is outside the plotted range. The signal region is indicated by the black arrow. Signal predictions are overlaid for several benchmark models. For the simplified model, LM, MM and HM refer to low, medium and high mass splitting scenarios, with $m_{\tilde{g}}$ ($m_{\tilde{\chi}_1^0}$) set to 1 065 GeV (825 GeV), 1 625 GeV (905 GeV) and 1 705 GeV (345 GeV), respectively. The GMSB benchmark scenario corresponds to $\Lambda = 120\,\mathrm{TeV}$ and $\tan\beta = 40$.

with its sensitivity to more models than only the four displayed benchmark scenarios. Details of this evaluation are presented in the forthcoming section. Additional information on the modelling of the other discriminating variables that are used in the signal region definitions are compiled in figs. A.14 and A.15 of appendix A.2.

Since five of the total of six signal regions are going to be evaluated as single-bin SRs, the agreement of the overall background prediction with the observed data in each region is a major subject of interest. A helpful tool to visualise said compatibility is a pull-plot as introduced in fig. 6.13. For all single-bin SRs as well as for the seven bins of the 2τ multibin SR, fig. 8.3 compiles the total background composition and its agreement with data. The qualitative analysis in the kinematic distributions can now be enhanced by a more detailed look at the total background and data yields in each SR. Both 1τ SRs exhibit a slight

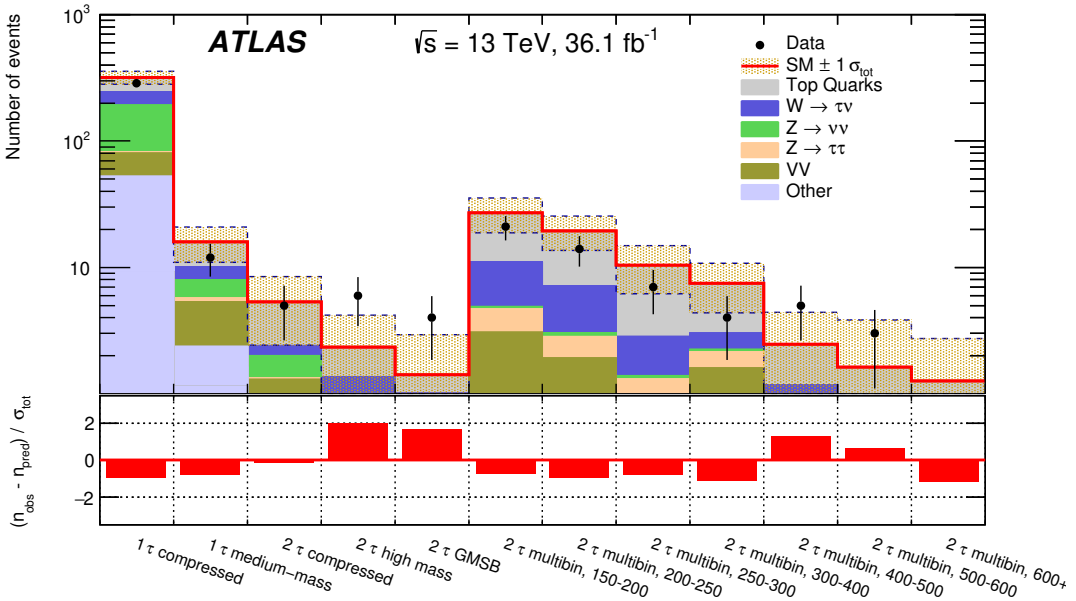

Figure 8.3: Number of observed events, n_{obs}, and predicted background yields after the fit, n_{pred}, in the signal regions of the 1τ and 2τ channels [8]. The background predictions are scaled using the normalisation-factors derived in the control regions. The total uncertainty in the background predictions, σ_{tot}, is shown as a shaded band. The error bars of the data points only represent the Poissonian statistical uncertainty of the measurement.

overestimation of the background. The deviation from the observation is, however, still well covered by one standard deviation, the total uncertainty on the background prediction. While the 2τ compressed SR is predicting the observation almost perfectly, the high-mass and GMSB SRs show a similar excess of data over the background between one and two standard deviations of the prediction[1]. Due to their similarity in phase-space (rather high requirements on the same two discriminating variables H_{T} and $m_{\text{T}}^{\tau_1}+m_{\text{T}}^{\tau_2}$), these small excesses are expected to be highly correlated. The number of observed data events and expected Standard Model background events for all single-bin SRs are summarised in table 8.1. In the seven bins of the 2τ multibin SR, the first four bins are subject to comparably strong overestimations of the background, all being, well covered by the total background uncertainty. The fifth and sixth bin show an opposite behaviour. Due to the very low statistics in these two bins, the low background prediction is, however, covered by the total uncertainty. The last bin does not contain any observed data but predicts a few Standard Model events. Due to the used fitting approach of a binned likelihood, this is still usable information (cf. appendix G).

Apart from the slight excess in the 2τ high-mass and GMSB signal regions, no deviations of the background prediction from the measured data are observed. The chances of actually discovering signal are hence negligibly small. The available results are, in turn, used to derive limits on either the different models' parameters, so-called *model-dependent* limits, or the number of potential signal events that are still compatible with the expected (observed) results, based only on background and data, the so-called *model-independent* limits. These results are presented and discussed in the forthcoming sections.

[1] The cover page of this thesis depicts a two-dimensional visualisation of one of the events found in the 2τ high-mass and GMSB SRs, obtained using the ATLANTIS reconstruction software [231], recorded on 2016-06-06 at 02:36:26 CEST in run 160155, luminosity block 519, having event number 10959.

Single-bin SR	observed events	fitted SM events
1τ compressed	286	319 ± 31.90
1τ medium-mass	12	15.90 ± 2.95
2τ compressed	5	5.36 ± 1.90
2τ high-mass	6	2.34 ± 0.70
2τ GMSB	4	1.41 ± 0.53

Table 8.1: Overview of the number of observed events in data and the number of expected SM background events after the background-only fit in the single-bin SRs of both channels. The uncertainty given on the background estimation is the total combination of statistical and systematic uncertainties.

8.2 Statistical evaluation

With fig. 8.3 not showing any significant excess of the observed data over the predicted Standard Model spectrum, the initially searched for signal models are now evaluated with respect to constraints on their defining parameters. Starting with model-dependent limits, for every signal scenario, an exclusion fit as described in appendix G.3 is performed in every signal region. The results of such fits and their applications are manifold.

$\mathbf{CL_S}$ The confidence level of the signal hypothesis being true is expressed by utilising the CL_S-method [232]. The resulting value of CL_S is derived separately for testing the nominal hypothesis of signal-plus-background against the observed data, giving $CL_S^{obs.}$, and against the best[2] hypothesis of signal and background, giving $CL_S^{exp.}$. Apart from just determining the confidence into an hypothesis, the CL_S values are used also in another context. CL_S being a measure of confidence, it can serve as a indicator of the performance of a signal regions being compared to each other. While mutually exclusive regions of phase-space can safely be fitted simultaneously, the individual results of SRs that overlap in phase-space can only be used one at a time. In the latter case, the results of the SR performing the best is obtained considering the signal region with the better, i.e. lower, value of $CL_S^{exp.}$.

Cross-section limits After deciding for a level of confidence with which a tested signal hypothesis is rejected—here, 95%—the fit can determine the value of the signal-strength μ with which the nominal signal had to be scaled in order to be excluded at the set value of CL_S. From this upper limit on the signal-strength parameter, in turn, upper limits on the production cross-section of the evaluated signal scenario can be derived: $\langle \epsilon\sigma \rangle^{95}_{exp.} = \sigma_{prod.} \times \mu^{95}_{obs.}$. This result is of particular interest for model-building and re-interpretation approaches of phenomenologists as further described in the forthcoming paragraphs.

Model-independent limits First, the Standard Model prediction and the observed data can be evaluated with respect to the potential presence of any new physics model. By comparing the background prediction to the observation, i.e. enforcing the absence of signal in the hypothesis test, statements about the amount of possibly present additional physics scenarios can be made – without any need for design or simulation of a particular model.

[2] Here, the *best* hypothesis refers to the estimator that maximised the unconditional likelihood, cf. appendix G.

Single-bin SR	$\langle\epsilon\sigma\rangle^{95}_{\text{obs.}}$ in fb	$S^{95}_{\text{obs.}}$	$S^{95}_{\text{exp.}}$	CL_B	$p(s=0)$ (Z)
1τ compressed SR	1.37	49.5	$64.3^{+24.1}_{-14.9}$	0.18	0.50 (0.0)
1τ medium-mass SR	0.21	7.7	$10.0^{+4.3}_{-2.7}$	0.24	0.50 (0.0)
2τ compressed SR	0.18	6.7	$6.7^{+2.8}_{-1.5}$	0.50	0.50 (0.0)
2τ high-mass SR	0.25	9.0	$5.0^{+1.9}_{-1.3}$	0.96	0.03 (1.83)
2τ GMSB SR	0.20	7.3	$4.4^{+1.5}_{-0.9}$	0.95	0.05 (1.68)

Table 8.2: Results of model-independent fits in the five single-bin signal region [8]. Left to right, the five columns give: the 95% CL upper limits on the visible cross section ($\langle\epsilon\sigma\rangle^{95}_{\text{obs.}}$) and on the number of signal events ($S^{95}_{\text{obs.}}$). The third column ($S^{95}_{\text{exp.}}$) shows the 95% CL upper limit on the number of signal events given the expected number (and $\pm1\sigma$ excursions on the expectation) of background events. The last two columns indicate the CL_B value, i.e. the confidence level observed for the background-only hypothesis and the discovery p-value ($p(s=0)$) as well as its corresponding significance Z. Due to the underlying one-sided hypothesis test, the p-value is capped at 0.50 for the case of an overestimation of the background.

2τ multbin SR	$\langle\epsilon\sigma\rangle^{95}_{\text{obs.}}$ in fb	$S^{95}_{\text{obs.}}$	$S^{95}_{\text{exp.}}$	CL_B	$p(s=0)$ (Z)
Bin $\mathcal{A}$	0.34	12.2	$14.6^{+5.4}_{-3.9}$	0.26	0.50 (0.0)
Bin $\mathcal{B}$	0.25	9.1	$11.3^{+4.6}_{-2.8}$	0.19	0.50 (0.0)
Bin $\mathcal{C}$	0.19	6.8	$8.3^{+3.4}_{-2.1}$	0.24	0.50 (0.0)
Bin $\mathcal{D}$	0.14	5.0	$7.0^{+2.7}_{-2.0}$	0.14	0.50 (0.0)
Bin $\mathcal{E}$	0.22	7.8	$5.0^{+2.0}_{-1.4}$	0.90	0.09 (1.31)
Bin $\mathcal{F}$	0.20	7.1	$5.7^{+2.0}_{-1.0}$	0.78	0.26 (0.63)
Bin $\mathcal{G}$	0.09	3.2	$3.6^{+1.4}_{-0.6}$	0.02	0.50 (0.0)

Table 8.3: Results of model-independent fits in the seven bin of the 2τ Multibin signal region [8]. Left to right, the five columns give: the 95% CL upper limits on the visible cross section ($\langle\epsilon\sigma\rangle^{95}_{\text{obs.}}$) and on the number of signal events ($S^{95}_{\text{obs.}}$). The third column ($S^{95}_{\text{exp.}}$) shows the 95% CL upper limit on the number of signal events given the expected number (and $\pm1\sigma$ excursions on the expectation) of background events. The last two columns indicate the CL_B value, i.e. the confidence level observed for the background-only hypothesis and the discovery p-value ($p(s=0)$) as well as its corresponding significance Z. Due to the underlying one-sided hypothesis test, the p-value is capped at 0.50 for the case of an overestimation of the background.

By means of such a model-independent fit[3], cf. appendix G.4, multiple characteristic quantities can be obtained, summarised in tables 8.2 and 8.3. Starting from the number of signal events which are compatible with the background prediction given the expected (observed) data at 95% CL, $S^{95}_{\text{exp.}}$ ($S^{95}_{\text{obs.}}$), the integrated luminosity available in this analysis is used to calculate an upper limit on the visible cross-section of a potential model, $\langle\epsilon\sigma\rangle^{95}_{\text{obs.}}$. These numbers already consider the limitations of the analysis in terms of detector effects and selection efficiency. In addition, the confidence level of the background-only hypothesis CL_B as well as the corresponding p-value and significance Z are provided. Due to the fact that the hypothesis test is performed using a one-sided profile-likelihood ratio and evaluated by means of a one-sided normal distribution, the p-value of the background-only hypothesis is capped to 0.50 (and the significance to 0.0) for the case of an overestimation of the background prediction.

[3] The term *model-independent* is only insofar correct as no particular signal model is used in the fit. Since the signal regions the fit is performed in are designed to target specific models in the first place, the fit is, from a strict philosophical point of view, not model-independent.

The visible excess of data events over the background prediction in the 2τ high-mass and GMSB signal regions can now be exactly quantified to be of 1.83 and 1.68 standard-deviations, respectively. Upper limits on the cross-sections vary from 0.18 fb in the 2τ compressed SR to 1.37 fb in the 1τ compressed SR. These results can be understood upon consideration of e.g. fig. 8.3: the 2τ compressed SR exhibits the lowest tension between the background prediction and the observation, hence being able to provide the strongest limit on an additional event contribution such as a model of new physics. The 1τ compressed SR, on the other hand, is the most inclusive of signal regions, rendering the inclusion of an additional signal model more difficult and giving hence the weakest limit.

Calculation of model-dependent limits The model-independent limits calculated in the last paragraph explicitly assumed the absence of any signal in the hypothesis tests to allow for quantitative statements of the general presence of any signal model. Statements about the two signal models searched for in the context of this thesis, the simplified model of gluino pair-production and the model of GMSB, are possible upon consideration of the different simulated signal scenarios in designated exclusion fits.

In a first step, the CL_S values, both for the expected and observed case, are computed from the exclusion fit of every signal-plus-background scenario. Based on a chosen threshold of $CL_S \leq 5\%$ to reject the hypothesis with the aforementioned 95% confidence, the decision of whether a particular scenario is excluded or still allowed, is made. Since both models of interest are described by two parameters, two-dimensional maps of the models' parameter-spaces and the decision of the exclusion fit can be drawn. Due to the finite number of parameters considered in the simulation of the signal models as MC events, only a discrete map of entries would be possible[4]. In order to allow for statements across the entire parameter-space, the gap between adjacent evaluated sets of parameters is closed via interpolation. Assuming that the behaviour of the selection is not too different between two adjacent signal points, the point of $CL_S = 0.05$ is determined by a linear interpolation between the two actually evaluated signal points. An illustrative example could be the following as shown in eq. (8.1): a certain signal point is excluded due $CL_S \leq 0.05$, while its closest neighbour is not, having $CL_S > 0.05$. Since the first point is barely excluded, the actual exclusion boundary is expected to be closer to it than to the non-excluded point.

$$\begin{aligned} &CL_S(m(\tilde{g}) = 600\,\text{GeV}) = 0.04 \\ &CL_S(m(\tilde{g}) = 700\,\text{GeV}) = 0.10 \\ &\Rightarrow m(\tilde{g})(CL_S = 0.05) = 617\,\text{GeV} \end{aligned} \tag{8.1}$$

This interpolation scheme allows for the derivation of continuous lines in the 2D parameter-plane that indicate areas of exclusion. Such lines are referred to as *exclusion contours*. They are calculated for both the expected and observed cases as well as their $\pm 1\sigma$-uncertainty cases. The picture of information obtained from the evaluation of the fit results across an entire parameter-plane can be enhanced further by overlaying the values of the obtained upper limits on the production cross-section at each simulated point.

[4] A set of model-defining parameters, for which a MC simulation is carried out, is referred to as a *point* in parameter-space or *signal point*.

8.2.1 Limits on the simplified model

Starting with the simplified model of gluino pair-production, results on the models specifically searched for in this analysis can be obtained and evaluated. Tests of all of the 169 simulated signal scenarios in separate exclusion fits in every signal region gives exclusion contour lines across the $m(\tilde{g})$-$m(\tilde{\chi}_1^0)$ parameter-plane. Figures 8.4(a) to 8.4(e) provide these results for the five individual SRs. As to be expected from the model-independent results, the observed limit in signal regions of the 1τ channel is stronger than the corresponding expected ones due to the overestimation of the background. While the good agreement between prediction and observation in the compressed SR of the 2τ channel results in agreement between the expected and observed limit contour, the high-mass SR exhibits a weaker observed limit due to its small excess in the observed data. In general, the observed limit contours follow the shape of the expected ones, as partially already introduced in the context of figs. 5.11 and 5.13. Due to the fact that the 2τ multibin SR is implemented as the simultaneous fit of its seven mutually exclusive bins treated as separate signal regions, the position and shape of the observed limit relative to the expected limit varies over the grid. This effect is explained by the same mechanisms as for the single-bin SRs when considering the predicted background and observed data results (cf. fig. 8.3 or tables A.10 and A.11 in appendix A.3): bins with an overestimation of the predicted background shape the contours differently than bins with an underestimation or high compatability. Already at this point the influence the increased amount of data available with respect to the extrapolation study [9] is visible: all individual signal regions are able to extend the earlier parameter limits in their respective target regions significantly.

The next step in unraveling the full potential of this analysis are combinations of the mutually exclusive signal regions by means of fitting them simultaneously in the respective exclusion fits. An overview of the different combinations of signal regions in the search for the simplified model is provided in fig. 8.5. The combination of the two SRs of the 1τ channel gives the result depicted in fig. 8.6(a). Despite the fact that the 1τ channel is mainly designed to target signal scenarios at lower gluino masses and towards lower mass-splittings, it is on its own able to extend the limit of the exploration study [9] across the entire parameter-plane. Figure 8.6(b) shows the combination of the two single-bin SRs of the 2τ channel. Although tailored towards high gluino masses and smaller differences between $m(\tilde{g})$ and $m(\tilde{\chi}_1^0)$, the 2τ single-bin combination also extends the earlier limit across large parts of the parameter-plane – only the signal scenarios with the smallest gluino masses are not covered. The combined sensitivity of both regions is almost reached by the 2τ multibin SR alone, cf. fig. 8.4(e). Only for scenarios with both heavy gluinos and LSPs, it is outperformed by the 2τ compressed SR. Its increased sensitivity in particular regions of the parameter-plane, for example around $m(\tilde{g}) = 1\,800\,\text{GeV}/m(\tilde{\chi}_1^0) = 900\,\text{GeV}$, can be exploited by considering the best result at each point, chosen from the multibin SR results and the 2τ single-bin combination, based on the value of $\text{CL}_\text{S}^{\text{exp.}}$ as described in section 8.1. The resulting exclusion contour in the parameter-plane is displayed in fig. 8.6(c). The obscure-looking distortions of the observed limit contour below $m(\tilde{\chi}_1^0) = 700\,\text{GeV}$ arise from the procedure of combination. Due to the expected limits of the multibin SR and the single-bin combination performing comparably while the observed limits are substantially different in this part of parameter-space, smallest fluctuations in $\text{CL}_\text{S}^{\text{exp.}}$ lead to abrupt changes in the preferred signal region choice and hence the observed limit contour. This effect is only an artefact of the interpolation approach applied between to simulated signal points and accounts for the correct treatment of the underlying statistics results.

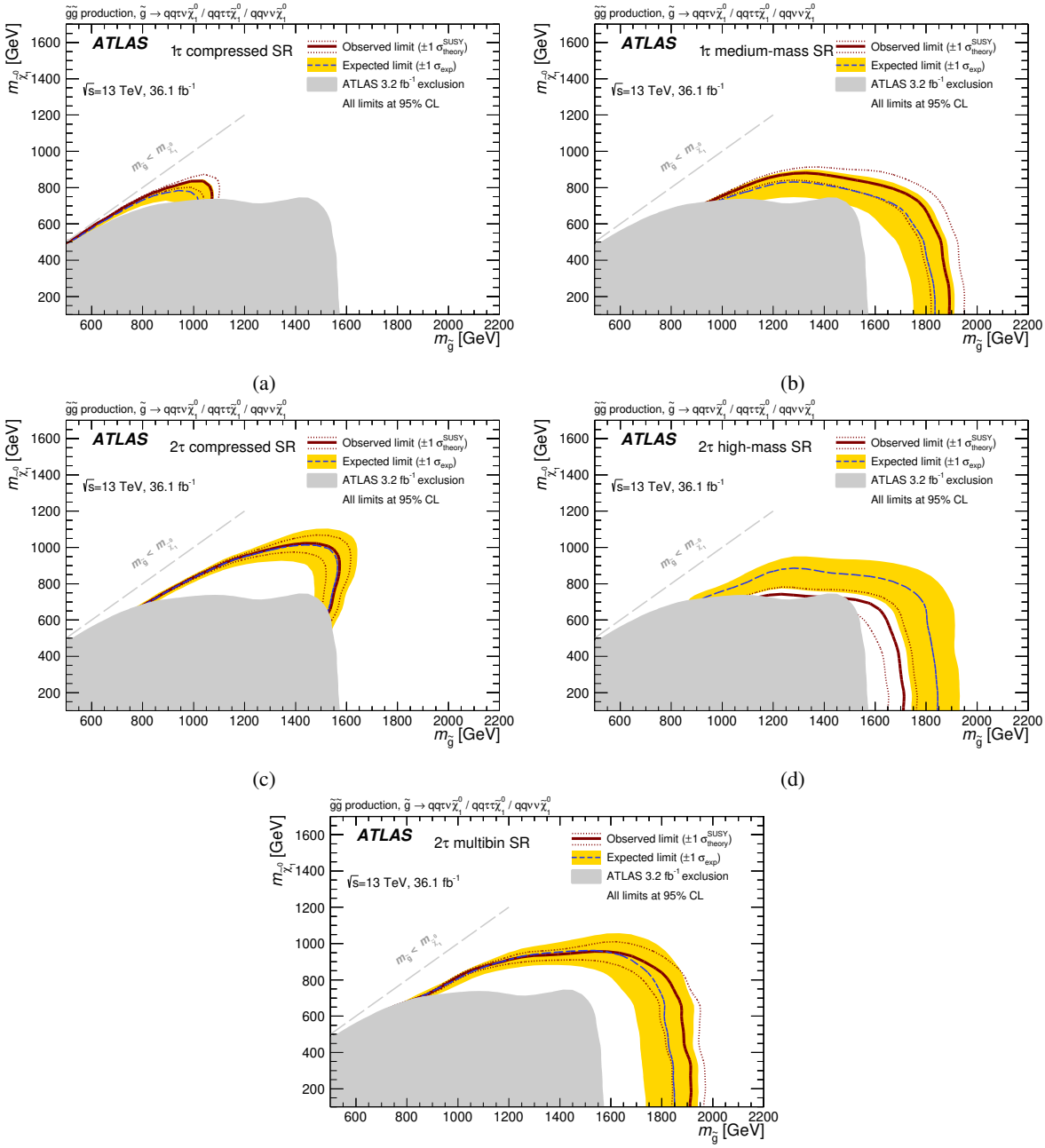

Figure 8.4: Exclusion contours at the 95% confidence level for the simplified model of gluino pair-production in the single-bin SRs of the 1τ channel ((a), (b)) and the 2τ channel ((c) to (e)) [8]. The red solid line and the blue dashed line correspond to the observed and median expected limits, respectively. The yellow band shows the one-standard-deviation spread of the expected limits around the median. The effect of signal cross-section uncertainties on the observed limits is shown as red dotted lines. The previous ATLAS result [9] obtained with $3.2\,\text{fb}^{-1}$ of $\sqrt{s} = 13\,\text{TeV}$ data is shown as a grey filled area.

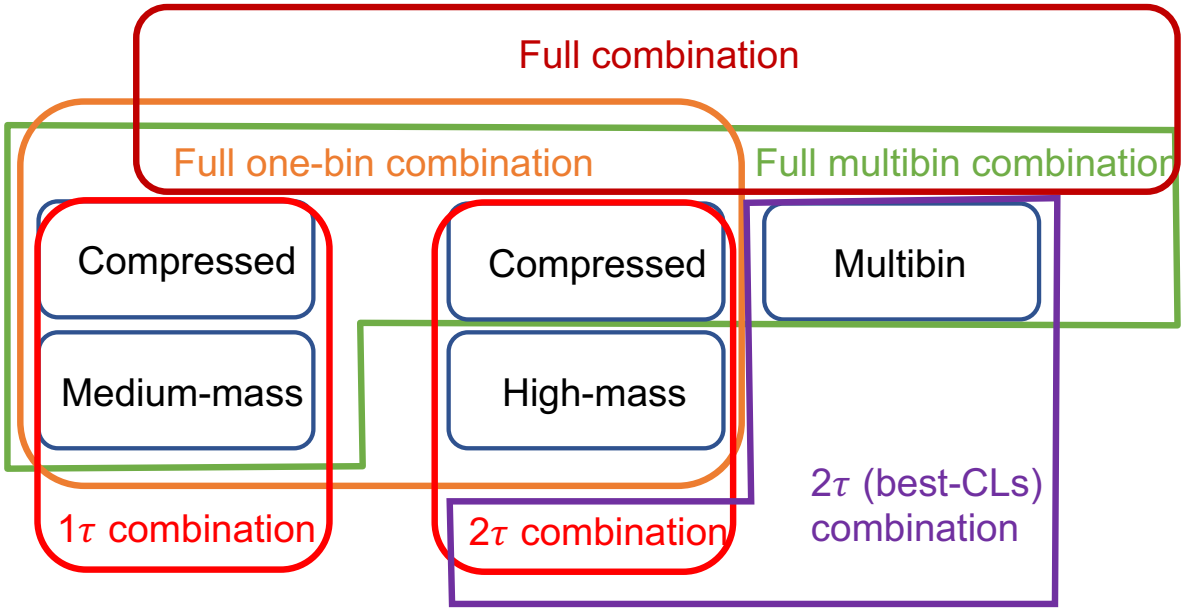

Figure 8.5: Flowchart visualising the signal region combinations performed in the search for the simplified model of gluino pair-production. The five SRs are labelled in black, the differently coloured frames and labels illustrate the various combinations and introduce the used nomenclature.

The combination efforts are continued by simultaneously fitting all combinations of mutually exclusive signal regions, giving rise to the results this analysis initially aimed for by its improved signal region design and background estimation approach with respect to [13, 219]. The combination of all four single-bin SRs is supposed to compile all the individual strengths and sensitivities of the individual, highly specified signal regions into one powerful result. Due to its comparable performance with respect to the combination of the 2τ single-bin SRs, the 2τ multibin SR is also fitted simultaneously with the two 1τ signal regions. The results of both combinations are displayed in fig. 8.7.

Comparing to the combinations of the individual channels, which are indicated as green (1τ channel) and magenta (2τ channel), the benefits of this setup of mutually exclusive signal regions and one mutual background estimation becomes evident. For both fit setups, the combined expected limit contour is clearly stronger than the individual channel expected limits. This effect arises from the simultaneous fit and is a signature feature of this approach that becomes clearest upon a comparison with the results of the earlier analysis [9]: ibid., no mutual background estimation is used and the combination of the two channels is only possible by means of a choice of one signal region at each point in parameter-space, based on the best $CL_S^{exp.}$. As a consequence, either the 1τ or the 2τ channel individual limits are chosen. This effect is visualised in fig. 8.7(c) by the blue line of the combined expected limit exactly following either the magenta or the green line of the individual channel limit contours. This approach prohibits the contribution of information on the tested signal points from the weaker of the two channels.

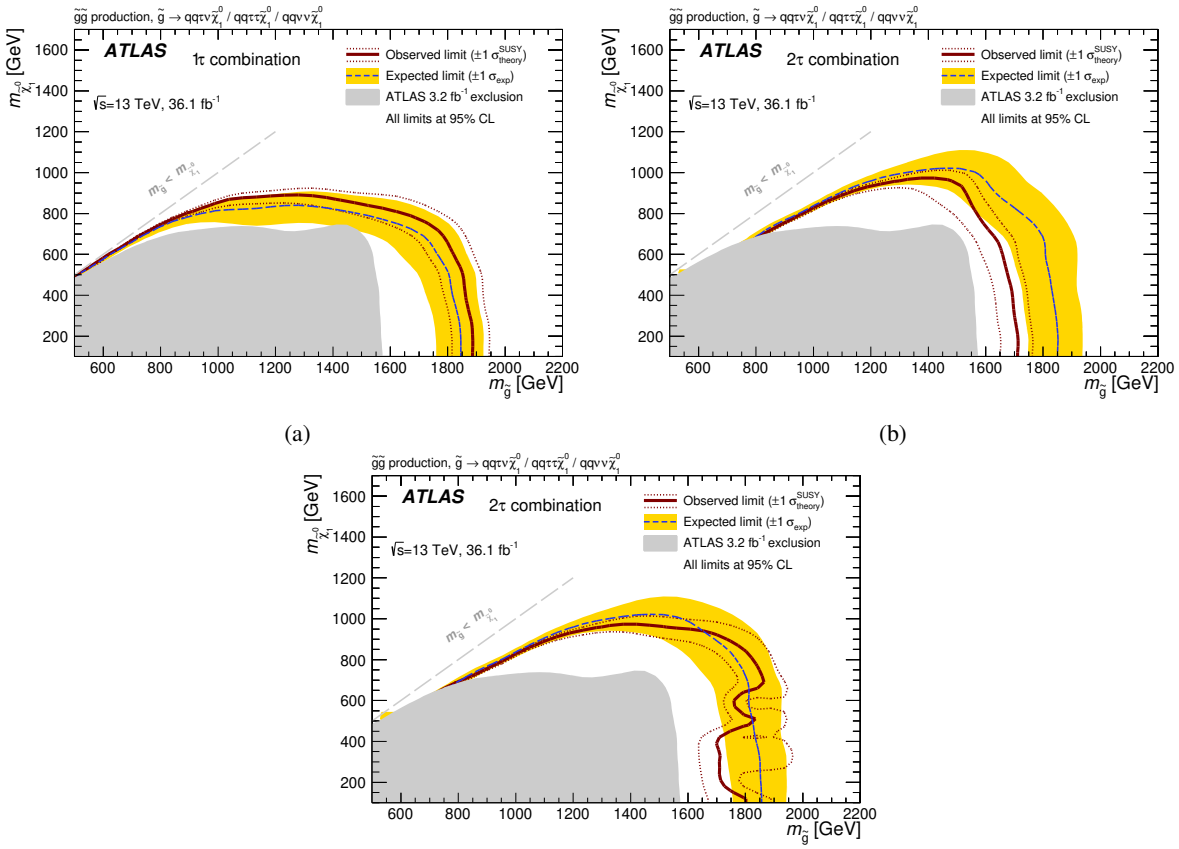

Figure 8.6: Exclusion contours at the 95% confidence level for the simplified model of gluino pair-production for the combinations of SRs in the 1τ channel (a) and the 2τ channel (b), (c) [8]. The results of the best performing 2τ setup at each point in parameter-space based on the value of $CL_S^{exp.}$, chosen between the single-bin combination and the multibin SR are given in (c). The red solid line and the blue dashed line correspond to the observed and median expected limits, respectively. The yellow band shows the one-standard-deviation spread of the expected limits around the median. The effect of signal cross-section uncertainties on the observed limits is shown as red dotted lines. The previous ATLAS result [9] obtained with 3.2 fb^{-1} of $\sqrt{s} = 13$ TeV data is shown as a grey filled area.

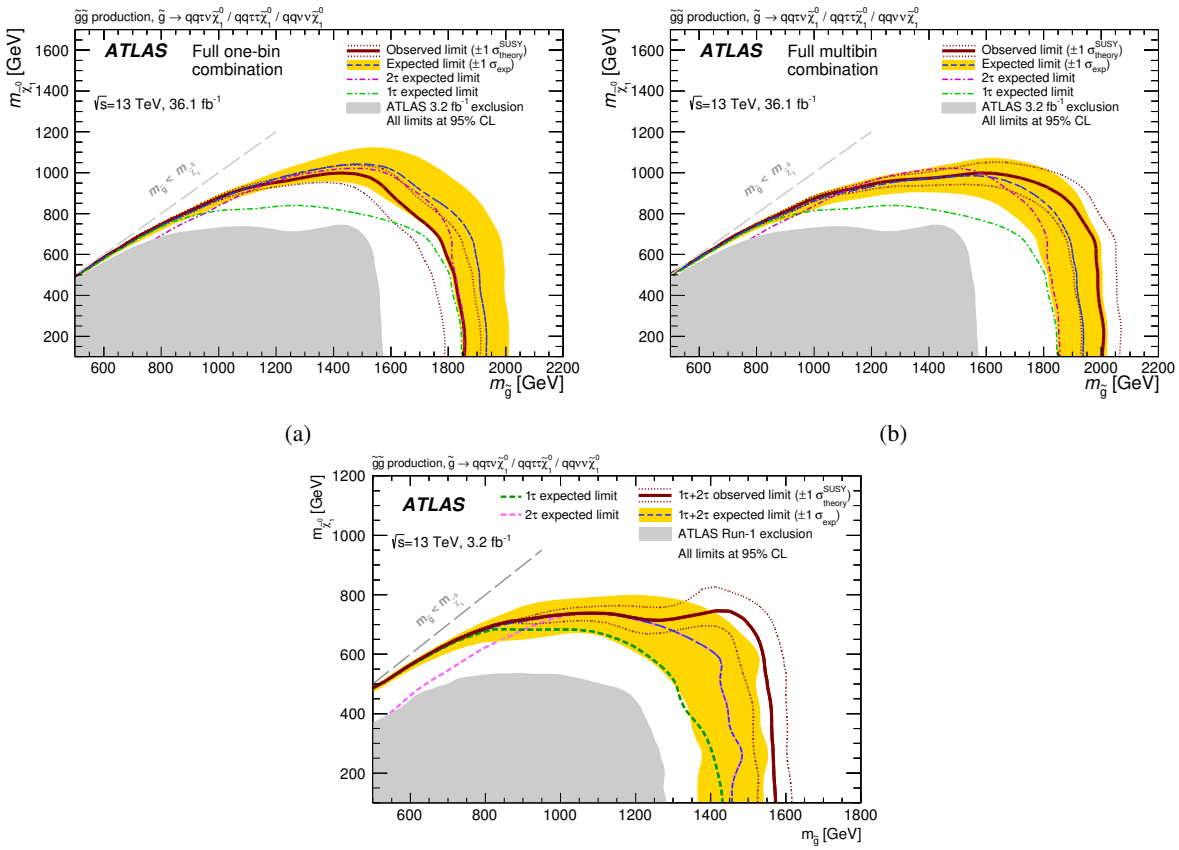

(a) (b)

(c)

Figure 8.7: Exclusion contours at the 95% confidence level for the simplified model of gluino pair-production for the combination of the compressed and medium-mass SRs of the 1τ channel with the compressed and the high-mass SRs of the 2τ channel, (a), and the combination of the compressed and the medium-mass SRs of the 1τ channel with the multibin SR of the 2τ channel, (b) [8]. The combination is realised by a simultaneous fit of the individual, mutually exclusive SRs. The red solid line and the blue dashed line correspond to the observed and median expected limits, respectively. The yellow band shows the one-standard-deviation spread of the expected limits around the median. The effect of signal cross-section uncertainties on the observed limits is shown as red dotted lines. The magenta and green dashed lines present the individual channel median expected limits as provided by figs. 8.6(a) and 8.6(c) in appendix A.5. The previous ATLAS result [9] obtained with 3.2 fb^{-1} of $\sqrt{s} = 13$ TeV data is shown as a grey filled area and depicted in detail in (c).

In the simultaneous fit of all SRs of both channels in this analysis, also the smallest piece of information on the tested signal scenario can be exploited to decide whether a signal point is excluded or not. This enormous benefit is reflected in the position of the combined expected limit relative to the individual channel limits. The expected structure of the 2τ channel being stronger for high values of $m(\tilde{g})$ and lower $m(\tilde{\chi}_1^0)$ is visible, as is the driving contribution of the 1τ channel along the diagonale of masses for the most compressed parts of the mass spectrum. At most points, however, the information from both channels—each being unable to claim an exclusion on their own—is combined to be sufficient to extend the exclusion significantly beyond the individual channel limit contours. An exception is the regime of smallest mass-differences, close to the diagonale, where the 2τ channel is not sensitive at all and the combined limit is purely driven by the 1τ channel.

The results show that this analysis is able to not only use the increased amount of available data for pushing the individual signal channel limits by approximately 400 GeV in $m(\tilde{g})$ and approximately 200 GeV in $m(\tilde{\chi}_1^0)$, but to extend the combined expected exclusion by another 100 GeV in $m(\tilde{g})$.

In a comparison of fig. 8.7(a) and fig. 8.7(b), the influence of the 2τ multibin SR becomes visible. Although not as much of an increase as in the 2τ combination only, an improvement of the combined expected limit is visible in the top right corner of the parameter-plane, for high values of $m(\tilde{g})$ and $m(\tilde{\chi}_1^0)$.

While the improvement in binary choice of whether a tested signal point is excluded or not is small, the confidence of the exclusions based on the 2τ multibin SR is higher. This effect is visualised in fig. 8.8. The plot displaying the ratio of the $\mathrm{CL_S^{exp.}}$ values of the results shown in figs. 8.7(a) and 8.7(b) highlights where the combination of signal regions including the 2τ multibin SR is stronger in red, its weaker regions in the parameter-plane in cyan. The latter is particularly the case for the highest values of $m(\tilde{g})$ and largest mass-splittings. Here, the 2τ high-mass SR is superior to the multibin SR due to its higher level of general background suppression.

The benefit of the multi-bin approach becomes clearest when studying the obtained limits on the model production cross-section. Strongly correlated to the improvement in the confidence of the hypothesis tests via $\mathrm{CL_S^{exp.}}$ is the obtained value of the signal strength that is fitted to scale the nominal signal hypothesis until it is excluded at 95% CL. Here, a similar improvement of the multi-bin approach with respect to the single-bin setup is expected. Figures A.16 and A.17 in appendix A.5 show the limit contours in the parameter-plane with the obtained upper limit values of the visible production cross-section at each point for the different signal regions and the channel combinations. Already at this point, the 2τ multibin SR provides stronger limits[5] than any other individual signal region, particularly within the bounds of the limit contour. This fact is of particular interest and importance. Since the four single-bin regions impose stronger selection criteria and are optimised towards selection efficiencies of the selected benchmark scenarios, it is possible for them to not be sensitive to signal scenarios their are not tailored towards. This lack of sensitivity can result in inadequate statements about the signal scenarios being excluded: a signal region not predicting enough events of a certain signal to be separated from the background because it selects events too strictly, will exclude said signal with less confidence. The more inclusive and less restrictive multi-bin approach, on the other hand, provides sensitivity and separation power also to signal scenarios which are difficult to assess with using the single-bin approach and can thus provide stronger exclusion statements. These enhanced exclusion capabilities of the multibin SR propagate on to the combined fit setups, depicted in fig. 8.9: the combination comprising the 2τ multibin SR provides the stronger upper limits on the visible production cross-section. Similarly to the illustration if the $\mathrm{CL_S^{exp.}}$ improvement, fig. 8.10 illustrates this increase graphically. In certain areas of the parameter-plane, the improvement reaches up to a factor of $3-4$.

[5] A stronger limit in the context of upper limits on the production cross-sections means that a lower value can be excluded at the same CL.

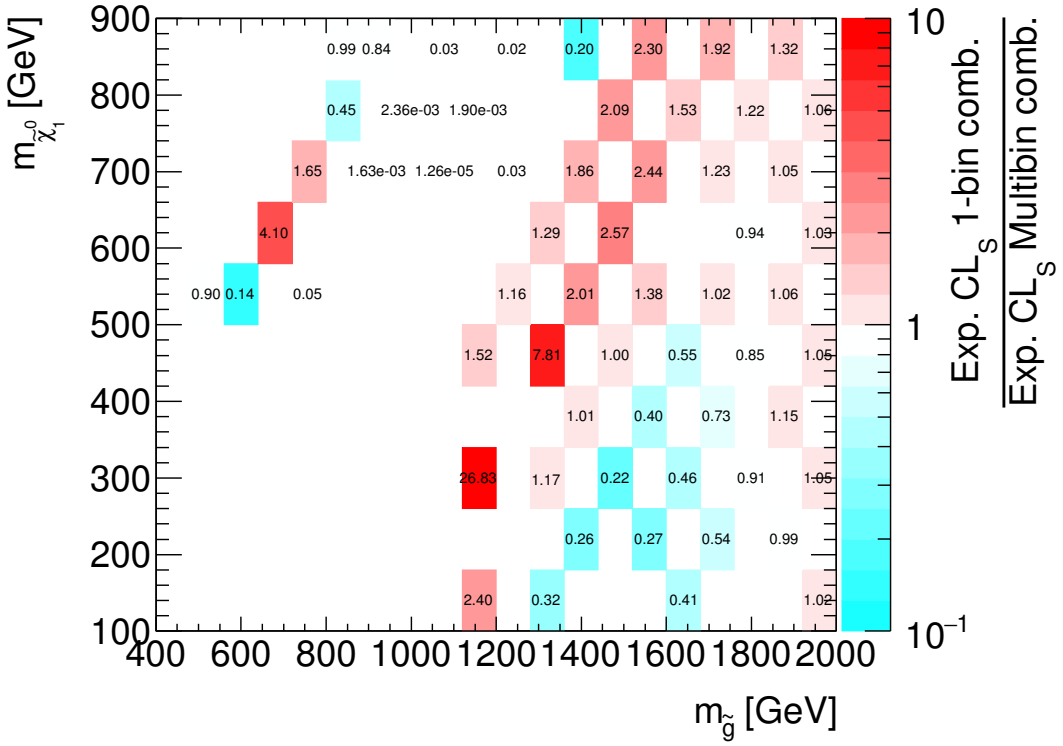

Figure 8.8: Ratio of $CL_S^{exp.}$ values of the combination of the 1τ compressed and medium-mass SRs with the 2τ compressed and high-mass SRs over the simultaneous fit of the 1τ compressed and medium-mass SRs with the 2τ multibin SR evaluated over the parameter grid of the simplified model. The numbers written onto the parameter grid give the exact ratio. Parameter points without such a printed value show insufficient quality of the underlying fit and cannot be evaluated. Overlaid values that fall beyond the range of the z-axis are printed on a white background.

Assuming that the relative systematic uncertainties would not change, a similar improvement of the limit, based solely on an increase in the available data, would require a factor of $9 - 16$ more integrated luminosity – a goal that is to be reached only by a significantly longer period of data-taking.

The differences between the single-bin and multi-bin results scrutinised so far motivate a final step in the evaluation of the results in the search for the studied simplified model of gluino pair-production. As outlined in section 8.1, the choice of the best-performing fit setup can be made for each signal point separately, preferably based on the value of $CL_S^{exp.}$. The results of such a combination of the different channel combination setups (cf. figs. 8.7(a) and 8.7(b)) gives fig. 8.11, the final set of exclusion limits on the simplified model.

The exact composition of this final result can be inferred from fig. A.19 in appendix A.5. Here, the overlaid labels give the final choice of the used fitting setup at each point, `S` referring to the pure single-bin combination, `M` being the multi-bin based combination. As to be expected from the earlier remarks, the multi-bin combination is preferred over large parts of the parameter-plane except for those where only the 2τ compressed SR is sensitive. The inward fluctuation of the -1σ observed limit contour is a result of the applied combination technique. At the affected region in the parameter-plane, a single signal point prefers the single-bin combination while its vicinity is described best by the multi-bin combination. Since the single-bin approach exhibits a weaker observed limit (cf. fig. A.18 in appendix A.5) in this region, the limit contour is interpolated under consideration of this local change, causing the observed fluctuation.

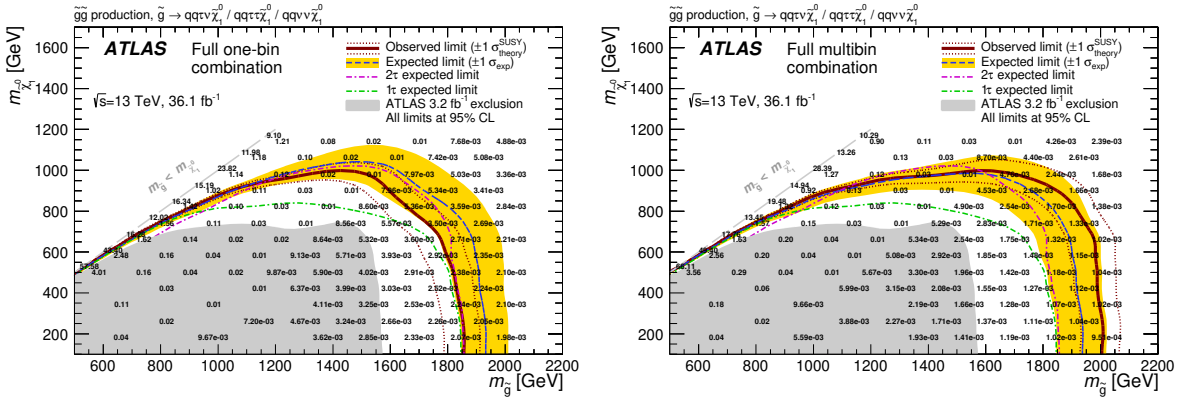

(a) (b)

Figure 8.9: Exclusion contours at the 95% confidence level for the simplified model of gluino pair-production for the combination of the compressed and medium-mass SRs of the 1τ channel with the compressed and the high-mass SR of the 2τ channel, (a), and the combination of the compressed and the medium-mass SR of the 1τ channel with the multibin SR of the 2τ channel, (b) [8]. The combination is achieved by a simultaneous fit of the individual, mutually exclusive SRs. The red solid line and the blue dashed line correspond to the observed and median expected limits, respectively. The yellow band shows the one-standard-deviation spread of the expected limits around the median. The effect of signal cross-section uncertainties on the observed limits is shown as red dotted lines. The magenta and green dashed lines present the individual channel median expected limits as provided by figs. 8.6(a) and A.17(e). The previous ATLAS result [9] obtained with 3.2 fb^{-1} of $\sqrt{s} = 13$ TeV data is shown as a grey filled area. The overlaid numbers give the excluded visible production cross-section at 95% CL, in pb.

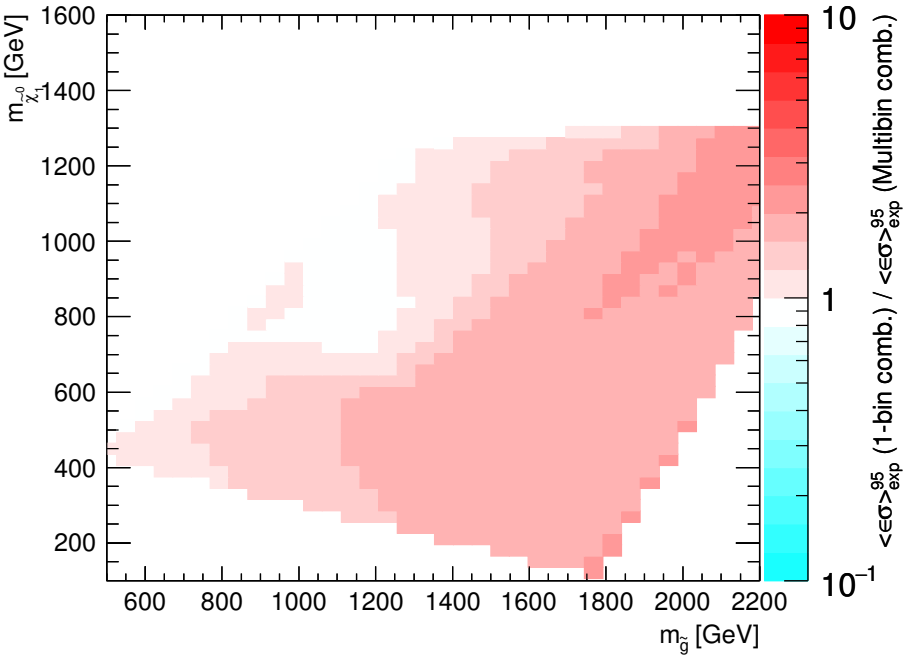

Figure 8.10: Ratio of the upper limits on $\langle \epsilon\sigma \rangle^{95}_{\text{exp.}}$ for the simultaneous fit of the 1τ compressed and medium-mass SRs and the 2τ compressed and high-mass SRs over the simultaneous fit of the 1τ compressed and medium-mass SRs and the 2τ multibin SR evaluated over the parameter grid of the simplified model. The white areas at the bottom left and right as well as the top center are, not evaluated due to insufficient quality of the underlying fit.

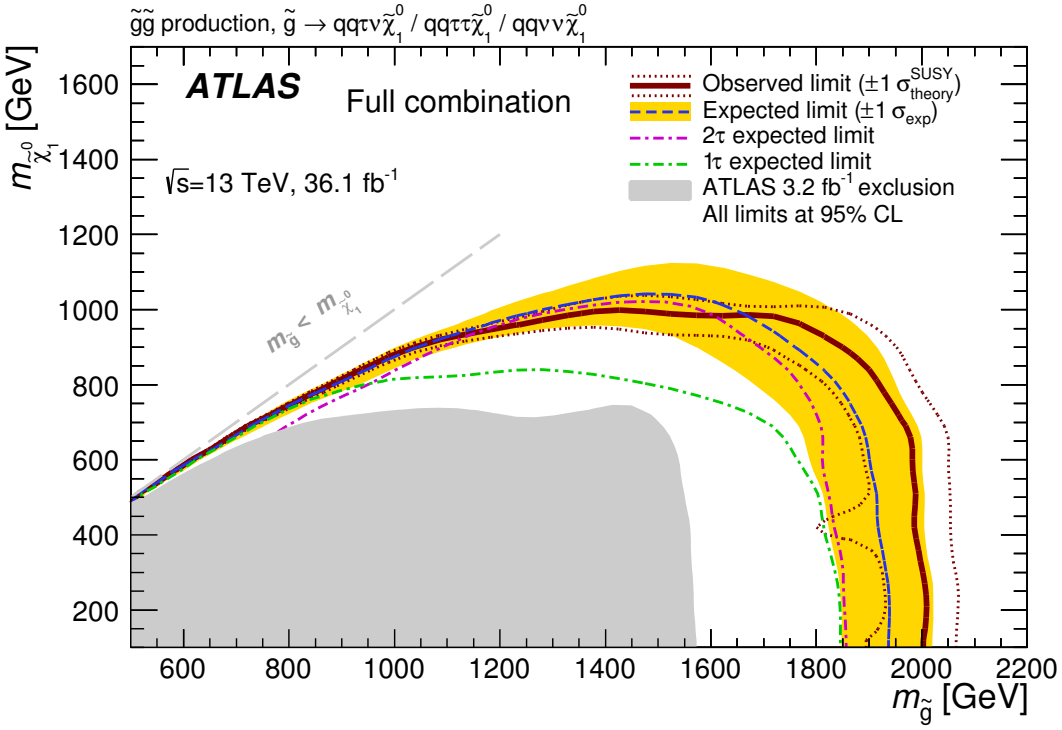

Figure 8.11: Exclusion contours at the 95% confidence level for the simplified model of gluino pair-production [8]. At each point, the result of either the single-bin combination of both channels (cf. fig. 8.7(a)) or the combination of the single-bin 1τ SRs with the 2τ Multibin SR (cf. fig. 8.7(b)) are chosen based on the value of $CL_S^{exp.}$. The red solid line and the blue dashed line correspond to the observed and median expected limits, respectively. The yellow band shows the one-standard-deviation spread of the expected limits around the median. The effect of signal cross-section uncertainties on the observed limits is shown as red dotted lines. The magenta and green dashed lines present the individual channel median expected limits as provided by figs. 8.6(a) and 8.6(c) in appendix A.5 The inward fluctuation of the -1σ observed limit line originates from the method employed to perform the combination. The previous ATLAS result [9] obtained with 3.2 fb^{-1} of $\sqrt{s} = 13$ TeV data is shown as a grey filled area.

8.2.2 Limits on the GMSB Model

Limits on the two free parameters of the studied GMSB model, Λ and $\tan\beta$, are firstly set in the only signal region that specifically addresses the expected GMSB signatures, the GMSB SR of the 2τ channel. The results of the exclusion fit in the GMSB SR are depicted in fig. 8.12.

Already this single signal region is able to extend the expected upper limit by ≈ 20 TeV in Λ for all values of $\tan\beta$ with respect to the earlier observed result, keeping a similar shape in $\tan\beta$. The difference of the presented GMSB SR with respect to its predecessor in [9], depicted as the grey filled area in fig. 8.12, ($m_{\mathrm{T}}^{\tau_1} + m_{\mathrm{T}}^{\tau_2} > 150$ GeV, $H_{\mathrm{T}} > 1\,700$ GeV) is small, rendering the increased amount of available data driving contributor to the improvement of the limits. The weaker limit on Λ for lower values of $\tan\beta$ arises from the lower number of expected τ-leptons in this Co-NLSP region, cf. section 2.2.2. Fewer τ-leptons being produced by the signal model results in even fewer reconstructed ones, lowering the efficiency of a 2τ-selection in this part of parameter-space.

Due to the sensitivity of this analysis to higher values of Λ with respect to [9, 13], not only gluino production is relevant at a hadron collider such as LHC, but also the production of squarks starts to contribute (cf. section 2.2.2). In fact, the production of squark pairs or a squark in association with a gluino is far more abundant in the 2τ GMSB SR than gluino pair production as can be inferred from

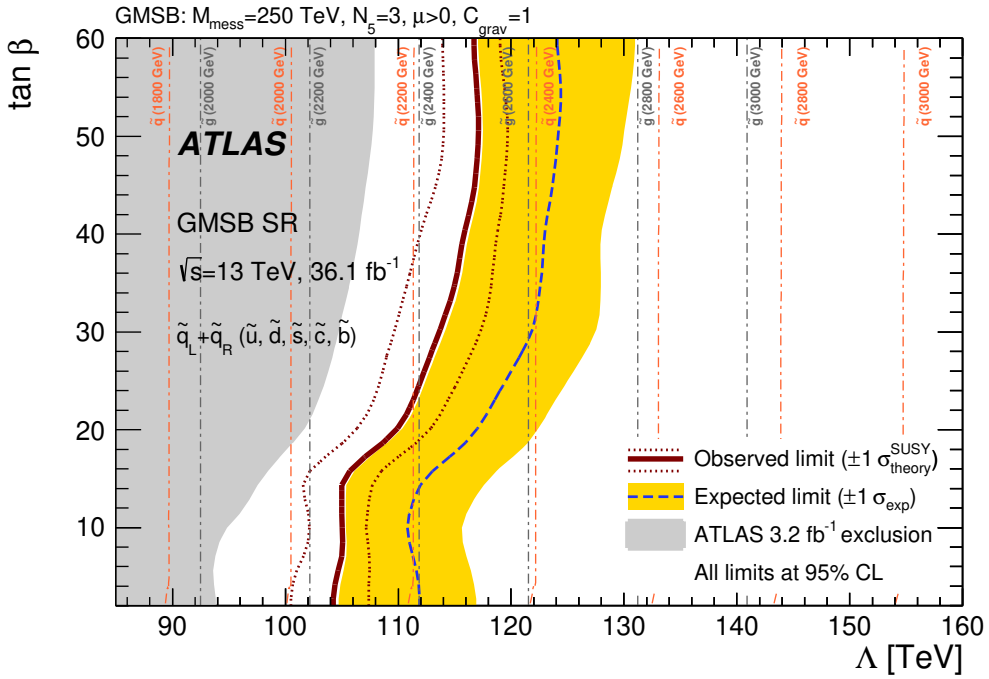

Figure 8.12: Exclusion contours at the 95% confidence level for the GMSB model in the 2τ GMSB SR [8]. The red solid line and the blue dashed line correspond to the observed and median expected limits. The yellow band shows the one-standard-deviation spread of the expected limits around the median. The effect of signal cross-section uncertainties on the observed limits is shown as red dotted lines. The grey and orange dashed lines indicate the masses of gluinos and mass-degenerate squarks, respectively. The previous ATLAS result [9] obtained with 3.2 fb^{-1} of $\sqrt{s} = 13$ TeV data is shown as a grey filled area.

fig. 8.13. In addition to the masses of gluinos which would be produced in the studied GMSB model, the masses of the 10-fold degenerate squarks are indicated in fig. 8.12.

Although no other signal region is specifically designed to search for GMSB signals, the combination of multiple different SRs in one combined fit has proven to be an effective measure to improve sensitivity further (cf. section 8.2.1). First, a combination of the GMSB SR with the 2τ compressed SR into a total 2τ result is performed. Moreover, a combination with the two 1τ SRs can be performed to gain additional sensitivity to signatures with only one reconstructed τ-lepton. Simultaneous fits of all of these configurations are possible due to the mutual exclusiveness of all involved SRs. The limit contours for the individual signal channel combinations in the GMSB parameter-plane are depicted in fig. A.23, the full combination of the 1τ channel and the 2τ channel signal regions is provided in fig. 8.14.

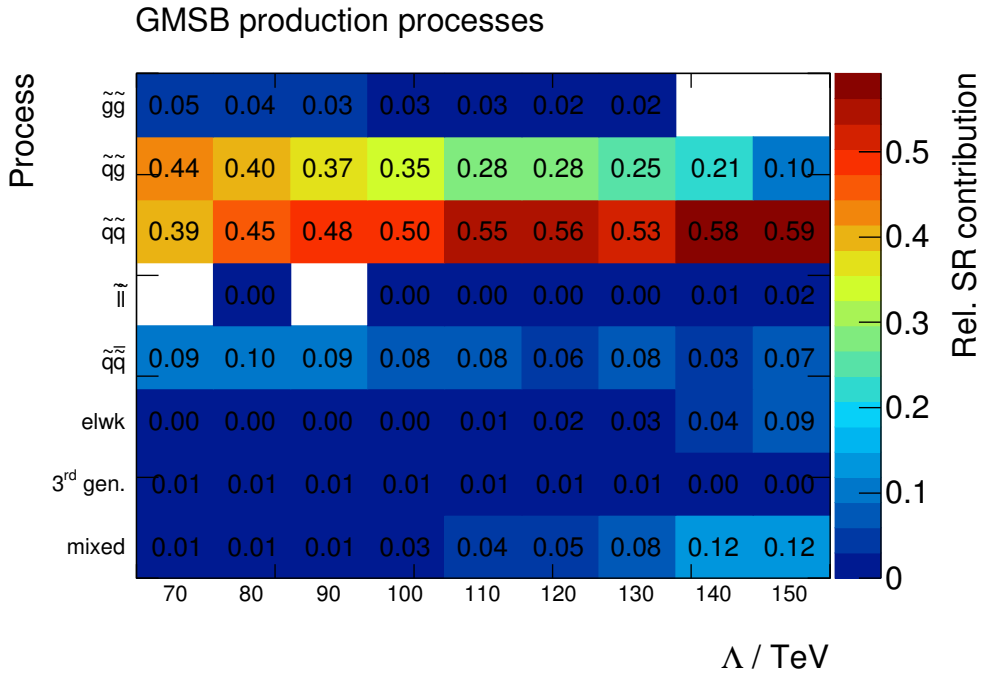

Figure 8.13: Relative contributions of the different production process over the GMSB parameter grid in the GMSB SR of the 2τ channel. $\tilde{g}\tilde{g}$ corresponds to gluino pair-production, $\tilde{q}\tilde{g}$ to squark–gluino production, $\tilde{q}\tilde{q}$ to squark–squark production (including sbottom quarks), $\tilde{l}\tilde{l}$ to slepton pair-production (including third generation sleptons and all sneutrinos), $\tilde{q}\bar{\tilde{q}}$ to squark–antisquark production (including sbottom quarks), *elwk* to gaugino production (including charged and neutral ones, across all generations), 3^{rd} *gen.* to stop quark production (including antisquarks, across both generations), and *mixed* to gaugino-squark and gaugino-gluino production (including antisquarks and sbottom quarks, across all generations).

While the 1τ combination shows the expected weaker limit with respect to the 2τ channel, the latter result benefits from the additional information contributed by the compressed SR already. As for the simplified model combination, the simultaneous fit of the four mutually exclusive SRs in fig. 8.14 gives a result which is stronger than the individual channel results. Once more, the benefit of combining different results on the signal model which individually would not allow for an exclusion statement is clearly visible along the full available range of $\tan\beta$. The original weakness of the 2τ GMSB SR at low values of $\tan\beta$ due to fewer reconstructible τ-leptons in the Co-NLSP regime is partially mitigated by the influence of the 1τ SRs and the compressed 2τ SR. For high Λ, the sensitivity is limited by the production cross-section contribution from the strong interaction.

While the analysis is mainly sensitive to squark and gluino production, the total GMSB production cross section for high Λ is dominated by electroweak production modes as depicted in fig. A.1 and outlined in section 2.2.2. As a result, the current limits on the model parameters and corresponding particle masses can be improved to $\Lambda > 110\,\text{TeV}$ for the full range of simulated values of $2 \leq \tan\beta \leq 60$. Above the Co-NLSP regime of $\tan\beta > 30$, the limit is even stronger: $\Lambda > 120\,\text{GeV}$. These values correspond to upper limits on the gluino (squark) mass of $m(\tilde{g}) > 2\,350\,\text{GeV}$ ($m(\tilde{q}) > 2\,200\,\text{GeV}$) for $2 \leq \tan\beta \leq 60$ and $m(\tilde{g}) > 2\,600\,\text{GeV}$ ($m(\tilde{q}) > 2\,300\,\text{GeV}$) for $\tan\beta > 30$.

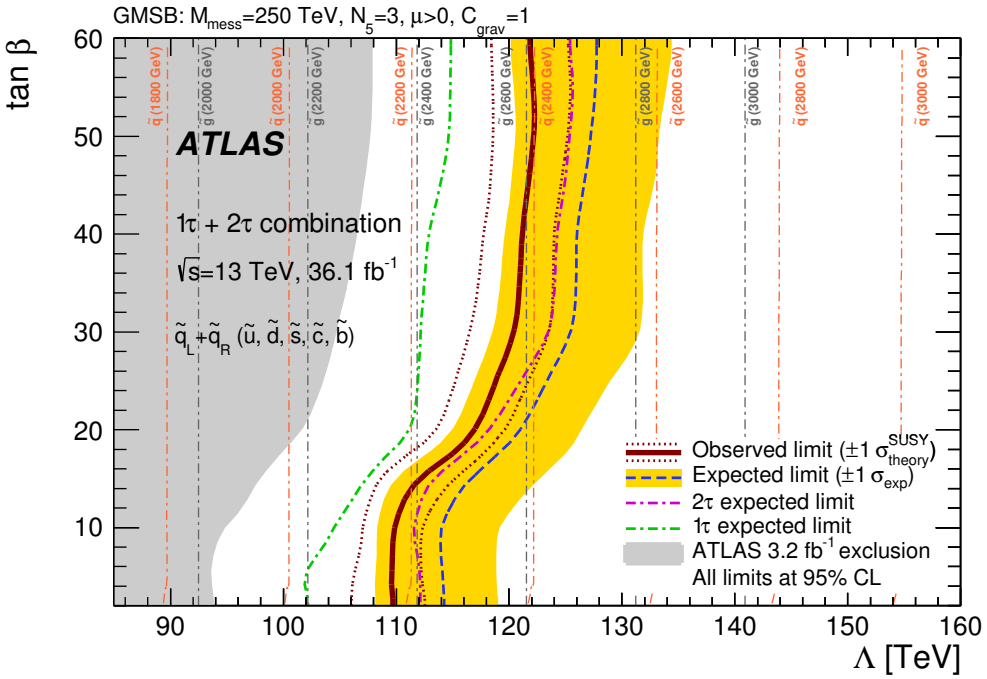

Figure 8.14: Exclusion contours at the 95% confidence level for the GMSB model [8]. The red solid line and the blue dashed line correspond to the observed and median expected limits, respectively, for the combination of the 1τ and 2τ channels. The combination is realised by a simultaneous fit of the individual, mutually exclusive SRs, the 1τ compressed and medium-mass SRs, and the 2τ compressed and GMSB SRs. The yellow band shows the one-standard-deviation spread of the expected limits around the median. The effect of signal cross-section uncertainties on the observed limits is shown as red dotted lines. The grey and orange dashed lines indicate the masses of gluinos and mass-degenerate squarks, respectively. The magenta and green dashed lines present the individual channel median expected limits as provided by figs. A.23(a) and A.23(b) in appendix A.5. The previous ATLAS result [9] obtained with 3.2 fb^{-1} of $\sqrt{s} = 13\,\text{TeV}$ data is shown as a grey filled area.

8.3 Conclusions and outlook

The presented analysis has obtained a multitude of different results, all of which representing significant improvements with respect to its predecessor of the early $\sqrt{s} = 13\,\text{TeV}$ ATLAS data-taking period [9]. The newly developed mutual background estimation allows for the simultaneous fit of multiple signal regions across both signal channels and a more robust prediction of the Standard Model background. Since no significant excess of observed data over the background prediction has been found, limits have been set on the defining parameters of both studied signal models as well as the general, model-independent, parameters of the evaluated signal regions. For both models, the upper limits on the parameters have been significantly improved, giving stronger limits. The newly introduced multibin signal region in the 2τ channel has been found to strongly improve both the confidence in the stated exclusions as well as to provide stronger upper limits on the visible model production cross-sections. Its increased versatility with respect to more exclusive single-bin signal regions can hence be considered proven, rendering this approach most prosperous for future searches.

Among aspects not considered in this analysis is a general issue of simplified models. The influence of other model parameters such as, in the case of the simplified model of gluino pair-production, the masses of the intermediate gauginos and tau sleptons/sneutrinos. Studies based only on two model parameters with fixed values for other important ones rely on the assumption that changes of these other, so-called *hidden* parameters neither influence the acceptance nor the selection efficiency of the analysis. Earlier studies both for the $\sqrt{s} = 8\,\text{TeV}$ analysis [99] and the early $\sqrt{s} = 13\,\text{TeV}$ exploration analysis [233], however, have shown a non-negligible influence of such hidden parameters. A possible solution are maps of the acceptance and efficiency for variations of these parameters to account for otherwise neglected effects and to hence provide better results.

The latter is also of particular interest to designers of new models of SUSY or beyond standard model physics in general. A common approach to find areas of phase-space into which new models could still fit, are re-interpretations of existent analysis results. They are usually performed by extrapolating published results to not yet studied scenarios and a subsequent evaluation of the predicted findings. Two frequently used toolkits for such re-interpretations are `SmodelS` [234] and `CheckMATE` [235, 236]. While `SmodelS` uses upper limit results on the production cross-sections and maps of the acceptance and efficiency to extrapolate existent results to new regions of phase-space, `CheckMATE` requires different inputs. Here, overviews of the total yields in the signal regions as well as the statistical and systematical uncertainties are used, while yields at the different stages of selection for each SR are used for validation. The additionally required maps of acceptance and efficiency for the analysis presented here are provided in figs. A.20 to A.22 and A.24 to A.26 of appendix A.5, while the yields of the signal benchmark scenarios at each selection step are summarised in tables A.15 to A.17 ibid..

CHAPTER 9

Summary and Conclusions

The well established and understood Standard Model of particle physics is a successful theory of the fundamental building blocks of matter and their interactions. Despite its predictive power and the high precision it has been tested to, the Standard Model is far from being the ultimate theory of the microcosm of elementary particles. A multitude of different measurements as well as theoretical considerations rather indicate that it is the low-energy approximation of some higher-order model. Supersymmetry (SUSY) is one of the best motivated and highly sought theories the Standard Model could be imbedded into. The ATLAS experiment at the Large Hadron Collider poses a unique experimental environment to search for new particles predicted by SUSY. Squarks and gluinos are the strongly interacting partners particles of quarks and gluons, and they are expected to be produced at the highest rate amongst the new particles. A search for squarks and gluinos using their promising decay signatures involving hadronically decaying τ-leptons and missing transverse momentum based on 36.1 fb^{-1} of data recorded in $\sqrt{s} = 13\,\text{TeV}$ proton–proton collisions has been presented. Two representations of SUSY are searched for, one model assuming a specific gauge mediated symmetric breaking mechanism, the other being a simplified model of gluino pair-production. The search is carried out in six regions of phase-space, five of which use a well-established approach of result extraction based only on the total number of expected SUSY and predicted Standard Model events in single signal regions. The sixth signal region exploits the large amount of available data to base the result extraction on an approach novel in the search for these signatures. The differences in the spectra of a discriminating variable between the expected SUSY signal and the predicted Standard Model background is used to search for deviations from the Standard Model prediction. This approach provides comparably strong mass limits but at much higher confidence levels, which directly translates into stronger upper limits on production cross-sections of the studied signal models. Equally powerful results from other extraction approaches would require substantially more data. A sophisticated estimation technique is developed to assess the Standard Model processes entering the analysis across all signal regions simultaneously. This mutual background estimation allows for a simultaneous result extraction in multiple signal regions. It thus enhances the predictive power of the analysis substantially. For all signal regions, the normalisations of the MC-simulated background from electroweak processes and the data-driven estimation of the multi-jet background are estimated in one common set of control regions. This procedure corrects for various shortcomings of the background modelling, particularly the simulation of quark and gluon jets being misidentified as τ-leptons.

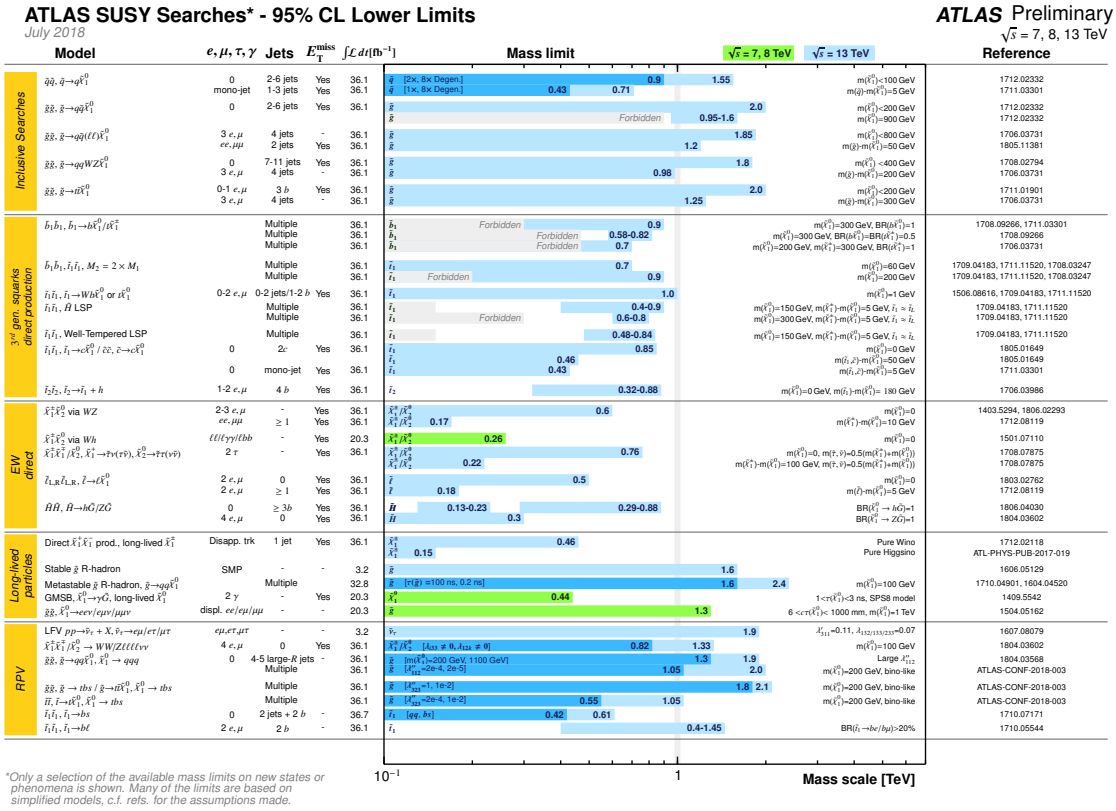

Figure 9.1: Comparison of the reaches of limits in ATLAS searches for SUSY to date [237]. The results on the simplified model of gluino pair-production obtained in this analysis are upper limits of $m(\tilde{g}) > 2\,000$ GeV for low values of $m(\tilde{\chi}_1^0)$ and $m(\tilde{g}) > 1\,400$ GeV for values of $m(\tilde{\chi}_1^0)$ around 1 000 GeV. Results on comparable models are depicted in the top box of *Inclusive Searches*.

The compatibility of the corrected background prediction with the observed data in the signal regions is found to be high – no significant hints towards the presence of any signal can be claimed. The lack of excess of the observation over the background prediction is cast into upper limits on the excluded number of events of any possible model of new physics in all signal regions. These fiducial limits range from 3.2 to 49.5 events at a confidence level of 95% and are valid for in respective signal regions for the studied integrated luminosity of 36.1 fb^{-1}. Statements about the realisations of the SUSY models searched for are based on upper limits on the free model parameters at 95% confidence level. In the simplified model of gluino pair-production, gluino masses up to 2 000 GeV can be excluded for low values of the mass of lightest neutralino, the LSP. Around gluino masses of 1 400 GeV, LSP masses up 1 000 GeV can be excluded. For the model of GMSB, values of the supersymmetry-breaking scale Λ are excluded below 110 TeV for all values of $\tan\beta$ in the range $2 \leq \tan\beta \leq 60$, and below 120 TeV for $\tan\beta > 30$. These values can be translated into upper limits on the gluino (squark) mass of $m(\tilde{g}) > 2\,350$ GeV ($m(\tilde{q}) > 2\,200$ GeV) and $m(\tilde{g}) > 2\,600$ GeV ($m(\tilde{q}) > 2\,400$ GeV), respectively. These numbers render the presented analysis competitive to the strongest limits on SUSY published by the ATLAS collaboration to date (cf. fig. 9.1). The results obtained in the search for the simplified model of gluino pair-production are of particular interest to phenomenologists and other model builders. They can be used to design more promising models which are specifically tailored to the remaining parameter-space of SUSY.

Certain shortcomings of the presented analysis limit its predictive power and hold room for future improvement. The fact that the 2τ multibin SR is not mutually exclusive with respect to the compressed SR of the 2τ prohibits their simultaneous fit and hence restricts mutual benefits. Furthermore, the design of a multi-bin SR for the 1τ channel is a promising prospect. The large increase in the confidence level with which exclusions are made due to the influence of the 2τ multibin SR strongly motivates the design of multi-bin signal regions also for the 1τ channel. A combination of the two is expected to yield even more powerful results without the expense of longer periods of data-taking. A prosperous yet challenging aspect of optimisation lies with the fitting procedure in general. Instead of obtaining the background normalisation in discrete control regions and applying it in discrete signal regions, the simultaneous fit of all Standard Model backgrounds and signals in a large number of bins of multiple discriminating variables would address several issues at once. Limitations in statistics due to the discrete nature of the individual regions of phase-space as well as effects originating from the extrapolation between control and signal regions would be reduced if not avoided. Moreover, the influence of systematic uncertainties could be studied in a less constrained way if the auxiliary measurements made to constrain them would be part of the global fit of the analysis itself. The generally necessary deep understanding of the Standard Model simulations as well as of the complex fit setup pose make this endeavour challenging.

Although the branching fraction of leptonic decays of the τ-lepton is smaller than the hadronic one, the inclusion of signal channels based on leptonic τ-lepton decays as in the corresponding $\sqrt{s} = 8\,\text{TeV}$ analysis [13] holds additional sensitivity. However, the necessary efforts of a background estimation mutual to all signal channels would be substantially more complicated due to the muon-based background estimation of jets being misidentified as τ-leptons presented here. First exploration studies have already been performed [217, 218].

The casting of results to input for new models of SUSY or new physics in general is not the only way to perform a reinterpretation of the obtained results. The designed signal regions exhibit strong exclusion capabilities as expressed by the model-independent limits. Using the full analysis setup to study different signal models is hence a manifest idea. While for the $\sqrt{s} = 8\,\text{TeV}$ dataset of ATLAS and the corresponding analysis [13] such a re-interpretation has already been performed successfully, e.g. providing exclusions on the pMSSM model in general [219], similar efforts are planned for the available $\sqrt{s} = 13\,\text{TeV}$ dataset. A first step is the analysis of the full available $\sqrt{s} = 13\,\text{TeV}$ dataset, including data taken in 2017 and 2018[1]. Here, certain of the aforementioned optimisation steps can already be included. In addition to a re-interpretation in the context of different models of SUSY, entirely different models of physics beyond the Standard Model can be studied using the presented analysis – e.g. models of leptoquarks [238]. First exploration studies of a search for leptoquark signals in the context of the presented analysis have been performed successfully [239]. While no discovery of squarks or gluinos can be claimed, the search has still been successful. Insight into the analysis design and result extraction procedures, as well as into the studied physics processes has been gained and represents a promising starting point for future developments in the search for SUSY and beyond.

[1] To date, the total recorded $\sqrt{s} = 13\,\text{TeV}$ dataset of ATLAS comprises $136\,\text{fb}^{-1}$. The recorded dataset used in the presented analysis comprised a total of $36.1\,\text{fb}^{-1}$.

Bibliography

[1] S. L. Glashow, *Partial Symmetries of Weak Interactions*, Nucl. Phys. **22** (1961) 579 (cit. on pp. 1, 6).

[2] A. Salam and J. C. Ward, *Electromagnetic and weak interactions*, Phys. Lett. **13** (1964) 168 (cit. on pp. 1, 6).

[3] S. Weinberg, *A Model of Leptons*, Phys. Rev. Lett. **19** (1967) 1264 (cit. on pp. 1, 6).

[4] G. Aad et al.,
Measurements of the Higgs boson production and decay rates and constraints on its couplings from a combined ATLAS and CMS analysis of the LHC pp collision data at $\sqrt{s} = 7$ *and 8 TeV*,
JHEP **08** (2016) 045, arXiv: 1606.02266 [hep-ex] (cit. on pp. 1, 14, 16, 22).

[5] L. Evans and P. Bryant, *LHC Machine*, JINST **3** (2008) S08001 (cit. on pp. 1, 37).

[6] G. Aad et al., *The ATLAS Experiment at the CERN Large Hadron Collider*,
JINST **3** (2008) S08003 (cit. on pp. 1, 40).

[7] S. Chatrchyan et al., *The CMS Experiment at the CERN LHC*, JINST **3** (2008) S08004 (cit. on pp. 1, 39).

[8] M. Aaboud et al.,
Search for squarks and gluinos in final states with hadronically decaying τ*-leptons, jets, and missing transverse momentum using pp collisions at* $\sqrt{s} = 13$ *TeV with the ATLAS detector*,
Phys. Rev. **D99** (2019) 012009, arXiv: 1808.06358 [hep-ex] (cit. on pp. 2, 66–68, 80, 82, 85, 108, 111, 122–124, 131, 141–144, 146, 149, 151, 152, 155–157, 159, 194, 195, 205–218).

[9] M. Aaboud et al., *Search for squarks and gluinos in events with hadronically decaying tau leptons, jets and missing transverse momentum in proton–proton collisions at* $\sqrt{s} = 13$ *TeV recorded with the ATLAS detector*, Eur. Phys. J. **C76** (2016) 683, arXiv: 1607.05979 [hep-ex] (cit. on pp. 2, 27–29, 34, 35, 66, 79–84, 87, 88, 92, 95, 96, 98, 101, 104, 111, 113, 114, 118, 127, 128, 131, 136, 138, 148–152, 155–157, 159, 205–208, 212, 225, 226, 231).

[10] M. Aaboud et al., *Search for new phenomena with large jet multiplicities and missing transverse momentum using large-radius jets and flavour-tagging at ATLAS in 13 TeV pp collisions*,
JHEP **12** (2017) 034, arXiv: 1708.02794 [hep-ex] (cit. on p. 2).

[11] M. Aaboud et al., *Search for supersymmetry in final states with two same-sign or three leptons and jets using 36* fb^{-1} *of* $\sqrt{s} = 13$ *TeV pp collision data with the ATLAS detector*,
JHEP **09** (2017) 084, arXiv: 1706.03731 [hep-ex] (cit. on p. 2).

[12] G. Aad et al.,
Search for Supersymmetry in Events with Large Missing Transverse Momentum, Jets, and at Least One Tau Lepton in 7 TeV Proton-Proton Collision Data with the ATLAS Detector,
Eur. Phys. J. **C72** (2012) 2215, arXiv: 1210.1314 [hep-ex] (cit. on pp. 2, 27, 79, 80, 136).

[13] ATLAS Collaboration,
Search for supersymmetry in events with large missing transverse momentum, jets, and at least one tau lepton in 20 fb^{-1} of $\sqrt{s}$ = 8 TeV proton–proton collision data with the ATLAS detector,
JHEP **09** (2014) 103, arXiv: 1407.0603 [hep-ex]
(cit. on pp. 2, 27, 28, 71, 76, 79–82, 85, 87, 101, 111, 113, 136, 138, 150, 156, 163).

[14] F. Halzen and A. D. Martin,
Quarks and Leptons: An Introductory Course in Modern Particle Physics,
Wiley India Pvt. Limited, 2008, ISBN: 978-8-126-51656-8 (cit. on p. 3).

[15] S. Schaepe, *Search for Supersymmetry in Tau Lepton Final States with the ATLAS Detector*,
PhD thesis: Bonn U., 2015, URL: http://hss.ulb.uni-bonn.de/2016/4238/4238.htm
(cit. on pp. 3, 6, 7, 26, 37, 42, 62, 71, 75–78, 104, 113, 125, 127, 132).

[16] S. P. Martin, *A Supersymmetry primer*,
(1997) 1, [Adv. Ser. Direct. High Energy Phys.18,1(1998)], arXiv: hep-ph/9709356 [hep-ph]
(cit. on pp. 3, 19–22, 25, 29, 30).

[17] A. Purcell, *The Standard Model, infographic*, 2012,
URL: https://cds.cern.ch/record/1473657/files/SMinfographic_image.png
(visited on 24/07/2018) (cit. on p. 4).

[18] D. Griffiths, *Introduction to Elementary Particles*, John Wiley & Sons, 2008,
ISBN: 978-3-527-61847-7 (cit. on p. 4).

[19] P. A. M. Dirac, *Quantum theory of emission and absorption of radiation*,
Proc. Roy. Soc. Lond. **A114** (1927) 243 (cit. on p. 4).

[20] J. D. Jackson, *Klassische Elektrodynamik*, Walter de Gruyter, 2014, ISBN: 978-3-110-33447-0
(cit. on p. 5).

[21] W. E. Lamb and R. C. Retherford, *Fine Structure of the Hydrogen Atom by a Microwave Method*,
Phys. Rev. **72** (1947) 241 (cit. on p. 6).

[22] C. S. Wu et al., *Experimental Test of Parity Conservation in Beta Decay*,
Phys. Rev. **105** (1957) 1413 (cit. on p. 6).

[23] M. Goldhaber, L. Grodzins and A. W. Sunyar, *Helicity of Neutrinos*, Phys. Rev. **109** (1958) 1015
(cit. on p. 6).

[24] N. Cabibbo, *Unitary Symmetry and Leptonic Decays*,
Phys. Rev. Lett. **10** (1963) 531, [,648(1963)] (cit. on p. 8).

[25] M. Kobayashi and T. Maskawa, *CP Violation in the Renormalizable Theory of Weak Interaction*,
Prog. Theor. Phys. **49** (1973) 652 (cit. on p. 8).

[26] M. Gell-Mann, *A Schematic Model of Baryons and Mesons*, Phys. Lett. **8** (1964) 214
(cit. on p. 8).

[27] G. Zweig, "An SU(3) model for strong interaction symmetry and its breaking. Version 2",
Developments in the quark theory of hadrons. Vol. 1. 1964–1978,
ed. by D. Lichtenberg and S. P. Rosen, 1964 22,
URL: http://inspirehep.net/record/4674/files/cern-th-412.pdf (cit. on p. 8).

[28] M. Gell-Mann and Y. Ne'eman, *The eightfold way*, W.A. Benjamin, 1964 (cit. on p. 8).

[29] D. Mendelejew, *Über die Beziehung der Eigenschaften zu den Atomgewichten der Elemente*,
Zeitschrift für Chemie (1869) 405 (cit. on p. 8).

[30] V. E. Barnes et al., *Observation of a Hyperon with Strangeness -3*, Phys. Rev. Lett. **12** (1964) 204 (cit. on p. 8).

[31] M. Y. Han and Y. Nambu, *Three Triplet Model with Double SU(3) Symmetry*, Phys. Rev. **139** (1965) B1006, [,187(1965)] (cit. on p. 8).

[32] H. Fritzsch, M. Gell-Mann and H. Leutwyler, *Advantages of the Color Octet Gluon Picture*, Phys. Lett. **47B** (1973) 365 (cit. on p. 9).

[33] D. J. Gross and F. Wilczek, *Ultraviolet Behavior of Nonabelian Gauge Theories*, Phys. Rev. Lett. **30** (1973) 1343, [,271(1973)] (cit. on p. 9).

[34] H. D. Politzer, *Reliable Perturbative Results for Strong Interactions?*, Phys. Rev. Lett. **30** (1973) 1346, [,274(1973)] (cit. on p. 9).

[35] U. Loring et al., *Relativistic quark models of baryons with instantaneous forces: Theoretical background*, Eur. Phys. J. **A10** (2001) 309, arXiv: hep-ph/0103287 [hep-ph] (cit. on p. 10).

[36] U. Loring, B. C. Metsch and H. R. Petry, *The Light baryon spectrum in a relativistic quark model with instanton induced quark forces: The Nonstrange baryon spectrum and ground states*, Eur. Phys. J. **A10** (2001) 395, arXiv: hep-ph/0103289 [hep-ph] (cit. on p. 10).

[37] U. Loring, B. C. Metsch and H. R. Petry, *The Light baryon spectrum in a relativistic quark model with instanton induced quark forces: The Strange baryon spectrum*, Eur. Phys. J. **A10** (2001) 447, arXiv: hep-ph/0103290 [hep-ph] (cit. on p. 10).

[38] C. Patrignani et al., *Review of Particle Physics*, Chin. Phys. **C40** (2016) 100001 (cit. on pp. 10, 11, 15–18, 22, 42, 54, 83, 107).

[39] J. Rojo et al., *The PDF4LHC report on PDFs and LHC data: Results from Run I and preparation for Run II*, J. Phys. **G42** (2015) 103103, arXiv: 1507.00556 [hep-ph] (cit. on p. 11).

[40] P. W. Higgs, *Broken symmetries, massless particles and gauge fields*, Phys. Lett. **12** (1964) 132 (cit. on p. 11).

[41] P. W. Higgs, *Broken Symmetries and the Masses of Gauge Bosons*, Phys. Rev. Lett. **13** (1964) 508, [,160(1964)] (cit. on p. 11).

[42] P. W. Higgs, *Spontaneous Symmetry Breakdown without Massless Bosons*, Phys. Rev. **145** (1966) 1156 (cit. on p. 11).

[43] F. Englert and R. Brout, *Broken Symmetry and the Mass of Gauge Vector Mesons*, Phys. Rev. Lett. **13** (1964) 321, [,157(1964)] (cit. on p. 11).

[44] *How to draw this particular Mexican hat potential*, 2015, URL: https://tex.stackexchange.com/questions/229178/how-to-draw-this-particular-mexican-hat-potential (visited on 07/09/2018) (cit. on p. 12).

[45] ATLAS Collaboration, *Cross-section measurements of the Higgs boson decaying to a pair of tau leptons in proton–proton collisions at* $\sqrt{s} = 13$ *TeV with the ATLAS detector*, (2018) (cit. on p. 14).

[46] N. Wermes, *Cartoon illustration of hadronic tau-lepton decay*, 2014, URL: https://twiki.cern.ch/twiki/pub/AtlasProtected/TauWG/TauDecay_NorbertWermes.png (visited on 24/08/2018) (cit. on p. 15).

[47] B. Andersson et al., *Parton Fragmentation and String Dynamics*, Phys. Rept. **97** (1983) 31 (cit. on p. 14).

[48] F. Abe et al., *Observation of top quark production in $\bar{p}p$ collisions*, Phys. Rev. Lett. **74** (1995) 2626, arXiv: hep-ex/9503002 [hep-ex] (cit. on p. 16).

[49] S. Abachi et al., *Search for high mass top quark production in $p\bar{p}$ collisions at $\sqrt{s} = 1.8$ TeV*, Phys. Rev. Lett. **74** (1995) 2422, arXiv: hep-ex/9411001 [hep-ex] (cit. on p. 16).

[50] K. Kodama et al., *Observation of tau neutrino interactions*, Phys. Lett. **B504** (2001) 218, arXiv: hep-ex/0012035 [hep-ex] (cit. on p. 16).

[51] S. Weinberg, *Implications of Dynamical Symmetry Breaking*, Phys. Rev. **D13** (1976) 974, [Addendum: Phys. Rev.D19,1277(1979)] (cit. on p. 17).

[52] E. Gildener, *Gauge Symmetry Hierarchies*, Phys. Rev. **D14** (1976) 1667 (cit. on p. 17).

[53] S. Weinberg, *Implications of Dynamical Symmetry Breaking*, Phys. Rev. **D13** (1976) 974, [Addendum: Phys. Rev.D19,1277(1979)] (cit. on p. 17).

[54] L. Susskind, *Dynamics of Spontaneous Symmetry Breaking in the Weinberg-Salam Theory*, Phys. Rev. **D20** (1979) 2619 (cit. on p. 17).

[55] S. Dimopoulos and H. Georgi, *Softly Broken Supersymmetry and SU(5)*, Nucl. Phys. **B193** (1981) 150 (cit. on p. 17).

[56] E. Witten, *Dynamical Breaking of Supersymmetry*, Nucl. Phys. **B188** (1981) 513 (cit. on p. 17).

[57] M. Dine, W. Fischler and M. Srednicki, *Supersymmetric Technicolor*, Nucl. Phys. **B189** (1981) 575 (cit. on p. 17).

[58] S. Dimopoulos and S. Raby, *Supercolor*, Nucl. Phys. **B192** (1981) 353 (cit. on p. 17).

[59] N. Sakai, *Naturalness in Supersymmetric Guts*, Z. Phys. **C11** (1981) 153 (cit. on pp. 17, 18).

[60] R. K. Kaul and P. Majumdar, *Cancellation of Quadratically Divergent Mass Corrections in Globally Supersymmetric Spontaneously Broken Gauge Theories*, Nucl. Phys. **B199** (1982) 36 (cit. on p. 17).

[61] H. Goldberg, *Constraint on the Photino Mass from Cosmology*, Phys. Rev. Lett. **50** (1983) 1419, [,219(1983)] (cit. on pp. 18, 23).

[62] J. R. Ellis et al., *Supersymmetric Relics from the Big Bang*, Nucl. Phys. **B238** (1984) 453, [,223(1983)] (cit. on pp. 18, 23).

[63] S. Dimopoulos, S. Raby and F. Wilczek, *Supersymmetry and the Scale of Unification*, Phys. Rev. **D24** (1981) 1681 (cit. on p. 18).

[64] L. E. Ibanez and G. G. Ross, *Low-Energy Predictions in Supersymmetric Grand Unified Theories*, Phys. Lett. **105B** (1981) 439 (cit. on p. 18).

[65] M. B. Einhorn and D. R. T. Jones, *The Weak Mixing Angle and Unification Mass in Supersymmetric SU(5)*, Nucl. Phys. **B196** (1982) 475 (cit. on p. 18).

[66] W. J. Marciano and G. Senjanovic, *Predictions of Supersymmetric Grand Unified Theories*, Phys. Rev. **D25** (1982) 3092 (cit. on p. 18).

[67] C. Giunti, C. W. Kim and U. W. Lee, *Running coupling constants and grand unification models*, Mod. Phys. Lett. **A6** (1991) 1745 (cit. on p. 18).

[68] J. R. Ellis, S. Kelley and D. V. Nanopoulos, *Probing the desert using gauge coupling unification*, Phys. Lett. **B260** (1991) 131 (cit. on p. 18).

[69] U. Amaldi, W. de Boer and H. Furstenau, *Comparison of grand unified theories with electroweak and strong coupling constants measured at LEP*, Phys. Lett. **B260** (1991) 447 (cit. on p. 18).

[70] P. Langacker and M.-x. Luo,
Implications of precision electroweak experiments for M_t, ρ_0, $\sin^2\theta_W$ and grand unification,
Phys. Rev. **D44** (1991) 817 (cit. on p. 18).

[71] I. J. R. Aitchison, *Supersymmetry and the MSSM: An Elementary introduction*, (2005), arXiv: hep-ph/0505105 [hep-ph] (cit. on p. 18).

[72] S. Deser and B. Zumino, *Consistent Supergravity*, Phys. Lett. B **62** (1976) 335 (cit. on pp. 19, 25).

[73] D. Z. Freedman, P. van Nieuwenhuizen and S. Ferrara,
Progress Toward a Theory of Supergravity, Phys. Rev. D **13** (1976) 3214 (cit. on pp. 19, 25).

[74] G. W. Bennett et al.,
Final Report of the Muon E821 Anomalous Magnetic Moment Measurement at BNL,
Phys. Rev. **D73** (2006) 072003, arXiv: hep-ex/0602035 [hep-ex] (cit. on p. 19).

[75] *A Combination of preliminary electroweak measurements and constraints on the standard model*, (2005), arXiv: hep-ex/0511027 [hep-ex] (cit. on p. 19).

[76] M. Huschle et al., *Measurement of the branching ratio of $\bar{B} \to D^{(*)}\tau^-\bar{\nu}_\tau$ relative to $\bar{B} \to D^{(*)}\ell^-\bar{\nu}_\ell$ decays with hadronic tagging at Belle*, Phys. Rev. **D92** (2015) 072014, arXiv: 1507.03233 [hep-ex] (cit. on p. 19).

[77] T. D. Lee, *A Theory of Spontaneous T Violation*, Phys. Rev. **D8** (1973) 1226, [,516(1973)] (cit. on p. 19).

[78] Y. A. Golfand and E. P. Likhtman,
Extension of the Algebra of Poincare Group Generators and Violation of p Invariance,
JETP Lett. **13** (1971) 323, [Pisma Zh. Eksp. Teor. Fiz.13,452(1971)] (cit. on p. 20).

[79] D. V. Volkov and V. P. Akulov, *Is the Neutrino a Goldstone Particle?*,
Phys. Lett. B **46** (1973) 109 (cit. on p. 20).

[80] J. Wess and B. Zumino, *Supergauge Transformations in Four-Dimensions*,
Nucl. Phys. B **70** (1974) 39 (cit. on p. 20).

[81] J. Wess and B. Zumino, *Supergauge Invariant Extension of Quantum Electrodynamics*,
Nucl. Phys. B **78** (1974) 1 (cit. on p. 20).

[82] S. Ferrara and B. Zumino, *Supergauge Invariant Yang-Mills Theories*,
Nucl. Phys. B **79** (1974) 413 (cit. on p. 20).

[83] A. Salam and J. A. Strathdee, *Supersymmetry and Nonabelian Gauges*,
Phys. Lett. B **51** (1974) 353 (cit. on p. 20).

[84] R. Haag, J. T. Lopuszanski and M. Sohnius,
All Possible Generators of Supersymmetries of the s Matrix,
Nucl. Phys. **B88** (1975) 257, [,257(1974)] (cit. on p. 20).

[85] S. R. Coleman and J. Mandula, *All Possible Symmetries of the S Matrix*,
Phys. Rev. **159** (1967) 1251 (cit. on p. 20).

[86] P. Fayet, *Supersymmetry and Weak, Electromagnetic and Strong Interactions*, Phys. Lett. B **64** (1976) 159 (cit. on p. 20).

[87] P. Fayet, *Spontaneously Broken Supersymmetric Theories of Weak, Electromagnetic and Strong Interactions*, Phys. Lett. B **69** (1977) 489 (cit. on p. 20).

[88] H. P. Nilles, *Supersymmetry, Supergravity and Particle Physics*, Phys. Rept. **110** (1984) 1 (cit. on p. 20).

[89] S. Dimopoulos and D. W. Sutter, *The Supersymmetric flavor problem*, Nucl. Phys. **B452** (1995) 496, arXiv: hep-ph/9504415 [hep-ph] (cit. on p. 24).

[90] M. Dine and W. Fischler, *A Phenomenological Model of Particle Physics Based on Supersymmetry*, Phys. Lett. B **110** (1982) 227 (cit. on p. 25).

[91] L. Alvarez-Gaume, M. Claudson and M. B. Wise, *Low-Energy Supersymmetry*, Nucl. Phys. B **207** (1982) 96 (cit. on p. 25).

[92] C. R. Nappi and B. A. Ovrut, *Supersymmetric Extension of the SU(3) x SU(2) x U(1) Model*, Phys. Lett. B **113** (1982) 175 (cit. on p. 25).

[93] W. Porod and F. Staub, *SPheno 3.1: Extensions including flavour, CP-phases and models beyond the MSSM*, Comput. Phys. Commun. **183** (2012) 2458, arXiv: 1104.1573 [hep-ph] (cit. on pp. 27, 28, 68).

[94] A. Buckley, *PySLHA: a Pythonic interface to SUSY Les Houches Accord data*, Eur. Phys. J. **C75** (2015) 467, arXiv: 1305.4194 [hep-ph] (cit. on pp. 27, 28).

[95] S. P. Martin and J. D. Wells, *Implications of gauge-mediated supersymmetry breaking with vector-like quarks and a 125 GeV Higgs boson*, Phys. Rev. **D86** (2012) 035017, arXiv: 1206.2956 [hep-ph] (cit. on p. 28).

[96] J. Alwall et al., *Searching for Directly Decaying Gluinos at the Tevatron*, Phys. Lett. B **666** (2008) 34, arXiv: 0803.0019 [hep-ph] (cit. on p. 32).

[97] J. Alwall, P. Schuster and N. Toro, *Simplified Models for a First Characterization of New Physics at the LHC*, Phys. Rev. D **79** (2009) 075020, arXiv: 0810.3921 [hep-ph] (cit. on p. 32).

[98] D. Alves et al., *Simplified Models for LHC New Physics Searches*, J. Phys. G **39** (2012) 105005, arXiv: 1105.2838 [hep-ph] (cit. on p. 32).

[99] O. Ricken, *Development and Analysis of Simplified Models in the Search for Supersymmetry with Tau Leptons in the Final State at the ATLAS Experiment*, M.Sc. thesis: Bonn U., 2013, URL: https://web.physik.uni-bonn.de/group/view.php?&group=1&lang=de&c=t&id=44 (cit. on pp. 33, 34, 160, 251).

[100] A. H. Chamseddine, R. L. Arnowitt and P. Nath, *Locally Supersymmetric Grand Unification*, Phys. Rev. Lett. **49** (1982) 970 (cit. on p. 35).

[101] R. Barbieri, S. Ferrara and C. A. Savoy, *Gauge Models with Spontaneously Broken Local Supersymmetry*, Phys. Lett. B **119** (1982) 343 (cit. on p. 35).

[102] G. L. Kane et al., *Study of constrained minimal supersymmetry*, Phys. Rev. D **49** (1994) 6173, arXiv: hep-ph/9312272 (cit. on p. 35).

[103] P. Bechtle et al., *Killing the cMSSM softly*, Eur. Phys. J. **C76** (2016) 96, arXiv: 1508.05951 [hep-ph] (cit. on pp. 35, 36).

[104] A. Djouadi et al., *The Minimal supersymmetric standard model: Group summary report*, 1998, arXiv: hep-ph/9901246 (cit. on p. 35).

[105] C. F. Berger et al., *Supersymmetry Without Prejudice*, JHEP **02** (2009) 023, arXiv: 0812.0980 [hep-ph] (cit. on p. 35).

[106] E. Bagnaschi et al., *Likelihood Analysis of the pMSSM11 in Light of LHC 13-TeV Data*, Eur. Phys. J. **C78** (2018) 256, arXiv: 1710.11091 [hep-ph] (cit. on p. 35).

[107] P. Bechtle et al., *SCYNet: Testing supersymmetric models at the LHC with neural networks*, Eur. Phys. J. **C77** (2017) 707, arXiv: 1703.01309 [hep-ph] (cit. on pp. 35, 36).

[108] K. Schindl, *The PS booster as preinjector for LHC*, Part. Accel. **58** (1997) 63 (cit. on p. 37).

[109] R. Cappi, *The PS in the LHC injector chain*, Part. Accel. **58** (1997) 79 (cit. on p. 37).

[110] P. Collier et al., *The SPS as injector for LHC: Conceptual design*, (1997) (cit. on p. 37).

[111] E. Mobs, *The CERN accelerator complex. Complexe des accélérateurs du CERN*, (2016), General Photo, URL: https://cds.cern.ch/record/2197559 (cit. on p. 38).

[112] T. Behnke et al., *The International Linear Collider Technical Design Report - Volume 1: Executive Summary*, (2013), arXiv: 1306.6327 [physics.acc-ph] (cit. on p. 38).

[113] M. Aicheler et al., *A Multi-TeV Linear Collider Based on CLIC Technology*, (2012) (cit. on p. 38).

[114] *LEP Design Report: Vol.2. The LEP Main Ring*, (1984) (cit. on p. 39).

[115] A. A. Alves Jr. et al., *The LHCb Detector at the LHC*, JINST **3** (2008) S08005 (cit. on p. 39).

[116] K. Aamodt et al., *The ALICE experiment at the CERN LHC*, JINST **3** (2008) S08002 (cit. on p. 39).

[117] J. Pequenao, "Computer generated image of the whole ATLAS detector", 2008, URL: https://cds.cern.ch/record/1095924 (cit. on p. 40).

[118] J. Pequenao, "Computer generated image of the ATLAS inner detector", 2008, URL: https://cds.cern.ch/record/1095926 (cit. on p. 41).

[119] ATLAS Collaboration, *ATLAS Insertable B-Layer Technical Design Report*, ATLAS-TDR-19, 2010, URL: https://cds.cern.ch/record/1291633, *ATLAS Insertable B-Layer Technical Design Report Addendum*, ATLAS-TDR-19-ADD-1, 2012, URL: https://cds.cern.ch/record/1451888 (cit. on p. 41).

[120] E. Abat et al., *The ATLAS Transition Radiation Tracker (TRT) proportional drift tube: Design and performance*, JINST **3** (2008) P02013 (cit. on p. 42).

[121] E. Abat et al., *The ATLAS TRT barrel detector*, JINST **3** (2008) P02014 (cit. on p. 42).

[122] E. Abat et al., *The ATLAS TRT end-cap detectors*, JINST **3** (2008) P10003 (cit. on p. 42).

[123] W. R. Leo, *Techniques for Nuclear and Particle Physics Experiments - A How-to Approach*, Springer Science & Business Media, 2012, ISBN: 978-3-642-57920-2 (cit. on p. 42).

[124] S. Zimmermann, *A search for stable massive particles carrying electric charges in the range of 2e to 6e in proton-proton collisions at $\sqrt{s}$ = 7 TeV recorded with the ATLAS detector at the LHC*, PhD thesis: Bonn U., 2013-04-29, URL: http://inspirehep.net/record/1296592/files/153892130_CERN-THESIS-2013-114.pdf (cit. on p. 42).

[125] J. Pequenao, "Computer Generated image of the ATLAS calorimeter", 2008, URL: https://cds.cern.ch/record/1095927 (cit. on p. 43).

[126] J. Pequenao, "Computer generated image of the ATLAS Muons subsystem", 2008, URL: https://cds.cern.ch/record/1095929 (cit. on p. 45).

[127] G. Aad et al., *Performance of the ATLAS Trigger System in 2010*, Eur. Phys. J. **C72** (2012) 1849, arXiv: 1110.1530 [hep-ex] (cit. on p. 46).

[128] M. Aaboud et al., *Performance of the ATLAS Trigger System in 2015*, Eur. Phys. J. **C77** (2017) 317, arXiv: 1611.09661 [hep-ex] (cit. on p. 46).

[129] M. Aaboud et al., *Luminosity determination in pp collisions at $\sqrt{s}$ = 8 TeV using the ATLAS detector at the LHC*, Eur. Phys. J. **C76** (2016) 653, arXiv: 1608.03953 [hep-ex] (cit. on pp. 47, 130).

[130] ATLAS Collaboration, *ATLAS Luminosity Public Results Run-2*, 2018, URL: https://twiki.cern.ch/twiki/bin/view/AtlasPublic/LuminosityPublicResultsRun2#Luminosity_summary_plots_for_AN2 (visited on 21/08/2018) (cit. on p. 49).

[131] V. Boisvert et al., *Final Report of the ATLAS Reconstruction Task Force*, (2003) (cit. on p. 48).

[132] A. Buckley et al., *Implementation of the ATLAS Run 2 event data model*, J. Phys. Conf. Ser. **664** (2015) 072045 (cit. on p. 48).

[133] R. Brun and F. Rademakers, *ROOT: An object oriented data analysis framework*, Nucl. Instrum. Meth. **A389** (1997) 81 (cit. on pp. 48, 50).

[134] J. Pequenao and P. Schaffner, "An computer generated image representing how ATLAS detects particles", 2013, URL: https://cds.cern.ch/record/1505342 (cit. on p. 51).

[135] S. D. Ellis and D. E. Soper, *Successive combination jet algorithm for hadron collisions*, Phys. Rev. **D48** (1993) 3160, arXiv: hep-ph/9305266 [hep-ph] (cit. on p. 52).

[136] Y. L. Dokshitzer et al., *Better jet clustering algorithms*, JHEP **08** (1997) 001, arXiv: hep-ph/9707323 [hep-ph] (cit. on p. 52).

[137] M. Wobisch and T. Wengler, "Hadronization corrections to jet cross-sections in deep inelastic scattering", *Monte Carlo generators for HERA physics. Proceedings, Workshop, Hamburg, Germany, 1998-1999*, 1998 270, arXiv: hep-ph/9907280 [hep-ph], URL: http://inspirehep.net/record/484872/files/arXiv:hep-ph_9907280.pdf (cit. on p. 52).

[138] M. Cacciari, G. P. Salam and G. Soyez, *The anti-k_t jet clustering algorithm*, JHEP **04** (2008) 063, arXiv: 0802.1189 [hep-ph] (cit. on p. 52).

[139] ATLAS Collaboration, *Quark versus Gluon Jet Tagging Using Charged-Particle Constituent Multiplicity with the ATLAS Detector*, ATL-PHYS-PUB-2017-009, 2017, URL: https://cds.cern.ch/record/2263679 (cit. on p. 52).

[140] ATLAS Collaboration, *Identification of Boosted, Hadronically-Decaying W and Z Bosons in $\sqrt{s}$ = 13 TeV Monte Carlo Simulations for ATLAS*, ATL-PHYS-PUB-2015-033, 2015, URL: https://cds.cern.ch/record/2041461 (cit. on p. 52).

[141] ATLAS Collaboration, *Boosted hadronic top identification at ATLAS for early 13 TeV data*, ATL-PHYS-PUB-2015-053, 2015, URL: https://cds.cern.ch/record/2116351 (cit. on p. 52).

[142] W. Lampl et al., *Calorimeter clustering algorithms: Description and performance*, (2008) (cit. on p. 52).

[143] G. Aad et al., *Jet energy measurement with the ATLAS detector in proton-proton collisions at $\sqrt{s}$ = 7 TeV*, Eur. Phys. J. **C73** (2013) 2304, arXiv: 1112.6426 [hep-ex] (cit. on pp. 52, 127, 128).

[144] *Jet Calibration and Systematic Uncertainties for Jets Reconstructed in the ATLAS Detector at $\sqrt{s}$ = 13 TeV*, tech. rep. ATL-PHYS-PUB-2015-015, CERN, 2015, URL: https://cds.cern.ch/record/2037613 (cit. on pp. 52, 127, 128).

[145] M. Aaboud et al., *Jet energy scale measurements and their systematic uncertainties in proton-proton collisions at $\sqrt{s}$ = 13 TeV with the ATLAS detector*, Phys. Rev. **D96** (2017) 072002, arXiv: 1703.09665 [hep-ex] (cit. on pp. 52, 127).

[146] M. Cacciari and G. P. Salam, *Pileup subtraction using jet areas*, Phys. Lett. **B659** (2008) 119, arXiv: 0707.1378 [hep-ph] (cit. on p. 52).

[147] G. Aad et al., *Performance of pile-up mitigation techniques for jets in pp collisions at $\sqrt{s}$ = 8 TeV using the ATLAS detector*, Eur. Phys. J. **C76** (2016) 581, arXiv: 1510.03823 [hep-ex] (cit. on p. 52).

[148] ATLAS Collaboration, *Selection of jets produced in 13 TeV proton–proton collisions with the ATLAS detector*, (2015) (cit. on p. 52).

[149] *Tagging and suppression of pileup jets with the ATLAS detector*, tech. rep. ATLAS-CONF-2014-018, CERN, 2014, URL: https://cds.cern.ch/record/1700870 (cit. on pp. 52, 128).

[150] G. Aad et al., *Performance of b-Jet Identification in the ATLAS Experiment*, JINST **11** (2016) P04008, arXiv: 1512.01094 [hep-ex] (cit. on pp. 53, 128).

[151] *Vertex Reconstruction Performance of the ATLAS Detector at " $\sqrt{s}$ = 13 TeV"*, tech. rep. ATL-PHYS-PUB-2015-026, CERN, 2015, URL: http://cds.cern.ch/record/2037717 (cit. on p. 53).

[152] *Optimisation of the ATLAS b-tagging performance for the 2016 LHC Run*, tech. rep. ATL-PHYS-PUB-2016-012, CERN, 2016, URL: https://cds.cern.ch/record/2160731 (cit. on p. 53).

[153] A. Collaboration, *Optimisation of the ATLAS b-tagging performance for the 2016 LHC Run*, tech. rep. ATL-PHYS-PUB-2016-012, CERN, 2016, URL: https://cds.cern.ch/record/2160731 (cit. on p. 53).

[154] *Measurement of b-tagging Efficiency of c-jets in $t\bar{t}$ Events Using a Likelihood Approach with the ATLAS Detector*, tech. rep. ATLAS-CONF-2018-001, CERN, 2018, URL: http://cds.cern.ch/record/2306649 (cit. on p. 53).

[155] ATLAS Collaboration, *Electron efficiency measurements with the ATLAS detector using the 2015 LHC proton–proton collision data*, ATLAS-CONF-2016-024, 2016, URL: https://cds.cern.ch/record/2157687 (cit. on p. 53).

[156] G. Aad et al., *Muon reconstruction performance of the ATLAS detector in proton–proton collision data at* $\sqrt{s} = 13$ *TeV*, Eur. Phys. J. **C76** (2016) 292, arXiv: 1603.05598 [hep-ex] (cit. on pp. 53, 129).

[157] ATLAS Collaboration, *Measurement of the photon identification efficiencies with the ATLAS detector using LHC Run-1 data*, Eur. Phys. J. C **76** (2016) 666, arXiv: 1606.01813 [hep-ex] (cit. on p. 53).

[158] ATLAS Collaboration, *Identification and energy calibration of hadronically decaying tau leptons with the ATLAS experiment in pp collisions at* $\sqrt{s} = 8$ *TeV*, Eur. Phys. J. C **75** (2015) 303, arXiv: 1412.7086 [hep-ex] (cit. on pp. 54, 55).

[159] *Measurement of the tau lepton reconstruction and identification performance in the ATLAS experiment using pp collisions at* $\sqrt{s} = 13$ *TeV*, tech. rep. ATLAS-CONF-2017-029, CERN, 2017, URL: https://cds.cern.ch/record/2261772 (cit. on pp. 54, 55, 58–61, 128, 129).

[160] A. Hocker et al., *TMVA - Toolkit for Multivariate Data Analysis*, (2007), arXiv: physics/0703039 [physics.data-an] (cit. on p. 55).

[161] *Reconstruction, Energy Calibration, and Identification of Hadronically Decaying Tau Leptons in the ATLAS Experiment for Run-2 of the LHC*, tech. rep. ATL-PHYS-PUB-2015-045, CERN, 2015, URL: https://cds.cern.ch/record/2064383 (cit. on pp. 56–58, 128, 129).

[162] G. Aad et al., *Reconstruction of hadronic decay products of tau leptons with the ATLAS experiment*, Eur. Phys. J. **C76** (2016) 295, arXiv: 1512.05955 [hep-ex] (cit. on p. 57).

[163] M. Aaboud et al., *Performance of missing transverse momentum reconstruction with the ATLAS detector using proton-proton collisions at* $\sqrt{s} = 13$ *TeV*, (2018), arXiv: 1802.08168 [hep-ex] (cit. on pp. 61, 129).

[164] A. Harmon, *Sherpa collision simulation*, 2014, URL: https://sciencenode.org/img/img_2014/sherpa_sim_0.jpeg (visited on 28/08/2018) (cit. on p. 64).

[165] T. Sjostrand, S. Mrenna and P. Z. Skands, *PYTHIA 6.4 Physics and Manual*, JHEP **05** (2006) 026, arXiv: hep-ph/0603175 [hep-ph] (cit. on pp. 64, 67).

[166] T. Sjostrand, S. Mrenna and P. Z. Skands, *A Brief Introduction to PYTHIA 8.1*, Comput. Phys. Commun. **178** (2008) 852, arXiv: 0710.3820 [hep-ph] (cit. on p. 64).

[167] G. Corcella et al., *HERWIG 6: An Event generator for hadron emission reactions with interfering gluons (including supersymmetric processes)*, JHEP **01** (2001) 010, arXiv: hep-ph/0011363 (cit. on p. 64).

[168] M. Bahr et al., *Herwig++ Physics and Manual*, Eur. Phys. J. C **58** (2008) 639, arXiv: 0803.0883 [hep-ph] (cit. on pp. 64, 67, 68).

[169] J. Bellm et al., *Herwig 7.0/Herwig++ 3.0 release note*, Eur. Phys. J. C **76** (2016) 196, arXiv: 1512.01178 [hep-ph] (cit. on p. 64).

[170] T. Gleisberg et al., *Event generation with SHERPA 1.1*, JHEP **02** (2009) 007, arXiv: 0811.4622 [hep-ph] (cit. on pp. 64, 67).

[171] S. Höche et al., *QCD matrix elements and truncated showers*, JHEP **05** (2009) 053, arXiv: 0903.1219 [hep-ph] (cit. on pp. 64, 66).

[172] T. Gleisberg and S. Höche, *Comix, a new matrix element generator*, JHEP **12** (2008) 039, arXiv: 0808.3674 [hep-ph] (cit. on pp. 64, 66).

[173] S. Schumann and F. Krauss, *A Parton shower algorithm based on Catani-Seymour dipole factorisation*, JHEP **03** (2008) 038, arXiv: 0709.1027 [hep-ph] (cit. on pp. 64, 66).

[174] M. L. Mangano et al., *ALPGEN, a generator for hard multiparton processes in hadronic collisions*, JHEP **07** (2003) 001, arXiv: hep-ph/0206293 (cit. on p. 65).

[175] S. Frixione and B. R. Webber, *Matching NLO QCD computations and parton shower simulations*, JHEP **06** (2002) 029, arXiv: hep-ph/0204244 (cit. on p. 65).

[176] S. Frixione, P. Nason and B. R. Webber, *Matching NLO QCD and parton showers in heavy flavour production*, JHEP **08** (2003) 007, arXiv: hep-ph/0305252 (cit. on p. 65).

[177] S. Frixione et al., *Single-top production in MC@NLO*, JHEP **03** (2006) 092, arXiv: hep-ph/0512250 (cit. on p. 65).

[178] S. Frixione et al., *Single-top hadroproduction in association with a W boson*, JHEP **07** (2008) 029, arXiv: 0805.3067 [hep-ph] (cit. on p. 65).

[179] S. Frixione et al., *NLO QCD corrections in Herwig++ with MC@NLO*, JHEP **01** (2011) 053, arXiv: 1010.0568 [hep-ph] (cit. on p. 65).

[180] P. Nason, *A New method for combining NLO QCD with shower Monte Carlo algorithms*, JHEP **11** (2004) 040, arXiv: hep-ph/0409146 (cit. on p. 65).

[181] S. Frixione, P. Nason and C. Oleari, *Matching NLO QCD computations with Parton Shower simulations: the POWHEG method*, JHEP **11** (2007) 070, arXiv: 0709.2092 [hep-ph] (cit. on p. 65).

[182] S. Alioli et al., *A general framework for implementing NLO calculations in shower Monte Carlo programs: the POWHEG BOX*, JHEP **06** (2010) 043, arXiv: 1002.2581 [hep-ph] (cit. on pp. 65, 67).

[183] S. Agostinelli et al., *GEANT4: A Simulation toolkit*, Nucl. Instrum. Meth. A **506** (2003) 250 (cit. on p. 65).

[184] G. Aad et al., *The ATLAS Simulation Infrastructure*, Eur. Phys. J. **C70** (2010) 823, arXiv: 1005.4568 [physics.ins-det] (cit. on p. 65).

[185] F. Cascioli, P. Maierhofer and S. Pozzorini, *Scattering Amplitudes with Open Loops*, Phys. Rev. Lett. **108** (2012) 111601, arXiv: 1111.5206 [hep-ph] (cit. on p. 66).

[186] S. Catani et al., *Vector boson production at hadron colliders: a fully exclusive QCD calculation at NNLO*, Phys. Rev. Lett. **103** (2009) 082001, arXiv: 0903.2120 [hep-ph] (cit. on p. 66).

[187] C. Anastasiou et al., *High precision QCD at hadron colliders: Electroweak gauge boson rapidity distributions at NNLO*, Phys. Rev. **D69** (2004) 094008, arXiv: hep-ph/0312266 [hep-ph] (cit. on p. 66).

[188] M. Czakon and A. Mitov,
Top++: A Program for the Calculation of the Top-Pair Cross-Section at Hadron Colliders,
Comput. Phys. Commun. **185** (2014) 2930, arXiv: 1112.5675 [hep-ph] (cit. on p. 66).

[189] P. Bechtle et al., *Search for squarks and gluinos in pp collisions at $\sqrt{s} = 13$ TeV in events with τ-leptons, jets and missing transverse energy.*, tech. rep. ATL-COM-PHYS-2016-1614, CERN, 2016, URL: https://cds.cern.ch/record/2231787
(cit. on pp. 66, 85, 87, 88, 90, 103, 107, 111, 114–117, 120, 130, 132, 137, 141, 225–228).

[190] M. Aliev et al., *HATHOR: HAdronic Top and Heavy quarks crOss section calculatoR*,
Comput. Phys. Commun. **182** (2011) 1034, arXiv: 1007.1327 [hep-ph] (cit. on p. 66).

[191] P. Kant et al., *HatHor for single top-quark production: Updated predictions and uncertainty estimates for single top-quark production in hadronic collisions*,
Comput. Phys. Commun. **191** (2015) 74, arXiv: 1406.4403 [hep-ph] (cit. on p. 66).

[192] M. Botje et al., *The PDF4LHC Working Group Interim Recommendations*, (2011),
arXiv: 1101.0538 [hep-ph] (cit. on p. 66).

[193] A. D. Martin et al., *Parton distributions for the LHC*, Eur. Phys. J. **C63** (2009) 189,
arXiv: 0901.0002 [hep-ph] (cit. on pp. 66, 67).

[194] A. D. Martin et al., *Uncertainties on alpha(S) in global PDF analyses and implications for predicted hadronic cross sections*, Eur. Phys. J. **C64** (2009) 653, arXiv: 0905.3531 [hep-ph] (cit. on p. 66).

[195] H.-L. Lai et al., *New parton distributions for collider physics*, Phys. Rev. **D82** (2010) 074024,
arXiv: 1007.2241 [hep-ph] (cit. on pp. 66, 67).

[196] R. D. Ball et al., *Parton distributions with LHC data*, Nucl. Phys. **B867** (2013) 244,
arXiv: 1207.1303 [hep-ph] (cit. on p. 66).

[197] Z. Czyczula, T. Przedzinski and Z. Was,
TauSpinner Program for Studies on Spin Effect in tau Production at the LHC,
Eur. Phys. J. **C72** (2012) 1988, arXiv: 1201.0117 [hep-ph] (cit. on p. 66).

[198] T. Sjöstrand et al., *An Introduction to PYTHIA 8.2*, Comput. Phys. Commun. **191** (2015) 159,
arXiv: 1410.3012 [hep-ph] (cit. on p. 67).

[199] *Summary of ATLAS Pythia 8 tunes*, (2012) (cit. on p. 67).

[200] R. D. Ball et al., *Parton distributions for the LHC Run II*, JHEP **04** (2015) 040,
arXiv: 1410.8849 [hep-ph] (cit. on p. 67).

[201] J. Pumplin et al.,
New generation of parton distributions with uncertainties from global QCD analysis,
JHEP **07** (2002) 012, arXiv: hep-ph/0201195 [hep-ph] (cit. on p. 67).

[202] P. Z. Skands, *Tuning Monte Carlo Generators: The Perugia Tunes*,
Phys. Rev. **D82** (2010) 074018, arXiv: 1005.3457 [hep-ph] (cit. on p. 67).

[203] R. D. Ball et al., *Parton distributions with QED corrections*, Nucl. Phys. **B877** (2013) 290,
arXiv: 1308.0598 [hep-ph] (cit. on p. 67).

[204] *ATLAS Run 1 Pythia8 tunes*, tech. rep. ATL-PHYS-PUB-2014-021, CERN, 2014, URL: https://cds.cern.ch/record/1966419 (cit. on p. 67).

[205] J. Alwall et al., *The automated computation of tree-level and next-to-leading order differential cross sections, and their matching to parton shower simulations*, JHEP **07** (2014) 079, arXiv: 1405.0301 [hep-ph] (cit. on p. 67).

[206] S. Gieseke, C. Rohr and A. Siodmok, *Colour reconnections in Herwig++*, Eur. Phys. J. **C72** (2012) 2225, arXiv: 1206.0041 [hep-ph] (cit. on p. 67).

[207] G. Marchesini and B. R. Webber, *Monte Carlo Simulation of General Hard Processes with Coherent QCD Radiation*, Nucl. Phys. **B310** (1988) 461 (cit. on p. 68).

[208] G. Marchesini and B. R. Webber, *Simulation of QCD Jets Including Soft Gluon Interference*, Nucl. Phys. **B238** (1984) 1 (cit. on p. 68).

[209] S. Gieseke, P. Stephens and B. Webber, *New formalism for QCD parton showers*, JHEP **12** (2003) 045, arXiv: hep-ph/0310083 [hep-ph] (cit. on p. 68).

[210] W. Beenakker et al., *Squark and gluino production at hadron colliders*, Nucl. Phys. **B492** (1997) 51, arXiv: hep-ph/9610490 [hep-ph] (cit. on p. 68).

[211] A. Kulesza and L. Motyka, *Threshold resummation for squark-antisquark and gluino-pair production at the LHC*, Phys. Rev. Lett. **102** (2009) 111802, arXiv: 0807.2405 [hep-ph] (cit. on p. 68).

[212] A. Kulesza and L. Motyka, *Soft gluon resummation for the production of gluino-gluino and squark-antisquark pairs at the LHC*, Phys. Rev. **D80** (2009) 095004, arXiv: 0905.4749 [hep-ph] (cit. on p. 68).

[213] W. Beenakker et al., *Soft-gluon resummation for squark and gluino hadroproduction*, JHEP **12** (2009) 041, arXiv: 0909.4418 [hep-ph] (cit. on p. 68).

[214] W. Beenakker et al., *Squark and Gluino Hadroproduction*, Int. J. Mod. Phys. **A26** (2011) 2637, arXiv: 1105.1110 [hep-ph] (cit. on p. 68).

[215] C. Borschensky et al., *Squark and gluino production cross sections in pp collisions at $\sqrt{s}$ = 13, 14, 33 and 100 TeV*, Eur. Phys. J. **C74** (2014) 3174, arXiv: 1407.5066 [hep-ph] (cit. on pp. 68, 132).

[216] ATLAS Collaboration, *ATLAS Standard Model Production Cross Section Measurements*, 2018, URL: https://atlas.web.cern.ch/Atlas/GROUPS/PHYSICS/CombinedSummaryPlots/SM/ATLAS_b_SMSummary_FiducialXsect/ATLAS_b_SMSummary_FiducialXsect.eps (visited on 21/09/2018) (cit. on p. 72).

[217] H. A. Junkerkalefeld, *Die Suche nach Supersymmetrie mit semileptonischen Zwei-Tau-Ereignissen beim ATLAS-Experiment für Schwerpunktsenergien von 13 TeV*, B.Sc. thesis: Bonn U., 2016, URL: https://web.physik.uni-bonn.de/group/view.php?&group=1&lang=de&c=t&id=68 (cit. on pp. 73, 163).

[218] I. Reinert, *Berücksichtigung von leptonischen Tau-Zerfällen bei der Suche nach Supersymmetrie am ATLAS-Experiment für $\sqrt{s}$ = 13 TeV*, B.Sc. thesis: Bonn U., 2017, URL: https://web.physik.uni-bonn.de/group/view.php?&group=1&lang=de&c=t&id=86 (cit. on pp. 73, 163).

[219] ATLAS Collaboration, *Summary of the searches for squarks and gluinos using $\sqrt{s} = 8$ TeV pp collisions with the ATLAS experiment at the LHC*, JHEP **10** (2015) 054, arXiv: 1507.05525 [hep-ex] (cit. on pp. 79–82, 150, 163).

[220] S. Schaepe, *Search for Supersymmetry in Tau Lepton Final States with the ATLAS Detector*, PhD thesis: Bonn U., 2015, URL: http://hss.ulb.uni-bonn.de/2016/4238/4238.htm (cit. on p. 80).

[221] F. Abe et al., *Measurement of the W boson mass*, Phys. Rev. **D52** (1995) 4784 (cit. on p. 83).

[222] C. G. Lester and D. J. Summers, *Measuring masses of semiinvisibly decaying particles pair produced at hadron colliders*, Phys. Lett. B **463** (1999) 99, arXiv: hep-ph/9906349 (cit. on p. 84).

[223] C. G. Lester and B. Nachman, *Bisection-based asymmetric M_{T2} computation: a higher precision calculator than existing symmetric methods*, JHEP **1503** (2015) 100, arXiv: 1411.4312 [hep-ph] (cit. on p. 84).

[224] P. Bechtle et al., *Search for strongly produced supersymmetry in 13 TeV p–p collisions with tau-leptons, jets and missing transverse energy in the final state.*, tech. rep. ATL-COM-PHYS-2015-1126, support note for planned SUSY CONF or paper on 2015 LHC data: CERN, 2015, URL: https://cds.cern.ch/record/2050716 (cit. on pp. 84, 85, 88, 90, 225, 226).

[225] M. Baak et al., *HistFitter software framework for statistical data analysis*, Eur. Phys. J. **C75** (2015) 153, arXiv: 1410.1280 [hep-ex] (cit. on p. 103).

[226] S. Owen, *Data-driven estimation of the QCD multijet background to SUSY searches with jets and missing transverse momentum at ATLAS using jet smearing*, URL: http://cdsweb.cern.ch/record/1423310 (cit. on p. 111).

[227] F. Beisiegel, *Jet-Smearing-based Multijet Background Determination for SUSY Searches with the ATLAS Detector*, M.Sc. thesis: Bonn U., 2017, URL: https://web.physik.uni-bonn.de/group/view.php?&group=1&lang=de&c=t&id=84 (cit. on pp. 111–113, 133).

[228] M. Tripiana, *Jet smearing status*, URL: https://indico.cern.ch/event/483393/contribution/3/attachments/1215449/1774722/jetsmearing_martin_210116.pdf (cit. on p. 114).

[229] *Electron identification measurements in ATLAS using $\sqrt{s} = 13$ TeV data with 50 ns bunch spacing*, tech. rep. ATL-PHYS-PUB-2015-041, CERN, 2015, URL: https://cds.cern.ch/record/2048202 (cit. on p. 129).

[230] ATLAS Collaboration, *Performance of the Fast ATLAS Tracking Simulation (FATRAS) and the ATLAS Fast Calorimeter Simulation (FastCaloSim) with single particles*, tech. rep. ATL-SOFT-PUB-2014-001, CERN, 2014, URL: https://cds.cern.ch/record/1669341 (cit. on p. 133).

[231] N. Konstantinidis et al., "The Atlantis event visualisation program for the ATLAS experiment", *Computing in high energy physics and nuclear physics. Proceedings, Conference, CHEP'04, Interlaken, Switzerland, September 27-October 1, 2004*, 2005 361, URL: http://doc.cern.ch/yellowrep/2005/2005-002/p361.pdf (cit. on p. 144).

[232] A. L. Read, *Presentation of search results: The CL(s) technique*, J. Phys. **G28** (2002) 2693, [,11(2002)] (cit. on pp. 145, 259).

[233] P. König, *Simplified Models with High Dimensionality in the Search for Supersymmetry at the ATLAS Experimen*, M.Sc. thesis: Bonn U., 2016, URL: https://web.physik.uni-bonn.de/group/view.php?&group=1&lang=de&c=t&id=79 (cit. on p. 160).

[234] S. Kraml et al., *SModelS: a tool for interpreting simplified-model results from the LHC and its application to supersymmetry*, Eur. Phys. J. **C74** (2014) 2868, arXiv: 1312.4175 [hep-ph] (cit. on p. 160).

[235] M. Drees et al., *CheckMATE: Confronting your Favourite New Physics Model with LHC Data*, Comput. Phys. Commun. **187** (2015) 227, arXiv: 1312.2591 [hep-ph] (cit. on p. 160).

[236] D. Dercks et al., *CheckMATE 2: From the model to the limit*, Comput. Phys. Commun. **221** (2017) 383, arXiv: 1611.09856 [hep-ph] (cit. on p. 160).

[237] ATLAS Collaboration, *ATLAS SUSY Searches*, 2018, URL: https://atlas.web.cern.ch/Atlas/GROUPS/PHYSICS/CombinedSummaryPlots/SUSY/ATLAS_SUSY_Summary/ATLAS_SUSY_Summary.pdf (visited on 01/10/2018) (cit. on p. 162).

[238] M. Aaboud et al., *Search for scalar leptoquarks in pp collisions at $\sqrt{s}$ = 13 TeV with the ATLAS experiment*, New J. Phys. **18** (2016) 093016, arXiv: 1605.06035 [hep-ex] (cit. on p. 163).

[239] L. Thimm, *Search for Leptoquarks with tau Lepton Final States in the ATLAS Experiment*, B.Sc. thesis: Bonn U., 2018 (cit. on p. 163).

[240] G. Cowan et al., *Asymptotic formulae for likelihood-based tests of new physics*, Eur. Phys. J. **C71** (2011) 1554, [Erratum: Eur. Phys. J.C73,2501(2013)], arXiv: 1007.1727 [physics.data-an] (cit. on pp. 219, 251, 262, 263).

[241] J. Neyman and E. Pearson, *On the problem of the most efficient tests of statistical hypotheses*, Philosophical Transactions of the Royal Society of London A: Mathematical, Physical and Engineering Sciences **231** (1933) 289, ISSN: 0264-3952, eprint: http://rsta.royalsocietypublishing.org/content/231/694-706/289.full.pdf, URL: http://rsta.royalsocietypublishing.org/content/231/694-706/289 (cit. on p. 251).

[242] G. Engeln-Müllges, K. Niederdrenk and R. Wodicka, *Numerik-Algorithmen - Verfahren, Beispiele, Anwendungen*, Springer-Verlag, 2010, ISBN: 978-3-642-13473-9 (cit. on p. 259).

APPENDIX A

Additional Information

This appendix presents additional information in the form of tables and figures to enhance the comprehension of the main document.

A.1 Additional signal model figures

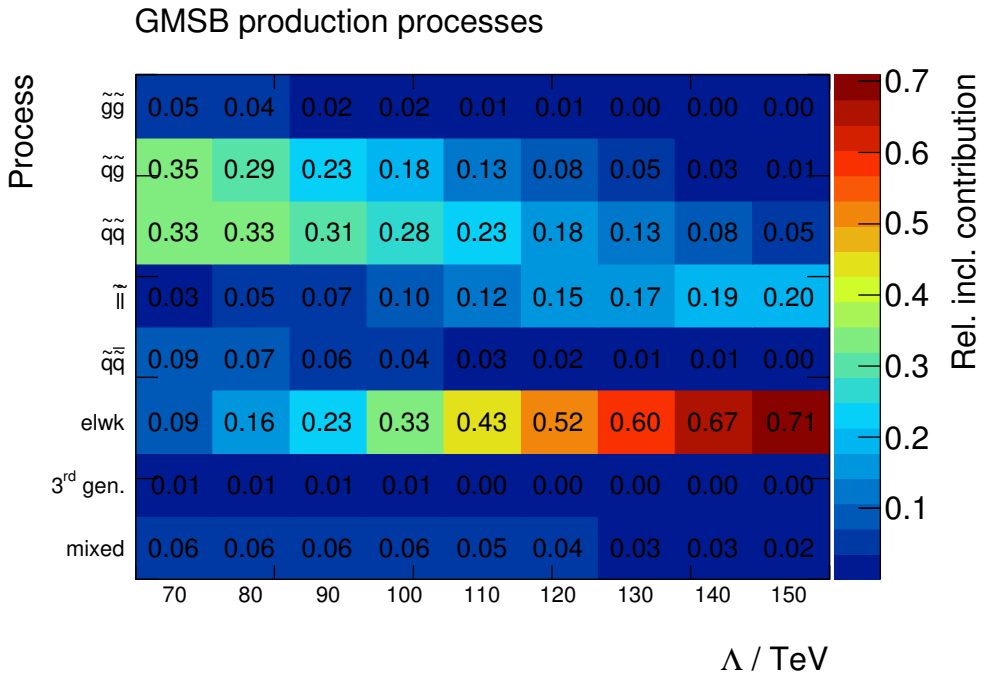

Figure A.1: Relative contributions of the different production process over the GMSB parameter grid for an inclusive phase-space. $\tilde{g}\tilde{g}$ corresponds to gluino pair-production, $\tilde{q}\tilde{g}$ to squark–gluino production, $\tilde{q}\tilde{q}$ to squark–squark production (including sbottom quarks), $\tilde{l}\tilde{l}$ to slepton pair-production (including third generation sleptons and all sneutrinos), $\tilde{q}\bar{\tilde{q}}$ to squark–antisquark production (including sbottom quarks), *elwk* to gaugino production (including charged and neutral ones, across all generations), 3^{rd} *gen.* to stop quark production (including antisquarks, across both generations), and *mixed* to gaugino-squark and gaugino-gluino production (including antisquarks and sbottom quarks, across all generations).

A.2 Additional kinematic distributions

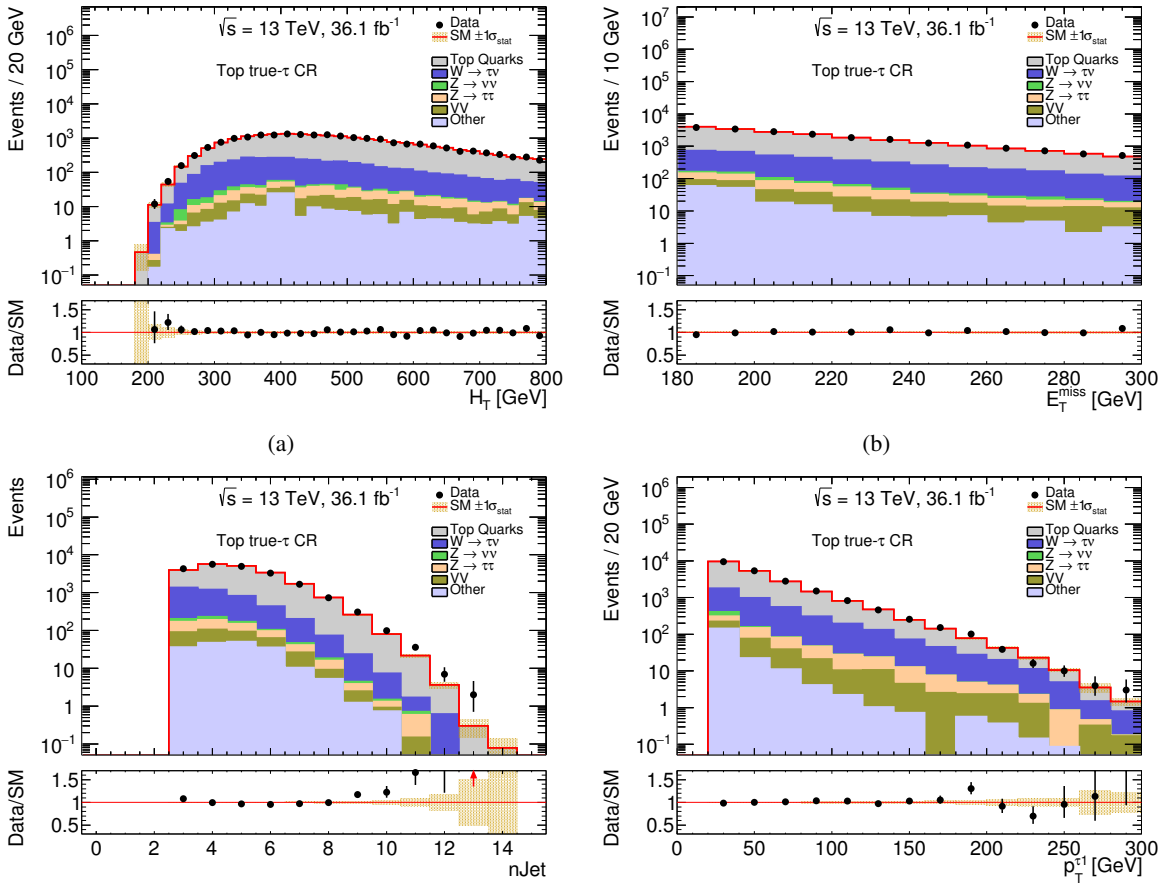

Figure A.2: Kinematic distributions of characteristic variables in the Top true-τ CR. The results shown are obtained after fitting the normalisation of the background in the control regions. The last bin of each distribution contains the overflow events. The uncertainties displayed consider only statistical limitations in the background modelling, illustrated by the shaded bands. Red arrows in the Data/SM ratio indicate bins where the corresponding entry falls outside the plotted range. The contribution labelled as *other* includes multi-jet events and V+Jets processes not explicitly listed in the legend.

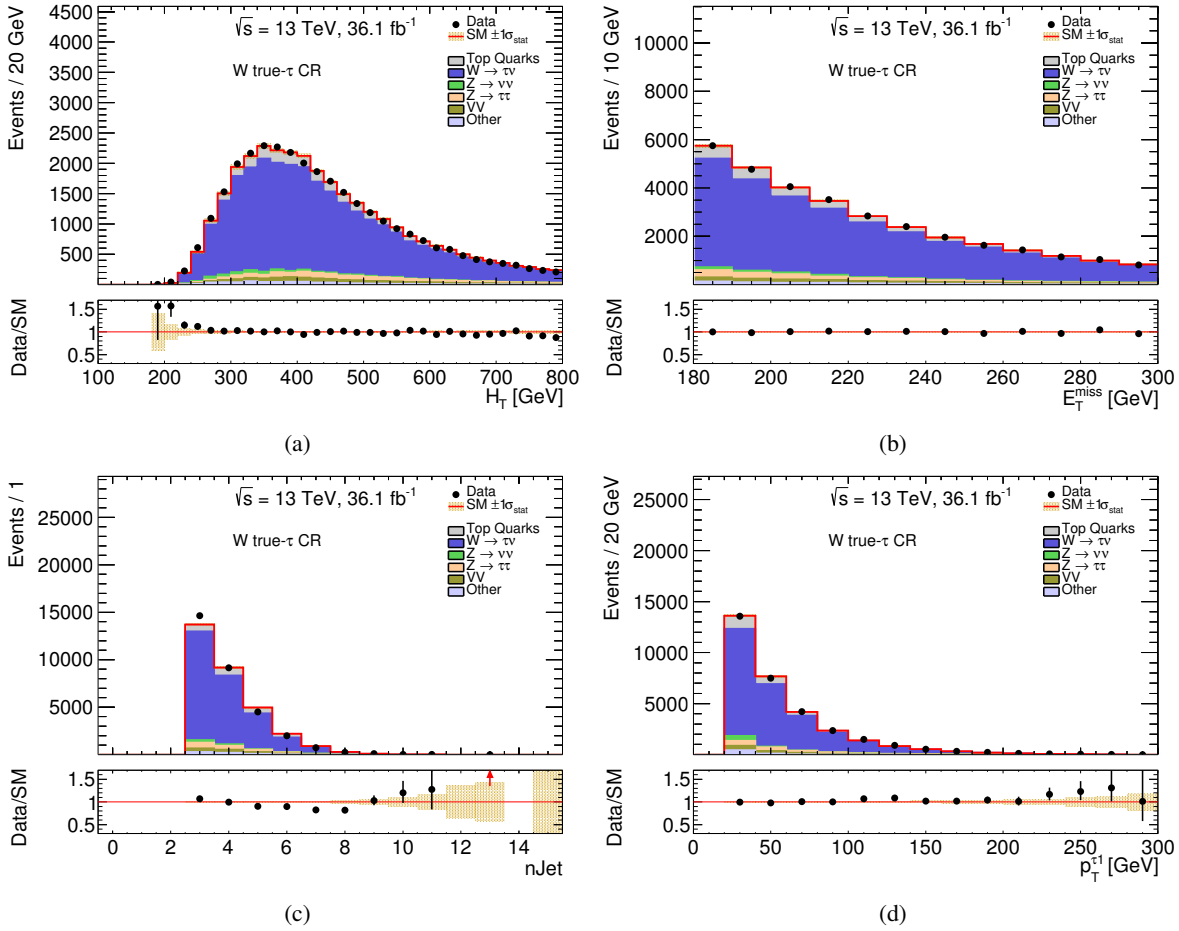

Figure A.3: Kinematic distributions of characteristic variables in the W true-τ CR. The results shown are obtained after fitting the normalisation of the background in the control regions. The last bin of each distribution contains the overflow events. The uncertainties displayed consider only statistical limitations in the background modelling, illustrated by the shaded bands. Red arrows in the Data/SM ratio indicate bins where the corresponding entry falls outside the plotted range. The contribution labelled as *other* includes multi-jet events and V+Jets processes not explicitly listed in the legend.

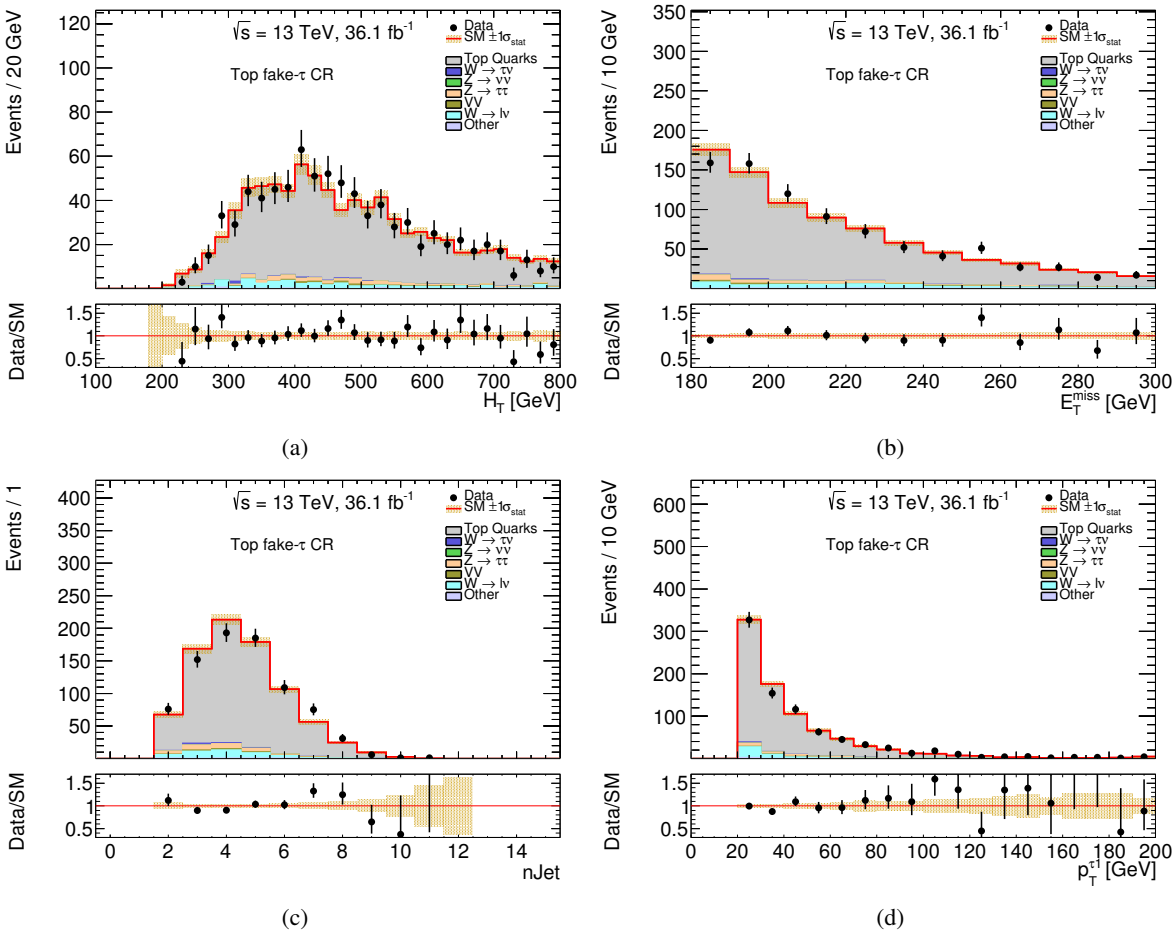

Figure A.4: Kinematic distributions of characteristic variables in the Top fake-τ CR. The results shown are obtained after fitting the normalisation of the background in the control regions. The last bin of each distribution contains the overflow events. The uncertainties displayed consider only statistical limitations in the background modelling, illustrated by the shaded bands. The contribution labelled as *other* includes multi-jet events and V+Jets processes not explicitly listed in the legend.

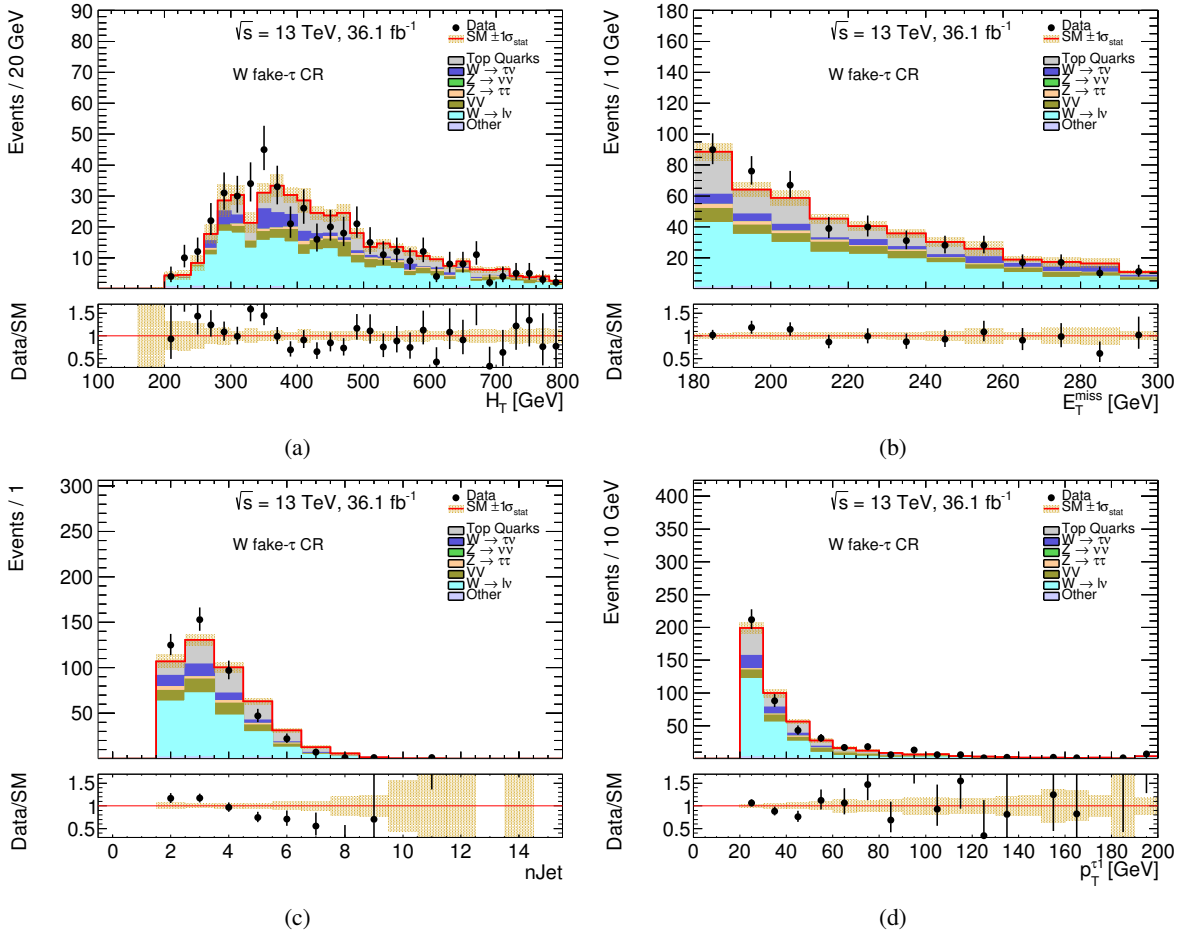

Figure A.5: Kinematic distributions of characteristic variables in the W fake-τ CR. The results shown are obtained after fitting the normalisation of the background in the control regions. The last bin of each distribution contains the overflow events. The uncertainties displayed consider only statistical limitations in the background modelling, illustrated by the shaded bands. The contribution labelled as *other* includes multi-jet events and V+Jets processes not explicitly listed in the legend.

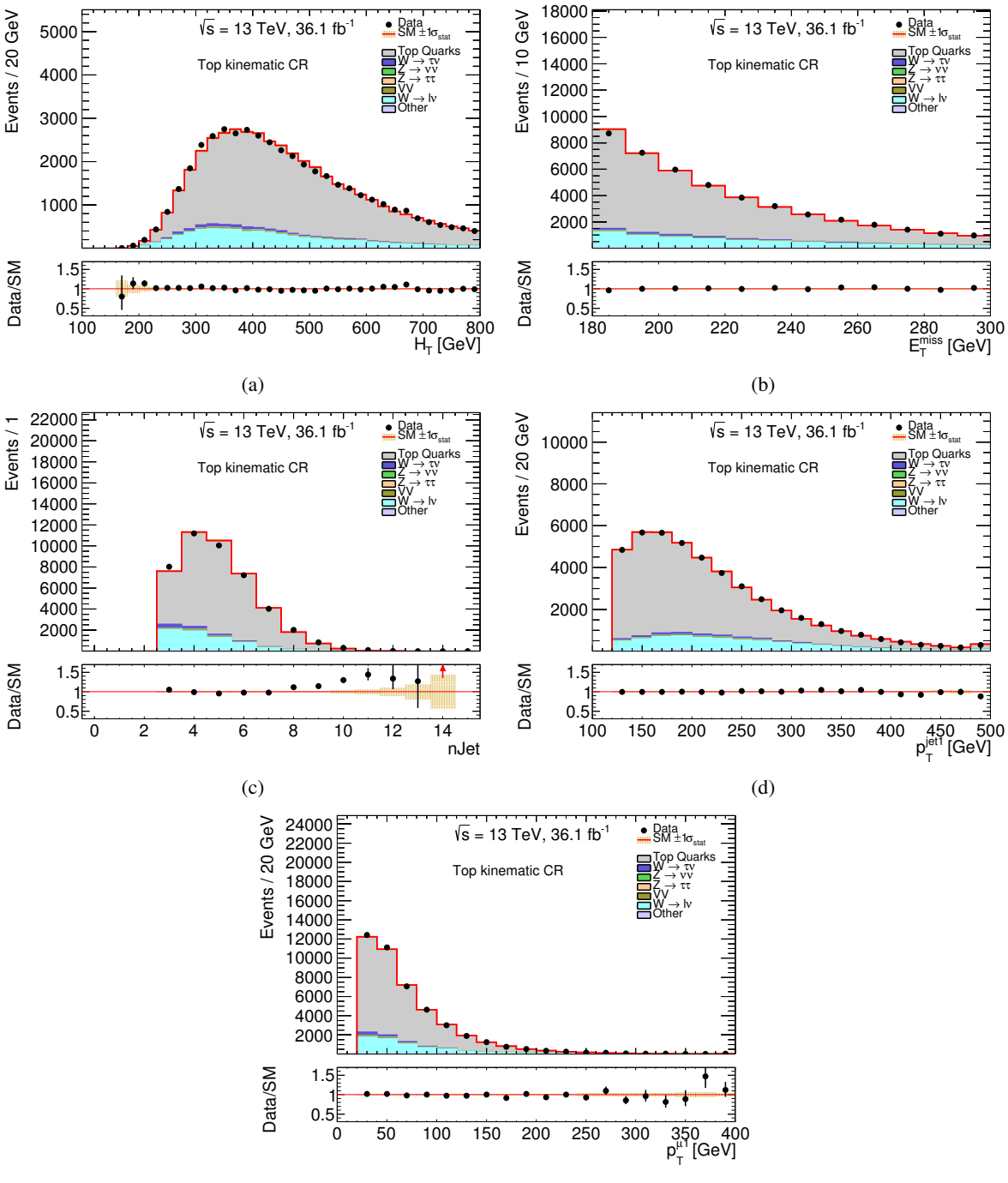

Figure A.6: Kinematic distributions of characteristic variables in the Top kinematic CR. The results shown are obtained after fitting the normalisation of the background in the control regions. The last bin of each distribution contains the overflow events. The uncertainties displayed consider only statistical limitations in the background modelling, illustrated by the shaded bands. Red arrows in the Data/SM ratio indicate bins where the corresponding entry falls outside the plotted range. The contribution labelled as *other* includes multi-jet events and V+Jets processes not explicitly listed in the legend.

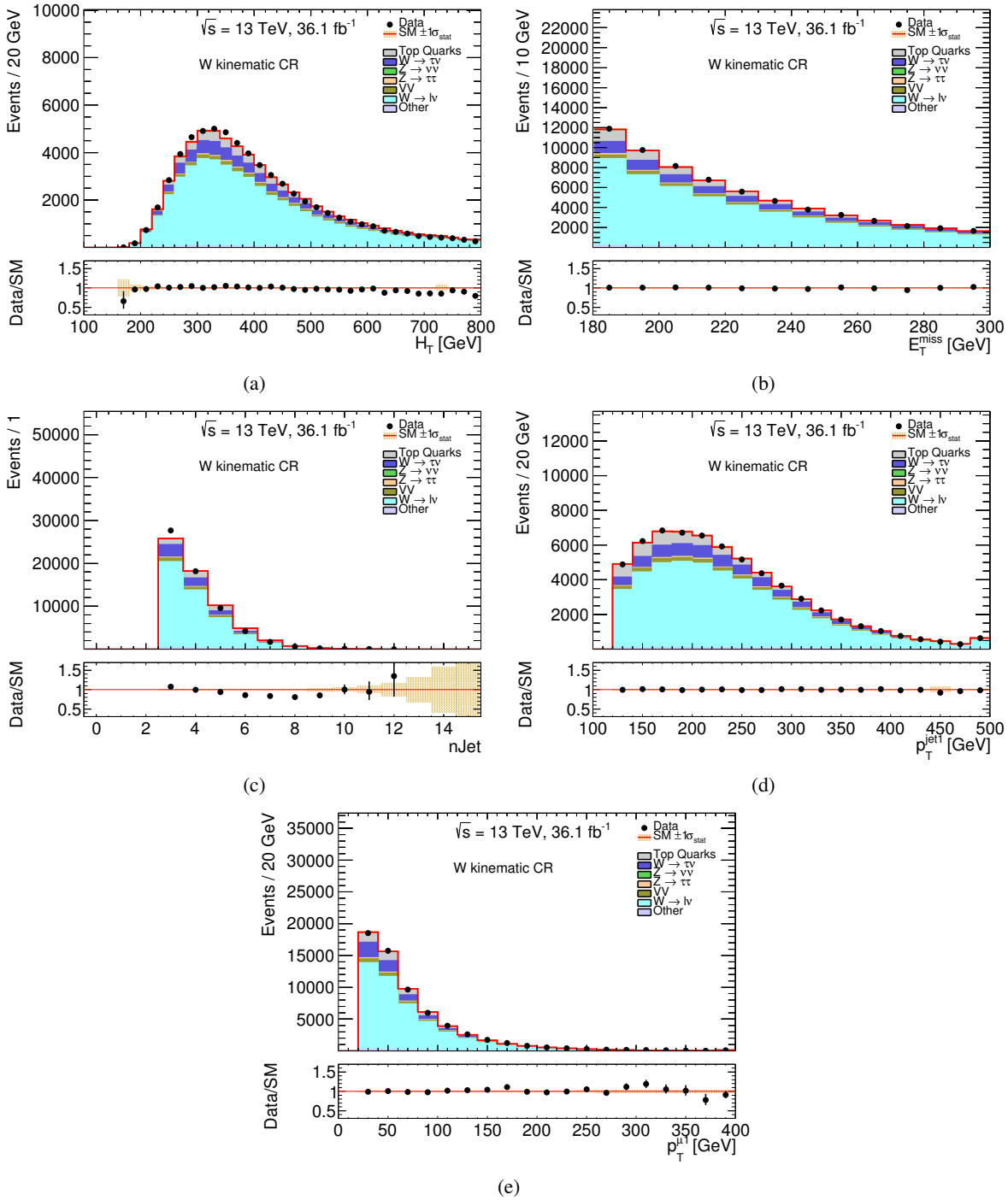

Figure A.7: Kinematic distributions of characteristic variables in the W kinematic CR. The results shown are obtained after fitting the normalisation of the background in the control regions. The last bin of each distribution contains the overflow events. The uncertainties displayed consider only statistical limitations in the background modelling, illustrated by the shaded bands. The contribution labelled as *other* includes multi-jet events and V+Jets processes not explicitly listed in the legend.

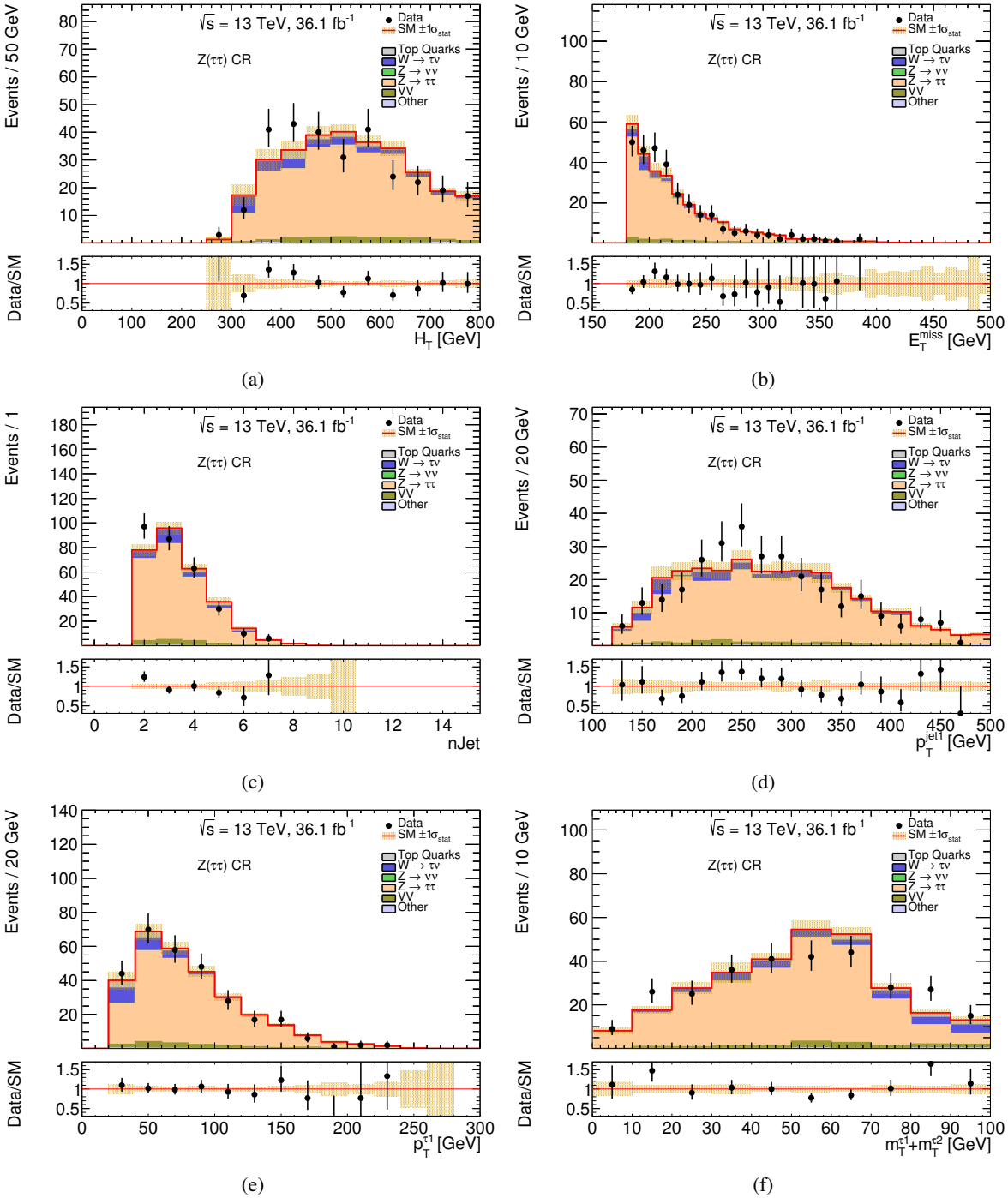

Figure A.8: Kinematic distributions of characteristic variables in the $Z(\tau\tau)$+jets CR. The results shown are obtained after fitting the normalisation of the background in the control regions. The last bin of each distribution contains the overflow events. The uncertainties displayed consider only statistical limitations in the background modelling, illustrated by the shaded bands. The contribution labelled as *other* includes multi-jet events and V+Jets processes not explicitly listed in the legend.

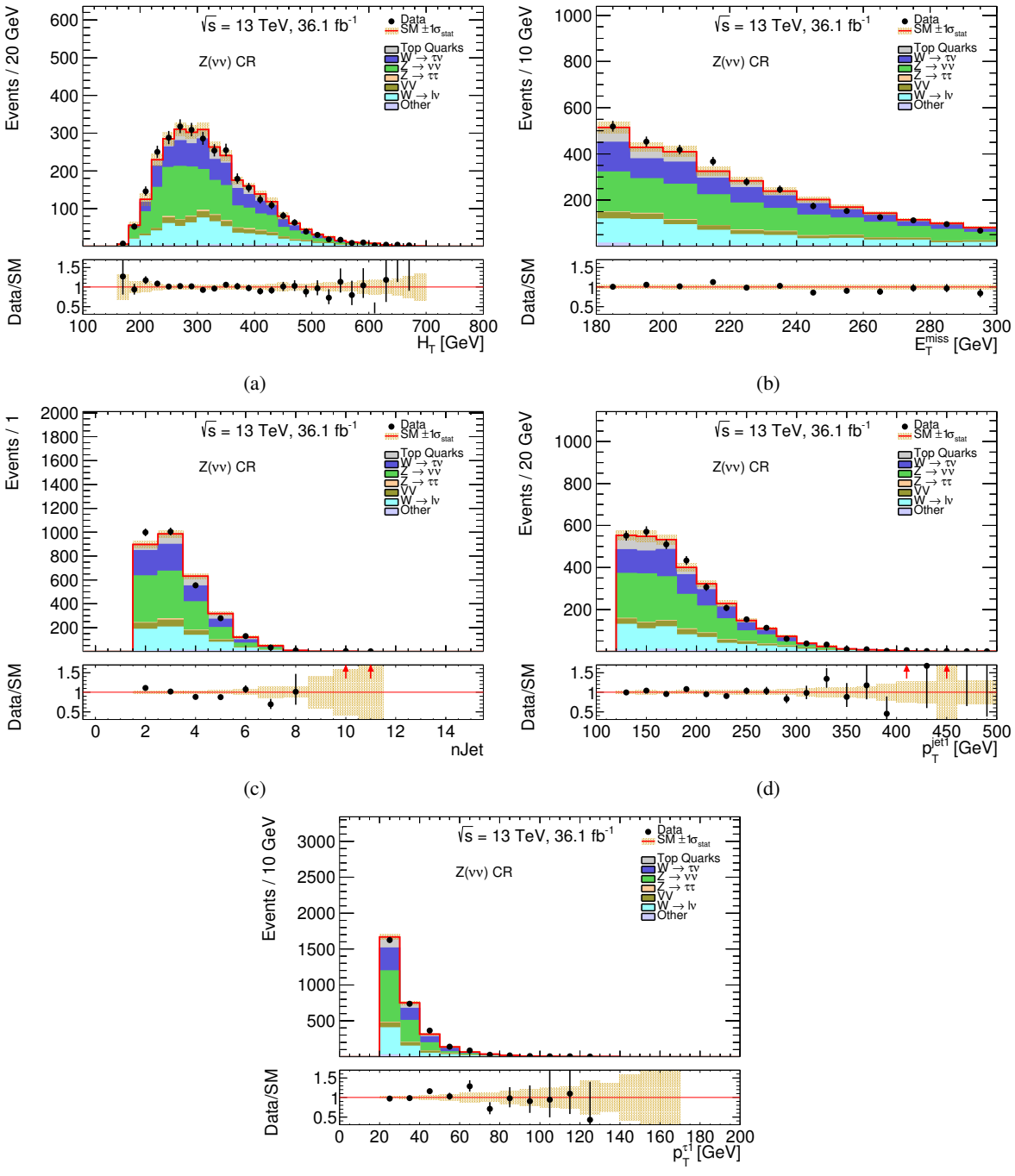

Figure A.9: Kinematic distributions of characteristic variables in the $Z(\nu\nu)$+jets CR. The results shown are obtained after fitting the normalisation of the background in the control regions. The last bin of each distribution contains the overflow events. The uncertainties displayed consider only statistical limitations in the background modelling, illustrated by the shaded bands. Red arrows in the Data/SM ratio indicate bins where the corresponding entry falls outside the plotted range. The contribution labelled as *other* includes multi-jet events and V+Jets processes not explicitly listed in the legend.

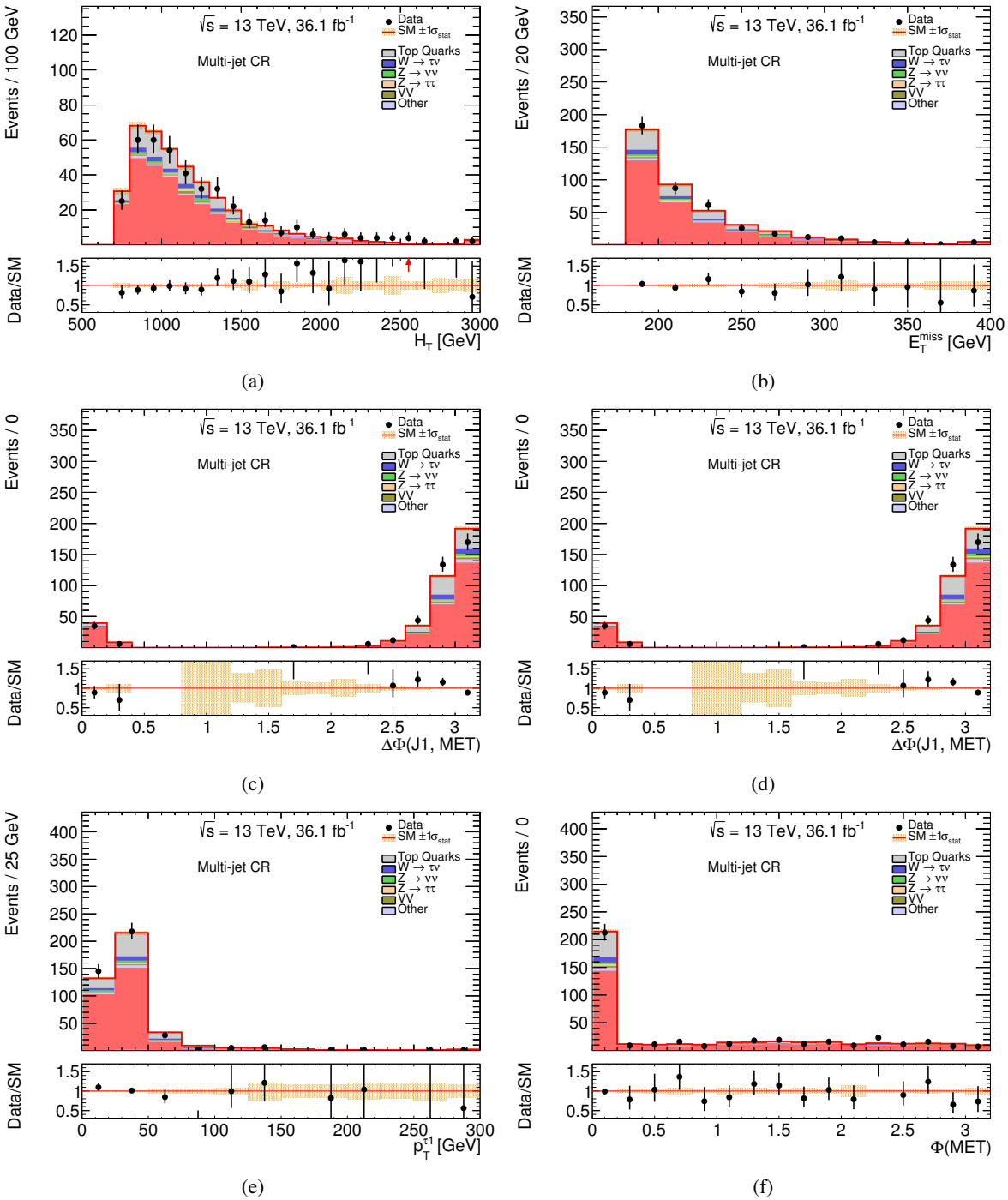

Figure A.10: Kinematic distributions of characteristic variables in the Multi-jet CR. The results shown are obtained after fitting the normalisation of the background in the control regions. The last bin of each distribution contains the overflow events. The uncertainties displayed consider only statistical limitations in the background modelling, illustrated by the shaded bands. Red arrows in the Data/SM ratio indicate bins where the corresponding entry falls outside the plotted range. The contribution labelled as *other* includes V+Jets processes not explicitly listed in the legend.

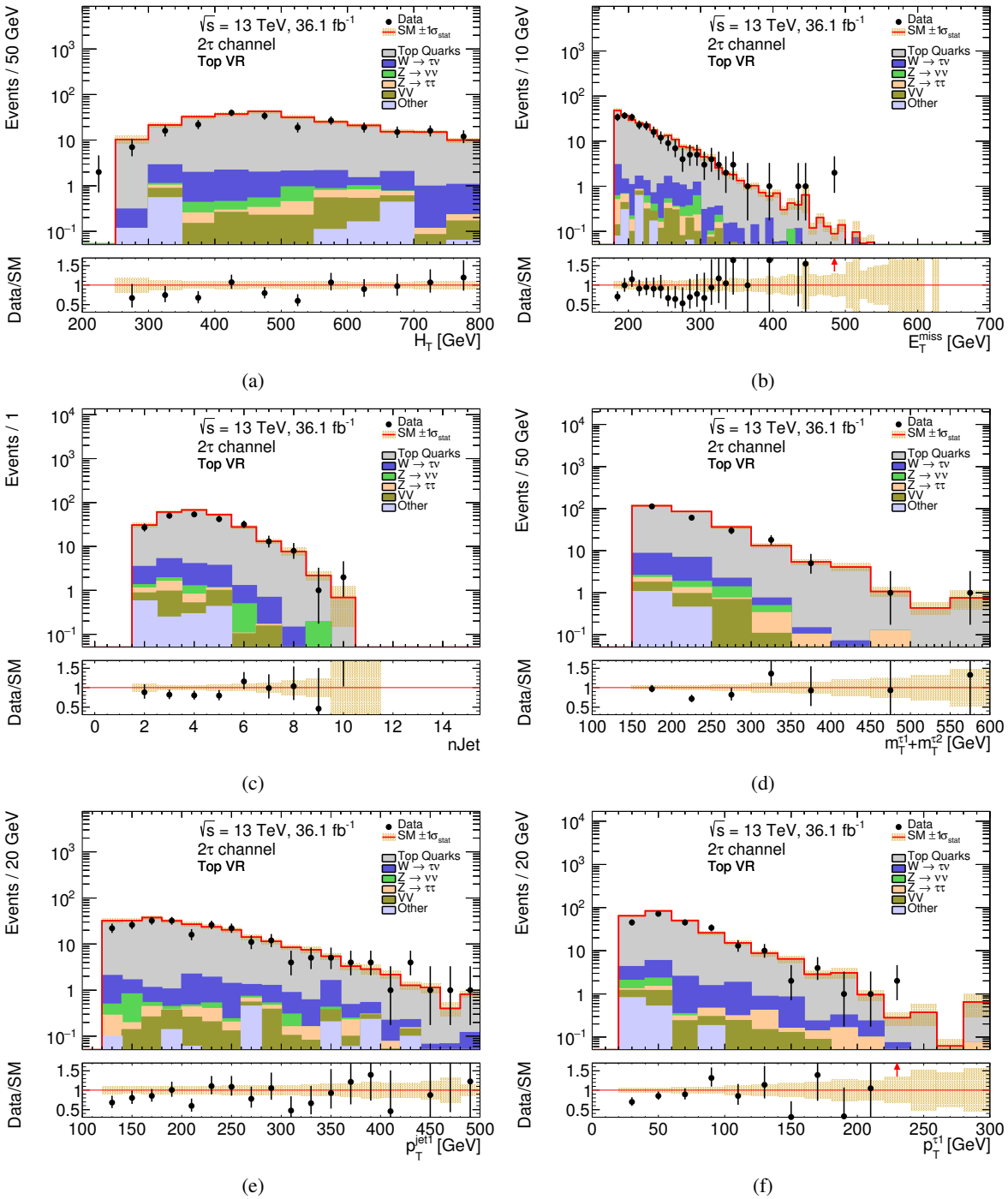

Figure A.11: Kinematic distributions of characteristic variables in the 2τ Top VR. The results shown are obtained after fitting the normalisation of the background in the control regions. The last bin of each distribution contains the overflow events. The uncertainties displayed consider only statistical limitations in the background modelling, illustrated by the shaded bands. Red arrows in the Data/SM ratio indicate bins where the corresponding entry falls outside the plotted range. The contribution labelled as *other* includes multi-jet events and V+Jets processes not explicitly listed in the legend.

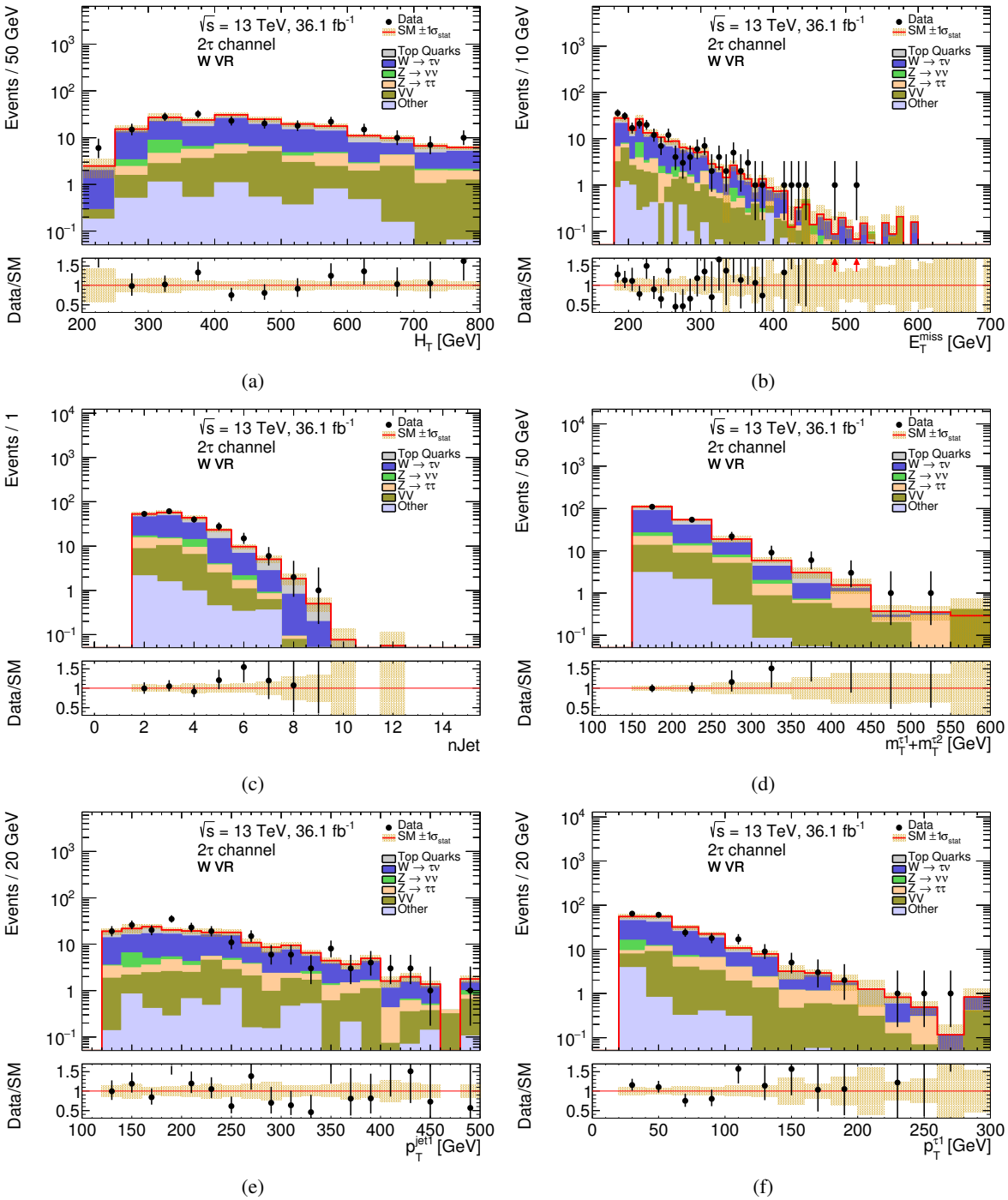

Figure A.12: Kinematic distributions of characteristic variables in the 2τ *W* VR. The results shown are obtained after fitting the normalisation of the background in the control regions. The last bin of each distribution contains the overflow events. The uncertainties displayed consider only statistical limitations in the background modelling, illustrated by the shaded bands. Red arrows in the Data/SM ratio indicate bins where the corresponding entry falls outside the plotted range. The contribution labelled as *other* includes multi-jet events and *V*+Jets processes not explicitly listed in the legend.

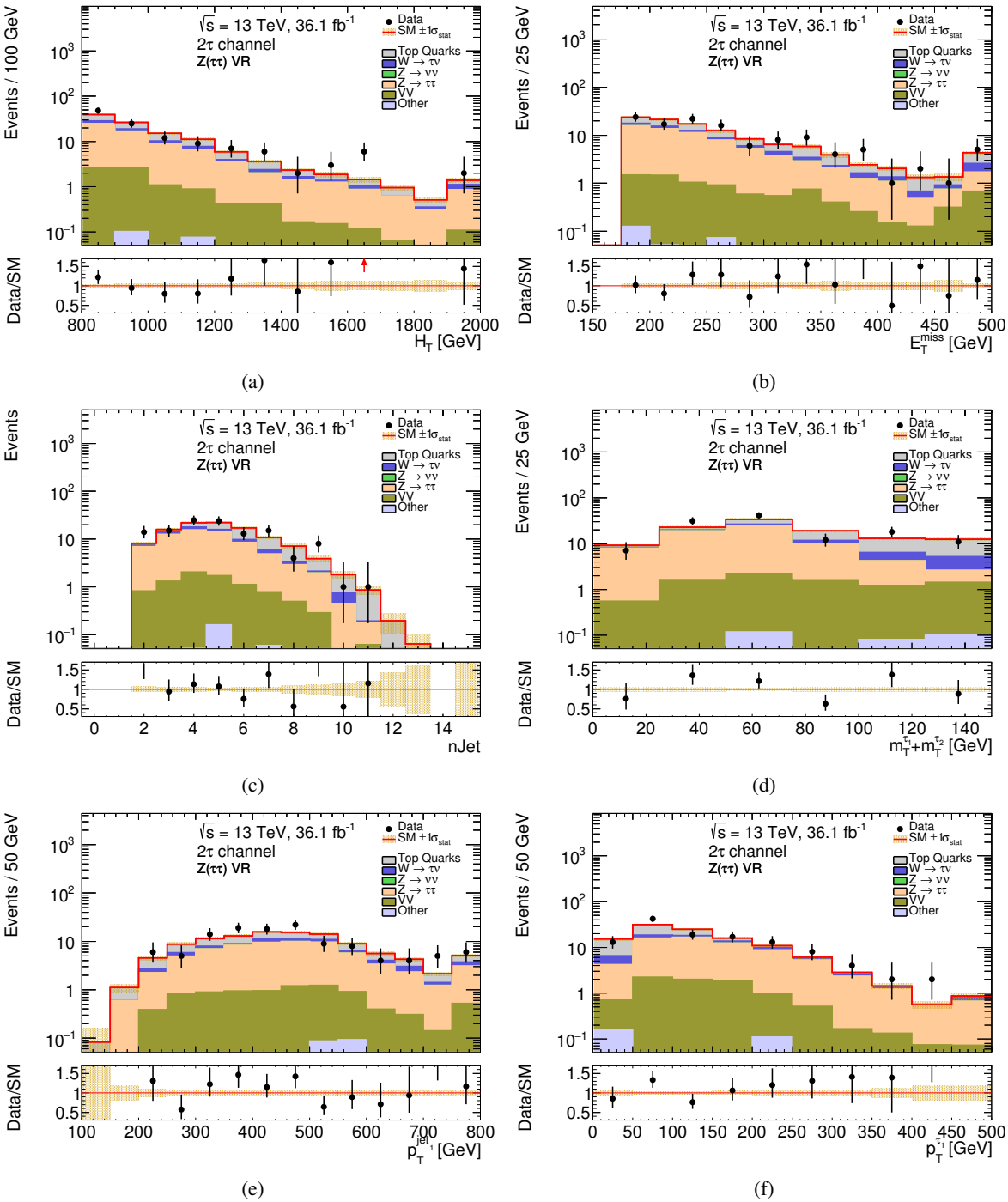

Figure A.13: Kinematic distributions of characteristic variables in the 2τ $Z \to \tau\tau$ VR. The results shown are obtained after fitting the normalisation of the background in the control regions. The last bin of each distribution contains the overflow events. The uncertainties displayed consider only statistical limitations in the background modelling, illustrated by the shaded bands. Red arrows in the Data/SM ratio indicate bins where the corresponding entry falls outside the plotted range. The contribution labelled as *other* includes multi-jet events and V+Jets processes not explicitly listed in the legend.

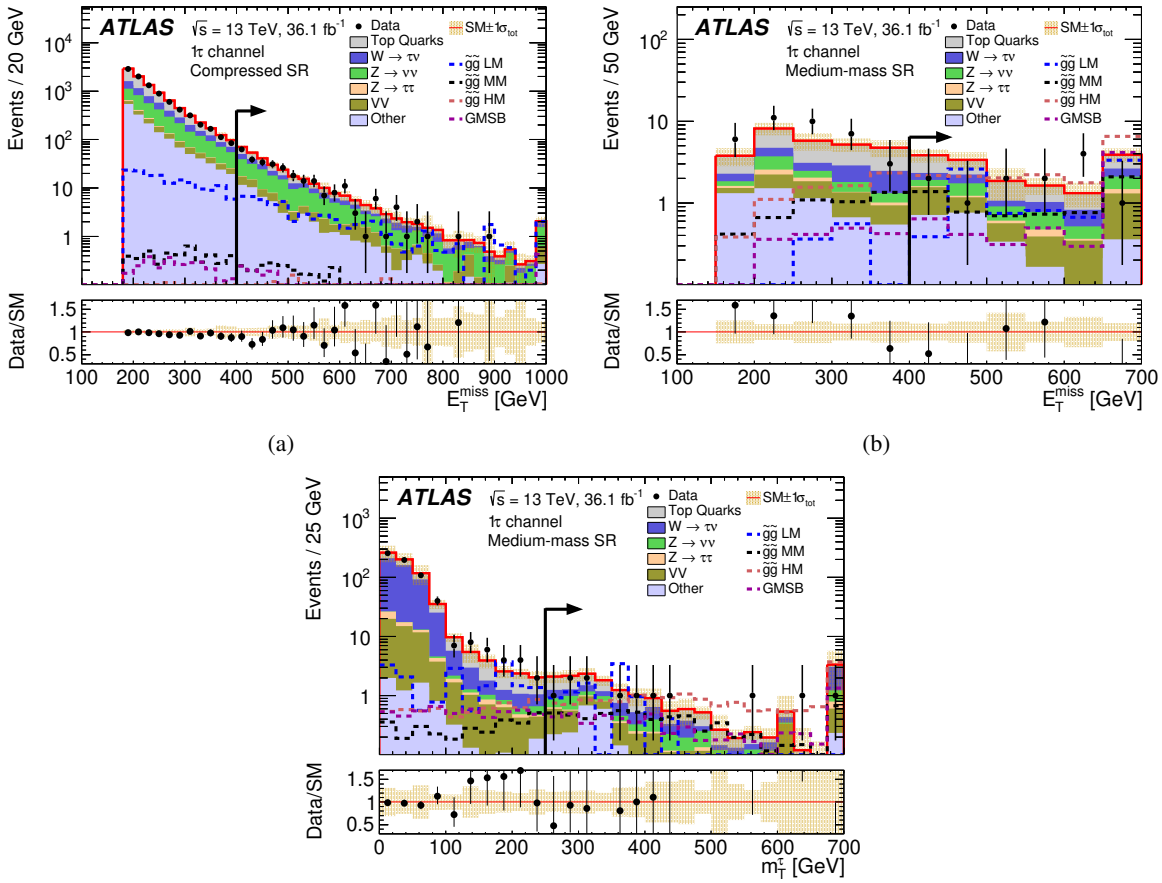

(a) (b)

(c)

Figure A.14: Kinematic distributions for extended SR selections of the 1τ channel after the fit: (a) $E_{\mathrm{T}}^{\mathrm{miss}}$ in the compressed SR without the $E_{\mathrm{T}}^{\mathrm{miss}} > 400\,\mathrm{GeV}$ requirement, (b) H_{T} in the medium-mass SR without the $E_{\mathrm{T}}^{\mathrm{miss}} > 400\,\mathrm{GeV}$ requirement and (c) m_{T}^{τ} in the medium-mass SR without the $m_{\mathrm{T}}^{\tau} > 250\,\mathrm{GeV}$ requirement [8]. The contribution labeled as *other* includes multi-jet events and the V + jets processes not explicitly listed in the legend. The last bin of each distribution includes overflow events. The total uncertainty in the background prediction is shown as a shaded band. The signal region is indicated by the black arrow. Signal predictions are overlaid for several benchmark models. For the simplified model, LM, MM and HM refer to low, medium and high mass splitting scenarios, with $m_{\tilde{g}}$ ($m_{\tilde{\chi}_1^0}$) set to 1 065 GeV (825 GeV), 1 625 GeV (905 GeV) and 1 705 GeV (345 GeV), respectively. The GMSB benchmark model corresponds to $\Lambda = 120\,\mathrm{TeV}$ and $\tan\beta = 40$.

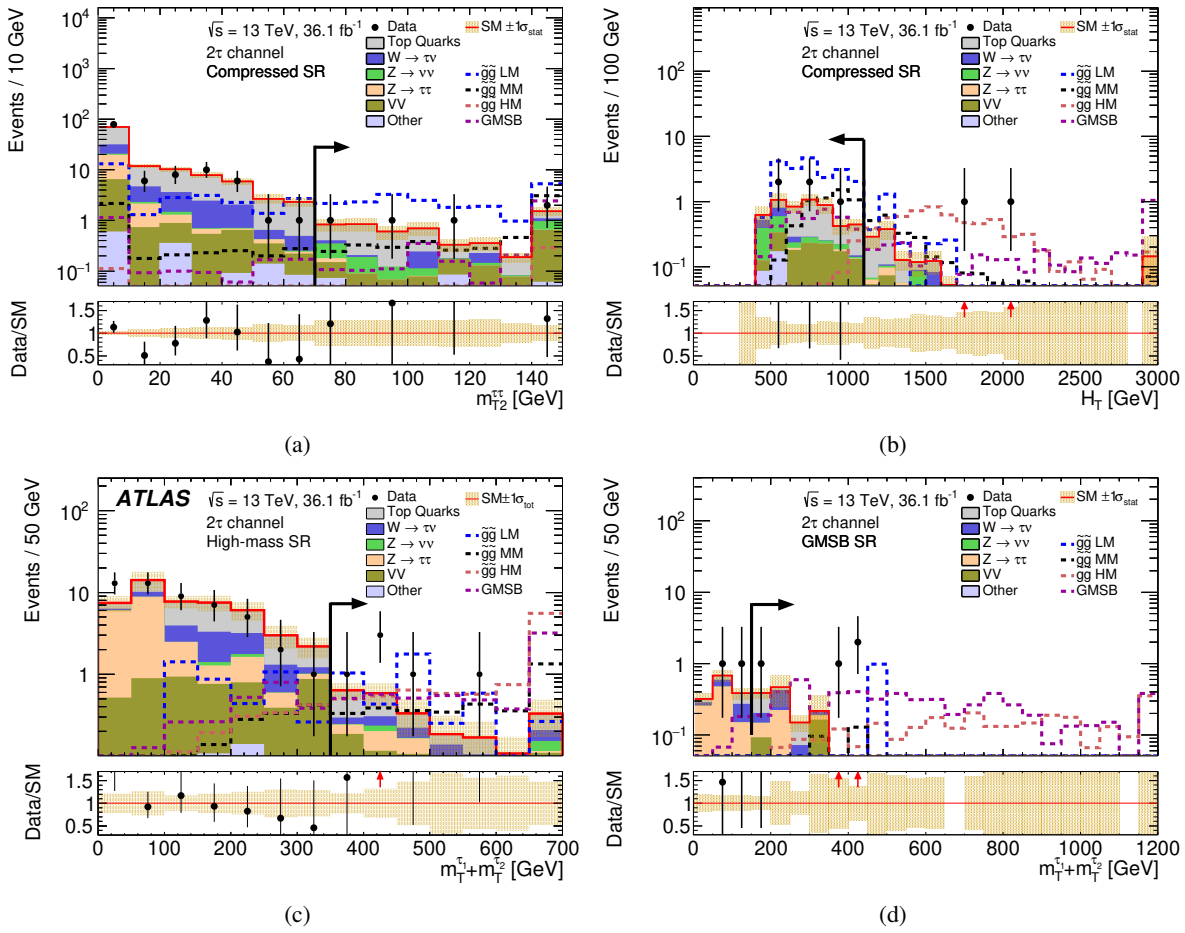

Figure A.15: Kinematic distributions for extended SR selections of the 2τ channel after the fit: (a) $m_{\mathrm{T2}}^{\tau\tau}$ in the compressed SR without the $m_{\mathrm{T2}}^{\tau\tau} > 70\,\mathrm{GeV}$ requirement, (b) H_{T} in the compressed SR without the $H_{\mathrm{T}} < 1\,100\,\mathrm{GeV}$ requirement, (c) $m_{\mathrm{T}}^{\tau_1} + m_{\mathrm{T}}^{\tau_2}$ in the high-mass SR without the $m_{\mathrm{T}}^{\tau_1} + m_{\mathrm{T}}^{\tau_2} > 350\,\mathrm{GeV}$ requirement [8] and (d) $m_{\mathrm{T}}^{\tau_1} + m_{\mathrm{T}}^{\tau_2}$ in the GMSB SR without the $m_{\mathrm{T}}^{\tau_1} + m_{\mathrm{T}}^{\tau_2} > 350\,\mathrm{GeV}$ requirement. The contribution labeled as *other* includes multi-jet events and the V + jets processes not explicitly listed in the legend. The last bin of each distribution includes overflow events. The statistical (total) uncertainty in the background prediction is shown as a shaded band. Red arrows in the Data/SM ratio indicate bins where the entry is outside the plotted range. The signal region is indicated by the black arrow. Signal predictions are overlaid for several benchmark models. For the simplified model, LM, MM and HM refer to low, medium and high mass splitting scenarios, with $m_{\tilde{g}}$ ($m_{\tilde{\chi}_1^0}$) set to 1 065 GeV (825 GeV), 1 625 GeV (905 GeV) and 1 705 GeV (345 GeV), respectively. The GMSB benchmark model corresponds to $\Lambda = 120\,\mathrm{TeV}$ and $\tan\beta = 40$.

A.3 Yield tables

CR	W true-τ	W fake-τ	Top true-τ	Top fake-τ
Observed events	31374	452	20964	829
Fitted SM events	31374.01 ± 232.35	451.97 ± 21.09	20963.73 ± 148.02	829.06 ± 28.26
Fitted $Z(\tau\tau)$ + jets events	1429.71 ± 229.42	12.40 ± 2.75	281.47 ± 57.54	28.24 ± 5.65
Fitted $Z(\nu\nu)$ + jets events	563.46 ± 122.14	0.00 ± 0.00	110.51 ± 25.69	0.00 ± 0.00
Fitted VV events	1063.84 ± 247.15	52.61 ± 7.49	205.71 ± 52.21	8.12 ± 2.01
Fitted $Z(\ell\ell)$ + jets events	20.84 ± 4.18	4.48 ± 1.61	2.13 ± 0.52	2.49 ± 1.06
Fitted $W(\mu\nu)$ + jets events	246.56 ± 48.85	226.49 ± 30.35	26.69 ± 7.47	41.62 ± 9.78
Fitted $W(e\nu)$ + jets events	387.27 ± 67.38	0.00 ± 0.00	60.85 ± 15.41	0.00 ± 0.00
Fitted $W(\tau\nu)$ + jets events	24847.16 ± 768.24	40.75 ± 14.59	3400.48 ± 639.71	6.81 ± 2.16
Fitted $t\bar{t}$ events	2494.06 ± 527.34	105.0 ± 19.8	15626.97 ± 720.35	693.2 ± 33.4
Fitted single-top + $t\bar{t}$ + V events	297.3 ± 89.9	10.2 ± 2.5	1149.3 ± 293.8	47.9 ± 10.7
Fitted Multi-jet events	23.45 ± 2.97	0.00 ± 0.00	99.49 ± 12.60	0.76 ± 0.10
MC exp. SM events	31366.10 ± 7468.80	451.63 ± 47.78	21001.50 ± 4419.91	828.00 ± 133.01
MC exp. $Z(\tau\tau)$ + jets events	1427.20 ± 371.05	12.38 ± 2.56	281.06 ± 69.74	28.20 ± 5.45
MC exp. $Z(\nu\nu)$ + jets events	575.03 ± 117.21	0.00 ± 0.00	112.81 ± 22.10	0.00 ± 0.00
MC exp. VV events	1063.53 ± 251.60	52.61 ± 7.56	205.73 ± 52.79	8.12 ± 2.02
MC exp. $Z(\ell\ell)$ + jets events	21.27 ± 3.99	4.57 ± 1.60	2.18 ± 0.49	2.55 ± 0.99
MC exp. $W(\mu\nu)$ + jets events	246.40 ± 55.30	226.36 ± 26.66	26.68 ± 6.82	41.61 ± 8.26
MC exp. $W(e\nu)$ + jets events	387.01 ± 64.75	0.00 ± 0.00	60.85 ± 12.87	0.00 ± 0.00
MC exp. $W(\tau\nu)$ + jets events	24824.97 ± 6640.54	40.72 ± 16.19	3398.81 ± 810.43	6.81 ± 1.95
MC exp. top quarks events	2795.35 ± 667.97	114.98 ± 22.21	16805.82 ± 4049.53	739.89 ± 127.86
data-driven exp. Multi-jet events	25.35 ± 10.14	0.00 ± 0.00	107.55 ± 43.02	0.83 ± 0.33

Table A.1: Yields of the expected backgrounds from the SM in the Top and W true-τ and fake-τ CRs. Expectation is given both with and without the normalisation-factors computed in the combined fit applied. The given uncertainties are statistical plus systematic. Only the subsamples contributing in the respective region are considered. For the MC exp. yields, contributions from single-top, $t\bar{t}$ + V and $t\bar{t}$ events are combined into one entry.

CR	W kinematic	Top kinematic
Observed events	62264	43785
Fitted SM events	62264.17 ± 375.50	43784.64 ± 216.90
Fitted $Z(\tau\tau)$ + jets events	581.31 ± 118.75	117.98 ± 29.37
Fitted $Z(\nu\nu)$ + jets events	1.87 ± 1.03	0.38 ± 0.14
Fitted VV events	2178.57 ± 358.92	405.68 ± 81.86
Fitted $Z(\ell\ell)$ + jets events	788.25 ± 185.99	115.66 ± 28.49
Fitted $W(\ell\nu)$ + jets events	46040.05 ± 1651.65	6246.45 ± 1080.48
Fitted $W(\tau\nu)$ + jets events	6797.56 ± 1244.18	1013.29 ± 217.58
Fitted $t\bar{t}$ events	5233.21 ± 1121.04	33100.1 ± 1304.5
Fitted single-top + $t\bar{t}$ + V events	598.8 ± 168.5	2541.6 ± 557.6
Fitted Multi-jet events	43.78 ± 5.55	243.53 ± 30.85
MC exp. SM events	62250.51 ± 12081.69	43935.20 ± 7656.08
MC exp. $Z(\tau\tau)$ + jets events	580.31 ± 110.56	117.80 ± 25.82
MC exp.$Z(\nu\nu)$ + jets events	1.90 ± 1.08	0.38 ± 0.14
MC exp. VV events	2178.07 ± 365.65	405.72 ± 82.73
MC exp. $Z(\ell\ell)$ + jets events	804.55 ± 194.56	118.09 ± 28.87
MC exp. $W(\ell\nu)$ + jets events	45995.61 ± 9732.99	6242.67 ± 1256.47
MC exp. $W(\tau\nu)$ + jets events	6790.31 ± 1805.38	1012.67 ± 220.03
MC exp. top quarks events	5852.44 ± 1204.62	35774.61 ± 7013.07
data-driven exp. Multi-jet events	47.33 ± 18.93	263.27 ± 105.31

Table A.2: Yields of the expected backgrounds from the SM in the Top and W kinematic CRs. Expectation is given both with and without the normalisation-factors computed in the combined fit applied. The given uncertainties are statistical plus systematic. Only the subsamples contributing in the respective region are considered. For the MC exp. yields, contributions from single-top, $t\bar{t}$ + V and $t\bar{t}$ events are combined into one entry.

CR	$Z(\nu\nu)$	multi-jet
Observed events	3011	408
Fitted SM events	3010.97 ± 53.66	407.65 ± 20.47
Fitted $Z(\nu\nu)$ + jets events	1191.75 ± 200.86	8.48 ± 1.60
Fitted VV events	170.27 ± 24.79	5.28 ± 1.24
Fitted $W(\tau\nu)$ + jets events	677.70 ± 198.90	19.28 ± 7.12
Fitted other V + jets events	641.80 ± 94.36	14.24 ± 6.29
Fitted $t\bar{t}$ events	279.44 ± 50.34	79.3 ± 24.7
Fitted single-top + $t\bar{t}$ + V events	24.77 ± 6.40	9.77 ± 2.00
Fitted Multi-jet events	25.24 ± 3.20	271.28 ± 34.36
MC exp. SM events	3036.20 ± 403.31	429.70 ± 120.05
MC exp. $Z(\nu\nu)$ + jets events	1216.47 ± 129.44	8.66 ± 0.96
MC exp. VV events	170.25 ± 25.04	5.28 ± 1.26
MC exp. $W(\tau\nu)$ + jets events	677.16 ± 266.49	19.28 ± 8.01
MC exp. other V + jets events	641.64 ± 84.06	14.24 ± 5.19
MC exp. top quarks events	303.39 ± 52.08	88.97 ± 22.74
data-driven exp. Multi-jet events	27.29 ± 10.91	293.27 ± 117.31

Table A.3: Yields of the expected backgrounds from the SM in the $Z(\nu\nu)$ and multi-jet CRs. Expectation is given both with and without the normalisation-factors computed in the combined fit applied. The given uncertainties are statistical plus systematic. Only the subsamples contributing in the respective region are considered. For the MC exp. yields, contributions from single-top, $t\bar{t}$ + V and $t\bar{t}$ events are combined into one entry.

CR	$Z(\tau\tau)$
Observed events	293
Fitted SM events	293.00 ± 16.81
Fitted $Z(\tau\tau)$ + jets events	239.40 ± 18.11
Fitted $Z(\nu\nu)$ + jets events	0.02 ± 0.01
Fitted VV events	15.98 ± 3.41
Fitted $W(\tau\nu)$ + jets events	0.62 ± 0.57
Fitted other V + jets events	24.94 ± 4.93
Fitted $t\bar{t}$ events	11.4 ± 3.7
Fitted single-top + $t\bar{t}$ + V events	0.62 ± 0.20
Fitted Multi-jet events	0.00 ± 0.00
MC exp. SM events	292.54 ± 64.10
MC exp. $Z(\tau\tau)$ + jets events	239.01 ± 57.70
MC exp. $Z(\nu\nu)$ + jets events	0.02 ± 0.00
MC exp. VV events	15.97 ± 3.46
MC exp. $W(\tau\nu)$ + jets events	0.62 ± 0.58
MC exp. other V + jets events	24.93 ± 4.06
MC exp. top quarks events	11.99 ± 4.99
data-driven exp. Multi-jet events	0.00 ± 0.00

Table A.4: Yields of the expected backgrounds from the SM in the $Z(\tau\tau)$ CR. Expectation is given both with and without the normalisation-factors computed in the combined fit applied. The given uncertainties are statistical plus systematic. Only the subsamples contributing in the respective region are considered. For the MC exp. yields, contributions from single-top, $t\bar{t}$ + V and $t\bar{t}$ events are combined into one entry.

2τ VR	W	Top	$Z(\tau\tau)$
Observed events	206	229	120
Fitted SM events	195.50 ± 19.70	263.47 ± 84.62	110.30 ± 23.91
Fitted $Z(\tau\tau)$ + jets events	15.86 ± 6.25	1.36 ± 0.44	59.45 ± 7.05
Fitted $Z(\nu\nu)$ + jets events	7.89 ± 2.05	1.59 ± 0.40	$0.01^{+0.02}_{-0.01}$
Fitted VV events	23.70 ± 4.65	2.05 ± 0.80	8.42 ± 2.10
Fitted $W(\tau\nu)$ + jets events	98.76 ± 14.63	12.24 ± 3.10	10.02 ± 6.01
Fitted other V + jets events	5.62 ± 2.01	1.00 ± 0.39	0.15 ± 0.07
Fitted $t\bar{t}$ events	40.77 ± 11.07	231.630 ± 85.007	29.45 ± 21.21
Fitted single-top + $t\bar{t}$ + V events	2.7 ± 0.9	13.07 ± 3.15	2.6 ± 0.8
Fitted Multi-jet events	0.19 ± 0.02	0.55 ± 0.07	0.19 ± 0.02
MC exp. SM events	195.40 ± 34.90	262.67 ± 103.37	110.10 ± 30.14
MC exp. $Z(\tau\tau)$ + jets events	15.82 ± 7.19	1.35 ± 0.60	59.34 ± 13.41
MC exp. $Z(\nu\nu)$ + jets events	8.06 ± 1.29	1.63 ± 0.34	$0.01^{+0.02}_{-0.01}$
MC exp. VV events	23.70 ± 4.70	2.05 ± 0.81	8.42 ± 2.13
MC exp. $W(\tau\nu)$ + jets events	98.70 ± 20.82	12.24 ± 2.35	10.01 ± 7.70
MC exp. other V + jets events	5.62 ± 1.11	1.00 ± 0.36	0.15 ± 0.06
MC exp. top quarks events	43.29 ± 15.24	243.81 ± 102.69	31.96 ± 21.06
data-driven exp. Multi-jet events	0.20 ± 0.08	0.60 ± 0.24	0.21 ± 0.08

Table A.5: Yields of the expected backgrounds from the SM in the VRs of the 2τ channel. Expectation is given both with and without the scalings computed in the combined fit applied. Uncertainties are statistical plus systematics. Only the subsamples contributing in the respective region are considered. For the MC exp. yields, contributions from single-top, $t\bar{t}$ + V and $t\bar{t}$ events are combined into one entry.

1τ VR	medium-mass m_{T}^{τ}	medium-mass H_{T}	medium-mass $E_{\mathrm{T}}^{\mathrm{miss}}$
Observed events	680	1871	1662
Fitted SM events	716.03 ± 113.29	1981.56 ± 438.63	1588.74 ± 441.33
Fitted $Z(\nu\nu)$ + jets events	87.10 ± 16.90	6.76 ± 1.86	11.18 ± 2.03
Fitted VV events	46.17 ± 7.94	109.17 ± 21.25	92.42 ± 14.27
Fitted $W(\tau\nu)$ + jets events	125.42 ± 28.86	992.89 ± 390.18	1173.02 ± 437.05
Fitted other V + jets events	71.51 ± 11.22	126.73 ± 17.49	40.27 ± 7.14
Fitted $t\bar{t}$ events	365.50 ± 104.00	672.6 ± 217.8	256.32 ± 49.32
Fitted single-top + $t\bar{t}$ + V events	17.4 ± 3.9	57.77 ± 14.00	14.3 ± 3.8
Fitted Multi-jet events	2.91 ± 0.37	15.57 ± 1.97	1.43 ± 0.18
MC exp. SM events	717.84 ± 149.55	1983.06 ± 595.94	1588.52 ± 613.21
MC exp. $Z(\nu\nu)$ + jets events	88.90 ± 6.42	6.90 ± 1.67	11.42 ± 1.62
MC exp. VV events	46.16 ± 8.00	109.15 ± 21.50	92.41 ± 14.44
MC exp. $W(\tau\nu)$ + jets events	125.32 ± 42.12	992.01 ± 507.24	1171.94 ± 594.00
MC exp. other V + jets events	71.48 ± 9.67	126.55 ± 19.00	40.23 ± 8.70
MC exp. top quarks events	382.83 ± 133.94	731.62 ± 252.10	270.97 ± 104.30
data-driven exp. Multi-jet events	3.15 ± 1.26	16.83 ± 6.73	1.54 ± 0.62

Table A.6: Yields of the expected backgrounds from the SM in the VRs of the medium-mass SR of the 1τ channel. Expectation is given both with and without the scalings computed in the combined fit applied. Uncertainties are statistical plus systematics. Only the subsamples contributing in the respective region are considered. For the MC exp. yields, contributions from single-top, $t\bar{t}$ + V and $t\bar{t}$ events are combined into one entry.

1τ VR	compressed $E_{\mathrm{T}}^{\mathrm{miss}}$	compressed m_{T}^{τ}
Observed events	1396	8982
Fitted SM events	1305.68 ± 295.80	9184.14 ± 764.42
Fitted $Z(\nu\nu)$ + jets events	25.69 ± 4.86	1946.17 ± 338.97
Fitted VV events	59.38 ± 8.01	338.08 ± 46.26
Fitted $W(\tau\nu)$ + jets events	903.33 ± 286.23	1508.09 ± 241.28
Fitted other V + jets events	52.36 ± 7.23	1390.03 ± 193.91
Fitted $t\bar{t}$ events	250.3 ± 84.6	3510.6 ± 759.5
Fitted single-top + $t\bar{t}$ + V events	12.1 ± 2.8	235.4 ± 47.5
Fitted Multi-jet events	2.59 ± 0.33	255.85 ± 32.41
MC exp. SM events	1306.08 ± 424.11	9236.88 ± 1333.55
MC exp. $Z(\nu\nu)$ + jets events	26.22 ± 3.12	1986.55 ± 211.08
MC exp. VV events	59.37 ± 8.09	338.05 ± 46.76
MC exp. $W(\tau\nu)$ + jets events	902.54 ± 397.67	1507.06 ± 427.16
MC exp. other V + jets events	52.39 ± 6.90	1389.66 ± 173.98
MC exp. top quarks events	262.75 ± 115.06	3738.98 ± 936.23
data-driven exp. Multi-jet events	2.80 ± 1.12	276.59 ± 110.63

Table A.7: Yields of the expected backgrounds from the SM in the VRs of the compressed SR of the 1τ channel. Expectation is given both with and without the scalings computed in the combined fit applied. Uncertainties are statistical plus systematics. Only the subsamples contributing in the respective region are considered. For the MC exp. yields, contributions from single-top, $t\bar{t}$ + V and $t\bar{t}$ events are combined into one entry.

1τ SR	medium-mass	compressed
Observed events	12	286
Fitted SM events	15.90 ± 2.95	319.74 ± 31.90
Fitted $Z(\nu\nu)$ + jets events	2.20 ± 0.50	110.16 ± 23.64
Fitted VV events	2.95 ± 0.57	28.18 ± 4.54
Fitted $W(\tau\nu)$ + jets events	2.15 ± 1.69	50.54 ± 17.79
Fitted other V + jets events	1.67 ± 0.38	44.85 ± 9.56
Fitted $t\bar{t}$ events	5.11 ± 1.00	69.8 ± 12.5
Fitted single-top + $t\bar{t}$ + V events	0.67 ± 0.16	7.0 ± 1.4
Fitted Multi-jet events	1.14 ± 0.14	9.22 ± 1.17
MC exp. SM events	16.03 ± 3.40	322.57 ± 42.15
MC exp. $Z(\nu\nu)$ + jets events	2.24 ± 0.34	112.45 ± 14.70
MC exp. VV events	2.95 ± 0.57	28.18 ± 4.56
MC exp. $W(\tau\nu)$ + jets events	2.15 ± 1.70	50.51 ± 21.47
MC exp. other V + jets events	1.67 ± 0.38	44.83 ± 8.01
MC exp. topquarks events	5.78 ± 1.96	76.64 ± 20.85
data-driven exp. Multi-jet events	1.24 ± 0.49	9.96 ± 3.99

Table A.8: Yields of the expected backgrounds from the SM in the SRs of the 1τ channel. Expectation is given both with and without the scalings computed in the combined fit applied. Uncertainties are statistical plus systematics. Only the subsamples contributing in the respective region are considered. For the MC exp. yields, contributions from single-top, $t\bar{t}$ + V and $t\bar{t}$ events are combined into one entry.

2τ SR	GMSB	high-mass	compressed
Observed events	4	6	5
Fitted SM events	1.41 ± 0.53	2.34 ± 0.70	5.36 ± 1.90
Fitted $Z(\tau\tau)$ + jets events	0.28 ± 0.10	0.32 ± 0.11	0.03 ± 0.01
Fitted $Z(\nu\nu)$ + jets events	0.01 ± 0.01	0.09 ± 0.03	0.67 ± 0.35
Fitted VV events	0.29 ± 0.08	0.56 ± 0.15	1.06 ± 0.25
Fitted $W(\tau\nu)$ + jets events	$0.37^{+0.38}_{-0.37}$	$0.36^{+0.43}_{-0.36}$	$0.40^{+0.47}_{-0.40}$
Fitted other V + jets events	$0.00^{+0.00}_{-0.00}$	0.02 ± 0.01	0.29 ± 0.08
Fitted $t\bar{t}$ events	0.31 ± 0.15	0.82 ± 0.18	2.4 ± 0.7
Fitted single-top + $t\bar{t}$ + V events	0.09 ± 0.04	0.17 ± 0.07	0.47 ± 0.14
Fitted Multi-jet events	0.06 ± 0.01	0.01 ± 0.00	0.02 ± 0.00
MC exp. SM events	1.42 ± 0.51	2.34 ± 0.70	5.36 ± 2.04
MC exp. $Z(\tau\tau)$ + jets events	0.28 ± 0.09	0.32 ± 0.10	0.03 ± 0.01
MC exp. $Z(\nu\nu)$ + jets events	0.01 ± 0.01	0.09 ± 0.02	0.69 ± 0.36
MC exp. VV events	0.29 ± 0.08	0.56 ± 0.15	1.06 ± 0.25
MC exp. $W(\tau\nu)$ + jets events	0.37 ± 0.32	$0.36^{+0.37}_{-0.36}$	$0.40^{+0.42}_{-0.40}$
MC exp. other V + jets events	$0.00^{+0.00}_{-0.00}$	0.02 ± 0.01	0.29 ± 0.05
MC exp. top quarks events	0.39 ± 0.23	0.98 ± 0.48	2.86 ± 1.82
data-driven exp. Multi-jet events	0.07 ± 0.03	0.01 ± 0.01	0.03 ± 0.01

Table A.9: Yields of the expected backgrounds from the SM in the normalisation-fit SRs of the 2τ channel. Expectation is given both with and without the scalings computed in the combined fit applied. Uncertainties are statistical plus systematics. Only the subsamples contributing in the respective region are considered. For the MC exp. yields, contributions from single-top, $t\bar{t}$ + V and $t\bar{t}$ events are combined into one entry.

2τ multibin SR	Bin $\mathcal{A}$	Bin $\mathcal{B}$	Bin C	Bin $\mathcal{D}$
Observed events	21	14	7	4
Fitted SM events	27.13 ± 6.44	19.51 ± 3.97	10.44 ± 2.88	7.51 ± 1.61
Fitted $Z(\tau\tau)$ + jets events	1.62 ± 0.40	0.92 ± 0.28	0.51 ± 0.14	0.55 ± 0.21
Fitted $Z(\nu\nu)$ + jets events	0.20 ± 0.07	0.19 ± 0.06	0.07 ± 0.04	0.09 ± 0.04
Fitted V events	2.80 ± 0.62	1.51 ± 0.39	0.62 ± 0.22	1.53 ± 0.37
Fitted $W(\tau\nu)$ + jets events	6.22 ± 3.91	4.09 ± 1.79	1.46 ± 0.79	0.76 ± 0.70
Fitted other V + jets events	0.15 ± 0.09	0.30 ± 0.12	0.11 ± 0.05	0.07 ± 0.05
Fitted $t\bar{t}$ events	14.8 ± 3.5	11.8 ± 2.6	6.98 ± 2.18	4.2 ± 0.7
Fitted single-top + $t\bar{t}$ + V events	1.4 ± 0.4	0.84 ± 0.25	0.66 ± 0.27	0.32 ± 0.13
Fitted Multi-jet events	0.11 ± 0.01	0.12 ± 0.02	0.07 ± 0.01	0.01 ± 0.00
MC exp. SM events	27.07 ± 6.33	19.47 ± 5.06	10.42 ± 3.66	7.49 ± 2.05
MC exp. $Z(\tau\tau)$ + jets events	1.62 ± 0.39	0.91 ± 0.26	0.51 ± 0.17	0.55 ± 0.22
MC exp. $Z(\nu\nu)$ + jets events	0.20 ± 0.06	0.19 ± 0.05	0.08 ± 0.04	0.10 ± 0.05
MC exp. VV events	2.80 ± 0.62	1.51 ± 0.40	0.62 ± 0.22	1.53 ± 0.37
MC exp. $W(\tau\nu)$ + jets events	6.22 ± 2.95	4.09 ± 1.55	1.46 ± 0.57	$0.75^{+0.82}_{-0.75}$
MC exp. other V + jets events	0.15 ± 0.08	0.30 ± 0.10	0.11 ± 0.05	0.07 ± 0.04
MC exp. top quarks events	15.96 ± 4.60	12.33 ± 4.37	7.57 ± 3.38	4.49 ± 1.48
data-driven exp. Multi-jet events	0.12 ± 0.05	0.13 ± 0.05	0.07 ± 0.03	0.01 ± 0.00

Table A.10: Yields of the expected backgrounds from the SM in the first four bins of the multibin SR of the 2τ channel. Expectation is given both with and without the scalings computed in the combined fit applied. Uncertainties are statistical plus systematics. Only the subsamples contributing in the respective region are considered. For the MC exp. yields, contributions from single-top, $t\bar{t}$ + V and $t\bar{t}$ events are combined into one entry.

2τ multibin SR	Bin $\mathcal{E}$	Bin $\mathcal{F}$	Bin $\mathcal{G}$
Observed events	5	3	0
Fitted SM events	2.47 ± 0.80	1.63 ± 1.60	1.26 ± 0.52
Fitted $Z(\tau\tau)$ + jets events	$0.26^{+0.30}_{-0.26}$	0.12 ± 0.09	$0.07^{+0.10}_{-0.07}$
Fitted $Z(\nu\nu)$ + jets events	$0.00^{+0.00}_{-0.00}$	$0.00^{+0.01}_{-0.00}$	0.08 ± 0.03
Fitted VV events	0.60 ± 0.22	0.24 ± 0.11	0.37 ± 0.11
Fitted $W(\tau\nu)$ + jets events	$0.30^{+0.36}_{-0.30}$	$0.36^{+0.46}_{-0.36}$	$0.15^{+0.21}_{-0.15}$
Fitted other V + jets events	$0.00^{+0.00}_{-0.00}$	0.01 ± 0.01	$0.01^{+0.10}_{-0.01}$
Fitted $t\bar{t}$ events	1.2 ± 0.5	$0.88^{+1.5}_{-0.88}$	$0.4^{+0.5}_{-0.4}$
Fitted single-top + $t\bar{t}$ + V events	0.17 ± 0.07	0.015 ± 0.011	0.16 ± 0.11
Fitted Multi-jet events	0.02 ± 0.00	0.00 ± 0.00	0.01 ± 0.00
MC exp. SM events	2.47 ± 1.02	$1.63^{+1.67}_{-1.63}$	1.26 ± 0.57
MC exp. $Z(\tau\tau)$ + jets events	$0.26^{+0.30}_{-0.26}$	0.12 ± 0.10	$0.07^{+0.10}_{-0.07}$
MC exp. $Z(\nu\nu)$ + jets events	$0.00^{+0.00}_{-0.00}$	$0.00^{+0.01}_{-0.00}$	0.08 ± 0.02
MC exp. VV events	0.60 ± 0.22	0.24 ± 0.11	0.37 ± 0.11
MC exp. $W(\tau\nu)$ + jets events	$0.30^{+0.31}_{-0.30}$	$0.36^{+0.41}_{-0.36}$	$0.15^{+0.18}_{-0.15}$
MC exp. other V + jets events	0.00 ± 0.00	0.01 ± 0.01	$0.01^{+0.04}_{-0.01}$
MC exp. top quarks events	1.29 ± 0.79	$0.90^{+1.57}_{-0.90}$	0.57 ± 0.51
data-driven exp. Multi-jet events	0.03 ± 0.01	0.00 ± 0.00	0.01 ± 0.00

Table A.11: Yields of the expected backgrounds from the SM in the last three bins of the multibin SR of the 2τ channel. Expectation is given both with and without the scalings computed in the combined fit applied. Uncertainties are statistical plus systematics. Only the subsamples contributing in the respective region are considered. For the MC exp. yields, contributions from single-top, $t\bar{t}$ + V and $t\bar{t}$ events are combined into one entry.

A.4 Additional information on systematic uncertainties

Uncertainty of CR	$Z(\nu\nu)$	$Z(\tau\tau)$	multi-jet
Total background expectation	3010.97	293.00	407.65
Total statistical $\left(\sqrt{N_{\text{exp.}}}\right)$	±54.87	±17.12	±20.19
Total background systematic	±53.66 [1.78%]	±16.81 [5.74%]	±20.47 [5.02%]
Background estimation	±389.36 [12.9%]	±64.71 [22.1%]	±111.87 [27.4%]
Jet reconstruction	±262.64 [8.7%]	±31.62 [10.8%]	±8.84 [2.2%]
Electroweak theory	±262.21 [8.7%]	±32.92 [11.2%]	±7.10 [1.7%]
Flavour tagging	±67.34 [2.2%]	±5.66 [1.9%]	±0.86 [0.21%]
$E_{\text{T}}^{\text{miss}}$ reconstruction	±66.78 [2.2%]	±4.28 [1.5%]	±4.89 [1.2%]
Pile-up	±65.43 [2.2%]	±2.80 [0.96%]	±0.05 [0.01%]
MC statistics	±50.53 [1.7%]	±8.58 [2.9%]	±4.02 [0.99%]
Tau identification	±31.72 [1.1%]	±36.52 [12.5%]	±3.81 [0.93%]
PDF variations	±27.45 [0.91%]	±3.11 [1.1%]	±1.98 [0.49%]
Top quark theory	±26.15 [0.87%]	±4.45 [1.5%]	±8.88 [2.2%]
Diboson theory	±21.37 [0.71%]	±1.61 [0.55%]	±0.76 [0.19%]
Multi-jet estimation	±9.70 [0.32%]	±0.00 [0.00%]	±105.81 [26.0%]
Electron reconstruction	±5.81 [0.19%]	±0.03 [0.01%]	±0.21 [0.05%]
Tau energy measurement	±5.48 [0.18%]	±21.61 [7.4%]	±1.43 [0.35%]
Muon reconstruction	±3.46 [0.11%]	±0.04 [0.01%]	±0.19 [0.05%]

Uncertainty of CR	W Kinematic	Top Kinematic
Total background expectation	62264.17	43784.64
Total statistical $\left(\sqrt{N_{\text{exp.}}}\right)$	±249.53	±209.25
Total background systematic	±375.50 [0.60%]	±216.90 [0.50%]
Background estimation	±11470.37 [18.4%]	±7467.38 [17.1%]
Jet reconstruction	±10789.50 [17.3%]	±4016.83 [9.2%]
Electroweak theory	±4332.18 [7.0%]	±485.07 [1.1%]
Flavour tagging	±1600.30 [2.6%]	±1436.47 [3.3%]
Top quark theory	±665.51 [1.1%]	±6058.74 [13.8%]
Muon reconstruction	±544.22 [0.87%]	±367.51 [0.84%]
PDF variations	±457.87 [0.74%]	±310.32 [0.71%]
$E_{\text{T}}^{\text{miss}}$ reconstruction	±380.30 [0.61%]	±426.68 [0.97%]
Diboson theory	±228.52 [0.37%]	±46.39 [0.11%]
Pile-up	±183.74 [0.30%]	±148.86 [0.34%]
Multi-jet estimation	±18.97 [0.03%]	±380.99 [0.87%]
Electron reconstruction	±3.43 [0.01%]	±12.49 [0.03%]
Tau energy measurement	±0.88 [0.00%]	±2.85 [0.01%]
Tau identification	±0.00 [0.00%]	±0.00 [0.00%]
MC statistics	±0.00 [0.00%]	±0.00 [0.00%]

Table A.12: Breakdown of the dominant systematic uncertainties on background estimates in the CRs. It is to be noted that the individual uncertainties can be correlated, and do not necessarily add up quadratically to the total background uncertainty. The percentages show the size of the uncertainty relative to the total expected background.

Uncertainty of 1τ compressed VR	$E_{\mathrm{T}}^{\mathrm{miss}}$	m_{T}^{τ}
Total background expectation	1305.68	9184.14
Total statistical ($\sqrt{N_{\mathrm{exp.}}}$)	±36.13	±95.83
Total background systematic	±295.80 [22.65%]	±764.42 [8.32%]
Electroweak theory	±385.57 [29.5%]	±385.15 [4.2%]
Background estimation	±270.01 [20.7%]	±1070.44 [11.7%]
Top quark theory	±109.91 [8.4%]	±852.94 [9.3%]
Jet reconstruction	±90.90 [7.0%]	±863.12 [9.4%]
Tau identification	±85.89 [6.6%]	±173.99 [1.9%]
PDF variations	±19.20 [1.5%]	±69.14 [0.75%]
MC statistics	±13.39 [1.0%]	±73.24 [0.80%]
Pile-up	±11.31 [0.87%]	±117.19 [1.3%]
Diboson theory	±5.67 [0.43%]	±39.53 [0.43%]
$E_{\mathrm{T}}^{\mathrm{miss}}$ reconstruction	±5.63 [0.43%]	±182.03 [2.0%]
Multi-jet estimation	±4.01 [0.31%]	±108.12 [1.2%]
Flavour tagging	±3.00 [0.23%]	±12.00 [0.13%]
Tau energy	±2.17 [0.17%]	±39.47 [0.43%]
Electron reconstruction	±0.46 [0.04%]	±17.83 [0.19%]
Muon reconstruction	±0.34 [0.03%]	±8.25 [0.09%]

Uncertainty of 2τ VR	W	Top	Z
Total background expectation	195.50	263.47	110.30
Total statistical ($\sqrt{N_{\mathrm{exp.}}}$)	±13.98	±16.23	±10.50
Total background systematic	±19.70 [10.08%]	±84.62 [32.12%]	±23.91 [21.68%]
Background estimation	±31.54 [16.1%]	±57.71 [21.9%]	±20.44 [18.5%]
Jet reconstruction	±18.82 [9.6%]	±20.12 [7.6%]	±13.90 [12.6%]
Electroweak theory	±16.62 [8.5%]	±1.20 [0.45%]	±9.07 [8.2%]
Tau identification	±14.65 [7.5%]	±23.61 [9.0%]	±12.52 [11.4%]
Top quark theory	±12.06 [6.2%]	±97.30 [36.9%]	±20.52 [18.6%]
MC statistics	±8.60 [4.4%]	±7.96 [3.0%]	±2.20 [2.0%]
$E_{\mathrm{T}}^{\mathrm{miss}}$ reconstruction	±7.06 [3.6%]	±7.02 [2.7%]	±1.25 [1.1%]
Flavour tagging	±6.66 [3.4%]	±6.75 [2.6%]	±0.59 [0.53%]
TauEnergy	±3.60 [1.8%]	±4.38 [1.7%]	±5.20 [4.7%]
Diboson theory	±3.35 [1.7%]	±0.36 [0.14%]	±1.37 [1.2%]
PDF variations	±2.53 [1.3%]	±1.80 [0.68%]	±1.50 [1.4%]
Pile-up	±0.64 [0.33%]	±0.51 [0.19%]	±2.20 [2.0%]
Electron reconstruction	±0.41 [0.21%]	±0.62 [0.23%]	±0.04 [0.03%]
Muon reconstruction	±0.40 [0.20%]	±0.29 [0.11%]	±0.03 [0.03%]
Multi-jet estimation	±0.08 [0.04%]	±2.04 [0.77%]	±0.49 [0.45%]

Table A.13: Breakdown of the dominant systematic uncertainties on background estimates in the VRs. It is to be noted that the individual nuisance parameters can be correlated, and do not necessarily add up quadratically to the total background uncertainty. The percentages show the size of the uncertainty relative to the total expected background.

Uncertainty of 2τ multibin SR	Bin $\mathcal{A}$	Bin $\mathcal{B}$	Bin $\mathcal{C}$	Bin $\mathcal{D}$
Total background expectation	27.13	19.51	10.44	7.51
Total statistical $\left(\sqrt{N_{\text{exp.}}}\right)$	±5.21	±4.42	±3.23	±2.74
Total background systematic	±6.44 [23.75%]	±3.97 [20.36%]	±2.88 [27.57%]	±1.61 [21.43%]
Background estimation	±4.31 [15.9%]	±3.20 [16.4%]	±1.85 [17.7%]	±1.16 [15.5%]
Jet reconstruction	±3.39 [12.5%]	±1.78 [9.1%]	±1.71 [16.4%]	±0.94 [12.5%]
Top quark theory	±2.97 [10.9%]	±3.61 [18.5%]	±2.74 [26.3%]	±1.07 [14.3%]
Electroweak theory	±2.66 [9.8%]	±0.88 [4.5%]	±0.50 [4.7%]	±0.77 [10.3%]
Tau identification	±2.25 [8.3%]	±1.60 [8.2%]	±0.87 [8.3%]	±0.69 [9.1%]
MC statistics	±1.40 [5.2%]	±1.22 [6.3%]	±0.90 [8.6%]	±0.73 [9.7%]
Pile-up	±0.92 [3.4%]	±0.44 [2.3%]	±0.11 [1.0%]	±0.24 [3.2%]
$E_{\text{T}}^{\text{miss}}$ reconstruction	±0.48 [1.8%]	±0.07 [0.34%]	±0.18 [1.8%]	±0.29 [3.8%]
PDF variations	±0.45 [1.7%]	±1.33 [6.8%]	±0.26 [2.5%]	±0.21 [2.8%]
Multi-jet estimation	±0.35 [1.3%]	±0.26 [1.3%]	±0.16 [1.6%]	±0.06 [0.84%]
Tau energy measurement	±0.25 [0.93%]	±0.47 [2.4%]	±0.15 [1.4%]	±0.14 [1.8%]
Electron reconstruction	±0.04 [0.14%]	±0.05 [0.24%]	±0.01 [0.11%]	±0.02 [0.28%]
Flavour tagging	±0.03 [0.11%]	±0.12 [0.61%]	±0.09 [0.88%]	±0.04 [0.59%]
Muon reconstruction	±0.03 [0.09%]	±0.01 [0.05%]	±0.01 [0.12%]	±0.00 [0.05%]
Diboson theory	±0.00 [0.00%]	±0.00 [0.00%]	±0.00 [0.00%]	±0.00 [0.00%]

Uncertainty of 2τ Multbin SR	Bin $\mathcal{E}$	Bin $\mathcal{F}$	Bin $\mathcal{G}$
Total background expectation	2.47	1.63	1.26
Total statistical $\left(\sqrt{N_{\text{exp.}}}\right)$	±1.57	±1.28	±1.12
Total background systematic	±0.80 [32.52%]	±1.60 [98.42%]	±0.52 [41.13%]
Top quark theory	±0.68 [27.5%]	±0.74 [45.7%]	±0.45 [35.3%]
Jet reconstruction	±0.41 [16.4%]	±0.29 [17.6%]	±0.13 [10.0%]
Background estimation	±0.38 [15.4%]	±0.30 [18.6%]	±0.15 [11.8%]
MC statistics	±0.33 [13.3%]	±0.61 [37.4%]	±0.22 [17.6%]
$E_{\text{T}}^{\text{miss}}$ reconstruction	±0.30 [12.1%]	±0.95 [58.5%]	±0.11 [8.4%]
Electroweak theory	±0.30 [12.0%]	±0.36 [22.4%]	±0.15 [11.9%]
Tau identification	±0.26 [10.3%]	±0.18 [10.8%]	±0.10 [7.7%]
Multi-jet estimation	±0.08 [3.1%]	±0.01 [0.37%]	±0.01 [0.53%]
Tau energy measurement	±0.06 [2.5%]	±0.72 [44.2%]	±0.07 [5.4%]
PDF variations	±0.06 [2.5%]	±0.05 [3.1%]	±0.05 [4.3%]
Flavour tagging	±0.06 [2.4%]	±0.04 [2.4%]	±0.01 [0.89%]
Pile-up	±0.03 [1.2%]	±0.33 [20.3%]	±0.05 [4.4%]
Electron reconstruction	±0.00 [0.09%]	±0.00 [0.10%]	±0.00 [0.16%]
Muon reconstruction	±0.00 [0.05%]	±0.00 [0.07%]	±0.00 [0.06%]
Diboson theory	±0.00 [0.00%]	±0.00 [0.00%]	±0.00 [0.00%]

Table A.14: Breakdown of the dominant systematic uncertainties on background estimates in the SRs in the background-only fit. It is to be noted that the individual nuisance parameters can be correlated, and do not necessarily add up quadratically to the total background uncertainty. The percentages show the size of the uncertainty relative to the total expected background. Uncertainties on the present signals are not given here.

A.5 Additional results plots and tables

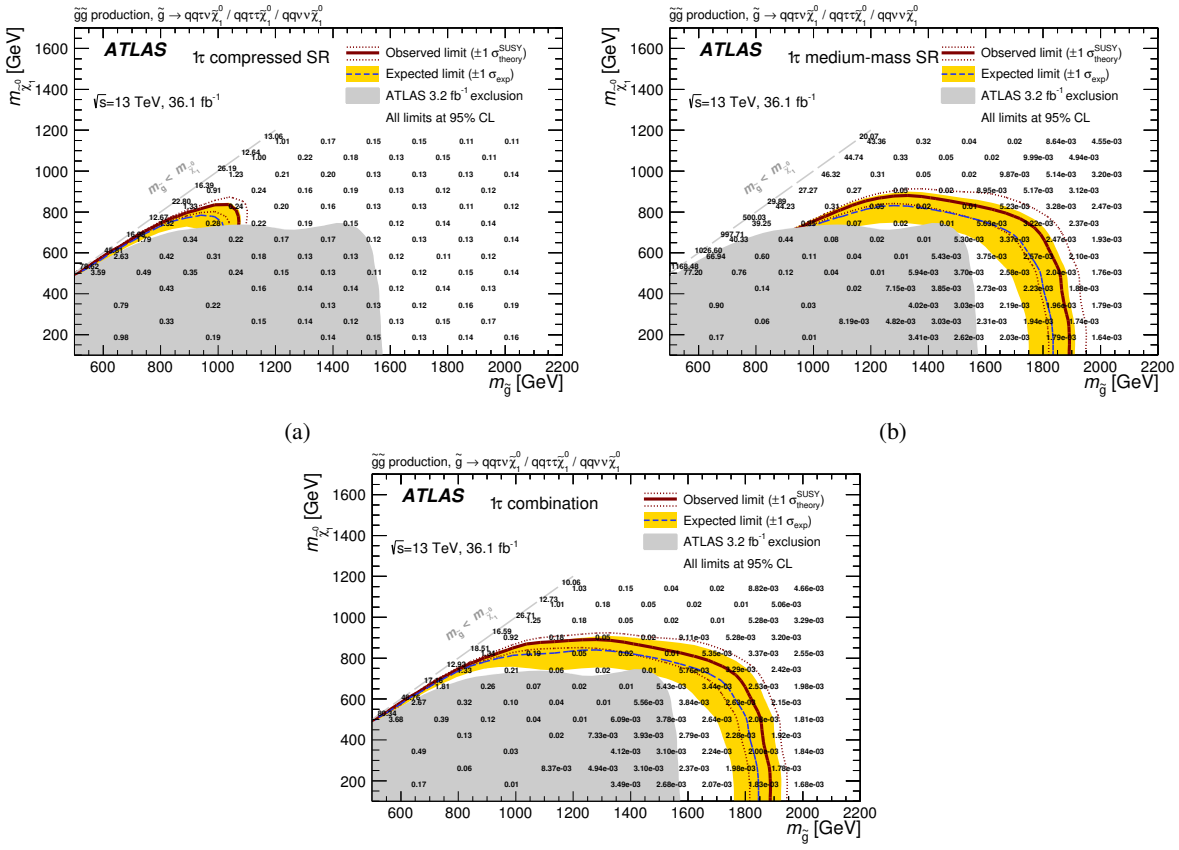

(a) (b)

(c)

Figure A.16: Exclusion contours at the 95% confidence level for the simplified model of gluino pair-production in the 1τ channel[8]. (a) and (b) show the results in the compressed and medium-mass SR, respectively, while (c) show the results of the combination of the two, i.e. their simultaneous fit. The red solid line and the blue dashed line correspond to the observed and median expected limits, respectively. The yellow band shows the one-standard-deviation spread of the expected limits around the median. The effect of signal cross-section uncertainties on the observed limits is shown as red dotted lines. The previous ATLAS result [9] obtained with 3.2 fb^{-1} of $\sqrt{s} = 13$ TeV data is shown as a grey filled area. The overlaid numbers give $\langle \epsilon\sigma \rangle^{95}_{\text{obs.}}$ in pb.

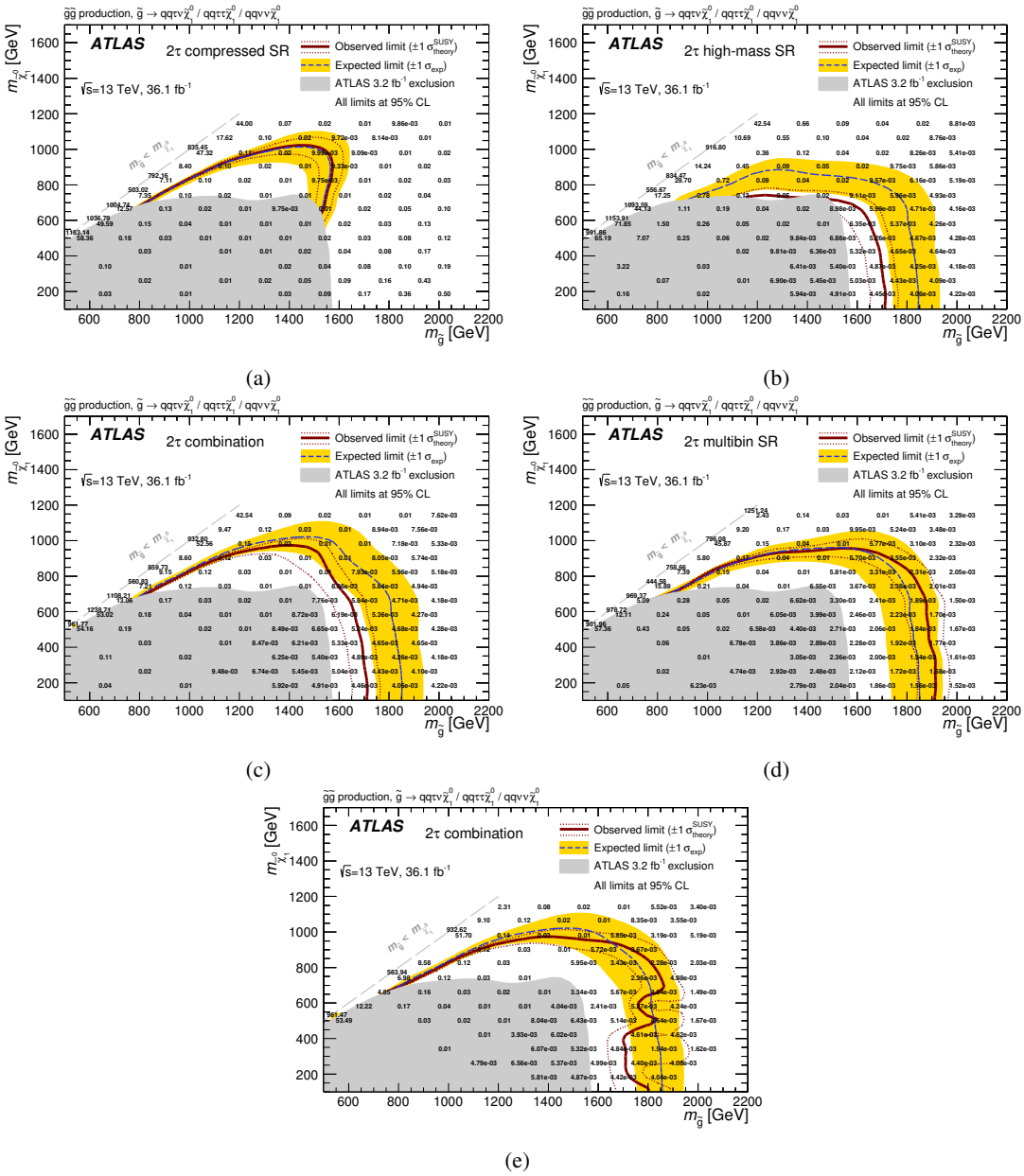

Figure A.17: Exclusion contours at the 95% confidence level for the simplified model of gluino pair-production in the 2τ channel [8]. (a) and (b) show the results in the compressed and high-mass SR, respectively, while (c) presents the results of the combination of the two, i.e. their simultaneous fit. (d) illustrates the exclusion obtained in the 2τ Multibin SR, (e) the results of the best performing setup at each point in parameter-space based on the value of $CL_S^{exp.}$, chosen between the single-bin combination and the multibin SR. The red solid line and the blue dashed line correspond to the observed and median expected limits, respectively. The yellow band shows the one-standard-deviation spread of the expected limits around the median. The effect of signal cross-section uncertainties on the observed limits is shown as red dotted lines. The fluctuation of the observed limit line originate from the method employed to perform the combination. The previous ATLAS result [9] obtained with 3.2 fb^{-1} of $\sqrt{s} = 13$ TeV data is shown as a grey filled area. The overlaid numbers give $\langle \epsilon\sigma \rangle_{obs.}^{95}$ in pb.

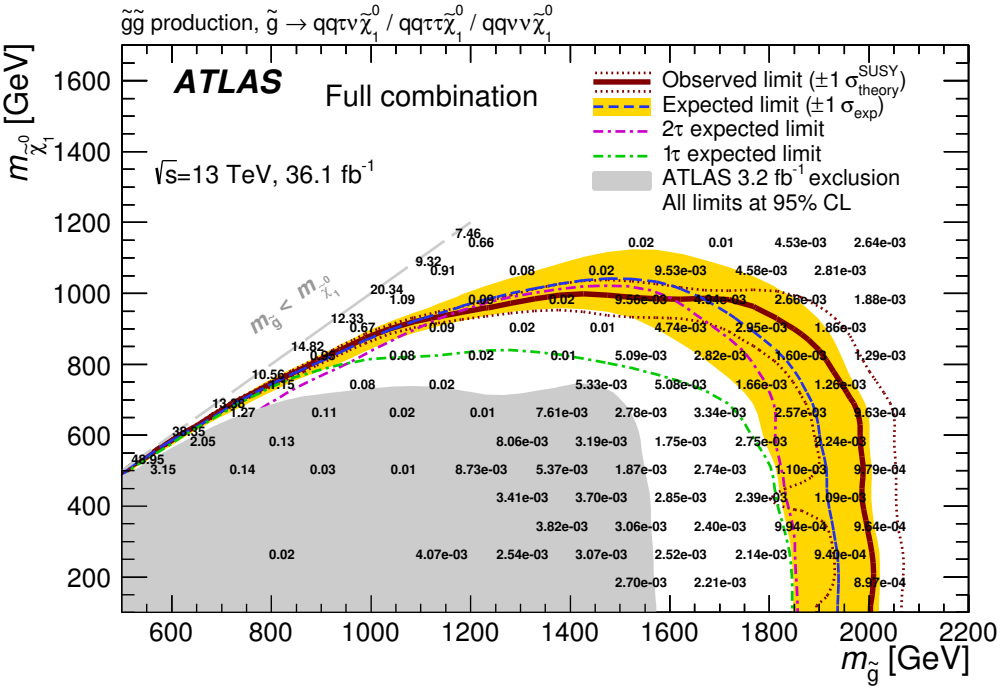

Figure A.18: Exclusion contours at the 95% confidence level for the simplified model of gluino pair-production [8]. At each point, the result of either the single-bin combination of both channels (cf. fig. 8.9(a)) or the combination of the single-bin 1τ SRs with the 2τ Multibin SR (cf. fig. 8.9(b)) are chosen based on the value of $CL_S^{exp.}$. The red solid line and the blue dashed line correspond to the observed and median expected limits, respectively. The yellow band shows the one-standard-deviation spread of the expected limits around the median. The effect of signal cross-section uncertainties on the observed limits is shown as red dotted lines. The magenta and green dashed lines present the individual channel median expected limits as provided by figs. 8.6(a) and 8.6(c). The inward fluctuation of the -1σ observed limit line originates from the method employed to perform the combination. The previous ATLAS result [9] obtained with 3.2 fb^{-1} of $\sqrt{s} = 13$ TeV data is shown as a grey filled area. The overlaid numbers give $\langle\epsilon\sigma\rangle^{95}_{obs.}$ in pb.

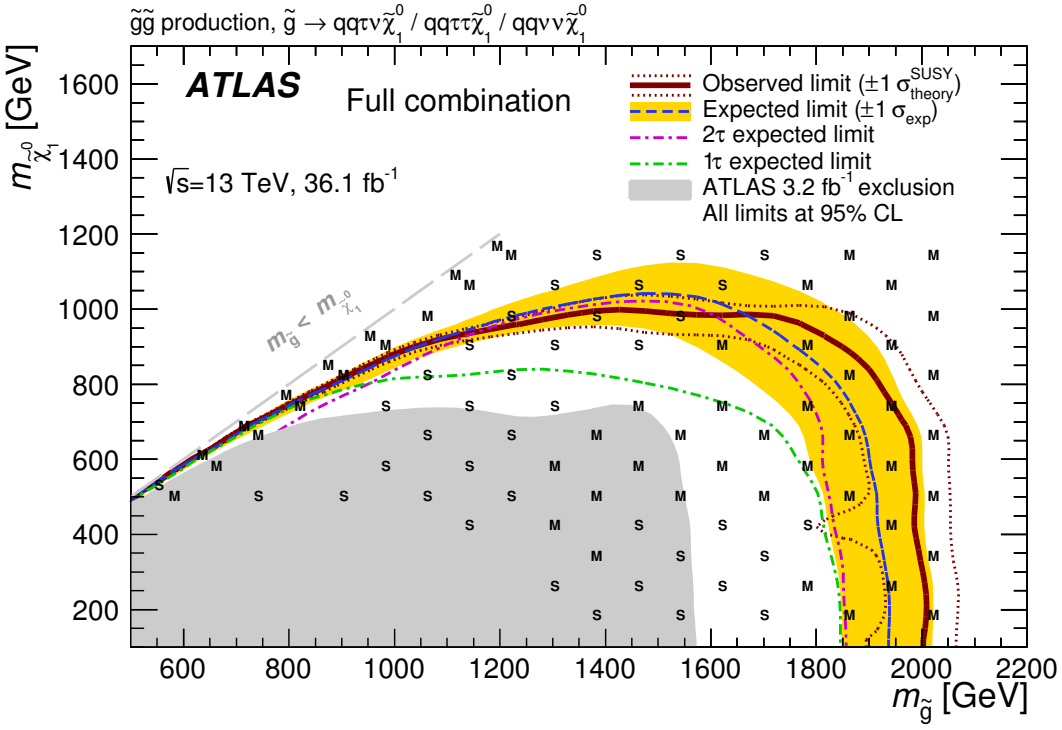

Figure A.19: Exclusion contours at the 95% confidence level for the simplified model of gluino pair-production [8]. At each point, the result of either the single-bin combination of both channels (cf. fig. 8.7(a)) or the combination of the single-bin 1τ SRs with the 2τ Multibin SR (cf. fig. 8.7(b)) are chosen based on the value of $CL_S^{exp.}$. The red solid line and the blue dashed line correspond to the observed and median expected limits, respectively. The yellow band shows the one-standard-deviation spread of the expected limits around the median. The effect of signal cross-section uncertainties on the observed limits is shown as red dotted lines. The magenta and green dashed lines present the individual channel median expected limits as provided by figs. 8.6(a) and 8.6(c). The inward fluctuation of the -1σ observed limit line originates from the method employed to perform the combination. The previous ATLAS result [9] obtained with 3.2 fb^{-1} of $\sqrt{s}$ = 13 TeV data is shown as a grey filled area. The overlaid labels indicate which of the two underlying sets of combined signal regions is chosen at each point. `S` referencing scenarios where the single-bin combination performs the best, `M` representing areas of parameter-space where the combination with the Multibin SR performs the best.

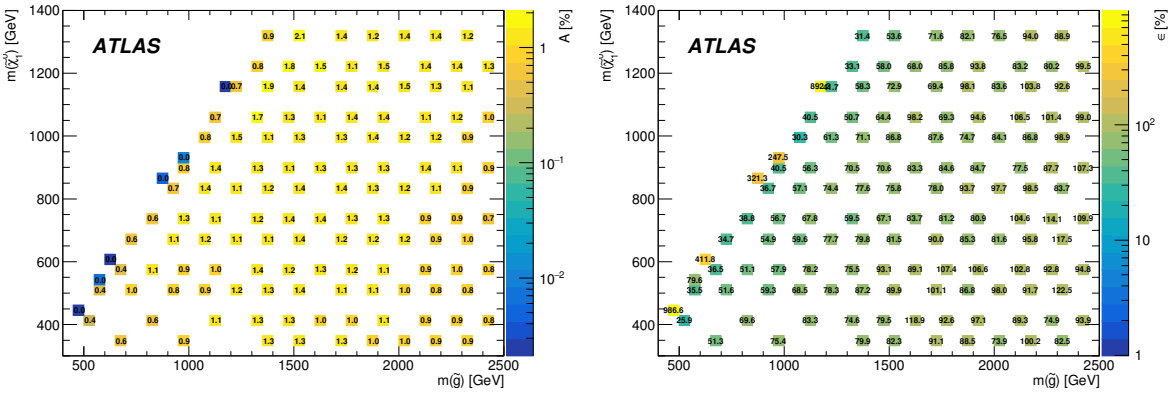

(a) 1τ Compressed SR, acceptance

(b) 1τ Compressed SR, efficiency

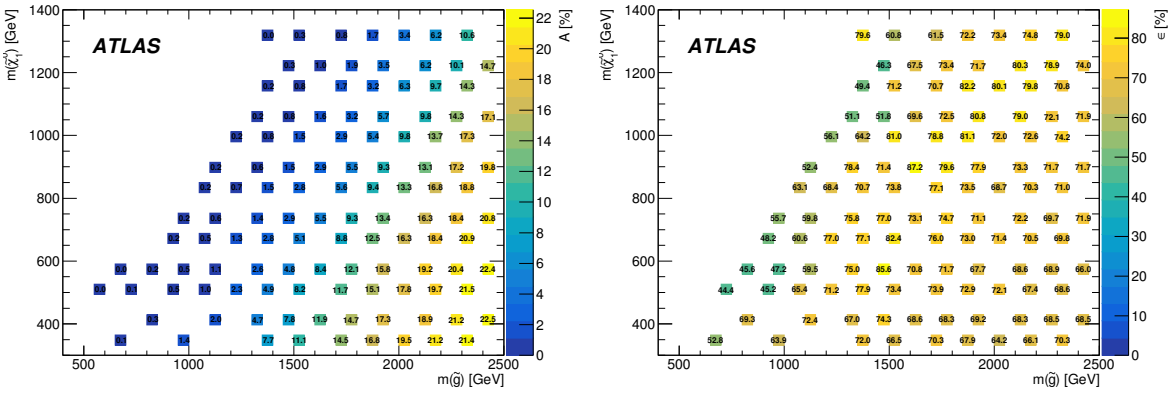

(c) 1τ Medium-Mass SR, acceptance

(d) 1τ Medium-Mass SR, efficiency

Figure A.20: Maps of acceptance ((a), (c)) and efficiency ((b), (d)) of the simplified model for the Compressed and Medium-Mass signal regions of the 1τ channel. The acceptance is calculated by application of the analysis cuts to truth-level objects. The efficiency includes reconstruction and identification efficiencies [8].

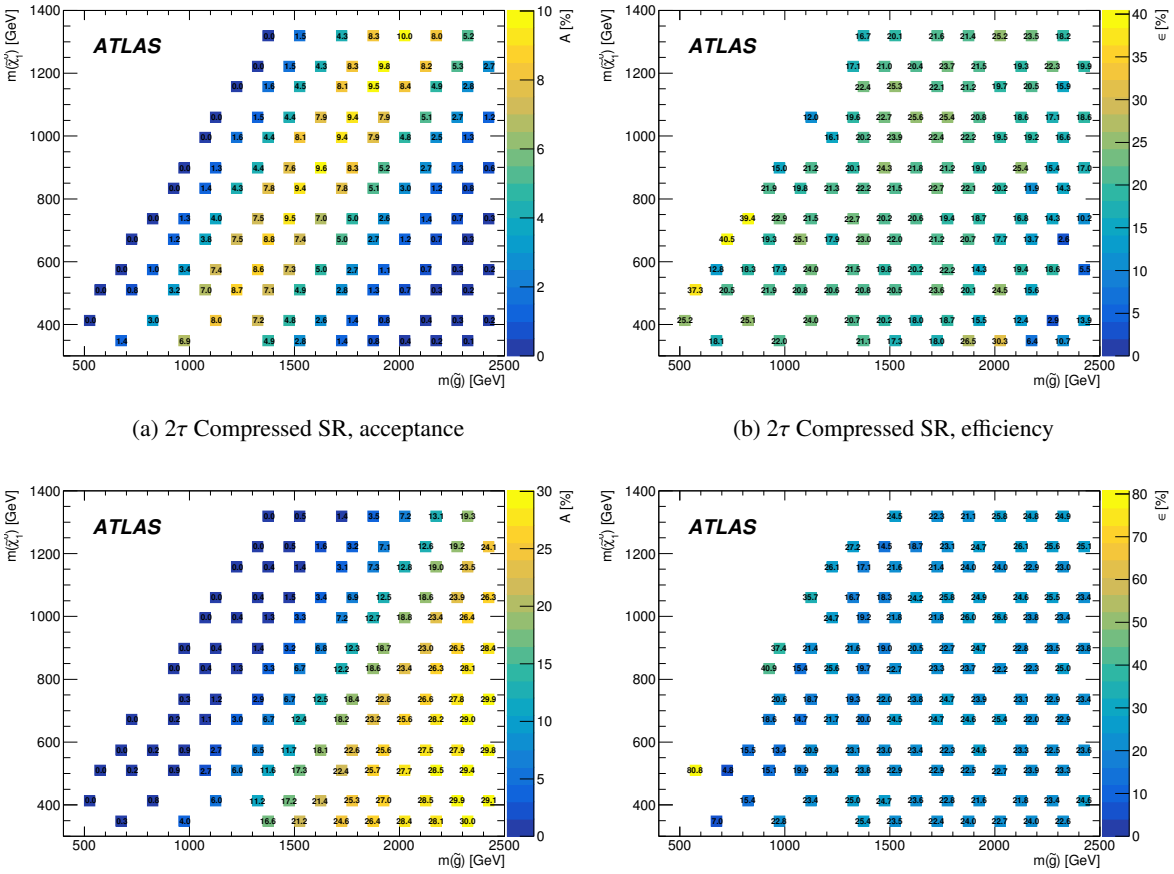

(a) 2τ Compressed SR, acceptance

(b) 2τ Compressed SR, efficiency

(c) 2τ High-Mass SR, acceptance

(d) 2τ High-Mass SR, efficiency

Figure A.21: Maps of acceptance ((a), (c)) and efficiency ((b), (d)) of the simplified model for the Compressed and High-Mass signal regions of the 2τ channel. The acceptance is calculated by application of the analysis cuts to truth-level objects. The efficiency includes reconstruction and identification efficiencies [8].

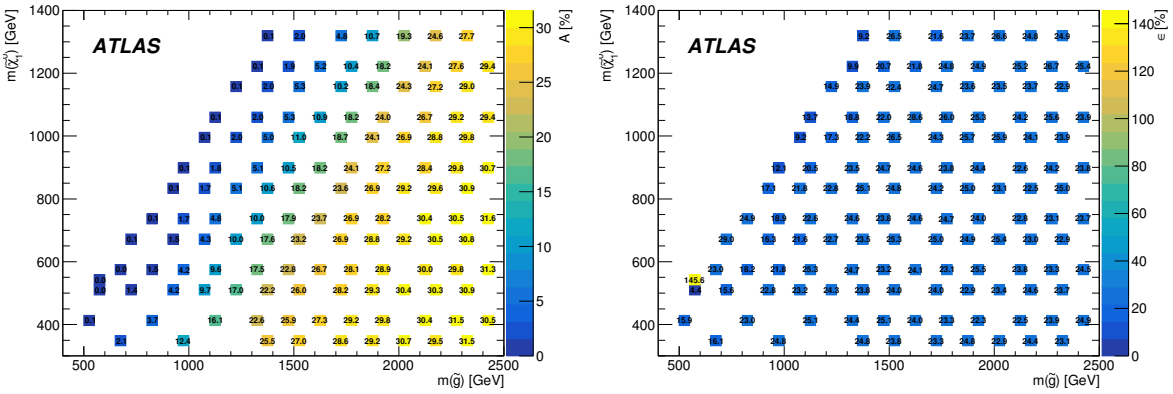

(a) 2τ Multibin SR, acceptance

(b) 2τ Multibin SR, efficiency

(c) 2τ GMSB SR, acceptance

(d) 2τ GMSB SR, efficiency

Figure A.22: Maps of acceptance ((a), (c)) and efficiency ((b), (d)) of the simplified model for the Multibin and GMSB signal regions of the 2τ channel. The acceptance is calculated by application of the analysis cuts to truth-level objects. The efficiency includes reconstruction and identification efficiencies [8].

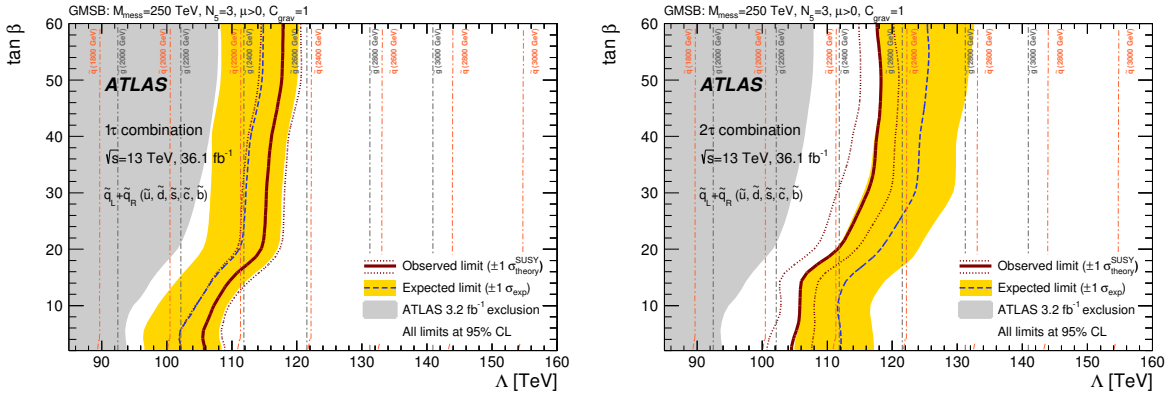

(a) 1τ combination

(b) 2τ combination

Figure A.23: Exclusion contours at the 95% confidence level for the GMSB model [8]. The red solid line and the blue dashed line correspond to the observed and median expected limits, respectively. (a) shows the results for the simultaneous fit of the 1τ Compressed and Medium-Mass SRs. (b) depicts the limits obtained in the simultaneous fit of the 2τ GMSB SR with the 2τ Compressed SR. The yellow band shows the one-standard-deviation spread of the expected limits around the median. The effect of signal cross-section uncertainties on the observed limits is shown as red dotted lines. The grey and orange dashed lines indicate the masses of gluinos and mass-degenerate squarks, respectively. The previous ATLAS result [9] obtained with 3.2 fb^{-1} of $\sqrt{s} = 13$ TeV data is shown as a grey filled area.

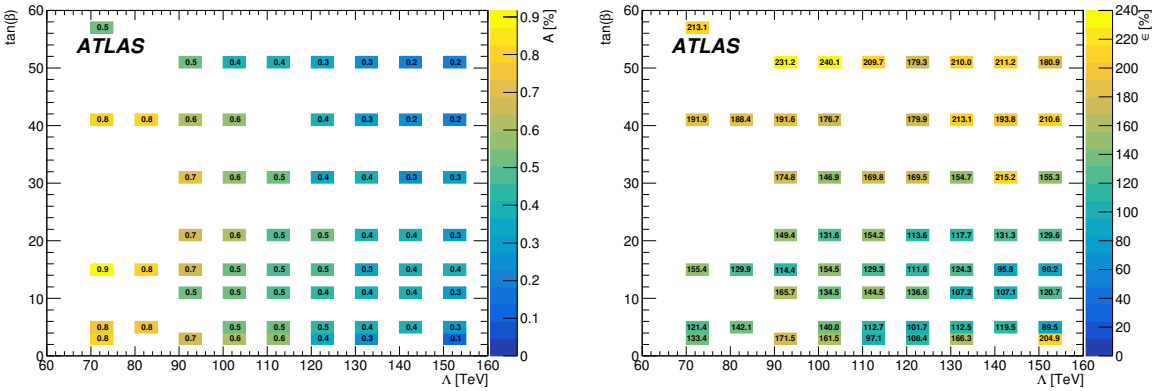

(a) 1τ Compressed SR, acceptance

(b) 1τ Compressed SR, efficiency

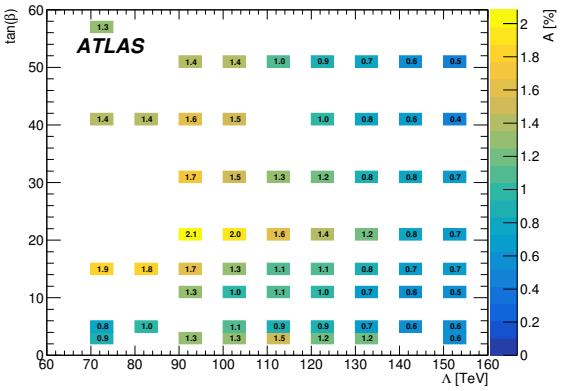

(c) 1τ Medium-Mass SR, acceptance

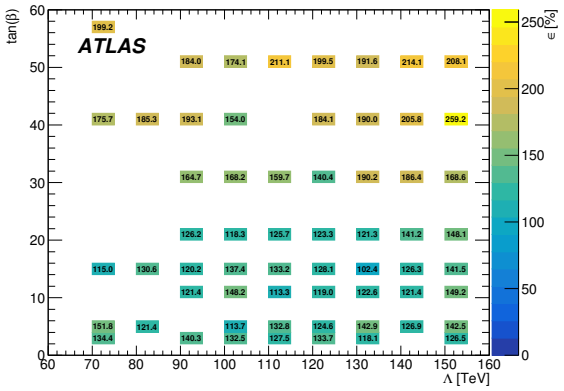

(d) 1τ Medium-Mass SR, efficiency

Figure A.24: Maps of acceptance ((a), (c)) and efficiency ((b), (d)) of the GMSB Model for the Compressed and Medium-Mass signal regions of the 1τ channel. The acceptance is calculated by application of the analysis cuts to truth-level objects. The efficiency includes reconstruction and identification efficiencies [8].

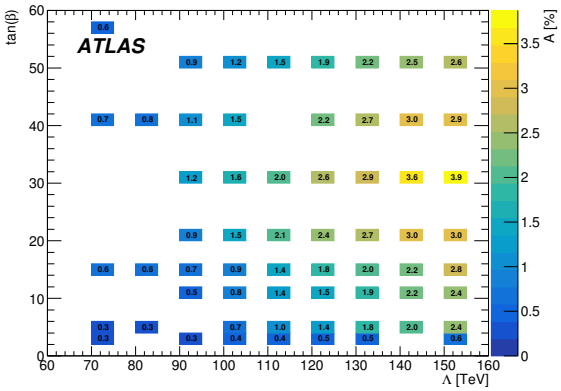

(a) 2τ Compressed SR, acceptance

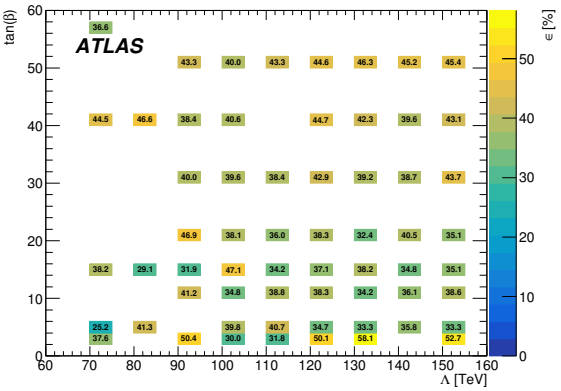

(b) 2τ Compressed SR, efficiency

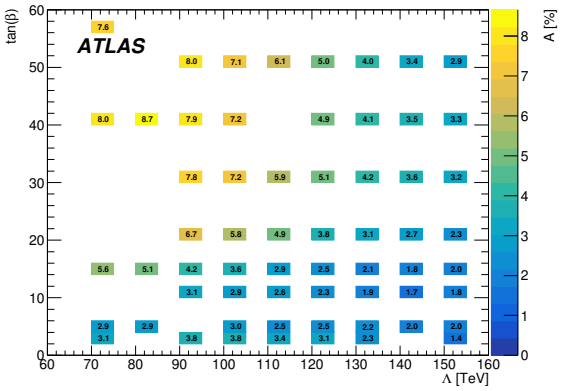

(c) 2τ High-Mass SR, acceptance

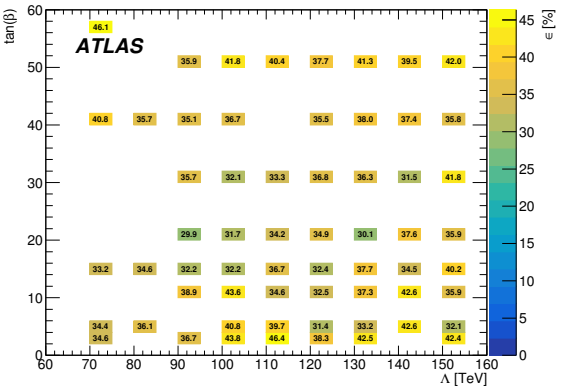

(d) 2τ High-Mass SR, efficiency

Figure A.25: Maps of acceptance ((a), (c)) and efficiency ((b), (d)) of the GMSB Model for the Compressed and High-Mass signal regions of the 2τ channel. The acceptance is calculated by application of the analysis cuts to truth-level objects. The efficiency includes reconstruction and identification efficiencies [8].

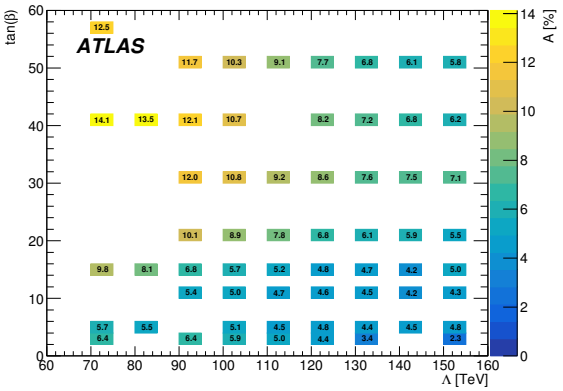

(a) 2τ Multibin SR, acceptance

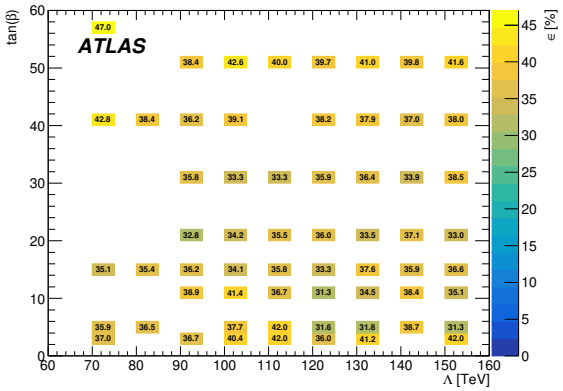

(b) 2τ Multibin SR, efficiency

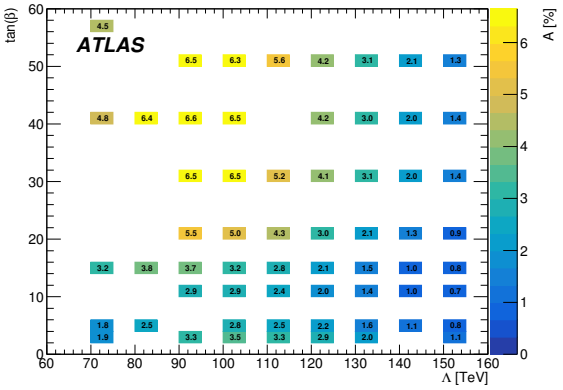

(c) 2τ GMSB SR, acceptance

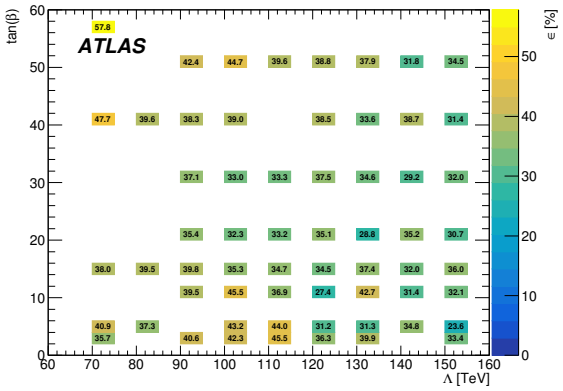

(d) 2τ GMSB SR, efficiency

Figure A.26: Maps of acceptance ((a), (c)) and efficiency ((b), (d)) of the GMSB Model for the Multibin and GMSB signal regions of the 2τ channel. The acceptance is calculated by application of the analysis cuts to truth-level objects. The efficiency includes reconstruction and identification efficiencies [8].

1τ compressed SR	$\tilde{g}\tilde{g}$ simplified model						GMSB model	
	$m(\tilde{g})$ = 1 065 GeV		$m(\tilde{g})$ = 1 265 GeV		$m(\tilde{g})$ = 1 705 GeV		Λ = 120 TeV	
	$m(\tilde{\chi}_1^0)$ = 825 GeV		$m(\tilde{\chi}_1^0)$ = 905 GeV		$m(\tilde{\chi}_1^0)$ = 345 GeV		$\tan\beta$ = 40	
Subject of selection	weighted	unweighted	weighted	unweighted	weighted	unweighted	weighted	unweighted
Total events	7473.62	25356.90	254.50	20000.0	165.16	20000.0	356.27	25000.0
Leading particle jet $p_T > 85$ GeV	5894.74	20000.0	254.50	20000.0	165.16	20000.0	356.27	25000.0
Data processing selection	2358.07	7508.0	131.51	9650.0	85.09	9653.0	163.86	10457.0
Event cleaning	2215.11	7087.0	124.18	9133.0	79.95	9097.0	155.56	9961.0
Trigger	1529.84	4835.0	109.0	7992.0	73.79	8392.0	130.13	8240.0
Multi-jet rejection	819.09	2503.0	90.32	6596.0	66.18	7535.0	81.5	4996.0
Taus	611.32	1862.0	63.93	4674.0	46.84	5398.0	50.07	3132.0
$E_T^{miss} > 400$ GeV	78.29	232.0	3.47	259.0	2.32	271.0	3.12	190.0
$m_T^\tau > 80$ GeV	59.26	175.0	2.78	210.0	1.93	226.0	2.48	149.0

1τ medium-mass SR	$\tilde{g}\tilde{g}$ simplified model						GMSB model	
	$m(\tilde{g})$ = 1 065 GeV		$m(\tilde{g})$ = 1 265 GeV		$m(\tilde{g})$ = 1 705 GeV		Λ = 120 TeV	
	$m(\tilde{\chi}_1^0)$ = 825 GeV		$m(\tilde{\chi}_1^0)$ = 905 GeV		$m(\tilde{\chi}_1^0)$ = 345 GeV		$\tan\beta$ = 40	
Subject of selection	weighted	unweighted	weighted	unweighted	weighted	unweighted	weighted	unweighted
Total events	7473.62	25356.90	254.50	20000.0	165.16	20000.0	356.27	25000.0
Leading particle jet $p_T > 85$ GeV	5894.74	20000.0	254.50	20000.0	165.16	20000.0	356.27	25000.0
Data processing selection	2358.07	7508.0	131.51	9650.0	85.09	9653.0	163.86	10457.0
Event cleaning	2215.11	7087.0	124.18	9133.0	79.95	9097.0	155.56	9961.0
Trigger	1529.84	4835.0	109.0	7992.0	73.79	8392.0	130.13	8240.0
Multi-jet rejection	819.09	2503.0	90.32	6596.0	66.18	7535.0	81.5	4996.0
Taus	611.32	1862.0	63.93	4674.0	46.84	5398.0	50.07	3132.0
$E_T^{miss} > 400$ GeV	53.73	155.0	17.34	1216.0	24.2	2736.0	16.25	942.0
$m_T^\tau > 250$ GeV	19.32	52.0	12.5	865.0	17.81	1999.0	9.4	546.0
$H_T > 1\,000$ GeV	8.54	22.0	6.44	446.0	16.86	1898.0	6.31	349.0

Table A.15: Cutflow tables of the 1τ compressed SR (top) and the 1τ medium-mass SR (bottom) for the four signal benchmark scenarios [8]. For each scenario, the number of events before (unweighted) and after application of all correction factors (weighted) is provided. The unweighted number of total events represents the number of generated events, while the weighted number of total events is derived from the inclusive production cross section of the respective sample and the integrated luminosity used in this analysis. In the case of the lowest gluino mass scenario of the Simplified Model ($m(\tilde{g})$ = 1 065 GeV), these initial numbers are corrected for the efficiency of a truth-level filter that requires the event to have a $p_T > 85$ GeV jet. The data processing selection step requires the presence of a loose tau candidate with $p_T > 15$ GeV and at least one of a selection of single-electron, single-muon, tau, jet and E_T^{miss} based triggers to be activated.

2τ compressed SR	$\tilde{g}\tilde{g}$ simplified model						GMSB model	
	$m(\tilde{g})$ = 1 065 GeV		$m(\tilde{g})$ = 1 265 GeV		$m(\tilde{g})$ = 1 705 GeV		Λ = 120 TeV	
	$m(\tilde{\chi}_1^0)$ = 825 GeV		$m(\tilde{\chi}_1^0)$ = 905 GeV		$m(\tilde{\chi}_1^0)$ = 345 GeV		tanβ = 40	
Subject of selection	weighted	unweighted	weighted	unweighted	weighted	unweighted	weighted	unweighted
Total events	7473.62	25356.90	254.50	20000.0	165.16	20000.0	356.27	25000.0
Leading particle jet $p_T > 85$ GeV	5894.74	20000.0	254.50	20000.0	165.16	20000.0	356.27	25000.0
Data processing selection	2358.07	7508.0	131.51	9650.0	85.09	9653.0	163.86	10457.0
Event cleaning	2215.11	7087.0	124.18	9133.0	79.95	9097.0	155.56	9961.0
Trigger	1529.84	4835.0	109.0	7992.0	73.79	8392.0	130.13	8240.0
Multi-jet rejection	819.09	2503.0	90.32	6596.0	66.18	7535.0	81.5	4996.0
Taus	142.44	428.0	20.64	1489.0	15.18	1645.0	25.5	1485.0
$m_{T2}^{\tau\tau} > 70$ GeV	34.87	113.0	8.62	621.0	6.96	738.0	9.94	565.0
$H_T > 1\,100$ GeV	32.49	105.0	6.14	440.0	0.43	49.0	6.41	384.0
$m_T^{sum} > 1\,600$ GeV	20.17	62.0	5.33	385.0	0.41	47.0	3.52	214.0

2τ high-mass SR	$\tilde{g}\tilde{g}$ simplified model						GMSB model	
	$m(\tilde{g})$ = 1 065 GeV		$m(\tilde{g})$ = 1 265 GeV		$m(\tilde{g})$ = 1 705 GeV		Λ = 120 TeV	
	$m(\tilde{\chi}_1^0)$ = 825 GeV		$m(\tilde{\chi}_1^0)$ = 905 GeV		$m(\tilde{\chi}_1^0)$ = 345 GeV		tanβ = 40	
Subject of selection	weighted	unweighted	weighted	unweighted	weighted	unweighted	weighted	unweighted
Total events	7473.62	25356.90	254.50	20000.0	165.16	20000.0	356.27	25000.0
Leading particle jet $p_T > 85$ GeV	5894.74	20000.0	254.50	20000.0	165.16	20000.0	356.27	25000.0
Data processing selection	2358.07	7508.0	131.51	9650.0	85.09	9653.0	163.86	10457.0
Event cleaning	2215.11	7087.0	124.18	9133.0	79.95	9097.0	155.56	9961.0
Trigger	1529.84	4835.0	109.0	7992.0	73.79	8392.0	130.13	8240.0
Multi-jet rejection	819.09	2503.0	90.32	6596.0	66.18	7535.0	81.5	4996.0
Taus	142.44	428.0	20.64	1489.0	15.18	1645.0	25.5	1485.0
$m_T^{\tau_1} + m_T^{\tau_2} > 350$ GeV	25.23	79.0	10.94	780.0	9.7	1026.0	14.49	823.0
$H_T > 1\,100$ GeV	4.35	13.0	3.56	258.0	9.12	962.0	6.18	327.0

Table A.16: Cutflow table of the 2τ compressed SR (top) and the 2τ high-mass SR (bottom) for the four signal benchmark scenarios [8]. For each scenario, the number of events before (unweighted) and after application of all correction factors (weighted) is provided. The unweighted number of total events represents the number of generated events, while the weighted number of total events is derived from the inclusive production cross section of the respective sample and the integrated luminosity used in this analysis. In the case of the lowest gluino mass scenario of the Simplified Model ($m(\tilde{g})$ = 1 065 GeV), these initial numbers are corrected for the efficiency of a truth-level filter that requires the event to have a $p_T > 85$ GeV jet. The data processing selection step requires the presence of a loose tau candidate with $p_T > 15$ GeV and at least one of a selection of single-electron, single-muon, tau, jet and E_T^{miss} based triggers to be activated.

2τ multibin SR	$\tilde{g}\tilde{g}$ simplified model						GMSB model	
	$m(\tilde{g})$ = 1 065 GeV		$m(\tilde{g})$ = 1 265 GeV		$m(\tilde{g})$ = 1 705 GeV		Λ = 120 TeV	
	$m(\tilde{\chi}_1^0)$ = 825 GeV		$m(\tilde{\chi}_1^0)$ = 905 GeV		$m(\tilde{\chi}_1^0)$ = 345 GeV		$\tan\beta$ = 40	
Subject of selection	weighted	unweighted	weighted	unweighted	weighted	unweighted	weighted	unweighted
Total events	7473.62	25356.90	254.50	20000.0	165.16	20000.0	356.27	25000.0
Leading particle jet $p_T > 85$ GeV	5894.74	20000.0	254.50	20000.0	165.16	20000.0	356.27	25000.0
Data processing selection	2358.07	7508.0	131.51	9650.0	85.09	9653.0	163.86	10457.0
Event cleaning	2215.11	7087.0	124.18	9133.0	79.95	9097.0	155.56	9961.0
Trigger	1529.84	4835.0	109.0	7992.0	73.79	8392.0	130.13	8240.0
Multi-jet rejection	819.09	2503.0	90.32	6596.0	66.18	7535.0	81.5	4996.0
Taus	142.44	428.0	20.64	1489.0	15.18	1645.0	25.5	1485.0
$n_{jet} > 2$	97.4	290.0	15.13	1079.0	11.26	1206.0	17.62	986.0
$m_T^{\tau_1} + m_T^{\tau_2} > 150$ GeV	86.51	259.0	14.67	1044.0	11.05	1181.0	16.96	950.0
$H_T > 800$ GeV	27.82	88.0	11.41	802.0	10.99	1175.0	11.11	604.0

2τ GMSB SR	$\tilde{g}\tilde{g}$ simplified model						GMSB model	
	$m(\tilde{g})$ = 1 065 GeV		$m(\tilde{g})$ = 1 265 GeV		$m(\tilde{g})$ = 1 705 GeV		Λ = 120 TeV	
	$m(\tilde{\chi}_1^0)$ = 825 GeV		$m(\tilde{\chi}_1^0)$ = 905 GeV		$m(\tilde{\chi}_1^0)$ = 345 GeV		$\tan\beta$ = 40	
Subject of selection	weighted	unweighted	weighted	unweighted	weighted	unweighted	weighted	unweighted
Total events	7473.62	25356.90	254.50	20000.0	165.16	20000.0	356.27	25000.0
Leading particle jet $p_T > 85$ GeV	5894.74	20000.0	254.50	20000.0	165.16	20000.0	356.27	25000.0
Data processing selection	2358.07	7508.0	131.51	9650.0	85.09	9653.0	163.86	10457.0
Event cleaning	2215.11	7087.0	124.18	9133.0	79.95	9097.0	155.56	9961.0
Trigger	1529.84	4835.0	109.0	7992.0	73.79	8392.0	130.13	8240.0
Multi-jet rejection	819.09	2503.0	90.32	6596.0	66.18	7535.0	81.5	4996.0
Taus	142.44	428.0	20.64	1489.0	15.18	1645.0	25.5	1485.0
$m_T^{\tau_1} + m_T^{\tau_2} > 150$ GeV	87.83	262.0	14.71	1047.0	11.05	1181.0	19.15	1092.0
$H_T > 800$ GeV	0.98	1.0	0.58	39.0	2.75	301.0	5.71	279.0

Table A.17: Cutflow table of the 2τ multibin SR (top) and the 2τ GMSB SR (bottom) for the four signal benchmark scenarios [8]. For each scenario, the number of events before (unweighted) and after application of all correction factors (weighted) is provided. The unweighted number of total events represents the number of generated events, while the weighted number of total events is derived from the inclusive production cross section of the respective sample and the integrated luminosity used in this analysis. In the case of the lowest gluino mass scenario of the Simplified Model ($m(\tilde{g})$ = 1 065 GeV), these initial numbers are corrected for the efficiency of a truth-level filter that requires the event to have a $p_T > 85$ GeV jet. The data processing selection step requires the presence of a loose tau candidate with $p_T > 15$ GeV and at least one of a selection of single-electron, single-muon, tau, jet and E_T^{miss} based triggers to be activated.

APPENDIX **B**

Asimov Significance

In studies where the occurrence of a rare signal in data, which is pre-dominantly background, is to be evaluated, different definitions of *significance* provide measures of how well the background-only hypothesis is separable from the hypothesis of the presence of signal and background. The two hypotheses are, in general, separable from each other, depending on the total signal and the uncertainty of the background. The easiest and least sophisticated way to determine a signal significance is the ratio of $S/\sqrt{B}$ with S and B denoting the total yields of signal and background, respectively. Under the assumption that no systematic uncertainties influence the measurement, $\sqrt{B}$ represents the total uncertainty—i.e. the uncertainty of a regular counting experiment—of the background. The more signal there is and the lower the uncertainty on the background estimation, the better the two hypotheses can be tested against each other. Taking statistical fluctuations of the signal prediction into account, this measure can be extended to $S/\sqrt{S+B}$. This approach is also valid for scenarios where no background at all is expected and hence the signal discovery can only be claimed if statistical fluctuations of the signal are incompatible with zero. Based on the hypothesis testing approach pursued in this analysis (cf. appendix G), a measure of significance that is directly deduced from the used test statistic can be formulated [240] expressed in eq. (B.1).

$$z = \sqrt{2 \cdot \left((S+B) \cdot \log\left(1 + \frac{S}{B}\right) - S \right)} \tag{B.1}$$

This so-called *Asimov significance* for discovery considers the total yields and the statistical uncertainties of the signal and background predictions. More importantly, this approach provides a measure of significance that is to be expected when using the exact result extraction approach that this analysis pursues. It is hence better suited than a generic measure such as $S/\sqrt{S+B}$. Equation (B.1) can be refined further by introducing a term that takes an estimation of a systematic uncertainty on the background into account. Although at the development stage of an analysis this estimation is difficult due to lacking studies of sources of systematic uncertainties, even a rough estimation gives a more realistic result than any other measure of significance. This so-called *modified Asimov significance* is defined in eq. (B.2).

$$z_{\mathrm{A}} = \sqrt{2 \cdot \left((S+B) \cdot \log\left(\frac{(S+B) \cdot (S + (\Delta B)^2)}{(\Delta B)^2 + (S+B) \cdot (\Delta B)^2} \right) - \frac{B^2}{(\Delta B)^2} \cdot \log\left(1 + \frac{S \cdot (\Delta B)^2}{B} \frac{1}{B + (\Delta B)^2}\right)\right)} \tag{B.2}$$

$$\Delta B = \sqrt{\left(\sqrt{B}\right)^2 + \left(0.3 \cdot \sqrt{B}\right)^2} \tag{B.3}$$

In this notation ΔB denotes the total background uncertainty. In the case of this analysis, it is formed by the uncorrelated combination of the statistical uncertainty and an additional systematic uncertainty of 30% as expressed in eq. (B.3). A scan of the modified Asimov significance for discovery z_A can now be used to find cut-values on distributions of signal and background that maximise the discovery potential of an analysis. The distribution of a variable of interest is scanned by imposing sequentially incremented cuts and the calculation of z_A based on the number of events surviving said cut. For the SR defining kinematic variables of both channels, the distributions at Pre-selection level and the corresponding significance scans are depicted in figs. B.1 to B.4. The significance of a lower cut on the variable depicted in the upper row, i.e. selecting only events that exhibit a higher value in that variable, can be inferred directly from the significance plot in the lower row. The significance value of a certain bin corresponds to a lower cut in the underlying kinematic distribution.

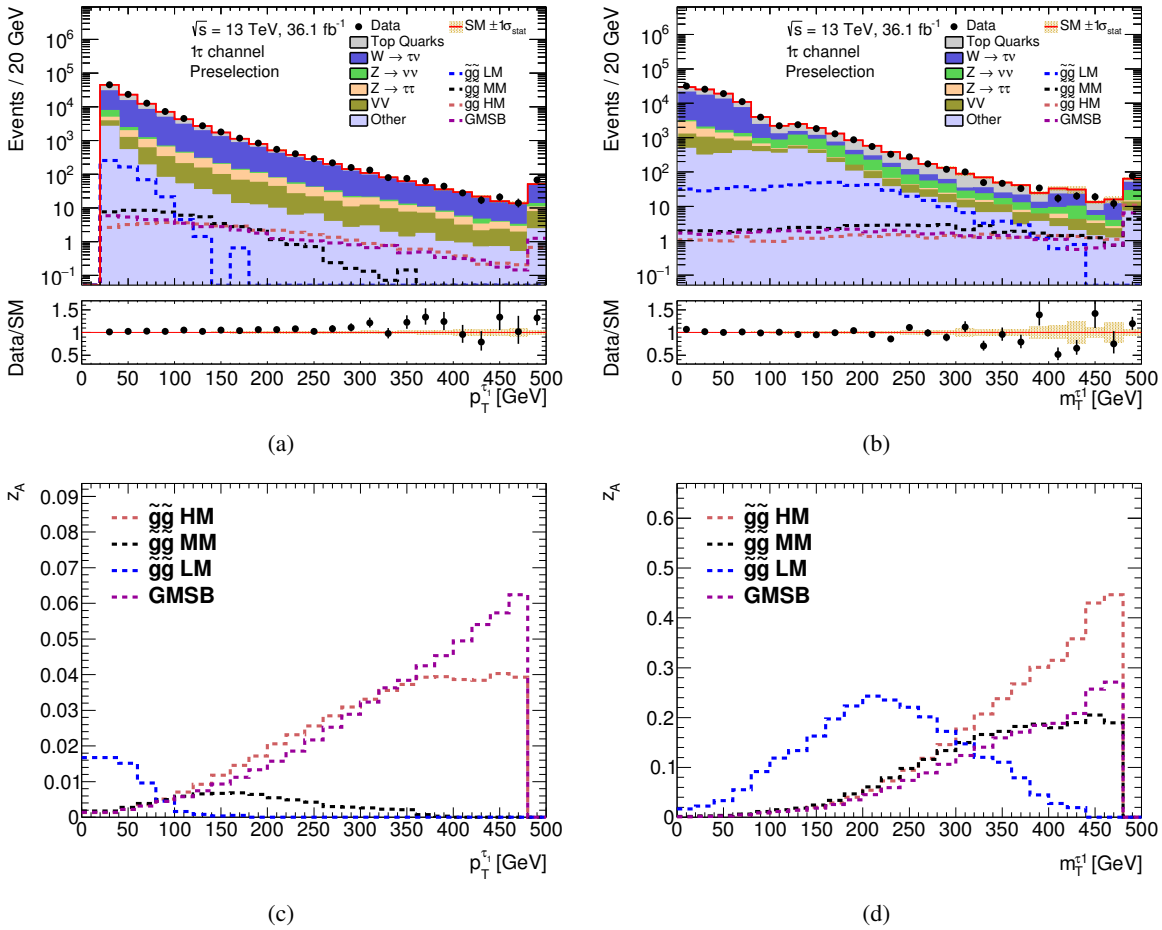

Figure B.1: The upper row shows kinematic distributions after the pre-selection in the 1τ channel. The results shown are obtained after fitting the normalisation of the background in the control regions. The last bin of each distribution contains the overflow events. The uncertainties displayed consider only statistical limitations in the background modelling, illustrated by the shaded bands. The contribution labelled as "other" includes multi-jet events and V+Jets processes not explicitly listed in the legend. The dashed lines represent the four signal model benchmark scenarios used in the design process of the analysis. The bottom row shows the corresponding scans of the modified Asimov significance z_A with an additional systematic background uncertainty of 30% taken into account.

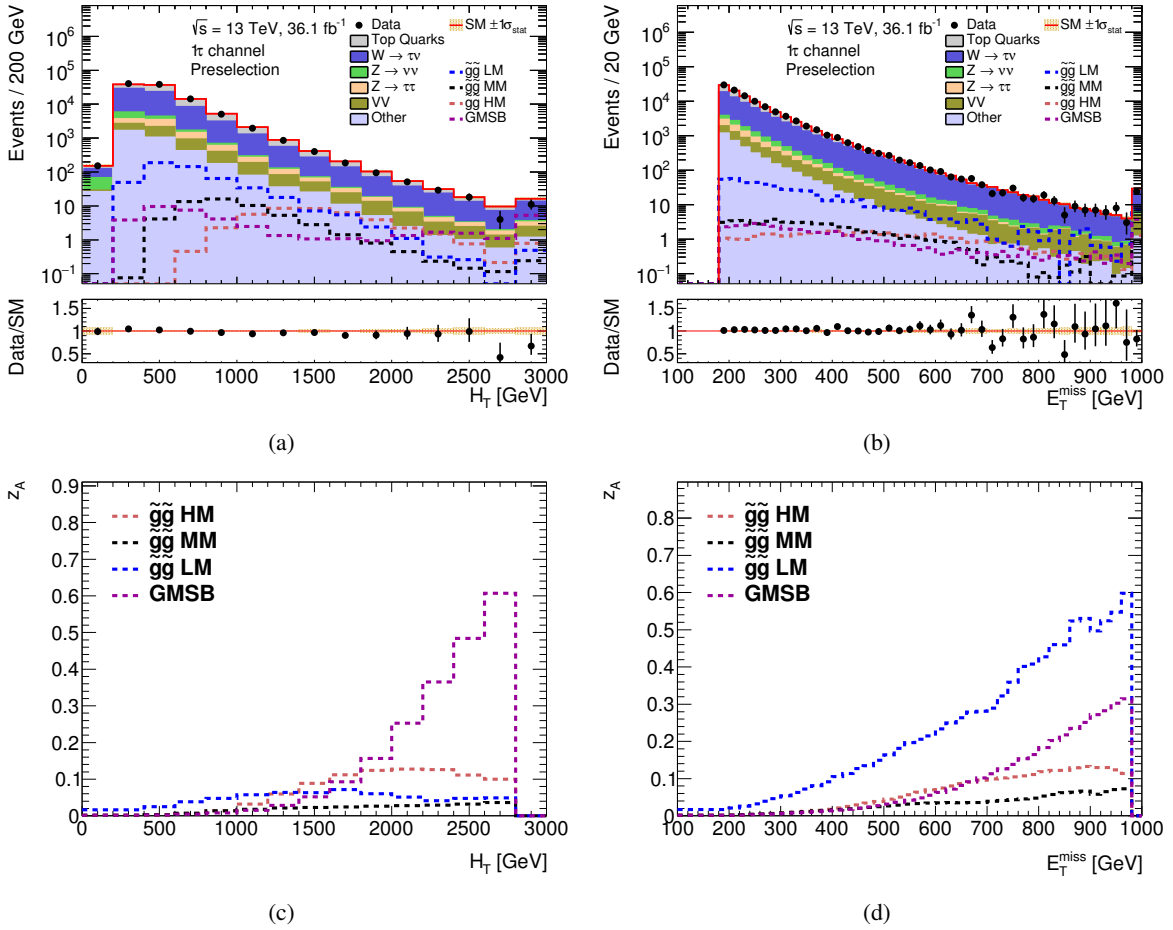

Figure B.2: The upper row shows kinematic distributions after the pre-selection in the 1τ channel. The results shown are obtained after fitting the normalisation of the background in the control regions. The last bin of each distribution contains the overflow events. The uncertainties displayed consider only statistical limitations in the background modelling, illustrated by the shaded bands. The contribution labelled as "other" includes multi-jet events and V+Jets processes not explicitly listed in the legend. The dashed lines represent the four signal model benchmark scenarios used in the design process of the analysis. The bottom row shows the corresponding scans of the modified Asimov significance z_A with an additional systematic background uncertainty of 30% taken into account.

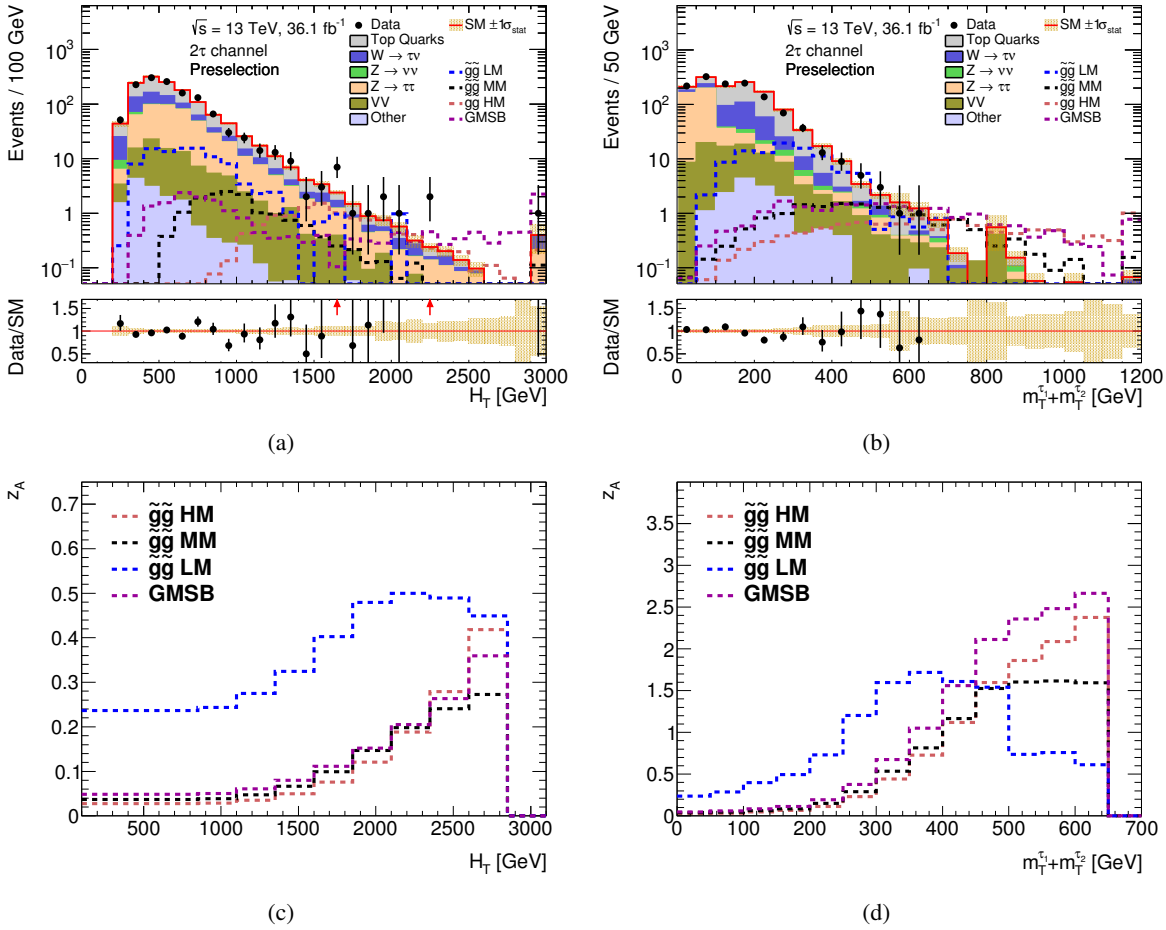

Figure B.3: The upper row shows kinematic distributions after the pre-selection in the 2τ channel. The results shown are obtained after fitting the normalisation of the background in the control regions. The last bin of each distribution contains the overflow events. The uncertainties displayed consider only statistical limitations in the background modelling, illustrated by the shaded bands. Red arrows in the Data/SM ratio indicate bins where the corresponding entry falls outside the plotted range. The contribution labelled as "other" includes multi-jet events and V+Jets processes not explicitly listed in the legend. The dashed lines represent the four signal model benchmark scenarios used in the design process of the analysis. The bottom row shows the corresponding scans of the modified Asimov significance z_A with an additional systematic background uncertainty of 30% taken into account.

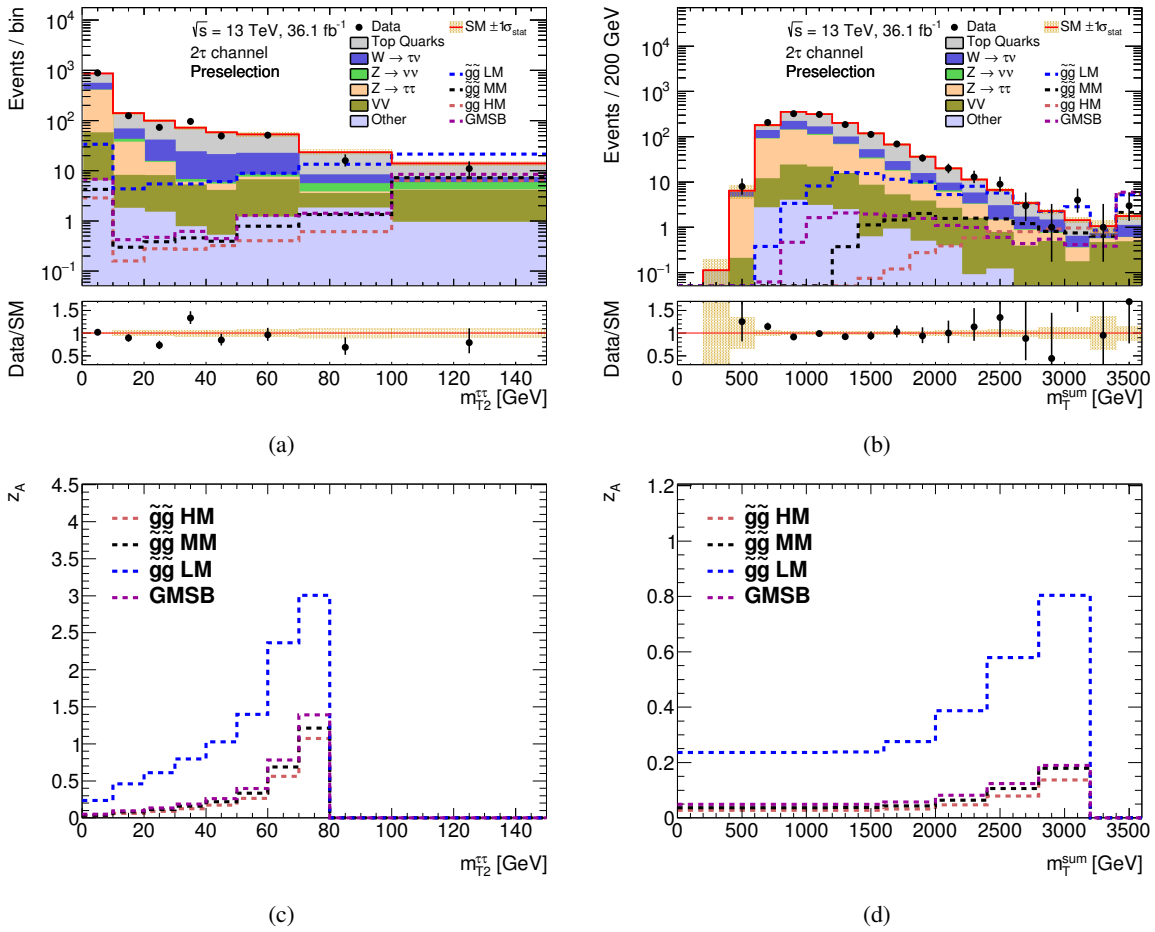

Figure B.4: The upper row shows kinematic distributions after the pre-selection in the 2τ channel. The results shown are obtained after fitting the normalisation of the background in the control regions. The last bin of each distribution contains the overflow events. The uncertainties displayed consider only statistical limitations in the background modelling, illustrated by the shaded bands. Red arrows in the Data/SM ratio indicate bins where the corresponding entry falls outside the plotted range. The contribution labelled as "other" includes multi-jet events and V+Jets processes not explicitly listed in the legend. The dashed lines represent the four signal model benchmark scenarios used in the design process of the analysis. The bottom row shows the corresponding scans of the modified Asimov significance z_A with an additional systematic background uncertainty of 30% taken into account.

APPENDIX C

Trigger Performance

This appendix summarises the studies performed to determine and optimise the trigger setup used to select recorded events for analysis as documented in [189]. It is closely based on ibid..

C.0.1 Trigger strategy

As outlined in section 5.5, triggers based on missing transverse momentum, jets, τ-leptons, or a combination of those, are potential trigger candidates for the presented analysis. In its earlier version [9], the missing transverse energy trigger `HLT_XE70` has been chosen as baseline trigger, for both 1τ and 2τ channels. It requires $E_{\mathrm{T}}^{\mathrm{miss}} > 50\,\mathrm{GeV}$ at Level-1 and $E_{\mathrm{T}}^{\mathrm{miss}} > 70\,\mathrm{GeV}$ at the HLT level. This trigger is the lowest-threshold non-prescaled $E_{\mathrm{T}}^{\mathrm{miss}}$-trigger for the whole 2015 data-taking period. Triggers based on τ-lepton + $E_{\mathrm{T}}^{\mathrm{miss}}$ signatures for the 1τ channel, di-tau or di-tau + $E_{\mathrm{T}}^{\mathrm{miss}}$ signatures for the 2τ channel, offer the possibility to cut looser on offline $E_{\mathrm{T}}^{\mathrm{miss}}$, at the expense of harder cuts on the offline τ-lepton p_{T}. For signal models with compressed sparticle mass spectra, where soft τ-leptons are expected, triggers based on τ-leptons are not appropriate. But in regions of phase-space where the $E_{\mathrm{T}}^{\mathrm{miss}}$-trigger strategy would not be optimal, τ-lepton-based triggers could have been an interesting alternative. Investigations were made about the use of a 2τ trigger in the 2τ channel in 2015, and no significant gain was found [189, 224].

Due to its overall good performance across the probed SUSY parameter-space, the $E_{\mathrm{T}}^{\mathrm{miss}}$-trigger is also used in the this analysis. The HLT trigger threshold has been raised during the data taking period to cope with the non-linear increase in rates at higher instantaneous luminosity. The non-prescaled triggers are `HLT_XE70_mht` for 2015, then `HLT_XE90_mht_L1XE50`, then `HLT_XE100_mht_L1XE50` and finally `HLT_XE110_mht_L1XE50`. The `mht` suffix indicates that $E_{\mathrm{T}}^{\mathrm{miss}}$ is built using HLT jets, unlike `HLT_XE70` which is computed directly from cells above noise threshold. Performance studies have shown a slightly better performance of `HLT_XE70_mht` over `HLT_XE70`.

C.0.2 Trigger efficiency measurement

The trigger efficiency measurement is carried out in two steps. First, the efficiency of HLT triggers is measured using a bootstrapping method. Utilising periods of data-taking when more than one of the target $E_{\mathrm{T}}^{\mathrm{miss}}$-triggers were non-prescaled, it is possible to find the efficiency by a direct comparison.

Since all non-prescaled $E_{\mathrm{T}}^{\mathrm{miss}}$-triggers used in 2016 have the same L1 part, `L1_XE50`, the bootstrapping method cannot access the L1 efficiency. Instead, orthogonal non-prescaled triggers based on single-muon signatures are utilised to determine the efficiency of `L1_XE50`. A basic selection of events that triggered either `HLT_mu50` or `HLT_mu26_ivarmedium` and contain at least one *loose* τ-lepton is performed and

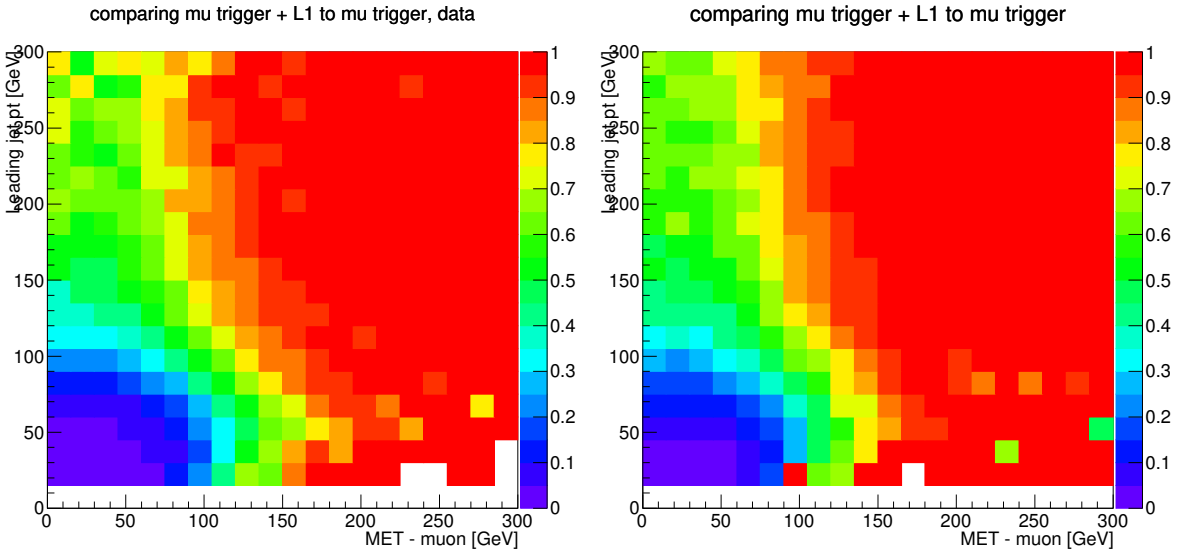

(a) Data (b) Simulation

Figure C.1: Efficiency of the `L1_XE50` trigger (L1-only) measured in data (a) and in simulation (b). In the simulation, all Standard Model backgrounds in the are included except the multi-jet contribution [189].

compared to the events passing both a single-muon trigger and `L1_XE50`. It is also possible to use this method to determine the full efficiency of the trigger, but the bootstrapping method provides more statistics for the HLT trigger efficiency.

For the trigger efficiency studies, the SUSY3 derivation (cf. section 3.2.5) is used. The selection is identical to the pre-selection described in section 5.6 except for the trigger plateau cuts and the *medium* ID τ-lepton. Instead, one *loose* τ-lepton with $p_{\mathrm{T}} > 20\,\mathrm{GeV}$ is required. For studies involving single-muon triggers, an additional muon with $p_{\mathrm{T}} > 30\,\mathrm{GeV}$ is required.

Triggers based on $E_{\mathrm{T}}^{\mathrm{miss}}$ do not use p_{T}^{μ} when calculating $E_{\mathrm{T}}^{\mathrm{miss}}$. Introducing any muon requirements would thus lead to a bias in the resulting $E_{\mathrm{T}}^{\mathrm{miss}}$. To address this, a new variable $E_{\mathrm{T}}^{\mathrm{miss}} - p_{\mathrm{T}}^{\mu}$ is introduced by excluding muons from the offline $E_{\mathrm{T}}^{\mathrm{miss}}$ calculation. $E_{\mathrm{T}}^{\mathrm{miss}} - p_{\mathrm{T}}^{\mu}$ of events containing muons is then directly comparable to $E_{\mathrm{T}}^{\mathrm{miss}}$ of events with a veto on muons.

Similar to the [9, 224], the possibility of a cut on the $p_{\mathrm{T}}^{\mathrm{j}_1}$ to improve the $E_{\mathrm{T}}^{\mathrm{miss}}$ cut-off is investigated. For that purpose, the efficiency of `L1_XE50` is binned in $E_{\mathrm{T}}^{\mathrm{miss}} - p_{\mathrm{T}}^{\mu}$ and $p_{\mathrm{T}}^{\mathrm{j}_1}$ as depicted in fig. C.1. The efficiency is determined by comparing the number of events that fire one of the single-muon triggers and `L1_XE50` to the number of events that fire one of the single-muon triggers. A cut on $p_{\mathrm{T}}^{\mathrm{j}_1} > 120\,\mathrm{GeV}$ is chosen. Figure C.2(a) depicts the efficiency of `L1_XE50` as a function of $E_{\mathrm{T}}^{\mathrm{miss}} - p_{\mathrm{T}}^{\mu}$ with the cut on $p_{\mathrm{T}}^{\mathrm{j}_1}$.

The analysis intends to use a single plateau region for all the different $E_{\mathrm{T}}^{\mathrm{miss}}$-triggers, so the efficiency of `HLT_XE110_mht_L1XE50` is of importance. Both `xe110` and `xe100` triggers were run non-prescaled during runs 302736-304009 which allows for a straightforward use of the bootstrapping method. A veto on muons is applied to make the selection orthogonal to events used for the determination of L1-trigger efficiencies. Figure C.3 shows the efficiency of the `HLT_XE110_mht` trigger in bins of $E_{\mathrm{T}}^{\mathrm{miss}} - p_{\mathrm{T}}^{\mu}$ and $p_{\mathrm{T}}^{\mathrm{j}_1}$. As a cross-check, the HLT trigger efficiency is also calculated using orthogonal single-muon triggers. The HLT trigger efficiency as a function of $E_{\mathrm{T}}^{\mathrm{miss}} - p_{\mathrm{T}}^{\mu}$ with the cut on $p_{\mathrm{T}}^{\mathrm{j}_1} > 120\,\mathrm{GeV}$ applied is depicted in fig. C.2(b).

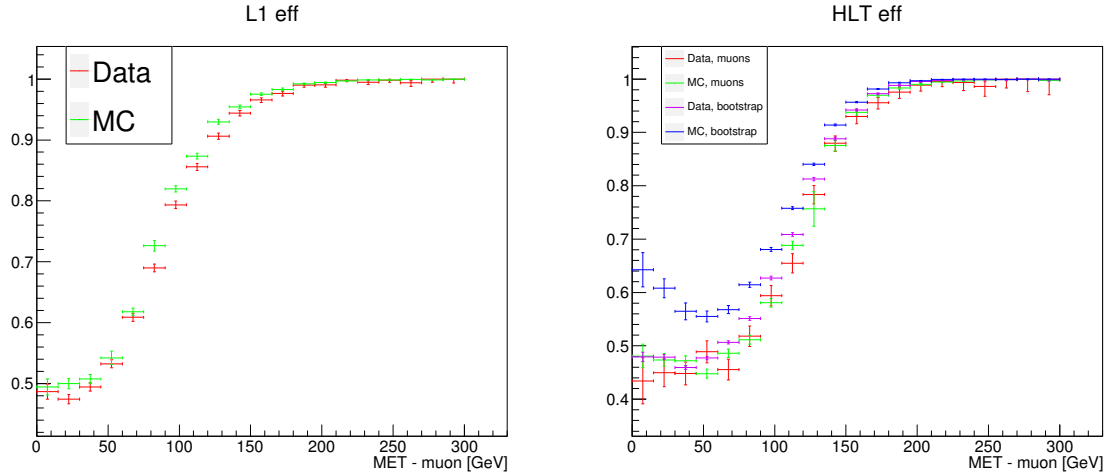

(a) `L1_XE50` (b) `HLT_XE110_mht`

Figure C.2: Efficiency of the `L1_XE50` trigger (L1-only) (a) and the `HLT_XE110_mht` trigger (HLT-only) (b) as a function of $E_{\mathrm{T}}^{\mathrm{miss}} - \mu_{p_{\mathrm{T}}}$ with the $p_{\mathrm{T}}^{\mathrm{j1}} > 120\,\mathrm{GeV}$ cut applied. In the simulation, all Standard Model backgrounds are included except the multi-jet contribution [189].

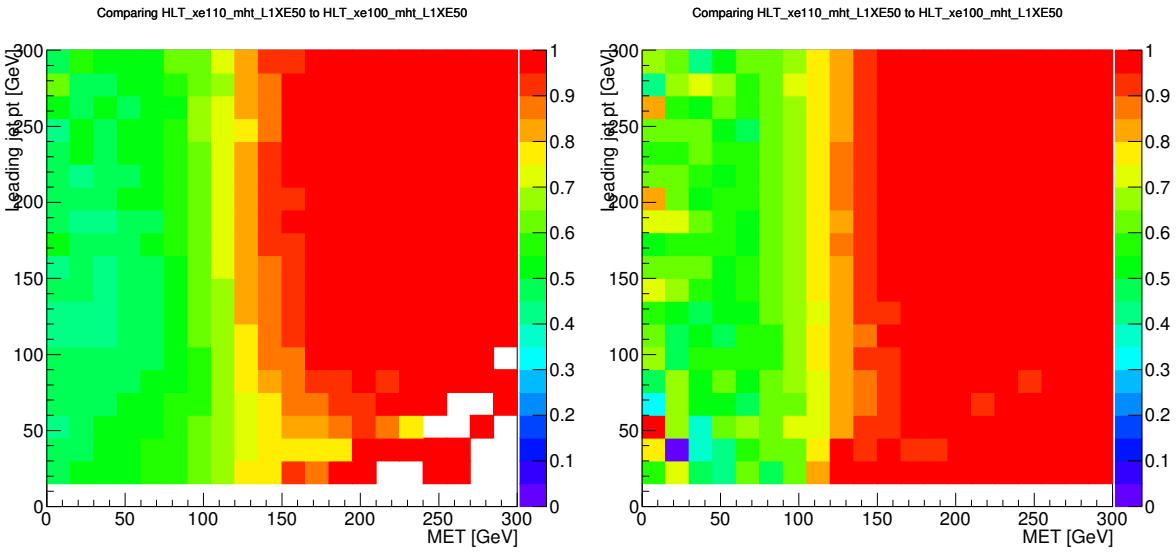

(a) Data (b) Simulation

Figure C.3: Efficiency of the `HLT_XE110_mht` trigger (HLT-only) measured in data (a) and in simulation (b). In the simulation, all Standard Model backgrounds are included except the multi-jet contribution [189].

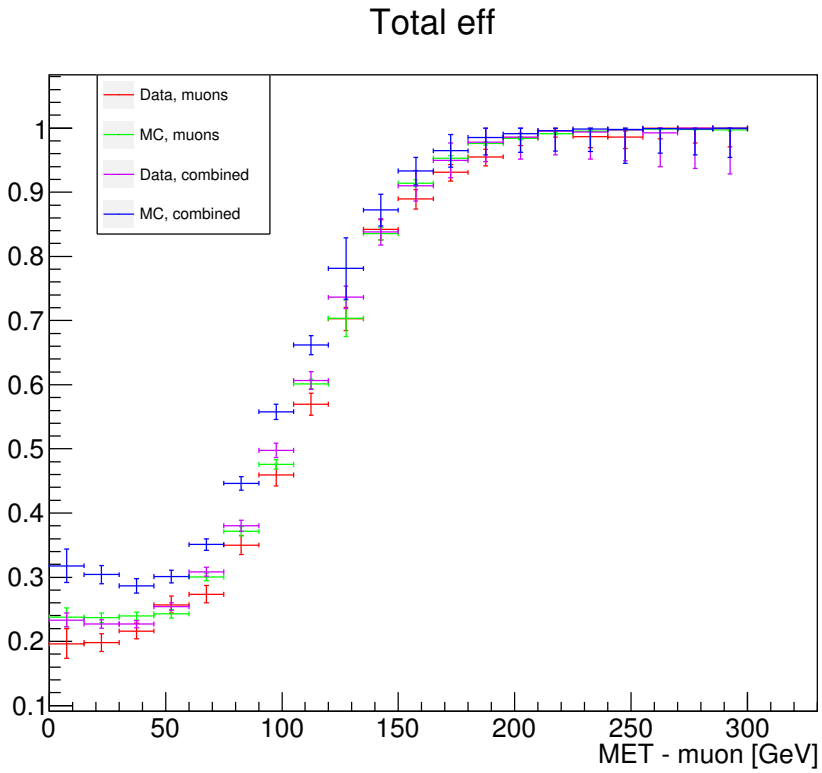

Figure C.4: Efficiency of the `HLT_XE110_mht_L1_XE50` trigger with the $p_{\mathrm{T}}^{\mathrm{j_1}} > 120\,\mathrm{GeV}$ cut applied. In the simulation, all Standard Model backgrounds in the are included except the multi-jet contribution [189].

Since the selections for L1 and HLT are orthogonal, they can be trivially combined to the total trigger efficiency. Figure C.4 illustrates the total trigger efficiency from the combination of the bootstrapping and the muon-trigger methods as well as the efficiency determined from the muon-trigger methods completely. Data and simulation agree well for both methods in the plateau region. As a consequence, the $E_{\mathrm{T}}^{\mathrm{miss}} > 180\,\mathrm{GeV}$ cut is chosen in addition to ensure the optimal performance of the chosen trigger setup.

APPENDIX D

W + jets H_{T}-correction

A discrepancy between data and the predicted background in the H_{T}-distributions in the W kinematic and true-τ CRs can be inferred from figs. A.3(a) and A.7(a). In both distributions, the predicted spectrum appears harder than the observed data. This mismatch can be corrected for by bin-specific scaling-factors. Based on H_{T}, they are derived in the W kinematic CR as the ratio of the $H_{\mathrm{T}}^{\mathrm{jets}}$ distributions of the background-subtracted data and the W + jets MC prediction. Here, all backgrounds are initially scaled using the background-only fit normalisation factors. The $H_{\mathrm{T}}^{\mathrm{jets}}$-variable is the scalar sum of the transverse momenta of all jets. It does not include the light lepton or tau p_{T}. This variable is preferred over the regular H_{T} definition in order to allow the re-weighting to be applicable to all leptonic W + jets decays. The binning of the $H_{\mathrm{T}}^{\mathrm{jets}}$ distribution used for the fit is chosen such that 100 events with all other weights applied are found in each bin. The results of this correction are depicted in fig. D.1. By design, the re-weighting enforces agreement between observed data and predicted MC in the H_{T} distribution of the W kinematic CR. However, it also corrects for minor disagreement in, for example, the n_{jet} distribution of the W kinematic CR. Its general influence is considered as an additional systematic uncertainty, parametrised by means of a designated nuisance parameter in the combined fit.

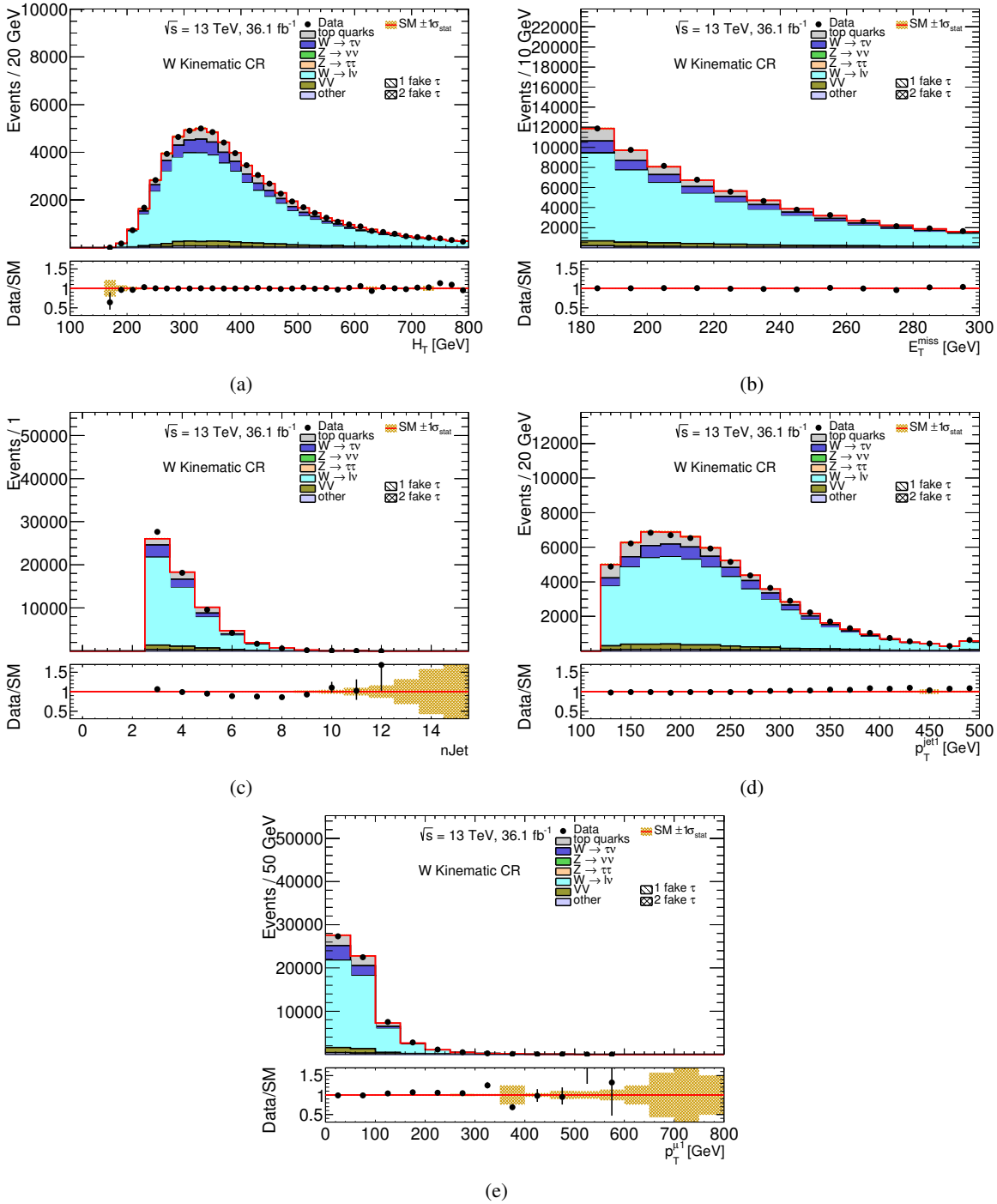

Figure D.1: Kinematic distributions of characteristic variables in the *W* Kinematic CR. The results shown are obtained after fitting the normalisation of the background in the control regions. The last bin of each distribution contains the overflow events. The uncertainties displayed consider only statistical limitations in the background modelling, illustrated by the shaded bands. The contribution labelled as "other" includes multi-jet events and *V*+Jets processes not explicitly listed in the legend. The black hatch-pattern illustrates contributions with fake τ-leptons. Here, the *W* + jets contributions are re-weighted by a fit of the unweighted—yet post-fit—distribution to the observed data distribution.

APPENDIX E

$t\bar{t}$ matrix element uncertainty

The systematic uncertainty introduced to the analysis by the description of the matrix element in the generation of $t\bar{t}$-events is evaluated by comparing two MC generators with different matrix element calculators, which use the same parton showering and hadronisation description: POWHEG and MG5_AMC@NLO both using HERWIG++ for the parton showering and hadronisation are compared to each other. Since neither of them is the nominal generator used in this analysis for predictions of the $t\bar{t}$ background, they cannot be compared directly in the simultaneous fit. Due to their substantially different statistical power, first their proper normalisation is ensured by performing the full background-only fit with the comparison samples substituting the nominal one. Based on these results, the relative difference between the post-fit yields of those generators in the signal and validation regions are computed and applied as weight-based systematic uncertainties to the nominal generator POWHEGBOX+PYTHIA6. Here, the yield difference is normalised to the yield of POWHEGBOX+HERWIG++ due to the fact that the nominal generator is also using POWHEG-BOX for the matrix element calculation.

As can be inferred from this line of argumentation, the predictive power and reliability of this estimation of the systematic uncertainty is heavily relying on the stability of the two alternate generators. In fact, this poses a challenge for the signal regions designed and used in this analysis. Since both samples used for comparison here contain fewer events than the nominal sample, their predictions of yields can only be trusted if enough (un-weighted) events are present in the regions of interest. Too few events modelling the final prediction cannot be trusted due to their high statistical uncertainty.

The latter is the case in most of the signal regions of this analysis as summarised in table E.1. While the nominal generator POWHEGBOX+PYTHIA6 has sufficient statistics in the nominal SRs, the two comparison generators exhibit low event yields in all SRs but the 1τ Compressed SR and the 2τ Multibin SR.

The resulting systematic uncertainties on the $t\bar{t}$ matrix element calculation in a complete background-only fit based on the numbers provided in table E.1 are summarised in the third column of table E.2. While in the 2τ high-mass SR the relative uncertainty is huge, in the 2τ compressed and GMSB SRs no uncertainty could be calculated at all. The huge uncertainty in the 1τ medium-mass SR is hence at least questionable to dubious.

In order to obtain sensible and reliable values, different approaches of estimating this systematic uncertainty are developed. Since similar problems already occurred in [9], the approach of less restrictive SR-like regions to estimate the uncertainties is pursued. A baseline selection is kept[1] from which cuts on the SR-defining variables are sequentially tightened until their descriptive power is too low to make a reliable estimate. From before the point of unreliability, the largest relative deviation between the

[1] All event quality and trigger-related criteria as well as cuts to suppress multi-jet events are applied, depending on the channel of interest, either one or two *medium*-ID τ-leptons are required in addition.

comparison generators and the nominal generator is taken as weight-based input to the combined fit for each region separately. SR-specific details on this estimation technique are described in the subsequent paragraphs.

The final results of this approach are summarised in table E.2. For each problematic SR, the outcome of the estimation process and the result in the full combined fit are provided. The latter can be compared to the results of a full combined fit that uses the direct comparison based on insufficient statistics in the signal regions. In the 2τ high-mass SR, the uncertainty drops from 153% to 17% while in the 1τ medium-mass SR it decreases from 50% to 7%. The estimation in the 2τ compressed SR as well as the 2τ GMSB SR is available now while before the re-assessment, the contribution was too small to be displayed or not calculable at all. Similar statements hold for the individual bins of the 2τ Multibin SR.

Region	Generator		
	PowhegBox+Pythia6	PowhegBox+Herwig++	MG5_aMC@NLO+Herwig++
2τ high-mass SR	73	14	3
2τ Compressed SR	96	29	1
2τ multibin SR	1868	449	47
2τ GMSB SR	34	9	0
1τ compressed SR	8450	944	89
2τ medium-mass SR	683	84	13

Table E.1: Overview of the un-weighted pre-fit event yields for all three generators related to the evaluation of the systematic uncertainty on $t\bar{t}$ matrix element calculation: PowhegBox+Pythia6 being the nominal generator used everywhere else across the analysis, PowhegBox+Herwig++ and MG5_aMC@NLO+Herwig++ being the two generators to be compared to each other to obtain an uncertainty on the modelling of the $t\bar{t}$ matrix element calculation.

Region	injected pre-fit TOPGEN uncertainty	nominal post-fit TOPGEN uncertainty	improved post-fit TOPGEN uncertainty
2τ high-mass SR	50%	153%	17%
2τ compressed SR	40%	0%	26%
2τ GMSB SR	50%	0%	11%
1τ medium-mass SR	20%	50%	7%

Table E.2: Improvement of the relative systematic uncertainty on the matrix element calculation in the generation of $t\bar{t}$ events (TOPGEN) using input weights that are obtained in separate regions of phase-space with a looser selection to ensure enough statistics for a more reliable estimation. The second column gives the injected weights that are obtained in the separate estimation-regions. The final values of the TOPGEN uncertainty resulting from full background-only fits comprising all systematic uncertainties are depicted for two scenarios. The results in column three are obtained in the nominal SRs, column four gives the results when using the injected pre-fit uncertainties of column two.

2τ high-mass SR As can be inferred from table E.1, the un-weighted event counts of the two comparison generators are low and not sufficient to provide a reliable estimate of the uncertainty. As a consequence, the aforementioned procedure of sequentially increasing cuts on H_{T} and $m_{\mathrm{T}}^{\tau_1}+m_{\mathrm{T}}^{\tau_2}$ is performed. Figure E.1 illustrates the results: for both generators, figs. E.1(a) and E.1(c) show the relative difference of the yield surviving an imposed cut (y-axes) plotted against the cut value (x-axes). The errors depicted represent the statistical uncertainties propagated to the displayed ratio. Figures E.1(b) and E.1(c) show the relative statistical uncertainties (statistical uncertainty normalised to bin content) of the un weighted events, hence representing the amount of statistical uncertainty being left when imposing a given cut. Based on those four plots, conclusions regarding a more robust estimation of the statistical uncertainty can be drawn. Starting from around 900 GeV in H_{T} and approximately 300 GeV in $m_{\mathrm{T}}^{\tau_1}+m_{\mathrm{T}}^{\tau_2}$, MG5_aMC@NLO+Herwig++ starts to run out of raw events and is dominated by few high-weight events resulting in huge statistical uncertainties rendering any statement beyond these cut values virtually useless. Since this is where the signal of interest begins, estimating the systematic uncertainty below these values where there are still enough events left becomes an obvious choice. PowhegBox+Herwig++, on the other hand, also loses statistical power with increasing cut strength but still remains reliable, i.e. enough un-weighted events survive to make a reliable prediction. Given these poor statistics for MG5_aMC@NLO+Herwig++, the following (conservative) choice is made in estimating the systematic uncertainty of the $t\bar{t}$ generator matrix element modelling (TOPGEN) in the 2τ High-Mass signal region: The largest deviation of MG5_aMC@NLO+Herwig++ from the nominal generator PowhegBox+Pythia6 that can be observed in regimes with acceptable statistics is approximately 50%. This number is visible in the distribution of H_{T} at around 750 GeV. This number is taken as a relative uncertainty and injected into the combined fit as a weight-based variation for all $t\bar{t}$ samples in the 2τ high-mass signal region of this analysis.

2τ compressed SR In the same fashion, the systematic uncertainty of the $t\bar{t}$ matrix element calculation in the 2τ compressed SR is estimated in a region with looser cuts than the nominal signal region. The discriminating variables defining the region are $m_{\mathrm{T}}^{\mathrm{sum}}$ and $m_{\mathrm{T2}}^{\tau\tau}$. Scanning those two variables with the aforementioned preselection and the upper cut of $H_{\mathrm{T}} < 1\,100$ GeV gives the results depicted in fig. E.2. Since the scan of $m_{\mathrm{T2}}^{\tau\tau}$ shows the stronger deviations of MG5_aMC@NLO+Herwig++ (PowhegBox+Herwig++ being comparable to the 2τ high-mass SR), the uncertainty is extracted from this plot to be set to 60% for all $t\bar{t}$ samples as a weight-based variation in the combined fit.

2τ Multibin SR In contrast to the 2τ high-mass and compressed signal regions, the un-weighted event yields of the two comparison generators are not too low to be used for a useful estimate of the systematic uncertainty. However, since HistFitter considers the Multibin SR bins (7 when using $m_{\mathrm{T}}^{\tau_1}+m_{\mathrm{T}}^{\tau_2}$ for the fit to be performed in), as individual signal regions each of which constraining background and signal in the combined fit, the uncertainties for each bin can become large. Given this fact and the nature of the individual bins being mutually exclusive, the only feasible approach is one mutual estimate of the uncertainty for all bins simultaneously. Since the baseline selection of this region being defined by moderate cuts on $m_{\mathrm{T}}^{\tau_1}+m_{\mathrm{T}}^{\tau_2}$ and H_{T} allows for such an estimate, cf. table E.1, the relative difference of MG5_aMC@NLO+Herwig++ and PowhegBox+Herwig++ weighted post-fit yields normalised to the yield of PowhegBox+Herwig++ is considered as the (symmetrical), weight-based uncertainty in the combined fit. Given the properly scaled post-fit yields of the two generators, this gives eq. (E.1). The final value of the relative difference is set to be 20% for all bins of the $m_{\mathrm{T}}^{\tau_1}+m_{\mathrm{T}}^{\tau_2}$ distribution of the 2τ Multibin signal region.

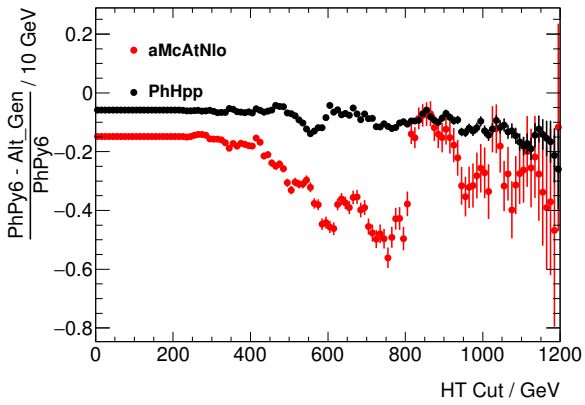

(a) H_{T}-scan, relative deviations

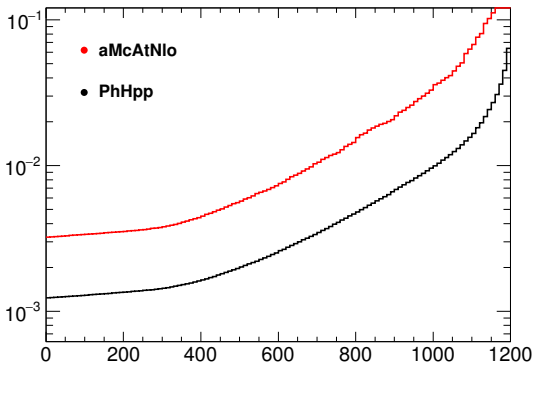

(b) H_{T}-scan, relative stat. uncertainty

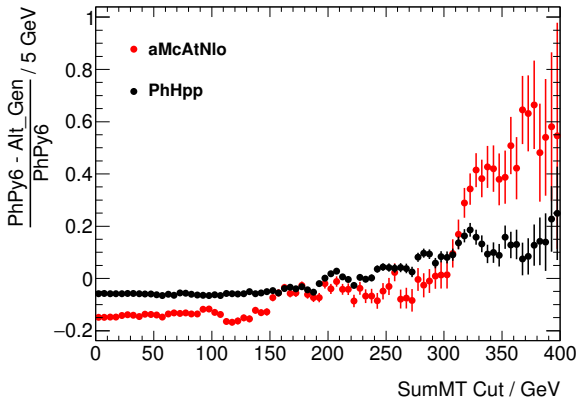

(c) $m_{\mathrm{T}}^{\tau_1}+m_{\mathrm{T}}^{\tau_2}$-scan, relative deviations

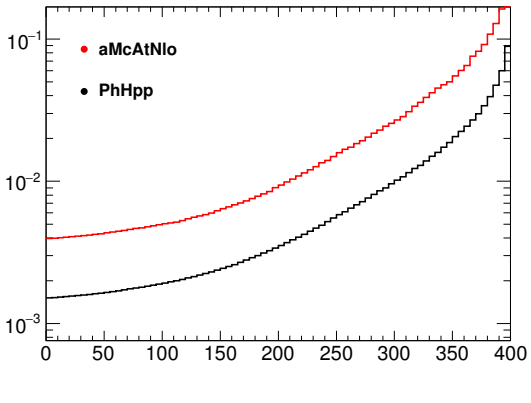

(d) $m_{\mathrm{T}}^{\tau_1}+m_{\mathrm{T}}^{\tau_2}$-scan, relative stat. uncertainty

Figure E.1: Scans of the region-defining variables H_{T} and $m_{\mathrm{T}}^{\tau_1}+m_{\mathrm{T}}^{\tau_2}$ after a baseline selection and requiring the presence of two τ-leptons. (a) and (c) show the weighted post-fit event yield differences of the two comparison generators normalised to the yield of the nominal generator. The x-axes show the cut values which are applied at each stage of the scan. (b) and (d) show the un-weighted post-fit relative statistical uncertainties at each cut stage. The statistical uncertainty at each point is normalised to the event yield at that point. All displayed error bars are obtained from propagated statistical uncertainties.

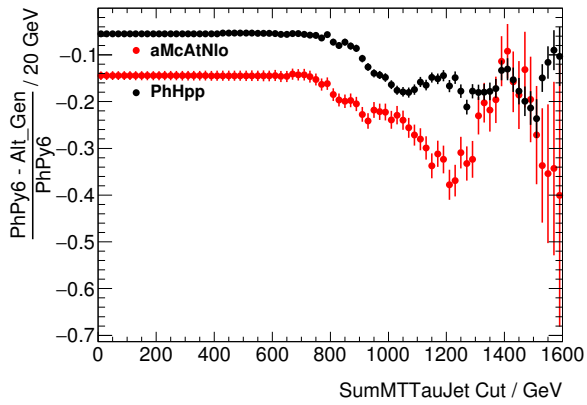

(a) $m_{\mathrm{T}}^{\mathrm{sum}}$-scan, relative deviations

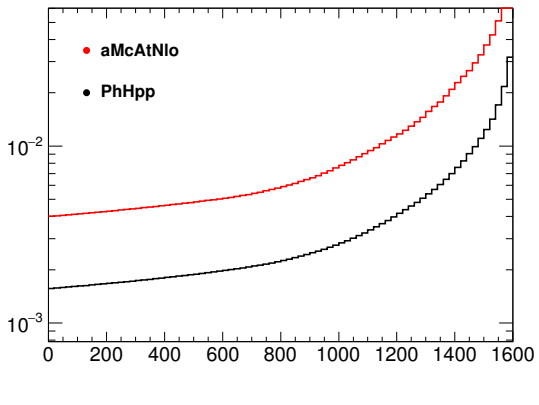

(b) $m_{\mathrm{T}}^{\mathrm{sum}}$-scan, relative stat. uncertainty

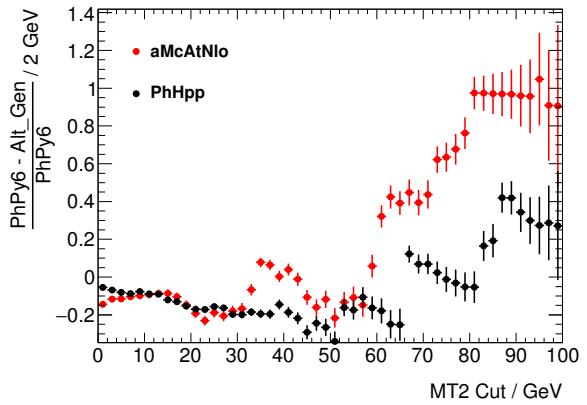

(c) $m_{\mathrm{T2}}^{\tau\tau}$-scan, relative deviations

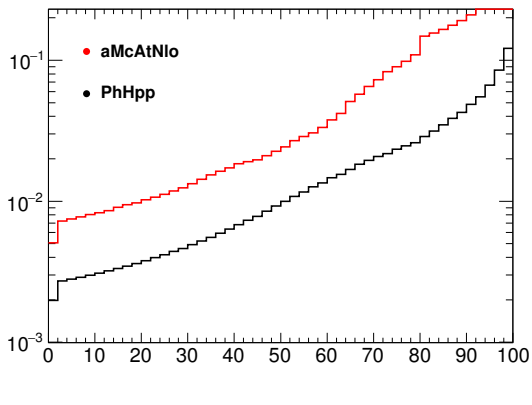

(d) $m_{\mathrm{T2}}^{\tau\tau}$-scan, relative stat. uncertainty

Figure E.2: Scans of the region-defining variables $m_{\mathrm{T}}^{\mathrm{sum}}$ and $m_{\mathrm{T2}}^{\tau\tau}$ after a baseline selection and requiring the presence of two τ-leptons. (a) and (c) show the weighted post-fit event yield differences of the two comparison generators normalised to the yield of the nominal generator. The x-axes show the cut values which are applied at each stage of the scan. (b) and (d) show the un-weighted post-fit relative statistical uncertainties at each cut stage. The statistical uncertainty at each point is normalised to the event yield at that point. All displayed error bars are obtained from propagated statistical uncertainties.

$$\Delta_{\text{Up,Down}} = \frac{\left|N_{\text{aMcAtNlo}}^{\text{weighted, post-fit}} - N_{\text{PhHpp}}^{\text{weighted, post-fit}}\right|}{N_{\text{PhHpp}}^{\text{weighted, post-fit}}} = \frac{|44.26 - 37.03|}{35.59} = 0.2032 \tag{E.1}$$

1τ medium-mass SR Since the number of un-weighted events of MG5_aMC@NLO+Herwig++ in the 1τ Medium-Mass signal region is also low, the same procedure as for the two single-bin signal regions of the 2τ channel is applied here. Using the three discriminating variables H_{T}, m_{T}^{τ} and $E_{\text{T}}^{\text{miss}}$, the largest relative deviation to the nominal generator in a less restrictive region (the regular pre-selection and a requirement of one *medium*-ID τ-lepton is imposed) is taken as the relative difference used as a weight-based variation in the combined fit. The corresponding scans of the variables are depicted in figure fig. E.3. Taken from the m_{T}^{τ} distribution, the final value of relative deviation is chosen to be 20%.

1τ compressed SR In contrast to the aforementioned signal regions, statistics of all considered generators are high enough to rely on the prediction of the $t\bar{t}$ matrix element uncertainty in the 1τ compressed signal region. Here, the relative difference between the two generators MG5_aMC@NLO+Herwig++ and PowhegBox+Herwig++ (normalised to PowhegBox+Herwig++) in the nominal region is considered as the weight-based uncertainty that is injected as a weight-based variation into the combined fit.

2τ GMSB SR Finally, in the same way as for the 2τ high-mass SR, the uncertainty in the GMSB SR of the 2τ channel is re-assessed. Here, the variables H_{T} and $m_{\text{T}}^{\tau_1} + m_{\text{T}}^{\tau_2}$ are scrutinised. Judging from fig. E.4, the H_{T} distribution suggests an uncertainty of 50% as for the 2τ HM SR.

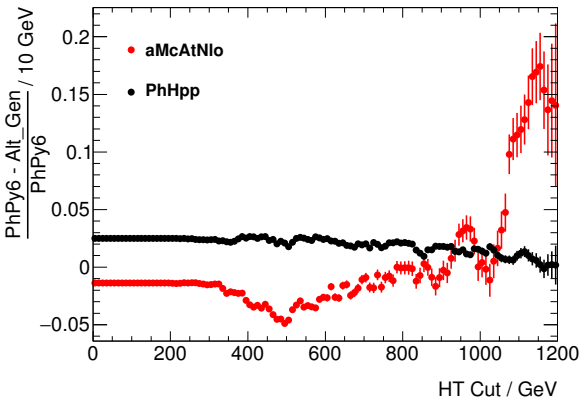

(a) H_T-scan, relative deviations

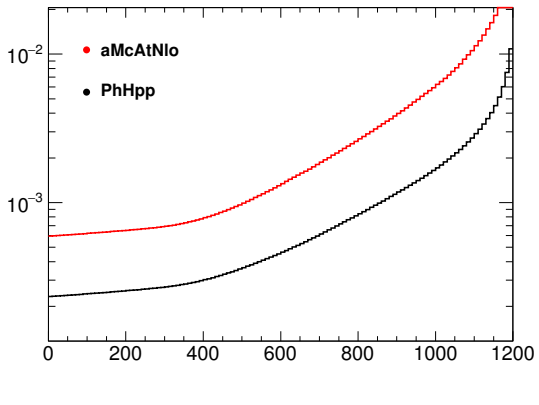

(b) H_T-scan, relative stat. uncertainty

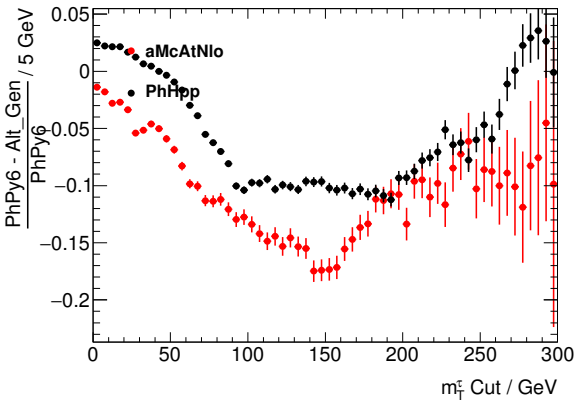

(c) m_T^τ-scan, relative deviations

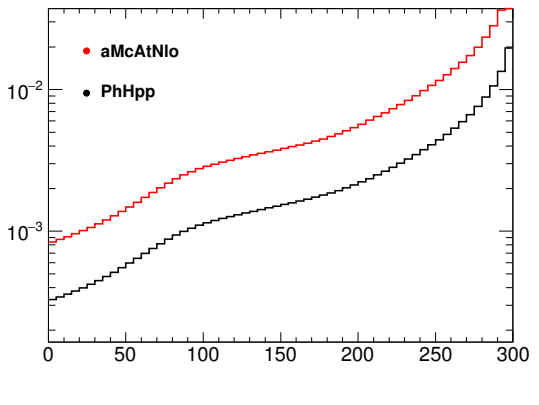

(d) m_T^τ-scan, relative stat. uncertainty

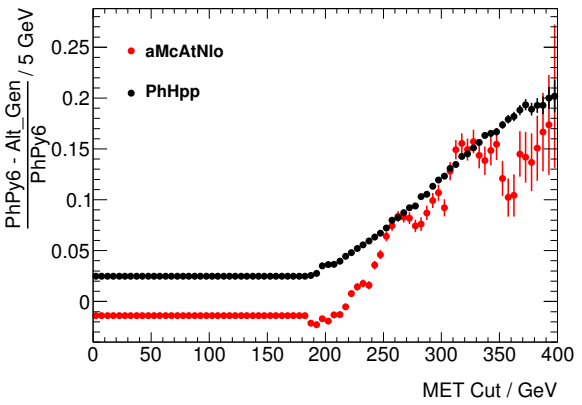

(e) E_T^{miss}-scan, relative deviations

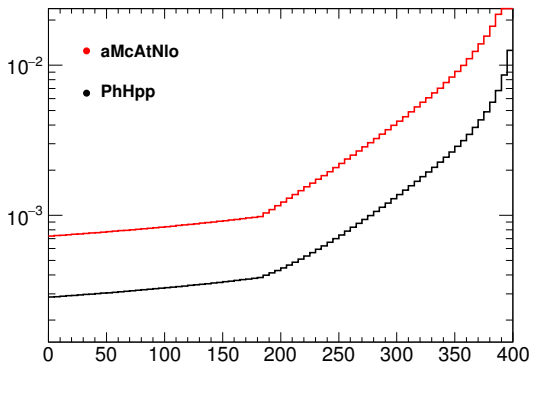

(f) E_T^{miss}-scan, relative stat. uncertainty

Figure E.3: Scans of the region-defining variables H_T, m_T^τ and E_T^{miss} after a baseline selection and requiring the presence of two taus. (a), (c) and (e) show the weighted post-fit event yield differences of the two comparison generators normalised to the yield of the nominal generator. The x-axes show the cut values which are applied at each stage of the scan. (b), (d) and (f) show the un-weighted post-fit relative statistical uncertainties at each cut stage. The statistical uncertainty at each point is normalised to the event yield at that point. All displayed error bars are obtained from propagated statistical uncertainties.

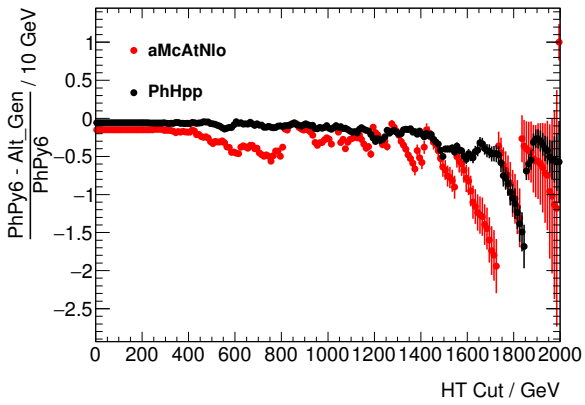

(a) H_{T}-scan, relative deviations

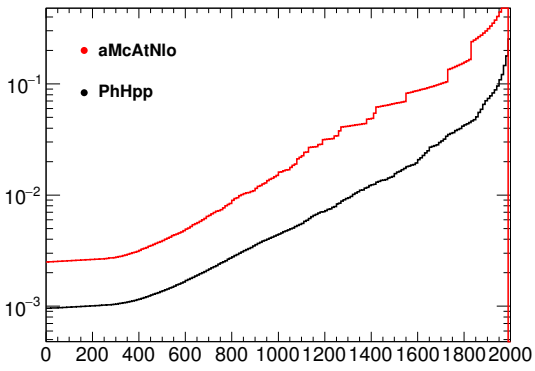

(b) H_{T}-scan, relative stat. uncertainty

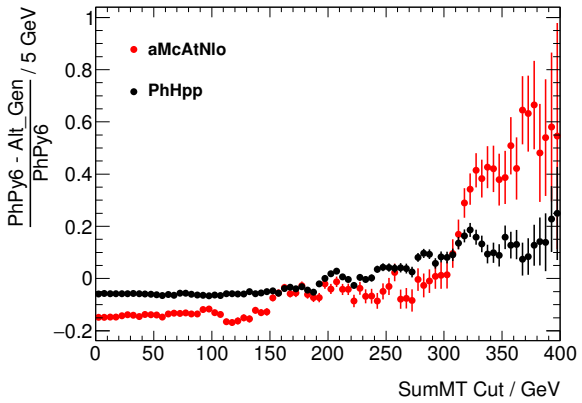

(c) $m_{\mathrm{T}}^{\tau_1}+m_{\mathrm{T}}^{\tau_2}$-scan, relative deviations

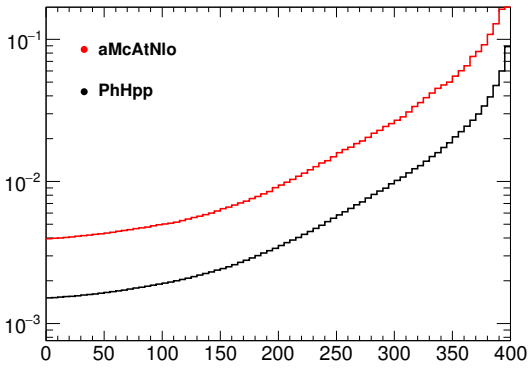

(d) $m_{\mathrm{T}}^{\tau_1}+m_{\mathrm{T}}^{\tau_2}$-scan, relative stat. uncertainty

Figure E.4: Scans of the region-defining variables H_{T} and $m_{\mathrm{T}}^{\tau_1}+m_{\mathrm{T}}^{\tau_2}$ after a baseline selection and requiring the presence of two taus. (a) and (c) show the weighted post-fit event yield differences of the two comparison generators normalised to the yield of the nominal generator. The x-axes show the cut values which are applied at each stage of the scan. (b) and (d) show the un-weighted post-fit relative statistical uncertainties at each cut stage. The statistical uncertainty at each point is normalised to the event yield at that point. All displayed error bars are obtained from propagated statistical uncertainties.

APPENDIX F

Used MC & Data samples

This appendix provides a detailed list of the data and MC samples used in this analysis.

ID	Name	Generator	σ[pb]	k-factor	filter eff.
410011	singletop_tchan_lept_top	PowhegPythia	43.74	1.01	1.00
410011	singletop_tchan_lept_top	PowhegPythia	43.74	1.01	1.00
410012	singletop_tchan_lept_antitop	PowhegPythia	25.78	1.02	1.00
410013	Wt_inclusive_top	PowhegPythia	34.01	1.05	1.00
410014	Wt_inclusive_antitop	PowhegPythia	33.99	1.05	1.00
407018	Wt_inclusive_top_HT500	PowhegPythia	34.01	1.05	0.09
407019	Wt_inclusive_top_MET200	PowhegPythia	34.01	1.05	0.01
407020	Wt_inclusive_tbar_HT500	PowhegPythia	33.99	1.05	0.09
407021	Wt_inclusive_tbar_MET200	PowhegPythia	33.99	1.05	0.01
410025	SingleTopSchan_noAllHad_top	PowhegPythia	2.05	1.00	1.00
410026	SingleTopSchan_noAllHad_antitop	PowhegPythia	1.26	1.02	1.00
410560	tZ_4fl_tchan_noAllHad	MadGraphPythia8	0.24	1.00	1.00
410017	singletop_tchan_lept_top	PowhegPythia	40.34	1.09	1.00
410018	singletop_tchan_lept_top	PowhegPythia	44.38	0.99	1.00
410019	singletop_tchan_lept_antitop	PowhegPythia	23.75	1.11	1.00
410020	singletop_tchan_lept_antitop	PowhegPythia	26.39	1.00	1.00
410062	Wt_DS_inclusive_top	PowhegPythia	32.38	1.05	1.00
410063	Wt_DS_inclusive_antitop	PowhegPythia	32.36	1.05	1.00
410099	Wt_inclusive_top	PowhegPythia	34.92	1.03	1.00
410100	Wt_inclusive_top	PowhegPythia	33.41	1.07	1.00
410101	Wt_inclusive_antitop	PowhegPythia	34.89	1.03	1.00
410102	Wt_inclusive_antitop	PowhegPythia	33.39	1.07	1.00
410107	SingleTopSchan_lept_top	PowhegPythia	2.08	0.99	1.00
410108	SingleTopSchan_lept_top	PowhegPythia	2.03	1.01	1.00
410109	SingleTopSchan_lept_antitop	PowhegPythia	1.28	1.01	1.00
410110	SingleTopSchan_lept_antitop	PowhegPythia	1.25	1.03	1.00

Table F.1: List of used single-t samples, their corresponding dataset ID, the used event generator, the production cross-section σ, the k-factor, and the filter efficiency.

ID	Name	Generator	σ[pb]	k-factor	filter eff.
407200	ttbarNp012p_MET0to200_HT0to500	MGPy8	435.44	1.87	0.49
407201	ttbarNp012p_MET0to200_HT500to700	MGPy8	436.63	1.87	0.03
407202	ttbarNp012p_MET0to200_HT700to1000	MGPy8	436.48	1.87	0.01
407203	ttbarNp012p_MET200p_HT0to1000	MGPy8	436.48	1.87	0.01
407204	ttbarNp012p_HT1000p	MGPy8	436.58	1.87	0.00
410249	NNPDF30NNLO_ttbar_AllHadronic_MEPS_NLO	Sherpa	330.54	1.15	1.00
410250	NNPDF30NNLO_ttbar_SingleLeptonP_MEPS_NLO	Sherpa	158.76	1.00	1.00
410251	NNPDF30NNLO_ttbar_SingleLeptonM_MEPS_NLO	Sherpa	158.97	1.00	1.00
410252	NNPDF30NNLO_ttbar_dilepton_MEPS_NLO	Sherpa	76.28	1.15	1.00
410501	ttbar_hdamp258p75_nonallhad	PowhegPythia8	730.17	1.14	0.54
410502	ttbar_hdamp258p75_allhad	PowhegPythia8	249.81	1.14	1.00
410503	ttbar_hdamp258p75_dil	PowhegPythia8	76.93	1.14	1.00
410525	tt_hdamp258p75_nonallhad	PowhegHerwig7	730.15	1.14	0.54
410526	tt_hdamp258p75_allhad	PowhegHerwig7	249.81	1.14	1.00
410527	tt_hdamp258p75_dilep	PowhegHerwig7	76.93	1.14	1.00
407009	ttbarHT6c_1k_hdamp172p5_nonAH	PowhegPythia	696.22	1.19	0.02
407010	ttbarHT1k_1k5_hdamp172p5_nonAH	PowhegPythia	696.23	1.19	0.00
407011	ttbarHT1k5_hdamp172p5_nonAH	PowhegPythia	696.23	1.19	0.00
407012	ttbarMET200_hdamp172p5_nonAH	PowhegPythia	696.22	1.19	0.01
407322	ttbarMET300_hdamp172p5_nonAH	PowhegPythia	696.21	1.19	0.00
407323	ttbarMET400_hdamp172p5_nonAH	PowhegPythia	696.23	1.19	0.00
407030	P2012radHiC6L1_ttbarHT1k_1k5_hdamp345_down_nonAH	PhPy	783.84	1.06	0.00
407031	P2012radHiC6L1_ttbarHT1k5_hdamp345_down_nonAH	PhPy	783.85	1.06	0.00
407032	P2012radHiC6L1_ttbarMET200_hdamp345_down_nonAH	PhPy	783.83	1.06	0.01
407033	P2012radLoC6L1_ttbarHT6c_1k_hdamp172_up_nonAH	PhPy	611.11	1.36	0.02
407034	P2012radLoC6L1_ttbarHT1k_1k5_hdamp172_up_nonAH	PhPy	611.11	1.36	0.00
407035	P2012radLoC6L1_ttbarHT1k5_hdamp172_up_nonAH	PhPy	611.12	1.36	0.00
407036	P2012radLoC6L1_ttbarMET200_hdamp172_up_nonAH	PhPy	611.10	1.36	0.01
407037	UE5C6L1_ttbarHT6c_1k_hdamp172p5_nonAH	PhHpp	696.33	1.19	0.02
407038	UE5C6L1_ttbarHT1k_1k5_hdamp172p5_nonAH	PhHpp	696.33	1.19	0.00
407039	UE5C6L1_ttbarHT1k5_hdamp172p5_nonAH	PhHpp	696.34	1.19	0.00
407040	UE5C6L1_ttbarMET200_hdamp172p5_nonAH	PhHpp	696.32	1.19	0.01
341177	CTEQ6L1_CT10ME_ttH125_dil	aMcAtNloHerwigpp	0.51	1.00	1.00
341270	CTEQ6L1_CT10ME_ttH125_semilep	aMcAtNloHerwigpp	0.51	1.00	0.44
341271	CTEQ6L1_CT10ME_ttH125_allhad	aMcAtNloHerwigpp	0.51	1.00	0.46
410066	ttW_Np0	MadGraphPythia8	0.18	1.32	1.00
410067	ttW_Np1	MadGraphPythia8	0.14	1.32	1.00
410068	ttW_Np2	MadGraphPythia8	0.14	1.32	1.00
410073	ttZnnqq_Np0	MadGraphPythia8	0.17	1.47	1.00
410074	ttZnnqq_Np1	MadGraphPythia8	0.17	1.47	1.00
410075	ttZnnqq_Np2	MadGraphPythia8	0.17	1.47	1.00
410081	ttbarWW	MadGraphPythia8	0.01	1.22	1.00
410111	ttee_Np0	MadGraphPythia8	0.01	1.51	1.00
410112	ttee_Np1	MadGraphPythia8	0.01	1.51	1.00
410113	ttmumu_Np0	MadGraphPythia8	0.01	1.51	1.00
410114	ttmumu_Np1	MadGraphPythia8	0.01	1.51	1.00
410115	tttautau_Np0	MadGraphPythia8	0.01	1.51	1.00
410116	tttautau_Np1	MadGraphPythia8	0.01	1.51	1.00
410156	A14N23LO_ttZnunu	aMcAtNloPythia8	0.15	1.11	1.00
410157	A14N23LO_ttZqq	aMcAtNloPythia8	0.53	1.11	1.00
410142	ttll_mll5	Sherpa	0.11	1.09	1.00
410143	ttZnnqq	Sherpa	0.69	1.10	1.00
410144	ttW	Sherpa	0.58	1.04	1.00
410000	ttbar_hdamp172p5_nonallhad	PowhegPythia	831.76	1.00	0.54
410001	ttbar_hdamp345_down_nonallhad	PowhegPythia	831.76	1.00	0.54
410002	ttbar_hdamp172_up_nonallhad	PowhegPythia	831.76	1.00	0.54
410003	nonallhad	aMcAtNloHerwigpp	831.76	1.00	0.54
410004	ttbar_hdamp172p5_nonallhad	PowhegHerwigpp	831.76	1.00	0.54
410007	ttbar_hdamp172p5_allhad	PowhegPythia	695.99	1.20	0.46

Table F.2: List of used $t\bar{t}$ samples, their corresponding dataset ID, the used event generator, the production cross-section σ, the k-factor, and the filter efficiency.

ID	Name	Generator	σ[pb]	k-factor	filter eff.
363331	Wtaunu_Pt0_70_CVetoBVeto	Sherpa	20 026.00	0.97	0.81
363332	Wtaunu_Pt0_70_CFilterBVeto	Sherpa	20 024.00	0.97	0.14
363333	Wtaunu_Pt0_70_BFilter	Sherpa	20 021.00	0.97	0.05
363334	Wtaunu_Pt70_140_CVetoBVeto	Sherpa	589.71	0.97	0.66
363335	Wtaunu_Pt70_140_CFilterBVeto	Sherpa	589.95	0.97	0.25
363336	Wtaunu_Pt70_140_BFilter	Sherpa	590.25	0.97	0.09
363337	Wtaunu_Pt140_280_CVetoBVeto	Sherpa	84.26	0.97	0.62
363338	Wtaunu_Pt140_280_CFilterBVeto	Sherpa	84.22	0.97	0.28
363339	Wtaunu_Pt140_280_BFilter	Sherpa	84.18	0.97	0.11
363340	Wtaunu_Pt280_500_CVetoBVeto	Sherpa	6.10	0.97	0.59
363341	Wtaunu_Pt280_500_CFilterBVeto	Sherpa	6.07	0.97	0.29
363342	Wtaunu_Pt280_500_BFilter	Sherpa	6.08	0.97	0.13
363343	Wtaunu_Pt500_700_CVetoBVeto	Sherpa	0.38	0.97	0.57
363344	Wtaunu_Pt500_700_CFilterBVeto	Sherpa	0.38	0.97	0.29
363345	Wtaunu_Pt500_700_BFilter	Sherpa	0.38	0.97	0.14
363346	Wtaunu_Pt700_1000_CVetoBVeto	Sherpa	0.07	0.97	0.57
363347	Wtaunu_Pt700_1000_CFilterBVeto	Sherpa	0.07	0.97	0.29
363348	Wtaunu_Pt700_1000_BFilter	Sherpa	0.07	0.97	0.15
363349	Wtaunu_Pt1000_2000_CVetoBVeto	Sherpa	0.01	0.97	0.58
363350	Wtaunu_Pt1000_2000_CFilterBVeto	Sherpa	0.01	0.97	0.29
363351	Wtaunu_Pt1000_2000_BFilter	Sherpa	0.01	0.97	0.16
363352	Wtaunu_Pt2000_E_CMS_CVetoBVeto	Sherpa	2.62×10^{-5}	0.97	0.56
363353	Wtaunu_Pt2000_E_CMS_CFilterBVeto	Sherpa	2.81×10^{-5}	0.97	0.27
363354	Wtaunu_Pt2000_E_CMS_BFilter	Sherpa	2.94×10^{-5}	0.97	0.17
364186	NNPDF30NNLO_Wtaunu_MAXHTPTV0_70_BFilter	Sherpa	19 148.00	0.97	0.05
364189	NNPDF30NNLO_Wtaunu_MAXHTPTV70_140_BFilter	Sherpa	945.71	0.97	0.10
364192	NNPDF30NNLO_Wtaunu_MAXHTPTV140_280_BFilter	Sherpa	339.35	0.97	0.11
364195	NNPDF30NNLO_Wtaunu_MAXHTPTV280_500_BFilter	Sherpa	71.95	0.97	0.14
364196	NNPDF30NNLO_Wtaunu_MAXHTPTV500_1000	Sherpa	15.05	0.97	1.00
364197	NNPDF30NNLO_Wtaunu_MAXHTPTV1000_E_CMS	Sherpa	1.23	0.97	1.00
364185	NNPDF30NNLO_Wtaunu_MAXHTPTV0_70_CFilterBVeto	Sherpa	19 149.00	0.97	0.13
364188	NNPDF30NNLO_Wtaunu_MAXHTPTV70_140_CFilterBVeto	Sherpa	946.23	0.97	0.24
364191	NNPDF30NNLO_Wtaunu_MAXHTPTV140_280_CFilterBVeto	Sherpa	339.66	0.97	0.28
364194	NNPDF30NNLO_Wtaunu_MAXHTPTV280_500_CFilterBVeto	Sherpa	71.99	0.97	0.32
364184	NNPDF30NNLO_Wtaunu_MAXHTPTV0_70_CVetoBVeto	Sherpa	19 155.00	0.97	0.82
364187	NNPDF30NNLO_Wtaunu_MAXHTPTV70_140_CVetoBVeto	Sherpa	945.02	0.97	0.68
364190	NNPDF30NNLO_Wtaunu_MAXHTPTV140_280_CVetoBVeto	Sherpa	339.78	0.97	0.60
364193	NNPDF30NNLO_Wtaunu_MAXHTPTV280_500_CVetoBVeto	Sherpa	72.09	0.97	0.55
361530	Wtaunu_Np0	MadGraphPythia8	13 935.00	1.20	1.00
361531	Wtaunu_Np1	MadGraphPythia8	1 892.10	1.20	1.00
361532	Wtaunu_Np2	MadGraphPythia8	642.23	1.20	1.00
361533	Wtaunu_Np3	MadGraphPythia8	179.16	1.20	1.00
361534	Wtaunu_Np4	MadGraphPythia8	71.07	1.20	1.00
363648	Wtaunu_Ht0_70_CVetoBVeto	MGPy8	16 702.00	1.12	0.84
363649	Wtaunu_Ht0_70_CFilterBVeto	MGPy8	16 702.00	1.12	0.14
363650	Wtaunu_Ht0_70_BFilter	MGPy8	16 701.00	1.12	0.02
363651	Wtaunu_Ht70_140_CVetoBVeto	MGPy8	755.08	1.12	0.71
363652	Wtaunu_Ht70_140_CFilterBVeto	MGPy8	755.24	1.12	0.24
363653	Wtaunu_Ht70_140_BFilter	MGPy8	755.14	1.12	0.05
363654	Wtaunu_Ht140_280_CVetoBVeto	MGPy8	315.27	1.12	0.67
363655	Wtaunu_Ht140_280_CFilterBVeto	MGPy8	315.97	1.12	0.27
363656	Wtaunu_Ht140_280_BFilter	MGPy8	315.63	1.12	0.07
363657	Wtaunu_Ht280_500_CVetoBVeto	MGPy8	72.22	1.12	0.62
363658	Wtaunu_Ht280_500_CFilterBVeto	MGPy8	72.24	1.12	0.29
363659	Wtaunu_Ht280_500_BFilter	MGPy8	72.21	1.12	0.10
363660	Wtaunu_Ht500_700_CVetoBVeto	MGPy8	11.44	1.12	0.59
363661	Wtaunu_Ht500_700_CFilterBVeto	MGPy8	11.46	1.12	0.30
363662	Wtaunu_Ht500_700_BFilter	MGPy8	11.46	1.12	0.12
363663	Wtaunu_Ht700_1000_CVetoBVeto	MGPy8	4.03	1.12	0.57
363664	Wtaunu_Ht700_1000_CFilterBVeto	MGPy8	4.03	1.12	0.30
363665	Wtaunu_Ht700_1000_BFilter	MGPy8	4.03	1.12	0.13
363666	Wtaunu_Ht1000_2000_CVetoBVeto	MGPy8	1.33	1.12	0.55
363667	Wtaunu_Ht1000_2000_CFilterBVeto	MGPy8	1.32	1.12	0.31
363668	Wtaunu_Ht1000_2000_BFilter	MGPy8	1.32	1.12	0.14
363671	Wtaunu_Ht2000_E_CMS_BFilter	MGPy8	0.04	1.12	0.17

Table F.3: List of used $W(\tau\nu)+$jets samples, their corresponding dataset ID, the used event generator, the production cross-section σ, the k-factor, and the filter efficiency.

ID	Name	Generator	σ[pb]	k-factor	filter eff.
363436	Wmunu_Pt0_70_CVetoBVeto	Sherpa	20 013.00	0.97	0.81
363437	Wmunu_Pt0_70_CFilterBVeto	Sherpa	20 028.00	0.97	0.14
363438	Wmunu_Pt0_70_BFilter	Sherpa	20 022.00	0.97	0.05
363439	Wmunu_Pt70_140_CVetoBVeto	Sherpa	590.67	0.97	0.66
363440	Wmunu_Pt70_140_CFilterBVeto	Sherpa	590.51	0.97	0.25
363441	Wmunu_Pt70_140_BFilter	Sherpa	589.90	0.97	0.09
363442	Wmunu_Pt140_280_CVetoBVeto	Sherpa	84.16	0.97	0.62
363443	Wmunu_Pt140_280_CFilterBVeto	Sherpa	84.19	0.97	0.28
363444	Wmunu_Pt140_280_BFilter	Sherpa	84.10	0.97	0.10
363445	Wmunu_Pt280_500_CVetoBVeto	Sherpa	6.08	0.97	0.59
363446	Wmunu_Pt280_500_CFilterBVeto	Sherpa	6.08	0.97	0.29
363447	Wmunu_Pt280_500_BFilter	Sherpa	6.07	0.97	0.14
363448	Wmunu_Pt500_700_CVetoBVeto	Sherpa	0.38	0.97	0.57
363449	Wmunu_Pt500_700_CFilterBVeto	Sherpa	0.38	0.97	0.29
363450	Wmunu_Pt500_700_BFilter	Sherpa	0.38	0.97	0.14
363451	Wmunu_Pt700_1000_CVetoBVeto	Sherpa	0.07	0.97	0.57
363452	Wmunu_Pt700_1000_CFilterBVeto	Sherpa	0.07	0.97	0.29
363453	Wmunu_Pt700_1000_BFilter	Sherpa	0.07	0.97	0.15
363454	Wmunu_Pt1000_2000_CVetoBVeto	Sherpa	0.01	0.97	0.58
363455	Wmunu_Pt1000_2000_CFilterBVeto	Sherpa	0.01	0.97	0.31
363456	Wmunu_Pt1000_2000_BFilter	Sherpa	0.01	0.97	0.15
363457	Wmunu_Pt2000_E_CMS_CVetoBVeto	Sherpa	2.77×10^{-5}	0.97	0.60
363458	Wmunu_Pt2000_E_CMS_CFilterBVeto	Sherpa	2.85×10^{-5}	0.97	0.32
363459	Wmunu_Pt2000_E_CMS_BFilter	Sherpa	2.70×10^{-5}	0.97	0.21
364158	NNPDF30NNLO_Wmunu_MAXHTPTV0_70_BFilter	Sherpa	19 138.00	0.97	0.04
364161	NNPDF30NNLO_Wmunu_MAXHTPTV70_140_BFilter	Sherpa	944.14	0.97	0.08
364164	NNPDF30NNLO_Wmunu_MAXHTPTV140_280_BFilter	Sherpa	339.64	0.97	0.11
364167	NNPDF30NNLO_Wmunu_MAXHTPTV280_500_BFilter	Sherpa	72.06	0.97	0.13
364168	NNPDF30NNLO_Wmunu_MAXHTPTV500_1000	Sherpa	15.01	0.97	1.00
364169	NNPDF30NNLO_Wmunu_MAXHTPTV1000_E_CMS	Sherpa	1.23	0.97	1.00
364157	NNPDF30NNLO_Wmunu_MAXHTPTV0_70_CFilterBVeto	Sherpa	19 142.00	0.97	0.13
364160	NNPDF30NNLO_Wmunu_MAXHTPTV70_140_CFilterBVeto	Sherpa	945.44	0.97	0.24
364163	NNPDF30NNLO_Wmunu_MAXHTPTV140_280_CFilterBVeto	Sherpa	339.77	0.97	0.29
364166	NNPDF30NNLO_Wmunu_MAXHTPTV280_500_CFilterBVeto	Sherpa	72.10	0.97	0.32
364156	NNPDF30NNLO_Wmunu_MAXHTPTV0_70_CVetoBVeto	Sherpa	19 149.00	0.97	0.82
364159	NNPDF30NNLO_Wmunu_MAXHTPTV70_140_CVetoBVeto	Sherpa	945.52	0.97	0.67
364162	NNPDF30NNLO_Wmunu_MAXHTPTV140_280_CVetoBVeto	Sherpa	339.70	0.97	0.60
364165	NNPDF30NNLO_Wmunu_MAXHTPTV280_500_CVetoBVeto	Sherpa	72.08	0.97	0.55

Table F.4: List of used $W(\mu\nu)$+jets samples, their corresponding dataset ID, the used event generator, the production cross-section σ, the k-factor, and the filter efficiency.

ID	Name	Generator	σ[pb]	k-factor	filter eff.
363460	Wenu_Pt0_70_CVetoBVeto	Sherpa	20 038.00	0.97	0.81
363461	Wenu_Pt0_70_CFilterBVeto	Sherpa	20 023.00	0.97	0.14
363462	Wenu_Pt0_70_BFilter	Sherpa	20 022.00	0.97	0.05
363463	Wenu_Pt70_140_CVetoBVeto	Sherpa	590.25	0.97	0.66
363464	Wenu_Pt70_140_CFilterBVeto	Sherpa	590.09	0.97	0.25
363465	Wenu_Pt70_140_BFilter	Sherpa	589.58	0.97	0.09
363466	Wenu_Pt140_280_CVetoBVeto	Sherpa	84.19	0.97	0.62
363467	Wenu_Pt140_280_CFilterBVeto	Sherpa	84.16	0.97	0.28
363468	Wenu_Pt140_280_BFilter	Sherpa	84.14	0.97	0.11
363469	Wenu_Pt280_500_CVetoBVeto	Sherpa	6.09	0.97	0.59
363470	Wenu_Pt280_500_CFilterBVeto	Sherpa	6.09	0.97	0.29
363471	Wenu_Pt280_500_BFilter	Sherpa	6.08	0.97	0.13
363472	Wenu_Pt500_700_CVetoBVeto	Sherpa	0.38	0.97	0.57
363473	Wenu_Pt500_700_CFilterBVeto	Sherpa	0.38	0.97	0.29
363474	Wenu_Pt500_700_BFilter	Sherpa	0.38	0.97	0.14
363475	Wenu_Pt700_1000_CVetoBVeto	Sherpa	0.07	0.97	0.56
363476	Wenu_Pt700_1000_CFilterBVeto	Sherpa	0.07	0.97	0.29
363477	Wenu_Pt700_1000_BFilter	Sherpa	0.07	0.97	0.15
363478	Wenu_Pt1000_2000_CVetoBVeto	Sherpa	0.01	0.97	0.55
363479	Wenu_Pt1000_2000_CFilterBVeto	Sherpa	0.01	0.97	0.29
363480	Wenu_Pt1000_2000_BFilter	Sherpa	0.01	0.97	0.16
363481	Wenu_Pt2000_E_CMS_CVetoBVeto	Sherpa	2.88×10^{-5}	0.97	0.49
363482	Wenu_Pt2000_E_CMS_CFilterBVeto	Sherpa	2.72×10^{-5}	0.97	0.32
363483	Wenu_Pt2000_E_CMS_BFilter	Sherpa	2.83×10^{-5}	0.97	0.18
364172	NNPDF30NNLO_Wenu_MAXHTPTV0_70_BFilter	Sherpa	19 138.00	0.97	0.04
364175	NNPDF30NNLO_Wenu_MAXHTPTV70_140_BFilter	Sherpa	945.57	0.97	0.10
364178	NNPDF30NNLO_Wenu_MAXHTPTV140_280_BFilter	Sherpa	339.70	0.97	0.11
364181	NNPDF30NNLO_Wenu_MAXHTPTV280_500_BFilter	Sherpa	72.09	0.97	0.14
364182	NNPDF30NNLO_Wenu_MAXHTPTV500_1000	Sherpa	15.05	0.97	1.00
364183	NNPDF30NNLO_Wenu_MAXHTPTV1000_E_CMS	Sherpa	1.23	0.97	1.00
364171	NNPDF30NNLO_Wenu_MAXHTPTV0_70_CFilterBVeto	Sherpa	19 145.00	0.97	0.13
364174	NNPDF30NNLO_Wenu_MAXHTPTV70_140_CFilterBVeto	Sherpa	945.74	0.97	0.24
364177	NNPDF30NNLO_Wenu_MAXHTPTV140_280_CFilterBVeto	Sherpa	339.88	0.97	0.29
364180	NNPDF30NNLO_Wenu_MAXHTPTV280_500_CFilterBVeto	Sherpa	72.11	0.97	0.32
364170	NNPDF30NNLO_Wenu_MAXHTPTV0_70_CVetoBVeto	Sherpa	19 153.00	0.97	0.82
364173	NNPDF30NNLO_Wenu_MAXHTPTV70_140_CVetoBVeto	Sherpa	944.98	0.97	0.67
364176	NNPDF30NNLO_Wenu_MAXHTPTV140_280_CVetoBVeto	Sherpa	339.67	0.97	0.60
364179	NNPDF30NNLO_Wenu_MAXHTPTV280_500_CVetoBVeto	Sherpa	72.07	0.97	0.55

Table F.5: List of used $W(e\nu)$+jets samples, their corresponding dataset ID, the used event generator, the production cross-section σ, the k-factor, and the filter efficiency.

ID	Name	Generator	σ[pb]	k-factor	filter eff.
363102	Ztautau_Pt70_140_CVetoBVeto	Sherpa	71.69	0.98	0.67
363103	Ztautau_Pt70_140_CFilterBVeto	Sherpa	71.69	0.98	0.20
363104	Ztautau_Pt70_140_BFilter	Sherpa	71.72	0.98	0.13
363105	Ztautau_Pt140_280_CVetoBVeto	Sherpa	11.03	0.98	0.63
363106	Ztautau_Pt140_280_CFilterBVeto	Sherpa	11.07	0.98	0.22
363107	Ztautau_Pt140_280_BFilter	Sherpa	11.07	0.98	0.15
363108	Ztautau_Pt280_500_CVetoBVeto	Sherpa	0.83	0.98	0.60
363109	Ztautau_Pt280_500_CFilterBVeto	Sherpa	0.83	0.98	0.25
363110	Ztautau_Pt280_500_BFilter	Sherpa	0.83	0.98	0.14
363111	Ztautau_Pt500_700_CVetoBVeto	Sherpa	0.05	0.98	0.59
363112	Ztautau_Pt500_700_CFilterBVeto	Sherpa	0.05	0.98	0.26
363113	Ztautau_Pt500_700_BFilter	Sherpa	0.05	0.98	0.16
363114	Ztautau_Pt700_1000_CVetoBVeto	Sherpa	0.01	0.98	0.58
363115	Ztautau_Pt700_1000_CFilterBVeto	Sherpa	0.01	0.98	0.26
363116	Ztautau_Pt700_1000_BFilter	Sherpa	0.01	0.98	0.16
363117	Ztautau_Pt1000_2000_CVetoBVeto	Sherpa	0.00	0.98	0.57
363118	Ztautau_Pt1000_2000_CFilterBVeto	Sherpa	0.00	0.98	0.27
363119	Ztautau_Pt1000_2000_BFilter	Sherpa	0.00	0.98	0.16
363120	Ztautau_Pt2000_E_CMS_CVetoBVeto	Sherpa	4.75×10^{-6}	0.98	0.57
363121	Ztautau_Pt2000_E_CMS_CFilterBVeto	Sherpa	4.54×10^{-6}	0.98	0.31
363122	Ztautau_Pt2000_E_CMS_BFilter	Sherpa	4.69×10^{-6}	0.98	0.19
363361	Ztautau_Pt0_70_CVetoBVeto	Sherpa	2 076.50	0.98	0.81
363362	Ztautau_Pt0_70_CFilterBVeto	Sherpa	2 078.40	0.98	0.12
363363	Ztautau_Pt0_70_BFilter	Sherpa	2 079.00	0.98	0.07
364130	NNPDF30NNLO_Ztautau_MAXHTPTV0_70_BFilter	Sherpa	1 982.10	0.98	0.07
364133	NNPDF30NNLO_Ztautau_MAXHTPTV70_140_BFilter	Sherpa	110.66	0.98	0.11
364136	NNPDF30NNLO_Ztautau_MAXHTPTV140_280_BFilter	Sherpa	40.74	0.98	0.16
364139	NNPDF30NNLO_Ztautau_MAXHTPTV280_500_BFilter	Sherpa	8.68	0.98	0.18
364140	NNPDF30NNLO_Ztautau_MAXHTPTV500_1000	Sherpa	1.81	0.98	1.00
364141	NNPDF30NNLO_Ztautau_MAXHTPTV1000_E_CMS	Sherpa	0.15	0.98	1.00
364129	NNPDF30NNLO_Ztautau_MAXHTPTV0_70_CFilterBVeto	Sherpa	1 981.70	0.98	0.11
364132	NNPDF30NNLO_Ztautau_MAXHTPTV70_140_CFilterBVeto	Sherpa	110.56	0.98	0.19
364135	NNPDF30NNLO_Ztautau_MAXHTPTV140_280_CFilterBVeto	Sherpa	40.72	0.98	0.23
364138	NNPDF30NNLO_Ztautau_MAXHTPTV280_500_CFilterBVeto	Sherpa	8.68	0.98	0.26
364128	NNPDF30NNLO_Ztautau_MAXHTPTV0_70_CVetoBVeto	Sherpa	1 981.70	0.98	0.83
364131	NNPDF30NNLO_Ztautau_MAXHTPTV70_140_CVetoBVeto	Sherpa	110.61	0.98	0.69
364134	NNPDF30NNLO_Ztautau_MAXHTPTV140_280_CVetoBVeto	Sherpa	40.77	0.98	0.62
364137	NNPDF30NNLO_Ztautau_MAXHTPTV280_500_CVetoBVeto	Sherpa	8.66	0.98	0.56
364210	NN30NNLO_Ztt_Mll10_40_MAXHTPTV0_70_BVeto	Sherpa	2 415.30	0.98	0.97
364211	NN30NNLO_Ztt_Mll10_40_MAXHTPTV0_70_BFilter	Sherpa	2 414.30	0.98	0.03
364212	NN30NNLO_Ztt_Mll10_40_MAXHTPTV70_280_BVeto	Sherpa	50.41	0.98	0.89
364213	NN30NNLO_Ztt_Mll10_40_MAXHTPTV70_280_BFilter	Sherpa	50.47	0.98	0.11
364214	NN30NNLO_Ztt_Mll10_40_MAXHTPTV280_E_CMS_BVeto	Sherpa	3.28	0.98	0.85
364215	NN30NNLO_Ztt_Mll10_40_MAXHTPTV280_E_CMS_BFilter	Sherpa	3.28	0.98	0.16
361510	Ztautau_Np0	MadGraphPythia8	1 398.80	1.23	1.00
361511	Ztautau_Np1	MadGraphPythia8	211.44	1.23	1.00
361512	Ztautau_Np2	MadGraphPythia8	67.20	1.23	1.00
361513	Ztautau_Np3	MadGraphPythia8	18.61	1.23	1.00
361514	Ztautau_Np4	MadGraphPythia8	7.26	1.23	1.00

Table F.6: List of used $Z(\tau\tau)+$jets samples, their corresponding dataset ID, the used event generator, the production cross-section σ, the k-factor, and the filter efficiency.

ID	Name	Generator	σ[pb]	k-factor	filter eff.
363364	Zmumu_Pt0_70_CVetoBVeto	Sherpa	2 077.90	0.98	0.81
363365	Zmumu_Pt0_70_CFilterBVeto	Sherpa	2 077.30	0.98	0.12
363366	Zmumu_Pt0_70_BFilter	Sherpa	2 077.80	0.98	0.07
363367	Zmumu_Pt70_140_CVetoBVeto	Sherpa	71.96	0.98	0.67
363368	Zmumu_Pt70_140_CFilterBVeto	Sherpa	71.58	0.98	0.20
363369	Zmumu_Pt70_140_BFilter	Sherpa	71.63	0.98	0.13
363370	Zmumu_Pt140_280_CVetoBVeto	Sherpa	11.10	0.98	0.63
363371	Zmumu_Pt140_280_CFilterBVeto	Sherpa	11.07	0.98	0.23
363372	Zmumu_Pt140_280_BFilter	Sherpa	11.06	0.98	0.15
363373	Zmumu_Pt280_500_CVetoBVeto	Sherpa	0.83	0.98	0.60
363374	Zmumu_Pt280_500_CFilterBVeto	Sherpa	0.83	0.98	0.24
363375	Zmumu_Pt280_500_BFilter	Sherpa	0.83	0.98	0.16
363376	Zmumu_Pt500_700_CVetoBVeto	Sherpa	0.05	0.98	0.59
363377	Zmumu_Pt500_700_CFilterBVeto	Sherpa	0.05	0.98	0.27
363378	Zmumu_Pt500_700_BFilter	Sherpa	0.05	0.98	0.17
363379	Zmumu_Pt700_1000_CVetoBVeto	Sherpa	0.01	0.98	0.58
363380	Zmumu_Pt700_1000_CFilterBVeto	Sherpa	0.01	0.98	0.26
363381	Zmumu_Pt700_1000_BFilter	Sherpa	0.01	0.98	0.16
363382	Zmumu_Pt1000_2000_CVetoBVeto	Sherpa	0.00	0.98	0.57
363383	Zmumu_Pt1000_2000_CFilterBVeto	Sherpa	0.00	0.98	0.28
363384	Zmumu_Pt1000_2000_BFilter	Sherpa	0.00	0.98	0.16
363385	Zmumu_Pt2000_E_CMS_CVetoBVeto	Sherpa	4.96×10^{-6}	0.98	0.61
363386	Zmumu_Pt2000_E_CMS_CFilterBVeto	Sherpa	5.03×10^{-6}	0.98	0.28
363387	Zmumu_Pt2000_E_CMS_BFilter	Sherpa	4.78×10^{-6}	0.98	0.17
364102	NNPDF30NNLO_Zmumu_MAXHTPTV0_70_BFilter	Sherpa	1 981.50	0.98	0.07
364105	NNPDF30NNLO_Zmumu_MAXHTPTV70_140_BFilter	Sherpa	108.98	0.98	0.12
364108	NNPDF30NNLO_Zmumu_MAXHTPTV140_280_BFilter	Sherpa	39.89	0.98	0.16
364111	NNPDF30NNLO_Zmumu_MAXHTPTV280_500_BFilter	Sherpa	8.53	0.98	0.18
364112	NNPDF30NNLO_Zmumu_MAXHTPTV500_1000	Sherpa	1.79	0.98	1.00
364113	NNPDF30NNLO_Zmumu_MAXHTPTV1000_E_CMS	Sherpa	0.15	0.98	1.00
364101	NNPDF30NNLO_Zmumu_MAXHTPTV0_70_CFilterBVeto	Sherpa	1 982.10	0.98	0.11
364104	NNPDF30NNLO_Zmumu_MAXHTPTV70_140_CFilterBVeto	Sherpa	108.81	0.98	0.20
364107	NNPDF30NNLO_Zmumu_MAXHTPTV140_280_CFilterBVeto	Sherpa	39.86	0.98	0.24
364110	NNPDF30NNLO_Zmumu_MAXHTPTV280_500_CFilterBVeto	Sherpa	8.53	0.98	0.27
364100	NNPDF30NNLO_Zmumu_MAXHTPTV0_70_CVetoBVeto	Sherpa	1 982.40	0.98	0.82
364103	NNPDF30NNLO_Zmumu_MAXHTPTV70_140_CVetoBVeto	Sherpa	109.13	0.98	0.69
364106	NNPDF30NNLO_Zmumu_MAXHTPTV140_280_CVetoBVeto	Sherpa	39.87	0.98	0.60
364109	NNPDF30NNLO_Zmumu_MAXHTPTV280_500_CVetoBVeto	Sherpa	8.53	0.98	0.56
364198	NN30NNLO_Zmm_Mll10_40_MAXHTPTV0_70_BVeto	Sherpa	2 414.30	0.98	0.97
364199	NN30NNLO_Zmm_Mll10_40_MAXHTPTV0_70_BFilter	Sherpa	2 414.40	0.98	0.03
364200	NN30NNLO_Zmm_Mll10_40_MAXHTPTV70_280_BVeto	Sherpa	50.33	0.98	0.89
364201	NN30NNLO_Zmm_Mll10_40_MAXHTPTV70_280_BFilter	Sherpa	50.27	0.98	0.11
364202	NN30NNLO_Zmm_Mll10_40_MAXHTPTV280_E_CMS_BVeto	Sherpa	3.24	0.98	0.85
364203	NN30NNLO_Zmm_Mll10_40_MAXHTPTV280_E_CMS_BFilter	Sherpa	3.28	0.98	0.16

Table F.7: List of used $Z(\mu\mu)$ + jets samples, their corresponding dataset ID, the used event generator, the production cross-section σ, the k-factor, and the filter efficiency.

ID	Name	Generator	σ[pb]	k-factor	filter eff.
363388	Zee_Pt0_70_CVetoBVeto	Sherpa	2 076.40	0.98	0.81
363389	Zee_Pt0_70_CFilterBVeto	Sherpa	2 079.10	0.98	0.12
363390	Zee_Pt0_70_BFilter	Sherpa	2 075.80	0.98	0.07
363391	Zee_Pt70_140_CVetoBVeto	Sherpa	71.68	0.98	0.67
363392	Zee_Pt70_140_CFilterBVeto	Sherpa	71.66	0.98	0.20
363393	Zee_Pt70_140_BFilter	Sherpa	71.74	0.98	0.13
363394	Zee_Pt140_280_CVetoBVeto	Sherpa	11.04	0.98	0.63
363395	Zee_Pt140_280_CFilterBVeto	Sherpa	11.05	0.98	0.23
363396	Zee_Pt140_280_BFilter	Sherpa	11.08	0.98	0.15
363397	Zee_Pt280_500_CVetoBVeto	Sherpa	0.83	0.98	0.60
363398	Zee_Pt280_500_CFilterBVeto	Sherpa	0.83	0.98	0.25
363399	Zee_Pt280_500_BFilter	Sherpa	0.83	0.98	0.16
363400	Zee_Pt500_700_CVetoBVeto	Sherpa	0.05	0.98	0.59
363401	Zee_Pt500_700_CFilterBVeto	Sherpa	0.05	0.98	0.25
363402	Zee_Pt500_700_BFilter	Sherpa	0.05	0.98	0.16
363403	Zee_Pt700_1000_CVetoBVeto	Sherpa	0.01	0.98	0.58
363404	Zee_Pt700_1000_CFilterBVeto	Sherpa	0.01	0.98	0.26
363405	Zee_Pt700_1000_BFilter	Sherpa	0.01	0.98	0.16
363406	Zee_Pt1000_2000_CVetoBVeto	Sherpa	0.00	0.98	0.59
363407	Zee_Pt1000_2000_CFilterBVeto	Sherpa	0.00	0.98	0.27
363408	Zee_Pt1000_2000_BFilter	Sherpa	0.00	0.98	0.16
363409	Zee_Pt2000_E_CMS_CVetoBVeto	Sherpa	4.90×10^{-6}	0.98	0.58
363410	Zee_Pt2000_E_CMS_CFilterBVeto	Sherpa	4.70×10^{-6}	0.98	0.53
363411	Zee_Pt2000_E_CMS_BFilter	Sherpa	4.80×10^{-6}	0.98	0.17
364116	NNPDF30NNLO_Zee_MAXHTPTV0_70_BFilter	Sherpa	1 982.10	0.98	0.07
364119	NNPDF30NNLO_Zee_MAXHTPTV70_140_BFilter	Sherpa	110.50	0.98	0.12
364122	NNPDF30NNLO_Zee_MAXHTPTV140_280_BFilter	Sherpa	40.67	0.98	0.15
364125	NNPDF30NNLO_Zee_MAXHTPTV280_500_BFilter	Sherpa	8.68	0.98	0.18
364126	NNPDF30NNLO_Zee_MAXHTPTV500_1000	Sherpa	1.81	0.98	1.00
364127	NNPDF30NNLO_Zee_MAXHTPTV1000_E_CMS	Sherpa	0.15	0.98	1.00
364115	NNPDF30NNLO_Zee_MAXHTPTV0_70_CFilterBVeto	Sherpa	1 981.50	0.98	0.11
364118	NNPDF30NNLO_Zee_MAXHTPTV70_140_CFilterBVeto	Sherpa	110.50	0.98	0.19
364121	NNPDF30NNLO_Zee_MAXHTPTV140_280_CFilterBVeto	Sherpa	40.67	0.98	0.23
364124	NNPDF30NNLO_Zee_MAXHTPTV280_500_CFilterBVeto	Sherpa	8.67	0.98	0.27
364114	NNPDF30NNLO_Zee_MAXHTPTV0_70_CVetoBVeto	Sherpa	1 981.60	0.98	0.82
364117	NNPDF30NNLO_Zee_MAXHTPTV70_140_CVetoBVeto	Sherpa	110.65	0.98	0.69
364120	NNPDF30NNLO_Zee_MAXHTPTV140_280_CVetoBVeto	Sherpa	40.68	0.98	0.62
364123	NNPDF30NNLO_Zee_MAXHTPTV280_500_CVetoBVeto	Sherpa	8.67	0.98	0.57
364204	NN30NNLO_Zee_Mll10_40_MAXHTPTV0_70_BVeto	Sherpa	2 415.30	0.98	0.97
364205	NN30NNLO_Zee_Mll10_40_MAXHTPTV0_70_BFilter	Sherpa	2 415.50	0.98	0.03
364206	NN30NNLO_Zee_Mll10_40_MAXHTPTV70_280_BVeto	Sherpa	50.33	0.98	0.89
364207	NN30NNLO_Zee_Mll10_40_MAXHTPTV70_280_BFilter	Sherpa	50.48	0.98	0.11
364208	NN30NNLO_Zee_Mll10_40_MAXHTPTV280_E_CMS_BVeto	Sherpa	3.25	0.98	0.85
364209	NN30NNLO_Zee_Mll10_40_MAXHTPTV280_E_CMS_BFilter	Sherpa	3.25	0.98	0.15

Table F.8: List of used $Z(ee)$ + jets samples, their corresponding dataset ID, the used event generator, the production cross-section σ, the k-factor, and the filter efficiency.

ID	Name	Generator	σ[pb]	k-factor	filter eff.
363412	Znunu_Pt0_70_CVetoBVeto	Sherpa	11 224.00	0.97	0.81
363413	Znunu_Pt0_70_CFilterBVeto	Sherpa	11 229.00	0.97	0.12
363414	Znunu_Pt0_70_BFilter	Sherpa	11 228.00	0.97	0.07
363415	Znunu_Pt70_140_CVetoBVeto	Sherpa	403.31	0.97	0.67
363416	Znunu_Pt70_140_CFilterBVeto	Sherpa	403.62	0.97	0.20
363417	Znunu_Pt70_140_BFilter	Sherpa	403.74	0.97	0.13
363418	Znunu_Pt140_280_CVetoBVeto	Sherpa	62.13	0.97	0.63
363419	Znunu_Pt140_280_CFilterBVeto	Sherpa	62.13	0.97	0.22
363420	Znunu_Pt140_280_BFilter	Sherpa	62.24	0.97	0.15
363421	Znunu_Pt280_500_CVetoBVeto	Sherpa	4.63	0.97	0.60
363422	Znunu_Pt280_500_CFilterBVeto	Sherpa	4.62	0.97	0.24
363423	Znunu_Pt280_500_BFilter	Sherpa	4.62	0.97	0.16
363424	Znunu_Pt500_700_CVetoBVeto	Sherpa	0.29	0.97	0.58
363425	Znunu_Pt500_700_CFilterBVeto	Sherpa	0.29	0.97	0.26
363426	Znunu_Pt500_700_BFilter	Sherpa	0.29	0.97	0.16
363427	Znunu_Pt700_1000_CVetoBVeto	Sherpa	0.05	0.97	0.59
363428	Znunu_Pt700_1000_CFilterBVeto	Sherpa	0.05	0.97	0.27
363429	Znunu_Pt700_1000_BFilter	Sherpa	0.05	0.97	0.16
363430	Znunu_Pt1000_2000_CVetoBVeto	Sherpa	0.01	0.97	0.58
363431	Znunu_Pt1000_2000_CFilterBVeto	Sherpa	0.01	0.97	0.27
363432	Znunu_Pt1000_2000_BFilter	Sherpa	0.01	0.97	0.18
363433	Znunu_Pt2000_E_CMS_CVetoBVeto	Sherpa	2.45×10^{-5}	0.97	0.57
363434	Znunu_Pt2000_E_CMS_CFilterBVeto	Sherpa	2.49×10^{-5}	0.97	0.27
363435	Znunu_Pt2000_E_CMS_BFilter	Sherpa	2.44×10^{-5}	0.97	0.54
364144	NNPDF30NNLO_Znunu_MAXHTPTV0_70_BFilter	Sherpa	10 705.00	0.97	0.07
364147	NNPDF30NNLO_Znunu_MAXHTPTV70_140_BFilter	Sherpa	607.97	0.97	0.12
364150	NNPDF30NNLO_Znunu_MAXHTPTV140_280_BFilter	Sherpa	222.38	0.97	0.16
364153	NNPDF30NNLO_Znunu_MAXHTPTV280_500_BFilter	Sherpa	47.42	0.97	0.18
364154	NNPDF30NNLO_Znunu_MAXHTPTV500_1000	Sherpa	9.91	0.97	1.00
364155	NNPDF30NNLO_Znunu_MAXHTPTV1000_E_CMS	Sherpa	0.82	0.97	1.00
364143	NNPDF30NNLO_Znunu_MAXHTPTV0_70_CFilterBVeto	Sherpa	10 705.00	0.97	0.11
364146	NNPDF30NNLO_Znunu_MAXHTPTV70_140_CFilterBVeto	Sherpa	607.59	0.97	0.19
364149	NNPDF30NNLO_Znunu_MAXHTPTV140_280_CFilterBVeto	Sherpa	222.31	0.97	0.23
364152	NNPDF30NNLO_Znunu_MAXHTPTV280_500_CFilterBVeto	Sherpa	47.40	0.97	0.26
364142	NNPDF30NNLO_Znunu_MAXHTPTV0_70_CVetoBVeto	Sherpa	10 706.00	0.97	0.82
364145	NNPDF30NNLO_Znunu_MAXHTPTV70_140_CVetoBVeto	Sherpa	607.65	0.97	0.69
364148	NNPDF30NNLO_Znunu_MAXHTPTV140_280_CVetoBVeto	Sherpa	222.33	0.97	0.62
364151	NNPDF30NNLO_Znunu_MAXHTPTV280_500_CVetoBVeto	Sherpa	47.42	0.97	0.56
361515	Znunu_Np0	MadGraphPythia8	7 521.20	1.23	1.00
361516	Znunu_Np1	MadGraphPythia8	1 199.90	1.23	1.00
361517	Znunu_Np2	MadGraphPythia8	387.10	1.23	1.00
361518	Znunu_Np3	MadGraphPythia8	110.08	1.23	1.00
361519	Znunu_Np4	MadGraphPythia8	43.47	1.23	1.00

Table F.9: List of used $Z(\nu\nu)$ + jets samples, their corresponding dataset ID, the used event generator, the production cross-section σ, the k-factor, and the filter efficiency.

ID	Name	Generator	σ[pb]	k-factor	filter eff.
361069	llvvjj_ss_EW4	Sherpa	0.03	1.00	1.00
361070	llvvjj_ss_EW6	Sherpa	0.04	1.00	1.00
361071	lllvjj_EW6	Sherpa	0.04	1.00	1.00
361072	lllljj_EW6	Sherpa	0.01	1.00	1.00
361073	gglllll	Sherpa	0.02	1.55	1.00
361077	ggllvv	Sherpa	0.85	0.91	1.00
363491	NNPDF30NNLO_llllv	Sherpa	4.59	1.00	1.00
363492	NNPDF30NNLO_llvv	Sherpa	12.47	1.00	1.00
363493	NNPDF30NNLO_lvvv	Sherpa	3.23	1.00	1.00
363494	NNPDF30NNLO_vvvv	Sherpa	0.60	1.00	1.00
363355	NNPDF30NNLO_ZqqZvv	Sherpa	15.56	1.00	0.28
363356	NNPDF30NNLO_ZqqZll	Sherpa	15.56	1.00	0.14
363357	NNPDF30NNLO_WqqZvv	Sherpa	6.80	1.00	1.00
363358	NNPDF30NNLO_WqqZll	Sherpa	3.43	1.00	1.00
363359	NNPDF30NNLO_WpqqWmlv	Sherpa	24.71	1.00	1.00
363360	NNPDF30NNLO_WplvWmqq	Sherpa	24.73	1.00	1.00
363489	NNPDF30NNLO_WlvZqq	Sherpa	11.42	1.00	1.00
364250	NNPDF30NNLO_llll	Sherpa	1.25	1.00	1.00
407311	NNPDF30NNLO_6l0v_EW6	Sherpa	0.00	1.00	1.00
407312	NNPDF30NNLO_5l1v_EW6	Sherpa	0.00	1.00	1.00
407313	NNPDF30NNLO_4l2v_EW6	Sherpa	0.00	1.00	1.00
407314	NNPDF30NNLO_3l3v_EW6	Sherpa	0.02	1.00	1.00

Table F.10: List of used VV samples, their corresponding dataset ID, the used event generator, the production cross-section σ, the k-factor, and the filter efficiency.

ID	$m(\tilde{g})$ [GeV]	$m(\tilde{\chi}_1^0)$ [GeV]	σ[pb]	filtereff.
373200	985	345	0.36	1.00
373201	665	345	4.86	1.00
373202	985	185	0.36	1.00
373203	665	185	4.86	1.00
373204	797	772	1.53	0.46
373205	717	692	3.03	0.45
373206	1865	825	0.00	1.00
373207	1705	825	0.00	1.00
373208	1545	825	0.01	1.00
373209	1385	825	0.03	1.00
373210	1225	825	0.07	1.00
373211	1065	825	0.21	0.79
373212	905	825	0.65	0.49
373213	1945	745	0.00	1.00
373214	1785	745	0.00	1.00
373215	1625	745	0.01	1.00
373216	1465	745	0.02	1.00
373217	1305	745	0.04	1.00
373218	1145	745	0.12	1.00
373219	985	745	0.36	0.79
373220	825	745	1.22	0.49
373221	1865	665	0.00	1.00
373222	1705	665	0.00	1.00
373223	1545	665	0.01	1.00
373224	1385	665	0.03	1.00
373225	1225	665	0.07	1.00
373226	1065	665	0.21	1.00
373227	905	665	0.65	0.79
373228	1945	585	0.00	1.00
373229	1785	585	0.00	1.00
373230	1625	585	0.01	1.00
373231	1465	585	0.02	1.00
373232	1305	585	0.04	1.00
373233	1865	505	0.00	1.00
373234	1705	505	0.00	1.00
373235	1545	505	0.01	1.00
373236	1385	505	0.03	1.00
373237	1945	425	0.00	1.00
373238	1785	425	0.00	1.00
373239	1625	425	0.01	1.00
373240	1465	425	0.02	1.00
373241	1305	425	0.04	1.00
373242	1865	345	0.00	1.00

ID	$m(\tilde{g})$ [GeV]	$m(\tilde{\chi}_1^0)$ [GeV]	σ[pb]	filtereff.
373243	1705	345	0.00	1.00
373244	1545	345	0.01	1.00
373245	1385	345	0.03	1.00
373246	1945	265	0.00	1.00
373247	1785	265	0.00	1.00
373248	1625	265	0.01	1.00
373249	1465	265	0.02	1.00
373250	1865	185	0.00	1.00
373251	1705	185	0.00	1.00
373252	1545	185	0.01	1.00
373253	1385	185	0.03	1.00
373254	1945	105	0.00	1.00
373255	1785	105	0.00	1.00
373256	1625	105	0.01	1.00
373257	1465	105	0.02	1.00
373258	825	105	1.22	1.00
373259	1145	105	0.12	1.00
373260	1305	105	0.04	1.00
373261	825	265	1.22	1.00
373262	1145	265	0.12	1.00
373263	1305	265	0.04	1.00
373264	825	425	1.22	1.00
373265	1145	425	0.12	1.00
373266	905	505	0.65	1.00
373267	1065	505	0.21	1.00
373268	1225	505	0.07	1.00
373269	985	585	0.36	1.00
373270	1145	585	0.12	1.00
373271	505	105	25.90	1.00
373272	505	265	25.90	0.75
373273	505	425	25.90	0.42
373274	585	505	10.75	0.44
373275	745	505	2.37	0.78
373276	665	585	4.86	0.46
373277	825	585	1.22	0.78
373278	745	665	2.37	0.47
373279	477	452	36.07	0.38
373280	557	532	14.50	0.41
373281	637	612	6.36	0.43
373282	1117	1092	0.15	0.50
373283	1037	1012	0.25	0.49
373284	957	932	0.44	0.48
373285	877	852	0.81	0.47

Table F.11: List of used simplified model signal samples, their corresponding dataset ID, the production cross-section σ, and the filter efficiency. The k-factor for all signal samples is 1.0.

ID	$m(\tilde{g})$ [GeV]	$m(\tilde{\chi}_1^0)$ [GeV]	σ[pb]	filtereff.
373286	1945	1065	0.00	1.00
373287	1785	1065	0.00	1.00
373288	1625	1065	0.01	1.00
373289	1465	1065	0.02	1.00
373290	1305	1065	0.04	0.79
373291	1145	1065	0.12	0.51
373292	1865	985	0.00	1.00
373293	1705	985	0.00	1.00
373294	1545	985	0.01	1.00
373295	1385	985	0.03	1.00
373296	1225	985	0.07	0.78
373297	1065	985	0.21	0.50
373298	1945	905	0.00	1.00
373299	1785	905	0.00	1.00
373400	1625	905	0.01	1.00
373401	1465	905	0.02	1.00
373402	1305	905	0.04	1.00
373403	1145	905	0.12	0.79
373404	985	905	0.36	0.50
393951	1277	1252	0.05	0.50
393952	1197	1172	0.09	0.50
393953	2345	1305	0.00	1.00
393954	2185	1305	0.00	1.00
393955	2025	1305	0.00	1.00
393956	1865	1305	0.00	1.00
393957	1705	1305	0.00	1.00
393958	1545	1305	0.01	0.79
393959	1385	1305	0.03	0.51
393960	2425	1225	0.00	1.00
393961	2265	1225	0.00	1.00
393962	2105	1225	0.00	1.00
393963	1945	1225	0.00	1.00
393964	1785	1225	0.00	1.00
393965	1625	1225	0.01	1.00
393966	1465	1225	0.02	0.78
393967	1305	1225	0.04	0.51
393968	2345	1145	0.00	1.00
393969	2185	1145	0.00	1.00
393970	2025	1145	0.00	1.00
393971	1865	1145	0.00	1.00
393972	1705	1145	0.00	1.00
393973	1545	1145	0.01	1.00
393974	1385	1145	0.03	0.79
393975	1225	1145	0.07	0.51
393976	2425	1065	0.00	1.00
393977	2265	1065	0.00	1.00
393978	2105	1065	0.00	1.00
393979	2345	985	0.00	1.00
393980	2185	985	0.00	1.00
393981	2025	985	0.00	1.00
393982	2425	905	0.00	1.00
393983	2265	905	0.00	1.00
393984	2105	905	0.00	1.00
393985	2345	825	0.00	1.00
393986	2185	825	0.00	1.00
393987	2025	825	0.00	1.00
393988	2425	745	0.00	1.00
393989	2265	745	0.00	1.00
393990	2105	745	0.00	1.00
393991	2345	665	0.00	1.00
393992	2185	665	0.00	1.00
393993	2025	665	0.00	1.00
393994	2425	585	0.00	1.00
393995	2265	585	0.00	1.00
393996	2105	585	0.00	1.00
393997	2345	505	0.00	1.00
393998	2185	505	0.00	1.00
393999	2025	505	0.00	1.00
394000	2425	425	0.00	1.00
394001	2265	425	0.00	1.00
394002	2105	425	0.00	1.00
394003	2345	345	0.00	1.00
394004	2185	345	0.00	1.00
394005	2025	345	0.00	1.00
394006	2425	265	0.00	1.00
394007	2265	265	0.00	1.00
394008	2105	265	0.00	1.00
394009	2345	185	0.00	1.00
394010	2185	185	0.00	1.00
394011	2025	185	0.00	1.00
394012	2425	105	0.00	1.00
394013	2265	105	0.00	1.00
394014	2105	105	0.00	1.00

Table F.12: List of used simplified model signal samples, their corresponding dataset ID, the production cross-section σ, and the filter efficiency. The k-factor for all signal samples is 1.0.

ID	Λ [TeV]	$\tan\beta$	σ[pb]
372820	70	5	0.20
372821	70	15	0.20
372822	70	40	0.21
372823	80	5	0.09
372824	80	15	0.09
372825	80	40	0.10
372826	90	2	0.04
372827	90	5	0.04
372828	90	10	0.05
372829	90	15	0.05
372830	90	20	0.05
372831	90	30	0.05
372832	90	40	0.05
372833	90	50	0.05
372834	90	60	0.06
372835	100	2	0.02
372836	100	5	0.02
372837	100	10	0.03
372838	100	15	0.03
372839	100	20	0.03
372840	100	30	0.03
372841	100	40	0.03
372842	100	50	0.03
372843	100	60	0.03
372844	110	2	0.01
372845	110	5	0.01
372846	110	10	0.01
372847	110	15	0.01
372848	110	20	0.02
372849	110	30	0.02
372850	110	40	0.02
372851	110	50	0.02
372852	110	60	0.02
372853	120	2	0.01
372854	120	5	0.01
372855	120	10	0.01

ID	*Lambda* [TeV]	$\tan\beta$	σ[pb]
372856	120	15	0.01
372857	120	20	0.01
372858	120	30	0.01
372859	120	40	0.01
372860	120	50	0.01
372861	120	60	0.01
372862	70	2	0.18
372863	70	57	0.24
372864	130	2	0.00
372865	130	5	0.01
372866	130	10	0.01
372867	130	15	0.01
372868	130	20	0.01
372869	130	30	0.01
372870	130	40	0.01
372871	130	50	0.01
372872	130	60	0.01
372873	140	2	0.00
372874	140	5	0.00
372875	140	10	0.00
372876	140	15	0.00
372877	140	20	0.00
372878	140	30	0.00
372879	140	40	0.00
372880	140	50	0.00
372881	140	60	0.01
372882	150	2	0.00
372883	150	5	0.00
372884	150	10	0.00
372885	150	15	0.00
372886	150	20	0.00
372887	150	30	0.00
372888	150	40	0.00
372889	150	50	0.00
372890	150	60	0.00

Table F.13: List of used GMSB model signal samples, their corresponding dataset ID, the production cross-section σ, and the filter efficiency. The k-factor and the filter efficiency are 1.0 for all signal samples.

APPENDIX G

Fitting procedure

The evaluation of the results of a search for new physics beyond the Standard Model requires certain statistical tools that are introduced here. Furthermore, the different approaches of interpretation of analysis results and the underlying procedures are outlined and discussed. The notation used in this chapter is adopted from [240].

G.1 The profile likelihood method

One method to claim the discovery of a model or to exclude it to a certain degree is based on a frequentist significance test [99]. It utilises a ratio of likelihoods as a test statistic as suggested by the Neyman-Pearson lemma [241]. In general, the signal and background models used in this test are described by parameters such as the model cross-sections and additional nuisance parameters (NPs). While the former are a priori known, for example given by the used physics generator, the latter have to be determined by a fit to data. In order for this approach to work, the model is assumed to be sufficiently flexibel such that for a particular set of parameters it can be regarded as true. Additional systematic uncertainties can be taken into account by introducing additional nuisance parameters to the fit.

As a starting point, the measurement of an observable x is considered. For each event, the result of the measurement is written into a histogram $\boldsymbol{n} = (n_1, n_2, \ldots, n_N)$ with N bins. The expectation value for the i-th bin of $\boldsymbol{n}$ can be written as

$$E[n_i] = \mu s_i + b_i \,, \tag{G.1}$$

$$s_i = s_{\text{tot.}} \int_{\text{bin}_i} f_s(x;\theta_s)\mathrm{d}x \,, \tag{G.2}$$

$$b_i = b_{\text{tot.}} \int_{\text{bin}_i} f_b(x;\theta_b)\mathrm{d}x \,. \tag{G.3}$$

Here, s_i (b_i) denote the mean number of entries in the i-th bin of the predicted signal (background), while μ represents the signal strength. Hence $\mu = 0$ corresponds to the background-only hypothesis with no signal present while $\mu = 1$ marks the nominal signal contribution as it is predicted. The individual signal and background contributions to each bin are, in turn, related to the total amount of signal ($s_{\text{tot.}}$) and background ($b_{\text{tot.}}$). The probability for an event to end up in a particular bin i when measuring the observable x is given by the probability density functions (PDF) $f_s(x;\theta_s)$ and $f_b(x;\theta_b)$.

They are specific to each observable and depend on the nuisance parameters θ that describe the different predictions. While $s_{\text{tot.}}$ is fixed to the value predicted by the nominal signal model, b_{tot} is a nuisance parameter itself that can be merged into one variable denoting a vector of all nuisance parameters $\boldsymbol{\theta} = (\theta_s, \theta_b, b_{\text{tot.}})$. The fact that $b_{\text{tot.}}$ is obtained in the fit is reflected in the floating background normalisation that is already introduced in sections 5.3 and 6.3. For the fit to describe the observed data properly, it is necessary to constrain the set of nuisance parameters as well as possible. One way of obtaining such constraints is to perform additional measurements, aside from the one of x. As an example of such measurements, signal-free control regions that are mutually exclusive with respect to the region in which x is measured (here, an SR), can be used. Similar to eq. (G.1), a histogram of an observable measured in a CR $\boldsymbol{m} = (m_1, m_2, \ldots, m_M)$ can be described by the expectation value of its bins

$$E[m_i] = u_i(\boldsymbol{\theta}) \tag{G.4}$$

with u_i denoting a calculable quantity depending on the set of nuisance parameters $\boldsymbol{\theta}$. In the presented analysis, u_i corresponds to the total background in each CR, constraining hence $b_{\text{tot.}}$ in the SR. In principle also possible is the construction of such measurements to constrain shape parameters of the signal and background predictions in observables of interest.

$$\mathcal{L}(\mu, \boldsymbol{\theta}) = \underbrace{\prod_{j=1}^{N} \frac{(\mu s_j + b_j)^{n_j}}{n_j!} e^{-(\mu s_j + b_j)}}_{\text{Poissonian for each bin of } \boldsymbol{n}} \times \underbrace{\prod_{k=1}^{M} \frac{u_k^{m_k}}{m_k!} e^{-u_k}}_{\text{Poissonian for each bin of } \boldsymbol{m}} \times \underbrace{\frac{1}{\sqrt{2\pi\sigma_\theta^2}} e^{-\frac{(\theta-\mu_\theta)^2}{2\sigma_\theta^2}}}_{\text{Gaussian for an example NP } \theta} \tag{G.5}$$

The likelihood $\mathcal{L}(\mu, \boldsymbol{\theta})$ for a measurement carried out that way can then look like eq. (G.5). The first term is a Poissonian distribution taking into account the bin-by-bin statistics of the studied observable x in the SR of interest. This term is unique for every measurement. In the presented analysis, it would be single Poissonian contributions for the normalisation fit SRs of both signal channels (i.e. $N = 1$) and the product of the seven bin contributions for the Multibin SR of the 2τ channel (i.e. $N = 7$). The second contribution is a bin-by-bin Poissonian distribution of the constraining measurement in an example CR. In principle there can be multiple CR measurements and corresponding contributions to the likelihood. Here, nine single contributions would account for the nine CRs of the analysis in which the background normalisation is fitted (i.e. nine contributions with each $M = 1$). The last term in eq. (G.5) represents the contribution from an example systematic uncertainty. For each of them, a designated nuisance parameter θ is introduced. This NP is constrained by external measurements, reflected in a constrain function such as a Gaussian. An example of such a contribution is the Jet Energy Resolution (JER) uncertainty in the presented analysis. Measurements of the performance of the ATLAS detector determine its spread σ_θ around a mean value μ_θ and find its Gaussian distributed. For all systematic uncertainties considered, such contributions are present in the likelihood. For several, external measurements can provide the required constraints, for others, it is given by theory or has to be estimated individually. In most cases, Gaussian constrain functions are appropriate. However, certain systematic uncertainties may require the usage of different functions, such as a log-normal distribution. The latter can, for example, occur when the possibility of a negative value of θ should be excluded by design.

By maximising this likelihood, the optimal set of parameters μ and $\boldsymbol{\theta}$ can be found, corresponding to a simultaneous fit of all involved parameters.

In order to test a hypothesised value of μ, the frequentist approach of hypothesis testing is pursued. This technique follows the frequentist paradigm of approaching the truth by performing as many repetitions of the measurement as possible. Since the measurement itself—in this case a huge number of experiments, i.e. recorded particle collisions—is not repeatable, so-called *toy experiments* are carried out.

The repetition of analysing a similar set of recorded data is emulated by substituting the measured data in the hypothesis to be tested with a number of events randomly drawn from the pool of possible predictions of the signal and background models. This pool is limited by the fluctuations introduced by the uncertainties of the various NPs considered.

For every toy experiment and the observed data, the aforementioned likelihood ratio $\lambda(\mu)$ is calculated as

$$\lambda(\mu) = \frac{\mathcal{L}(\mu, \hat{\hat{\boldsymbol{\theta}}}|d)}{\mathcal{L}(\hat{\mu}, \hat{\boldsymbol{\theta}}|d)} \,. \tag{G.6}$$

The likelihood in the numerator is maximised for $\boldsymbol{\theta} = \hat{\hat{\boldsymbol{\theta}}}$, testing the hypothesised value of μ given the data d. In a computational implementation, μ is fixed to the desired valued. While d is either given by the observation or randomly generated in the case of a toy experiment, $\boldsymbol{\theta}$ is varied systematically until the maximum of the likelihood is found at the value
hathat$\boldsymbol{\theta}$. The numerator hence represents the best representation of the tested hypothesis given the data. The denominator is given by the maximum of the unconditional likelihood. Here, the parameters μ and $\boldsymbol{\theta}$ are both varied given the data d until the likelihood value is maximal at the values $\hat{\mu}$ and $\hat{\boldsymbol{\theta}}$. The data against which the prediction is optimised is again given either by the observation or the randomly generated for one of the toy experiments. The denominator hence represents the best matching unconditional hypothesis given the data.

For the ratio $\lambda(\mu)$, the condition $0 \leq \lambda \leq 1$ holds, rendering higher values of lambda an indicator for good agreement of data and the hypothesised value of μ. As a consequence of this behaviour, a test statistic as the basis of frequentist test can be defined via eq. (G.7). Higher values of t_μ then correspond to worse agreement between the two hypotheses.

$$t_\mu = -2 \ln \lambda(\mu) \tag{G.7}$$

The *profile* characteristics of this approach stems from the fact that the distribution of the ratio of likelihoods or the difference of their logarithms—referred to as Δ(NLL)—can be used to directly extract the standard deviation of the estimated parameter of interest. An example distribution of such a likelihood profile is depicted in fig. G.1.

The resulting values of -2Δ(NLL) for testing the hypothesis of the combined model of $(\mu s + b)$ against the nominal combined model of $(s + b)$ are plotted against the hypothesised value of μ. In a well-working fit environment, the expected shape of the distribution is a symmetric parabola with its minimum being the best-fitting value of μ giving $-2\Delta(\text{NLL}) = 0$. Deviations of the shape of the parabola such as asymmetries or offsets of the minimum can point towards problems in the fitting procedure or underlying models. From the profile of the curve, the $\pm 1\sigma$ ($\pm 2\sigma$) variations of the parameter of interest can be directly extracted as the intersections with $-2\Delta(\text{NLL}) = 1$ ($-2\Delta(\text{NLL}) = 4$), giving rise to the nomenclature of the approach. In an analogue way, the behaviour and uncertainty of the NPs of systematic uncertainties can be studied. For the simple example, the outcome is as expected by the design: a parabola-shaped profile is visible, exhibiting a minimum at $\mu = 1$ with $-2\Delta(\text{NLL})(\mu = 1) = 0$.

A quantification of the disagreement between two hypotheses tested against each other can be obtained by means of a so-called p-value as defined in eq. (G.8).

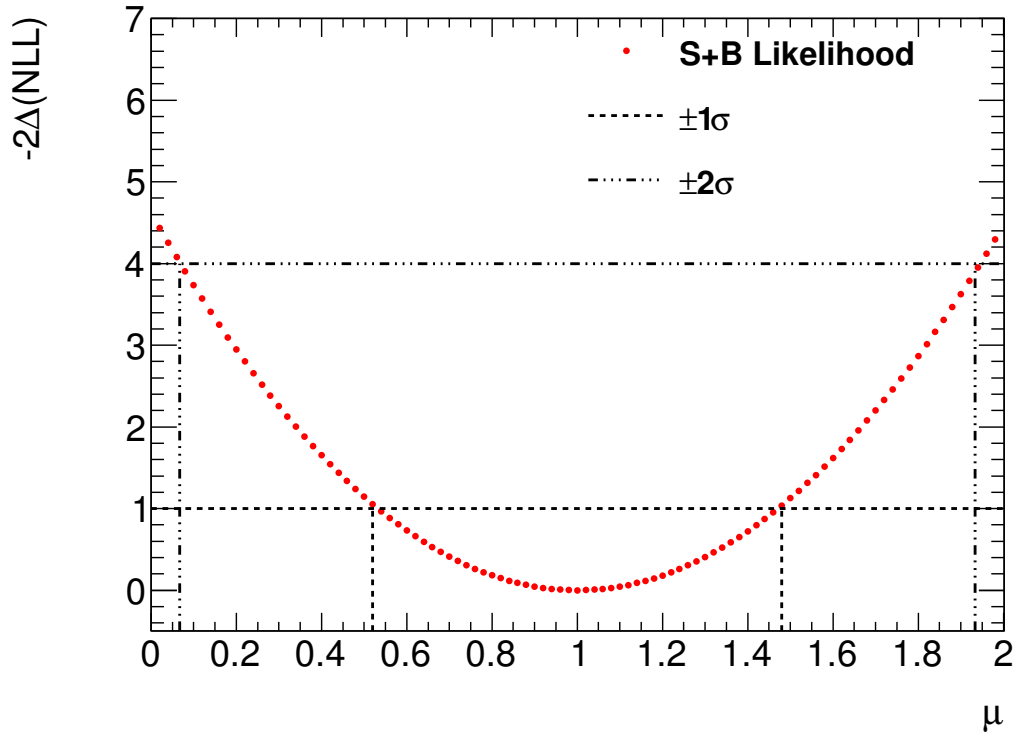

Figure G.1: Example illustration of the likelihood profile of a simple exclusion fit. In a single-bin fit with 100 background and 50 signal events, the expected combined signal and background model is considered to be the nominal one. For different tested values of the signal strength parameter μ the value of the difference between the two logarithmic likelihoods $-2\Delta(\mathrm{NLL})$ is displayed. The μ-values of the resulting profile at $-2\Delta(\mathrm{NLL}) = 1$ ($-2\Delta(\mathrm{NLL}) = 4$) give the $\pm1\sigma$ ($\pm2\sigma$) variations of the best estimated value of μ being the global minimum.

$$p_\mu = \int_{t_{\mu,\mathrm{obs.}}}^{\infty} f(t_\mu|\mu)\mathrm{d}t_\mu \tag{G.8}$$

In this notation, $t_{\mu,\mathrm{obs.}}$ is the value of the test statistic observed in data or the median of the corresponding toy experiment distribution of the test statistic (referred to as $t_{\mu,\mathrm{exp.}}$). In the latter case, the median is the best justified estimator due to the absence of any knowledge constraining the hypothesis tested against further – predicting more or fewer events is hence equally probable. When the p-value is calculated using $t_{\mu,\mathrm{obs.}}$ arising from the actual observed data, the derived quantities are referred to as being *observed*. When the median of a toy experiment-based test statistic is used, the affix *expected* is used since the underlying pseudo-data arises from smearing of the predicted outcome and is not related to the actual observation. $f(t_\mu|\mu)$ denotes the PDF of t_μ under the assumption of the tested signal strength value μ. This context is visualised in fig. G.2(a). By comparison to a standard normal distribution, any p-value can be translated into the significance of the hypothesis test Z as illustrated in fig. G.2(b), typically given in multiples of the standard deviation. Since regardless of the way of interpreting the obtained results, any signal hypothesis is only considered to contribute with an overall non-negative event yield (i.e. $\mu \geq 0$), every hypothesis test performed in this analysis is one-sided. As a consequence, the p-value and its derivations stem from one-sided distributions.

A common criterion to decide to reject a tested hypothesis is an obtained p-value of $p < 0.05$. This

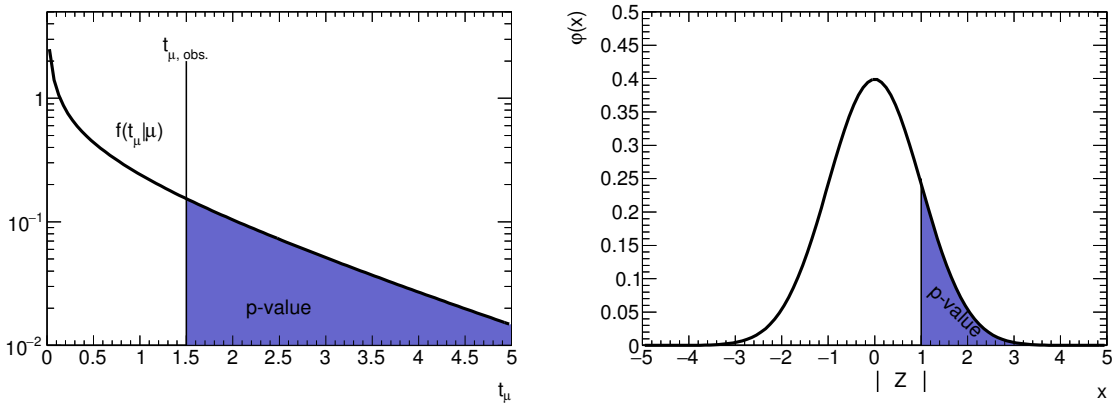

(a) p-value extraction from example test statistic

(b) significance extraction from p-value

Figure G.2: Graphical illustration of properties of the p-value. (a) depicts how the p-value is obtained from a performed hypothesis test given the observed value of the test statistic $t_{\mu,\text{obs.}}$ and the PDF of the test statistic of the tested hypothesis $f(t_\mu|\mu)$ according to eq. (G.8). (b) illustrates the relation between the p-value and the significance Z via its fraction of the integral of a standard normal distribution $\varphi(x)$. For the interpretations performed out in this analysis, only one-sided hypothesis tests are carried out.

boundary corresponds to a probability of less than 5% to observe data that describes the tested hypothesis properly or worse. Such an exclusion is typically referred to as being at a so-called *confidence level* (CL) of 95%.

G.2 The discovery fit

When searching for new physics beyond the Standard Model, the ultimate goal is to claim the discovery of a new model. In order to do so with adequate confidence, the probability of having accidentally observed anything but the desired model needs to be sufficiently small. As introduced in appendix G.1 and visualised in fig. G.2, the p-value is a measure of confidence that comes with the pursued profile likelihood approach. The translation of the p-value into multiples of the standard deviation of a standard normal distribution gives the typical measure of discovery significance, e.g. $Z \geq 5\sigma$ corresponding to an approximate probability of a false-positive result of $1/3,500,000$. Following this procedure, any model can be tested for its compatibility with measured data and its probability to exist can be quantified by means of a discovery significance.

Using the afore introduced method of a profile likelihood, the discovery significance of a proposed signal model can be determined by what is referred to as a discovery fit. In such a setup the probability of the hypothesis of only the background describing the data being true is evaluated. This is achieved by comparing the background-only hypotheses given the two cases of only the background and the combination of signal and background describing the observed data.

As a first step, the test statistic distribution for the background-only hypothesis describing background-like pseudo-data is calculated based on the likelihood ratio given in eq. (G.9). For sake of comprehension in this illustrative description, a simple model is assumed. The total number of background and signal events, $b_{\text{tot.}}$ and $s_{\text{tot.}}$, is set to large enough values to provide results convenient for interpretation, while the only systematic uncertainty considered is a normal-distributed NP with a width of 20%. No CRs to constrain the background are taken into account. If not given explicitly, no binning of the SR is considered but only the total event yields are fitted and evaluated.

$$\lambda(\mu = 0) = \frac{\mathcal{L}(\mu = 0, \hat{\hat{\boldsymbol{\theta}}} | d = b)}{\mathcal{L}(\hat{\mu}, \hat{\boldsymbol{\theta}} | d = b)} \tag{G.9}$$

$$\lambda(\mu = 0, d = d(\mu_{\text{test}})) = \frac{\mathcal{L}(\mu = 0, \hat{\hat{\boldsymbol{\theta}}} | d = \mu_{\text{test}} \cdot s + b)}{\mathcal{L}(\hat{\mu}, \hat{\boldsymbol{\theta}} | d = \mu_{\text{test}} \cdot s + b)} \tag{G.10}$$

The following steps are repeated for every toy experiment:

1. From the Gaussian distribution constraining the NP that is assigned to the background ($\mu_{\text{Gauss,NP}} = 1.0$, $\sigma_{\text{Gauss,NP}} = 0.2$) a value of the NP θ is drawn.

2. The value of the expected data is calculated by drawing a random value from a Poissonian distribution with the smeared pseudo-data being the expectation value:

$$P(d_{\text{toy}} | d = s + \theta \cdot b_{\text{tot.}}) = \frac{(\theta \cdot b_{\text{tot.}})^{d_{\text{toy}}}}{d_{\text{toy}}!} e^{-(\theta \cdot b_{\text{tot.}})}. \tag{G.11}$$

   This point represents the repetition of the actual measurement within its statistical and systematic uncertainties under the assumption, the observed data is described by the background-only model.

3. The conditional likelihood $\mathcal{L}(\mu = 0, \hat{\hat{\boldsymbol{\theta}}} | d = \theta \cdot b_{\text{tot.}})$ and the unconditional likelihood $\mathcal{L}(\hat{\mu}, \hat{\boldsymbol{\theta}} | d = \theta \cdot b_{\text{tot.}})$, based on the **same** pseudo-data d, are separately maximised. As mentioned afore, the resulting ratio $\lambda(\mu = 0)$ gives an estimate of how likely the background-only hypothesis describes the pseudo-data.

4. The value of the test statistic $t_{\mu=0}$ is calculated. The fact that no negative overall signal contributions are allowed is a characteristic of the interpretations in this analysis and is reflected in this calculation by capping the test statistic to zero for negative values of $\hat{\mu}$:

$$t_{\mu=0} = \begin{cases} -2 \ln \lambda(\mu = 0), & \hat{\mu} \geq 0, \\ 0, & \hat{\mu} < 0. \end{cases} \tag{G.12}$$

   Example distributions of $t_{\mu=0}$ for different scenarios are depicted in fig. G.3.

Repeating steps 1-4 with $d = \mu_{\text{test}} \cdot s + b$ (cf. eq. (G.10)) gives the corresponding distribution of the test statistic arising from a test of the background-only hypothesis describing the combined signal and background model[1]. Again, example distributions are depicted in fig. G.3.

The median value of the resulting distribution of $t_{\mu=0}$ is calculated, providing $t_{\mu,\text{exp.}}$. When calculating *observed* quantities, no toy experiments are needed for the test of the combined signal and background model. Since in a discovery fit, the observed data is considered to arise from said combined model, it is sufficient to calculate the one value of $t_{\mu=0} = t_{\mu,\text{obs.}}$ that stems from the likelihoods where d is the actually observed data.

By integrating over the normalised test statistic distribution of the background-only case from $t_{\mu=0} = t_{\mu,\text{exp.}}$ onwards, the p-value $p_0^{\text{exp.}}$ is obtained. The confidence level of the background-only hypothesis CL_B, in turn, is related to it via $p_0^{\text{exp.}} = 1 - \text{CL}_\text{B}^{\text{exp.}}$. The values of the corresponding observed quantities are obtained in the same way.

[1] The signal is expected to be accessible already at its nominal cross-section, setting $\mu_{\text{test}} = 1$ without loss of generality.

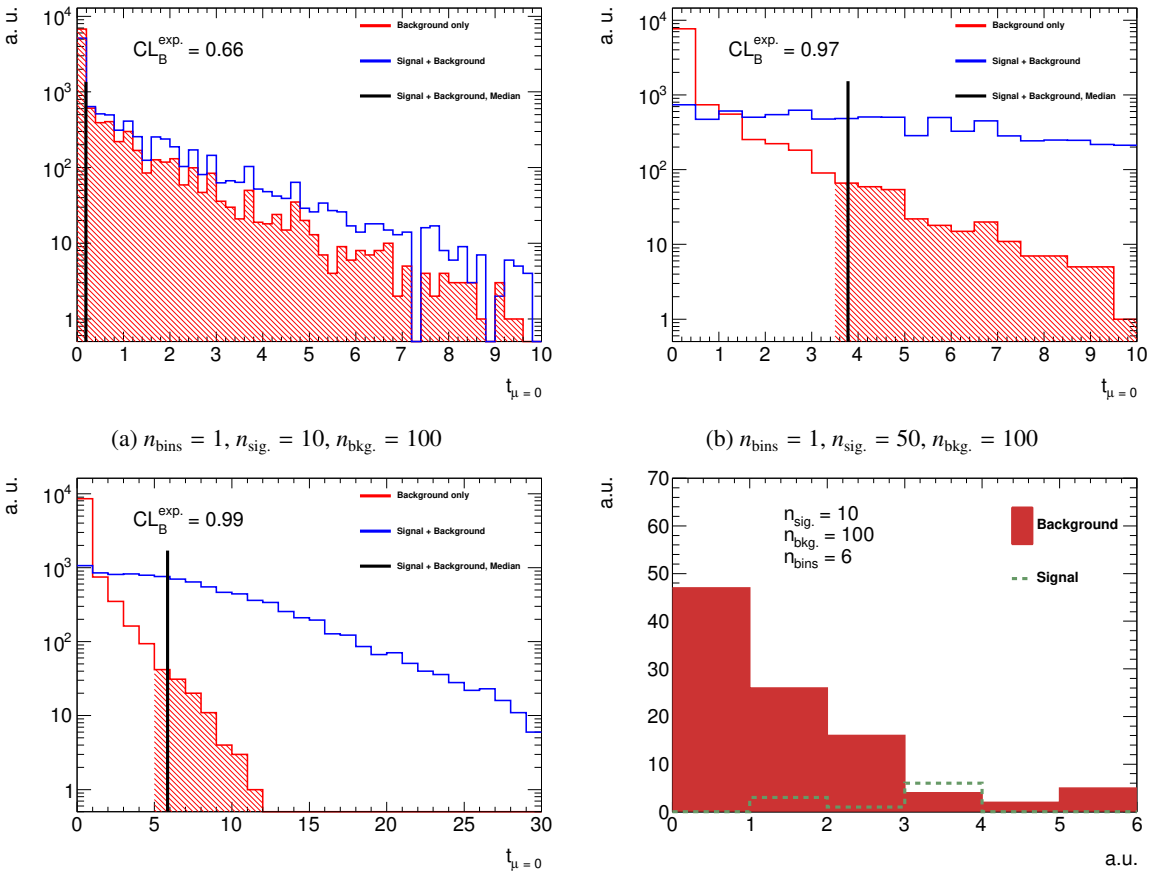

(a) $n_{\text{bins}} = 1$, $n_{\text{sig.}} = 10$, $n_{\text{bkg.}} = 100$

(b) $n_{\text{bins}} = 1$, $n_{\text{sig.}} = 50$, $n_{\text{bkg.}} = 100$

(c) $n_{\text{bins}} = 6$, $n_{\text{sig.}} = 10$, $n_{\text{bkg.}} = 100$

(d) Signal and Background distribution

Figure G.3: Illustration of a discovery fit. Figures (a) to (c) show the test statistic distributions obtained for different configurations, each time using 10,000 toy experiments. The blue histogram represents the combined hypothesis of signal and background, the red histogram the background-only hypothesis. The red hatched area shows the integral of the background-only test statistic distribution beyond the median of the combined signal and background test statistic marked as the black line. The integral extending below the median line is due to the finite binning and not part of the calculation of the given value of $CL_B^{exp.}$. Figure (d) shows the underlying model of signal and background for the case of a fit with multiple bins such as (c).

Figure G.3 illustrates the expected behaviour of different models of signal and background. In the case of a fit in a single bin (i.e. a normalisation-fit) where ten signal events are to be studied for a discovery over 100 background events, the expected outcome of $\mathrm{CL}_\mathrm{B}^{\mathrm{exp.}} = 66\%$ is found (cf. fig. G.3(a)). The ten signal events correspond to the statistical uncertainty of the 100 background events, hence (in a one-sided hypothesis test) the background-only hypothesis is expected to be one standard-deviation away from full confidence. This simplest of examples thus serves as a successful sanity-check of the approach. Increasing the number of signal events to 50 increases the confidence in the background-only hypothesis as expected: it is less likely for the background to fluctuate up by 50% to be in agreement with the combined hypothesis of signal and background (cf. fig. G.3(b)). Finally the case of using a binned distribution to perform the fit in is studied (i.e. a multi-bin fit). Given the different shapes in distributions of an arbitrary observable, signal and background are separable from each other (cf. fig. G.3(d)). The increased discrimination power is expressed in a higher value of $\mathrm{CL}_\mathrm{B}^{\mathrm{exp.}}$ for this fit setup with respect to the single-bin approach and the same underlying signal and background statistics. It is less likely for multiple bins of the background distribution to fluctuate upwards and mimic the combined signal and background model.

This increased sensitivity to the separation of signal from background in a quantitative approach such as the presented profile likelihood ratio test is one of the most striking arguments to pursue analyses in more than one bin, fostering the point of the multi-bin approach developed and studied in this analysis.

G.3 The exclusion fit

In the case of not being able to claim the discovery of a new model, it is possible to quantify to which degree it can be excluded. The underlying approach of the exclusion fit is similar to the the procedure of the discovery fit, testing not the background-only hypothesis but the hypothesis of the combined model of signal and background. A hypothesised value $\mu = \mu_{\mathrm{test}}$ is now tested, modifying eqs. (G.9) and (G.10) to eqs. (G.13) and (G.14).

$$\lambda(\mu = \mu_{\mathrm{test}}) = \frac{\mathcal{L}(\mu = \mu_{\mathrm{test}}, \hat{\hat{\boldsymbol{\theta}}} | d = b)}{\mathcal{L}(\hat{\mu}, \hat{\boldsymbol{\theta}} | d = b)} \tag{G.13}$$

$$\lambda(\mu = \mu_{\mathrm{test}}, d = d(\mu_{\mathrm{test}})) = \frac{\mathcal{L}(\mu = \mu_{\mathrm{test}}, \hat{\hat{\boldsymbol{\theta}}} | d = \mu_{\mathrm{test}} \cdot s + b)}{\mathcal{L}(\hat{\mu}, \hat{\boldsymbol{\theta}} | d = \mu_{\mathrm{test}} \cdot s + b)} \tag{G.14}$$

$$t_{\mu=\mu_{\mathrm{test}}} = \begin{cases} -2 \ln \lambda(\mu = 0), & \hat{\mu} < 0, \\ -2 \ln \lambda(\mu = \mu_{\mathrm{test}}), & 0 \leq \hat{\mu} \leq \mu_{\mathrm{test}}, \\ 0, & \hat{\mu} > \mu_{\mathrm{test}} \end{cases} \tag{G.15}$$

The test statistic distributions are obtained accordingly, summarised in eq. (G.15), resulting in an inverted picture for the tested background-only and combined signal and background hypotheses as illustrated in fig. G.4. In contrast to the background-only fit, the test statistic is modified to protect against two effects: if an the background prediction is overestimated, the unconditional estimator of the signal strength would become negative. For such cases, the value of the test statistic arising from the corresponding background-only fit is considered. In the case of the signal model predicting too few events, it is not desired to exclude the model – only models with a prediction too strong to be compatible with the observation (expectation) are to be excluded. By means of integrating the the normalised test statistic distribution of the combined signal and background model from the median of the background-only distribution $t_{\mu_{\mathrm{test}}}^{\mathrm{exp.}}$, the exclusion p-value is obtained. It is equal to the confidence

level of the tested hypothesis: $p^{\text{exp.}}_{\mu_{\text{test}}} = \text{CL}^{\text{exp.}}_{\text{S+B}}$. Similarly, $p^{\text{obs.}}_{\mu_{\text{test}}} = \text{CL}^{\text{obs.}}_{\text{S+B}}$ is calculated using the value of the test statistic using the actually observed data.

By means of this procedure, it is possible to exclude the combined hypothesis of signal and background as indicated by the subscript of $\text{CL}_{\text{S+B}}$. In principle more desired is information on the signal model as a stand-alone hypothesis on its own. Such information becomes accessible when using the CL_{S}-technique as explained in detail in [232]. As a result, a measure for the confidence in the signal hypothesis is obtained in the form of eq. (G.16).

$$\text{CL}_{\text{S}} = \frac{\text{CL}_{\text{S+B}}}{\text{CL}_{\text{B}}} \tag{G.16}$$

The used value of CL_{B} is either calculated from the actual test statistic value of the observed data (*observed* case, cf. appendix G.2) or $\text{CL}^{\text{exp.}}_{\text{B}} = 0.5$. The latter equality originates from the fact that test statistic distributions for the background-only and the combined signal and background hypotheses are the same for $\mu = \mu_{\text{test}}$ as can be inferred from eqs. (G.13) and (G.14).

Results of exclusion fits for different scenarios are depicted in fig. G.4. Similar as for the single-bin case of the discovery fit with 100 background and ten signal events relativ to the case of 50 signal events, the confidence in the tested hypothesis changes as expected: When more signal events are tested against the same amount of background, the confidence in the signal hypothesis decreases. The absence of more signal is easier to claim than the absence of signal that is with the background uncertainty. Adding more information to the fit by performing it again in bins of a discriminating distribution (cf. fig. G.3(d)), even the weaker of the two signal scenarios can be excluded ($\text{CL}^{\text{exp.}}_{\text{S}} < 0.05$). This point strengthens the motivation for using multi-bin fits when performing analyses searching for a rare signal once more.

With CL_{S} introduced as the desired measure of confidence, it is possible to not only test and possibly exclude nominal signal hypotheses, but to estimate values of $\mu = \mu'$ at which a studied signal signature would be excluded. This, in turn, allows for statements about the production cross-sections of the studied scenarios.

By varying the values of μ_{test} that are used in the exclusion fit, a value $\mu_{\text{test}} = \mu'$ is found that satisfies $\text{CL}_{\text{S}}(\mu') = 5\%$. The signal strength obtained this way is just not compatible with the expected (observed) results and allows for the calculation of an upper bound on the production cross-section of the studied signal scenario: $\sigma_{95} = \sigma_{\text{prod.}} \times \mu'$. In the presented example, the variation of μ is performed using an implementation of the Newton-Raphson [242] method with a tolerance of 10% to achieve quick convergence in the search for μ'. The results are summarised in fig. G.5. By incrementing μ until the transition from a not-excluded to an excluded value is found, a starting interval for the Newton-Raphson method is obtained. Further exclusion fits of values of μ performed until $\mu' = 4.42$ is found.

A final use-case for the results of an exclusion fit are contours in the signal model parameter-space that indicate the CL = 95% exclusion on combinations of the parameters that describe the model searched for, cf. sections 8.2.1 and 8.2.2. For every available signal scenario, i.e. set of parameters available for analysis, an exclusion fit with the nominal signal hypothesis is carried out. Signal scenarios exhibiting $\text{CL}_{\text{S}} > 0.05$ are excluded while parameter combinations with $\text{CL}_{\text{S}} < 0.05$ are considered to be possible realisations that cannot be excluded (yet). Since the amount of studied parameter sets is finite and hence discrete, the exclusion contour is extrapolated between excluded and not-yet excluded points in parameter-space in order to be as smooth as possible. The actual point in parameter-space which would be excluded if it were subject to the analysis is obtained by a linear interpolation between adjacent points between which the CL = 95% exclusion would lie. The same procedure is carried out for the signal hypotheses with production cross-sections varied up and down by one standard deviation, giving rise to the uncertainty bands depicted in typical exclusion maps.

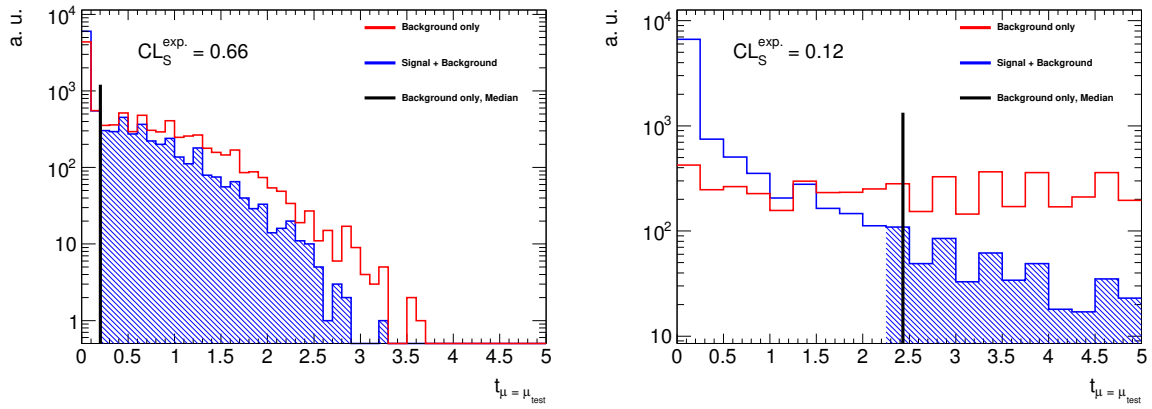

(a) $n_{\text{bins}} = 1$, $n_{\text{sig.}} = 10$, $n_{\text{bkg.}} = 100$

(b) $n_{\text{bins}} = 1$, $n_{\text{sig.}} = 50$, $n_{\text{bkg.}} = 100$

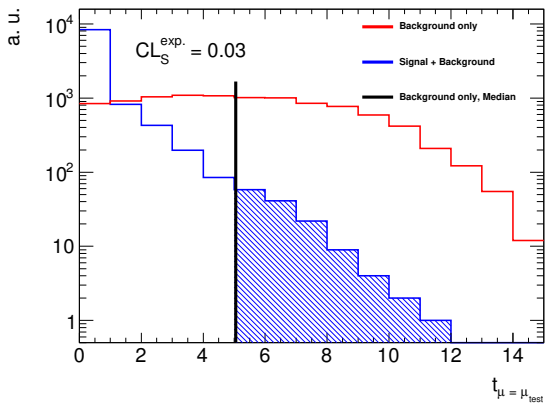

(c) $n_{\text{bins}} = 6$, $n_{\text{sig.}} = 10$, $n_{\text{bkg.}} = 100$

Figure G.4: Illustration of an exclusion fit. Figures (a) to (c) show the test statistic distributions obtained for different configurations, each time using 10,000 toy experiments. The blue histogram represents the combined hypothesis of signal and background, the red histogram the background-only hypothesis. The blue hatched area shows the integral of the combined signal and background test statistic distribution beyond the median of the background-only test statistic marked as the black line. The integral extending below the median line is due to the finite binning and not part of the calculation of the given value of $CL_S^{exp.}$.

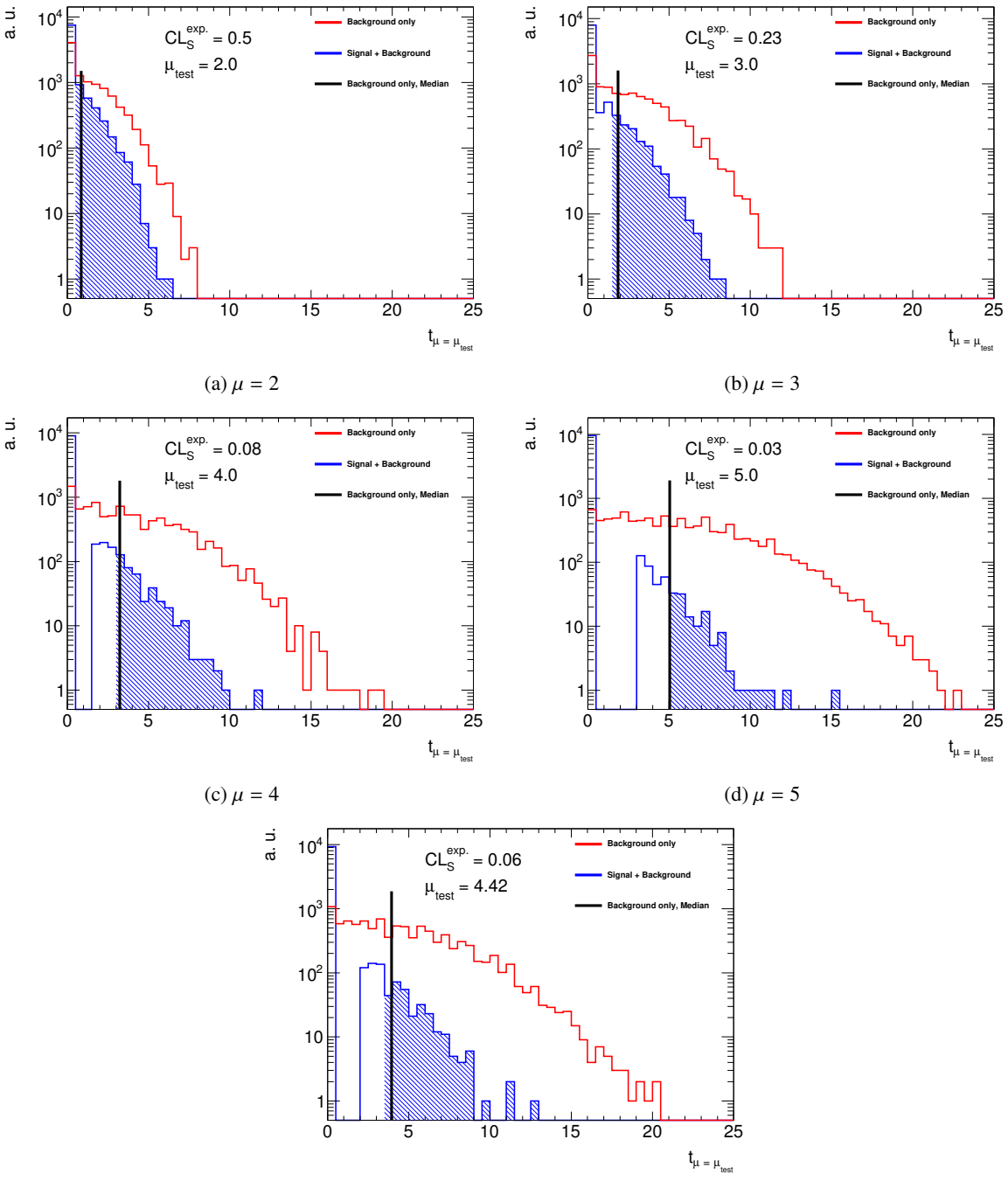

(a) $\mu = 2$

(b) $\mu = 3$

(c) $\mu = 4$

(d) $\mu = 5$

(e) $\mu = 4.42 = \mu'$

Figure G.5: Illustration of a scan of μ to find $\mu = \mu'$ with $CL_S^{exp.}(\mu') = 0.05 \pm 0.005$. The tested signal strength is incremented until an excluded value is found (d). Within the interval of the excluded value of μ and the last not-excluded value (c), a Newton-Raphson method is applied to find μ' with a tolerance of 10% (e).

G.4 Special cases

The model-independent fit is a special variation of the exclusion fit (assuming $s = 1$ signal event) scanning the signal strength parameter to find its value that gives $\mathrm{CL_S} = 5\%$. The regular exclusion fit as described in appendix G.3 can set limits on any model for which a simulation of the physics is available. By evaluating the agreement between the predicted background and the observed data, a statement about the potential presence of **any** model ist possible – this procedure is referred to as a model-independent fit. If the agreement between background and data is good, not much signal of any kind can be present. If there is more data than background and the agreement is hence bad, chances of a potential signal are higher. Finally, more background than data allows for no statement about signal models but lowers the confidence in the background hypothesis due to effects such as mis-modelling.

Practically, the model-independent fit works in the very same way as the scan of μ to find μ', substituting the actual signal model for a single signal event. This makes μ' equivalent to the number of arbitrary signal events that are compatible with the predicted background given the observed data at a confidence level of 95%. In the typical nomenclature of analyses as the one presented here, this found value of μ' would be referred to as $S^{95}_{\mathrm{obs.}}$ or $S^{95}_{\mathrm{exp.}}$, respectively. This upper limit on the event yield can be transformed in an upper limit of the production cross-section $\langle\sigma_{\mathrm{vis.}}\rangle^{95}_{\mathrm{obs.}}$, referred to as *visible cross-section*. Finally, it is common to quote the corresponding values of $\mathrm{CL_B}$ of the observed data and the discovery p-value p_0 and significance Z. The latter numbers are obtained by performing a discovery fit with the afore obtained μ' as the signal hypothesis. Typically, $p_0 > 0.5$ is truncated to $p_0 = 0.5$ and the corresponding significance to $Z = 0.0$ since the underlying hypothesis test is one-sided. Hence a $p > 0.5$ would neither make any sense to quote nor to transform into a value of Z.

The background-only fit is a tool frequently mentioned in this analysis, its outcome is the basis of many statements and feeds into various diagrams and calculations. Its purpose is to fit the normalisation of the backgrounds in the signal-free and mutually exclusive CRs, giving rise to its name. Its results can be applied in VRs to study the quality of the prediction or in SRs to investigate the background spectrum expected upon result extraction. Its implementation can be viewed as a fit like the one given in eq. (G.5), substituting the contribution of the combined model of signal and background for one of the background NPs. Contributions from systematic uncertainties remain considered as before. The result of this fit provides the normalisation-factors ω as introduced in section 6.3 along with their uncertainties and further information regarding correlations between parameters and on the influence of systematic uncertainties as described in section 7.5.

G.5 Approximations

In most cases of the fitting scenarios described in this chapter, a large number of toy experiments needs to be performed to obtain the distribution of the test statistic from which the quantities of interest are then deduced. While in the case of *expected* quantities two such distributions need to be available, for *observed* values it is still one. Not having to calculate the median of a distribution saves computational efforts in the latter case.

However, performing $O(100,000)$ toy experiments for each available signal scenario, in each toy experiment performing another $O(10,000 - 100,000)$ calls of a minimisation algorithm is still computationally extensive. As proven in [240], it is possible to approximate both distributions of test statistic that are in general needed by single calculated values or known analytical functions.

It can be shown that the likelihood ratio for a tested value μ given data that is distributed according to a signal strength parameter μ'' is distributed in a Gaussian fashion, yielding

$$-2\ln\lambda(\mu) = \frac{(\mu-\mu'')^2}{\sigma^2} + O(1/\sqrt{N})\,. \tag{G.17}$$

For a sufficiently large number of events to base the fit on, the correction term can be neglected, allowing for a pure Gaussian description of the likelihood ratio.

As a consequence, the test statistic distribution which represents the hypothesis that is tested (i.e. the background-only model in the case of a discovery fit and the combined signal and background model in the case of an exclusion fit) can be approximated by a non-central χ^2 distribution $\chi^2(x, \mathrm{ndf}, \Lambda)$ with the number of degrees of freedom $\mathrm{ndf} = 1$ and the de-centrality parameter Λ.

The test statistic distribution which represents the hypothesis that is supposed to describe the observed data (i.e. the combined signal and background model in the case of a discovery fit and the background-only model in the case of an exclusion fit), on the other hand, cannot be approximated in such an analytical way. However, since only its median value is of actual interest, an estimation of said value is already sufficient. It can, in fact, be estimated by calculating value of the test statistic based on the likelihood ratio which arises from using the nominal, non-smeared model of background and signal: $d = b$ ($d = s + b$), without any values of μ or nuisance parameters θ.

Reversing the approach, a dataset that is regarded as true is assumed to be existent and referred to as the *Asimov dataset*, giving this approximation its name – the "*Asimov approximation*.

Further details on the validity of these approximations, the determination of Λ and other necessary parameters can be found in [240].

A comparison of these approximations in the context of the illustrative setups presented so far is provided in fig. G.6. In both cases, the approximations model the toy-based results well, particularly the estimation of the median of the background-only test statistic distribution. While a slight discrepancy between the χ^2 approximation and the test statistic distribution of the combined signal and background hypothesis is visible, the shape of the distribution is still described well. The difference in the final value of $\mathrm{CL}_\mathrm{S}^{\mathrm{exp.}}$ can be attributed to the slightly different normalisations due to the first bin of the test statistic distribution. Here, the toy experiment approach gives a higher value than the approximation, driving a difference in the value of the normalised integrals.

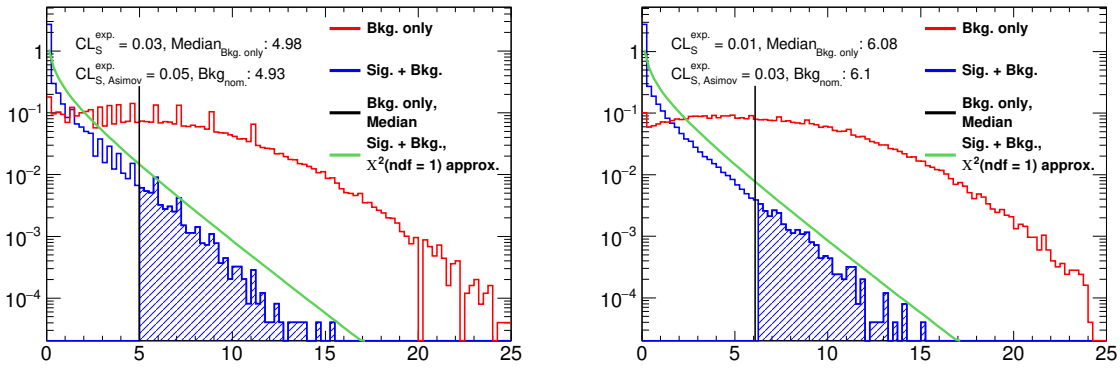

(a) $n_{\text{bins}} = 1$, $n_{\text{sig.}} = 50$, $n_{\text{bkg.}} = 100$

(b) $n_{\text{bins}} = 1$, $n_{\text{sig.}} = 500$, $n_{\text{bkg.}} = 1000$

Figure G.6: Illustration of the approximations made to avoid the simulation of toy experiments in an exclusion fit. (a) depicts the example of a single-bin fit with 100 background and 50 signal events, (a) depicts the same setup with 1000 background events and 500 signal events. For both cases, 100,000 toy experiments are performed to obtain the test statistic distributions. The median of the background-only test statistic is approximated by the value of the test statistic arising from a fit with the nominal, unsmeared background hypothesis being used as data. The test statistic distribution of the combined signal and background hypothesis is approximated by a non-central χ^2-distribution with one degree of freedom. The de-centrality value is set to $\lambda = 0$ since the signal strength in data is set to be the hypothesised nominal signal strength. The numbers given in the figures provide the results of both the toy-based approach and the approximation.

List of Figures

List of Tables

Acknowledgements

First of all, I would like to thank my granny Lisbeth, from whom I learned much more about life than I was able to thank her for while there still was time. I am most grateful to my parents. They raised me as the curious child I still am, they tried to answer all of my questions, no matter how nosey or obscure, and they stopped at every spot in time and place, to which I felt drawn. Without their unconditional support in numerous ways, none of this would have been possible and I would have missed so much in life that I have enjoyed experiencing. Here is to my brother Markus, the first player with whom I joined teams. Thank you for showing me the joys and value of companionship and being the mirror in whose reflection I develop myself continuously.

I want to thank Klaus Desch for accepting me as his student, for fuelling my fascination for physics and science. Thank you for showing and explaining to me the phenomena of nature. Thank you for your continuous motivation and your help, whenever I asked for it. Thank you for being an inspirational leader, scientist, and friend. I am deeply grateful to Philip Bechtle, my supervisor and mentor. Your endless motivation for science and your infinite curiosity are inspiring. You helped me countless times, scientifically and as a companion. Without Steffen Schaepe, non of this would have been possible – thank you! Your joy for physics and science, and your optimism drew me to this group. With your help and encouragement I developed to the self-reliant researcher I am. Thank you for being a great mentor, colleague, and friend.

I would like to thank my colleagues from Bergen, Norway, for their collaboration that made this research endeavour possible. Thank you, Alexander Kastanas, for teaching me so many programming skills. I am deeply grateful to Bertrand Martin dit Latour. Thank you for your scientific support and answering all of questions in endless phone calls and emails. Your contributions and your endurance made this research endeavour possible in the first place. In this context, my friend and former colleague Wolfgang Ehrenfeld deserves my gratitude, too. Thank you for helping and supporting me countless times during your time in our group and well beyond.

I want to thank my colleagues from CERN, Artem Maevskiy, Alexey Antonov, and Andrey Loginov. Your help and company during my field work at CERN is not forgotten. I would like to thank Anatoli Romaniouk for his efficient supervision of my research time at CERN. To Christian Grefe I am thankful for his constant encouragement, endless help and lessons on programming as well as his French negotiation skills. I owe special gratitude to my friends Sarah Aull and Christoph Krieger – you made my stay at CERN the joyful and memorable time it is. Thank you for your support and friendship.

I would like to thank all my colleagues at the Physics Institute of Bonn University for countless helpful discussions and moments of fun and joy – you helped make my work and time enjoyable. I want to explicitly mention Tobias Schiffer, Anjishnu Bandyopadhyay, Philipp König, and, again, Christoph Krieger. Your company and friendship strengthened my will to finish this thesis. To my former colleagues Till Nattermann, Mathias Uhlenbrock, Björn Sarrazin, Christian Limbach, Robert Zimmermann, Thorsten Krautscheid, Michael Lupberger, and Christoph Brezina I owe also a great deal of stamina. Your example continuously showed me that success is possible.

I had a great time working in the IT-department of the Physics Institute and gained much knowledge from the work with Jan Stillings, Peter Wienemann, and Oliver Freyermuth. Thank you for your productive collaboration, answering all my questions and being great team leaders.

A big thanks to all my friends from school and throughout my time at university. Thank you for accepting and confirming me in the way I am. In your presence, I have been able to develop to this point and will keep doing so. Thank you for your patience and your smiles, when things were weird. Thank you for your encouragement, when times were tough. Thank you for making so many moments so memorable. A special thanks I owe Thomas Velz, who mentored me from my very first exercise class up to this point – you are somewhat the end and the beginning of all of this, thank you.

Finally, I would like to thank Marike Menchen, for her patience and for her open ears, listening to my concerns. Thank you for being by my side, throughout the good and the bad times.

With you, there is no fear.